NASA CR 65657

MANNED MISSION PHOTOVOLTAIC POWER SYSTEM STUDY NAS 9-5266

VOLUME II TECHNICAL DISCUSSION

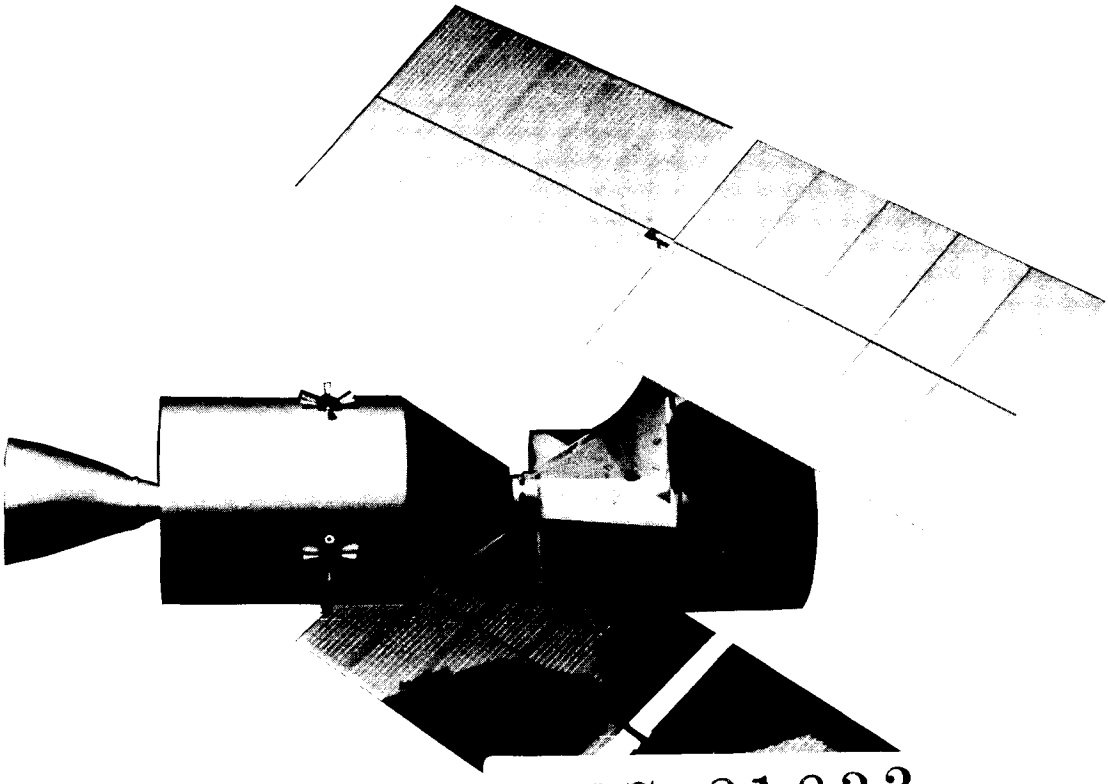

LIBRARY COPY

JUL 10 1967

MANNED SPACECRAFT CENTER
HOUSTON, TEXAS

FACILITY FORM 602

N67-31832 (ACCESSION NUMBER)
(THRU)
519 (PAGES)
1 (CODE)
CR-65657 (NASA CR OR TMX OR AD NUMBER)
03 (CATEGORY)

Prepared for

PROPULSION AND POWER DIVISION
MANNED SPACECRAFT CENTER
NATIONAL AERONAUTICS AND SPACE ADMINISTRATION
HOUSTON, TEXAS

Prepared by

ASTRO-ELECTRONICS DIVISION
DEFENSE ELECTRONIC PRODUCTS
RADIO CORPORATION OF AMERICA
PRINCETON, NEW JERSEY

AED-R-3155

June 9, 1967

MANNED MISSION PHOTOVOLTAIC POWER SYSTEM STUDY NAS 9-5266

VOLUME II TECHNICAL DISCUSSION

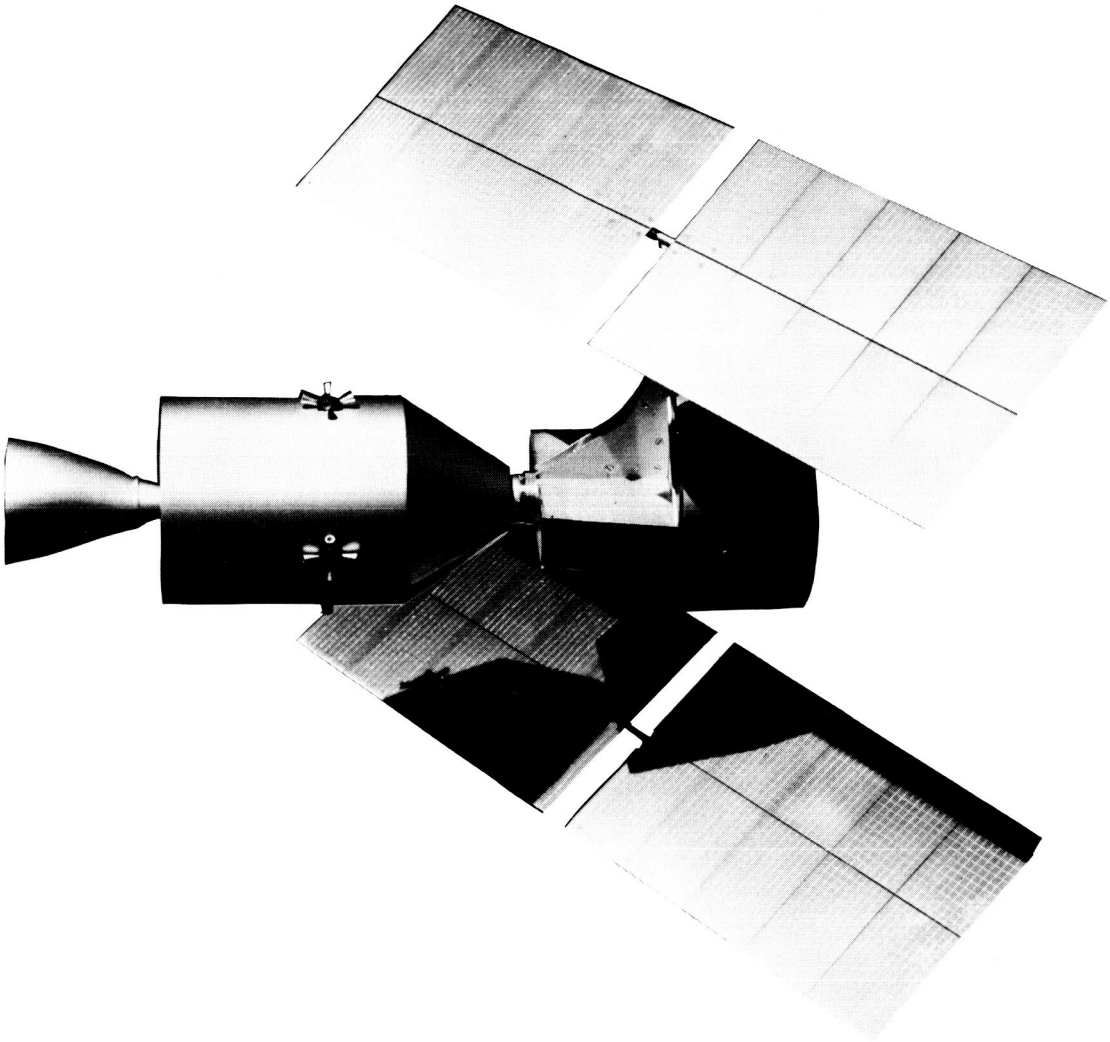

Prepared for

PROPULSION AND POWER DIVISION
MANNED SPACECRAFT CENTER
NATIONAL AERONAUTICS AND SPACE ADMINISTRATION
HOUSTON, TEXAS

Prepared by

ASTRO-ELECTRONICS DIVISION
DEFENSE ELECTRONIC PRODUCTS
RADIO CORPORATION OF AMERICA
PRINCETON, NEW JERSEY

AED-R-3155

June 9, 1967

FOREWORD

This is Volume II of the final engineering report on the "Manned Mission Photovoltaic Power System Study". This report was prepared by the Astro-Electronics Division of the Radio Corporation of America, Princeton, New Jersey, under Contract NAS 9-5266 for the Propulsion and Power Division, Manned Spacecraft Center, National Aeronautics and Space Administration, Houston, Texas. This volume contains a detailed technical discussion of the study program. Volume I contains a summary of the program and Volume III contains documentation that supports the technical discussion.

PRECEDING PAGE BLANK NOT FILMED.

TABLE OF CONTENTS

Section		Page
VI	POWER SYSTEM ANALYSIS	VI-1
	A. INTRODUCTION	VI-1
	1. Study Definition	VI-1
	2. Study Milestones	VI-1
	B. TECHNICAL TASK RELATIONSHIPS	VI-2
	1. Optimization Criteria	VI-2
	2. Intra-Section Relationships	VI-3
	3. Inter-Section Relationships	VI-3
	4. Total System Weight	VI-4
	5. Dynamics Loop Complexity	VI-5
	C. POWER SYSTEM CONSIDERATIONS	VI-5
	1. System Concepts	VI-5
	a. Integrated Power System (IPS)	VI-5
	b. Power System Module (PSM)	VI-7
	c. Recommendation	VI-7
	2. Modular Concepts	VI-9
	a. System Paralleling	VI-10
	b. Functional Element Paralleling	VI-10
	c. Comparison	VI-10
	d. Recommendation	VI-11
	D. GROUND RULES AND GUIDELINES	VI-11
	1. General Guidelines	VI-11
	2. Specific IPS Ground Rules	VI-14
	3. Specific PSM Ground Rules	VI-14
	E. SUMMARY	VI-17
VII	MECHANICAL SYSTEM ANALYSIS CONCEPT A (IPS)	VII-1
	A. INTRODUCTION AND SUMMARY	VII-1
	B. STOWAGE ANALYSIS	VII-4
	1. General Requirements	VII-4
	a. Array Support Requirements	VII-4
	b. Position Requirements for Stowed Panels	VII-4
	c. Deployment Requirements	VII-4
	2. Evaluation of Stowage Requirements	VII-4
	3. MMSS and Solar-Array Stowage	VII-7
	C. ARRAY STRUCTURE ANALYSIS	VII-8
	1. Introduction	VII-8
	2. Concept Development	VII-9
	3. Factors of Safety and Design Criteria	VII-9
	4. Array Structural Design Comparison	VII-13

TABLE OF CONTENTS (Continued)

Section		Page
	5. Comparison of Beryllium and Aluminum for Structural Members	VII-13
	6. Bowed-Panel Concept	VII-19
	7. Beam of Constant Stress Concept	VII-21
	8. Thermal Stress and Deflection	VII-21
	9. Conclusions	VII-23
D.	SOLAR ARRAY DESIGN CONCEPTS AND TECHNIQUES	VII-23
	1. Solar-Array Structure	VII-23
	2. Transition Panel	VII-25
	3. Array Assembly Procedure	VII-25
	a. Solar-Array Panel Assembly	VII-25
	b. Solar-Array - MMSS Integration	VII-27
	4. Energy Transfer Across Rotating Joint	VII-28
	a. Flexible Cable	VII-28
	b. Rotary Transformers	VII-29
	c. Step Rings	VII-29
	5. Brush Electrical Design	VII-33
	6. Hinges and Locks	VII-36
	7. Array Orientation Drive	VII-37
	a. Motor Drive Gear Box	VII-37
	b. Sealing and Lubrication	VII-40
E.	DEPLOYMENT	VII-41
	1. Sequence	VII-41
	2. Actuators	VII-43
	a. Motion	VII-43
	b. Weight	VII-43
	c. Size	VII-43
	d. Reliability	VII-43
	e. Force Levels	VII-43
	f. Compatibility	VII-45
	g. Spring-Loaded Hinge	VII-45
	h. Single-Actuator, Multi-Link Scissors	VII-45
	i. Individual Electric-Motor Drives	VII-45
	j. Individual Pneumatic Cylinder	VII-45
	3. Pneumatic Distribution System	VII-46
F.	SATELLITE ORBITAL CONFIGURATION	VII-46
	1. Docking Configuration	VII-48
	2. Docking Cycle	VII-52
	3. Service Propulsion System (SPS) Engine Firing	VII-52
	a. Boom Sizing	VII-52
	b. Array Orientation	VII-55
G.	WEIGHT SUMMARY	VII-55

TABLE OF CONTENTS (Continued)

Section		Page
VIII	MECHANICAL SYSTEM ANALYSIS, CONCEPT B (PSM)	VIII-1
	A. INTRODUCTION AND SUMMARY	VIII-1
	B. STOWAGE ANALYSIS (POWER SYSTEM MODULE)	VIII-6
	1. Evaluation of Storage Location	VIII-6
	2. PSM Structure Configuration	VIII-7
	3. Array Support, Stowed	VIII-8
	4. Array-PSM Structure Integration	VIII-8
	C. ARRAY STRUCTURE ANALYSIS	VIII-9
	1. Introduction	VIII-9
	2. Factors of Safety	VIII-9
	3. Design Criteria	VIII-10
	4. Design Analysis for Launch	VIII-10
	5. Additional Considerations	VIII-14
	a. Comparison of Aluminum and Beryllium	VIII-14
	b. Thermal Stress	VIII-14
	D. COMPONENT STRUCTURAL DESIGN	VIII-15
	1. Array Orientation Drive Assembly	VIII-15
	2. Sealing and Lubrication	VIII-15
	3. Energy Transfer Across a Rotating Joint	VIII-15
	4. Electrical Bus Design	VIII-16
	5. Details for Initial Panel Concept	VIII-16
	E. DEPLOYMENT	VIII-16
	1. Boom Actuation	VIII-20
	2. Primary Panel Deployment	VIII-20
	3. Secondary Panel Deployment	VIII-22
	4. Advanced Array Folding	VIII-22
	5. Retraction	VIII-24
	F. SATELLITE ORBITAL CONFIGURATION	VIII-25
	1. Docking Activity	VIII-25
	a. T/C Mode Docking	VIII-26
	b. Weak-Axis Bending (WAB) Docking Mode	VIII-28
	c. Strong-Axis Bending (SAB) Docking Mode	VIII-30
	2. SPS Engine Firing Activity	VIII-31
	a. Tensile-Compressive (T/C) Mode SPS Activity	VIII-32
	b. Weak-Axis Bending Mode SPS Activity	VIII-36
	c. Strong-Axis Bending Mode SPS Activity	VIII-37
	d. Boom-Deployed Array-Retracted SPS Activity	VIII-38
	3. Advanced Design Concept Array Structure	VIII-38
	G. THERMAL CONTROL ANALYSIS	VIII-40
	1. Introduction and Summary	VIII-40
	2. Considerations Affecting Thermal Design	VIII-41
	3. Equipment Temperature Control	VIII-43
	a. Radiation-Surface Requirements	VIII-43

TABLE OF CONTENTS (Continued)

Section		Page
	b. Temperature Differential Between Radiating Surface and Equipment	VIII-45
	c. 200-NMI Mission Analysis	VIII-47
	d. 19,400-NMI Mission Analysis	VIII-53
	4. Radiator Weight	VIII-57
	5. Fluid-Loop Heat Transfer Section	VIII-58
	6. Auxiliary Heater Temperature Control	VIII-58
	7. Conclusion	VIII-59
	H. WEIGHT SUMMARY	VIII-60
IX	ARRAY ORIENTATION ANALYSIS	IX-1
	A. INTRODUCTION AND SUMMARY	IX-1
	B. CONFIGURATION ANALYSIS	IX-1
	C. PERTURBATIONS AND EFFECTS	IX-10
	1. Aerodynamic Forces	IX-11
	2. Gravity Gradient Torques	IX-16
	3. Solar-Radiation Pressure	IX-21
	4. Magnetic Torques	IX-24
	D. FUEL CONSUMPTION ANALYSIS	IX-29
	E. MOMENTUM STORAGE DEVICE (MSD)	IX-32
	1. MSD Weight Calculation for "Z" Configuration (4900 Square-Foot Area)	IX-33
	a. Reaction Wheel	IX-33
	b. Control Moment Gyro	IX-34
	c. Addition Considerations	IX-35
	(1) "Z" Configuration	IX-35
	(2) "H" Configurations	IX-37
	2. Roll- and Yaw-Axis Momentum Compensation	IX-38
	F. ARRAY CONFIGURATION ANALYSIS	IX-39
	1. Spacecraft-Array Dynamic Interactions	IX-39
	a. General	IX-39
	(1) Action of Disturbing Torques	IX-40
	(2) Array-Torquing Reactions	IX-40
	b. Sun Tracking	IX-40
	(1) Spacecraft-Mounted Array, Two Degrees of Freedom	IX-41
	(2) Outboard Array, Zero Degrees of Freedom	IX-41
	c. System Block Diagrams	IX-41
	d. Analytical Approach	IX-44
	2. Orientation Servo System	IX-44
	a. System Description	IX-44
	b. Modes of Operation	IX-45
	(1) Initial Acquisition	IX-47

TABLE OF CONTENTS (Continued)

Section		Page
	(2) Normal Operation	IX-47
	(a) Sun Tracking	IX-47
	(b) Occultation and Reacquisition	IX-47
	(3) Docking and SPS Engine Firing	IX-48
	(4) Polar Orbit Stow	IX-48
	G. SHADOW ANALYSIS	IX-48
	1. Procedure	IX-49
	2. Results	IX-49
	3. Discussion	IX-50
	4. Array Boom Length	IX-54
X	ELECTRICAL SYSTEMS ANALYSIS	X-1
	A. INTRODUCTION	X-1
	B. POWER SYSTEM TRADEOFFS	X-2
	1. General Approach	X-2
	2. Assumptions, Requirements, and Definitions	X-4
	a. Design Philosophy	X-4
	b. Load Requirements	X-5
	c. Numerical Assumptions	X-7
	3. Block Diagram Tradeoffs	X-8
	a. Generalized System Block Diagram	X-8
	b. Specific Configurations	X-10
	c. Investigation of the Storage System Operating Parameters	X-16
	d. Systems Efficiency Tradeoffs	X-23
	e. Effects of Thermal Design on Systems Choice	X-31
	f. Reliability Estimate	X-36
	g. Peak Charge Rates in Tracker System	X-36
	4. Results and Conclusions	X-40
	a. Purpose	X-40
	b. Choice of Components	X-40
	c. Power System Configuration Summary	X-42
	d. Selected System Configuration	X-43
	C. COMPONENT STUDIES	X-43
	1. Introduction	X-43
	2. Solar Array	X-44
	a. Parametric Optimization	X-44
	b. Solar-Cell Tradeoff Analysis	X-53
	c. Cell Data Stored in the Computer Program	X-88
	d. Array Electrical Design	X-88
	e. Array Mechanical Design	X-94
	3. Storage System	X-111
	a. Battery Data	X-111

TABLE OF CONTENTS (Continued)

Section		Page
	b. Battery Weight Tradeoff Study	X-115
	c. Battery Charge Control Methods	X-122
	d. Battery Mechanical Configuration	X-132
	4. Electronics	X-146
	a. Discription of the Major Blocks	X-146
	b. Major Components	X-148
	c. Electromagnetic Compatibility (EMC) Considerations	X-173
	d. Electronic Packaging Concept	X-174
	e. Busbar Design	X-176
	f. Data and Analysis	X-186
D.	SYSTEM OPERATIONAL PHILOSOPHY	X-195
	1. Introduction	X-195
	2. The Protective Process	X-195
	3. Inspection and Preventive Maintenance; Performance Degradation	X-196
	a. General	X-196
	b. Parameters	X-196
	4. Automatic Protection; Malfunctions	X-198
	5. Crew Participation	X-200
	a. Presence of the Crew as a Factor in Systems Safety	X-200
	b. Critical Component Failure	X-201
	c. Non-critical Component Failure	X-201
	d. Location	X-201
	e. Corrective Action	X-201
	f. Maintenance	X-202
	g. Daily Inspections	X-202
	h. Weekly Inspections	X-202
	6. Equipment Reliability and Redundancy Recommendations	X-203
	a. Discussion	X-203
	b. Redundancy Apportionment for Electronic Power Modules	X-205
	c. Battery Reliability Analysis	X-209
	d. Summary of Redundance Recommendations	X-212
	7. Probability of Crew Survival	X-212
E.	COMPUTER PROGRAMS	X-214
	1. Summary of the Programs Developed	X-214
	2. Main Program	X-214
	a. Introduction and General Description	X-214
	b. Input Information	X-215
	c. Detailed Description of the Approach	X-219
	d. Main Program Outputs	X-230
	e. Modification of the Main Computer Program to Provide Solutions Based on Discrete Module Sizes	X-231

TABLE OF CONTENTS (Continued)

Section		Page
	3. Solar Cell Program	X-233
	a. Introduction	X-233
	b. Calculation of the 1-MeV Electron Flux	X-234
	c. Irradiation Degradation of Solar-Cell I-V Curve	X-242
	d. Degradation of Solar Cell I-V Curve for Factors Other Than Irradiation	X-246
	e. Solar-Array Weight	X-248
	f. Summary	X-249
	4. Program Options	X-249
F.	PARAMETRIC SYSTEMS STUDY	X-252
	1. Introduction	X-252
	2. Programmed Input Information	X-252
	3. Effect of Load Variation on Array Area	X-253
	4. Effect of Array Area on Array Weight, Number of Solar Cells, and Array Power	X-253
	5. Effect of Load Variation on Required Battery Capacity	X-256
	6. Effect of Battery Capacity on Battery Weight and Volume	X-256
	7. Effect of Load Variation on Total Electronics Weight and Volume	X-258
	8. Effect of Major System Parameters on Total System Weight	X-258
	9. Conclusions	X-262
G.	CONCEPTUAL POWER SYSTEM DESIGNS	X-264
	1. Introduction	X-264
	2. Discussion of the Conceptual Design Cases	X-264
	a. Horizontal Rows	X-266
	b. Vertical Columns	X-266
	c. Summary	X-269
	3. Resupply as a Weight Factor	X-269
	a. Resupply Philosophy	X-269
	b. Effect of Resupply Cycle Duration on Liftoff and Resupply Weights	X-270
	4. Final Recommendations	X-273

LIST OF ILLUSTRATIONS

Figure		Page
VI-1	Power System Technical Study Tasks	VI-2
VI-2	Partial Orientation System Analysis Tasks	VI-3
VI-3	Orientation Axes	VI-4
VI-4	Integrated Power System, Deployed Configuration	VI-6
VI-5	Integrated Power System Interfaces	VI-6
VI-6	Power System Module Configuration	VI-8
VI-7	Power System Module Interfaces	VI-8
VI-8	System Paralleling	VI-9
VI-9	Functional Element Paralleling	VI-9
VI-10	Launch Vehicles	VI-13
VI-11	Load Power Profile	VI-13
VI-12	IPS Configuration	VI-15
VI-13	PSM Configuration	VI-16
VI-14	Solar Array Terminology	VI-18
VI-15	Battery Terminology	VI-18
VII-1	MMSS and Solar Array Stowage in Launch Vehicle	VII-1
VII-2	MMSS with Solar Array Orbital Configuration	VII-2
VII-3	Preferred Docking Configuration	VII-3
VII-4	Desirable SPS Engine Firing Mode, Solar Array in Strong-Axis Bending Mode	VII-3
VII-5	Existing Stowage Location	VII-6
VII-6	Alternative Stowage Locations Considered	VII-6
VII-7	MMSS and Solar Array Stowage in Launch Vehicle	VII-7
VII-8	Truss Arrangement, Stowed Panels	VII-8
VII-9	Substrate Concepts; Night-Time Temperature Comparison; Thermal Mass Effect	VII-11
VII-10	Design Specification for Sinusoidal Vibration	VII-14
VII-11	Design Specification for Random Vibration	VII-14
VII-12	Acoustic Noise Design Specification	VII-15
VII-13	Axial Acceleration versus Flight Time	VII-15
VII-14	Panel Structural Cross Sections	VII-18
VII-15	Tensile Chordal Tie	VII-21
VII-16	Solar-Panel Temperature Distribution during Orbit	VII-22
VII-17	Detailed Solar-Panel Temperature Distribution	VII-22
VII-18	Array-Width Determination	VII-24
VII-19	Bowed-Array Solar Incidence Angles	VII-24
VII-20	Solar-Array Panel	VII-25
VII-21	Solar-Array Transition Panel	VII-26
VII-22	Deformation Forces	VII-26
VII-23	Panel Segment	VII-27
VII-24	Panel Mounting to Shear Fitting	VII-28

LIST OF ILLUSTRATIONS (Continued)

Figure		Page
VII-25	Array Actuator (Slip-Ring Assembly)	VII-32
VII-26	Joint Connection Motion	VII-34
VII-27	Solar Panel Double Cable Interconnection	VII-35
VII-28	Alternate Hinge and Hinge-Mounting Concepts	VII-36
VII-29	Orientation Drive Assembly Schematic	VII-37
VII-30	Orientation Drive Assembly Outline	VII-38
VII-31	Drive Motor and Reduction Gears	VII-39
VII-32	Lubricant Weight Loss vs. Temperature	VII-41
VII-33	Solar Array Deployment Sequence	VII-42
VII-34	Array Booms, Time-Velocity Profile	VII-43
VII-35	Panel Actuation	VII-44
VII-36	Panel Snubber Pads	VII-44
VII-37	Solar Panel Actuator Deployment	VII-47
VII-38	Double-Acting Pneumatic Cylinder Actuator	VII-47
VII-39	Array Configuration; Primary Load Orientation	VII-49
VII-40	Array Load Capability	VII-50
VII-41	Amplification Factor	VII-51
VII-42	Docking Cycle	VII-53
VII-43	Simplified Diagram of Array-Boom Structure	VII-54
VII-44	Space-Truss Boom Concept	VII-55
VIII-1	PSM Stowage and Launch Outline	VIII-2
VIII-2	PSM Launch Configuration	VIII-3
VIII-3	Array Deployment Concepts	VIII-4
VIII-4	Orbital Array Configuration	VIII-5
VIII-5	Power System Module Configuration	VIII-7
VIII-6	Aspect Ratio of Solar Panel	VIII-10
VIII-7	Spacecraft Array Details, Normal Position	VIII-11
VIII-8	Array Stowed for Launch	VIII-12
VIII-9	Array Panel Stowed for Launch	VIII-13
VIII-10	Schematic Representation of Orientation Drive Assembly	VIII-15
VIII-11	Structural Details of Array Elements	VIII-17
VIII-12	Schematic Diagram of Array Deployment	VIII-19
VIII-13	Array Deployment, Advanced Concept	VIII-23
VIII-14	Retracted Position for Initial and Advanced Design Concepts	VIII-25
VIII-15	Docking Modes	VIII-27
VIII-16	SPS Modes	VIII-33
VIII-17	Boom-Deployed Array-Retracted SPS Activity	VIII-39
VIII-18	Vehicle Orbital Configuration	VIII-42
VIII-19	Average Incident Solar Radiation on Radiating Surfaces versus Sun Angle 200-nmi Orbit	VIII-46

Figure		Page
VIII-20	Radiating Area per Unit of Power Dissipation versus Orbit Average Surface Temperature for Various Sun Angles; Sun and Shadow Sides of Orbit Plane at 200-nmi Altitude	VIII-46
VIII-21	Proposed Arrangement of Equipment on Radiating Surface	VIII-49
VIII-22	Thermal Dissipation Profiles	VIII-50
VIII-23	Orbit Component Temperature Range for Sections A and C of Vehicle Surface in Two Operating Modes at 200-nmi Altitude	VIII-52
VIII-24	Power Profiles for Sections A through D at 90° Sun Angle, 19,340-nmi Altitude	VIII-55
VIII-25	Temperature of Battery Mounting Surface versus Time From Start of Orbit Day for 90° Sun Angle at 19,340-nmi Altitude	VIII-56
IX-1	Orbital Configuration "H"	IX-2
IX-2	Solar Array Configurations (2 sheets)	IX-3
IX-3	Analysis of Gravity Gradient and Inertial Effects on Various Configurations (12 sheets)	IX-4
IX-4	Orbit Geometry	IX-8
IX-5	Spacecraft in Orbit with a 4900-square-foot Solar Array	IX-9
IX-6	Configurations for PSM Concept	IX-11
IX-7	Drag Coefficient (C_D) for Solar Panels versus Angle of Attack (γ)	IX-12
IX-8	Lift Coefficient (C_L) for Solar Panels versus Angle of Attack (γ)	IX-12
IX-9	Average Orbital Drag Coefficient versus ϕ's	IX-13
IX-10	Average Orbital Lift Coefficient versus ϕ's	IX-14
IX-11	Absolute Sun Angle to the Orbit Plane ($/\phi$'s$/$) versus Days from Epoch (200-nmi, 28.5° Orbit)	IX-15
IX-12	Absolute Sun Angle to the Orbit Plane ($/\phi$'s$/$) versus Days from Epoch (200-nmi, 90° Orbit)	IX-15
IX-13	Average Orbital Aerodynamic Drag versus Days from Epoch (200-nmi, 28.5° Orbit; Array Area 1944 Sq. Ft.)	IX-16
IX-14	Average Orbital Aerodynamic Lift versus Days from Epoch (200-nmi, 28.5° Orbit; Array Area 1944 Sq. Ft.)	IX-16
IX-15	Average Orbital Aerodynamic Drag versus Days from Epoch (200-nmi, 90° Orbit; Array Area 1944 Sq. Ft.)	IX-17
IX-16	Average Orbital Aerodynamic Lift versus Days from Epoch (200-nmi, 90° Orbit; Array Area 1944 Sq. Ft.)	IX-17
IX-17	Pitch Gravity-Gradient Torque versus $\omega_o t$ ("Z" Configuration, Array Area 4900 Sq. Ft.)	IX-19
IX-18	Roll Gravity-Gradient Torque versus $\omega_o t$ ("Z" Configuration, Array Area 4900 Sq. Ft.)	IX-19
IX-19	Pitch Gravity-Gradient Torque versus $\omega_o t$ ("Z" Configuration, Array Area 1900 Sq. Ft.)	IX-20
IX-20	Roll Gravity-Gradient Torque versus $\omega_o t$ ("Z" Configuration, Array Area 1900 Sq. Ft.)	IX-20

LIST OF ILLUSTRATIONS (Continued)

Figure		Page
IX-21	Pitch Gravity-Gradient Torque versus $\omega_0 t$ ("H" Configuration, Array Area 1944 Sq. Ft.)	IX-21
IX-22	Magnetic Disturbances; Total Momentum per Year versus Residual Dipole Moment (h=200 nmi)	IX-29
IX-23	Location of Propulsion Systems	IX-30
IX-24	Dynamic Control Loop Block Diagram	IX-43
IX-25	Control Axis Configuration	IX-45
IX-26	Panel Orientation Control System	IX-46
IX-27	Model Used for Shadow Analysis	IX-50
IX-28	Percentage of Shadow versus Orbit Angle for Various Sun Angles ("Z" Configuration)	IX-51
IX-29	Percentage of Shadow versus Orbit Angle for Various Sun Angles ("H" Configuration)	IX-52
IX-30	Average Percentage of Shadow versus Sun Angle ("Z" Configuration)	IX-52
IX-31	Average Percentage of Shadow versus Sun Angle ("H" Configuration)	IX-53
IX-32	Average Array Illumination versus Sun Angle ("Z" Configuration)	IX-53
IX-33	Average Array Illumination versus Sun Angle ("H" Configuration)	IX-54
IX-34	Boom Length versus Sun Angle for Start of Array-on-Array Shadowing	IX-55
X-1	Laboratory Module Power Supply, Functional Diagram	X-3
X-2	Generalized Power Subsystem, Block Diagram	X-8
X-3	Generalized Lead and Source Power Variation with Time in Orbit	X-9
X-4	PWM Regulator System	X-12
X-5	Series Tracker System	X-13
X-6	Direct Energy Transfer System	X-14
X-7	Earth Orbit Characteristics, Circular Orbits	X-19
X-8	Battery Operating Characteristics as a Function of Altitude, Earth Circular Orbits	X-20
X-9	Battery Watt-Hours of Discharge per Watt, $P_{Ln_{avg}}$	X-21
X-10	Typical Variation of Charge Parameters with Altitude, Ni-Cd Battery	X-23
X-11	Non-Tracking Series System with Ni-Cd Battery	X-25
X-12	Tracking Series System with Ni-Cd Battery	X-25
X-13	Non-Tracking Parallel System with Ni-Cd Battery	X-26
X-14	Tracking Parallel System with Ni-Cd Battery	X-26
X-15	Power Ratios for Series and Parallel Systems	X-28
X-16	Power Ratios for Tracking and Non-tracking Parallel Systems	X-28

LIST OF ILLUSTRATIONS (Continued)

Figure		Page
X-17	Power Ratios for Parallel Tracking to Series Non-Tracking System . . .	X-28
X-18	Relative Solar-Array Output	X-32
X-19	Peak-to-Average Charge Ratios as a Function of Altitude for Ni-Cd Battery	X-37
X-20	Average and Maximum Charge Rate Variation as a Function of Altitude for Ni-Cd Battery	X-38
X-21	Temperature Comparison	X-46
X-22	Temperature-Time Transients vs. Altitude	X-47
X-23	Effective Thermal Weight vs. Array Temperature for Various Back Emmissivities	X-48
X-24	Solar-Cell Temperature and Per Cell P_{max} vs. Back Emissivity	X-48
X-25	Effective Thermal Pounds/ft^2 vs. Watts/ft^2 for Various Assumed Low-Temperature Limits	X-49
X-26	Relationship of the Effective Thermal Unit Array Weight to Actual Total Unit Weight	X-49
X-27	Array Power Density at Steady-State Temperature vs. ϵ_b for Various Allowable Values of T_{min}	X-50
X-28	Optimum Back Emissivity as a Function of Array Temperatures, Synchronous Orbit	X-52
X-29	Weight and Area per 1000 Watts vs. Minimum Temperature	X-54
X-30	Blue-Reflecting Solar Cell Cover vs. Fused Silica	X-62
X-31	Transmission Curve for Microsheet Before and After Radiation by 50 KeV X-Rays	X-64
X-32	Irradiation Curve for Helietek 1-ohm-cm, 8-mil Solar Cell	X-68
X-33	Irradiation Curve for Heliotek 10-ohm-cm, 14-mil Solar Cell	X-68
X-34	Irradiation Curve for Hoffman 10-ohm-cm, 14-mil Solar Cell	X-68
X-35	Irradiation Curve for Texas Instrument 10-ohm-cm, 14-mil Solar Cell	X-69
X-36	Irradiation Curve for Westinghouse 10-ohm-cm, 14-mil Solar Cell . . .	X-69
X-37	Irradiation Curve for Ion Physics 10-ohm-cm, 14-Mil Solar Cell	X-69
X-38	Radiation Resistance of Vendor Cells vs. RCA Cells	X-70
X-39	Radiation Resistance of Heliotek Cells vs. RCA Cells	X-71
X-40	I-V Curve for RCA MT 1-ohm-cm Solar Cell	X-74
X-41	I-V Curve for RCA MT 10-ohm-cm Solar Cell	X-74
X-42	Cross Section of Solar Array	X-75
X-43	Maximum Power of 1-ohm Solar Cells	X-83
X-44	Maximum Power of 10-ohm Solar Cells	X-83
X-45	Maximum Power of 1- and 10-ohm Solar Cells	X-84
X-46	Maximum Power vs. Temperature for Silicon, P-en-N, Lithium-Doped Solar Cell	X-87
X-47	End-of-Life, Worst Case, Solar Cell Maximum Power vs. Temperature and 1 MeV Flux (1-ohm-cm)	X-89

LIST OF ILLUSTRATIONS (Continued)

Figure		Page
X-48	End-of-Life, Worst Case, Solar Cell Maximum Power vs. Temperature and 1 MeV Flux (10-ohm-cm)	X-89
X-49	Power System Voltage Drops, Schematic Diagram	X-90
X-50	Maximum Power Solar Cell Voltage vs. Temperature (Worst-Case, End of Life)	X-91
X-51	Open Circuit Solar Cell Voltage vs. Temperature (Best Case, Beginning of Life)	X-91
X-52	Solar Array Panel Layout	X-93
X-53	Dimensions of Conventional Contact Cell	X-96
X-54	Dimensions of Other Configuration Cells	X-96
X-55	Interconnection Techniques for Conventional Contact Cells (Exploded View of Typical Portion)	X-97
X-56	Interconnection Techniques for Wrap-Around Contact Cells	X-97
X-57	Array Weight vs. Cover Glass Thickness	X-102
X-58	Array Weight vs. Cell Thickness	X-102
X-59	Typical Portion, Solar Cell Module	X-103
X-60	Solar Cell Transfer Fixture	X-105
X-61	Array Current Distribution	X-106
X-62	Aluminum Conductor Weight vs. Average Voltage Drop	X-107
X-63	Conductor Weight vs. Array Panel Area	X-107
X-64	Maximum Conductor Cross Section vs. Panel Area	X-107
X-65	Temperature-Time Profile, Quick-Cycle Test	X-109
X-66	Cycle Life vs. Depth of Discharge	X-111
X-67	Cell Voltage vs. Depth of Discharge (Ni-Cd Cell at 25° C)	X-113
X-68	Cell Voltage vs. Depth of Dischrage (Ag-Cd Cell at 25° C)	X-113
X-69	Battery Efficiency vs. Charge Rate (Ag-Cd and Ni-Cd Cells at 25° C)	X-113
X-70	Orbital Characteristics	X-115
X-71	Battery Discharge Requirements	X-117
X-72	Depth of Discharge vs. Altitude	X-117
X-73	Required Battery Size, Watt-Hours per Watt Lead vs. Altitude	X-119
X-74	Required Battery Capacity; Ni-Cd Cells	X-120
X-75	Required Battery Capacity; Ag-Cd Cells	X-120
X-76	Required Battery Weight; Ag-Cd and Ni-Cd Cells	X-120
X-77	Battery Weight Comparison	X-121
X-78	Battery Weight Ratio	X-121
X-79	Beginning of Array Life, Ni-Cd Battery, 200 NM Orbit	X-125
X-80	End of Array Life, Ni-Cd Battery, 200 NM Orbit	X-125
X-81	Beginning of Array Life, Ni-Cd Battery, Synchronous Orbit	X-127
X-82	End of Array Life, Ni-Cd Battery, Synchronous Orbit	X-127
X-83	Beginning of Array Life, Ag-Cd Battery, 200 NM Orbit	X-128
X-84	End of Array Life, Ag-Cd Battery, 200 NM Orbit	X-128
X-85	Beginning of Array Life, Ag-Cd Battery, Synchronous Orbit	X-129

LIST OF ILLUSTRATIONS (Continued)

Figure		Page
X-86	End of Array Life, Ag-Cd Battery, Synchronous Orbit	X-129
X-87	Battery Arrangement, Ni-Cd	X-134
X-88	Battery Arrangement, Ag-Cd	X-135
X-89	Battery Stack and Control Module Wiring	X-136
X-90	Battery Module	X-137
X-91	Battery Module Wiring	X-138
X-92	Battery Stack and Control Unit Wiring	X-138
X-93	Storage Cell Voltages	X-143
X-94	Power Supply, Electronics Module	X-147
X-95	Battery Charge Electronics, Functional Diagram	X-150
X-96	Variation in Operating Point with Change of Impedance	X-151
X-97	Ideal PWM Impedance Transformer	X-151
X-98	Variation in Load Resistance with Variation in α	X-152
X-99	Determination of Maximum Power Transfer	X-152
X-100	Substitution of Battery for R_L	X-153
X-101	Short Term I-V Characteristic	X-153
X-102	Array Current Flow with Respect to I-V Characteristics	X-154
X-103	Battery/Battery Charger Automatic Protection, Functional Diagram	X-161
X-104	Battery-Charger Ampere-Hour Meter	X-162
X-105	Failure Detection and Switchover (FD and SO) Logic for Battery Charger Control and Auxiliary Regulator Unit	X-164
X-106	D-C Regulator, Logic Diagram	X-166
X-107	Functional Diagram of +28 VDC Over/Under Voltage Protection	X-169
X-108	Overvoltage Protection, Functional Diagram	X-170
X-109	High-Temperature Protection Circuit for D-C Regulator	X-171
X-110	Inverter Weight vs. Power Rating	X-172
X-111	D-C Regulator Concept	X-175
X-112	Battery Charge Power Module (Concept)	X-177
X-113	Battery Charger Control and Auxiliary Regulator Container	X-178
X-114	Unregulated Power Distribution Unit, Bus Bar Assembly	X-179
X-115	MMSS Floor Plan Showing Power Equipment Location and Bus Bar Routing	X-180
X-116	Array Bus Weight vs. Voltage Drop	X-182
X-117	Array Bus Area vs. Voltage Drop	X-182
X-118	Parameters for Battery-PDU-Regulator Assumptions	X-183
X-119	Bus Bar Resistance Relations	X-184
X-120	Plot of β vs. V_1	X-185
X-121	D-C Regulator Efficiency (Estimated)	X-188
X-122	Typical Power Dissipation in Flyback Diodes vs. Regulator Load Current	X-188
X-123	Inverter Efficiency	X-190

LIST OF ILLUSTRATIONS (Continued)

Figure		Page
X-124	Battery Charge Electronics Power Transfer Efficiency vs. Percent of Rated Load	X-190
X-125	Weight vs. Volat-Ampere Rating for Static Inverter (120/208 Volts, 3 ϕ, 400 Hz)	X-192
X-126	D-C Regulator Power Module Weight vs. Maximum Output Current Module	X-192
X-127	Battery Charge Electronics Module Weight vs. Maximum Charge Current	X-192
X-128	D-C Regulator Assembly, Specific Volume vs. Number of Power Modules	X-193
X-129	Battery Charge Electronics Assembly, Specific Volume vs. Number of Power Modules	X-193
X-130	Schematic Representation of Protective Processes	X-197
X-131	Reliability Mathematical Model, Power Subsystem	X-204
X-132	Portion of Subsystem to be Allocated	X-206
X-133	Battery Parameter Function	X-220
X-134	Battery Design Function	X-222
X-135	Electronics Function	X-224
X-136	Source Requirements Function	X-226
X-137	Array Design Function	X-227
X-138	Array Output Function	X-229
X-139	Self-Check and Monitoring Function	X-230
X-140	Total Weight Function	X-230
X-141	Adjustment of C and d for Modular Hardware Approach	X-232
X-142	Computerized Study Flow Chart Solar-Cell Subroutine	X-235
X-143	Damage Equivalent for Normally Incident 1-MeV Electron Flux vs. Monoenergetic Isotropic Electron Flux	X-238
X-144	Damage Equivalent for Normally Incident 1-MeV Electron Flux vs. Monoenergetic Isotropic Proton Flux	X-239
X-145	Damage Equivalent for Normally Incident 1 MeV Electrons per Omnidirectional Alpha Particle	X-239
X-146	Air-Mass-Zero Short Circuit and Maximum Power Current Degradation	X-244
X-147	Air-Mass-Zero Maximum Power Voltage Degradation	X-244
X-148	Air-Mass-Zero Open Circuit Voltage Degradation	X-244
X-149	I-V Curve Shape Change	X-245
X-150	Solar Array Area for Three Orbits vs. Night Load	X-254
X-151	Solar Array Area for Three A-C/D-C Ratios vs. Night Load	X-254
X-152	Total Array Weight and No. of Solar Cells vs. Array Area	X-254
X-153	Total Array Weight and No. of Solar Cells vs. Array Area	X-255
X-154	Solar Array Power in Three Orbits vs. Array Area	X-255

LIST OF ILLUSTRATIONS (Continued)

Figure		Page
X-155	Required Battery Capacity for Three A-C/D-C Ratios vs. Night Load	X-257
X-156	Required Battery Capacity for Three Resupply Intervals vs. Night Load	X-257
X-157	Battery Weight and Volume vs. Battery Capacity	X-257
X-158	Electronics Weight for 0 and 100-Percent D-C Loads vs. Night Load	X-259
X-159	Electronics Volume for 0 and 100-Percent D-C Loads vs. Night Load	X-259
X-160	Electronics Weight for Three Day/Night Load Ratios vs. Night Load	X-259
X-161	Electronics Volume for Three Day/Night Load Ratios vs. Night Load	X-260
X-162	Effect of System Operating Parameters on Total System Weight, Ni-Cd Batteries, 200 NM Orbit	X-261
X-163	Effect of System Operating Parameters on Total System Weight, Ag-Cd Batteries, 200 NM Orbit	X-261
X-164	Effect of System Operating Parameters on Total System Weight, Ag-Cd Batteries, Synchronous Orbit	X-262

LIST OF TABLES

Table		Page
VI-1	Mission and Orbit Guidelines	VI-12
VI-2	Manned Spacecraft Guidelines	VI-12
VI-3	Specific IPS Guidelines	VI-15
VI-4	Specific PSM Guidelines	VI-16
VII-1	Array Stowage Locations	VII-5
VII-2	Existing Solar-Array Structure Designs	VII-10
VII-3	Solar Panel Structural Concepts	VII-12
VII-4	Design Limit Input Loads	VII-16
VII-5	Panel Design Data	VII-17
VII-6	Comparison of the Characteristics of Beryllium and Aluminum Structures	VII-20
VII-7	Slip-Ring Characteristics	VII-31
VII-8	Weight Summary	VII-56
VIII-1	Array Design Comparison	VIII-2
VIII-2	Stowed Array Area Potential, Accordion-Folded Stowage Concept (IPS)	VIII-6
VIII-3	Design Limit Input Loads	VIII-11
VIII-4	Configuration Criteria	VIII-12
VIII-5	Launch-Mode Stresses and Safety Margins	VIII-13
VIII-6	Solar Array Weights (Estimated)	VIII-14
VIII-7	Tensile-Compressive Mode Docking	VIII-28
VIII-8	WAB Docking Mode	VIII-30
VIII-9	T/C Mode SPS Engine Activity	VIII-35
VIII-10	Weak-Axis Bending Mode SPS Activity	VIII-37
VIII-11	Boom-Deplayed Array-Retracted SPS Activity	VIII-38
VIII-12	T/C Mode SPS Activity, Advanced Design	VIII-40
VIII-13	Results of System Thermal Analysis	VIII-41

LIST OF TABLES (Continued)

Table		Page
VIII-14	Thermal External Environment Factors	VIII-42
VIII-15	Surface Finish Comparison	VIII-47
VIII-16	Temperature Values for 200-NMI Mission	VIII-48
VIII-17	Radiation Surface Requirements	VIII-51
VIII-18	Component Temperatures	VIII-57
VIII-19	Auxiliary Heater Power Requirements	VIII-59
VIII-20	Weight Summary	VIII-60
IX-1	Moment Arms for Several Configurations	IX-14
IX-2	Summary of Momentum Produced by Perturbations for a Worst-Case, 45-Day Period	IX-25
IX-3	Summary of Yearly Momentum Produced by Perturbations	IX-26
IX-4	Summary of Propellant Requirements to Cancel Perturbations for a Worst-Case, 45-Day Period, IPS Concept	IX-31
IX-5	Summary of Yearly Propellant Requirements to Cancel Perturbations, PSM Concept	IX-31
IX-6	Fuel Weights With and Without MSD	IX-32
IX-7	Net "Δ" Propellant Consumption Compared with Weight of Momentum Storage Device for a Worst-Case, 45-Day Period, IPS Concept	IX-38
IX-8	Yearly Net "Δ" Propellant Consumption Compared with Weight of Momentum Storage Device (Pounds), PSM Concept	IX-39
IX-9	Advantages and Disadvantages of Various Sem-Sansom Mountings	IX-42
X-1	Load Requirements for Typical Missions	X-6
X-2	Symbol and Parameter Assignments for Various Systems	X-11
X-3	Calculated Values of r_H ($I_{ch_{max}}/I_{ch_{avg}}$)	X-41
X-4	Optimum Array Design	X-51
X-5	Designs Under Evaluation	X-52
X-6	Solar-Flare Protons, Number/Cm^2/Year	X-57
X-7	Solar Flare Alpha Particles, Number/Cm^2/Year	X-58
X-8	Van Allen Belt Protons, Number/Cm^2/Year	X-59

LIST OF TABLES (Continued)

Table		Page
X-9	Van Allen Belt Electrons, Number/Cm^2/Year	X-60
X-10	Charged Particle Radiation Data for Microsheet and Corning 7940	X-63
X-11	Comparison of Weights of Integral and Bonded Cell Covers	X-66
X-12	Radiation Exposure of Various Cells	X-67
X-13	Equivalent 1 MeV Electrons/Cm^2 at End of Life (1 Yr.)	X-72
X-14	Summary of Solar-Cell Design Factors	X-77
X-15	Maximum Solar-Cell Power	X-82
X-16	Maximum Power for Cells of 1- and 10-ohm Resistivity	X-85
X-17	Outputs of Cells with Various Filter-Substrate Thickness	X-85
X-18	Comparison of 1-ohm-cm N-on-P Cells with Lithium-Daped P-on-N Cells	X-88
X-19	Summary of Parameters for Various Cell Configurations	X-99
X-20	Weights of Cell Components in lbs/ft^2	X-101
X-21	Lunar Orbiter Components	X-110
X-22	Evaluation of Existing Commerical Adhesives at Very Low Temperatures	X-110
X-23	Battery Design Factors for Computer Storage	X-114
X-24	Electronic Modules	X-148
X-25	Power Supply, +28 VDC Bus Over/Under Voltage Protection Logic	X-168
X-26	Length of Bus Bar Runs	X-181
X-27	Battery Regulator Bus Bar Constants	X-185
X-28	Estimated Size and Weight Data	X-194
X-29	Power System Parameters to be Monitored on Board	X-197
X-30	Power Subsystem Telemetry Points	X-199
X-31	Battery Charge Electronics, Power Modules	X-206
X-32	D-C Regulator, Power Modules	X-207
X-33	Inverter Modules (MTBF = 20,000 Hours)	X-207
X-34	Inverter Modules (MTBF = 40,000 Hours)	X-208
X-35	Inverter Modules (MTBF = 60,000 Hours)	X-208

LIST OF TABLES (Continued)

Table		Page
X-36	Spares and Reliability Apportionments for Nickel-Cadmium Modules. .	X-210
X-37	Spares and Reliability Apportionments for Silver-Cadmium Modules. .	X-210
X-38	Electron Flux Format	X-236
X-39	Proton Flux Format	X-236
X-40	Solar Flare Proton Flux Format	X-237
X-41	Solar Flare Alpha Particle Flux Format	X-237
X-42	Equivalent Thickness of Shielding	X-239
X-43	Damage Factors for Electrons	X-240
X-44	Damage Factors for Protons	X-240
X-45	Damage Factors for Alpha Particles	X-241
X-46	Summary of Conceptual Design Cases	X-265
X-47	Power Module Breakdown	X-268
X-48	Resupply Interval as a Weight Factor	X-272
X-49	Final Recommendation; Conceptual Designs	X-274

SECTION VI

POWER SYSTEM ANALYSIS

A. INTRODUCTION

1. Study Definition

A nine-month study entitled "Manned-Mission Photovoltaic Power System Study" has been performed under contract NAS 9-5266 for the NASA Manned Spacecraft Center at Houston, Texas by the Astro-Electronics Division of Radio Corporation of America in Princeton, New Jersey. The primary goals of this program were to define the major problems associated with large-area solar-array power systems and to perform power-system studies which would result in a conceptual design (adaptable to a variety of missions) with a hardware development plan for that design.

2. Study Milestones

Two major milestones in the program became significant because of their effect on the technical approach to the study. The first of these, which occurred early in the contract period, was a change in the intent of the program from a "design and integration study" to a "conceptual design study".* As a result, a modified work statement (see Appendix G) was prepared along with a revised technical task plan. A discussion of technical task relationships in a power system conceptual study is contained in Paragraph VI. B.

A review of the results of the first six months' effort showed that the constraints on the power system design were directly related to the many broadly defined vehicle power-system interfaces. An array stowage trade-off analysis subsequently performed (See Appendix A) and a desire to reduce the power-system design constraints provided the second significant milestone. This milestone was the redirection of the effort from the integrated power system (IPS) concept toward a separate power system module (PSM) that could be utilized with a variety of vehicle and mission combinations and that would reduce the constraints on the power-system conceptual design. A comparison of the salient features of an IPS and a PSM is contained in Paragraph VI. C.

---

* A design and integration study yields a detailed design of a power system and is based on a specific vehicle detailed description and a defined mission or group of missions. A conceptual design study yields, as a result of parametric and trade-off analyses, a power system concept consistent with a gross vehicle description, and a generalized definition of the mission or group of missions.

B. TECHNICAL TASK RELATIONSHIPS

Power system analysis and design requires effort in three basic, interrelated areas: the electrical system, the mechanical system, and the orientation system. The major tasks within each area and their relationships for a parametric conceptual study are shown diagrammatically in Figure VI-1.

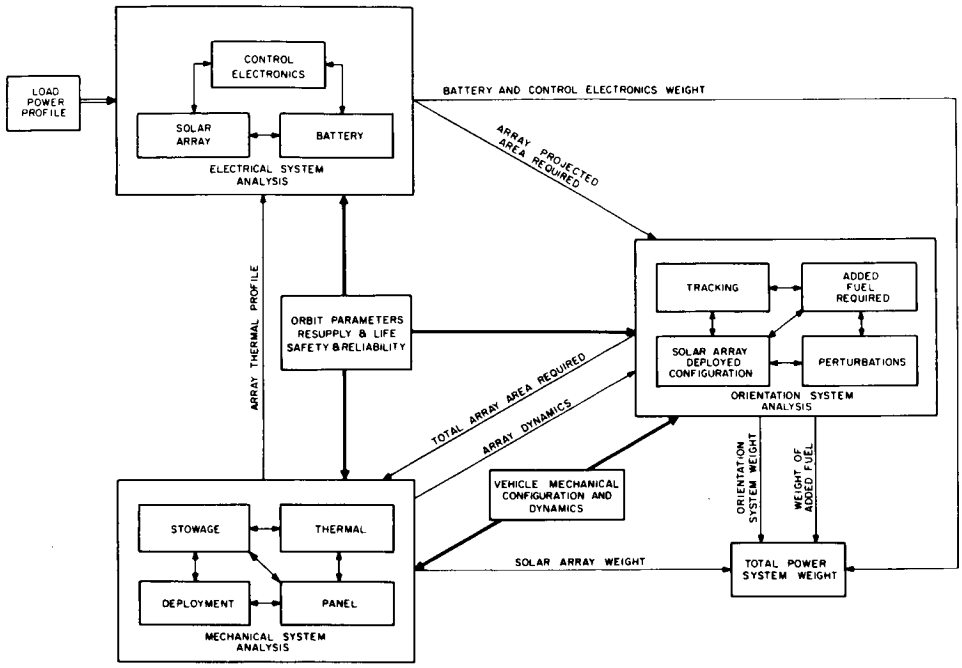

Figure VI-1. Power System Technical Study Tasks

The baseline definitions, guidelines, and assumptions will be applied as needed to reduce the number of variables and to narrow the range of parameters studied. (See Paragraph VI. D.)

1. Optimization Criteria

For the purposes of this conceptual study, minimum total system weight was chosen as the optimization criterion since reliability, cost, and/or development time are more appropriate as optimization criteria for a design and integration study where the inputs are defined in detail. The total system weight includes the weight of batteries, control electronics, solar array with deployment and stowage mechanisms, the array orientation drive system, and the additional fuel necessary for the vehicle attitude-control system to overcome the effects resulting from the gravity gradient, atmospheric drag, magnetic field, and solar pressure perturbations.

2. Intra-Section Relationships

Figure VI-2 shows some of the detail tasks within the Orientation System Analysis. Note that the feedback path indicated is but one of many in this section that will require several iterations before a satisfactory result is obtained.

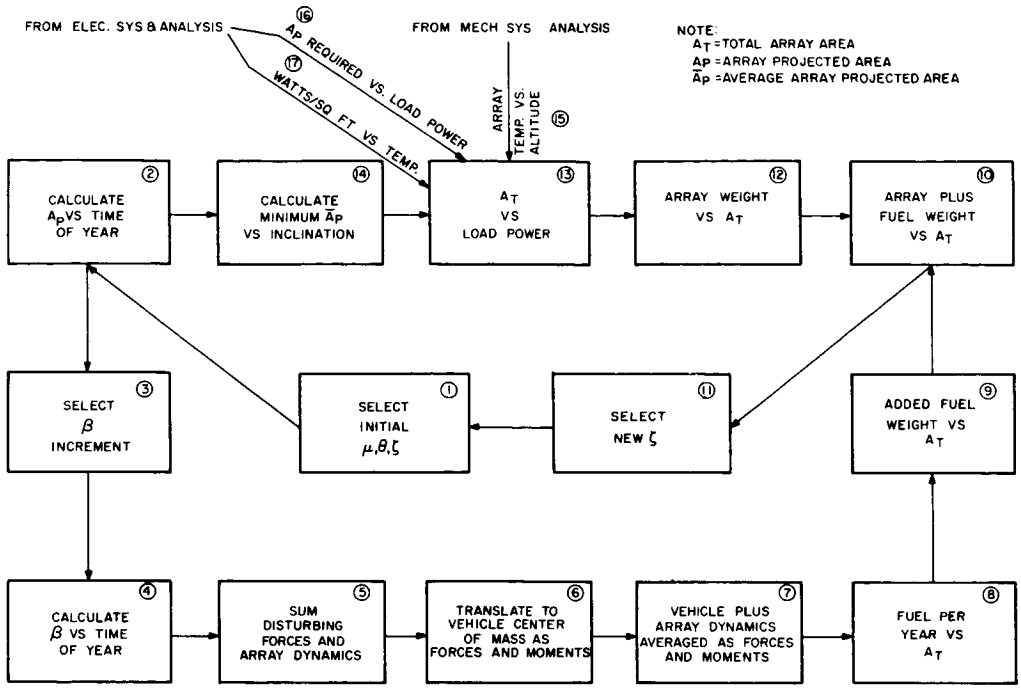

Figure VI-2. Partial Orientation System Analysis Tasks

Consider the loop containing the blocks numbered 1, 2, 14, 13, 12, 10, and 11 (see Figure VI-3 for a description of the angles). The forward part of this loop yields total array area A_T as a function of load power for a particular set of μ, θ, and ζ angles (utilizing additional inputs 15, 16, and 17). From this, array weight with regard to array area can be calculated. Another loop (1, 2, 3, 4, 5, 6, 7, 8, and 9) provides the added fuel weight required as a function of A_T (taking into account the disturbing forces and the array-vehicle dynamics). Combining blocks 12 and 9, a total array plus added fuel weight can be plotted against A_T (10). Then a new ζ is selected (11) and the process repeated, yielding another weight-versus-area curve (10). Iteration continues until a determination can be made of the optimum ζ angle (that which yields minimum array-plus-fuel weight).

3. Inter-Section Relationships

In addition to the feedback loops within each system analysis section, there is a closed-loop dependency of one section on another, particularly in a parametric study.

The electrical system (see Figure VI-1) lends itself to a parametric type of study, since the inputs affecting the design are limited in number and may be bounded realistically. These inputs are the load power requirement as a function of orbit time, the altitude and inclination

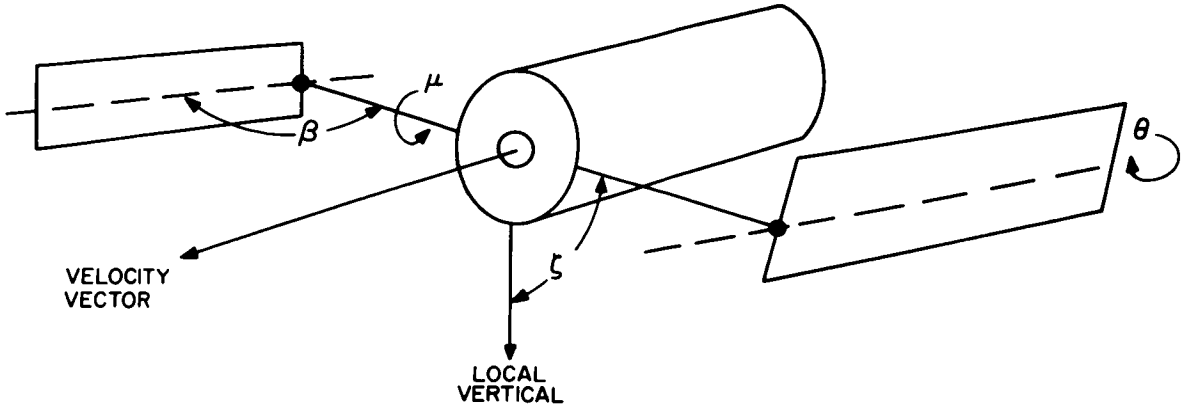

Figure VI-3. Orientation Axes

of the orbit, and the resupply period and life time of the mission. Reliability and crew safety are not treated parametrically, but are based on specific requirements.

Within the electrical system, parametric and trade-off studies are performed to yield the battery size and the solar array projected area required to support the load power profile as a function of orbit altitude. This range of solar array projected areas is then utilized in the orientation system analysis to define the range of total array areas required. These requirements are the result of analyses of various array geometric configurations as described in previous paragraphs.

The total array area requirement boundaries are employed, along with inputs shown, to establish array stowage requirements, a deployment technique, and a deployed array mechanical configuration. The solar array panel design will be influenced by the orbit altitude and the specific materials used, because the sun-time to dark-time ratio and the absorptivity and emmissivity of the array surfaces define the panel temperature-time profile. Since solar-cell power output varies inversely with temperature, the array temperature-time profile is utilized to modify the solar array projected area requirement through electrical system parametric analyses. This loop is iterated until no significant changes are necessary and all of the constraints and limitations are satisfied.

The numerous other iterative loops that exist among and within the electrical, orientation, and mechanical system analyses are resolved in a similar fashion.

4. Total System Weight

The weight of each area and its components can be determined as a function of the load power profile, the orbit parameters, and the life and resupply period. Summation of these outputs yields total system weight as a function of mission parameters.

In this conceptual study of a power system, the electrical system parameters have been optimized parametrically (through the use of a computer program as described in Paragraphs X. E and X. F and Appendix C), the orientation system analysis has been performed with limited iteration (see Section IX), and the mechanical system analysis has been based on two "point design" concepts (see Sections VI (C), VII, and VIII) that provide a means for preliminary comparison of an integrated power system and a power system module.

5. Dynamics Loop Complexity

One loop has been considered only superficially because the complexity involved is far beyond the scope of this study. Since the spacecraft is to supply the attitude control for the manned vehicle with the deployed solar array, there is a dynamic interaction between the spacecraft and its attitude control system and between the solar array and its orientation system. This iterative loop is very intricate, for it involves the mechanical response characteristics of the deployed solar array, the response characteristics of the two-degree-of-freedom solar-array-orientation servo system, the sun sensor type and location, the vehicle transmissibility and attenuation characteristics, the spacecraft three-axis attitude-control system performance, and the vehicle attitude stability requirements. Further discussion of this loop is contained in Section IX.

C. POWER SYSTEM CONSIDERATIONS

1. System Concepts

Photovoltaic-power-system concepts and design may be approached in two different ways. One method (integrated power system) considers the power-system components as an integral part of the mission vehicle; the other (power system module) provides a separate power module that can be utilized by a variety of vehicles.

a. INTEGRATED POWER SYSTEM (IPS)

The first method, hereafter called the integrated power system (IPS), requires the detail definition of many vehicle-power system interfaces. The battery and control electronics are packaged within the spacecraft, while the solar array is packaged for launch in a fashion consistent with the spacecraft peripheral envelope and the launch-vehicle shroud envelope. Solar array deployment and sun orientation, if required, provide additional constraints and interfaces. Usually the mission must be well defined and the spacecraft design well under way before definition of the interfaces is adequate to permit power system detail design. Furthermore, each mission or spacecraft change leads to power system modification or redesign.

Figure VI-4 depicts a spacecraft with an IPS (for a manned multi-kilowatt mission) while the major vehicle-IPS interfaces are shown in Figure VI-5. Each of the five functional elements of the power system has an electrical and a mechanical interface with the manned spacecraft. The electrical interfaces can usually be identified with sufficient accuracy to permit electrical system design to proceed early in a program. The mechanical interfaces, however, are more elusive and cannot be defined adequately until a firm spacecraft design approach is

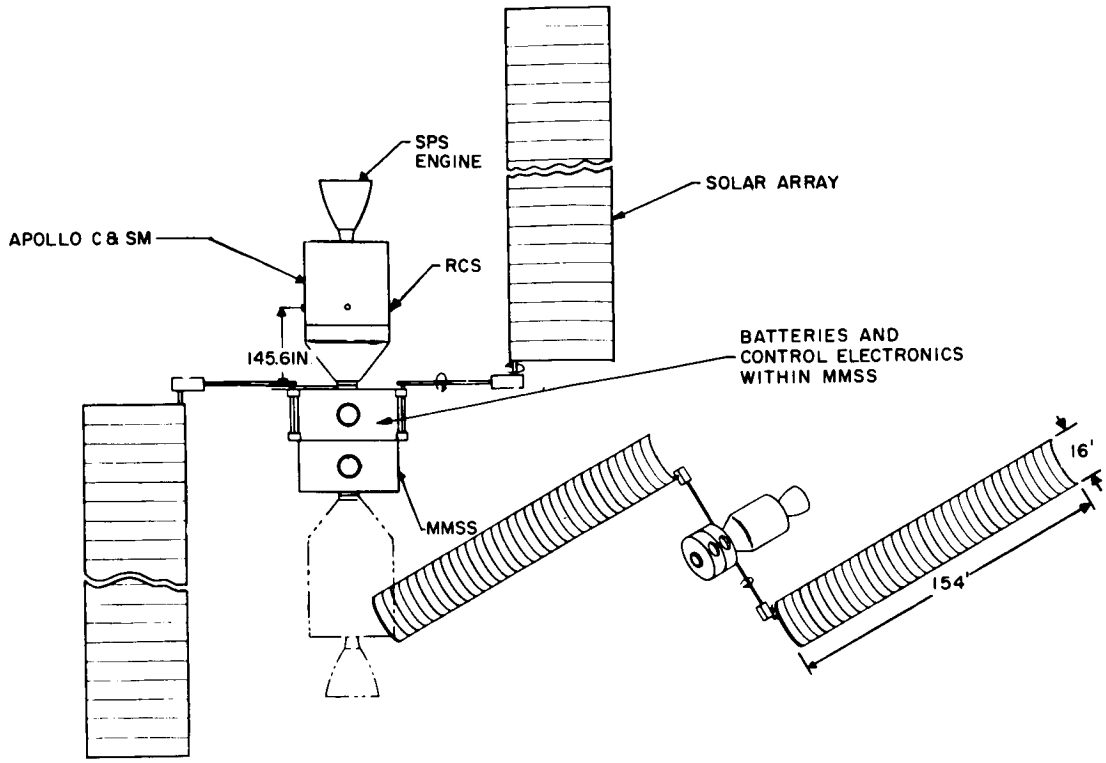

Figure VI-4. Integrated Power System, Deployed Configuration

INTEGRATED POWER SYSTEM—A POWER SYSTEM WHOSE COMPONENTS ARE AN INTEGRAL PART OF THE VEHICLE

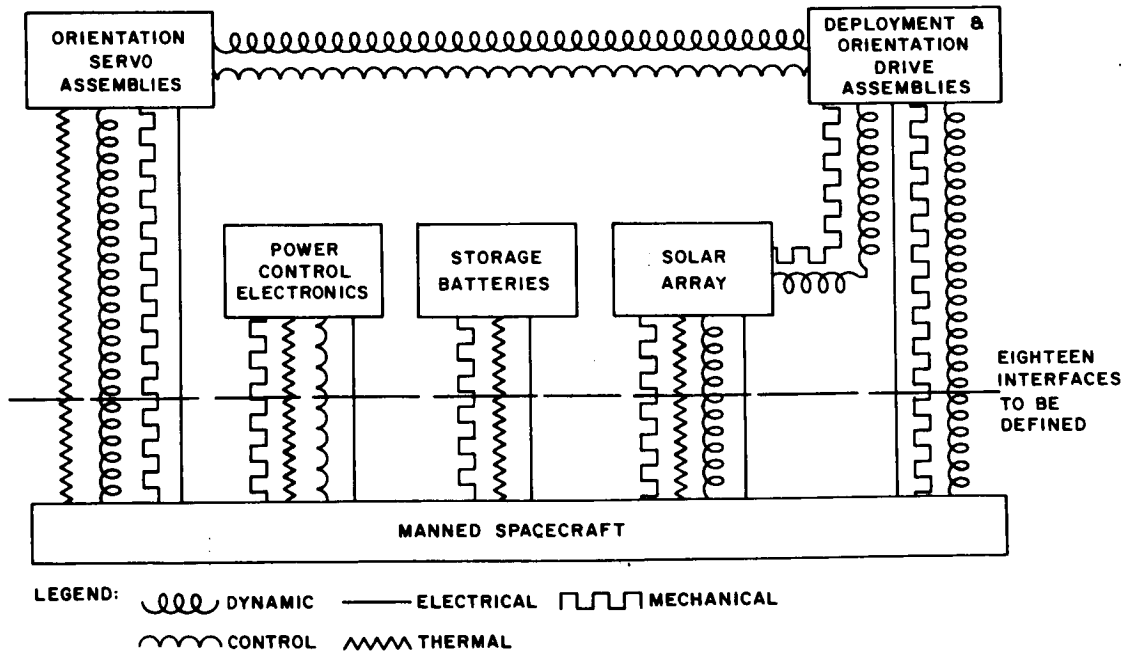

Figure VI-5. Integrated Power System Interfaces

established and many spacecraft problems are resolved. Four of the functional elements are contiguous with the spacecraft and, therefore, have thermal interfaces that will require iterative, concurrent design. The control interface between the power control electronics and the spacecraft is related to the degree of astronaut participation in load programming and system monitoring and maintenance. The three dynamic interfaces, as discussed in Paragraph VI. B, provide the most complex and intricate definition problem.

There are, then, eighteen specific interfaces between an IPS and the manned spacecraft that must be defined by the integration or prime contractor during the course of a program.

b. POWER SYSTEM MODULE (PSM)

A separate power system module (PSM) approach can reduce the number of interfaces to nine. A PSM is a separate unit, whose primary function is to provide a multi-kilowatt source of electrical power for a variety of spacecraft over a range of missions. A preliminary concept of such a PSM is shown in Figure VI-6 with the major interfaces between the PSM and the manned spacecraft schematically presented in Figure VI-7.

In this concept, the batteries and control electronics are contained in the component housing assembly with the solar array packaged for launch in the quadrants adjacent to this assembly. It can be seen that the number of electrical interfaces has been reduced to one (the IPS had five), the mechanical and thermal interfaces have been reduced to two each (the IPS had five mechanical and four thermal), and the dynamic interfaces reduced from three to two. This reduction in interfaces has been accomplished by transferring some design and hardware complexity from the spacecraft to the PSM.

As an example of this increased complexity, the component housing assembly provides mechanical support and thermal control for the batteries and the control electronics. In the IPS, the spacecraft environmental control system was required to provide the necessary battery and electronics heat-sink temperature control.

It is thus possible to begin detail design of the PSM early in a program where spacecraft design changes are occurring with great frequency. In fact, a PSM can be designed and built before a spacecraft design has been implemented, provided, of course, that the spacecraft design will be tailored to the mechanical and performance characteristics of the PSM. The PSM then becomes somewhat analogous to the aircraft jet engine of today wherein the engine is an off-the-shelf type of item, whose performance and mechanical characteristics are defined in detail by the manufacturer. Airframe manufacturers utilize these characteristics in designing an aircraft for specific load capacity and performance. This approach, for aircraft or spacecraft, permits major mission or vehicle design changes without requiring a new power system design.

c. RECOMMENDATION

Although the PSM approach reduces the manned-spacecraft/power-system interfaces, the power system penalties, if any (in terms of system complexity and overall mission cost)

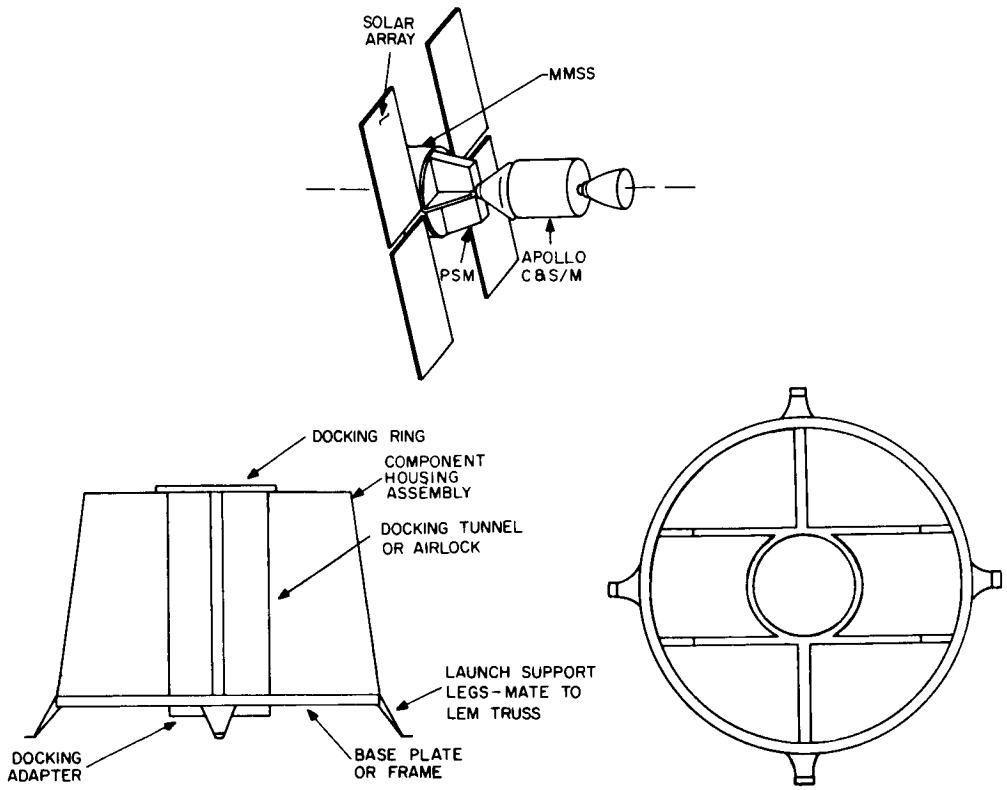

Figure VI-6. Power System Module Configuration

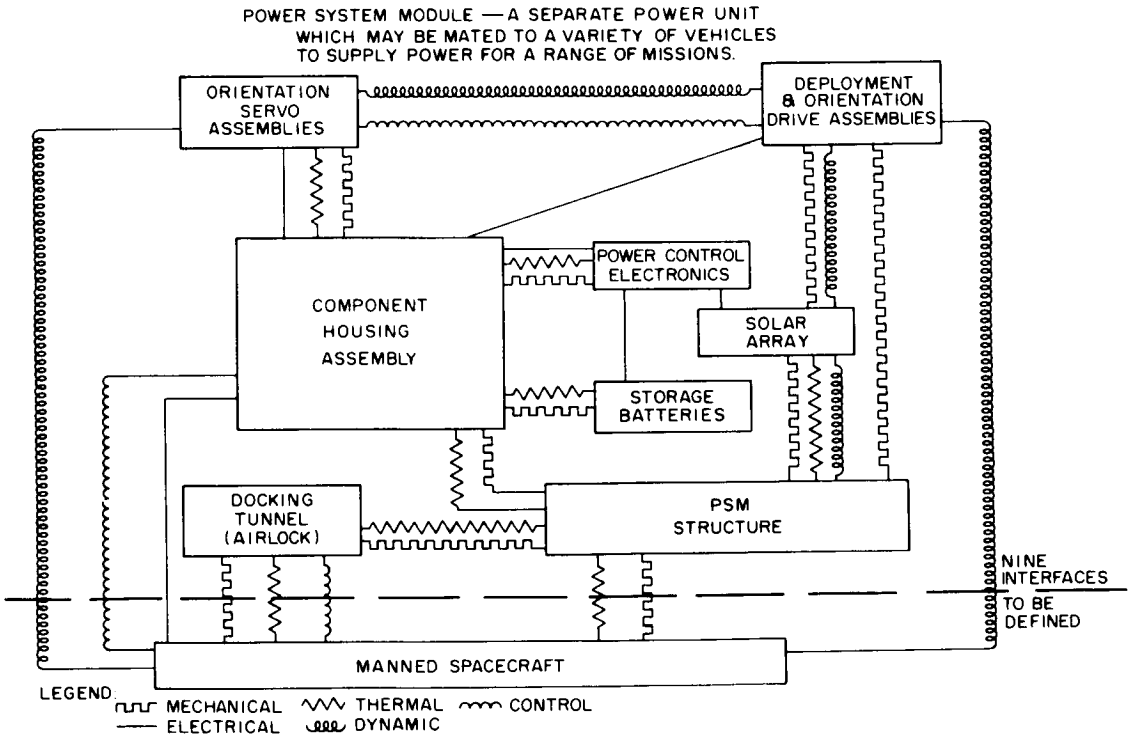

Figure VI-7. Power System Module Interfaces

have not been evaluated. It is therefore recommended that a cost effectiveness comparison be performed between the IPS and the PSM.

2. Modular Concepts

A modular power-system design can be achieved in several ways:

(1) By assembling multiples of the basic complete system (see Figure VI-8);

(2) By assembling building blocks of basic system functional elements (see Figure VI-9); or

(3) By a combination of (1) and (2).

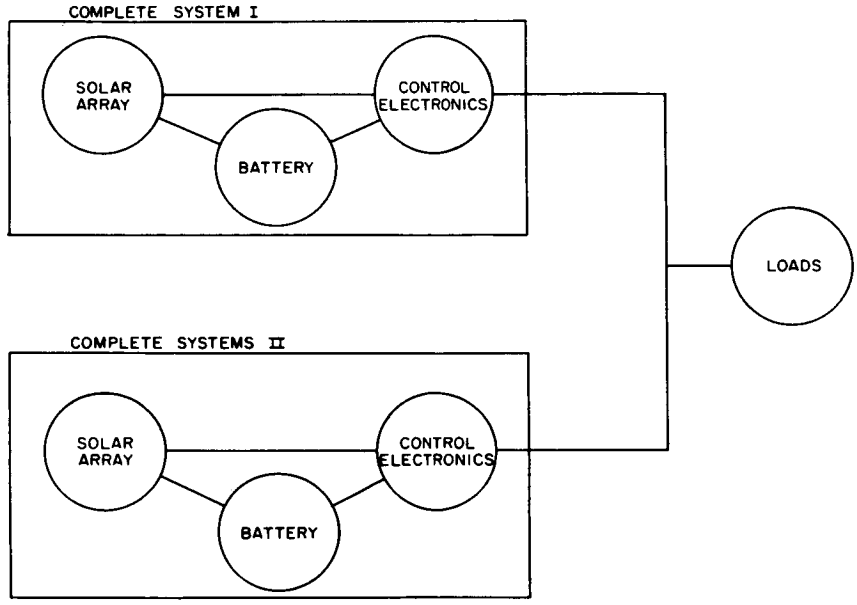

Figure VI-8. System Paralleling

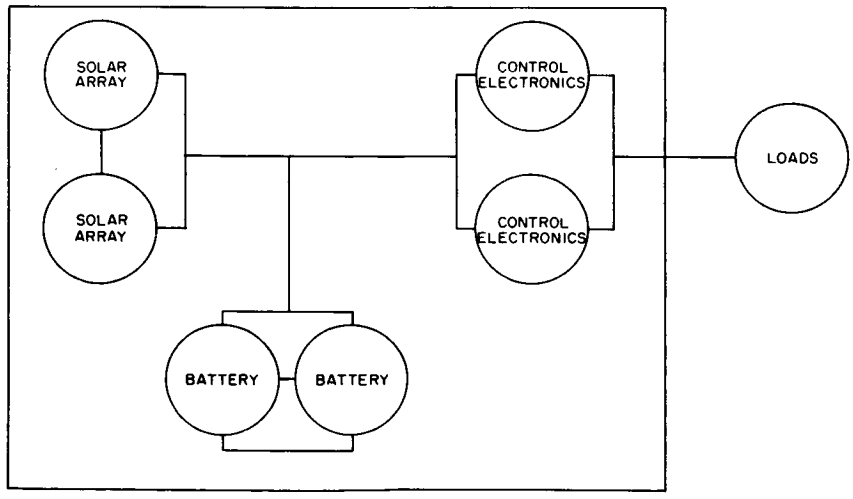

Figure VI-9. Functional Element Paralleling

a. SYSTEM PARALLELING

In technique (1), system paralleling, a basic power system is designed for a specific minimum load requirement. If subsequent missions require a greater load capability, two identical units of the basic system are paralleled.

For example, consider a basic power system of 1-kilowatt capability (with 0.5 kW at d-c and 0.5 kW at a-c). For a mission requirement of 2-kilowatts (1 kW at d-c and 1 kW at a-c), two basic systems would be required. For a 4-kilowatt load (2 kW at d-c and 2 kW at a-c), four of the basic 1-kilowatt systems would be utilized. If it is arbitrarily assumed that each 1-kilowatt system weighs 1000 pounds, the total weight for a 2-kilowatt mission would be 2000 pounds and for a 4-kilowatt load, 4000 pounds.

b. FUNCTIONAL ELEMENT PARALLELING

In technique (2), functional element paralleling, basic functional elements are designed and paralleled as necessary to increase capability. As an example, consider a basic system whose functional elements (i.e., solar array, battery, and control electronics) have been designed to handle a 1-kilowatt (0.5 kW d-c and 0.5 kW a-c) load requirement. For the 2-kW load requirement, two solar array elements, two parallel battery elements, and two parallel control electronics elements would be assembled as a system. For the 4-kilowatt mission, four parallel elements of each would be needed. If, again arbitrarily, the basic 1-kilowatt system is assumed to weigh 1000 pounds, consisting of 200 pounds of array, 600 pounds of batteries, and 200 pounds of control electronics (75 pounds of d-c and 125 pounds of a-c), then the 2-kilowatt mission requirement would weigh:

$$(2 \times 200) + (2 \times 600) + (2 \times 200) = 2000 \text{ pounds},$$

and in a like manner, the 4-kilowatt load system would weigh 4000 pounds.

c. COMPARISON

As a practical matter, however, when functional elements are paralleled, a weight saving may be achieved (through more efficient packaging) and an improvement in total system reliability obtained, compared with method (1). In addition, technique (2) provides greater flexibility. This may be shown by considering the same basic system design and weight assumptions as before. Then, for a new mission, where the load power level stays the same but is all at d-c, technique (1) would require two basic systems (2000 pounds) while technique (2) would permit paralleling of d-c elements and elimination of a-c elements, with the total weight:

$$200 + 600 + (2 \times 75) = 950 \text{ pounds}.$$

Similarly, if the mission day-to-night load ratio decreased significantly (or if the altitude or mission life time increased significantly), the weight of approach (1) would be greater than that of approach (2). Thus it can be seen that the functional element paralleling method may provide a greater flexibility and a weight saving along with an improvement in reliability.

Technique (3) is more applicable to the PSM than it is to the IPS, since large increases in mission and load requirements could be accommodated by providing additional PSM's, while small variations could be handled by functional element paralleling.

d. RECOMMENDATION

For this study, with the ground rules and guidelines as defined (see Paragraph VI.D) approach (2), functional element paralleling, is the recommended method, although final evaluation and selection can be performed only after the mission limits have been bounded and the manned vehicle defined.

D. GROUND RULES AND GUIDELINES

As described in Paragraph VI.A.2, the study program was separated by a revision of the ground rules into two distinct efforts. However, a number of the ground rules, guidelines, and assumptions that did not change. Paragraph VI.D.1 provides a description of these, while Paragraph VI.D.2 defines those specifically applicable to the IPS study, and Paragraph VI.D.3, those pertaining to the PSM effort.

1. General Guidelines

The guidelines related to the general mission are tabulated in Table VI-1 while those related to the spacecraft are shown in Table VI-2.

Since the launch period is defined as 1970 to 1972, power system development must begin in the 1968 period (assuming that three to four years will be realistically required to achieve flight-qualified, power-system hardware). Therefore, only current state-of-the-art methods, materials, and techniques may be utilized. State of the art is defined, for this study, to mean that no technological breakthrough is required to achieve a demonstrated capability.

The power system must be modular so that it may meet the requirements of a broad range of missions (see Paragraph VI.C.2). The electrical load power profile will have a form as shown in Figure VI-11 where P_{LD} is the day-time load and P_{LN} is the night-time load. Typical vehicle subsystems that will require this power are as follows:

(1) EC/LSS, Environmental Control and Life Support System, consisting of oxygen regeneration, waste processing, manned vehicle pressurization, etc.

(2) COMM, Communications System, consisting of voice and data transmission facilities, both primary and secondary.

(3) N/G, Navigation and Guidance System, consisting of orbit parameter computers, star trackers, etc.

(4) S & C, Stabilization and Control System, consisting of vehicle orientation and attitude sensors, thrusters, momentum storage devices, etc.

TABLE VI-1. MISSION AND ORBIT GUIDELINES

Item	Delineation
Launch period	1970 to 1972
Mission life	1 year
Probability of Mission Success	0.995
Three specific circular orbits considered	200 NM 28.5° inclination 200 NM 90° inclination 19340 NM 30° inclination
Radiation Environment for the three orbits	To be defined by RCA (for solar-cell degradation effects)
Atmosphere to be used	1962 ICAO* standard

* International Civil Aviation Organization

TABLE VI-2. MANNED SPACECRAFT GUIDELINES

Item	Delineation
Modular multipurpose space station (MMSS) compartment	To be the manned spacecraft
Launch vehicle	Saturn IB or Saturn V (3) (Figure VI-10)
Orientation of vehicle in orbit	Roll axis always coincident with velocity vector Yaw axis always coincident with local vertical
Spacecraft attitude control	Provided by Apollo Command and Service Module Reaction Control System (RCS).
Spacecraft maneuvering and Orbit Changes	Provided by Apollo Service Propulsion System (SPS)

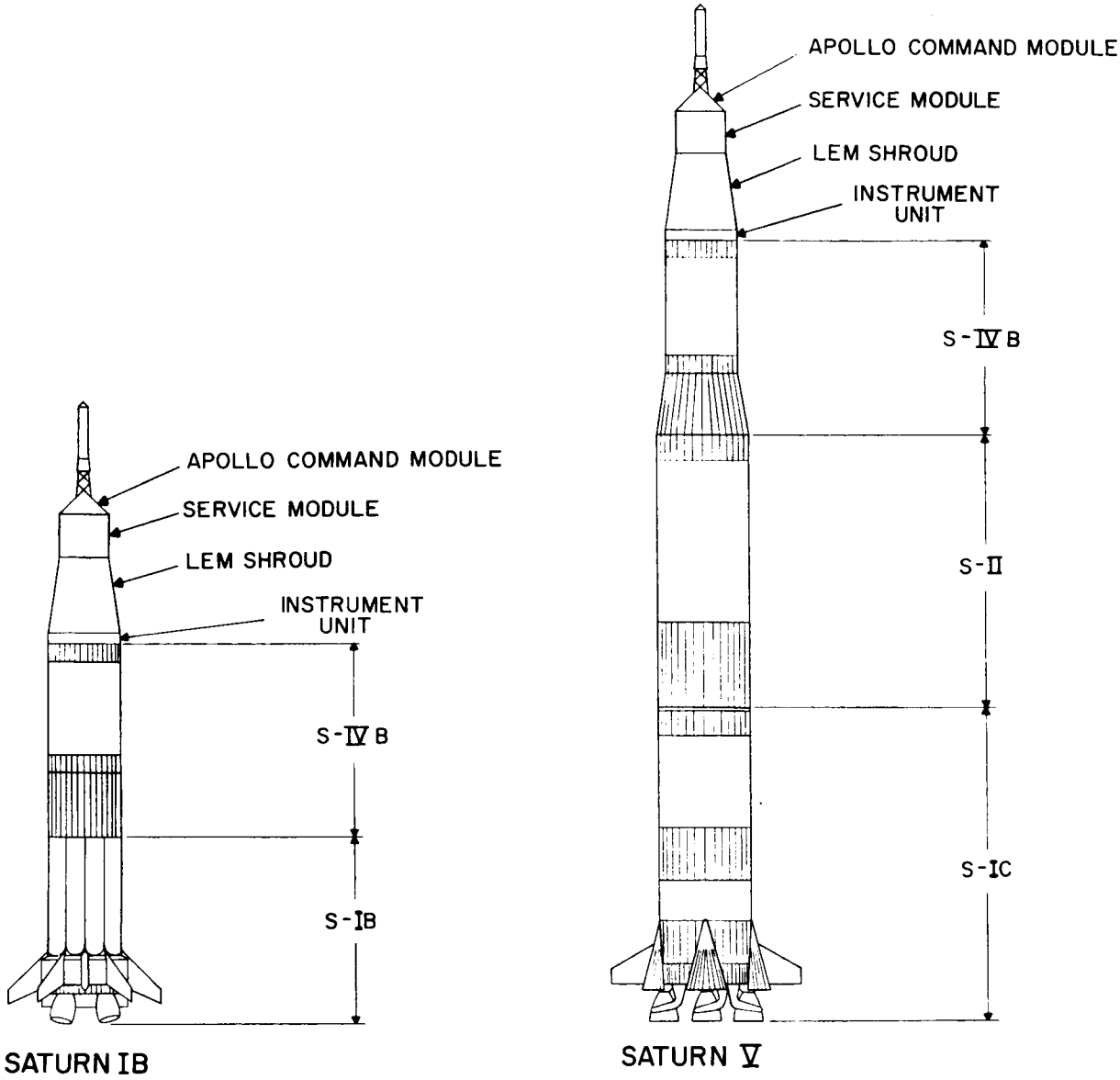

Figure VI-10. Launch Vehicles

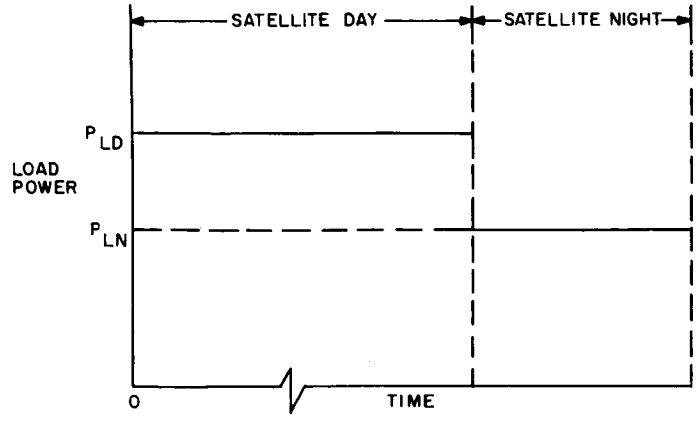

Figure VI-11. Load Power Profile

(5) PROP, Auxiliary Propulsion System, which has not been defined.

(6) HKPG, Vehicle 'housekeeping' requirements, consisting of displays, data management, signal processing, lighting, TV, maintenance, etc.

(7) EXP, Experiments, consisting of the scientific programmable experiments, i.e. the primary purpose of the mission.

A detailed breakdown for each of these is contained in Section X, Paragraph X.B.2.b. Specific values of P_{LD} and P_{LN} for the IPS and the PSM are contained in Paragraphs VI.D.2 and VI.D.3.

An a-c bus voltage of 120/208 volts, 400 Hz, three phase and a d-c bus voltage of +28 volts in accordance with MIL-STD-704 will be required.

Since this study is concerned with a manned mission, the astronauts may be required to perform routine monitoring of performance and periodic preventive maintenance, provided the average daily time requirements are relatively small. Emergency maintenance may be performed at any time without restriction.

Two significant assumptions have been made. First, the solar array density will be less than 1 pound per square foot, since the current state of the art is close to that value. Second, the solar array will rotate with two degrees of freedom always sun oriented (so that the projected area is equal to the total area) in order to provide the maximum mission flexibility.

Finally, the mechanical system concepts shall be based on a point design approach and will not be the result of parametric trade-off analyses.

2. Specific IPS Ground Rules

For the IPS study portion of the program, the specific ground rules as listed in Table VI-3 are applicable. In addition, the load power profile will have a range of 5 kW P_{LD} and 2 kW P_{LN} to 15 kW P_{LD} and 10 kW P_{LN} (see Figure VI-11). The ratio of a-c loads to d-c loads may vary from zero to infinity. A preliminary worst-case analysis shows that approximately 4900 square feet of solar array are required to support the largest load requirement (i.e., 200-nautical-mile altitude, nickel cadmium batteries and all a-c loads). Therefore, for mechanical system analysis, 4900 square feet of solar array must be stowed for launch and deployed for orbiting. For the specific design case, a P_{LD} of 8.2 kW and a P_{LN} of 5 kW with 67 percent of the load d-c and 33 percent a-c will be used.

3. Specific PSM Ground Rules (See Appendix H)

For the PSM concept, the ground rules established are as shown in Table VI-4. The basic PSM structure will house the solar array (during launch), the batteries, and the control electronics of the power system. A separate thermal control system will be

TABLE VI-3. SPECIFIC IPS GUIDELINES

Item	Delineation
Shroud and truss	Modifications permitted
Peripheral docking ports	Must be unobscured
Launch and orbiting configurations	As shown in Figure VI-12
Manned spacecraft equipment heat sinks	Will be held between 21 and 32°c regardless of equipment heat load
Resupply	Will be available in 45-day increments

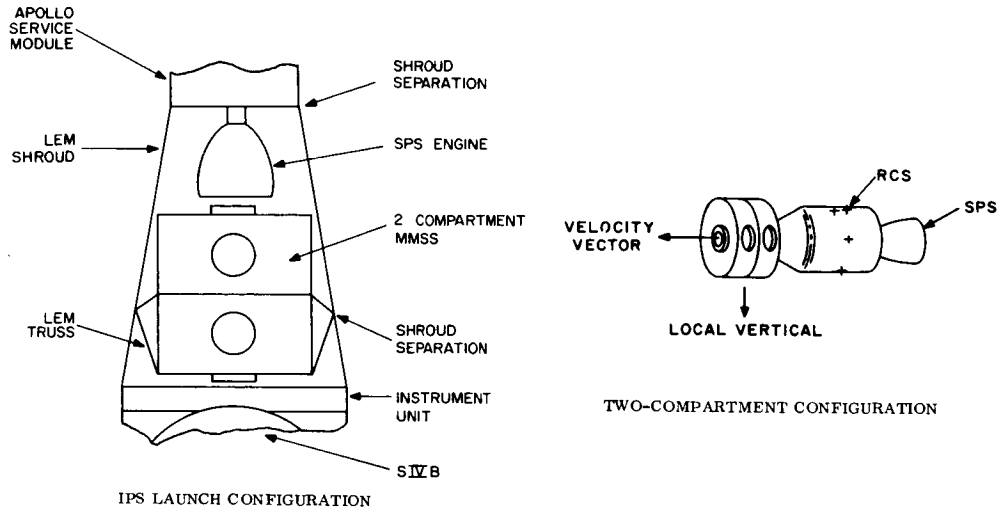

Figure VI-12. IPS Configuration

incorporated in the PSM to maintain the battery and electronic modules within permissible operating temperature limits.

The docking tunnel (airlock) is not defined in any detail but it may have cryogenic tankage and the equipment associated with it. Therefore, space must be left available for this requirement.

The load power profile will be 5 kW P_{LN} and 8.2 kW P_{LD} with loads of 67 percent d-c and 33 percent a-c. The specific solar-array area required, and the quantity of battery and electronics modules are based on the electrical system analysis performed during the IPS study (see Appendix H for details).

For the purpose of sizing a thermal-control system, power system thermal dissipation profiles for 200 NM and 19,340-nmi altitudes have been generated (see Appendix H).

TABLE VI-4. SPECIFIC PSM GUIDELINES

Item	Delineation
Shroud and truss	Modifications not permitted
Peripheral docking ports	Not to be considered
Configuration	As shown in Figure VI-13 and VI-14
Thermal Control System	Separate system to be incorporated for power system batteries and electronics
Resupply	Not considered
Rotation of spacecraft	Permitted occasionally about roll axis if required
Docking tunnel (Airlock)	Required
Solar array	Retraction to be considered. Array to be planar.

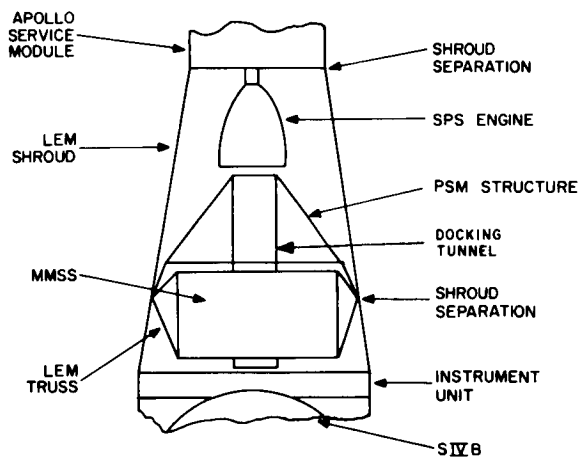

PSM LAUNCH CONFIGURATION

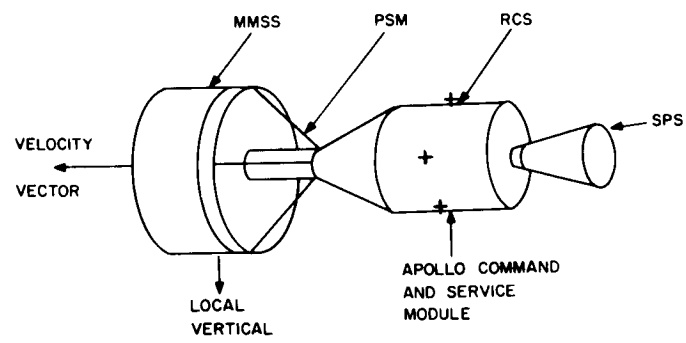

PSM ORBITAL CONFIGURATION

Figure VI-13. PSM Configuration

E. SUMMARY

The foregoing are the basic concepts and ground rules with which the detail study was undertaken.

Section VII presents the IPS mechanical analysis. It should be noted that, in some areas, detail conceptual design has not been performed. This is the result of the redirection from an IPS study to a PSM study.

Section VIII presents the PSM mechanical analysis. In some areas, it has not been possible to make a specific recommendation due to the limited depth of this portion of the study. For example, the thermal control system concepts have not been iterated with revised temperature limits on the batteries or with the possibility of occasional vehicle roll.

In Section IX, the solar-array orientation analysis presented is equally applicable to the IPS concept or the PSM concept.

Section X, the electrical system analysis, is the result of the effort during the IPS study, but its conclusions are generally applicable to both IPS and PSM. The primary areas of specific application to only the IPS concept are the battery and electronics mechanical packaging and power system maintenance philosophy.

The computer program and the results reported are applicable to the IPS since battery watt-hours per pound reflect IPS battery packaging. Limited program modification (in the form of revised stored computer data) will be necessary to provide realistic PSM concept results.

Figures VI-14 and VI-15 show the terminology applicable to the solar array and the batteries.

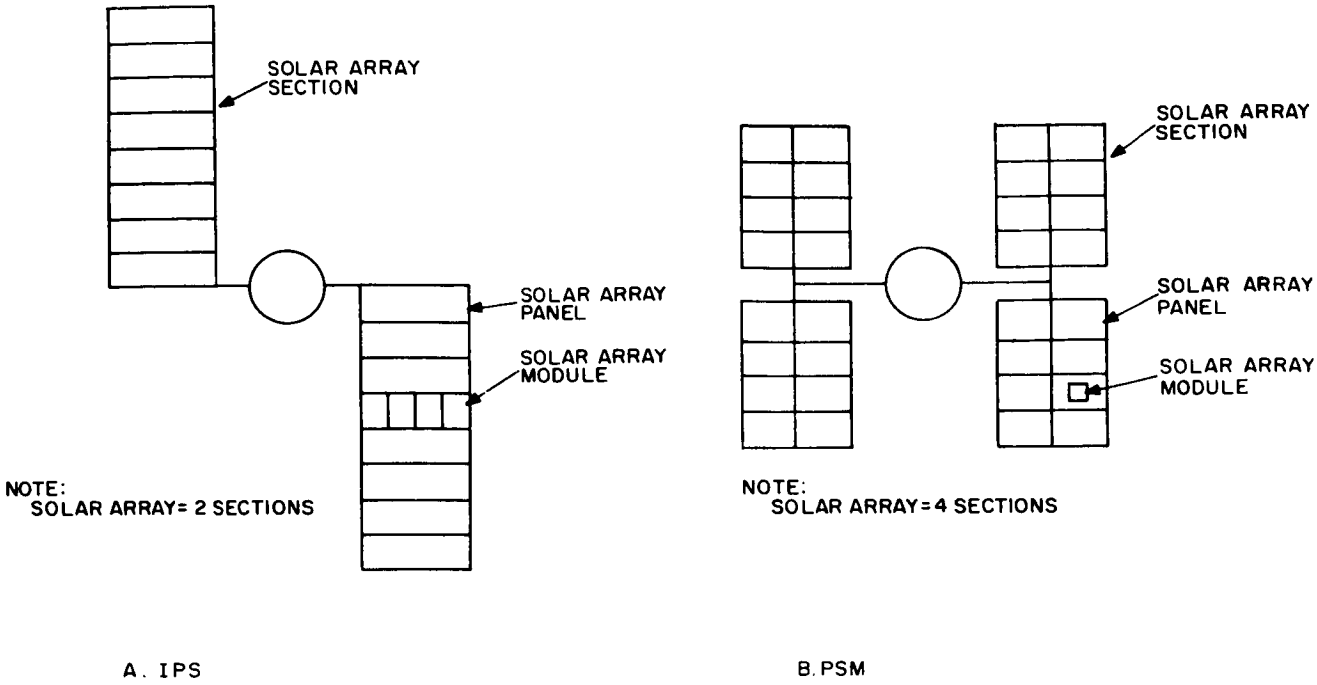

Figure VI-14. Solar Array Terminology

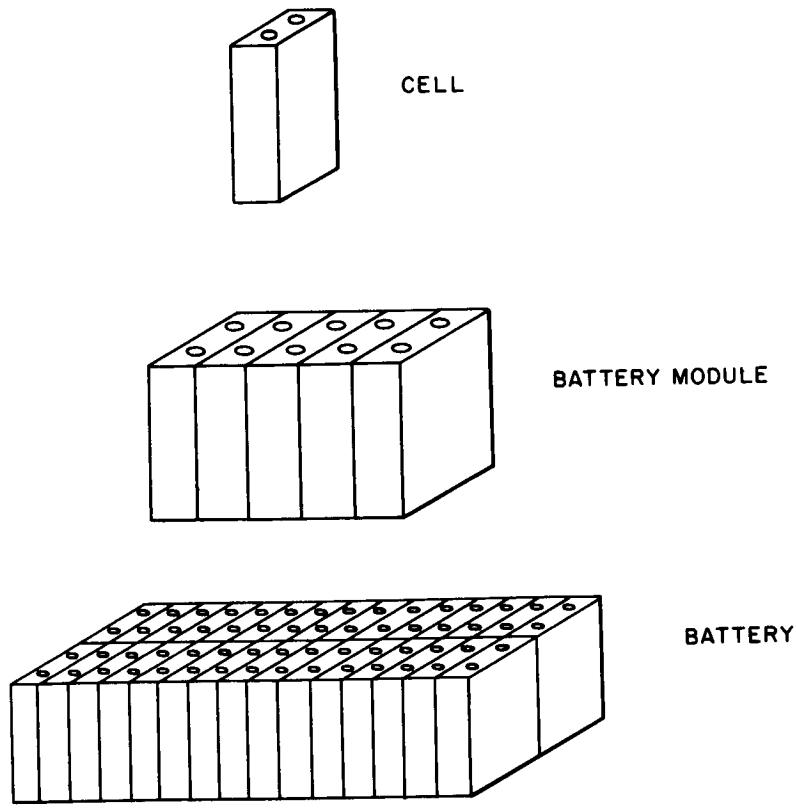

Figure VI-15. Battery Terminology

SECTION VII

MECHANICAL SYSTEM ANALYSIS, CONCEPT A (IPS)

A. INTRODUCTION AND SUMMARY

This section covers the mechanical system design and analyses for a 4900-square-foot solar array and the mechanical and electrical components necessary to orient the plane of the solar-cell array normal to the sun vector for all orbit inclinations. Analyses indicated that modifications to the payload launch configuration would be required to house the 4900-square-foot solar array within the LEM shroud. These modifications involve the shroud profile and will require the relocation of the MMSS shroud separation point and a new MMSS S-IV-B adapter. The launch configuration for the entire assembly is shown in Figure VII-1.

After considering a number of possible solar array structural design concepts, an all-aluminum, bowed-frame, honeycomb combination was selected. The design permits flat stowage of the array for the launch condition and a bowed configuration when deployed. The

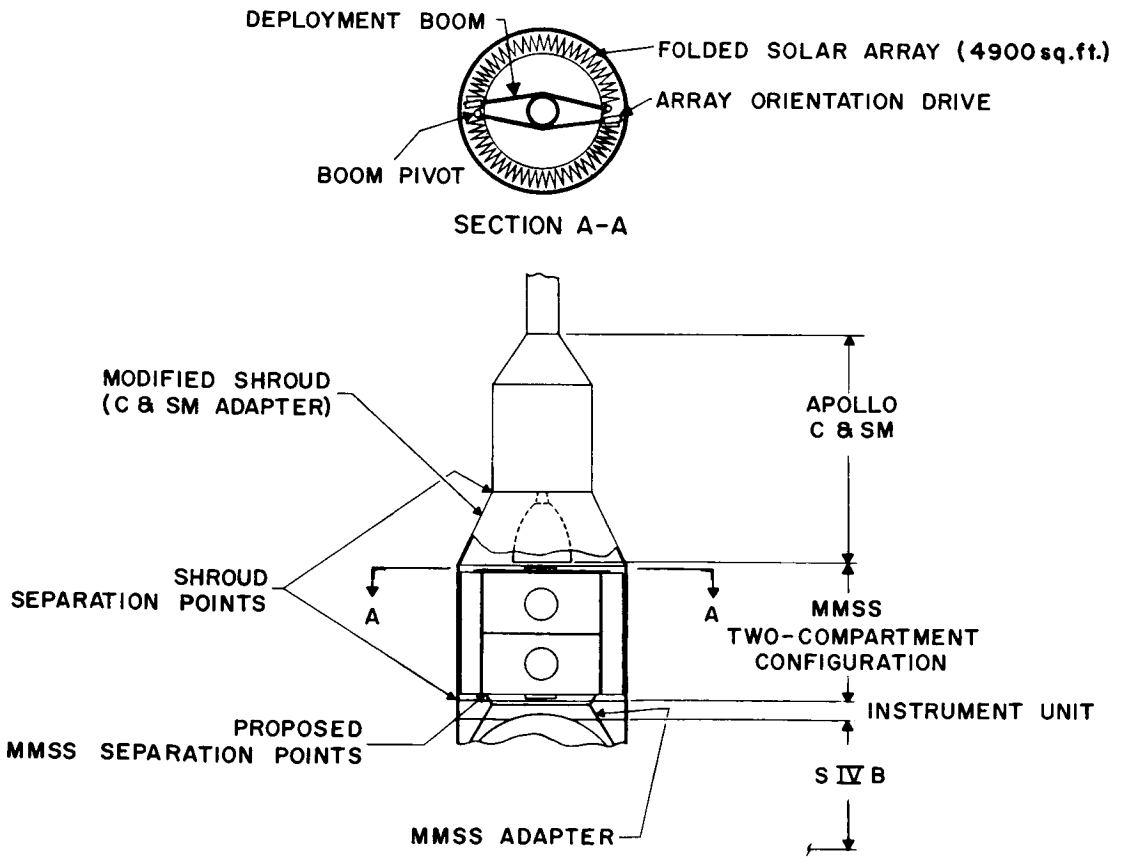

Figure VII-1. MMSS and Solar Array Stowage in Launch Vehicle

design chosen was lighter than other concepts considered and when bowed has better section properties than a flat configuration. With this concept the solar array weight is 0.823 lbs per square foot. The deployed solar array nighttime temperature, when in synchronous altitude, was calculated to be -155°C. While this temperature represents an extension of what has been space proven, it is considered achievable without major problems or utilization of unproven techniques.

Two degrees of rotational freedom are required to position the array normal to the sun. With this design requirement in mind an orientation drive for the solar array was selected and conceptually designed. Slip rings will be used for power transfer through the rotating joints. The choice was made after consideration of a number of other methods. The orientation drive assembly (which consists of slip rings, torque motors, and a gear reduction unit) will be sealed by a labyrinth seal.

The array is deployed from the stowed to the deployed position by double-acting pneumatic cylinders with cables and pulleys. The satellite orbital configuration shown in Figure VII-2 permits rotation about two axes. These axes were chosen to eliminate array-on-array shadowing and to minimize vehicle-on-array shadowing. Docking loads and Service Propulsion System (SPS) engine firing loads applied to the array and booms were investigated. Various orientations of the array relative to these applied loads were considered. For docking, any orientation except column compression can be utilized. The preferred orientation, which permits maximum maneuvering clearance for the docking vehicle is shown in Figure VII-3.

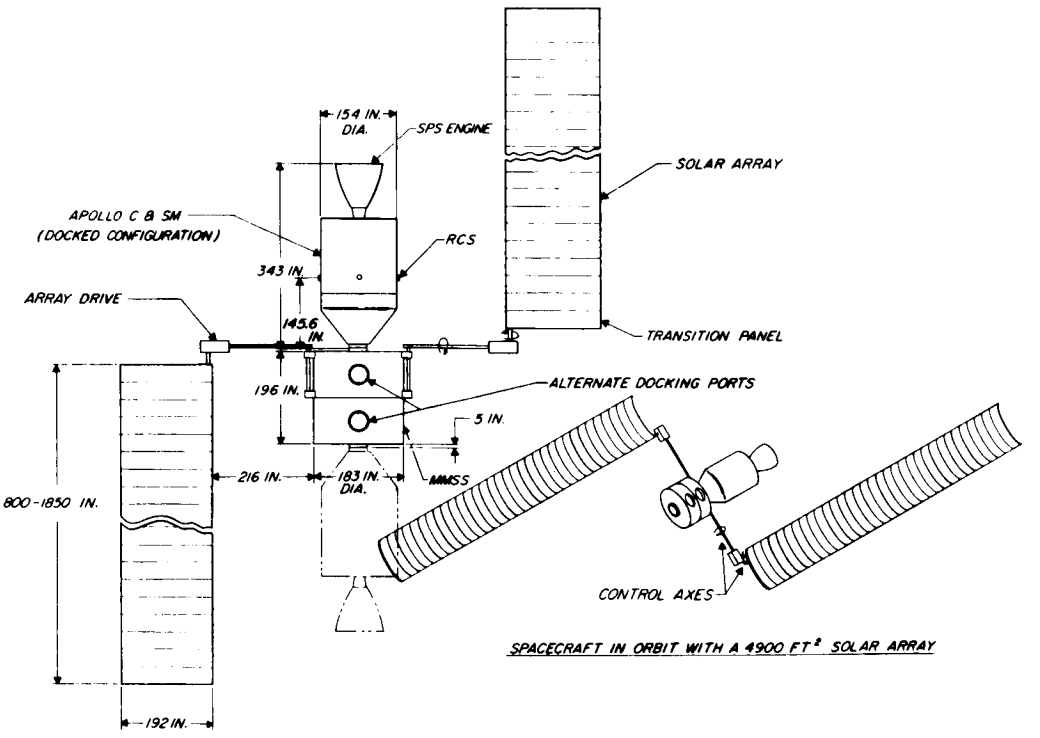

Figure VII-2. MMSS with Solar Array Orbital Configuration

With the present structural configuration of the array, only an orientation mode that places the array in a tensile mode may be used for SPS engine firing. In this mode, the effects of the SPS engine plume must be considered. However, by the addition of a presently undetermined quantity of structural weight, an orientation may be attained to place the array in the strong-axis bending mode, as shown in Figure VII-4, to eliminate the effects of the plume.

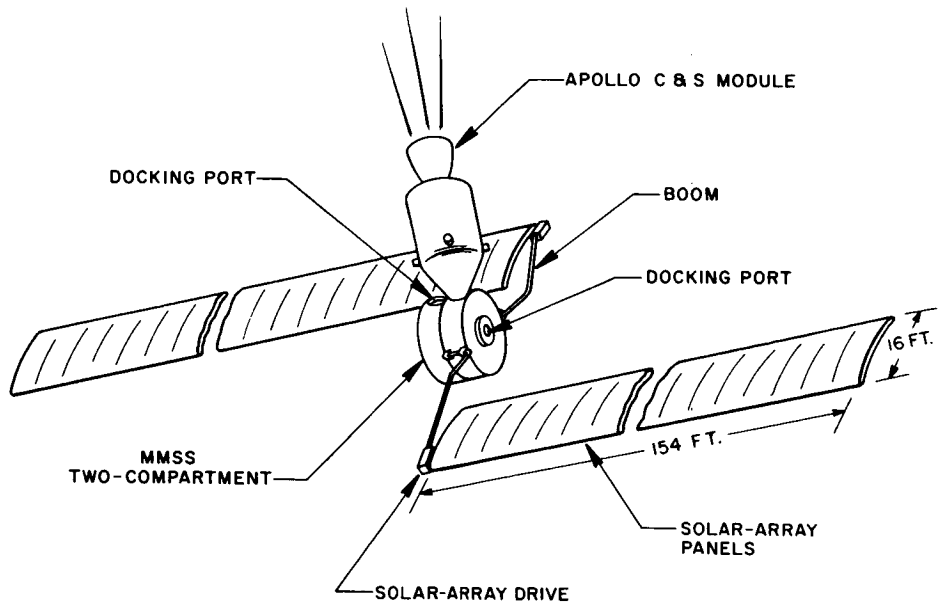

Figure VII-3. Preferred Docking Configuration

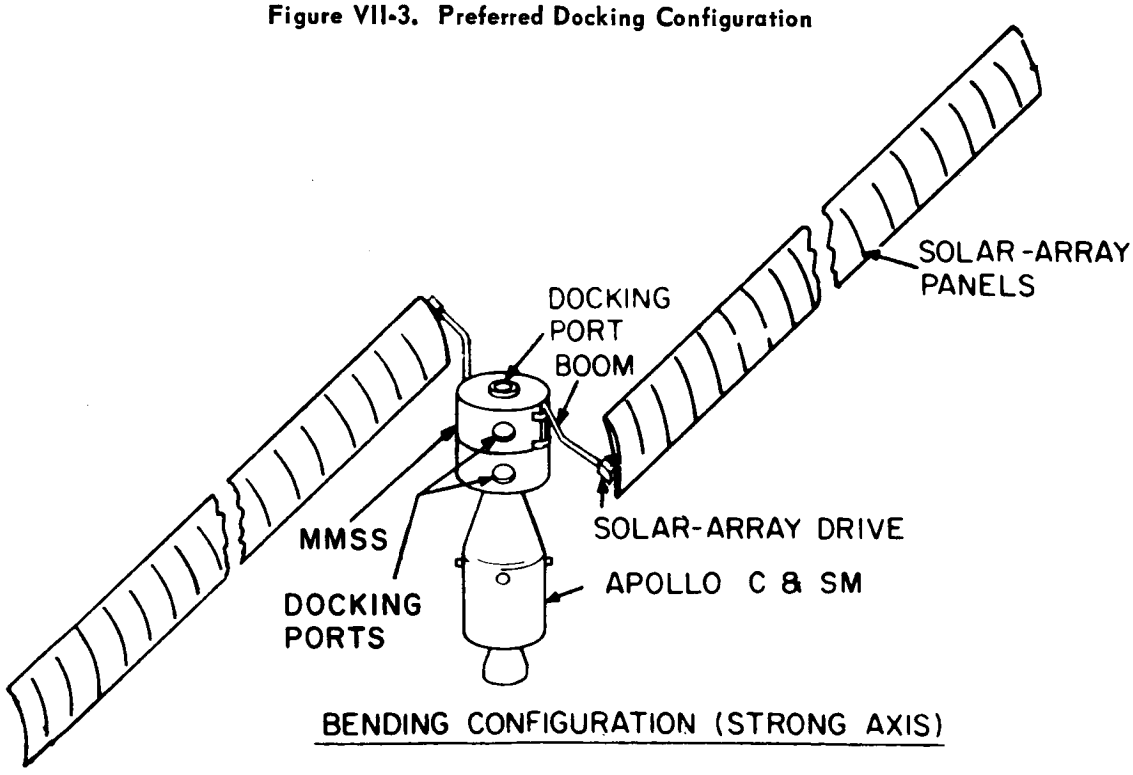

Figure VII-4. Desirable SPS Engine Firing Mode, Solar Array in Strong-Axis Bending

B. STOWAGE ANALYSIS

1. General Requirements

An array area of 4900 square feet was established as the maximum requirement based on predicted worst-case mission parameters and maximum electrical load. Before investigating specific stowage methods, a set of stowage guidelines was generated.

a. ARRAY SUPPORT REQUIREMENTS

The stowed array will be entirely supported by the MMSS during launch. This would eliminate the following requirements or conditions:

(1) An additional array/launch-vehicle interface.

(2) Problems caused by relative motion of more than one interface attachment.

(3) A dual interface separation mechanism.

This concept also allows the MMSS-solar array combination to be separately assembled and tested prior to mating with the launch vehicle, thus simplifying both procedures.

b. POSITION REQUIREMENTS FOR STOWED PANELS

The array should be stowed and the panels efficiently supported so that launch-induced stresses are minimized. Since the launch acoustic-noise environment is omnidirectional, the method of stowed panel support (rather than stowed orientation) is critical. However, when sine and random vibration environments are considered, the higher magnitude thrust-axis inputs indicate that, for optimum panel mounting, large surface areas should be oriented parallel to the thrust axis to minimize the resultant membrane response. The dynamic panel deflections must not physically damage or degrade the solar cells.

c. DEPLOYMENT REQUIREMENTS

The stowed array should be capable of deployment to an acceptable operational (orbital) configuration with a minimum of complex kinematics. This requirement is closely related to the orbital configuration and the two axis array orientation technique.

2. Evaluation of Stowage Locations

The volume initially available for solar-array stowage within the existing LEM shroud and external to the two-compartment MMSS is shown in Figure VII-5. Locations A and B were chosen as the most feasible volumes for array stowage. As indicated in Table VII-1, neither volume is large enough to stow the required 4900 square feet. The array area indicated for location A is optimistic since neither the LEM Truss Adapter interface nor the 15° separation angle clearance requirement was included in the analysis. Volume A, while providing greater array storage capability, requires small panels which, because of

TABLE VII-1. ARRAY STOWAGE LOCATIONS

AREA REQUIRED: 4900 FT^2

PARAMETER \ LOCATION	A	B	ALTERNATES 1	2	3	4
TOTAL AREA, FT^2	3985	1575	4900	4900	4900	4900
PANEL SIZE, FT^2	24	197	45	45	52	197
*NO. OF PANELS	166	8	109	109	95	25
FOLD AXES	NONE	ONE	ONE	ONE	ONE	TWO
DEPLOYMENT	MANUAL	AUTO	AUTO	AUTO	AUTO	AUTO
MODIFICATIONS REQ'D.	NONE	NONE	SHROUD AND ADAPTER	192" CYL. SHROUD AND ADAPTER	149" CYL. SHROUD AND COLUMN LENGTH	87" CYL. SHROUD LENGTH
REMARKS	ASSEMBLE ARRAY IN ORBIT	DUAL AXIS DEPLOYMENT	---	---	SUPPORT COLUMN PROTRUDES	DUAL AXIS DEPLOYMENT

* ASSUMED PANEL THICKNESS PLUS CLEARANCE 2.5 INCHES

their triangular shape, would require an extremely complex automatic deployment scheme. Realistic deployment from this configuration would necessitate manual assembly of individual panels by the astronauts, once orbit was achieved.

The relatively large (15-foot-diameter) panels stowed in Volume B would require more complex mounting methods, stiffer panels, or snubbers to minimize panel deflection due to vibratory loads. Due to these restrictive limitations, the possibilities of a shroud modification were evaluated. NASA-MSC's approval was given to consider and propose modifications to the LEM shroud. Figure VII-6 and Table VII-1 summarize four alternatives investigated.

The following observations were made for the alternate stowage concepts. See Figure VII-6 for illustrations.

- All the concepts require shroud modifications.
- Concepts 2, 3, and 4 require a dimensional change between the instrument unit (IU) and the Apollo command and service (C & S) module, thus lengthening the payload configuration.
- Concepts 2, 3, and 4 require a more complex method of removal of the payload by the Apollo C & S module unless another separation point is provided.
- Concepts 1 and 2 require a modified MMSS adapter.
- Concept 3 requires a protuding column; this column may, however, be used for a docking tunnel or for additional equipment housing.

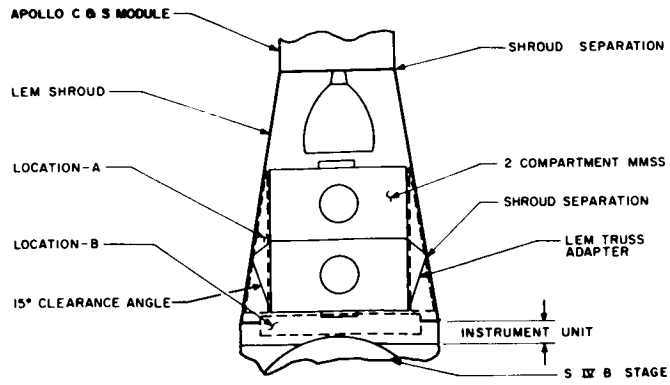

Figure VII-5. Existing Stowage Location

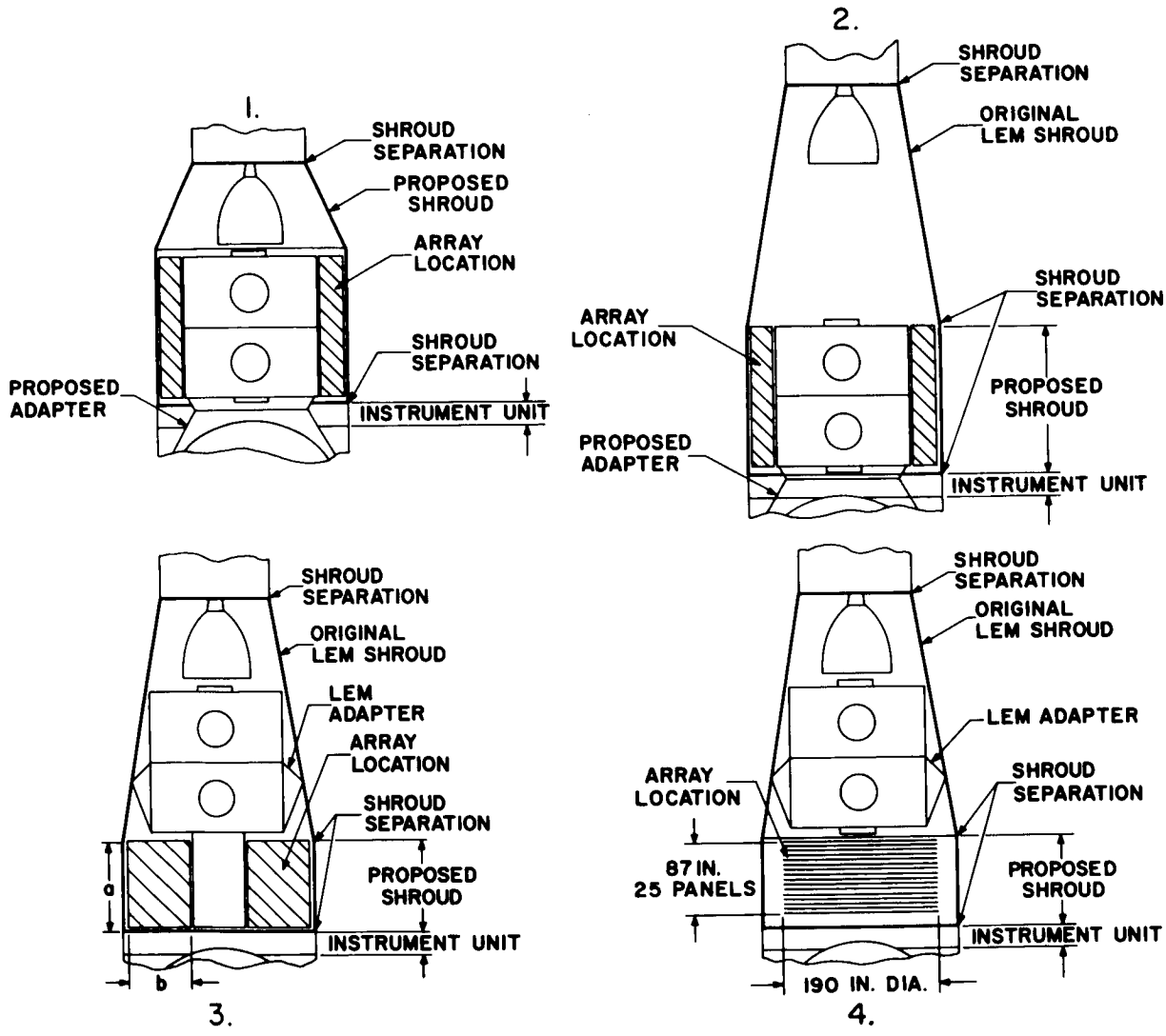

Figure VII-6. Alternative Stowage Locations Considered

In consideration of the preceding, concept 1 was selected for further study, primarily because of maximum utilization of volume between the existing IU and Apollo C&S module stations and the requirement for only two shroud separation points.

3. MMSS and Solar-Array Stowage

Figure VII-7 shows the adapter-mounted MMSS with the solar array in the stowed position. The array interfaces with the MMSS only and is therefore independent of launch-vehicle mounting and spacecraft separation mechanism. The solar array is divided into symmetric halves, each half consisting of 26 identical panel segments and associated deployment and orientation hardware. 180 degrees of MMSS circumference is allotted for the stowage of each half array.

The array panel segments are folded in an accordion fashion around the MMSS. Although the frame members of the individual panels are fabricated in a curved profile*, they are elastically deformed into a flat configuration when folded about their vertical (parallel to thrust axis) hinge lines. This flat-panel stowage method makes good use of the cylindrical stowage volume.

---

*The curved profile is NOT required for stowage, but results from orbital configuration loads and deflections.

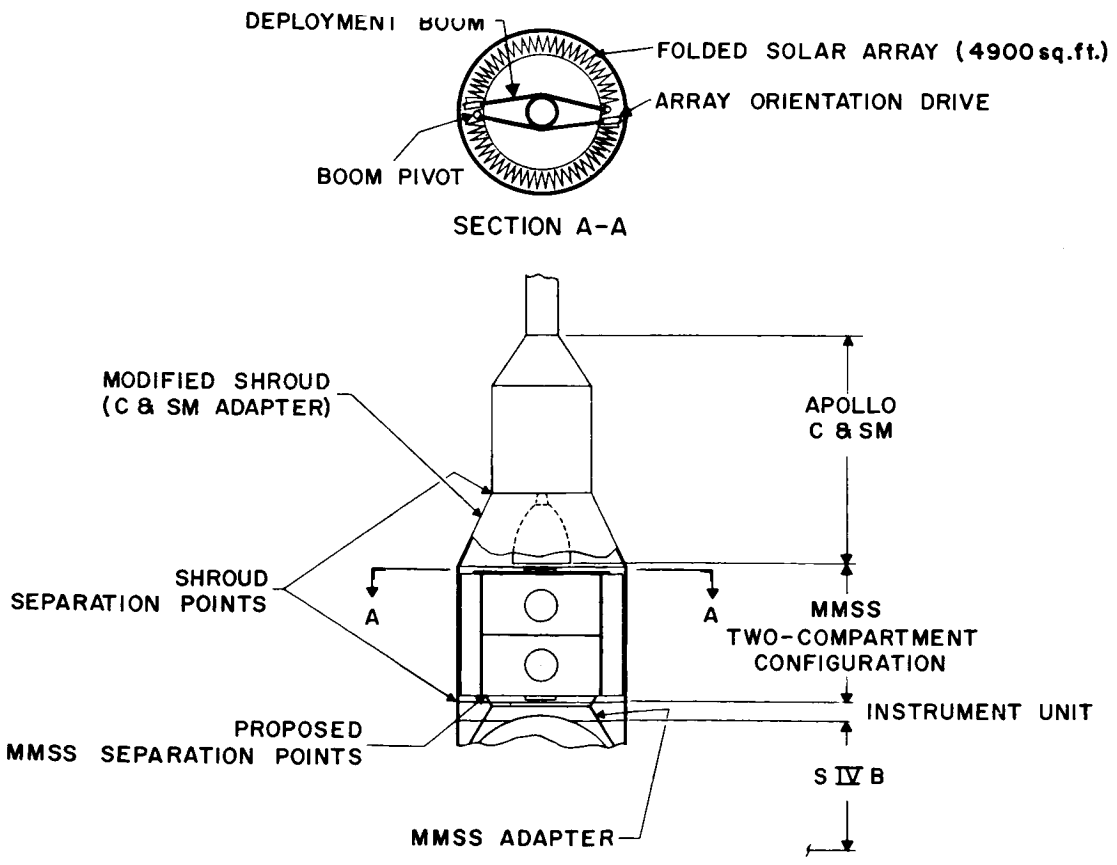

Figure VII-7. MMSS and Solar Array Stowage in Launch Vehicle

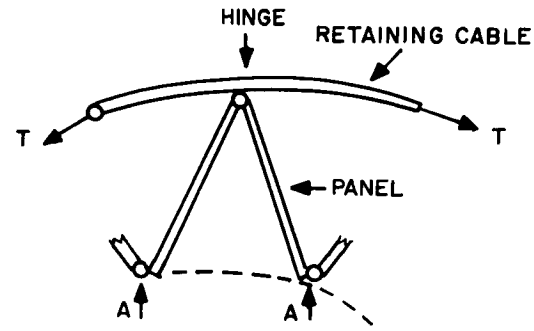

Figure VII-8. Truss Arrangement, Stowed Panels

Figure VII-8 shows the triangular truss that is basic to the panel-support method. Two preloaded circumferential cables (7800-pound tensile load) bear against the outer hinges of the folded array and hold the hinged panels against the MMSS. Points A represent shear fittings on the MMSS circumference which mate with the hinges of each panel. The truss concept permits ample dynamic clearance between the panels and shroud and provides a stable, self-reinforcing structural module.

Two shear fitting mounting rings (Figure VII-7) are attached to the MMSS structure to permit variation in the circumferential spacing of the shear fittings according to the number of panels (i.e. total array area) used on a specific mission. Separation of the array from the shear fittings is accomplished by severing the preloaded retaining cables. The portions of the shear fitting track crossing the side docking ports will have provision for explosive jettisoning after deployment. The vertical distance between shear fitting mounting rings on the MMSS must be accurately located to minimize vibration response. If the stored energy in the array released by cutting the cables is not sufficient to cause the array to separate from the shear ties, spring loaded plungers in the shear ties will provide a positive separation force.

The two booms necessary for array deployment are folded across the top of the MMSS, with their free (array) ends supported during the launch phase. These booms are so shaped that with the array stowed, the upper docking port of the MMSS remains accessible. A transition panel (discussed later) joins the end of the boom and the first solar-panel segment.

C. ARRAY STRUCTURE ANALYSIS

1. Introduction

The design of the array structure was governed by the requirements for a light-weight (less than 1 pound-per-square-foot design goal) sun-oriented array, fabricated with existing state-of-the-art methods and materials. Limitations were imposed on the array structure by the launch-vehicle mounting interface, geometry of the stowage volume, and the deployment concept employed. Environmental loads during the launch, ascent, orbital flight, docking and orbital-maneuver phases of the mission were considered in developing the array structural configuration.

The primary function of the structure is to mechanically support the solar cells during the various mission phases and also provide the functions listed in the following:

(1) A two axis, sun-oriented platform for maintaining the solar cell plane normal to the sun vector.

(2) A support for electrical power buses that transfer energy from panel to panel and from the panels to MMSS.

(3) A low-impedance thermal path from the sun side to dark side of the panels in order to maintain a high solar-cell efficiency (low day-time temperature) and to minimize thermal distortion in the structure.

2. Concept Development

Some of the existing and proposed satellite solar array structures were reviewed in making a comparison of present "state-of-the-art" concepts. Included in the comparisons were flight experience, structural materials, fabrication techniques, and solar-cell temperature extremes. Table VII-2 provides a list of the various satellite solar-array structures.

The review revealed that lightweight array designs were achieved through the use of beryllium, new methods of fabrication such as electroforming or prestressed tape or trampoline concepts. The use of beryllium as a primary structural member was ruled out due to the high costs involved and the unavailability of sheet stock in the size required. (However, an analysis was made in Paragraph VII-C-5 to show the weight savings involved utilizing beryllium for the concept used in this study.) At the present time, beryllium is not produced in the sheet size required (4 ft. x 8 ft. x 0.0037 in.) for honeycomb facings. The prestressed tape and diaphragm concepts, which also use beryllium for supporting frames, were not adopted because of the material used, the unknown dynamic response of these concepts, and the very low temperature (approximately -200°C, see Figure VII-9) that these types of solar arrays would reach at a synchronous altitude. Of the remaining two concepts (corrugated and honeycomb sandwiches) the weight differential is negligible and either choice would be acceptable. In Paragraph VII-C-4, a honeycomb sandwich is compared with a combination honeycomb plus structural frame concept. In this comparison the honeycomb plus frame proved to be the minimum-weight design. This method will meet the structural design goals and satisfy the requirement for state of the art. These factors led to the choice of this method for further study. In addition, RCA has a considerable amount of experience on similar structures that have been flight-proven on satellites such as Lunar Orbiter, Nimbus, Relay, and other (classified) programs.

3. Factors of Safety and Design Criteria

The factors of safety used provide a high degree of structural reliability for manned spaceflight. In addition these factors of safety are commensurate to those employed by the Lockheed Aircraft Company in the design of the MMSS laboratory. (See Reference VII-4) The design ultimate load is 1.5 times the limit load; the limit load is established as the maximum actual load experienced during all phases of the mission. This includes ground handling,

TABLE VII-2. EXISTING SOLAR ARRAY STRUCTURE DESIGNS

Satellite	Brief Structural Description
Tiros	Stiffened sheet-metal panels (0.062" thick - aluminum)
Classified	Honeycomb panels (0.38 lb./sq ft. solar-cell substrate only)
Relay	Honeycomb (0.375" thick)
Nimbus	Honeycomb - Internal stiffeners (aluminum), variable core density
Ranger	Corrugated sheet - 0.016 aluminum (1.03 lb./sq ft., solar-cell substrate & fittings)
Lunar Orbiter	Combined aluminum honeycomb and sheet metal stiffeners (0.25" honeycomb core)
Mariner/Venus	Corrugated sheet - .016 aluminum (1.013 lb./sq ft. solar-cell substrate & fittings)
Pegasus	14' x 48' detection panels (two), polyurethane foam cure with aluminum mylar copper laminate skin (Solar Panels - Aluminum honeycomb)
Transit V-A	Corrugated sheet 0.008" aluminum (0.6 lb./sq ft. solar-cell substrate & fittings)
Mariner/Mars	Corrugated sheet 0.012" aluminum with facing on one side (0.978 lb./sq ft. solar-cell substrate & fittings)
Explorer 22	Corrugated core laminate assembly
OGO	0.40" cross rolled sheet beryllium
OSO	Aluminum alloy sheet metal

ground testing (qualification tests), pre-launch, launch, and orbital flight. Design yield load is 1.15 times the limit load for the launch and pre-launch environment; 1.20 times the limit load for the flight mission, and 2.0 the limit load for ground-handling phases.

Limit loads established for the design of the solar array are based upon the launch environment of the Saturn V and Saturn I-B launch vehicles (higher load level used), the loads due to docking of the Apollo C&SM and the thrust loads resulting from firing of the Apollo SPS engine. Orbital environmental loads are contingent upon the particular orbit selected and,

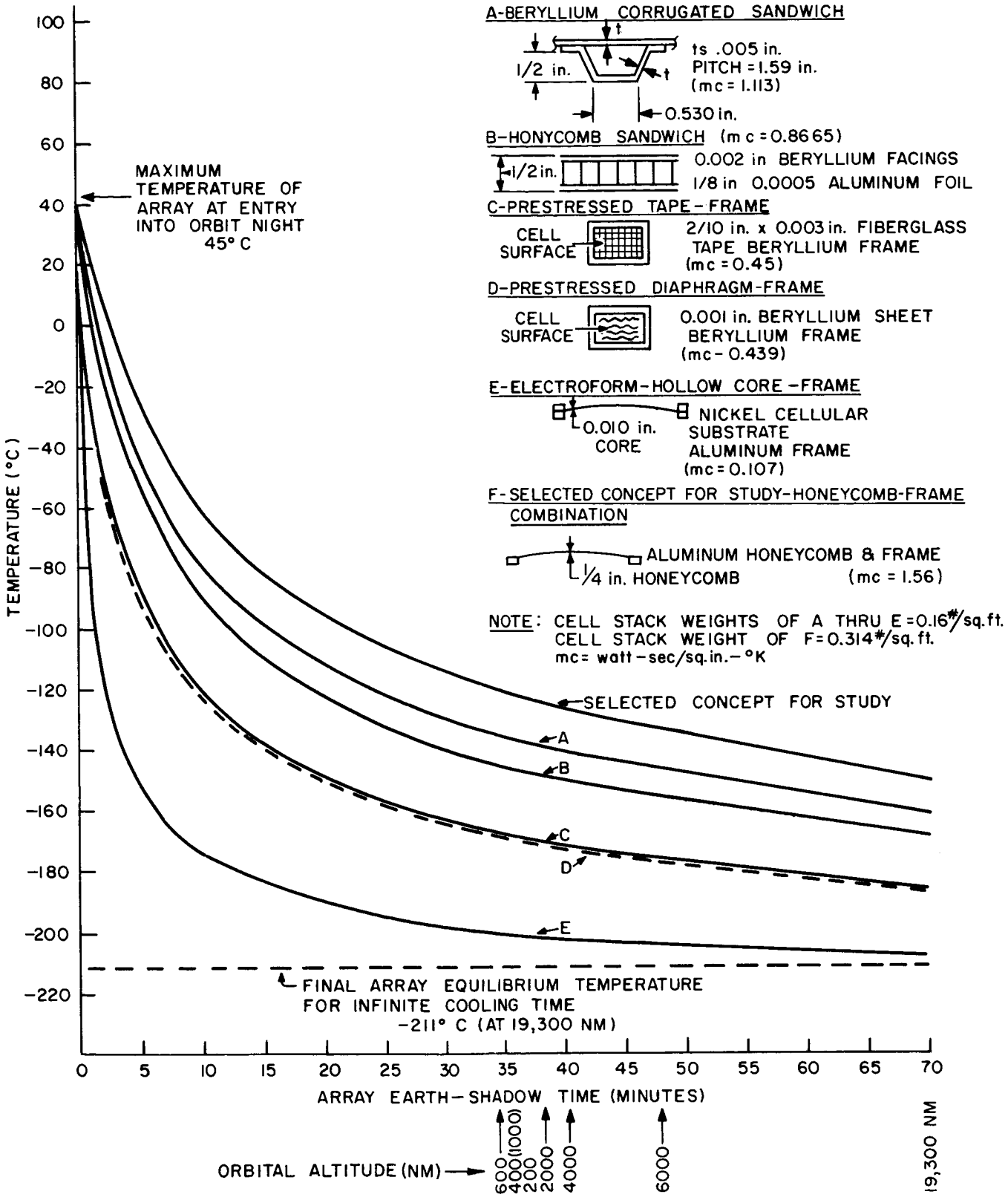

Figure VII-9. Substrate Concepts; Nighttime Temperature Comparison; Thermal-Mass Effect

TABLE VII-3. SOLAR PANEL STRUCTURAL CONCEPTS

Panel Configuration	Source	Loads	Structural Configuration	Structural Specific Weight (lb/sq ft)	Weight Index	Remarks
A						
1. Corrugated sandwich	Ref. VII-5	Based on solar cell stack weight of 0.16 lb./sq ft	58.6 in. x 120.1 in. simply supported at ends with over-hung sides	0.2528	1.370	Fabrication utilizes beryllium material. Present state-of-art is aluminum or magnesium
2. Honeycomb sandwich 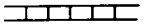		** Q = 40 for panel Q = 10 for frame	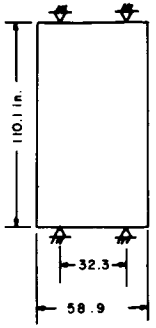	0.2548	1.380	1/2 in. aluminum core x 0.002 in. beryllium facing, 1/8 in. core density with 0.005 in. aluminum foil. Present state-of-art is aluminum.
3. Prestressed tapes (trampoline)				0.1890	1.022	0.20 in. x 0.003 in. fiberglass tape stretched over a beryllium frame. Requires development for response of membrane to vibratory loading, and development of solar cell stack to survive -190°C nighttime temperature in synchronous altitude.
4. Prestressed diaphragm				0.1849	1.000	0.001 in. beryllium foil over a beryllium frame. Requires development for response of membrane to vibratory loading and for solar cell stack to survive -190°C nighttime temperature in synchronous altitude.
5. Hollow core biconvex design (electroform)				0.1907	1.030	Nickel substrate and aluminum frame. Top and bottom facing supported by cylinders. Predicted to provide optimum lightweight design by 1970 in aluminum substrate and beryllium frame. Synchronous altitude nighttime temperature is -208°C.
B						
1. Corrugated sandwich	Ref. VII-6	Based on solar cell weight 0.3 lb./sq ft 10 watts/sq ft 20 watts/lb. design goals	Based upon simply supported beam lengths which vary from one concept to another	0.20 0.50 (total)*	—	Study indicates beryllium could deliver 18 watts/lb. Not considered present state-of-the-art, for fabrication and material availability. Aluminum could not meet design goals.
				—	—	Beyond the present state-of-the-art, could deliver 10.5 watts/sq ft.
2. Flexible rollup				0.1988 0.4988 (total)*	—	Selected by Boeing as design for 20 watt/lb. solar array.
3. Prestressed tape						

*Includes Cell Stack
**Transmissibility

to a lesser extent on the stability of the orbiting vehicle. Launch vehicle environmental data was obtained from References VII-1, VII-2, and VII-3. These environmental launch loads are shown in Figures VII-10 through VII-13. The orbital perturbation environmental loads are covered in Section IX. However, these loads are small in magnitude and do not influence the structural design of the array. An analysis of the launch loads (when the solar array is in the stowed position) indicates that the governing environmental load for this phase is acoustic noise, which results in a design requirement for the array of 20-g response. The governing orbital loads are docking and the firing of the SPS engine. These two loads are handled in a special way and are discussed in Paragraph VII-F (Satellite Orbital Configuration). A summary of the design limit loads appear in Table VII-4.

4. Array Structural Design Comparison

An analysis of three potential structural configurations was made to provide a basis for selection. These configurations were:

(1) Flat honeycomb

(2) Bowed honeycomb

(3) Bowed frame plus honeycomb

The results of this analysis are shown in Table VII-5. Comparison of these results clearly shows the advantage of the bowed honeycomb design in both weight and stiffness. For similar weight the bowed honeycomb shows a stiffness advantage of 17.8 in^4/1.94 in^4 or 9.18. This is further demonstrated in the array tip deflection due to docking loads, where the comparison is between 160 inches (bowed) and 1515 inches (flat). (The 1515-inch deflection is equal to 82 percent of the array length). The stiffness of the flat panel can be increased to a value comparable to that of the bowed panel, but at a significant increase in structural weight.

In comparing a bowed-frame-plus-honeycomb structure to the bowed honeycomb, it is seen that for a comparable stiffness the weight penalty amounts to 23 percent. It is clear that the bowed-frame-honeycomb is superior to the other concepts listed in Table VII-5. For this concept, the primary load-carrying members are the frame with the honeycomb acting as a solar cell substrate but carrying its share of the load. The frame members carry the stowage loads at the MMSS interface and also act as hinge mounting points for tension or compression load paths in the deployed configuration. Because of stowing ease (See Paragraph VII-C-6) and the other reasons discussed previously, the bowed-frame-honeycomb has been selected as the structural concept for the panel. The panel structural cross section is shown in Figure VII-14.

5. Comparison of Beryllium and Aluminum for Structural Members

In view of the high stiffness and low-density advantage of beryllium, a comparison was made of beryllium and aluminum as structural materials. A 43 percent weight reduction of the structure is possible if beryllium is used for the structure instead of aluminum. If

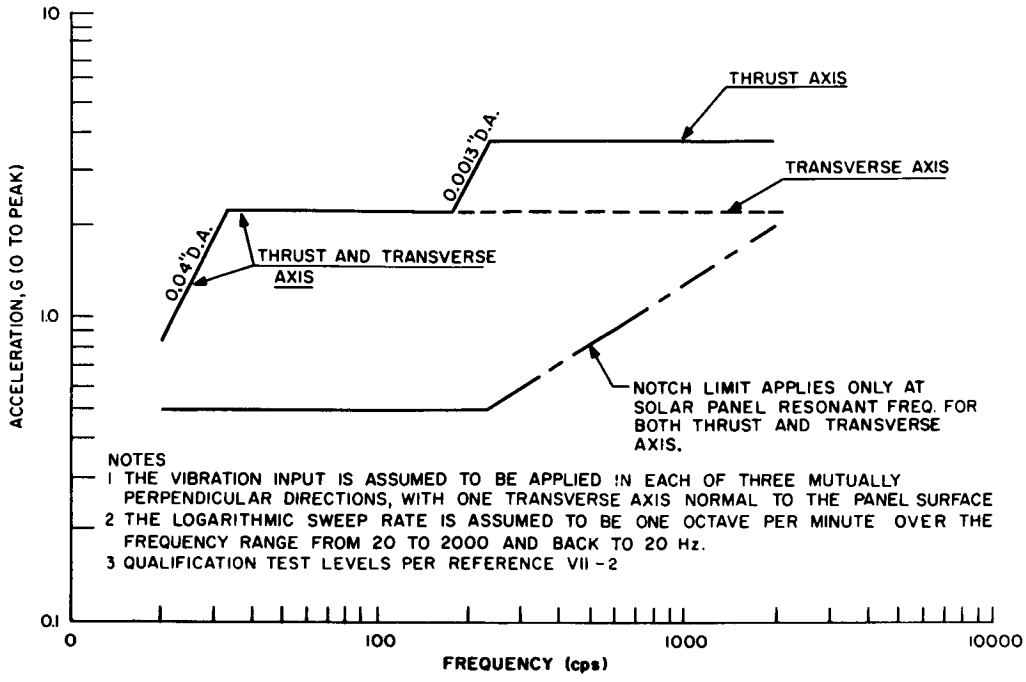

Figure VII-10. Design Specification for Random Vibration

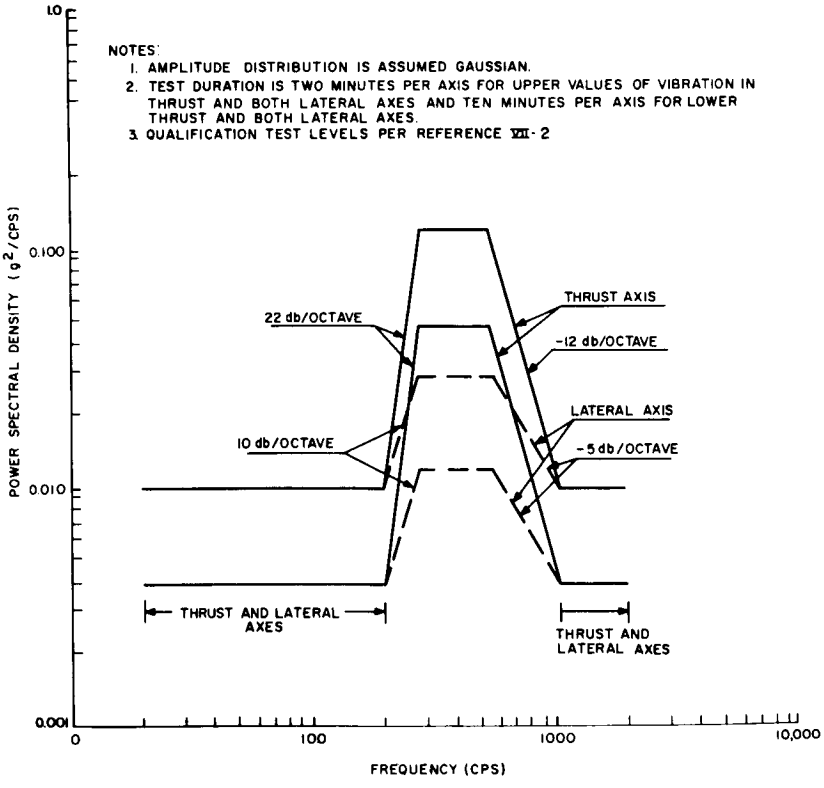

Figure VII-11. Design Specification for Sinusoidal Vibration

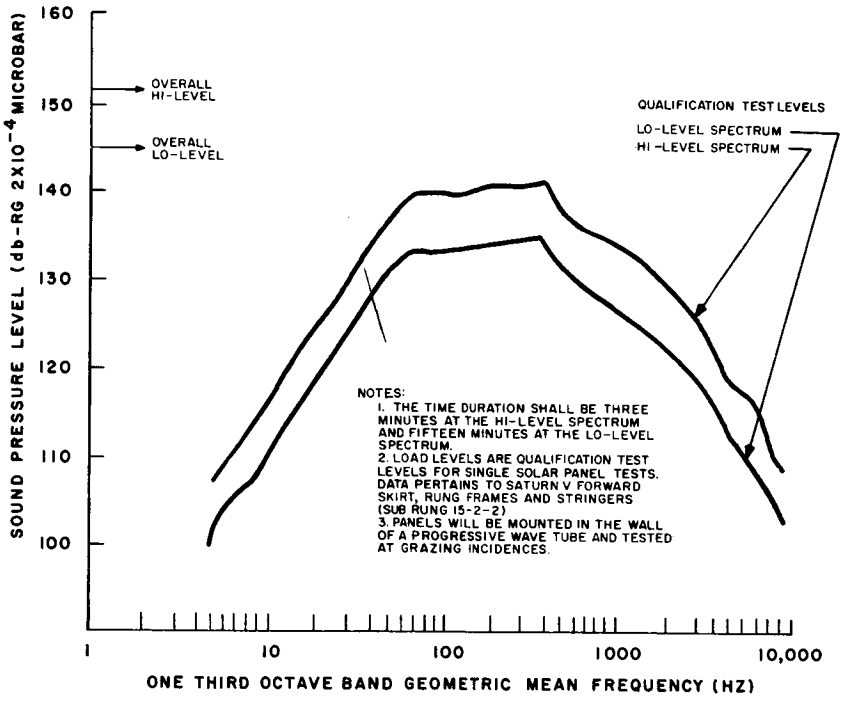

Figure VII-12. Acoustic Noise Design Specification

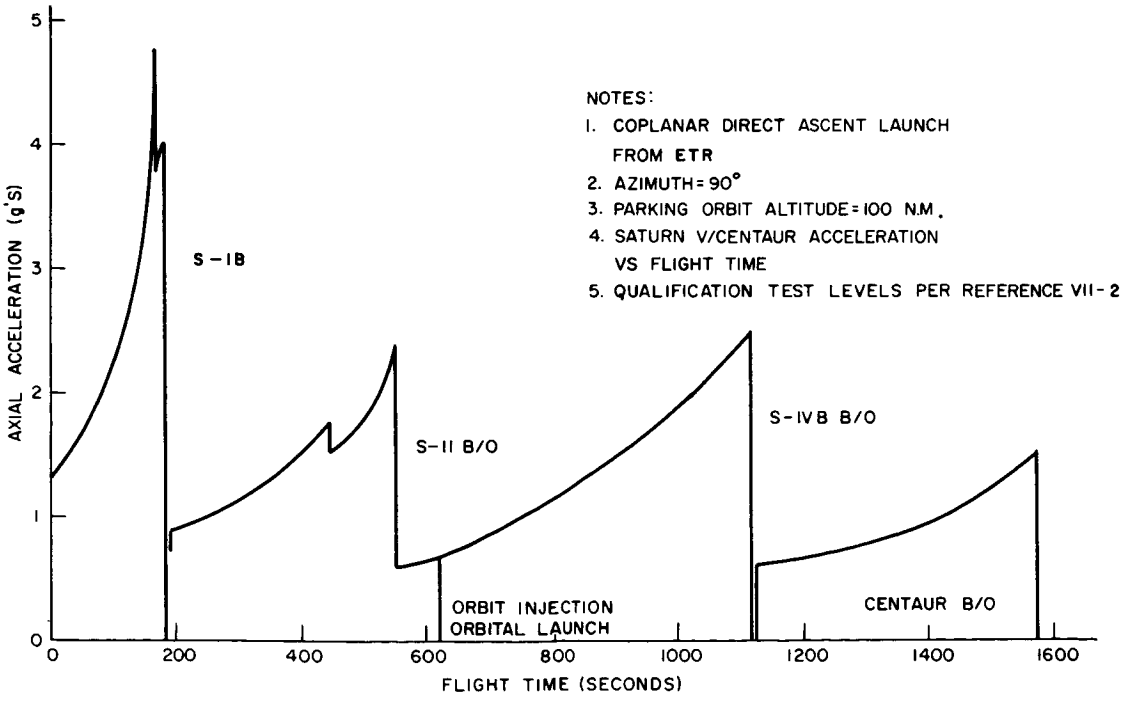

Figure VII-13. Axial Acceleration versus Flight Time

TABLE VII-4. DESIGN LIMIT INPUT LOADS

Load Applied	Design Limit Values
Prelaunch	
Hoisting	2 g
Ground deployment	See Note
Launch	
Sinusoidal vibration	See Figure VII-10
Random vibration	See Figure VII-11
Shock vibration	20 g peak, half-sine wave, 10 milliseconds
Acoustic noise vibration	See Figure VII-12
Ascent acceleration	See Figure VII-13
Orbital flight	
Array orientation angular acceleration	6.6×10^{-5} radians/sec^2
Docking	0.11 g (at Boom-MMSS attach point)
SPS engine firing	0.84 g (at Boom-MMSS attach point)
Orbital perturbation loads	See Section IX

Note:

A ground rule for this study is that deployment of array in a 1-g field (ground testing) shall not govern the structural design of the array.

TABLE VII-5. PANEL DESIGN DATA

Panel Configuration (Material: Aluminum)	Total Array Weight (lbs/ft^2)	Facing Thickness (Inches)	Moment of Inertia (Inch^4)	Docking Tip Deflection (Inches)	Margin of Safety (Stress)	
					Stowed	Deployed
Bowed Frame Plus Honeycomb 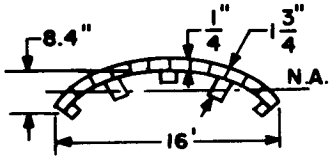	0.82	0.0037	21.92	134	(Frame) 0.13 Honeycomb 0.28	(Frame) 1.7 Honeycomb 0.21
Bowed Honeycomb 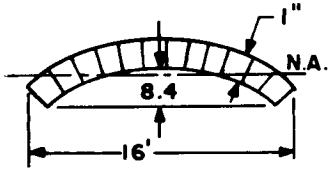	1.09	0.0037	17.8	160	0.91	0.05
Flat Honeycomb 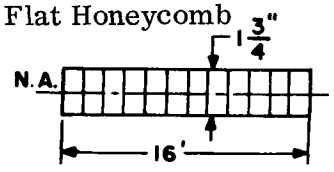	3.17	0.0825	21.92	134	Large	Large
	1.09	0.0054	1.94	1515	Large	0
	1.71	0.032	8.8	333	Large	Large

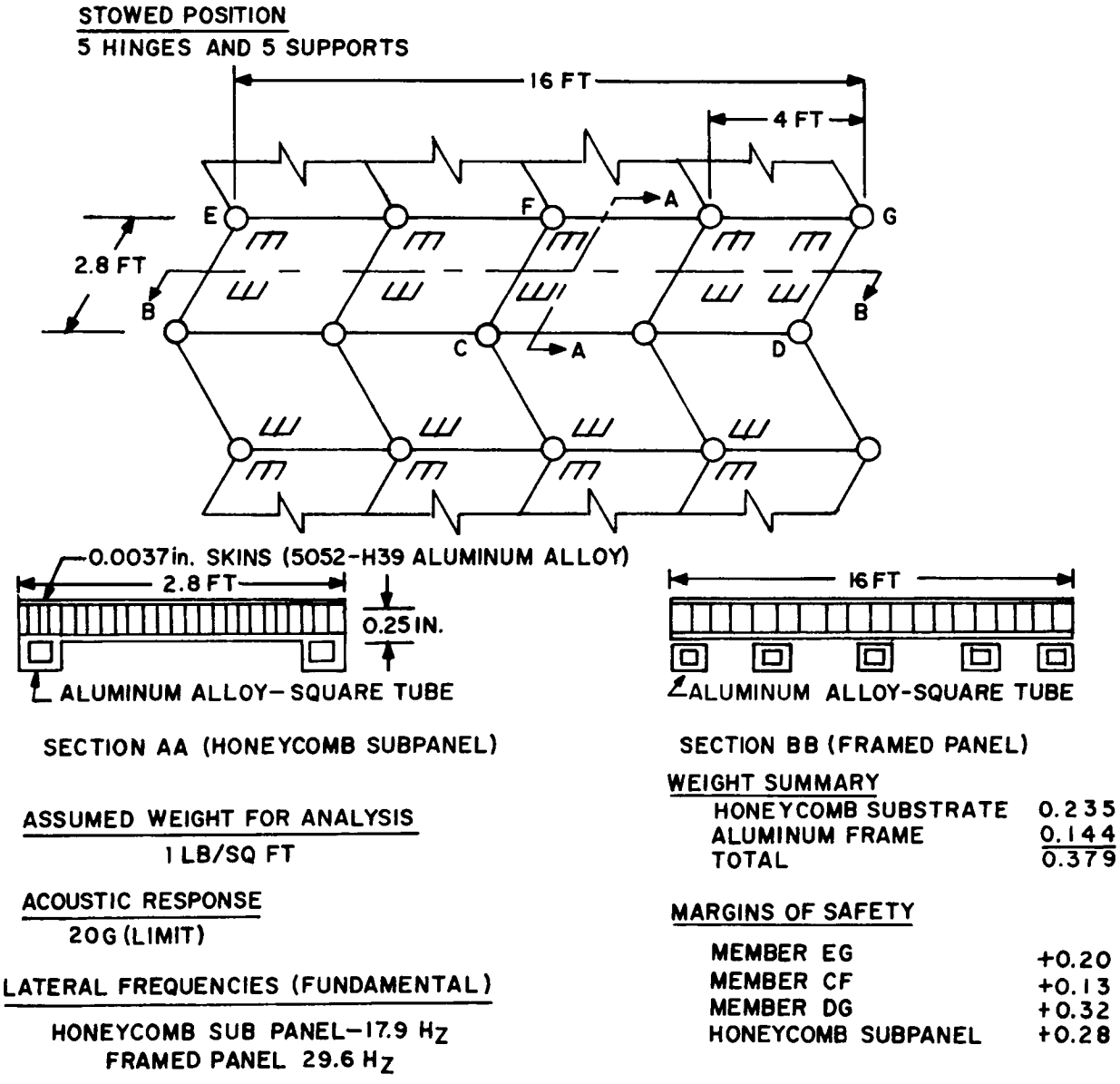

Figure VII-14. Panel Structural Cross Sections

beryllium frames and beryllium facings are used with aluminum honeycomb core, a 41 percent weight reduction of the structure is possible. (However, if the entire array weight is considered, a reduction of approximately 20 percent can be achieved by using beryllium as the structural material.) Unfortunately the size of sheets (4 ft. x 2.8 ft.) in the gauge necessary are not readily available, requiring an undesirable "patch work quilt" type of fabrication. Furthermore, the cost of beryllium is extremely high in comparison to aluminum. The past experience of RCA on the Lunar Orbiter and Nimbus solar panels has provided data for evaluation and prediction of the dynamic performance for an aluminum structure, while there is very limited fatigue data available on beryllium material subjected to cyclic loading. Thus, assuming that the response load for the beryllium and aluminum structures is the same, then the weight advantage that beryllium analytically provides is overshadowed by the uncertainties of its dynamic performance. Table VII-6 gives the detailed breakdown and comparison of the structural weight (analytical) of an aluminum and a beryllium solar panel.

6. Bowed-Panel Concept

The bowed panel, when stowed flat for launch, will experience higher hinge loads than will a flat panel. This is outweighed by the fact that the bowed-panel hinges are not subjected to primary bending moments when in the deployed (bowed) configuration. As a result, the bowed-panel concept does not require locking devices when the array is deployed. On the other hand, the flat panel requires either in-plane or out-of-plane locks to transfer bending moments across the length of the deployed array.

As discussed in Paragraph VII-D-3, the honeycomb substrate would not be prestressed when in the flat stowed configuration. When deployed, however, the honeycomb panel would have 12,300 psi tensile prestresses compared with the allowable value of 40,000 psi. Since compression buckling is generally the critical failure mode for honeycomb construction, this tensile prestress could be advantageous since it would in effect reduce the resultant compression load on the substrate. In addition, the direction of prestress would be along the 16-foot length of the array panels, which is the less significant load direction. The frame members, because of the bow, would be prestressed in the stowed position and because of the relative stiffness of the honeycomb and the frame, would be relatively unstressed in the deployed (bowed) configuration.

Several small scale models of the bowed array demonstrated a "snapping" action during the final phase of deployment. This action, which was anticipated, is the result of a sudden release of the stored energy in the panel during the final phase of transition from the flat to the bowed state. It is expected that the panel and solar cells would successfully survive this "snapping" acceleration without the need for damping, but an analytical determination followed by an equivalent "spring rate" model test would be required to establish this.

Since the increased stiffness factor of the bowed panel is dependent upon the maintenance of the panel bow, the desirability of lightweight chordal ties were investigated (see Figure VII-15). While the study showed that no problem existed under normal operating conditions, such a device could provide for a measure of increased reliability of the structure. The weight penalty for these ties would be negligible, but their implementation would require additional design study.

TABLE VII-6. COMPARISON OF THE CHARACTERISTICS OF BERYLLIUM AND ALUMINUM STRUCTURES

Typical Honeycomb Array Structure

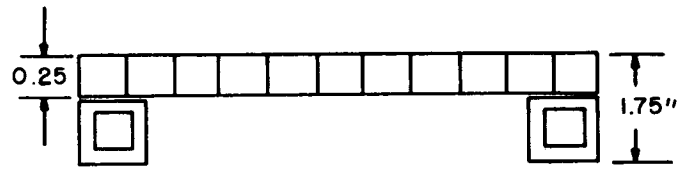

Honeycomb Structure Item	Honeycomb Array Structures		
	Aluminum Core - Cell size - 1/4 in. Aluminum Facings - 0.0037 in. thick Aluminum Frame Members	Beryllium Core - Cell size - 3/8 in. Beryllium Facings - 0.002 in. thick Beryllium Frame Members	Aluminum Core - Cell size - 3/8 in. Beryllium Facings - 0.002 in. thick Beryllium Frame Members
Facings (2)	0.107 lb/sq ft	0.047 lb/sq ft	0.047 lb/sq ft
Core	0.048	0.022	0.034
Adhesive	0.080	0.080	0.080
Frame Members	0.144	0.064	0.064
Total	0.379 lb/sq ft	0.213 lb/sq ft	0.225 lb/sq ft

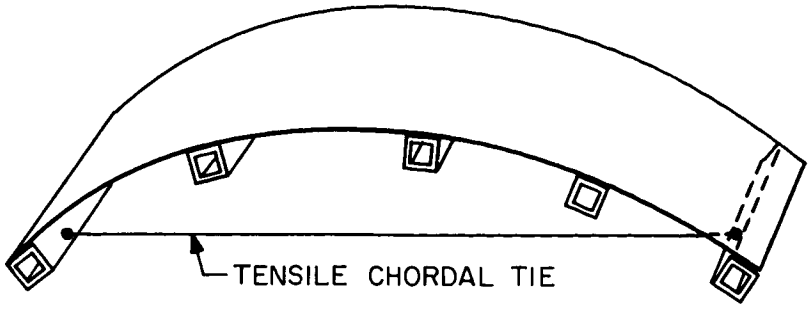

Figure VII-15. Tensile Chordal Tie (Array Bow Exaggerated)

7. Beam of Constant Stress Concept

The desirability of panel grading to enhance array capability in the deployed mode was considered. As described in Paragraph VII-F, the bending capability of the constant cross-section array about its strong axis is 0.75 g. If the panels adjacent to the boom end of the deployed array were designed to have increased section properties (for example, increased frame member cross-section) then for a small increase in total weight of the array, a significant improvement in array capability could be achieved. This modification would then permit the array to be positioned either in the tensile or bending (strong axis) modes for SPS engine firing, thus eliminating heating and other effects of the SPS plume. A detailed analysis will be required to determine the weight penalty involved.

8. Thermal Stress and Deflection

The effect of panel temperature gradients that result from a difference in cross-section within the panel (frame portion - honeycomb portion) was analyzed for stress and deflections. A temperature-time profile of the panel at synchronous altitude was established (nighttime ΔT_{max}, 24°C and daytime ΔT, 52°C) as shown in Figure VII-16. At the points indicated in the figure, a temperature distribution across a typical 48-inch module was determined; this distribution is shown in Figure VII-17.* Thermal-stress and thermal-deflection calculations were based on these curves.

The thermal stress resulting from the thermal gradient between the frame and honeycomb portion of a module were analyzed. The analysis included the consideration of frame flexibility and showed that, along the 2.8-foot width of a module, a compressive buckling stress in the honeycomb of 57 psi existed and a stress of similar magnitude exists in the chordwise (4-foot) direction. The allowable compressive buckling stress for the honeycomb is well in excess of these values and therefore, a large margin of safety exists for thermal loading.

---

*For stress calculation, a $\Delta T'$ maximum of 56°C was used and the distribution of this temperature difference across the panel section was ratioed in accordance with Figure VII-17.

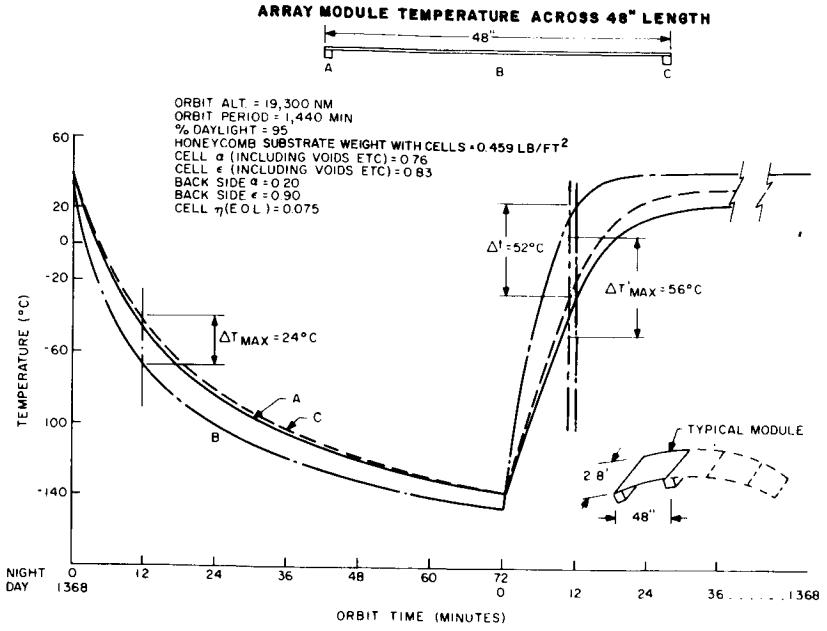

Figure VII-16. Array Module Temperature Distribution During Orbit

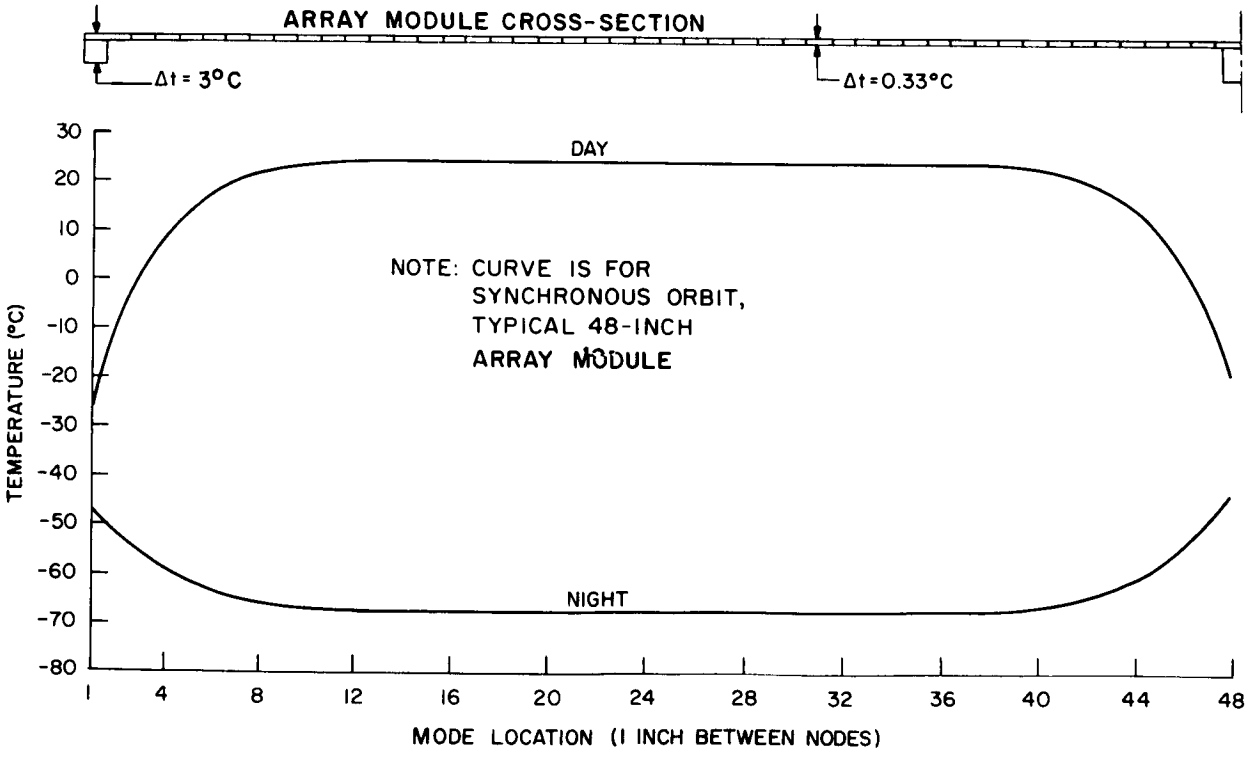

Figure VII-17. Detailed Array Module Temperature Distribution

Calculations for stress and deflection of the array section along its 154-foot span were made utilizing 1.5°C (see Figure VII-17) as the temperature difference between the frame and the adjacent substrate. This temperature difference resulted in a tip deflection of only 2.68 feet, with negligible stress being developed. Thus, it is concluded that thermal gradients do not significantly affect array mechanical performance.

9. Conclusions

The selection of a bowed-frame, aluminum-honeycomb panel structure for the solar array was made after a review of a number of possible concepts and materials. Considerations of the launch-vehicle interface, geometry of stowage volume, array-area requirements, environmental loads, lightweight structural goals, and the utilization of state-of-the-art techniques and materials were important factors contributing to the selection. In addition, flight experience on aluminum-honeycomb-frame, solar-array structures (gained by RCA on the Lunar Orbiter and Nimbus programs) establishes design data experience that results in a high degree of confidence in the design concept selected.

The bowed panel introduces a potential problem area with regard to the transition from the flat stowed position to the bowed deployed position. It is believed that analysis and subsequent testing will prove the ability of the panel and solar cells to withstand the "snapping" acceleration without the need for special precautions. Until this investigation is made, however, the transition acceleration remains an open question.

D. SOLAR ARRAY DESIGN CONCEPTS AND TECHNIQUES

In this portion of the report, structural and electrical elements of the array are discussed. Design approach is indicated and analyses are shown. Those elements of design that either do not lend themselves to parametric analysis or are beyond the conceptual scope of this study are discussed qualitatively.

1. Solar-Array Structure

Having selected the manner in which the array is to be stowed for the launch environment, the dimensions of the individual panels of the array may be determined. The length of the panel is made approximately equal to the height of a two compartment (16 ft) with the width being determined by the clearance between the MMSS and the LEM shroud dynamic clearance envelope. Since the array is stowed in truss fashion around the MMSS, the width dimension of a panel may be larger than the difference in the radial dimension between the MMSS and the dynamic clearance envelope. The extent to which the width dimension can be made larger depends on the array area required. This is apparent as shown in Figure VII-18.

A panel width dimension of 2.8 feet was selected, based on the mechanical requirement of 4900 square feet of solar array. The panel structure is shown in Figure VII-19. As was demonstrated in previous paragraphs, a bowed array (in the deployed mode) yields an increase in section properties without a sacrifice in weight. The radius of the panel bow

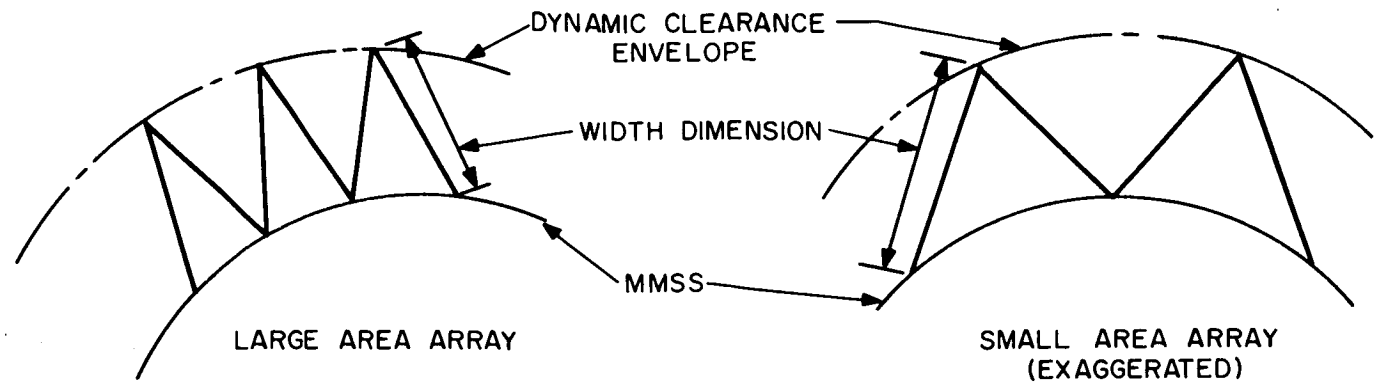

Figure VII-18. Array-Width Determination

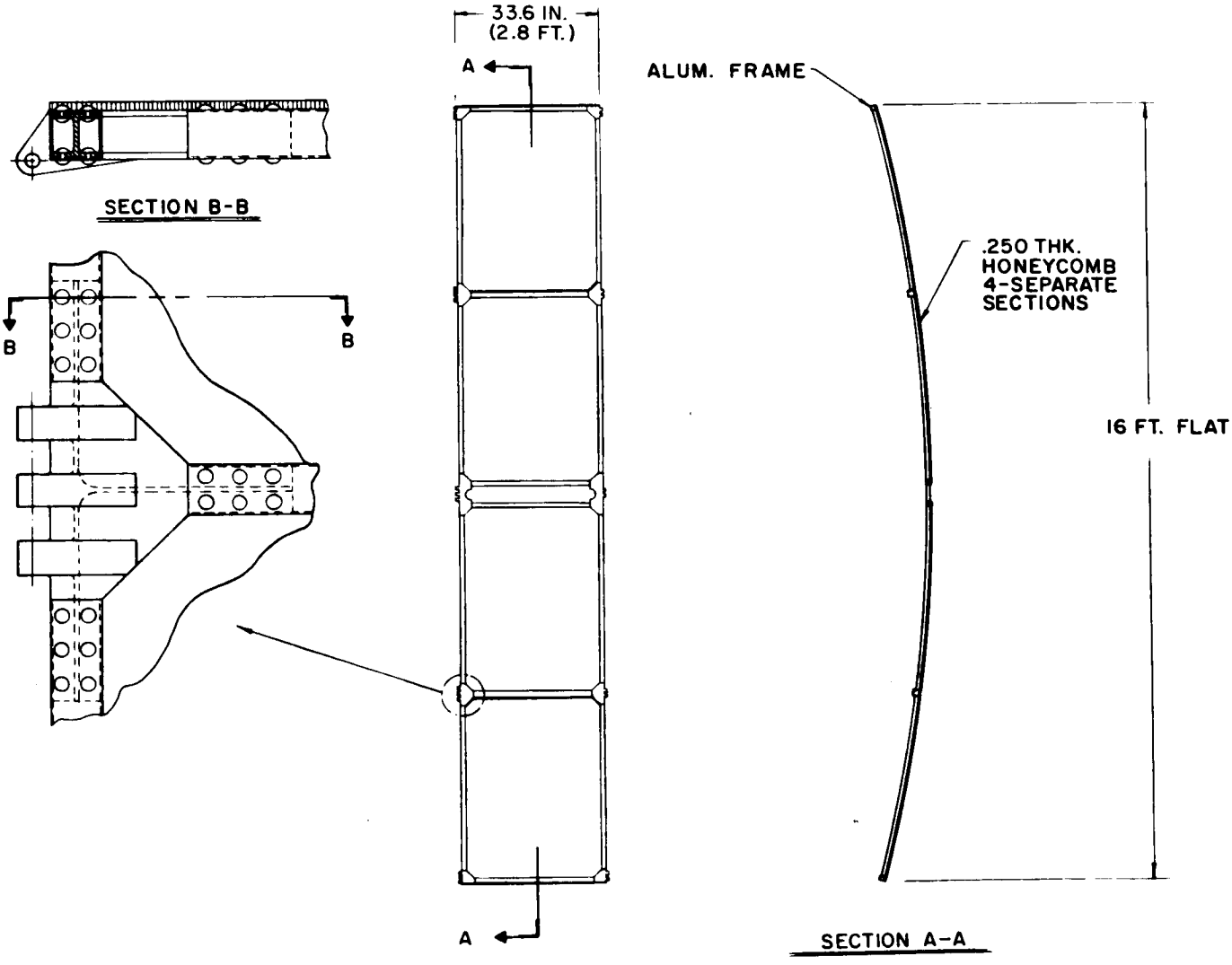

Figure VII-19. Solar Array Panel

determines the improvement in the section properties in that the smaller the radius of curvature, the greater the improvement in section properties. However, the smaller the radius of curvature, the lower the array projected area and consequently the lower the electrical power output.

The power output of a solar array varies approximately as the cosine of the angle of incidence between the array normal and the sun vector. Therefore, if the power output loss due to the angle of incidence of the sun vector is to be limited to approximately 1 percent, the maximum angle of incidence permitted is 10° (see Figure VII-20). It can be shown that a bow of 8.4 inches over a 16-foot length will yield approximately a 10° angle of incidence for solar cells at the extremities.

2. Transition Panel

The transition panel provides a flat profile for array stowage and a bowed profile for array orbital operation. It provides, additionally, a structural joint between the complete solar array and the array orientation drive. The transition panel's flexible member, which is fabricated in the bowed condition, duplicates solar-array panel stiffness and is independently deformable to the flat (stowage) shape of these segments. When the array is completely deployed, this flexible member and the panel will return to their initial bowed shapes. In this configuration, the transition panel will lock by means of a detent, thus providing a rigid chordal tie that maintains the bowed profile of the deployed array and lessens the possibility of array panel flattening under load.

Because of anticipated machine tolerance buildups in the array during assembly to the MMSS a provision has been made for transition-panel width adjustment. Provisions for absorbing both deployment and operational shock loadings may be added to the transition panel as shown in Figure VII-21. Details such as hinges, actuators, and electrical connections are common to both the transition and solar-array panels and are described elsewhere.

3. Array Assembly Procedure

a. SOLAR-ARRAY PANEL ASSEMBLY

Panels will be fabricated so that margins of safety while stowed will be maximized. The aluminum framework of each panel will be fabricated in the bowed (deployed) shape and subsequently elastically deformed into the flat (stowage) profile. Figure VII-22 indicates

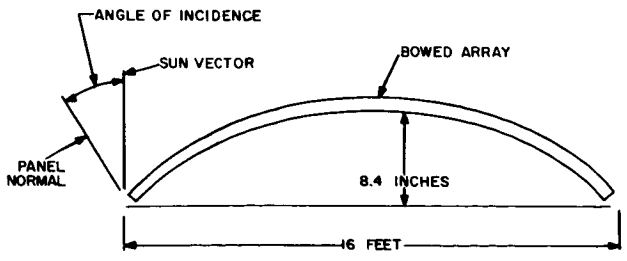

Figure VII-20. Bowed Array Solar Incidence Angles

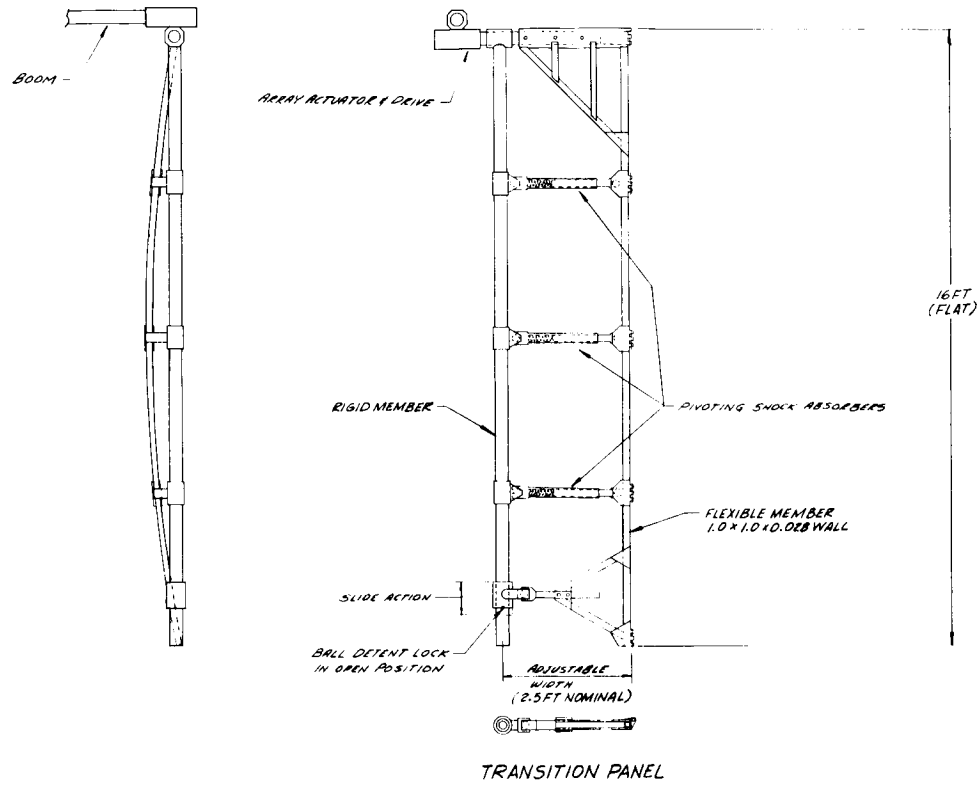

Figure VII-21. Solar Array Transition Panel

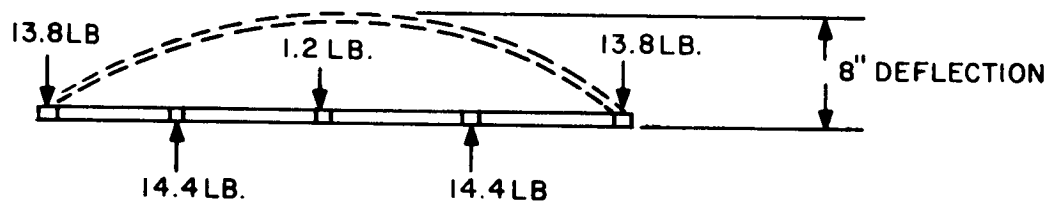

Figure VII-22. Deformation Forces

the forces needed for this operation. Following this deformation, the flat honeycomb substrate is rigidly attached to the frame. Release of the flattening forces allows the panel to return to the final bowed profile. Solar-cell modules and associated wiring are then installed on the bowed substrate.

When the completed panel is flattened and stowed on the MMSS, the honeycomb substrate has no initial stress. Subsequent launch environmental loads stress both the panel and the frame to approximately the same percentage of fatigue strength. If the honeycomb substrate were formed and assembled in the curved configuration, the increase in honeycomb facing stress due to panel flattening would lower the stowed margin of safety.

b. SOLAR ARRAY - MMSS INTEGRATION

The initial integration phase involves only the MMSS. First the shear fitting mounting rings are installed on the MMSS structure. With the number of array panels determined, the circumferential spacing of the shear fittings is computed and the shear fittings are then positioned and permanently pinned in place. The use of fixtures will simplify these operations. The deployment booms and associated mechanisms such as boom deployment actuator, boom latch, and electrical connectors are next assembled to hard points provided on the MMSS structure.

The solar array panels are installed in segments (consisting of two panels and one actuator), each weighing approximately 75 pounds (see Figure VII-23). Folding of this subassembly about its common hinge line causes partial panel flattening; flattening of the panel free ends is accomplished by means of fixtures. Subassemblies are consecutively installed from the free array ends, and held within the shear fittings by temporary locating pins (see Figure VII-24). As segments are joined, actuators, pneumatic tubing, and electrical links are permanently established. The last segment is installed in conjunction with the transition panel where width adjustment of the latter unit is made. Assembly fixtures are removed and the two array retaining cables are installed and preloaded. At this point, the locating pins holding the panels to the shear fittings are removed. Integration is complete when final electrical connections are made.

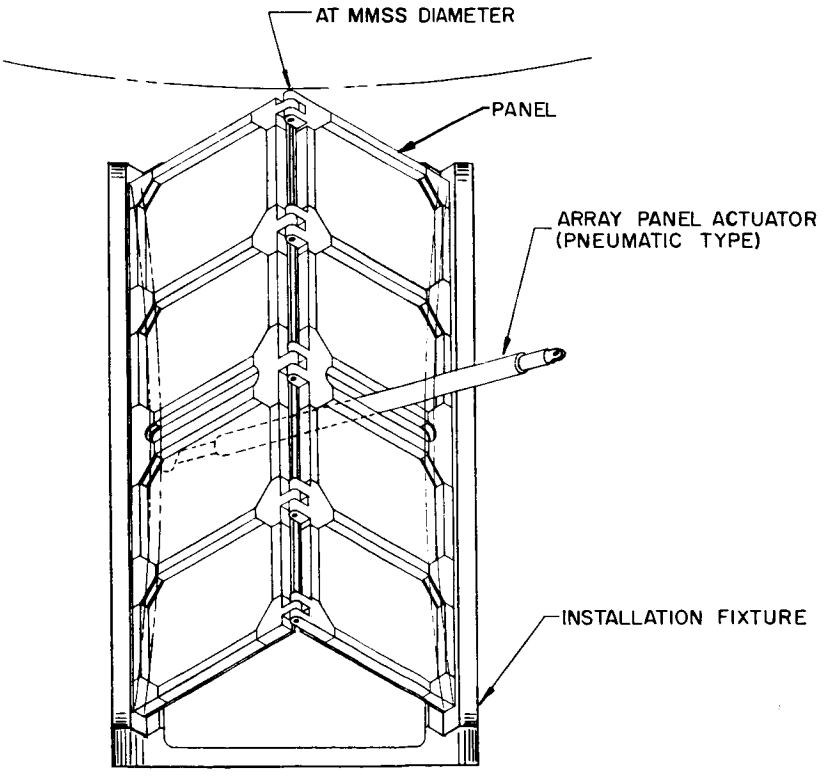

Figure VII-23. Panel Segment

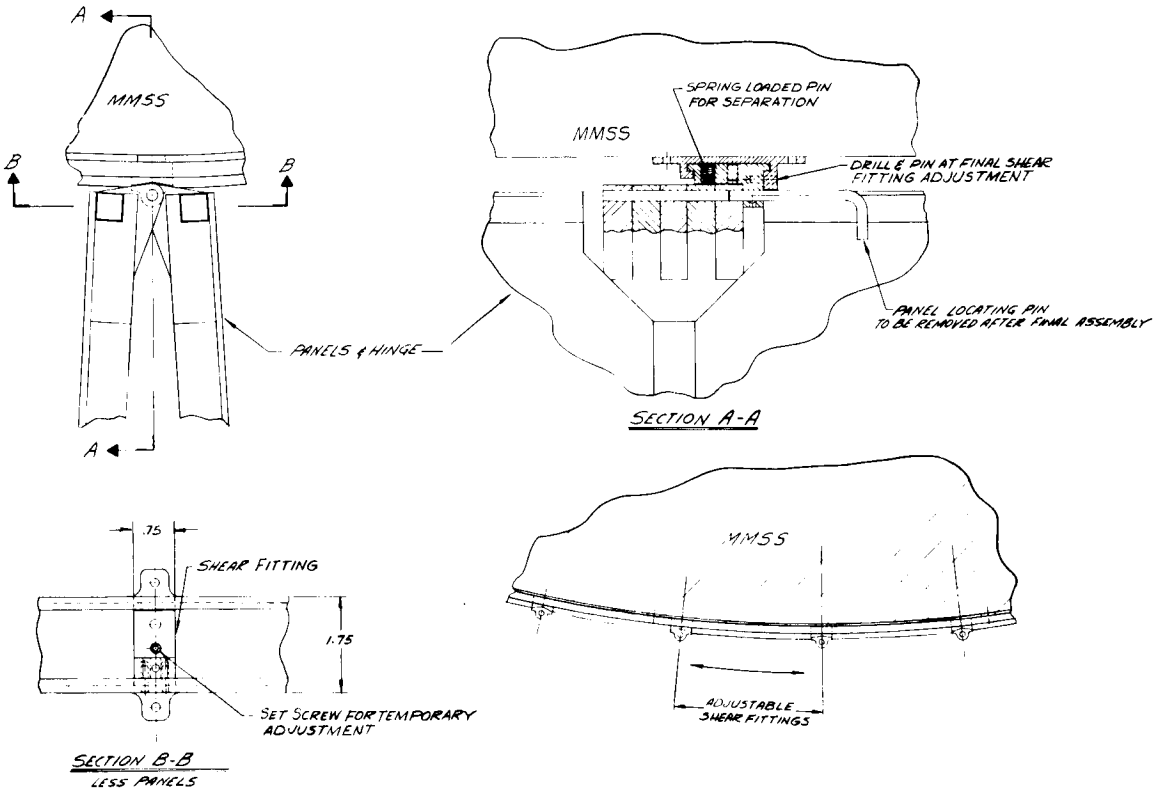

Figure VII-24. Panel Mounting to Shear Fitting

4. Energy Transfer Across a Rotating Joint

Three specific techniques for transferring energy across a rotating joint were investigated: flexible cables, rotary transformers, and slip rings. Of the three, slip rings are the recommended approach, since flexible cables have an inherently limited capability for rotation and rotary transformers are inefficient. In addition, slip rings have been successfully space-proven on the OSO and Nimbus programs.

a. FLEXIBLE CABLES

Flexible cables offer a simple means of power transfer across a rotating joint, particularly when low currents (low cross-sectional cable area) and small angular motions are employed. When the limit of angular motion (as defined by the initial cable windup or torsional properties of the cables) is reached, cessation of rotation or unwinding of the system becomes necessary. By using stranded cables and absorbing the joint angular motion through torsion of a long, straight cable length, the magnitude of cable fatigue stress can be minimized. This is one approach that can be used in the interpanel cable joints, where the requirements are limited to a single operation through 180° of motion.

Cable unwinding about the long axis of the array can be accomplished by periodically rotating the array counter to its normal rotation. Cable unwinding in the orthogonal axis requires one rotation per day. In view of the constraints unwinding would impose on the mission, this technique was not considered acceptable.

b. ROTARY TRANSFORMERS

Rotary transformers using adjacent moving coils transfer power without physical contact and the attendant friction and wear problems. This approach is limited to alternating currents and to a limited number of independent circuits. Internal heat generation, associated electrical inefficiencies (approximately 85 percent for the transformer circuitry), and the weight of the transformer and circuitry add to the disadvantages of this method. Therefore, this approach was not adopted.

c. SLIP RINGS

Electrical power and signal transmission across the motor-driven orientation shafts can be accomplished by two essentially identical slip ring assemblies housed within each orientation drive assembly. Slip rings provide a relatively simple method of transferring electrical signals or power across a rotating joint of unlimited rotation. The many aspects of their design for earth-based application have been thoroughly investigated and their use is commonplace for both signal and power applications. Considerable investigation of slip ring vacuum applications has been made and power slip-ring assemblies are operating on several successful space vehicles. However, each space application must be independently evaluated, tested, and qualified to ensure reliable operation.

The primary requirements of reliability and predictable minimum orbit lifetime are influenced by a set of factors which are intimately interrelated. Materials, lubrication, contact speeds, and electrical and mechanical loadings must be optimized if these requirements are to be met. To indicate the approach to an acceptable slip-ring design, examples of a space proven design and of recent research are cited.

The Orbiting Solar Observatories (OSO-1 and -2) have successfully employed relatively low-current, slip-ring assemblies containing coin silver (90 percent silver, 10 percent copper) and rings and brushes comprised of a 75 percent silver, 20 percent carbon, and 5 percent molybdenum disulfide alloy. The OSO-1 spacecraft, launched on March 7, 1962, was still functioning without any measurable deterioration of the electrical and mechanical interfaces when interrogated after 16 months in space.

A key item in the successful operation of the OSO slip-ring assembly was the Vac-Kote process for contact lubrication developed by the Ball Brothers Research Corporation. Ball Brothers has conducted additional tests on slip-ring assemblies of the same construction as those used on the OSO satellite, with the Vac-Kote process applied. Accelerated life testing at speeds as low as one revolution per day, in a vacuum of less than 10^{-8} torr, showed a small but acceptable slip ring and brush deterioration after the equivalent of 5 years of orbit operation. The Vac-Kote process, coupled with the molybdenum disulphide component of the brush material, constitutes the primary slip-ring lubrication system. A secondary system

in the OSO slip-ring unit provides lubrication for the shaft bearings and additional lubrication for the slip rings. This system consists of labyrinth shaft seals and a porous lubricant reservoir.

The labyrinth seal, which maintains a predetermined clearance between the housing and the shaft, is used to meter molecular exit from the otherwise entrapped atmosphere. As the interior becomes a vacuum harder than the vapor pressure of the stored oil, evaporation from the porous retainer occurs with resulting molecular oil movements that provide lubrication of the slip rings and bearings. Molecular leakage past the labyrinth allows this process to be continued for the life of the satellite. A Vac-Kote lubricant impregnated in a Nylasint retainer of approximately 2 cubic inches will supply bearing lubrication for approximately 5 years. Vac-Kote provides a low vapor pressure and a relatively high (5×10^{10} ergs/gm) radiation dosage damage threshold level.

Recent research by Westinghouse Electric Corporation evaluated self-lubricating brush materials that were designed for use on silver slip rings at high current densities. Brushes of silver/molybdenum disulfide and silver/niobium disulfide operating in a vacuum of 2×10^{-8} torr and at a speed of 0.43 revolutions per hour (3.4 inches per hour) were subjected to a 1000-hour test. The test disclosed that the niobium disulfide has a lower and more stable contact-voltage drop and a lower body temperature. Based on an anode wear rate of 0.094 cubic mm for 1035 hrs, a life of 242 years was predicted. Additional research conducted under Air Force contract AF 40 (600)-1070 supports the above findings. A summary of these results appears in Table VII-7.

By adapting similar methods and techniques for material, construction, and lubrication, the same success can be obtained for the slip ring assemblies of this program. Additional investigation would be necessary in the following areas to establish total reliability.

(1) Insulation resistance

(2) Dielectric strength

(3) Brush contact force

(4) Contact resistance

(5) Radio-frequency Interference

(6) Torque

(7) Environmental factors

(8) Redundancy

A conceptual design of the slip ring assembly is presented in Figure VII-25. An arbitrary number of signal and power rings have been shown in order to present the concepts of overall unit size, preliminary housing configuration, multi-brush slip ring contact and resolver

TABLE VII-7. SLIP-RING CHARACTERISTICS

Item	Lockheed		Westinghouse	OSO
Brush materials	Ag-graphite Ag-Cu-MoS_2* Ag-Mo-MoS_2	Ag-graphite Ag-Cu-MoS_2	*Ag-NbS_2 Ag-MoS_2	Ag-graphite-MoS_2 with Vac-Kote
Ring material	silver gold	silver gold	Ag-Cu	Ag-Cu
Ring size (inches)	2.25 dia. x 3/16 wide	6.75 dia. x 1/2 wide	3.00 dia.	--
Brushes per ring	2	4	14. max.	--
Brush area (sq. in.)	0.0135	0.328	0.375	--
Pressure (psi)	6-10	6-10	3.6 to 4.8	--
Current (amperes)	4.05 (300 amp./sq. in.)	75 (229 amp./sq. in.)	30 (80 amp./sq. in.)	4
Speed (rpm)	60 (424 in./min.	15 (318)	0.43	0-30 rpm, space operation 120 rpm, earth test
Atmosphere (torr)	10^{-6}	10^{-8} to 10^{-9}	2×10^{-8}	10^{-8}
Total hours	847 max.	700	1035 hrs 242 years, predicted life	12,000, space 456, earth
Potential drop (millivolts)	-	60-84	37	-

*Best material combination

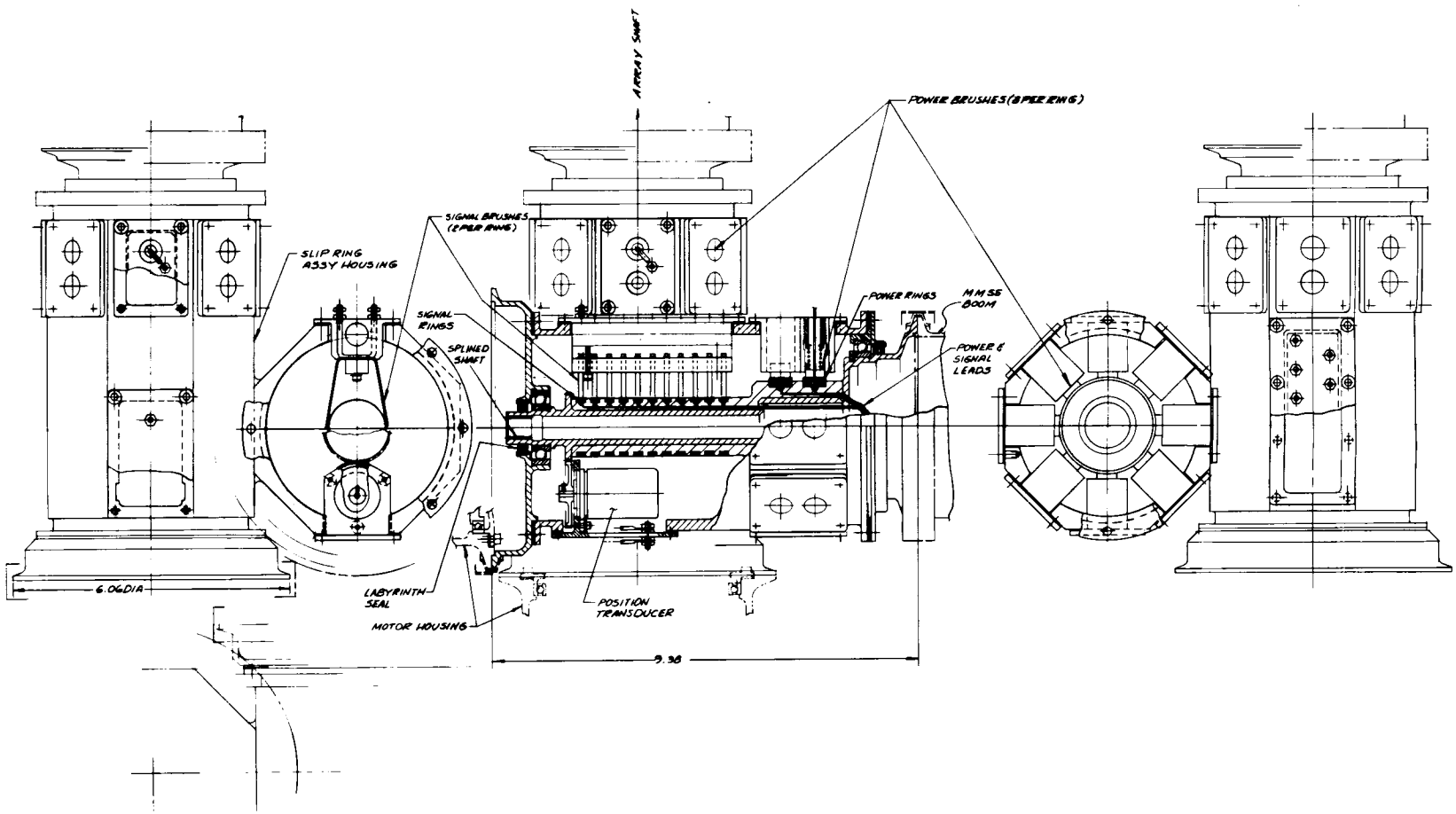

Figure VII-25. Array Actuator (Slip Ring Assembly)

installation. The entire two-shaft slip-ring assembly is independent of the motor-gear reduction unit and may be separately replaced in orbit by using a temporary support between the boom and transition panel.

The following characteristics based on the information in Table VII-7 have been used for the conceptual sizing of the primary array power brushes:

- Current: 150 amperes
- No. brushes: 8 per ring
- Current density: 150 amperes per square inch
- Brush area: 0.125 square inch each (1.00 square inch total)
- Brush diameter: 0.40 inch.

The motor and signal brushes transmit much lower currents and, because of their correspondingly smaller physical size, permit more latitude in design. The following slip ring characteristics for signal information usage lead to a brush size that can easily be increased for higher currents:

- Current: 0.5 ampere
- No. brushes: 2 per ring
- Current density: 90 amperes per square inch
- Brush area: 0.0028 square inch
- Brush diameter: 0.06 inch.

5. Electrical Bus Design

The power conductor system consists of primary power buses and interpanel power joints. The decision between using load-bearing structural buses or electrically independent conductors has been made in favor of the latter concept. The weight savings achieved by using structural buses are offset for the present by the complexity of maintaining reliable insulation between the buses and the remaining structure as well as the requirement for this insulated joint to transfer mechanical loads to the structural buses. This problem is further complicated by the necessity to minimize the thermal gradients through this region in order to avoid the creation of high thermal stress. Assuming that 100 percent of an electrical bus network could be converted to an efficient insulated structure, the weight savings would amount to 0.050 pound per square foot, based on an aluminum bus, which has a better conductivity-to-density ratio than copper. This weight saving is appreciable and comprises approximately 250 pounds for the array (4900 square feet). The resolution of this problem is of such a nature that it can be undertaken during a detail design effort.

The net area between the two buses (positive and negative), summed over the entire solar array, must be kept to a minimum to eliminate major magnetic perturbation torques. This requirement is more easily satisfied on interpanel buses than on the interpanel power connections.

The interpanel connections must provide low-resistance, reliable power joints within the size envelope of both the stowed and deployed array configurations. The mechanical torque contribution of the electrical power joint to the over-all hinge line restraining torque should be small to minimize required array deployment mechanisms. The restrictions of parallel (positive and negative) buses and easy assembly of joints during the array MMSS integration cycle add to the design complexity.

The main electrical bus is designed to have a tapered crossection, which gradually decreases from the boom end of the array to the free end. With an array area requirement of 4900 square feet, each of the conductors at the boom end will have a cross-section area of 0.68 square inch. This represents a cable diameter of 0.93 inch or in flat ribbon form (4 inch width), a thickness of 0.17 inch. This dimension may be made up of 5 individual ribbons each approximately 1/32 inch thick. (Installation thickness has not been included in these values.)

Two alternate solutions for inter-panel buses are possible. The first is the flat ribbon approach with its attendant spring force and clearance requirements for the stowed position. This solution is simple and straight forward, but requires more detail layouts for clearance requirements. However, this is the recommended approach.

A concept that satisfies the power joint requirements is presented in Figure VII-26.

The joint motion resulting from panel opening is absorbed by long lengths of stranded wire, resulting in low unit strains and subsequent low hinge torque. The figure schematically represents the motion of one of the two power connections at the joint. Cable A twists through approximately 150° while cable B deflects (bends) through about three inches. A and B are joined by a detachable link and move in Teflon-lined guides. The second connection is a mirror image of the first with stranded cables running parallel to A and B. Additional details are presented in Figure VII-27.

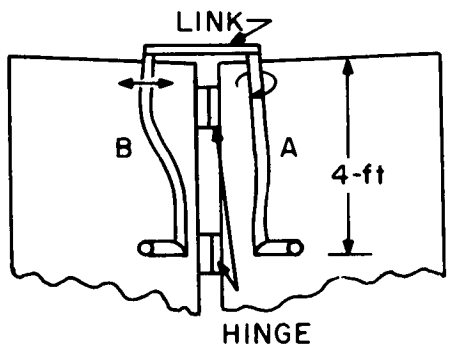

Figure VII-26. Joint Connection Motion

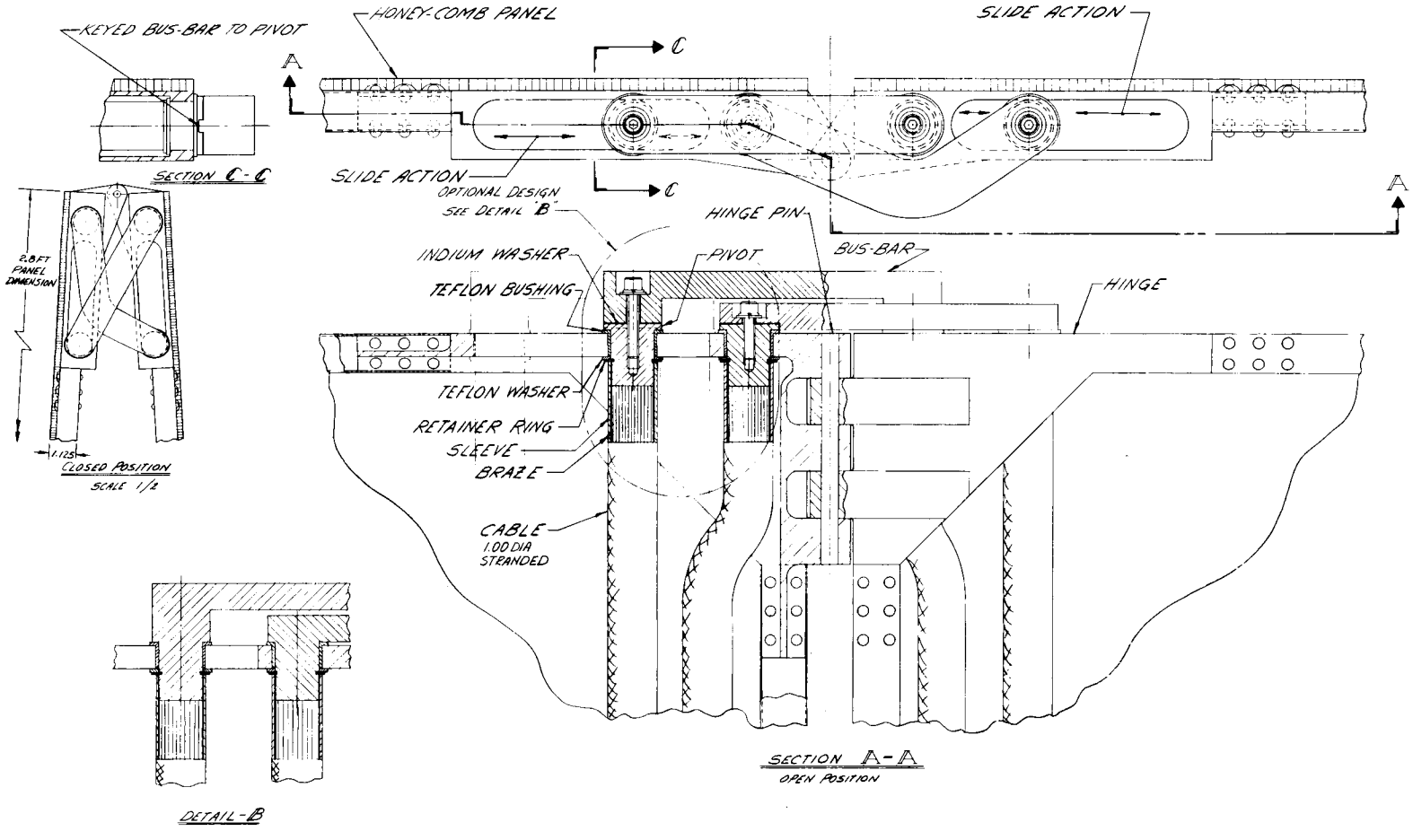

Figure VII-27. Solar Panel Double Cable Interconnection

6. Hinges and Locks

In addition to providing for panel folding, the hinges support and position the preloaded retaining cable used for array stowage and provide the mating half of the MMSS-array shear fitting. Two hinge designs have been considered although only a butt hinge is shown on the applicable drawing (Figure VII-28). A ball and socket hinge, by nature of its construction, eliminates local bending moments and resulting stresses about all three orthogonal axes. The physical size of this hinge is offset by the redundant action (two concentric turning axes) provided about the hinge axis. However, this feature complicates the design of shear fitting and stowage retaining cable interfaces and makes the mating of hinges during the array-MMSS integration operation more difficult.

Butt hinges allow considerable design latitude in making provisions for cable and shear fitting interfaces. Hinge mating requires only the installation of a hinge pin. The initial alignment of the hinge axis is critical and will require accurate fixtures if local bending moments and hinge-axis friction are to be minimized. Butt hinges offer the minimum size envelope necessary for stowing the maximum area (4900 square feet) of solar array and hence have been tentatively selected. No requirement exists at present for locking either hinge design in the deployed position. At final deployment, the change from a flat to curved panel profile will serve to lock the solar array.

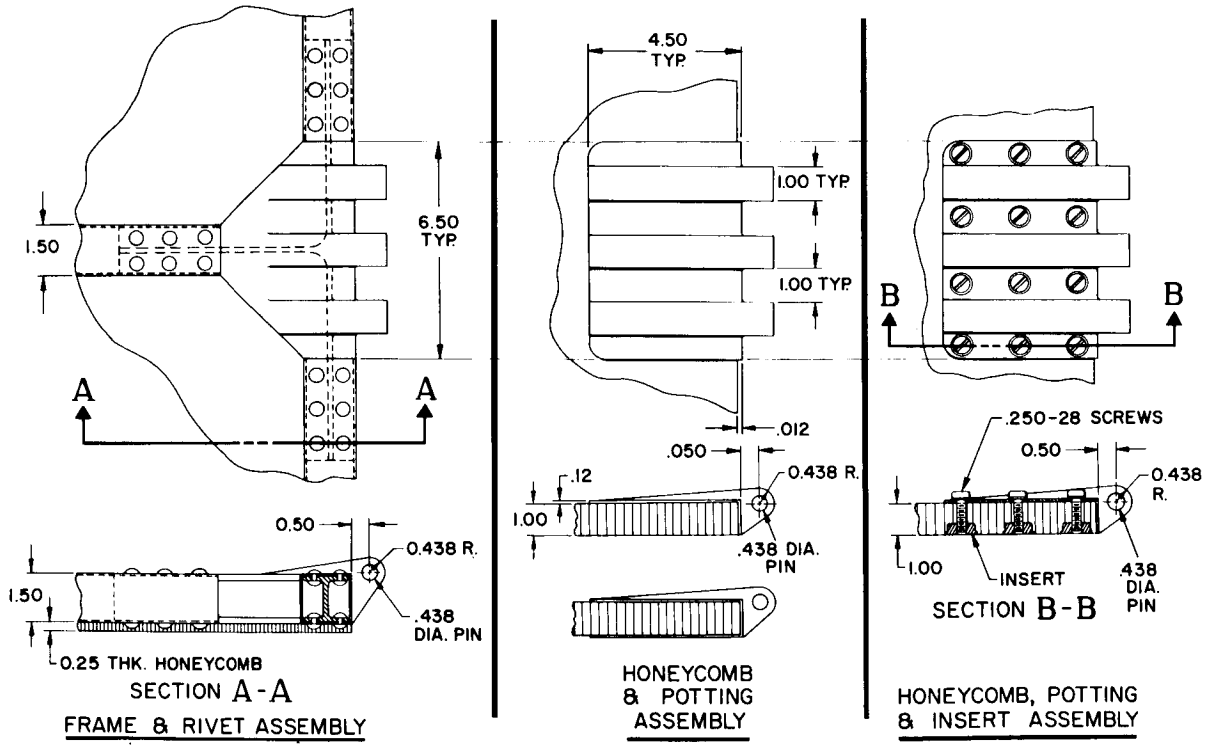

Figure VII-28. Alternate Hinge and Hinge-Mounting Concepts

7. Array Orientation Drive

The array orientation drive assembly joins the deployment boom to the solar array via the transition panel and provides a dual-axis, orthogonal-orientation system for the deployed array. Figure VII-29 is a schematic representation of the orientation drive assembly attached to the deployment boom and the array transition panel; Figure VII-30 gives the details of this assembly. In addition to drive motors and associated reduction gear, (see Figure VII-31) each drive assembly provides slip rings for power and signal transmission and synchros for array orientation definition.

The input shaft is rigidly joined to the outboard end of the deployment boom. The housing and array drive shaft both rotate about the input shaft. The array drive shaft rotates within the housing drive shaft and provides the second axis of rotation. Rotation of each shaft with respect to the housing is provided by two gear reduction torque motor units mounted to the housing by a quick disconnect V-band coupling. A splined joint connects the motor to the drive shaft. These features permit simple, rapid replacement of the drive motor in orbit by removing the motor power connector, disconnecting the V-band coupling and withdrawing the splined shaft from the slip-ring assembly.

a. MOTOR DRIVE GEAR BOX

The motor drive shown in Figure VII-31 provides 1.8 foot-pounds of torque and was chosen on the basis of reliability, power consumption, adequate torque capability, and packaging. Both a-c and d-c motors were considered; since 400-Hz power and direct current are available, they are equally suitable from this standpoint. The 400-Hz motor, although possessing a weight and size advantage and not requiring a commutator, has a poorer efficiency than the d-c motor. In addition, it is inherently a high-speed device, requiring several high-ratio gear passes for reduction to orbital or slewing velocity.

The choice of a motor type is intimately associated with lubrication and sealing. To avoid the problems associated with a hermetically sealed motor, a labyrinth seal system (utilizing a low-pressure vapor lubrication) was chosen. A high degree of confidence exists for this system with a low-speed drive, since test data is available to substantiate this. In addition,

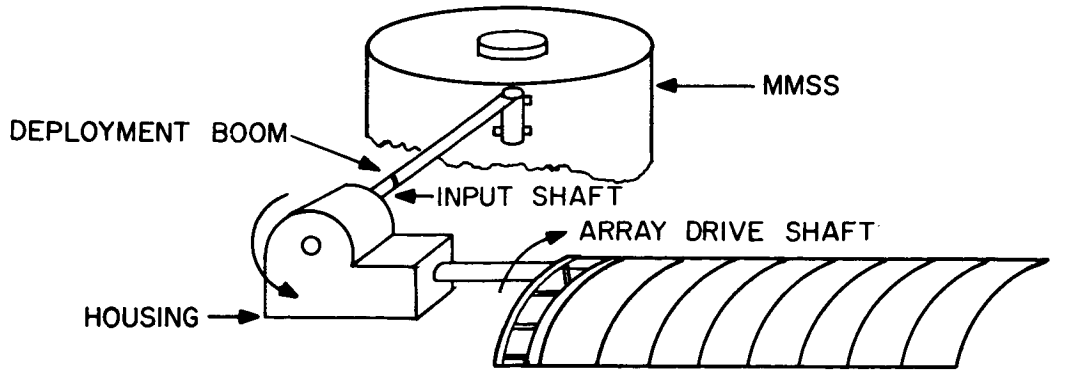

Figure VII-29. Orientation Drive Assembly Schematic

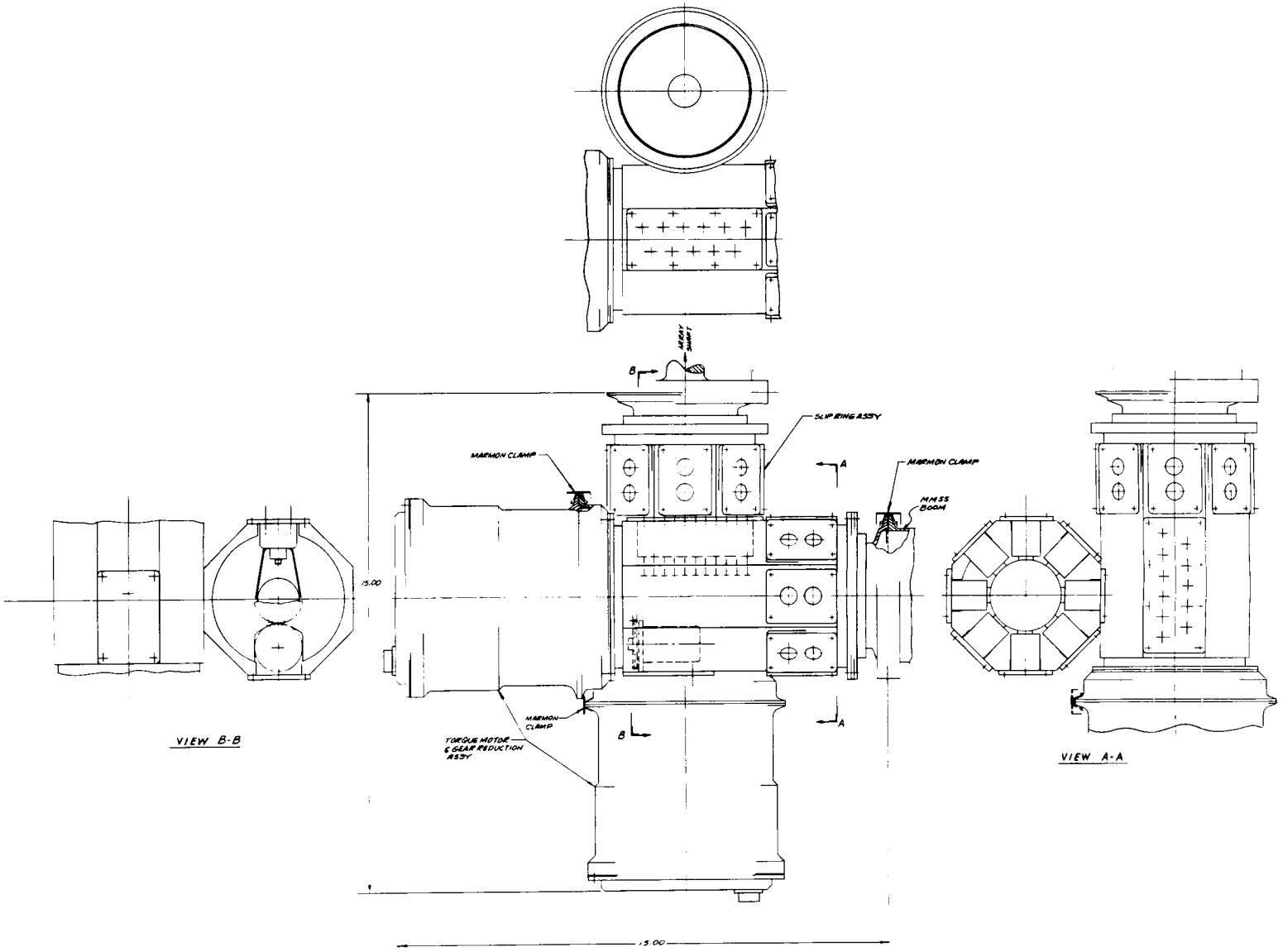

Figure VII-30. Orientation Drive Assembly Outline

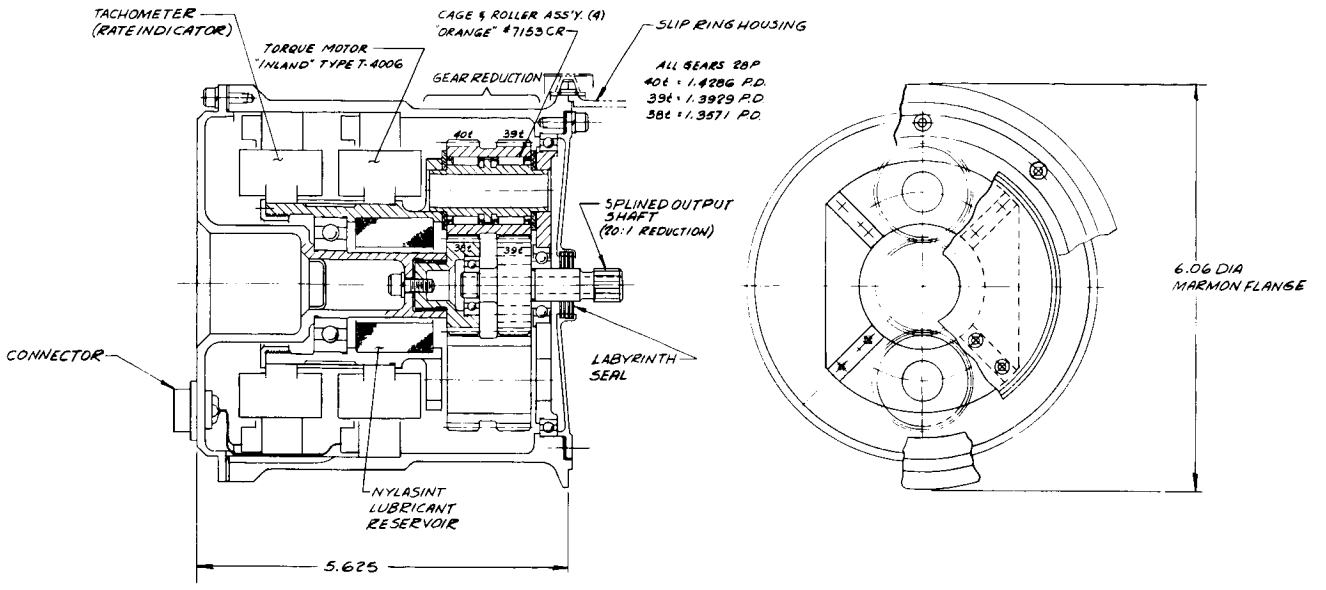

Figure VII-31. Drive Motor and Reduction Gears

with low-vapor-pressure lubrication, thermal hot-spot conditions are aggravated and the small size of an a-c motor is of no advantage. As an example, it is believed that the solar-panel-drive failure on a Nimbus I satellite (which utilized a small, high-speed a-c motor with a large reduction-gear train) was due to poor motor cooling, followed by bearing overheating and seizure.

For these reasons a d-c, low-speed torque motor has been selected. Consideration was then given to eliminating the commutator by going to a brushless d-c motor. However, on a parts-count basis, the brushless motor (137 parts) is less reliable than a brush motor (7 parts).

The test data referred to earlier was obtained from an RCA test of a d-c torque motor as part of a phase lock loop (servo). The test conditions were six months of continuous 150-rpm operation at temperatures ranging from 0°C to 25°C. Vapor lubrication with dioctyl adipate was used on the ball bearings and brushes. The ambient pressure ranged from 5×10^{-6} to 4×10^{-7} torr. The average measured brush wear rate of 2.3×10^{-2} mils per 10^6 feet of travel is less by an order of magnitude than predicted wear rate even for atmospheric conditions. For 40.5 million revolutions, or 46.6 million feet of brush travel, the average brush wear was 1.07 mil. Bearing wear could not be detected by measurement and there were no visible signs of wear. The test was terminated by schedule; no failures

occurred.* A single gear pass was chosen because it provided better matching between motor and load and increased torque for modes other than tracking. Without the gear pass, a large motor would be required for the same torque capability. In the tracking mode, a gear ratio of 20:1 increases the low level d-c tachometer signal by this factor, thus providing a higher level, less noisy signal for the servo.

b. SEALING AND LUBRICATION

Consideration has been given to both a sealed-drive unit mounted in a spacecraft at the ambient pressure (7 psia) and to a low-vapor-pressure system vented to space by means of a labyrinth seal on the output shaft. The first approach requires hull penetration and a rotating seal in the spacecraft for the boom drive. This is undesirable from a safety standpoint, since the MMSS is a pressure vessel. When it was determined that penetration of the hull (to provide mechanical manual backup operation for panel drive) was not feasible, the decision was made to leave the hull intact (except for electrical feed-throughs), position the drives outboard, and utilize low-vapor-pressure lubrication.

The derivation of the equation that predicts lubricant loss is contained in Appendix D. Dioctyl adipate has been used at RCA in experimental testing with loss rates less than theoretically predicted values. This particular lubricant was chosen on the basis of providing a minimum vapor pressure of 10^{-5} Torr for adequate d-c motor brush lubrication at 4°C. The recent tests described in the preceding subparagraph show excellent results in brush and bearing wear. Lubricant storage under zero-g conditions is obtained by impregnation of "Nylasint", a commercial product composed of porous nylon. The loss rate per year can be predicted from the following equation and is evaluated for the parameters indicated.

$$W = \frac{1.180 \times 10^{-5} (T_K - 248)^{5.63} \; T_K^{-1/2} Da}{\frac{n}{2}\left(\frac{L}{2a} + 1\right) + 1} \text{ grams per year,} \qquad \text{(VII-1)}$$

where

$$272°K < T_K < 394°K$$

$$1.5 < \frac{L}{a} < 40.$$

T_k is temperature, in degrees K,

n is number of elements in labyrinth seal, = 12,

L is element path length, = 0.381 cm,

*Internal RCA Memo. L. Muhlfelder to H. Perkel Dated 10-18-66 Subject "Stabilite Test with d-c Brush Motor"

a is clearance, = 0.0254 cm, and

D is diameter, = 7.62 cm

Substitution of the values into the equation results in

$$W = 4.38 \times 10^{-8} (T_k - 248)^{5.63} T_K^{-1/2}$$

The weight loss is plotted in Figure VII-32. Thus for this typical example, the loss rate is several grams per year for temperatures in the 10° to 15°C range. The six-month test described utilized a labyrinth seal of similar design and experienced 0.8 gram loss although it operated at lower average temperatures.

E. DEPLOYMENT

1. Sequence

The deployment sequence for the array is shown schematically in Figure VII-33. The sequence is initiated by simultaneous explosive separation of the two array retaining cables. The release of the strain energy originating from the 7800-pound tensile preload will cause the severed cables to fly clear of the spacecraft. Coincident with cable release is the separation of the panels from the MMSS mounted shear fittings. This separation will result from the release of compressive strain energy in the solar panel framing or, if needed, from

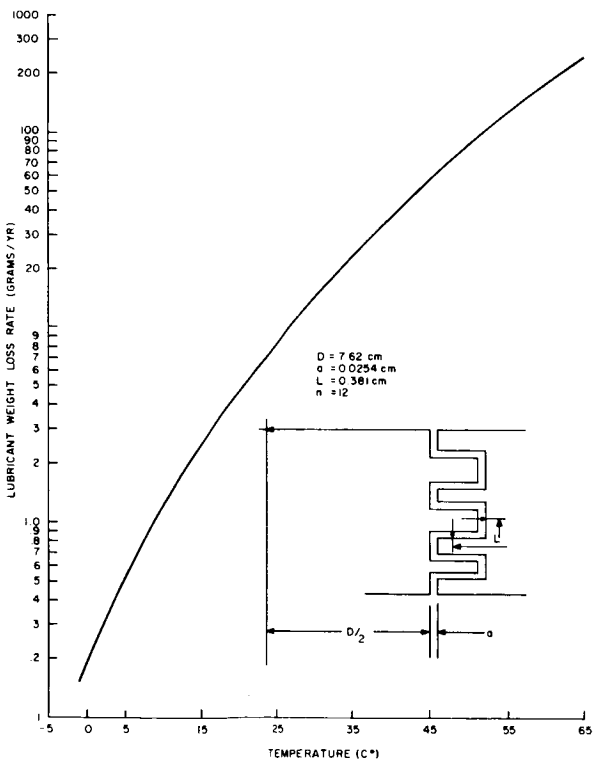

Figure VII-32. Lubricant Weight Loss Versus Temperature

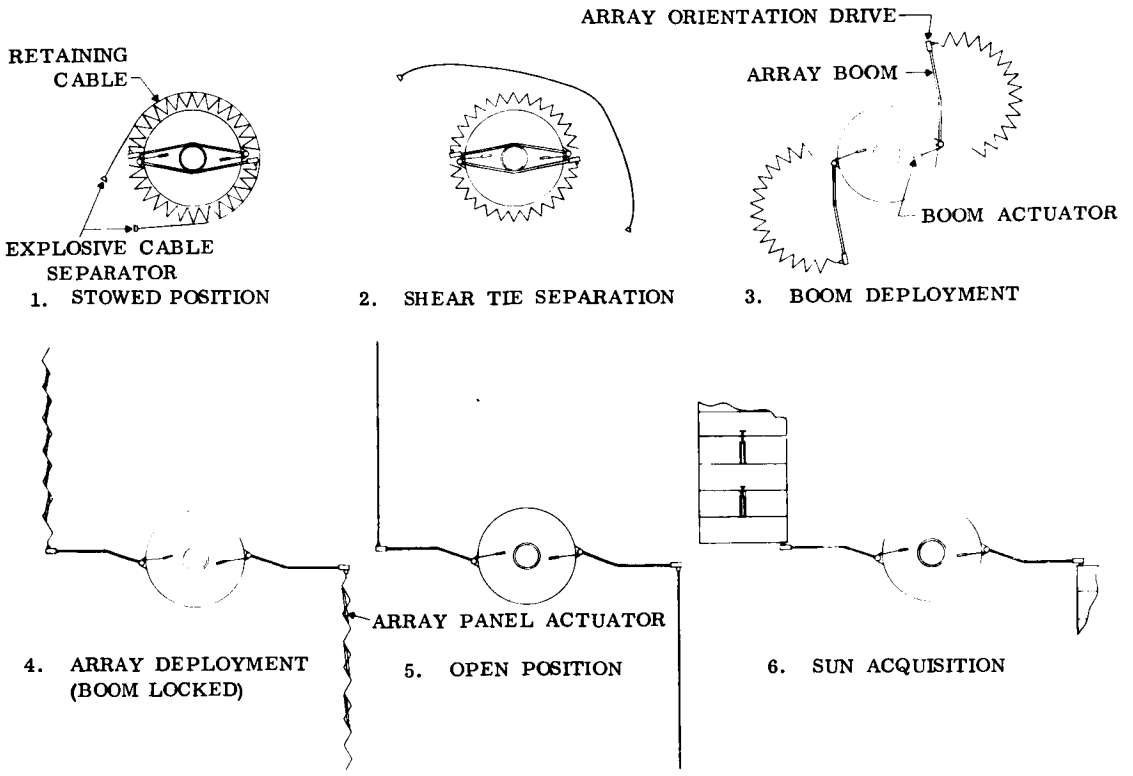

Figure VII-33. Solar Array Deployment Sequence

the separation spring system located in the shear fitting. Verification of these portions of the deployment sequence will require additional analysis followed by scale model (or full size) testing, specifically in the area of shear fitting separation. Such testing will verify the optimum geometric interfaces for reacting loads in the stowed position and for interference-free parting during deployment. The design parameters for positive separation springs, if required, would also be verified during the scale-model tests.

Following separation of the shear fittings, the array booms are simultaneously deployed to the full open position by penumatic piston actuators. For this operation, a time interval of approximately five minutes with the velocity profile of Figure VII-34 has been tentatively selected such that boom acceleration and angular velocity are minimized. This alloted time interval will result in small size boom actuators being used and low (angular) kinetic energy being developed. The dissipation of this energy can be accomplished by the use of a viscous damper or an overtravel spring with coulomb damping, with the latter approach favored for its simplicity. When the full open position is reached and the kinetic energy is dissipated, a detent will lock the boom in the final deployed configuration.

The next position of the array deployment sequence is the unfolding of the solar-panel segments. This part of the sequence is also being based on a five minute time cycle. The sequence of panel unfolding is dependent upon hinge friction, total mass inertia about each hinge axis, and whether the pneumatic actuators are in a parallel or series arrangement. In general, deployment motions will take place in order of increasing energy requirements.

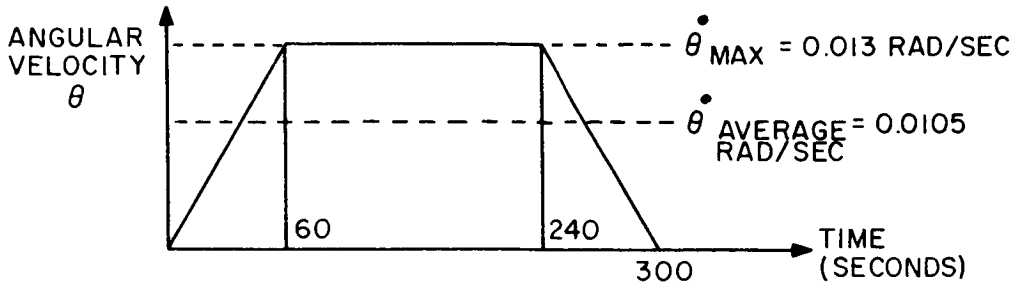

Figure VII-34. Array Booms, Time-Velocity Profile

2. Actuators

Series actuation applies equal pressure throughout the system. The initial motion, that of lowest energy, is shown in Figure VII-35, (A, Series). The next phase of the motion will depend on whether B or C has higher total friction and inertia loads. Since the exact unfolding motion is so highly dependent on friction levels, only experimental testing can verify the sequence. Parallel actuation can, due to pressure variations among sets of actuators, provide a sequence similar to that of Figure VII-35 (Parallel). The pressure ratios for such motion have not been determined.

In either system , the relatively low mass of the panels and corresponding low panel inertia will permit the kinetic energy of deployment to be absorbed by small elastic snubber pads positioned between panels (see Figure VII-36). At full deployment, the flat panels will revert to their original bowed profile, thus locking the array in the open position. The consequences of rapid transition of the panels from flat to bow configuration is discussed in Paragraph VII-C-6.

The requirements for the panel actuator can be summarized as follows:

a. Motion. The kinematic pattern must provide controlled and predictable forces, torques, and motions. Truly random motion is considered predictable. Sufficient force must be available from initial actuation to final curvature to overcome friction and inertia forces and guarantee locking.

b. Weight. The weight should be minimized.

c. Size. Small size is desirable in order to limit local shadowing of the solar cells.

d. Reliability. Should be high.

e. Force levels. Force and torque levels, within the actuation system and applied to the panels, must be minimized to avoid weight penalties. Actuation loads should be isolated from the panels during the already severe launch phase environment.

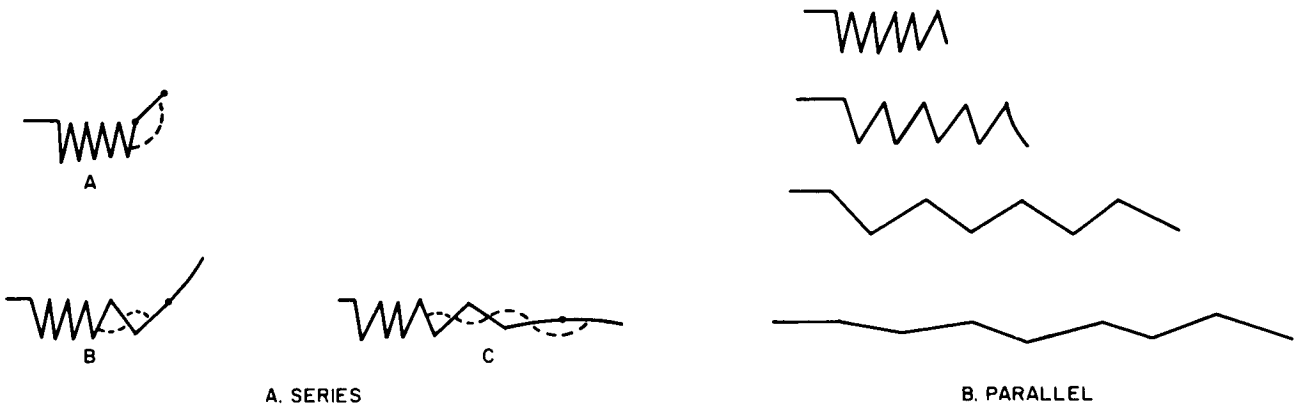

Figure VII-35. Panel Actuation

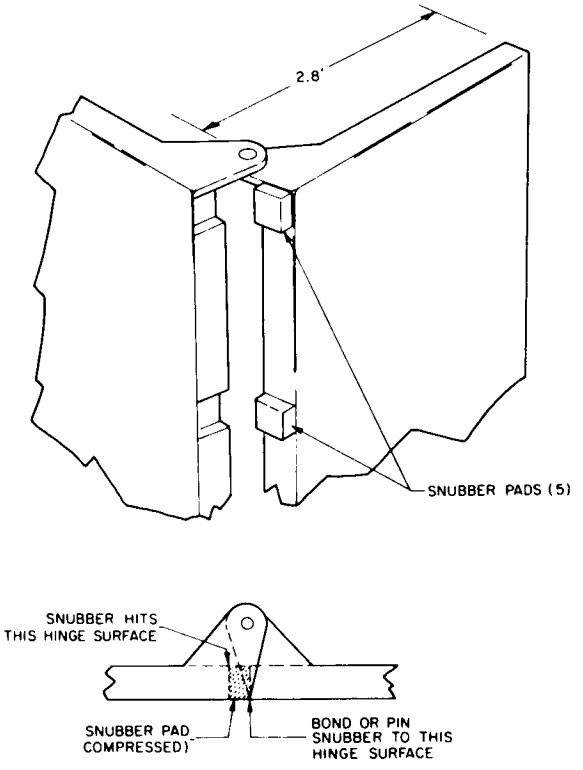

Figure VII-36. Panel Snubber Pads

f. Compatibility. The geometry of the actuation system must be dimensionally compatible with both the stowed and deployed configurations and must preclude the possibility of "hanging-up".

Several generalized methods of panel deployment, which are listed in the following, may be qualitatively evaluated against these basic requirements:

g. Spring-loaded hinges.

(1) High "cocked spring" stress imposed on panels in stowed position.

(2) High deployment acceleration and velocity

(3) Mechanically simple and compact

h. Single-actuator, multi-link scissors.

(1) Predictable and controllable deployment

(2) Single actuator required - redundant unit may be added

(3) High link forces may require stiffening of links to prevent buckling

(4) Freedom of choice for actuating drive

i. Individual electric-motor drives.

(1) Excellent control

(2) System requires additional slip rings (or electrical wiring)

(3) Weight penalty due to motor size and/or gear reduction

j. Individual pneumatic cylinder.

(1) Excellent control

(2) Many simple units

(3) Light weight (both unit and tubing)

(4) Some designs create geometric problems

Since the deployment motion is a one-time, non-reversible occurrence, pneumatic activation was initially chosen over other systems, such as electrical motors or mechanical linkages. Deployment by spring methods, while mechanically simple, causes problems of high localized

forces in the stowed configuration and does not offer the controlled, yet variable, deployment force obtainable in a pressure-regulated pneumatic system.

A double-ended extension cylinder was investigated in some detail (see Figure VII-37). Geometric studies revealed that this device required 40 square inches of panel area for operation and was incompatible with the closely folded panel stowage needed for a 4900-square-foot array. In addition, the deployment torque was variable, approaching zero at the critical initial and final opening points. At these points a high torque would be required, causing a high axial compressing force in the cylinder rod which would lead to a weight penalty to prevent column buckling.

The final actuator choice is shown in Figure VII-38. By utilizing a retracting double-ended cylinder, rod bucking is eliminated and weight is conserved, since a tension loaded cable is the only necessary linkage. No panel area is sacrificed for this device and deployment torque can be controlled.

3. Pneumatic Distribution System

Pneumatic pressure in the 50 to 100 psi range will be used for boom and panel actuation. Air for this system may be stored in a central MMSS mounted reservoir or in separate vessels adjacent to the boom actuators and on the transition panels. If a central-reservoir concept is chosen, thus reducing the system parts count, the pneumatic joint across the array orientation drive must be severed after deployment to allow for unrestrained solar tracking. Such separation may be explosively actuated.

Sizing of the actuators for an air pressure of 50 psi, indicates a piston bore of 0.25 inch. (Actual scale testing will be required to verify the dynamic and friction level assumptions used in this analysis.) The pneumatic distribution system will be composed of light weight flexible extruded nylon or silicone tubing. With a diameter of approximately 0.25 inches, complex mechanical joints will not be required to allow bending about the boom deployment axis and solar panel interfaces.

F. SATELLITE ORBITAL CONFIGURATION

The selection of the satellite orbital configuration was based upon the following requirements:

(1) Maintaining normal sun incidence for all orbiting conditions of the solar array; and

(2) Minimizing shadows (to prevent loss of array power).

The selection of axes of rotation for the array is discussed in Section IX. The orbiting configuration and axes of rotation selected are shown in Figure VII-2. Panel structure initial size for the stowed configuration loadings was determined for an acoustic noise critical load. The resulting structure was analyzed for deployed condition loadings.

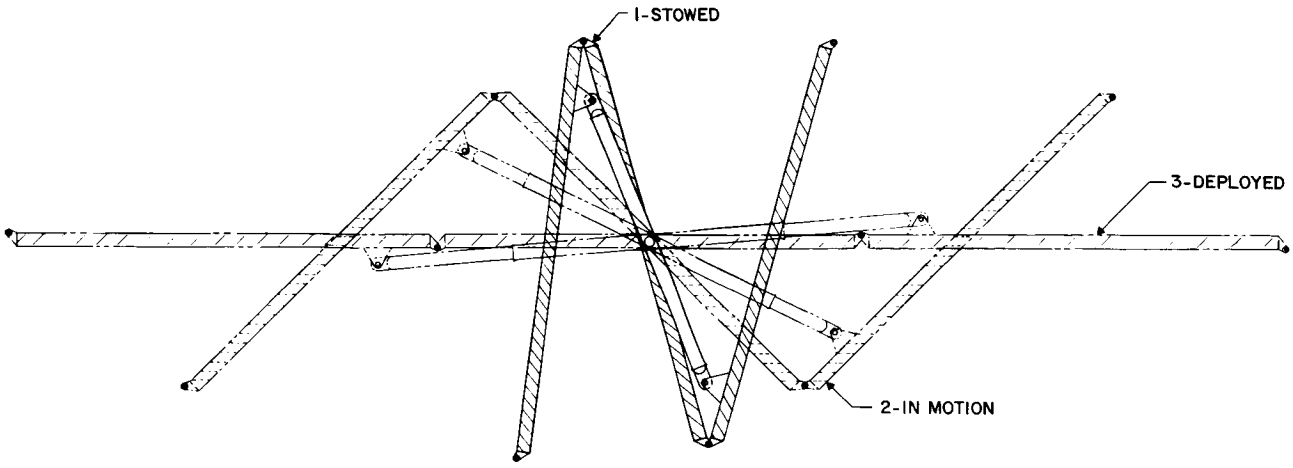

Figure VII-37. Solar Panel Actuator Deployment

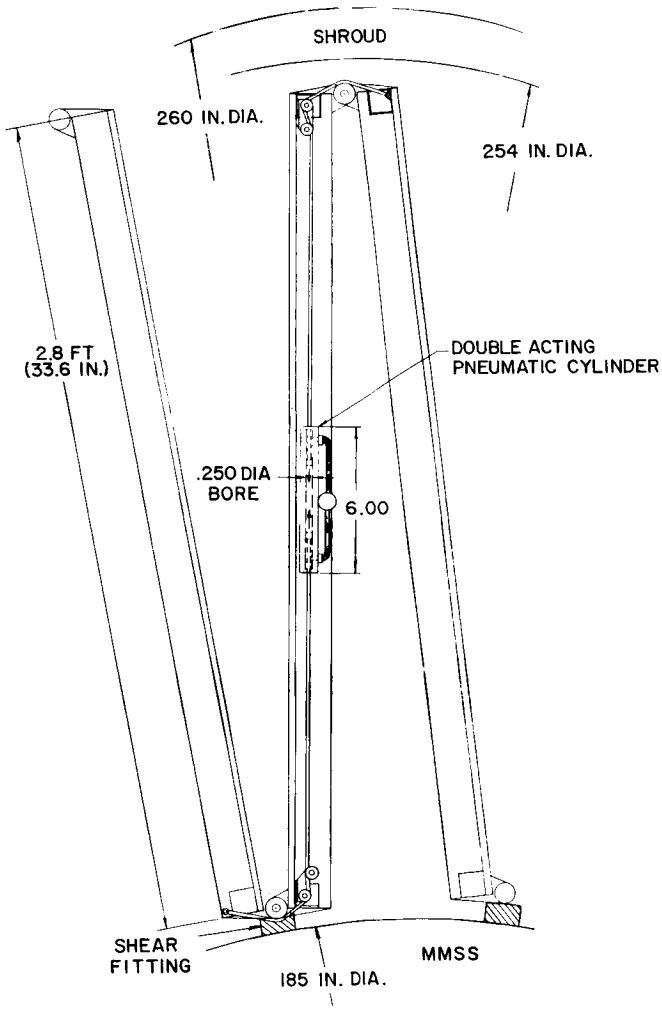

Figure VII-38. Double-Acting Pneumatic Cylinder Actuator

The critical loads developed in orbital flight result from Apollo Command and Service Module docking to the MMSS and from SPS engine firing. The solar array can be rotated relative to the MMSS with the primary load carrying orientations shown in Figure VII-39. For each of these orientations the load carrying capability of the array was determined, as shown in Figure VII-40.

1. Docking Configuration

The orbiting configuration used to illustrate the structural analysis is shown in Figure VII-3. Docking loads developed are based on the following information supplied in Reference VII-4.

Relative Docking Velocity: 2 feet per second;

Docking Stroke: 7 inches or 0.582 foot;

Apollo Command and Service Module Weight:	16,690 lb
Two Compartment MMSS & Solar Array Weight:	16,610 lb
Total Weight	33,300 lb

The determination of the input limit load is as follows: Equating the impact energy to the resisting energy,

$$1/2\ mv^2 = F \times S \qquad \text{(VII-2)}$$

where

m is equivalent docking mass (lb sec^2/ft),

v is relative docking velocity (ft/sec),

F is impact force, and

S is stroke of impact (ft).

The equivalent weight is

$$W_e = \frac{(W_1)(W_2)}{W_1 + W_2} = 8320 \text{ lb.}$$

where

W_1 is Apollo C&SM, lbs, and

W_2 is Two-compartment MMSS and Solar Array, lbs.

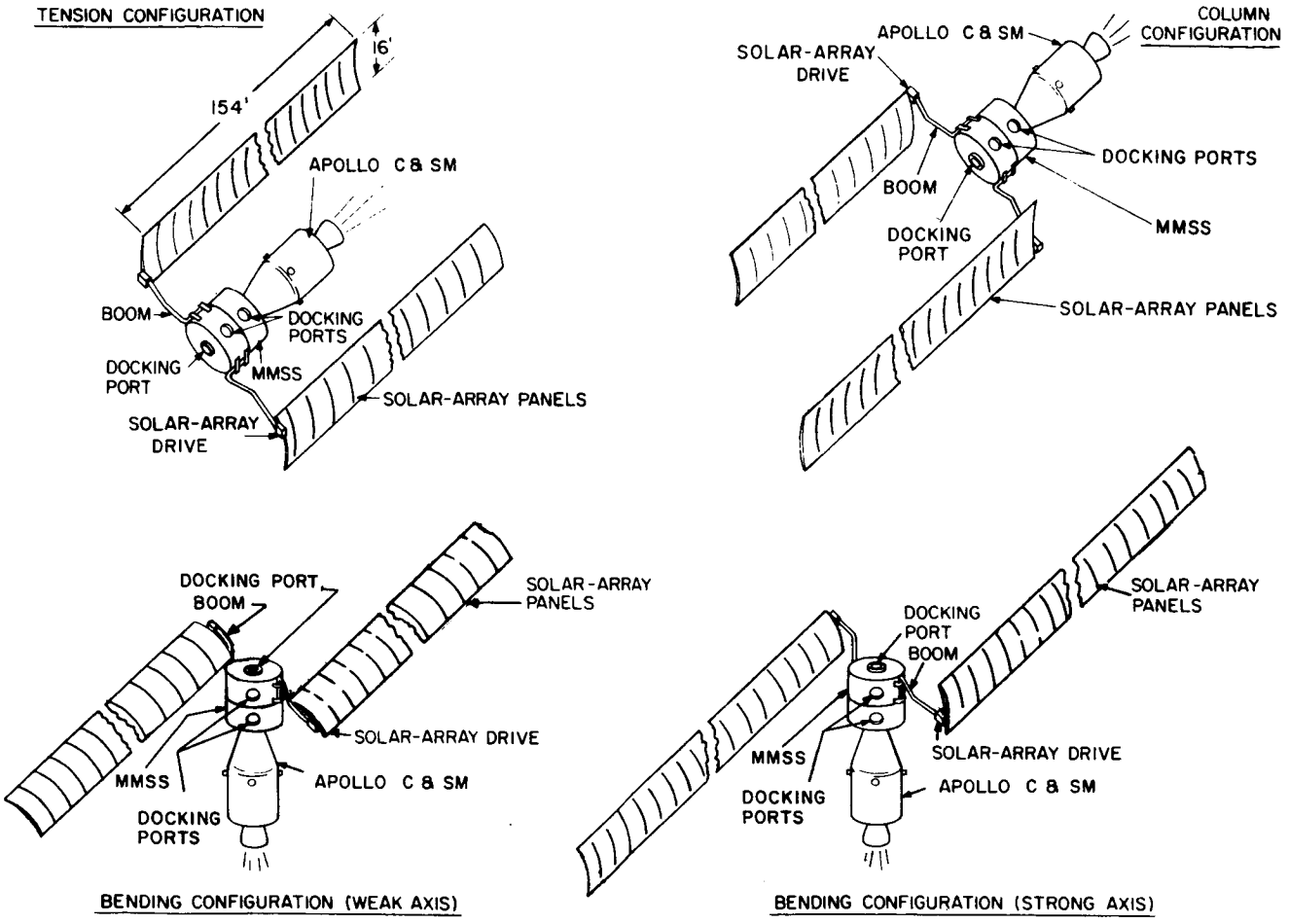

Figure VII-39. Array Configuration; Primary Load Orientation

Then the equivalent mass is

$$m = \frac{W_e}{g} = \frac{8320}{32.2} = 285.5 \text{ lbs. sec}^2/\text{ft}$$

Substitution in Equation VII-2

$$F_{avg} = \frac{mv^2}{2S} = \frac{285.5\ (2)^2}{2\ (0.582)} = 887 \text{ lbs., average docking force}$$

Assuming shock loading,

$$F_{peak} = 2\ F_{ave} = 1774 \text{ lb} = \text{limit docking load}$$

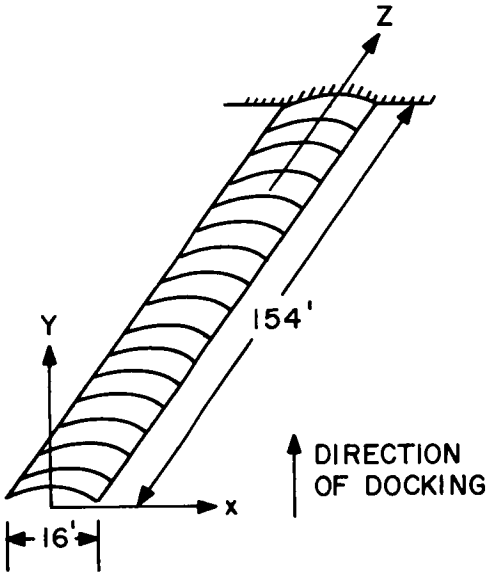

DEPLOYED POSITION

55 PANELS @ 2.8 FT X 16 FT
AREA/ARRAY SIDE = 2470 FT^2

*TIP DEFLECTIONS

PANEL CHARACTERISTICS

I_{x-x} = 21.92 in^4
I_{y-y} = 7280 in^4
* J_{max} = 137 @ TIP (ult) - DOCKING COND.
* θ_{max} = 5.74 @ TIP (ult) - DOCKING COND.

LATERAL FREQUENCY = 0.026 Hz
TORSIONAL FREQUENCY = 2.10 Hz

ARRAY LOADINGS (in g's)

TENSION ORIENTATION	35.0
COLUMN COMPRESSION BUCKLING ORIENTATION	0.23
BENDING ORIENTATION	
WEAK AXIS	0.02
STRONG AXIS	0.75

Figure VII-40. Array Load Capability

The equivalent input "g" load to the panels (assume rigid boom and rigid attachment to the MMSS is

$$\frac{1774}{16,610} = 0.1608 \text{ g (limit)}$$

As previously stated, the analysis assumes that the array docking position relative to the direction of the docking load is in bending about the "weak axis". Then the "g" response of the array is determined by the frequency ratio fundamental natural frequency of the array to the excitation frequency using the assumption of a half sine-wave pulse (see Figure VII-41) is as follows.

The period of docking pulse

$$\tau_o = \frac{S}{V} = \frac{7}{12} \times \frac{1}{2} = 0.292 \text{ second}$$

Then

$$f = \frac{1}{2\tau_o} = 1.712 \text{ cps (docking-pulse frequency)}$$

For the solar array, $f_n = 0.043$ cps (fundamental bending natural frequency in the deployed condition).

$$\frac{f_n}{f} = \frac{0.043}{1.712} = 0.0251.$$

From Figure VII-41, where A_o is amplification factor

$$A_o = \frac{Y_o}{X_o} \approx 0.1$$

Therefore, the effective docking response load becomes

$$gA_o = (0.1068)(0.1) = 0.011 \text{ g (limit)}$$

This response load is within the capability of the array as shown in Figure VII-40. The bending-weak axis orientation of the array was chosen for illustration since this mode yields the maximum maneuvering clearance for the docking vehicle.

Ideally, the column compression mode is capable of sustaining the docking load. However, temperature gradients through the array and manufacturing tolerances will cause a "droop" in the array which will result in application of an eccentric column load. Since manufacturing tolerance build-up is unknown at this time, it is not possible to calculate the eccentricity of the load vector and therefore the "g" loading. For this reason this mode is not recommended.

The array is capable of sustaining the docking loads in all other primary orientations.

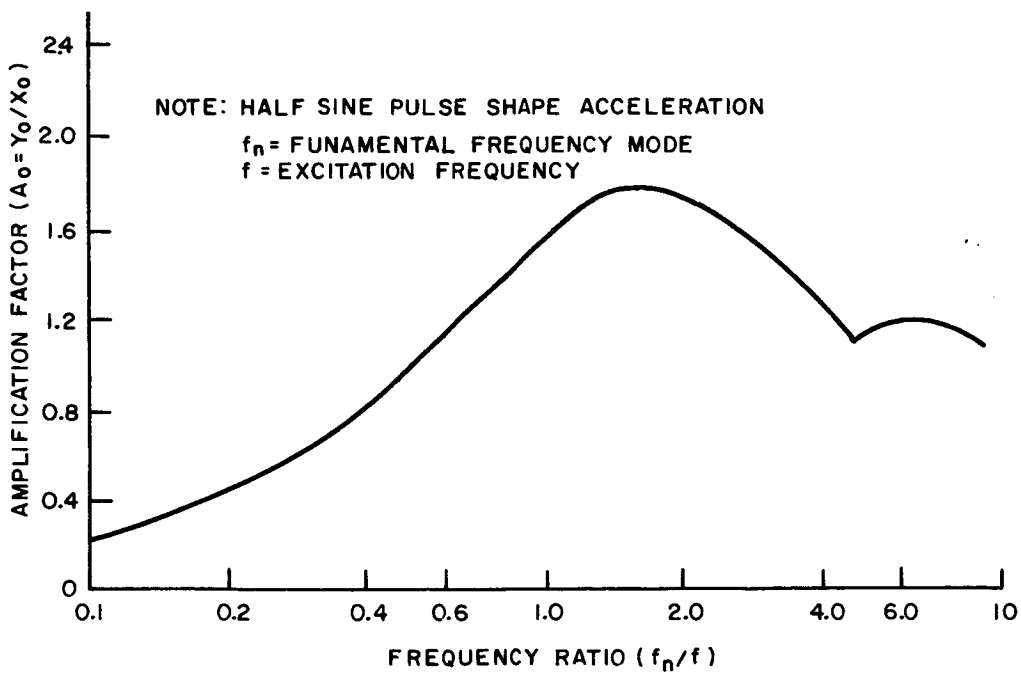

Figure VII-41. Amplification Factor

2. Docking Cycle

The load developed by docking normal to the array (Figure VII-3) will cause the array to rotate about the longitudinal axis of the boom. The rotation will be resisted by the electric-motor/gear-box assembly of the array orientation drive. This assembly will react to the angular acceleration of the array and will reposition the array normal to the sun vector.

A brief description of the docking cycle is given in this paragraph and is shown graphically in Figure VII-42. The analysis was made using a conservative rigid-body model and assuming that the torque developed by the motor is constant at the stalled rotor torque value of 1.8 foot-pounds.

At the conclusion of the docking impulse, the solar array is rotating at an angular velocity of 6.5×10^{-3} radian per second. With a motor capability of 1.8 foot-pounds of torque and a gear-box reduction ratio of 20:1, the angular deceleration of the array is 5.95×10^{-5} radians per second per second. The time required to reduce the angular velocity to zero is 110 seconds, at which time the array has rotated 20.6°. Deceleration of the array continues for an additional 77 seconds until the angular velocity is -4.4×10^{-3} radian per second and the angular displacement is 10.3° from the initial start of docking position. At this time the motor/gear-box assembly acts as a brake on the array and reduces the angular velocity of the array to zero in an additional 77 seconds. At this point the array has assumed its normal operational position. This completes the docking cycle in a total time of 264 seconds. For this type of operation reverse current protection for the motor must be included so as not to demagnetize the motor.

3. Service Propulsion System (SPS) Engine Firing

Firing of the SPS engine will be required to provide orbit charges. Since SPS engine firing represents the critical orbital load, the array orientation boom has been sized for this condition. The position of the array relative to the SPS engine load vector places the array in the tensile mode.

a. BOOM SIZING

Considering the worst case, where the boom is assumed to be rigid and the array is in a tensile mode, (see Figure VII-39) the following analysis was made:

$$a = \frac{T}{W} g;$$

where

T is engine thrust = 21,900 lb and

W is vehicle weight = 26,100 lb,

Based on a conservative estimate, the MMSS weight is 28,370 lb. Less expendables of 2,270 lb, the total weight is 26,100 lb.

$$a = \frac{21,900}{26,100} = 0.84 \text{ g.}$$

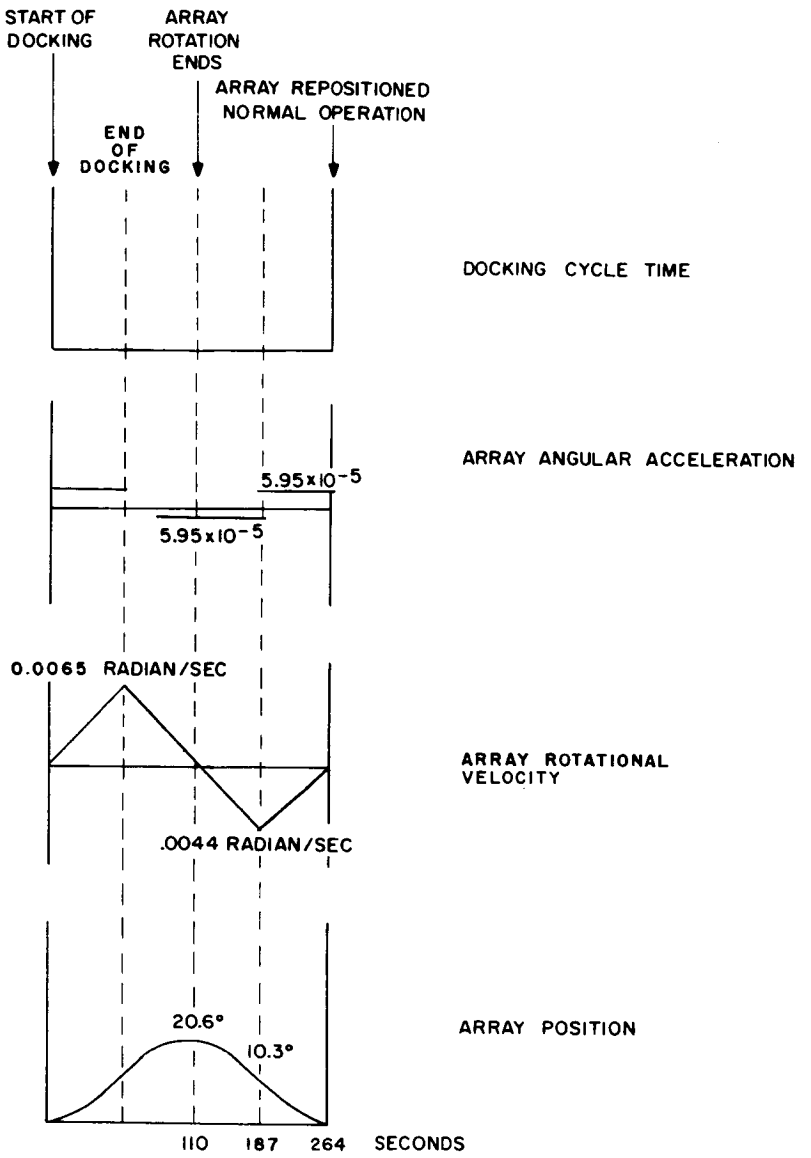

Figure VII-42. Docking Cycle

The ultimate design load in terms of g for the boom is:

$$g = 0.84\ (1.2)\ (1.5) = 1.515$$

where

1.2 is the magnification factor and

1.5 is the ultimate design load factor.

Then, as a cantilever beam as in Figure VII-43,

$$M = P\ell$$

where

M is bending moment

P is array weight x g loading and

ℓ is application of load distance (312 in.)

and

$P = 2470\ (1.515) = 3,740$ lb

$M = 3740\ (312) = 1.168 \times 10^6$ in lb. ultimate.

Using 78,000 psi as the ultimate strength of 7075T-6,

$$\text{Section modulus Z required} = \frac{1.168 \times 10^6}{78,000} = 15.0 \text{ Cu in.}$$

This requirement can be met with a standard 8-inch-diameter by 3/8-inch wall thickness aluminum alloy tube, where Z is 16.36 cu. in.; the weight for this boom will be 190 lb. To reduce the weight of the boom, a space-truss configuration such as shown in Figure VII-44 can be utilized. This configuration has the following weight breakdown:

Cylindrical boom	91 lb
Space truss members	53 lb
Total	144 lb

With this configuration, however, an astronaut would be required to perform an assembly (space truss to boom) prior to and post SPS engine firing. For the additional weight of 46 pounds per cantilevered boom, this requirement can be eliminated. Therefore, the single cylindrical boom of 190 pounds is recommended. It is interesting to note that if firing the SPS engine is not a requirement, a 2-3/4-inch O. D. by 1/8-inch wall thickness aluminum tube can be used at a weight of 21.85 pounds per boom.

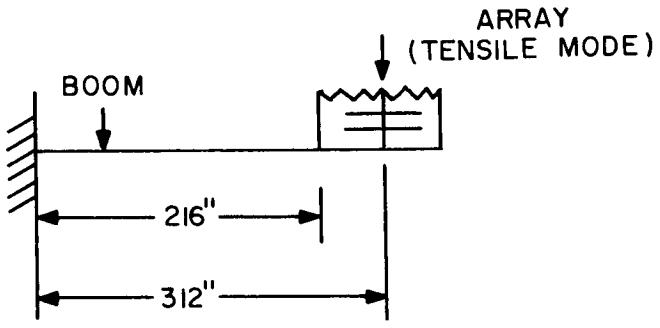

Figure VII-43. Simplified Diagram of Array-Boom Structure

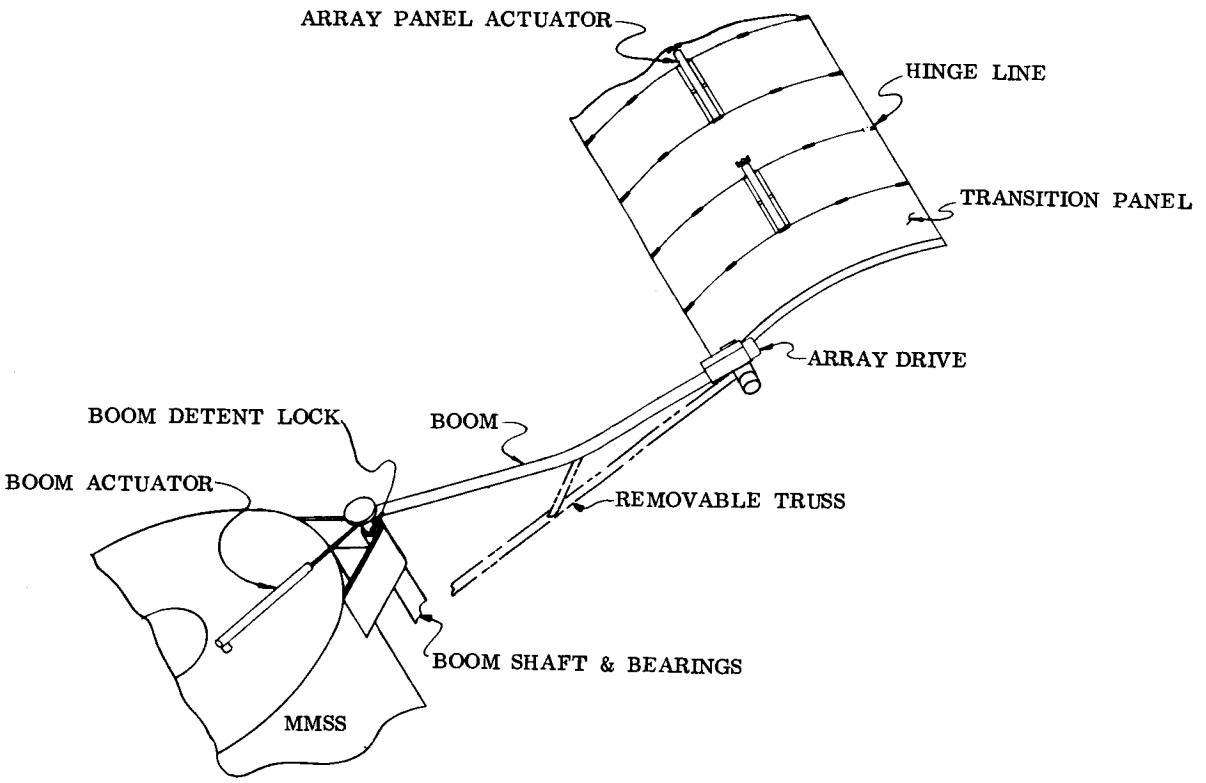

Figure VII-44. Space-Truss Boom Concept

b. ARRAY ORIENTATION

As shown in Figure VII-40, the array in the tensile mode is capable of withstanding the "g" loading imposed by the SPS engine firing. Similarly, it can be seen that placing the array in a bending mode about the weak or strong axis is prohibitive.* However, only the tensile mode can be employed to survive the engine firing without increasing the panel cross section, although in this mode, the plume effects of the SPS engine on the array (both thermal and particle) must be considered.

G. WEIGHT SUMMARY

A weight summary for all items required to fabricate the array and maintain normal sun incidence is shown in Table VII-8. Because of the conceptual nature of the study, it was not possible to size all members based on a stress analysis. Consequently, some of the values listed represent engineering estimates based on previous experience.

---

*The concept of a beam of constant stress (discussed in Paragraph VII.C.7) if adopted, would permit placing the array in hard mode bending for engine firing. As noted previously, this approach would virtually eliminate the effects of the engine plume on the array.

TABLE VII-8. WEIGHT SUMMARY

Item	Weight	
	lb per sq. ft.	lb
Solar Array (4900 sq ft)		
Solar Cells & Electrical Components	0.314	
Aluminum Structural Frame	0.144	
Aluminum Honeycomb - 1/4 in. thick	0.235	
Hinges	0.034	
Panel Fold-Out Actuators & Fittings	0.019	
Electrical Harness	0.050	
Miscellaneous Hardware	0.027	
Total	0.823	4033
Deployment Mechanisms		
Boom Assembly (2 req.)		380
Transition Panel (2 req.)		180
Drive Shaft & Bearings (2 req.)		50
Boom Actuator Assembly (2 req.)		10
Array Retaining Cables & Hardware (2 req.)		45
Electrical Connectors		10
	Total	675
Servo Control System		105
Array Orientation Drive Assembly (2 req.)		
Electronics		
Sensors		

LIST OF REFERENCES FOR SECTION VII

VII-1. Douglas Aircraft Company, Inc., Saturn 1B Payload Planner's Guide, Missile and Space Systems Division, Santa Monica, California.

VII-2. Douglas Aircraft Company, Inc., Saturn V Payload Planner's Guide, Missile and Space Systems Division, Santa Monica, California.

VII-3. George C. Marshall Space Flight Center, Preliminary Vibration, Acoustic, and Shock Specifications for Components on Saturn V Vehicle, Report No. IN-P+VE-S-63-2.

VII-4. Lockheed-California Company, Modular Multipurpose Space Station Study, Report LR 18906, July 30, 1965.

VII-5. Electro-Optical Systems, Inc., Development of a Lightweight Rigid Solar Panel, Report No. 7027-IDR, May 18, 1966.

VII-6. Boeing Company, Final Report, Fabrication Feasibility Study of a 20-Watt per Pound Solar-Cell Array, Report No. D2-23942-5.

SECTION VIII

MECHANICAL SYSTEM ANALYSIS, CONCEPT B (PSM)

A. INTRODUCTION AND SUMMARY

The mechanical and thermal analysis of a power system module (PSM) concept is presented in this section.

As a result of the stowage analysis performed (Appendix A), a basic PSM structure was defined by NASA and a revised set of ground rules was provided (Appendix H). Major differences in the ground rules are as follows:

- No modification to the LEM shroud or truss adapter.
- Planar array with retraction capability.
- 5 kW baseline load requirement.

The lower (5 kW) load requirement can be supported by an 1800 square foot array. Thus shroud modification is not needed to provide adequate stowage volume. Figure VIII-1 shows the PSM stowage and launch envelope and dimensions; Figure VIII-2 shows the PSM conceptual design in the launch configuration. Appendix H gives the ground rules and assumptions used in the PSM conceptual effort. A retractable flat array was designed, with a weight of approximately 0.8 pound per square foot, substantially better than the one pound per square foot maximum. This array is composed of primary (major load-carrying members in the deployed mode) panels and secondary panels. Revision of this design concept led to a structurally more efficient array, which, when deployed, loaded all panels equally. Figure VIII-3 shows the initial and final concepts in schematic form. Table VIII-1 lists the load capability and natural frequency, in torsion and bending modes, of the deployed array.

Tentatively, for the initial design, a scissor linkage driven by a motor-gearbox deploys the array stack. By means of this linkage, the primary panels are locked in the flight position. The secondary panels are deployed by means of spring-actuated, fluid-damped mechanism with a permanent locking feature. This mechanism is a modified, flight-proven device.

The locks on the primary panel must be capable of being unlocked, but the secondary-panel locks do not require this capability. Retraction of the array is accomplished by unlocking the primary panels and folding them back along a single hinge line (primary) axis. The mechanism that locks the array in the retracted position so that it is a single folded stack requires considerable additional design effort.

For the final concept, retraction for load purposes (as indicated in Table VIII-1) is not required. It is therefore assumed that little or no load capability is required of the retracted array. The deployment and lock-unlock mechanisms have not been designed, although there are many possibilities.

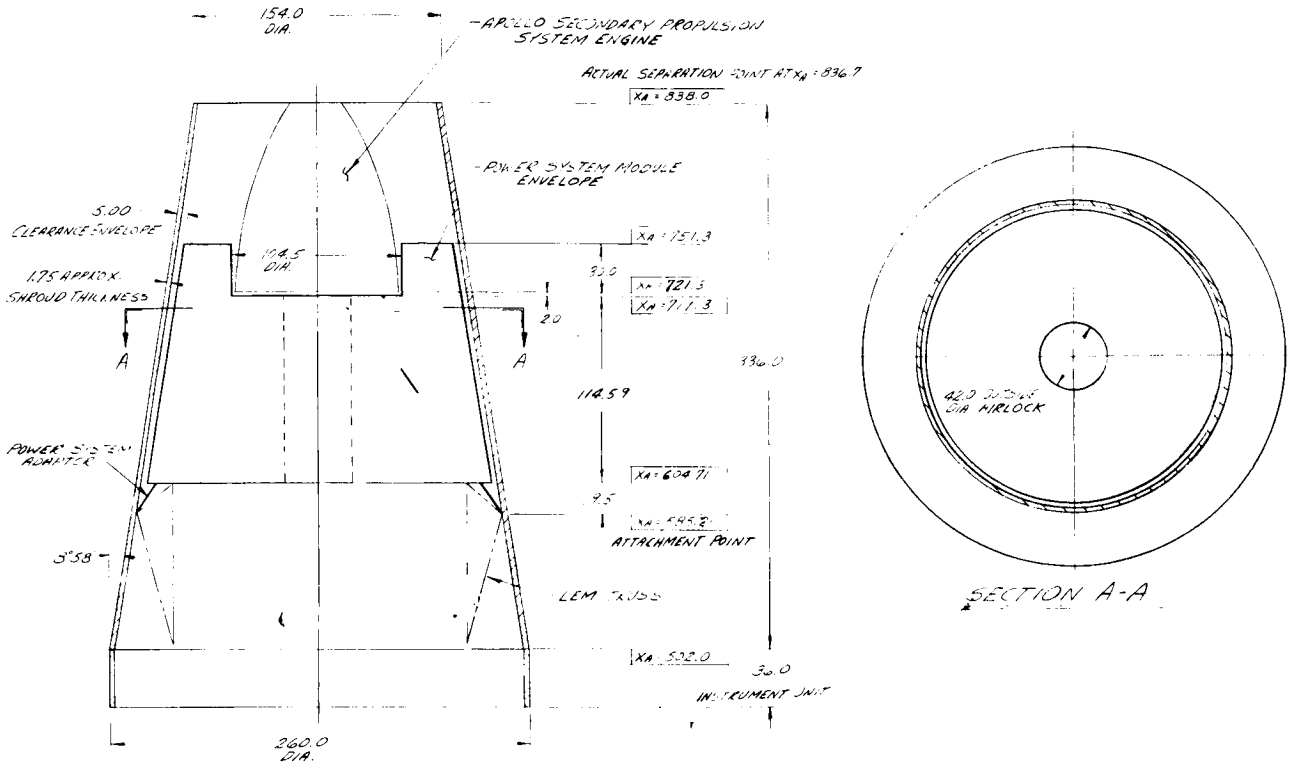

Figure VIII-1. PSM Stowage and Launch Outline

TABLE VIII-1. ARRAY DESIGN COMPARISION

Concept	Mode for Docking	Mode for SPS Firing	Natural Frequency (Hz)*	
			In Bending	In Torsion
Initial (Preliminary)	Deployed	Retracted (for loading)	0.18	0.14
Final	Deployed	Deployed (tension-compression orientation)	0.26	0.38

*The discussion in Paragraph VIII. F. mentions a small negative stress margin (-0.1) for the final concept when in the deployed mode during firing of the SPS engine. Further iteration will lead to satisfaction of the stress requirements with little or no weight penalty.

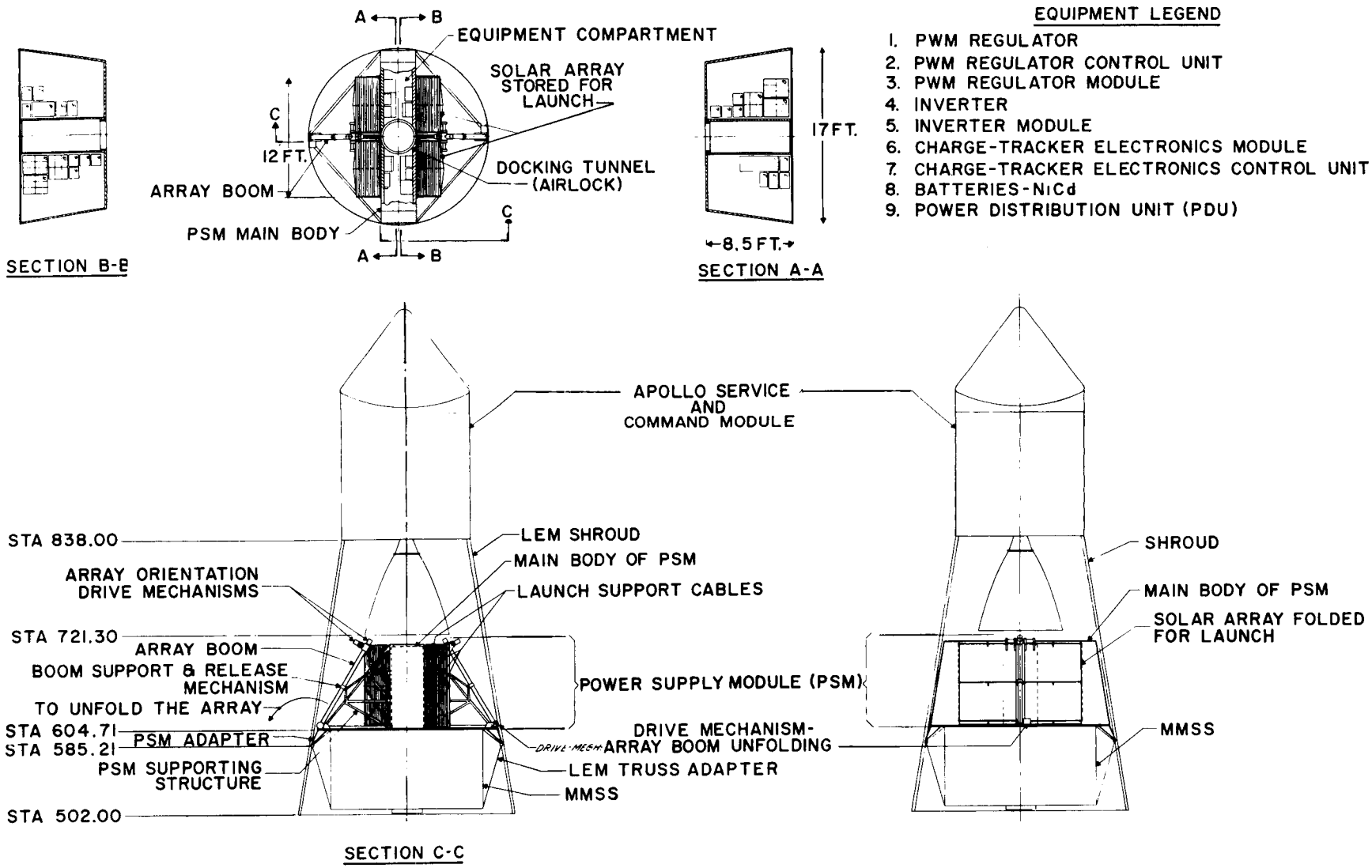

Figure VIII-2. PSM Launch Configuration

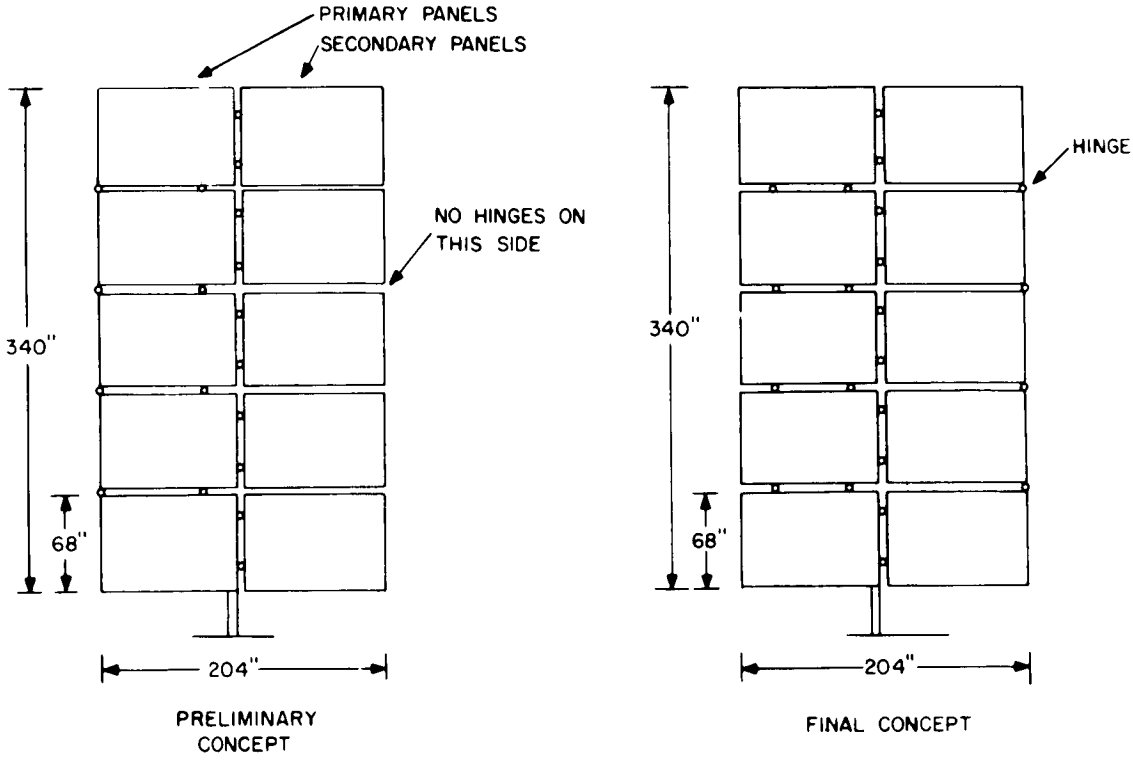

Figure VIII-3. Array Deployment Concepts

The orientation drive used on the IPS array (Section VII) is adapted for use on this array. Power transfer across the rotating joint, as before, utilizes slip rings.

The orbital configuration, shown in Figure VIII-4, employs the "H" type array concept (See Section IX). This symmetrical design eliminates cyclical gravity gradient and its attendant fuel requirements. Shadowing of one array on another presents no mission capability curtailment since this condition occurs at or near 100 percent sun time when the power demand is at a minimum, i.e., no battery recharge power requirement. However, full power array capabilities can be reacquired by rolling the vehicle slightly for a polar orbit. In a 28-1/2 degree inclined orbit, this maneuver is not required at all since array on array shadowing does not occur. The additional discussion of shadowing is covered in Section IX.

The orbital configuration has dimension such that the aspect ratio is 3.36:1 with a length of 28.75 feet from the boom axis. Because of this length, the plume effects of the firing of the SPS engine with the array deployed (final concept) will have little or no effect on the array.

The thermal control system for the battery compartments must be active, whereas the electronic compartments may be passively controlled. This results from the narrow acceptable temperature limit for the batteries of 15 to 30°C, whereas the electronics temperature range is 0 to 55°C. The radiating surfaces for all compartments use second-surface mirrors. A very brief discussion in this Section points to some advantage of a fluid-loop thermal-control system.

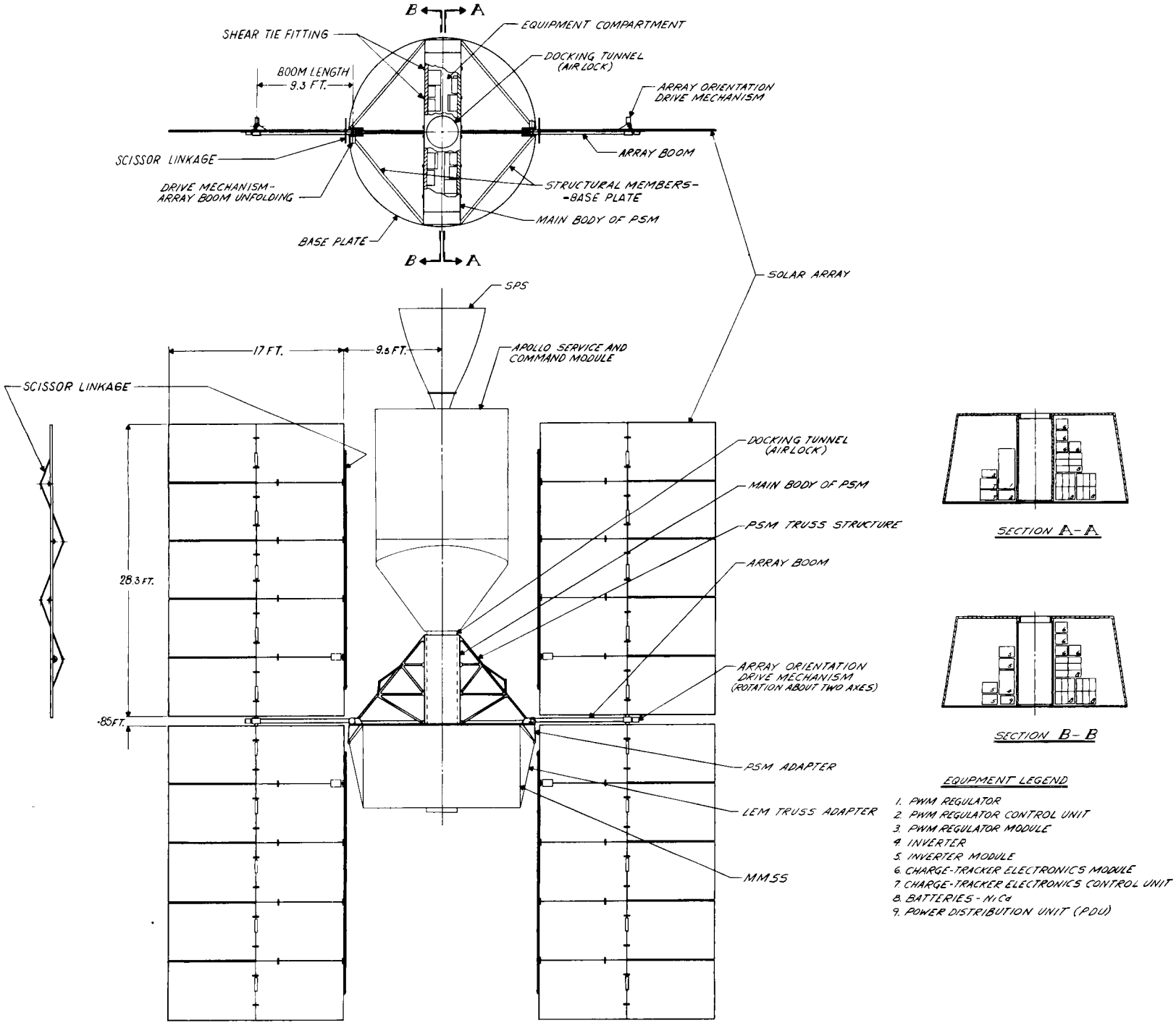

Figure VIII-4. Orbital Array Configuration

B. STOWAGE ANALYSIS (POWER SYSTEM MODULE)

1. Evaluation of Stowage Location

To avoid modifications to the existing LEM shroud, an investigation was made of alternate stowage locations within the volume of the original two-module MMSS volume (See Appendix A). The array stowage concept of accordion-folded panel segments about a mounting circumference, used in the IPS design, was used in all cases studied so as to form a common basis for comparison of stowage possibilities. Details of deployment concepts were not evaluated for this comparison, but were assumed similar to those of the IPS concept.

Table VIII-2 summarizes the stowed array area potential of the various locations. Based on these results, Case I was translated into an independent power supply module (PSM) concept adaptable to various space vehicles. The volume within the LEM shroud, as defined in Figure VII-1, was chosen as the limiting envelope size of the PSM launch configuration. Since only 1800 square feet of array area is required to support the reduced mission load, no shroud or truss modification was necessary.

The initial concept of the PSM framework is shown in Figure VIII-5. Four equally spaced struts serve as docking tunnel (airlock) supports and PSM primary attachment points to the LEM shroud separation points. The "H" shaped, deployed array configuration can be folded and stowed for launch within this structural configuration.

TABLE VIII-2. STOWED ARRAY AREA POTENTIAL
ACCORDION-FOLDED STOWAGE CONCEPT (IPS)

Case*	Array Area (Sq. Ft.)	
	9 in. Packing Factor	7-1/2 in. Packing Factor
I	1750	2400
IIA	740	1000
IIB	1130	1420
IIC	1515	1775
III	750	1000
IVA	675	900
VIB	875	1140
IVC	1200	1550
IVD	1200	1590

*See Appendix A

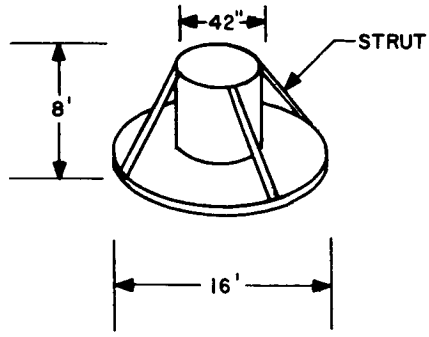

NOTE: ALL DIMENSIONS APPROXIMATE

Figure VIII-5. Power System Module Configuration

2. PSM Structure Configuration

The Power Supply Module (PSM) must provide for launch support and functional orbital operation of both the docking tunnel (airlock) and the entire power supply system. The docking-tunnel design, while not part of the scope of this study, is briefly considered so that docking-tunnel/PSM-structure interfaces can be discussed.

The main body of the PSM consists of the docking tunnel and power supply equipment compartment. The walls of the equipment compartment will support all the power supply electronic packages, such as the stowed solar-array, batteries, battery charge regulators, voltage regulators, and inverters and will provide the surface area required for radiative cooling of these units. The structural design of these walls will be strongly influenced by the requirements of the thermal control system.

The thermal control system (tentative) requires relatively thick walls (average of 0.4 inch) for a thermally conductive radiator and the power supply equipment will utilize these walls for structural support. Local reinforcements will be provided at equipment mounting locations and shear fitting points will be provided for the solar array in stowage position. The relatively sturdy construction of these walls will allow the omission of two of the original four docking tunnel supporting struts (see Figure VIII-2).

The two remaining docking tunnel supporting struts will themselves be strengthened against buckling loads by a secondary truss system.

The docking tunnel will be functionally independent of the power supply equipment compartment, since its integrity as a pressure vessel must be preserved. Local "hard" points on the docking tunnel will be required for interconnection with the PSM structure.

The PSM baseplate supports the lower end of the docking tunnel and the deployment-boom mounting points and provides the bottom wall of the power supply equipment compartment. As such, the baseplate provides a major load-carrying path.

Construction may be similar to that of the equipment compartment walls, or may be of truss-type construction with local reinforcement as required. An adapter structure, which mates with the baseplate and attaches to the existing hard points on the LEM shroud, will be provided.

3. Array Support, Stowed

The array in the launch configuration is shown in Figure VIII-2. Each array half, consisting of a deployment boom and four identical folded sections, is stored in two of the adjacent quadrants formed by the docking tunnel (airlock) supporting structure. Each array section is folded and supported for launch in identical fashion. A tightly folded, large-panel array was chosen over the IPS accordion-folded system because of the interference of the supporting struts, the volumetric stowage efficiency, and the larger dimensions available for stowed panels. This approach requires consideration of large-panel dynamic response and necessitates a revised concept of array launch support.

The basic requirements for array stowage discussed in the IPS design are still applicable to the PSM concept. The stowed array, when folded into the compact rectangular shape for stowage, must be adequately supported against launch loadings and must be capable of deployment with a minimum of kinematics.

Panel support for each stowed array section will be provided by a shear tie-cable tension member system as shown in Figure VIII-2. Folded adjacent panels will interlock through nine mating shear fittings. The tapered design of these shear fittings will prevent shock loadings by absorbing small variations in panel spacing and permit easy separation of panel-shear fitting during the initial phase of array deployment. Similar shear fittings, having a retracting capability, will join the inboard panel of each array section to the PSM structure. As the shear fitting system provides support in only the thrust and one lateral axis, tension bands or cables are employed to complete the support system and to secure the entire array section assembly to the PSM structure. Truss members, integral with the outboard panel, provide support for the centrally located shear fittings.

Support at the center of the deployment boom will be provided during the launch phase by a latch capable of explosively initiated opening. Such support is necessary to minimize the inertial-mass loading of the array-orientation drive unit on the adjacent panels and to control dynamic deflections of the center portion of the boom.

4. Array-PSM Structure Integration

Prior to array integration with the PSM structure, batteries and associated electronics are installed within the electronic compartment of the PSM. This procedure will require, in addition to mechanical assembly, electrical harness connection, electrical tests, and final inspection of both the docking tunnel assembly and the electronic compartments.

To avoid solar-cell damage and to simplify interpanel connections, each array section will be separately assembled in the deployed configuration in a controlled environmental area. By reversing the deployment sequence, the array quadrant will be refolded with hinge, actuator, electrical, and similar connections being made as the process continues. The resulting folded-array quadrant will be secured by temporary tension bands and placed in a handling fixture.

Each array section may now be handled and installed on the PSM as a unit. Once the inboard shear-tie assemblies are mated with the adjacent panel and the final tension members secured, the fixture is removed and final connection of the array section to the deployment boom is completed. The handling of large weight (the 500-pound weight of each array section assembly) is offset by the ease and simplicity of array-PSM integration. Fixtures can be designed to minimize the handling problem and provide protection to the folded array (see Section V).

With the PSM concept, the entire power supply system is now complete and may be independently tested, qualified, and stored, prior to mating with an MMSS or launch vehicle.

C. ARRAY STRUCTURE ANALYSIS

1. Introduction

The Power System Module (PSM) concept was investigated with the following goals:

(1) The utilization of a flat solar-panel design with a low aspect ratio for the array when in the deployed mode.

(2) The consideration of an array retraction capability for the SPS propulsion engine firing mode. Retraction need not be to launch mode.

(3) Density of one pound per square foot (or less) for the assembled solar array.

The investigations and analyses were based upon the structural requirements dictated by the stowed mode. The resulting design was then analyzed for loadings in the deployed mode.

The final solar array structural configuration chosen was based on results of the concept development discussed in Section VII, and on flight-proven techniques used on the Lunar Orbiter and Nimbus Solar Arrays. This configuration incorporates a flat honeycomb sandwich panel structure, framed and stiffened with channels and hat sections as required for stress and deflection considerations. The aspect ratio (length to width ratio) for one side of the solar array is 3.38 as demonstrated in Figure VIII-6.

2. Factors of Safety

For the PSM concept, the factors of safety were the same as those incorporated in the IPS concept. They are commensurate with the factors utilized by the Lockheed Aircraft Company for the design of the MMSS (Reference VIII-1). These factors of safety are necessary in order to provide for the structural integrity and the high degree of reliability required for manned spaceflight.

As before, the limit load is established as the maximum actual load experienced by the structure during the prelaunch, launch, ascent, and orbital phases of the mission. The structure must not fail when subjected to the ultimate design load, which is defined as 1.5 times the limit load. In addition, the yield design load shall be equal to 1.15 times the

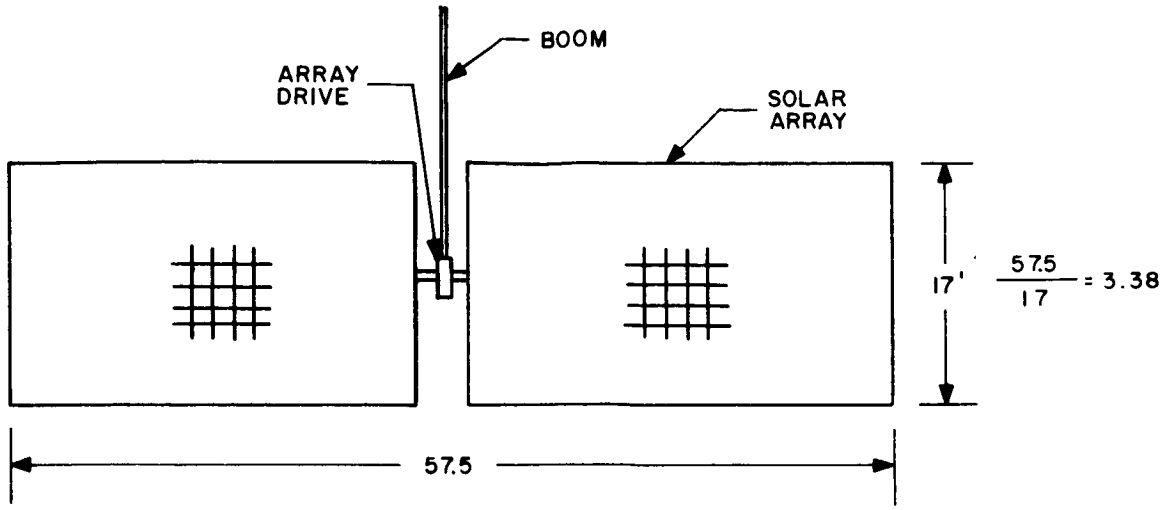

Figure VIII-6. Aspect Ratio of Solar Panel

limit load (during the prelaunch and launch phases) and ... 1.20 times the limit load (during the orbital phases) and 2.0 times the limit load (during the ground handling phases).

3. Design Criteria

The design limit input loads used for this portion of the study were as defined in Section VII of this report. Shown in Table VIII-3 is a summary of the loads in the prelaunch and launch environments. An analysis of these loads indicated that acoustic noise was the critical launch phase load (as in Section VII).

The critical loads for orbital flight are those associated with the docking and SPS engine firing activities. The magnitude of these loads and the manner in which they are handled are developed in Paragraph VIII. F.

Figure VII-7 shows the array-spacecraft layout with the array positioned normal to the velocity vector or roll-axis of the PSM.

4. Design Analysis for Launch

As was previously indicated, the launch (or stowed) conditions dictated a particular structural design and a subsequent design analysis was performed based upon the configuration criteria (Table VIII-4).

Figure VIII-8 depicts the array configuration for launching in the stowed position.

Figure VIII-9 shows the panel structural elements and support points for the launch mode.

Section A-A of Figure VIII-7 indicates the framing layout from which the critical inertia is determined. This value was computed as 0.514 in^4.

TABLE VIII-3. DESIGN LIMIT INPUT LOADS
(Reference, Section VII)

Item	Load Criterion
Prelaunch	
Hoisting	2.0 g
Ground deployment	See NOTE
Launch	
Vibration:	
Sinusoidal	Described in Section VII
Random	Described in Section VII
Shock	20 g peak, half-sine, 10 milliseconds
Acoustic noise	Described in Section VII
Lift-off acceleration	Described in Section VII

NOTE: Deployment of the array in a 1.0g field (ground testing) shall not govern the structural design of the array.

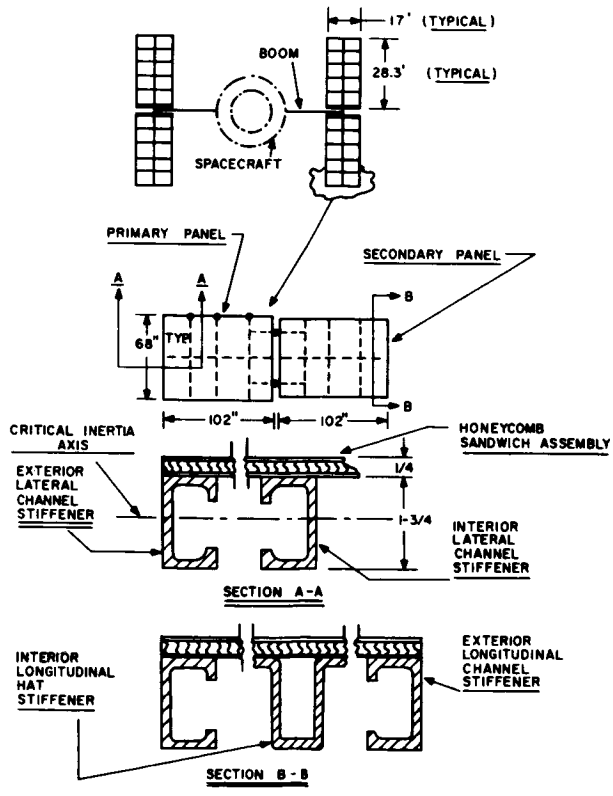

Figure VIII-7. Spacecraft Array Details, Normal Position

TABLE VIII-4. CONFIGURATION CRITERIA

Item	Criterion
Honeycomb panel height and core size	1/4 in., as used in IPS concept
Total structural height	2 in.
Honeycomb panel treatment	To be uniformly loaded and simply supported on all four edges
Dead weight of panel	Not to exceed 1.0 lb per sq. ft.
Honeycomb facing material	To be aluminum alloy 5052-H39; tensile yield strength of 40,000 psi; fatigue strength of 26,000 psi at 10^6 Hz
Honeycomb intercell buckling stress allowable	17,000 psi
Frame stiffener material	To be aluminum alloy 2024-T4; tensile yield strength 46,000 psi; fatigue strength 26,000 psi at 10^6 Hz

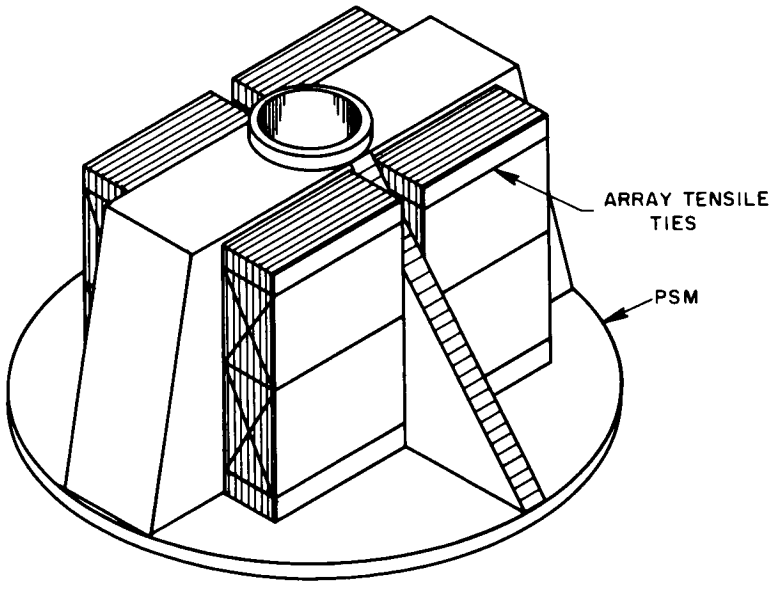

Figure VIII-8. Array Stowed for Launch

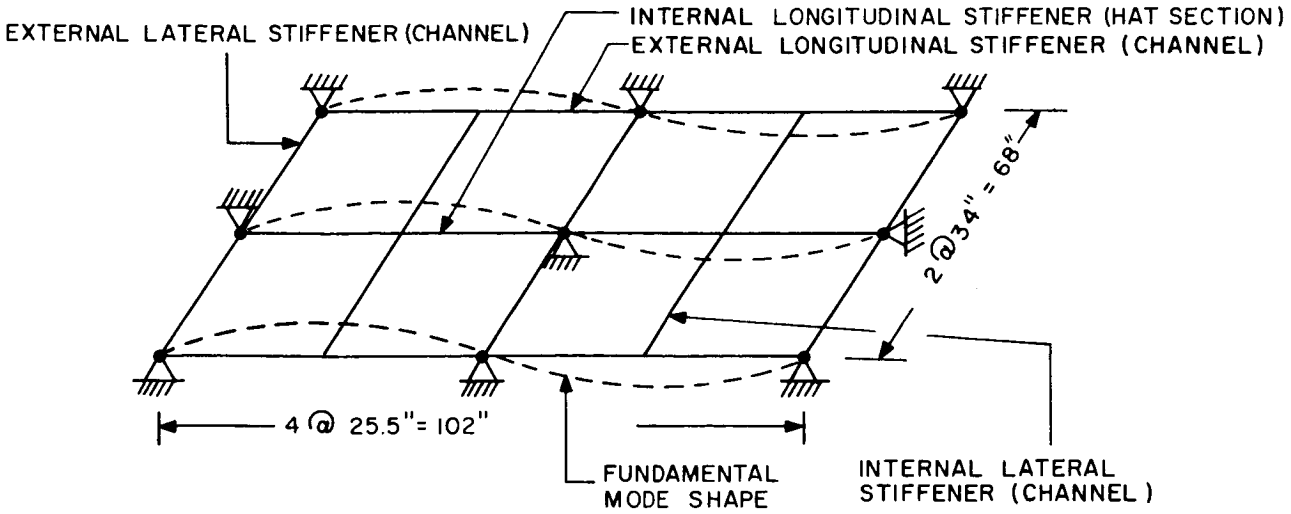

Figure VIII-9. Array Panel Stowed for Launch

Table VIII-5 lists the stresses and associated margins of safety for the various elements of the array structure.

TABLE VIII-5. LAUNCH-MODE STRESSES AND SAFETY MARGINS

Element	f_{Max}* (psi)	Margin of Safety **
Honeycomb substrate	10,500	+0.62
Composite honeycomb/interior longitudinal stiffener section (1.75 x 0.032 in. "hat") ***	17,550	-0.03
Composite honeycomb/exterior longitudinal stiffener section (1.75 x 0.032 in. channel)	17,550	-0.03
Composite honeycomb/interior lateral stiffener section (1.75 x 0.025 in. channel)	15,000	+0.13
Composite honeycomb/exterior lateral stiffener section (1.75 x 0.025 in. channel)	7,500	+1.26

* maximum bending stress based on an ultimate design load factor of 1.50

** based on 1.0 lb per sq. ft. loading condition

*** $f_{allowable}$ is 17,000 psi, critical honeycomb intercell buckling stress

In reviewing this table, attention is directed to the negative margins of safety associated with the bending stress analysis of the exterior and interior longitudinal stiffeners. It is pointed out that these figures are based on a loading condition of one pound per square foot, whereas in reality, the loading to which the panel is subjected is 0.808 pound per square foot (see Table VIII-6). Using this latter value and reiterating, the maximum bending stress in the stiffeners is calculated to be 14,200 psi and the associated margins of safety are +0.20. The other margins shown will also increase positively, thereby affording additional reliability in the design and/or permitting a reduction in the size and weight of the members.

The solar array weight estimate is shown in Table VIII-6.

TABLE VIII-6. SOLAR ARRAY WEIGHTS (ESTIMATED) *

Item	Weight (lb/ft^2)	lbs
Solar cells & components	0.314	
Array structure	0.413	
Hinges & panel unfold actuators	0.053	
Harness	0.008	
Miscellaneous hardware	0.020	
Total, lb/ft^2	0.808	
Total, lb		1,558
*Solar array = 1927 ft^2 (total)		

5. Additional Considerations

a. COMPARISON OF BERYLLIUM AND ALUMINUM

As discussed in Section VII, a weight advantage for beryllium over aluminum can be shown analytically. However, for the same reasons, as discussed in Section VII, namely: (1) cost, (2) material size availability in the required gauge, and (3) limited test data, the choice of material for this design is aluminum.

b. THERMAL STRESS

Solar-array temperatures are primarily based upon the distributed mass and not on local concentrated masses such as the structural stiffeners. In order to maintain a night-time temperature at the synchronous altitude of no lower than -155°C, the honeycomb substrate

(which is a distributed mass) must be at least as dense as that determined in Section VII. As a result, the honeycomb section utilized in the IPS analysis is used in this portion of the study.

Thermal stresses and the associated deflections resulting from thermal gradients within the array structure were proven to have a negligible affect upon the structural performance of the array. As a result, these analyses were not duplicated here.

D. COMPONENT STRUCTURAL DESIGN

1. Array Orientation Drive Assembly

The orientation drive assembly mounted on the end of the boom and connected to the array contains the torque motors (for control of both axes of rotation), gear reduction units, and slip ring assemblies. This unit is similar to that of the IPS concept with the exception that two output shafts are required. These shafts each actuate one section of the array, located on one side of the vehicle. The drive unit is shown schematically in Figure VIII-10.

2. Sealing and Lubrication

Demonstrated in Section VII was the justification for and advisability of using a labyrinth sealing system and low-pressure lubrication. An identical approach will be adopted for this PSM concept.

3. Energy Transfer Across a Rotating Joint

Three approaches were investigated for transferring energy across a two-axis rotating joint: wind-up cable, rotary transformers, and slip rings. Because of the continuous rotation required by the array relative to the spacecraft in one axis (one revolution per orbit) and the complexity of counter-rotating the array to unwind for the orthogonal axis, this approach was not pursued. The rotary transformers (required in two axes) plus the required

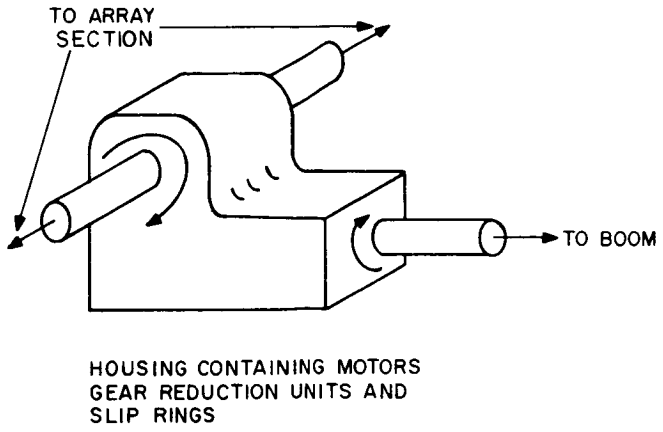

Figure VIII-10. Schematic Representation of Orientation Drive Assembly

power-conditioning electronics associated with the transformers result in an overall transfer efficiency of approximately 85 percent. When compared with the slip rings, this is too severe a penalty.

The slip rings, which are a very efficient means of transferring energy across a rotating joint, have been flight-tested (Nimbus and OSO) and can readily be made redundant. The potential drop across a typical ring-brush pair is approximately 50 millivolts. This value will vary, depending on electrical and mechanical parameters in the design. For the reasons mentioned here and in the discussion presented in Section VII, this approach is adapted for use for this conceptual PSM design.

4. Electrical Bus Design

The electrical current requirements and the aspect ratio of the array combine to simplify the design requirements for the buses as compared to the IPS concept. The cross-section area required of each bus at the root end of the array is only 0.025 square inch, gradually tapering in cross section toward the free end of the array. A rather simple and satisfactory approach for the bus is the use of flat ribbon. For example, if a two-inch width is used, the thickness of the ribbon (without insulation) need be only 0.013 inch thick. It is not expected that any bending stress problem will result, even for multi-cycle retraction of the array.

5. Details for Initial Panel Concept

Figure VIII-11 presents details of various structural and kinematic elements used for the solar array. Included are: a description of the primary panel actuators (scissor linkage and drive motor), secondary panel actuator and locking mechanism, shear fittings, the design of a redundant rotating joint, and structural description of an array panel. Some of these details are discussed in other sections of this report.

E. DEPLOYMENT

The deployment of the "H" configuration array is influenced by the biaxial folded-panel concept and by the desire to provide partial array retraction. Although the general considerations for deployment discussed in the IPS concept still are applicable (motion, force level, and geometric compatibility), the new requirements call for additional design considerations.

Specific problems of deployment are best explained by first describing the deployment sequence without discussing means of activation. The sequence, schematically represented in Figure VIII-12, begins with the severing of the tension bands or cables holding the folded array sections to the PSM structure and with the axial retraction of the inboard panel-to-PSM structure shear fittings. These operations can be accomplished by explosive cable cutters and explosively actuated, spring-loaded shear fittings respectively. Unlatching of the boom from the PSM strut completes the first phase of deployment.

The still folded array sections are rotated out and away from the PSM by the deployment boom, which will lock in its final position. The array-panel deployment mechanism will be designed so that the panels will remain folded in a compact shape during this motion.

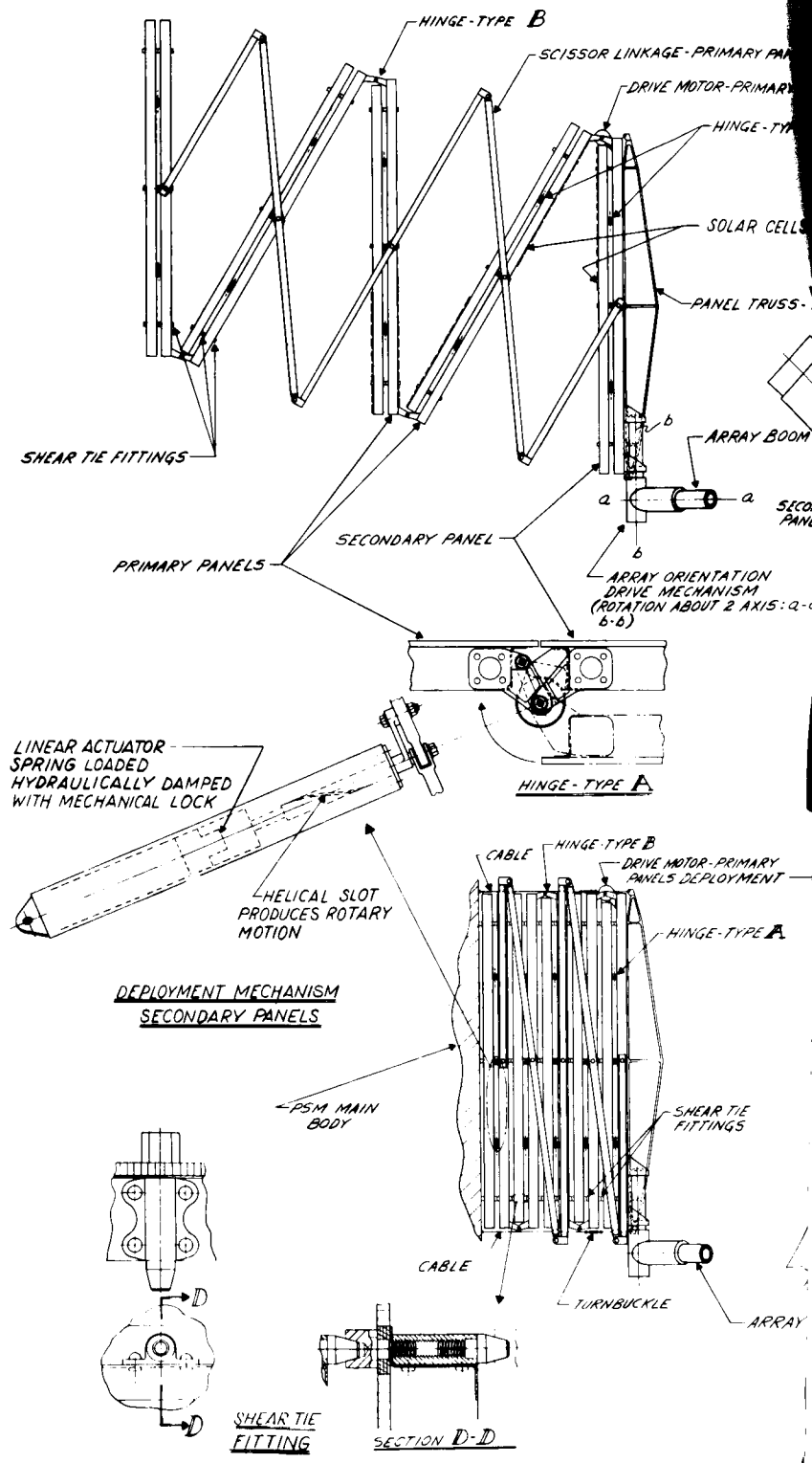
HINGE-TYPE B
SCISSOR LINKAGE-PRIMARY PA
DRIVE MOTOR-PRIMARY
HINGE-TY
SOLAR CELLS
PANEL TRUSS-
SHEAR TIE FITTINGS
ARRAY BOOM
SECONDARY PANEL
PRIMARY PANELS
ARRAY ORIENTATION DRIVE MECHANISM (ROTATION ABOUT 2 AXIS: a-a b-b)
HINGE-TYPE A
LINEAR ACTUATOR SPRING LOADED HYDRAULICALLY DAMPED WITH MECHANICAL LOCK
HELICAL SLOT PRODUCES ROTARY MOTION
CABLE
HINGE-TYPE B
DRIVE MOTOR-PRIMARY PANELS DEPLOYMENT
HINGE-TYPE A
DEPLOYMENT MECHANISM SECONDARY PANELS
PSM MAIN BODY
SHEAR TIE FITTINGS
CABLE
TURNBUCKLE
ARRAY
SHEAR TIE FITTING
SECTION D-D

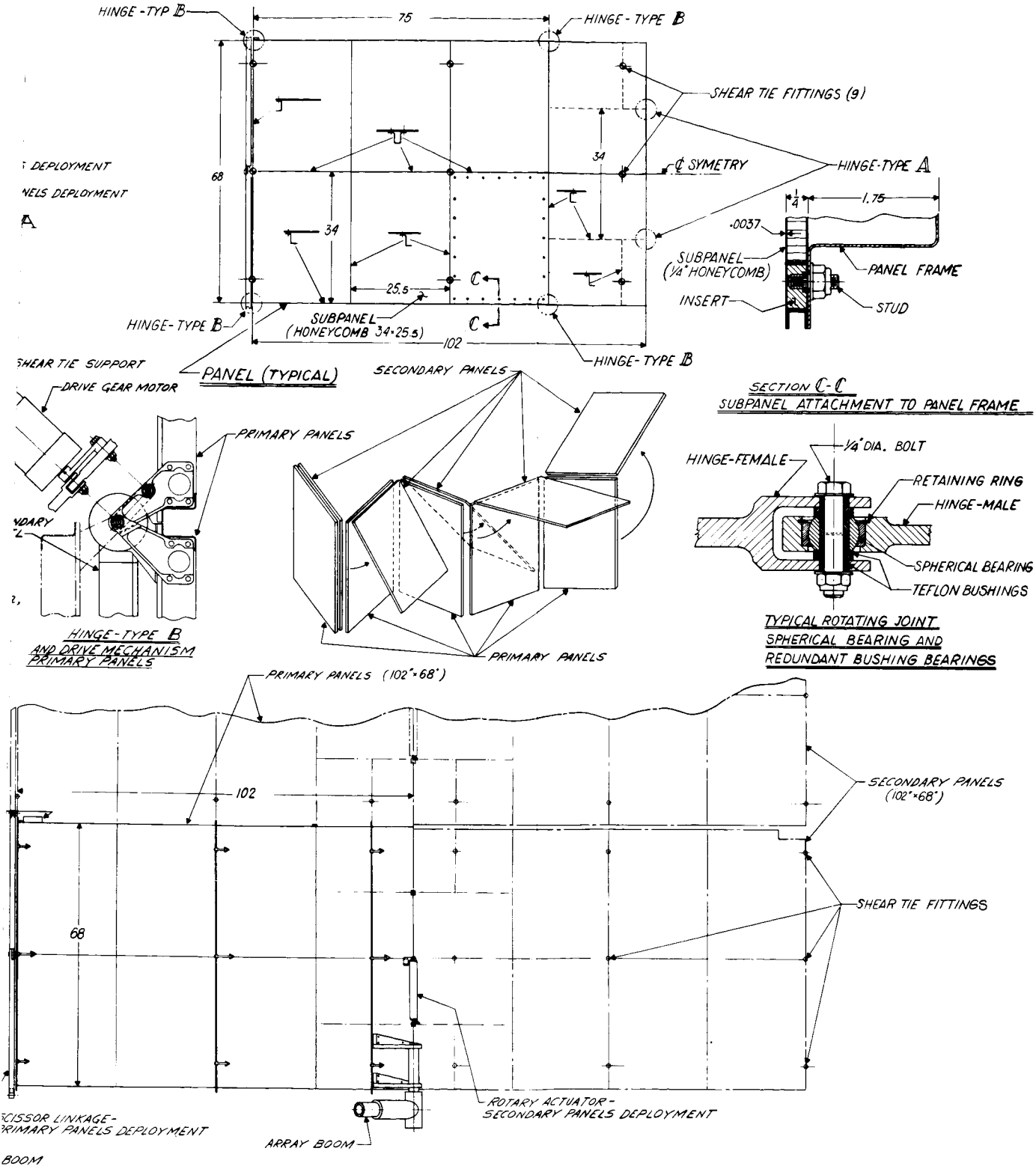

Figure VIII-11. Structural Details of Array Elements

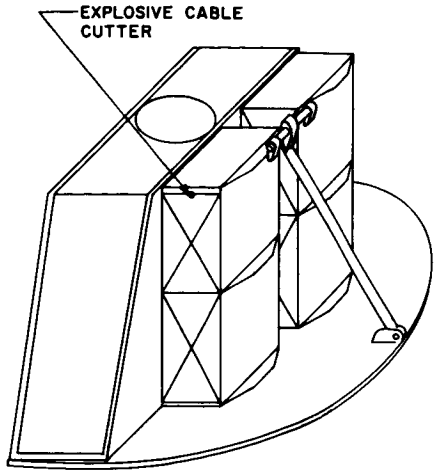

SHEAR FITTING AND CABLE SEPARATION

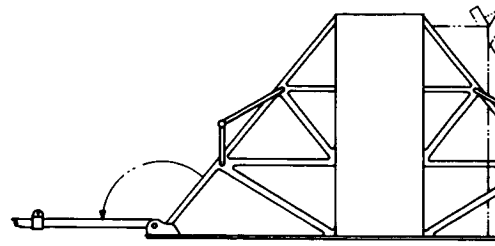

BOOM DEPLOYMENT AND LOCKI

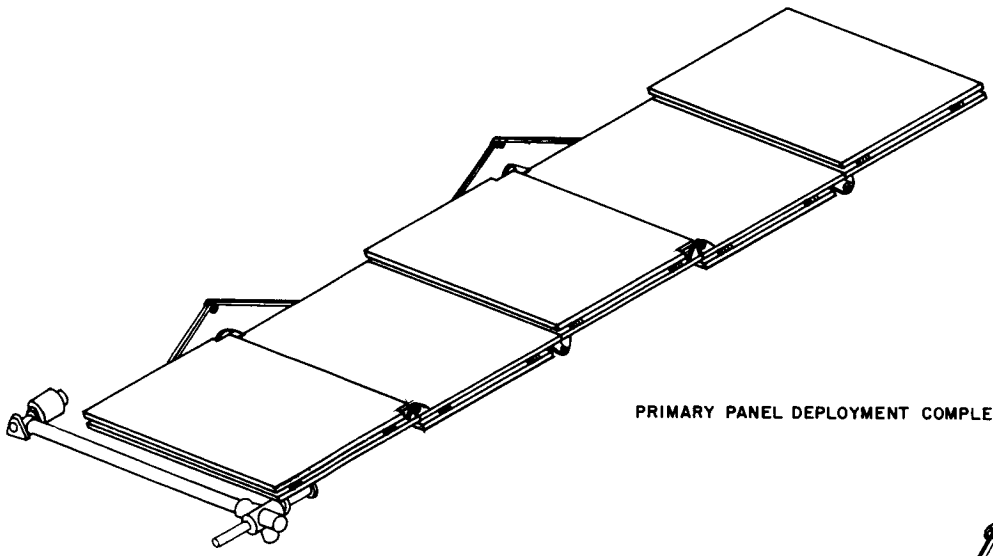

PRIMARY PANEL DEPLOYMENT COMPLETE

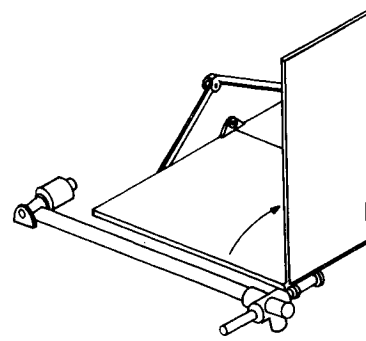

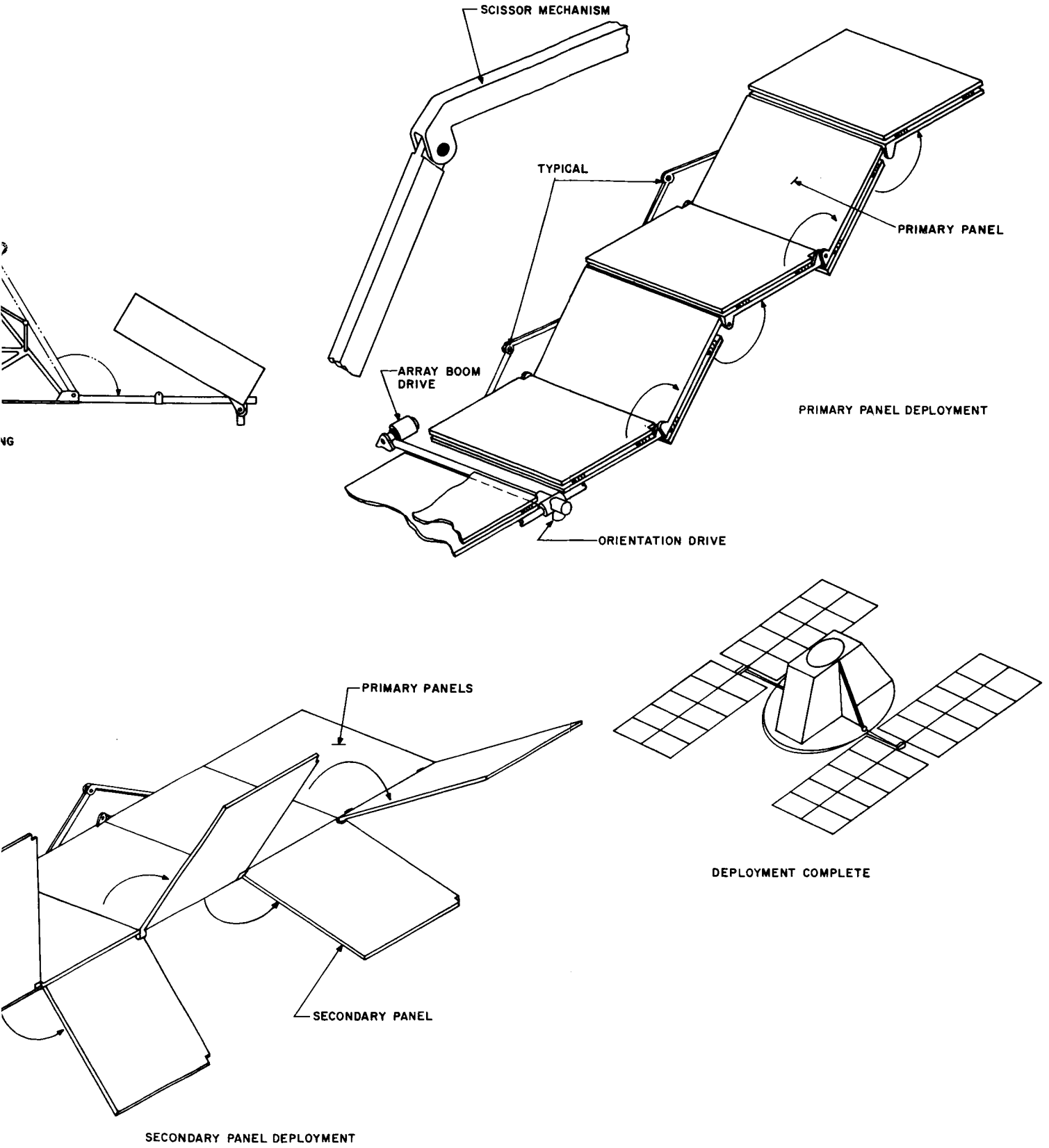

Figure VIII-12. Diagram of Array Deployment

With the boom locked in the operational position, the primary array panels are extended to their full length. At or near the end of this motion, the folded secondary panels are released by a mechanism automatically initiated by the primary-panel extension or by a separately activated explosive latch. These secondary panels will lock in their open position by the locking device included as part of the actuator. At this point, the sequence is completed and the orientation servo system takes over.

1. Boom Actuation

A number of methods are available for rotating the deployment boom into its operational position. A motor-drive, gear-reduction assembly, a pneumatic cylinder, or a spring-powered unit are all possible choices. The pneumatic cylinder and cable linkage, coupled with a spring or fluid shock absorber, will fit within the space confines of the stowed position and provide a controlled-force actuator at a reasonable weight expense. The ability to control velocity is important as it will minimize the shock loads when full boom deployment is reached.

A spring-powered, fluid-damped actuator, as successfully used on Ranger, Mariner, and Lunar Orbiter, can also be employed. This type of actuation modified to rotary motion, as shown in Figure VIII-11, is probably the simplest approach.

2. Primary Panel Deployment

The desirability of partial array retraction, the limitations of array stowage volume, and the desirability of a low aspect ratio of the deployed array combine to yield the double-folded array concept. Hence, deployment activation methods, as well as design of hinges, electrical connections across hinges, and panel locks, must be adapted to both stowage-volume restrictions and multi-cycle retraction operations.

Primary array panel extension and retraction will be accomplished by one or more reversible actuators coupled with appropriate linkage systems. Although a deployment system for the primary panels is shown in Figure VIII-11, various modifications are possible.

With only four moving hinge axes in the primary deployment sequence of each array section, the choice between a single-actuator linkage system and a localized four-actuator system is available. Although the decision is primarily one of overall reliability, certain observations can be made.

The small number of hinges and the low total hinge friction permit a single actuator of reasonable size to be used. The corresponding linkage forces will also be low and excessive weight penalties will not arise. Because of the array folding geometry and limited stowage volume, the position of a hinged-bar linkage is limited to one edge of each array section. This non-symmetry is not considered a problem due to low friction loads and the rigidity of the small (five-panel) primary system.

A bar linkage can be replaced by the use of a cable and pulley system similar to that found on drafting machines. This entire system may then be housed within the cross-section of the

individual panels. Some weight (not calculated) is saved by the replacement of rigid bars with the cable linkage.

The cable system can be divided into four subsystems and four separate actuators. The advantage of this approach is that of lower linkage forces and smaller actuators. In this design, individual actuators will tend to decrease system reliability by increasing the moving parts count.

The power system for actuating the deployment mechanisms must be reversible and capable of repetitive use after varying periods of idleness. Electrical and pneumatic systems can be used for this application, but both methods share the common problem of transmitting the power, in some form, across the dual-axis rotating joint formed by the array orientation drive assembly.

Three concepts are available for supplying power to the chosen actuator: electrically through slip rings, by means of manually detachable couplings engaged only during the operation of the actuator, and by an independent power source mounted on the array panels.

Detachable couplings, while the simplest and most reliable, necessitate astronaut involvement in extra-vehicular maneuvers both before and following array retraction. Electrical slip rings are feasible and can be designed with the existing array orientation drive concept, subject to the design criteria discussed in the IPS concept study. Pneumatic slip rings, though commercially available for industrial applications, are too complex for use in space vehicles. Independent power sources, mounted on the array, have the disadvantage of limited power-storage capacity. Although storage batteries with charging circuits could negate this criticism, their complexity would far outweigh that of supplying the electrical power through slip rings. Pressurized gas presents a more realistic though still limited energy storage system, in addition to the sealing problems it presents. This system would, however, require electrical slip-ring circuits for valve actuation and pressure monitoring.

As a result of these considerations, the preliminary choice is an electric motor drive unit as the power source for driving the bar linkage system, as shown in Figure VIII-11.

Linkage joints and hinges in the primary deployment system will be designed with a self-aligning and redundant action to insure continuous operation in the vacuum environment. This redundancy will be accomplished by providing two independent surfaces of rotation about a common axis. A Teflon bushing, as shown in Figure VIII-11, will reduce friction levels and eliminate the problem of cold welding. This type of bearing will be utilized for the hinges and scissor linkage pins.

Electrical interconnections across the hinge lines of the primary deployment system must, in addition to meeting the design parameters of the earlier study, be capable of repeated flexing. A flat ribbon type of electrical conductor is used to meet the electrical current requirements of this array.

3. Secondary Panel Deployment

Since array retraction will be accomplished with the secondary panels locked in the open position (for the initial concept), the deployment of these panels reduces to a one-time occurrence with an associated simplification of mechanisms. The prime restrictions on actuation include a minimum actuator space envelope to allow initial high-density stowage, a controllable deployment motion, and an actuator that will not interfere with subsequent array retraction.

A linear, spring-powered, damped actuator with a linear-to-angular motion converter is shown in Figure VIII-11. "Cocked spring" forces of the stowed mode are contained entirely within the actuator. The linear portion of this actuator, including the damping mechanism, is a space-proven design manufactured by Adel.* The damping feature allows the worst-case (maximum) spring energy to be absorbed when a best-case (minimum) hinge friction exists. To ensure that secondary panels remain fixed in their deployed position and do not interfere with the retraction sequence, a locking feature is incorporated in the spring actuator. Self-aligning hinges will be used to minimize friction. The cross-sectional area requirement of the buses for each secondary panel, combined with the one-time unfolding motion, will permit electrical connections across the hinge line to be made through service loops in stranded wire or flat-ribbon type conductors.

4. Advanced Array Folding

To increase the rigidity of the array panel (shown in Figures VIII-3 and VIII-13) an advanced method of panel hinging was developed. This design allows the secondary panels to be joined, by hinges, to the primary-panel edges and also to the edges of adjacent secondary panels. Hence, the width of array cross-section available to resist torsional and bending loads is doubled.

Figure VIII-13 is a schematic diagram of view of the deployment sequence using the advanced folding method. The shear-tie separation and boom-deployment portions are identical with those of Figure VIII-12. The remaining kinematics are similar, for the increase in array stiffness is achieved by a unique hinge configuration.

The geometry of the hinges and the position of the hinge axes allows both sets of panels to unfold about a common hinge line, while still interconnected along three edges. This motion is shown in progress in Figure VIII-13. A single actuator scissors linkage, or individual actuator system, may power the Phase I motion.

Completion of this motion extends the array section to its full length and brings all primary and secondary hinge axes into a common line. At this point, an electrically actuated hinge driving system is engaged. The interconnected secondary panels are now unfolded, Phase II, as a unit by a single actuator into the final deployed configuration and locked.

---

* Adel Division General Metals Corp., P.O. Box 671, 10777 Vanowen Street, Burbank, California.

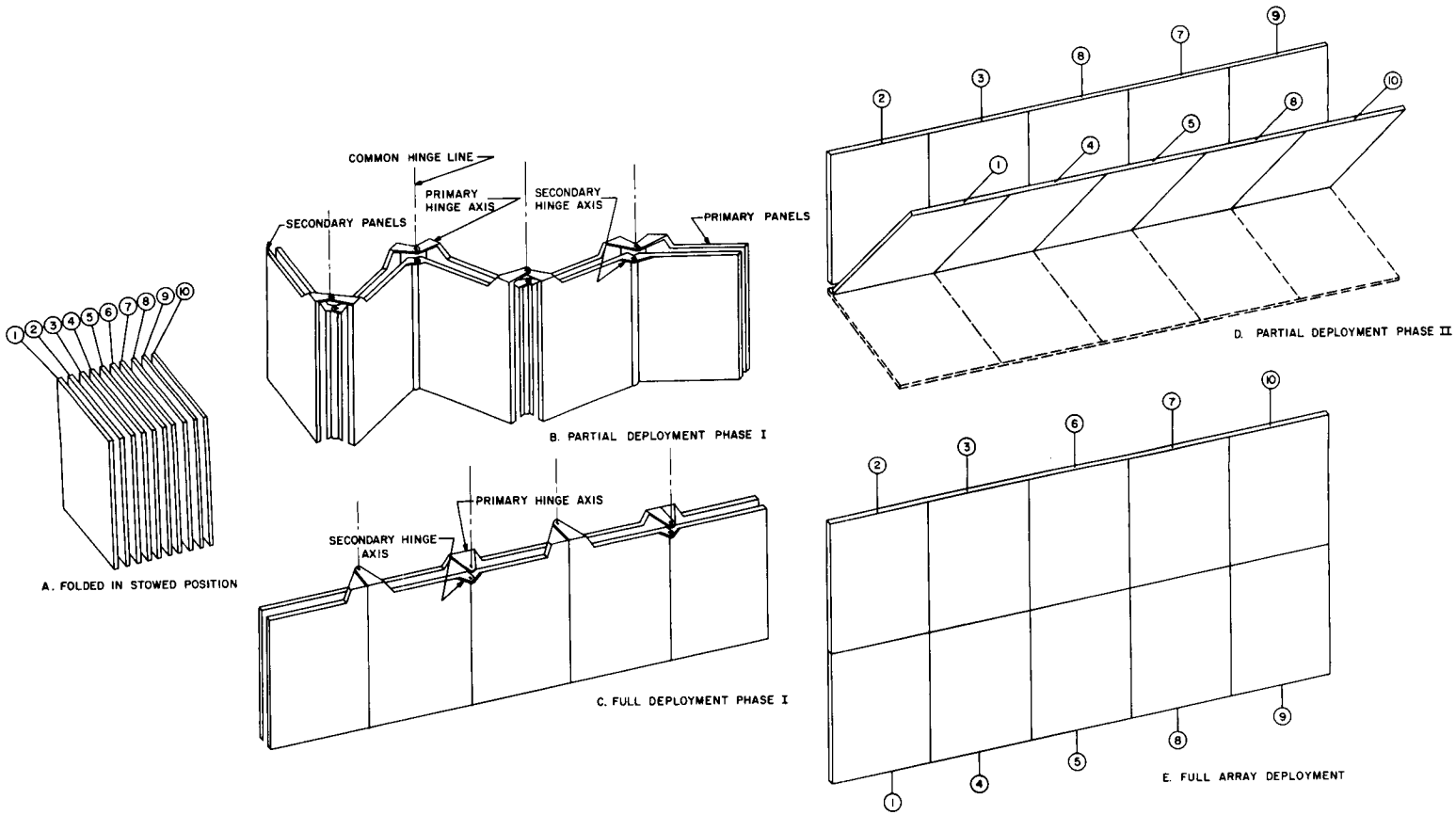

Figure VIII-13. Array Deployment, Advanced Concept

Due to the directional characteristics of the hinge axes, this method of unfolding does not lend itself to the partial array retraction of Figure VIII-14, View B. Instead, the entire sequence is reversed so that both primary and secondary panels are refolded to the initial position shown in Figure VIII-14, View A.

The hinge designs for this advanced folding method must have the ability to latch in the extended position and unlatch for retraction. A reliable spring loaded latch is envisioned for this application with electromagnetic unlatching. Since this approach requires electrical power over a short time span, it is not considered a deterrent, even though all hinge latch releases about any given hinge line must be in the "open" position prior to actuation.

The design of the electrical connections across the hinges, and of the actuators will be similar to those already described. An electrically operated hinge locking-unlocking system will be necessary on all hinge-axis actuators to maintain deployed rigidity yet allow complete retraction.

5. Retraction

The reasons for considering retraction of the array could be manifold and encompass such possibilities as meteoroid shower avoidance, increased docking reliability, reduction of aerodynamic drag during non-operating periods, minimization of solar-flare effects on the array, etc. All of these considerations except docking require very little load carrying capability from the folded array. However, herein lies an important distinction between the initial and advanced folding concepts previously described. Due to the inability of the initial folding design to withstand SPS engine firing when extended, the array must be retracted for this mode of operation. This means that it must be arranged into a configuration capable of withstanding a major load. This situation requires a good load path for all panels back to the array boom. The complexity of this could well dictate astronaut involvement in providing and securing the needed structural members. On the other hand the advanced design can take all loads when extended and need retract only for the reasons previously listed (which provide small load environments). However, if it is required to subject the retracted array to a high load environment, the advanced concept of panel folding provides a good load path to the array boom. Retraction for this design is merely a reversal of deployment and the retracted form factor and interpanel load transfer points are, in general, intact. What is missing is the tensile banding that held all panels in a stack. Without this banding, large dynamic load capacity is probably not possible. Extending the previous requirement for a latching hinge design to also latch in the retracted position will provide considerable load capacity when retracted. It is not inconceivable that even the docking and SPS loading environment can be withstood under these conditions. Certainly if the latched hinges and panel structure can withstand SPS loading when extended, they can withstand the same static loading when retracted and latched since the bending moments are vastly reduced. However, the absence of the aforementioned tensile banding raises concern for the vibratory effects on the panels which are closely stacked. Definition of the detailed requirements for each mode of operation must be established before design and analysis can be logically performed.

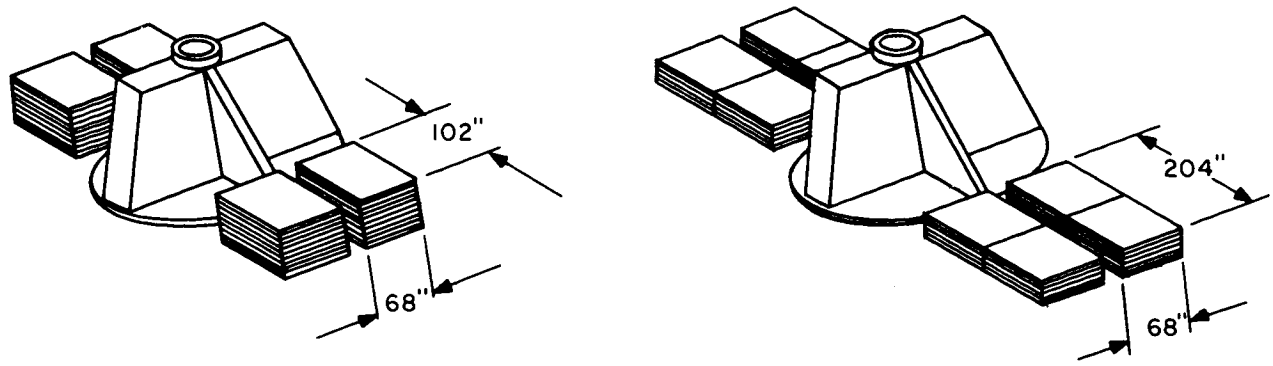

A. ADVANCED DESIGN CONCEPT

B. INITIAL DESIGN CONCEPT

Figure VIII-14. Retracted Position for Initial and Advanced Design Concepts

F. SATELLITE ORBITAL CONFIGURATION

The selection of the orbital configuration was based upon the requirements for maintaining normal sun incidence for the solar array for all orbits and for minimizing the effects of gravity gradient. This effect is of particular importance for this portion of the study effort since there will be no resupply during the one-year mission. This consideration necessitates a symmetrical-array geometry with respect to the spacecraft (See Section IX).

The array control axes of rotation chosen for the original concept proved to be advantageous and were adopted for this configuration. Figure VIII-4 shows the orbiting configuration of the satellite. As in the IPS concept, design analysis of the panel structure was first made for the launch environment and subsequently analyzed for the deployed conditions. The critical loads in this condition are docking and SPS engine firing. The analyses for these loads (based upon a panel loading of one pound per square foot) and their effects on the array structure are given in this Section.

1. Docking Activity

While various docking configurations may be feasible, three in particular were analyzed, as follows:

1. Tensile/compressive T/C (or hard mode) array orientation,

2. Weak-axis bending WAB (or soft mode) array orientation,

3. Strong axis bending SAB array orientation.

The preceding configurations represent the extreme positions of possible array orientations.

The following is the docking analysis of the array structure utilizing the design configuration that met the launch load requirements of Paragraph VIII. C.

a. T/C MODE DOCKING

This activity is shown in Figure VIII-15. As is indicated, the array structure is deployed so that the docking load vector places the array in a tensile/compressive mode. That is, the docking-load vector is parallel to the roll axis of the PSM and is applied along the long axis of the array structure.

The following information is repeated from Paragraph VII. F. 1:

- Docking vehicle velocity, 2 fps (maximum relative velocity)
- Stroke, 7 inches
- Weight of Apollo C/S Module, 15,730 pounds
- Weight of PSM, MMSS, Solar Array, 21,750 pounds.

The limit and ultimate "g" load inputs to the inboard end of the boom were found to be 0.0896 g and 0.134 g respectively. Then, assuming the time per cycle to be twice the stroke-docking velocity, the forcing frequency was computed to be 1.718 Hz. Comparing this forcing frequency with the system "T/C Mode" natural frequency of the array (0.88, Hz as noted in Paragraph VIII. F. 2.) yields a frequency ratio ($f_{n/f}$) of 0.512. The amplification factor (0.95) is then found utilizing the graph of amplification factor versus frequency ratio for the half-sine pulse. The product of amplification factor and the limit and ultimate equivalent "g" loads (as previously mentioned) determine the limit and ultimate docking loads experienced by the solar array in the "T/C (hard) docking" mode. They are:

- Limit docking load: 0.085 g
- Ultimate docking load: 0.127 g

The critical section inertia was also computed at a value of 0.514 in^4. The array-structure, when deployed, consists of primary and secondary panels (see Figure VIII-3). Since the primary panels and their stiffeners are continuous (via hinges and locks), they carry the loads and therefore contribute all the inertia of the array structure. That is, the secondary panels and associated framing do not contribute inertia to the array in the deployed mode of orientation. As will be seen for the "advanced concept" (Paragraph VIII. F. 3), all panels contribute to the array inertia and are therefore load bearing.

With the foregoing data, the analysis now centered about the following three critical points:

*(1) Boom bending stress,

(2) Boom-Array deflection,

(3) Array Structure, longitudinal buckling effects.

---

*See Paragraph VIII. F. 2. a. for "boom sizing".

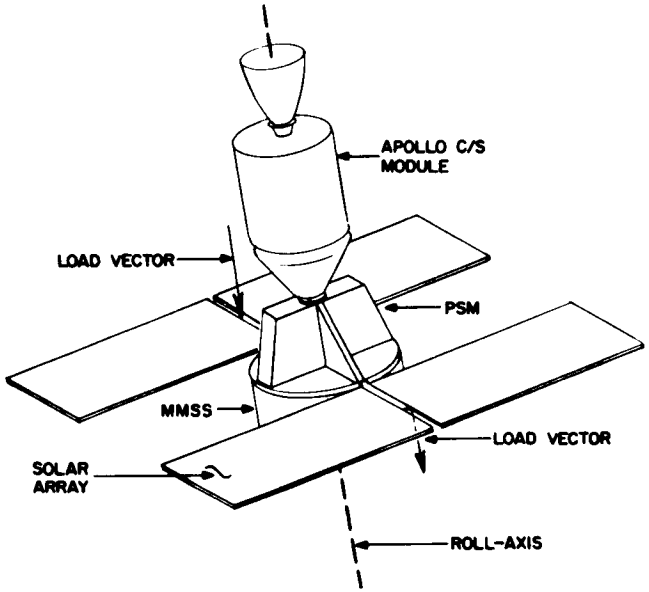

WEAK - AXIS BENDING MODE

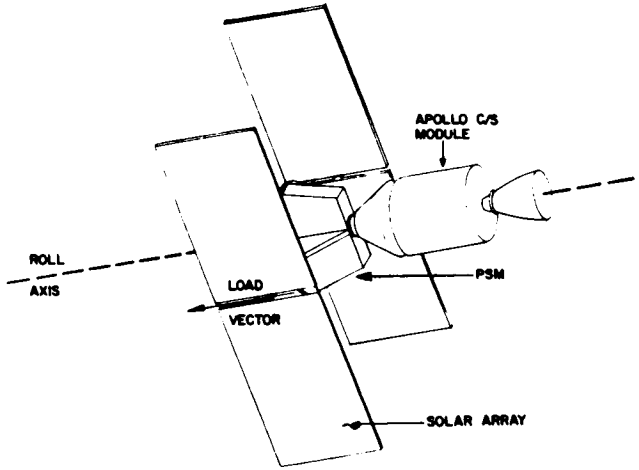

STRONG - AXIS BENDING MODE

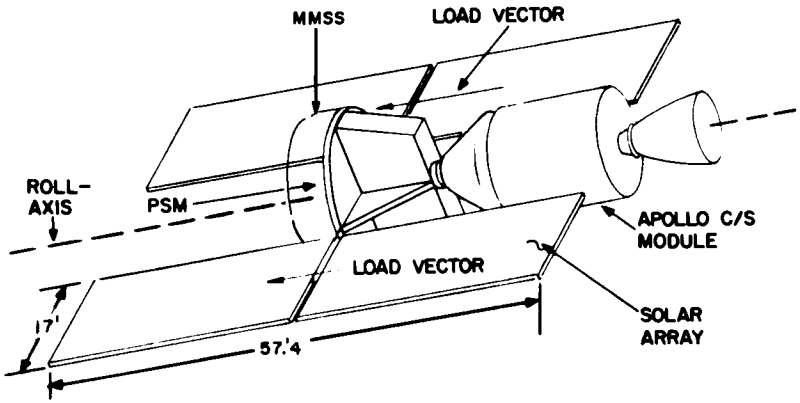

TENSION - COMPRESSION MODE

Figure VIII-15. Docking Modes

The analysis was then made considering that the honeycomb and stiffeners act as a composite body reinforced with adequate shear ties. It should be pointed out that whereas many parameters were investigated concerning this and subsequent modes, only those conditions listed are considered as critical.

The results of the analysis are tabulated in Table VIII-7.

TABLE VIII-7. TENSILE-COMPRESSION MODE DOCKING

Element	Condition	Results
Solar array response loads	Limit load	0.085 g
Solar array response loads	Ultimate load	0.127 g
Boom	Bending	*Ample margin of safety
Boom-array	Deflection	2.37 inches
Array-structure	Longitudinal buckling	Ample margin of safety
	Tensile	Ample margin of safety

In reviewing the results, it is apparent that T/C Mode docking poses no problem from a structural standpoint. Since the clearance between the array sections is approximately 18 feet, one must also consider the ability of the astronauts performing this docking maneuver. A certain amount of skill is necessary in order to avoid any contact with the array structure, as this contact could conceivably damage the array structure and/or components. However, the primary consideration is the damage to the docking vehicle and its effect on crew safety. Subsequent analysis utilizes array orientations wherein maximum clearance between the docking vehicle and the array is afforded.

b. WEAK-AXIS BENDING (WAB) DOCKING MODE

The weak-axis bending (WAB) docking mode (or soft mode) is shown in Figure VIII-15. As indicated, the array structure is oriented so that the docking load vector is perpendicular to it and parallel to the roll-axis of the PSM.

The natural frequency of this boom-array system was computed. In this orientation, the array is the soft link in the multi-mass array-boom system. The general formula for the computation of the 1st Mode Natural Frequency is as follows:

$$\omega_{N_1} = \frac{\alpha_1}{2\pi}\sqrt{\frac{EI}{\mu_1 \ell^4}}\ Hz.$$

*Ample Margin of Safety means greater than unity.

where

EI is the bending stiffness of array section which is equal to 0.514×10^7 lb-in^2,

ℓ is the length of the beam (340 inches)

μ_1 is the mass per unit length . . . $W/_{gL} = 37.1 \times 10^{-4} \dfrac{\text{lb - sec}^2}{\text{in}^2}$,

$\alpha_1 = 3.52$,

and

$$\omega_{N_1} = \frac{3.52}{6.28} \sqrt{\frac{0.514 \times 10^7}{37.1 \times 10^{-4} \times 133.63 \times 10^8}} \; ;$$

$$\omega_{N_1} = \frac{3.52}{6.28} \quad (0.32) = 0.179 \; Hz.$$

Computing the 2nd Mode

$$\omega_{N_2} = \frac{\alpha_2}{\alpha_1} \; \omega_{N_1} .$$

where

$$\alpha_2 = 22.0,$$

$$\alpha_1 = 3.52,$$

$$\omega_{N_1} = 0.179 \; Hz.$$

and

$$\omega_{N_2} = \frac{22.0}{3.52} \quad (0.179)$$
$$= 1.120 \; Hz$$

As previously shown, the 1st mode natural frequency is 0.179 Hz and, since the docking effects are of short time duration, the 2nd mode was neglected. *

The frequency ratio was then calculated to be 0.104 Hz (with a forcing frequency of 1.718 Hz). The amplification factor (0.30) is found by utilizing the graph of amplification factor versus

---

*1st mode effects are generally predominant (viz, least-energy concept) so 2nd mode response was neglected.

frequency ratio for the half-sine pulse. The product of amplification factor and the limit and ultimate input g loads (0.0896 g and 0.134 g respectively), determine the limit and ultimate docking response loads experienced by the solar array in the "WAB" docking mode; these are:

Limit docking load, 0.026 g;

Ultimate docking load, 0.040 g.

With the foregoing data, the analysis now centered upon the following four critical points:

(1) Panel-intercell buckling;

(2) Stiffener frame (lateral), compressive buckling;

(3) Array structure, linear deflection; and

(4) Array structure, angular deflection.

The results of this analysis are tabulated in Table VIII-8.

TABLE VIII-8. WAB MODE DOCKING

Element	Condition	Results
Solar array response load	Limit load	0.026 g
Solar array response load	Ultimate load	0.040 g
Solar panel	Intercell buckling	Ample margin of safety
Stiffener frame (lateral)	Compressive buckling	+0.01 margin of safety
Array structure	Tip Linear deflection	1.53 feet
Array structure	Tip angular deflection	4.125 degrees

In reviewing these results, it is safe to conclude that performing the docking activity with the array structure oriented for the weak-axis bending mode (i.e., soft mode) is both feasible and practical. In addition, the orientation of the array in this mode reduces the possibility of docking interference and therefore makes for a more reliable docking activity.

c. STRONG-AXIS BENDING (SAB) DOCKING MODE

The strong-axis bending (SAB) docking mode is shown in Figure VIII-15. As indicated, the array structure is so oriented that the docking-load vector is perpendicular to the long axis of the array and parallel to the roll axis of the PSM.

A brief analysis was made for the SAB configuration and the results were similar to those obtained for the T/C and WAB docking modes. That is:

(1) The array structure buckling margin of safety is ample,

(2) The stiffener frame buckling margin of safety is ample, and

(3) The boom-array deflection is minimal.

These results were expected since the requirements for the extreme conditions (i.e., T/C and WAB modes) were met. It can therefore be concluded that the "strong-axis" docking activity is practical from docking vehicle - any clearance point of view and is not deleterious to the system.

2. SPS Engine Firing Activity

The SPS activity places the most stringent requirements upon the solar array structure and/or components during the orbital phases of the mission. In general, there are four possible deployment orientations of the solar array when performing this activity. These are:

(1) Tensile/compressive (T/C) or hard mode,

(2) Weak-axis bending (WAB) or soft mode,

(3) Strong-axis bending (SAB), and

(4) Boom deployed, array retracted.

Since the array structure itself (less the boom) was "sized" for the launch phase, as discussed in Paragraph VIII.C.4, there remains the analysis which "sizes" the boom and the analysis of the various deployment modes listed for the SPS activity. The SPS engine firing acceleration was computed as shown in the following:

Given

Total Vehicle Weight (W_T) = 37,480 lb*

Weight of Expandables (W_E) = -2,280 lb

Net Weight (W_N) = 35,200 lb;

Engine Thrust (F) = 21,000 lb

$$F = \frac{W_N}{g} (a) \qquad \text{(VIII-3)}$$

$$a = \frac{F}{W_N} (g) \qquad \text{(VIII-4)}$$

*Apollo C/S Module	=	15,730 lb
PSM	=	8,200 lb
MMSS	=	11,600 lb
Solar Array (1 lb/ft^2)	=	1,950 lb
W_T	=	37,480 lb

Substituting the given values into Equation (VIII-4):

$$a = \frac{(21,000 \text{ lb.})}{35,200 \text{ lb.}} g = 0.597 \text{ g (input at boom - PSM interface)}$$

The response loads on the array structure can now be calculated as noted previously as a function of the shock-pulse frequency and the first mode natural frequency of the array-boom system. For T/C mode firing, the array is stiff relative to the boom. The shock amplification factor is primarily determined by the boom stiffness and the array/boom masses, whereas, for the WAB firing condition, the array is the soft link in the multi-mass array/boom system (see Paragraph VIII. F. 1. b).

For the T/C mode firing, a peak amplification factor of 1.8 was assumed in order to size the boom. This assumption was verified in subsequent calculations.

Using the 1.8 amplification factor, the limit and ultimate response loads are:

Limit response "g" = (0.597) (1.8) = 1.075;

Ultimate Response "g" = (1.5) (1.075) = 1.610.

NOTE: Reducing the weight of the vehicle by removal of the "expendable" weights is a conservative assumption leading to a higher "g" value.

a. TENSILE/COMPRESSIVE (T/C) MODE SPS ACTIVITY

This orientation for the SPS engine firing is depicted in Figure VIII-16. As shown, the array structure is deployed so that the SPS load vector places the array in a tensile/compressive mode. That is, the SPS load vector is parallel to the roll axis of the PSM and is applied along the long axis of the array structure.

With this array orientation, the boom was sized for the critical bending stress encountered in its deployed mode. Extruded aluminum high-strength tubing is used and boom length of approximately 10-1/2 feet was chosen, based upon the "stowed" space limitations. (Actual boom length of 9.3 feet is shown in Figure VIII-4.)

The bending stress calculations are based on the following:

$$S = \frac{M}{Z}, \qquad \text{(VIII-5)}$$

where

M is the maximum moment based upon the lumped mass of solar array at a distance of 10.5 feet with the boom in a cantilevered orientation and with the application of the ultimate load factor of 1.61 g, and

S is the ultimate bending strength of the 7057-T6 aluminum material (80,000 psi.)

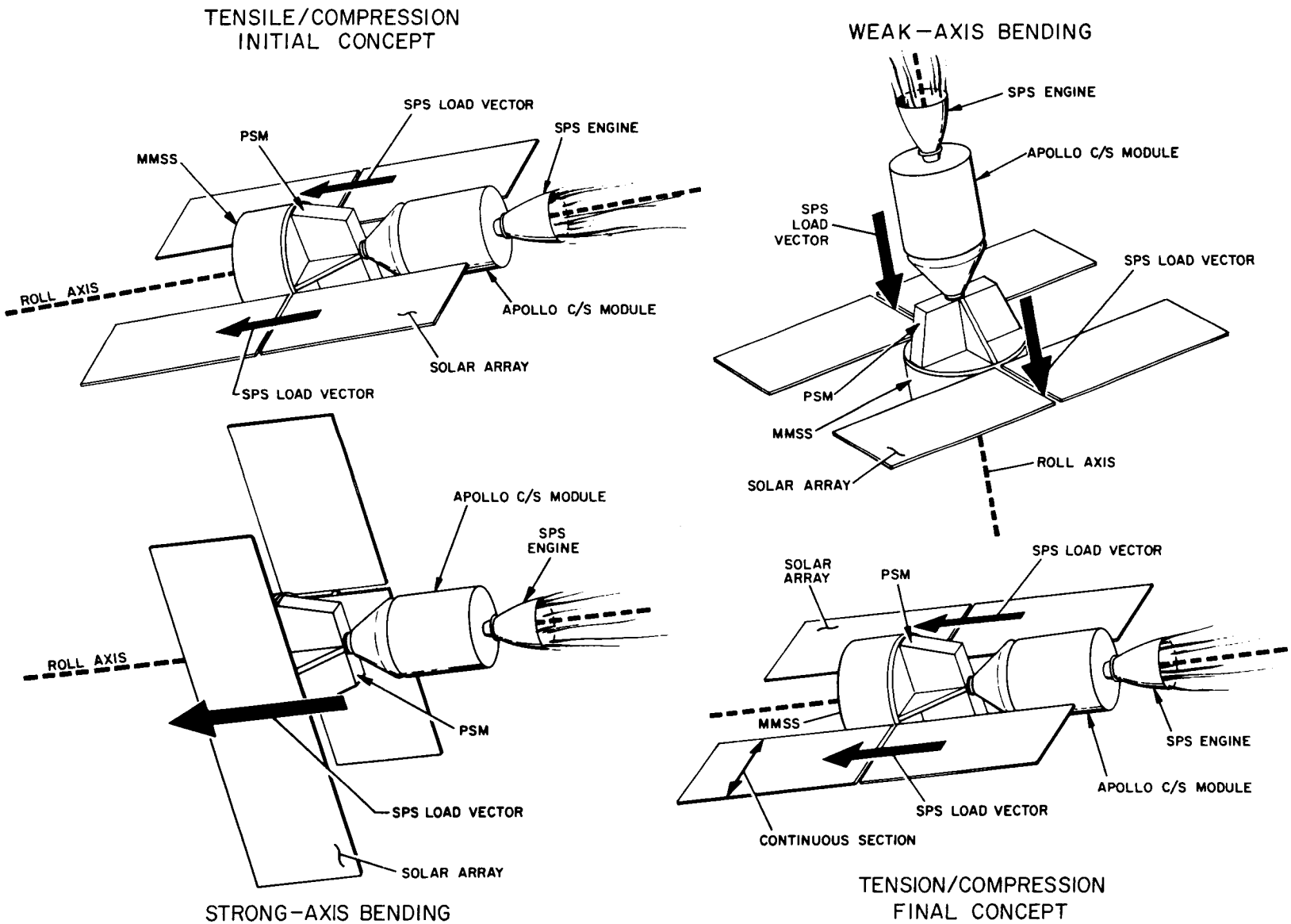

Figure VIII-16. SPS Modes

The required section modulus, Z, is

$$Z = \frac{M}{S}. \qquad \text{(VIII-6)}$$

Computing the required section modulus:

$$Z = \frac{PL}{S}$$

$$= \frac{(2 \times 487.5 \text{ lb})\ (1.61 \text{ g})\ (126 \text{ in.})}{80,000}$$

$$= 2.48 \text{ cubic inches,}$$

where

P is the weight of the array structure times the ultimate g response (in pounds); and

L is the length of the boom (in inches).

The most economical section, from both the weight and availability standpoint is

- Standard 4-inch (outer diameter) tubing; 1/4-inch wall thickness;
- Cross-section area= 2.945 square inches;
- Section modulus (Z) = 2.60 cubic inches;
- Bending inertia (I) = 5.20 inches^4;
- Weight (w)= 3.463 pounds per linear foot.

The actual ultimate bending stress is

$$S = \frac{M}{Z}$$

$$= \frac{198,000 \text{ in.-lb}}{2.6 \text{ in.}^3},$$

$$S = 76,300 \text{ psi.}$$

$$\text{M.S. (margin of safety)} = \frac{f_{allowable}}{f_{actual}} - 1 = \frac{80,000}{76,300} - 1 = +0.05.$$

This margin would be reduced a negligible amount if the weight of the boom (which is 36.4 lb) were included in the loading.

It was now necessary to verify the amplification factor (1.8) used to calculate the ultimate "g" loading condition. The natural frequency of array-boom in the T/C mode orientation was computed using conventional means and is shown as

$$f_n = \frac{1}{2\pi} \sqrt{g/\delta_{max}} \text{ Hz,} \qquad \text{(VIII-7)}$$

where

$$\delta_{max} = \frac{fL^3}{3EI},$$

f is the weight of the solar array plus the dead weight of the boom superimposed = 984 lb.,

L is the boom length = 126 inches;

E is the elastic modulus = 10×10^6 psi; and

I is the bending inertia = 5.20 $inch^4$.

The T/C mode natural frequency (f_n) for the system was calculated as 0.88 Hz. Additional information (Reference 3) enabled determination of the forcing frequency, which was 0.455 Hz. The frequency ratio was then calculated to be 1.935, and upon application to the amplification vs. frequency graph (Figure VII-41), yielded an amplification factor of 1.80, thus verifying the earlier assumption.

In addition to the bending stress margin of safety computed earlier, there remained two other critical areas of investigation for the T/C mode orientation. These were:

(1) Boom-array deflection, and

(2) Array-structure longitudinal buckling effects.

An analysis was made in the above mentioned area and the results are shown in Table VIII-9.

TABLE VIII-9. T/C MODE SPS ENGINE ACTIVITY

Element	Condition	Results
Boom-solar array response load	Limit load	1.075 g
Boom-solar array response load	Ultimate load	1.610 g
Boom	Bending	+0.05 Margin of safety
Boom	Deflection (tip)	1.675 feet
Array structure	Longitudinal buckling effects	-0.55 Margin of safety

In reviewing the table, it can be immediately concluded that T/C Mode SPS activity should not be undertaken as buckling failure in the solar array structure will result. However, two alternatives exist, as follows:

(1) Retraction of the solar array prior to firing of the SPS engine.

(2) Modification of the array structural design so that the critical section inertia is increased approximately 2-1/2 times, thereby affording a positive longitudinal buckling margin of safety.

For alternative (1), the design and implementation of an array-retracting device to handle the magnitude of load indicated is unique. Considerably more design effort is required in this area to implement this alternative. It is also to be pointed out that additional reliability requirements would be introduced in the system design, as well as additional weight required for retraction. The conditions for SPS activity with orientation of a "boom-deployed/array-retracted" mode will be discussed later in this report.

Alternative (2) can be readily implemented at the expense of an increase in weight or by a design change of the deployed array configuration (see Paragraph VIII. F. 3). It is estimated that with the present configuration, this increase would amount to 25 to 30 percent above the one pound per square foot loading condition. However, two additional critical considerations to include before the T/C mode SPS activity can be implemented; these are:

(1) Droop in the array caused by thermal gradients; and

(2) Manufacturing tolerance buildup.

The effect of these items upon the solar array would be to cause eccentricities and thereby possibly alter the loading conditions appreciably; an unpredictable performance of the system could thus result. However, the problem of the droop in the array could be alleviated by delaying the SPS activity until after the array attains (or is close to) thermal equilibrium and by establishing more stringent controls upon tolerances. With the implementation of such measures and with the strengthening of the array structure, T/C SPS activity would be acceptable.

b. WEAK-AXIS BENDING MODE SPS ACTIVITY

The weak-axis bending (WAB) SPS activity (or soft) mode is shown in Figure VIII-16. As indicated, the array structure is so oriented that the SPS load vector is perpendicular to it.

Utilizing the 1st mode natural frequency (0.179 Hz) as computed for the "WAB Mode" docking activity (Paragraph VIII. F. 1. b) and the SPS forcing frequency (0.455 Hz) yields a frequency ratio of 0.394. Consultation of the graph of amplification factor versus frequency ratio (for the half-sine wave shock pulse) elicits an amplification factor of 0.80. The limit and ultimate 'g' loads are now computed by taking the product of the amplification factor and the SPS

engine firing g load (0.597 g) for the limit conditions; 1.5 times the limit load establishes the ultimate condition. The computation is as follows:

Limit SPS load = (0.80) (0.597 g) = 0.478 g,

Ultimate SPS load = (1.5) (0.478 g) = 0.717 g

These loads are the response loads on the array structure during the "WAB Mode" SPS activity. The analysis now centered upon four critical points consisting of:

(1) Panel-intercell buckling;

(2) Stiffener-frame compressive buckling;

(3) Array-structure linear deflection; and

(4) Array-structure angular deflection.

The analysis was made by means of a technique similar to that employed for "WAB Mode" docking, since only the "g-load" differed from that activity. The results of this analysis are shown in Table VIII-10.

TABLE VIII-10. WEAK-AXIS BENDING MODE SPS ACTIVITY

Element	Condition	Results
Solar panel response load	Limit load	0.478 g
Solar panel response load	Ultimate load	0.717 g
Solar panel	Intercell buckling	-0.70 Margin of safety
Stiffener frame (lateral)	Compressive buckling	-0.94 Margin of safety
Array structure	Tip linear deflection	27.8 feet
Array structure	Max. angular deflection	73.6 degrees

A brief perusal of the foregoing table is sufficient to determine that WAB Mode SPS activity should not be undertaken and therefore, it is not recommended.

c. STRONG-AXIS BENDING MODE SPS ACTIVITY

The strong-axis bending (SAB) mode SPS activity is shown in Figure VIII-16. As is indicated, the array structure is oriented so that the SPS load vector is perpendicular to the long axis of the array and parallel to the roll axis of the PSM.

A brief analysis was made for the SAB mode SPS activity. This analysis was similar to that discussed in Paragraph VIII. F. 1. c except that the SPS "g" load input was utilized. The results, as expected, indicated that this mode of SPS activity should not be attempted in that failure in the structural stiffeners would result.

d. BOOM-DEPLOYED ARRAY-RETRACTED SPS ACTIVITY

The array orientation for this mode is shown in Figure VIII-17. As depicted, this mode is identical with the T/C Mode (for calculation purposes) for SPS activity discussed previously except that the array is retracted (with primary and secondary panels assumed locked). However, since the panel "column length" has been reduced to one-fifth of that present in the T/C mode SPS activity, it was anticipated that this alternative orientation would be feasible.

An analysis was made for the retracted configuration and the results appear in Table VIII-11.

TABLE VIII-11. BOOM-DEPLOYED ARRAY-RETRACTED SPS ACTIVITY

Element	Condition	Results
Boom-Solar Array Response Load	Limit Load	1.075 g
Boom-Solar Array Response Load	Ultimate Load	1.610 g
Boom	Bending	0.05 Margin of Safety
Boom	Tip Deflection	1.675 feet
Array Structure	Longitudinal Buckling Effects	Ample margin of Safety

In addition to the array orientation shown in Figure VIII-17, two other orientations are possible as shown in the inset of Figure VIII-17, which shows the SPS load vector applied either parallel to the long axes of the panels (vector 2) or normal to the panels (vector 3). However, neither of these orientations offer any particular advantage over the orientation that was analyzed.

It is therefore concluded that this mode of SPS activity is both practical and feasible. However, the implementation of a suitable structural tie when the array is retracted requires additional design effort.

3. Advanced Design Concept Array Structure

It was previously shown (Paragraph VIII. F. 2) that the SPS engine activity was not advisable unless the solar array was retracted prior to engine firing. Two other alternatives were discussed; by alteration of the array structure in order to increase the array inertia at the expense of weight or by deployed configuration design iteration.

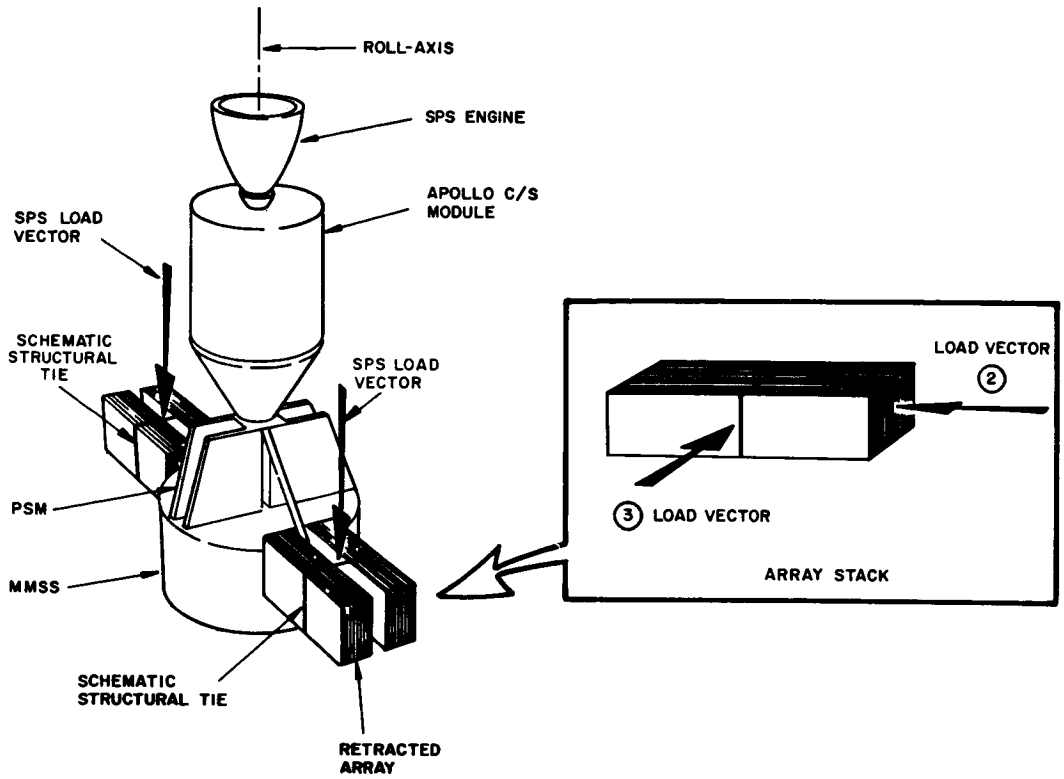

Figure VIII-17. Boom-Deployed Array-Retracted SPS Activity

It was felt that additional consideration should be given to the design of the latter system so that SPS activity could be undertaken without retraction and without altering the basic array structure as discussed. This was done and a schematic of the configuration is shown in Figure VIII-16.

The SPS load vector is applied along the long axis of the array. This is the same configuration as discussed in Paragraph VIII. F. 2. a, but with one important exception. In the latter configuration, the primary solar array panels contributed all the inertia. That section inertia was deficient and failure occurred due to longitudinal buckling of the array when the array was subjected to the T/C mode SPS activity. In the advanced design, the concept of primary and secondary panels is eliminated. That is, the design makes use of a continuous section (total array width), which will now afford a total inertia of 1.028 inch^4 about the critical axis (double the initial concept value) with no increase in array weight.

An analysis was made of this advanced configuration and the results are shown in Table VIII-12.

The results of the above table are similar to those of Paragraph VIII. F. 2. a. with the exception of longitudinal buckling effects. The negative margin of safety as previously determined, has been significantly reduced (viz., from -0.55 to -0.10). This indicates the merit of the new design. What remains then, is to further increase the critical inertia slightly, approximately 12 percent (from 1.028 inch^4 to 1.150 inch^4), with little or no increase in system weight.

TABLE VIII-12. T/C MODE SPS ACTIVITY, ADVANCED DESIGN

Element	Condition	Results
Boom-solar array response load	Limit load	1.075 g
Boom-solar array response load	Ultimate load	1.610 g
Boom	Bending	0.05 margin of safety
Boom	Tip deflection	1.675 feet
Array structure	Longitudinal buckling effects	-0.10 margin of safety

It is also noted that this advanced configuration will meet all the docking requirements discussed in Paragraph VIII. F. 1 and that the system will function more efficiently (viz. higher margins of safety).

The foregoing, coupled with the fact that the array droop effects can be minimized (as discussed in Paragraph VIII. F. 2. a.), show that the T/C mode SPS activity can be readily undertaken if the advanced design concept is implemented. It is therefore recommended that future areas of investigation be undertaken utilizing the concept discussed in this portion of the report.

G. THERMAL CONTROL ANALYSIS

1. Introduction and Summary

The thermal control systems considered include (1) passive, (2) active, and (3) auxiliary liquid loop heaters combined with a passive system. Additional study effort together with further definition of mission constraints are required to select a system that can be recommended for the thermal conditions considered. The two orbits under discussion are at 200 NM, 90° and 19,340 NM (synchronous), 28.5°; for additional assumptions and ground rules, see Appendix H.

The results of the calculations are tabulated in Table VIII-13. Temperature limits for the electronics and battery packages are indicated in the table, together with the temperature limits achieved by each of the systems investigated. Note that in accordance with the ground rules, a roll is a permissible maneuver if not performed too frequently. Use of this maneuver would reduce the amount of radiating surface area required by the batteries from 110 to 74 square feet during the 200-nmi-altitude mission, but provides no significant advantage during the 19,340 NM altitude mission.

The radiating surfaces for both passive (electronic equipment compartment) and active (battery compartment) thermal control systems utilize second-surface mirrors.

2. Considerations Affecting Thermal Design

The magnitudes of external environmental factors such as orbit time, fractional suntime, earthshine, and albedo (that affect the thermal design) are controlled by the orbit altitude and inclination. Table VIII-14 indicates the values of these factors for the two orbits considered.

Note that at the synchronous altitude, the values of earthshine and albedo are so small that they can be neglected in thermal-design calculations. Orbital inclinations for the 200 NM altitude missions may vary from equatorial to polar. Since the polar orbit experiences worst-case change in sun load, this orbit has been investigated. For the synchronous altitude only a 28-1/2° inclination is planned and investigated for thermal control.

For a 200 NM polar orbit, the possible range of sun angles (angle between orbit normal and sun direction) is 0 to 90°. The range of sun angles for a 28-1/2° inclined orbit is 39 to 90°. The effect of these sun angles upon the incident solar radiation on the vehicle surfaces is discussed later in greater detail.

The planned general configuration of the orbiting vehicle is shown in Figure VIII-18. The vehicle will be earth-oriented and the external radiating surfaces for the dissipating electronic equipment will be in the orbit plane. Thus, these surfaces will experience varying solar inputs as the sun angle changes during the 1-year mission. The local surfaces that will affect the effective emittance of the external radiating surfaces are the Apollo vehicle surfaces, the solar-array panels, and the PSM baseplate. Since the view factor between the radiating surfaces and the Apollo vehicle will be small, the effect on the surface effective emittance has been neglected in the thermal calculations. The effect of the other surfaces are included and will vary with the orbital position of the vehicle.

TABLE VIII-13. RESULTS OF SYSTEM THERMAL ANALYSIS

Orbit	*Vehicle Operating Mode	Power Conditioning Electronics (Operating Temperature Limits 0 to 55°C)				Batteries (Operating Temperature Limits 15 to 30°C)						
		Radiator Surface Finish	Passive Temp. Control			Radiator Surface Finish	Passive Temp. Control			Active Temp. Control		
			Area (ft^2)	Max (°C)	Min (°C)		Area (ft^2)	Max (°C)	Min (°C)	Area (ft^2)	Max (°C)	Min (°C)
200 nmi, polar orbit	I	Second-Surface Mirrors	76	55	15	Second-Surface Mirrors	110	30	-13	10	30	15
200 nmi, polar orbit	II		76	55	18		74	30	8	74	30	15
Synchronous, 28-1/2 inclined	I		85	55	20		5	30	-10	5	30	15

*Mode I : Local vertical of vehicle maintained fixed with respect to vehicle axes.
Mode II: Rotation of vehicle permitted about roll axes.

TABLE VIII-14. THERMAL EXTERNAL ENVIRONMENT FACTORS

Altitude (NM)	Maximum Incident Power (watts/inch^2) on horizontal flat plate		Orbit Time (minutes)	Maximum Orbital Nighttime (minutes)
	Earthshine	Albedo		
200	0.128	0.291	92	37
19,340	0.0033	0.0074	1440	70

The dissipating electronic equipment will be mounted on the internal face of the radiating surface. The equipment complement and the location of the equipment on the various sections of the radiator will be somewhat different for the two altitudes. Detailed data on this will be presented in later sections that consider the temperature profiles for these altitudes.

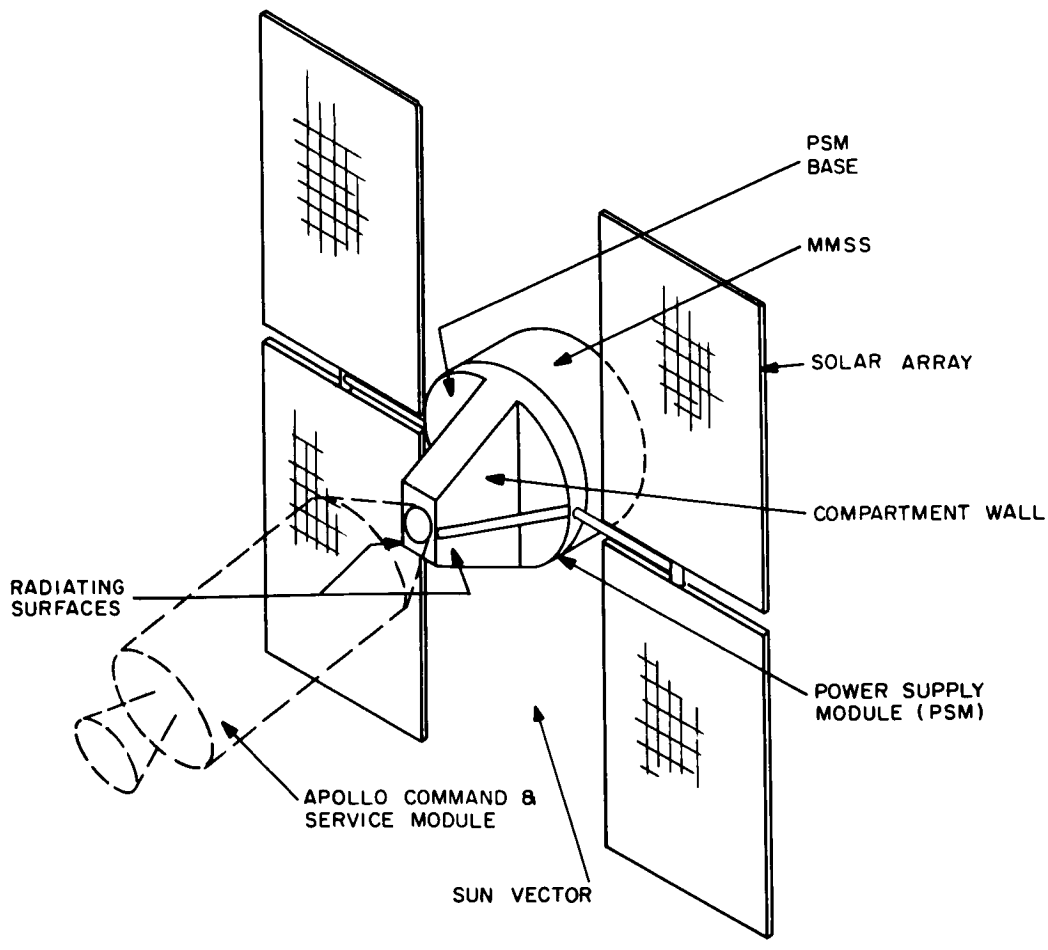

Figure VIII-18. Vehicle Orbital Configuration

The electronic equipment required for the vehicle mission consists of batteries, regulating and charging units, and an inverter for providing a-c power. The operating temperature ranges desired for this equipment are as follows:

Equipment	Temperature Range (°C)	
	Minimum	Maximum
Batteries	15	30
Power Conditioning	0	55

3. Equipment Temperature Control

a. RADIATION-SURFACE REQUIREMENTS

The equation that relates the various radiation-surface parameters at steady state conditions is:

$$A_r = \frac{1}{\epsilon' \sigma T_s^4 - P_S}, \qquad \text{(VIII-8)}$$

where

A_r (Area-power ratio) is the radiating area per unit dissipation (in^2/watt),

ϵ' is the effective emittance of the surface,

σ is the Stefan-Boltzmann Constant (3.657×10^{-11} watts/in^2 - °K^4),

T_s is the average surface temperature, °K, and

P_s is the Solar power absorbed by surface (watts/in^2).

The values of ϵ' and P_s are functions of the surface thermal characteristics and external environmental factors.

The effective emittance (ϵ') is determined by:

$$\epsilon' = \epsilon - \sum_{j=1}^{N} F_{sj} \frac{\sigma T_j^4}{\sigma T_s^4} = \epsilon - \frac{\sum}{\sigma T_s^4}, \qquad \text{(VIII-9)}$$

where

ϵ is the emittance of the radiating surface,

F_{sj} is the unit radiation exchange factor between the radiating surface and the jth external sink, and

T_j is the temperature of the jth external sink, (°K).

The value of F_{sj} is a function of geometric factors and surface thermal properties, and will vary with the orbit and position of the vehicle in the orbit. The external sinks which affect ϵ' are the earth, the solar-array panels, and the PSM baseplate. T_j, the external-sink temperature, will vary with the position of the solar array and PSM baseplate. These variations are a function of the orbit and of the position of the vehicle within the orbit.

The solar radiation absorbed by the surface depends on the incident radiation and the surface solar absorptance α_s or

$$P_s = \alpha_s \; P_{si} , \qquad \text{(VIII-10)}$$

where

P_{si} is the total incident solar radiation on the surface.

The incident solar radiation on the surface will be the sum of the direct radiation, earth albedo, and radiation reflected from local surfaces. The magnitude of incident direct radiation will be

$$P_{sid} = s \; \alpha_s \; F_s \; \text{Cos} \; \phi' \qquad \text{(VIII-11)}$$

where

s is the solar constant at earth distance ($0.87 \leq S \leq 0.93$), watts/in^2,

F_s is the shadowing factor, and

ϕ' is the angle between surface normal and sun direction.

As noted previously, the albedo and local surface-reflected radiation will vary with orbit and vehicle position. Figure VIII-19 presents curves of orbit-average incident solar radiation on the external radiating surfaces from each of the three possible sources as a function of sun angle for the 200-nmi altitude.

Note from equation (VIII-8) that the magnitude of absorbed radiation (P_s) will have a large effect on the magnitude of radiating surface required per unit of power dissipation. For example, suppose it is desired to maintain the average radiating surface temperature (T_s) at a value of 30°C when the total incident solar radiation on the surface is 0.75 watt per square inch with a surface effective emittance of 0.7. The value of A_r required for this condition depends on P_s. It is apparent that a low value of α_s is desired to give a low value of P_s (equation (VIII-10)). Available surface finishes that have low values of α_s are second-surface mirrors and certain white paint coatings. Table VIII-15 indicates the value of A_r, required for these two finishes and the surface equilibrium temperature for these values when the incident solar radiation is 0.75 watt per square inch and when the absorbed solar power equals zero (nighttime or long periods of shadow).

The second-surface mirror finish has a considerable advantage in the area power ratio (A_r) required, in temperature variation from maximum-sun to no-sun conditions and in degradation of surface properties. The temperature noted in the table are based on steady-state conditions and occur when the radiating surfaces are shadowed for a long period of time.

The use of A_r for computations permits easy redetermination of temperature or radiator area if power dissipation is changed. A revised value of A_r (A_r') is calculated by:

$$A'_r = \frac{A_r}{P_r},$$

where

$$P_r = \frac{\text{Revised power dissipation}}{\text{Original power dissipation}}$$

The value of A_r' can be used in equation (VIII-8) to determine the new surface temperature T_s':

$$\sigma T_s'^{\,4} = \frac{1}{\epsilon'}\left[\frac{1}{A_r'} + P_s\right]$$

A series of curves of A_r versus surface temperature, T_s, for various vehicle orientations based on equation (VIII-8), can be useful in the rapid determination of radiation surface required and steady-state temperature for various vehicle orientations and magnitudes of power dissipation (see Figure VIII-20).

b. TEMPERATURE DIFFERENTIAL BETWEEN RADIATING SURFACE AND EQUIPMENT

The surface temperature (T_s) involved in Equation (VIII-8) is the average temperature of the external radiating surface. The component temperature (T_c) will be higher than T_s because a temperature drop is required between the component and the contact area on

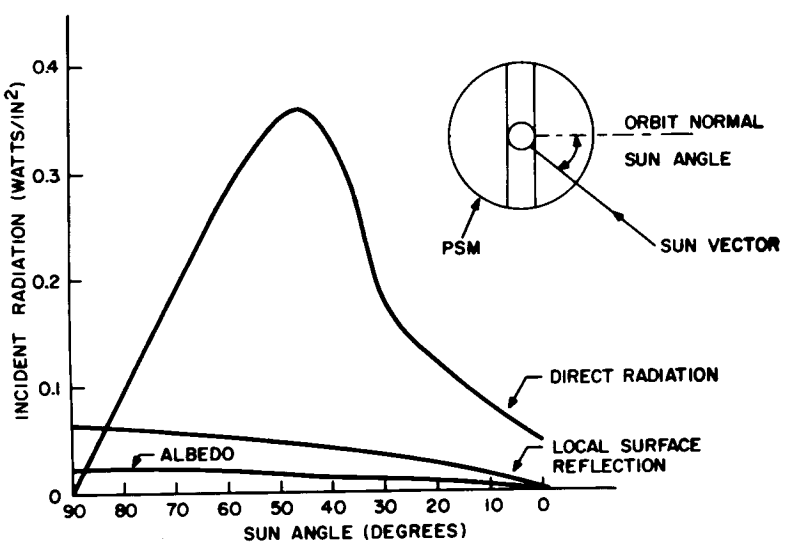

Figure VIII-19. Average Incident Solar Radiation on Radiating Surfaces versus Sun Angle; 200-nmi Orbit

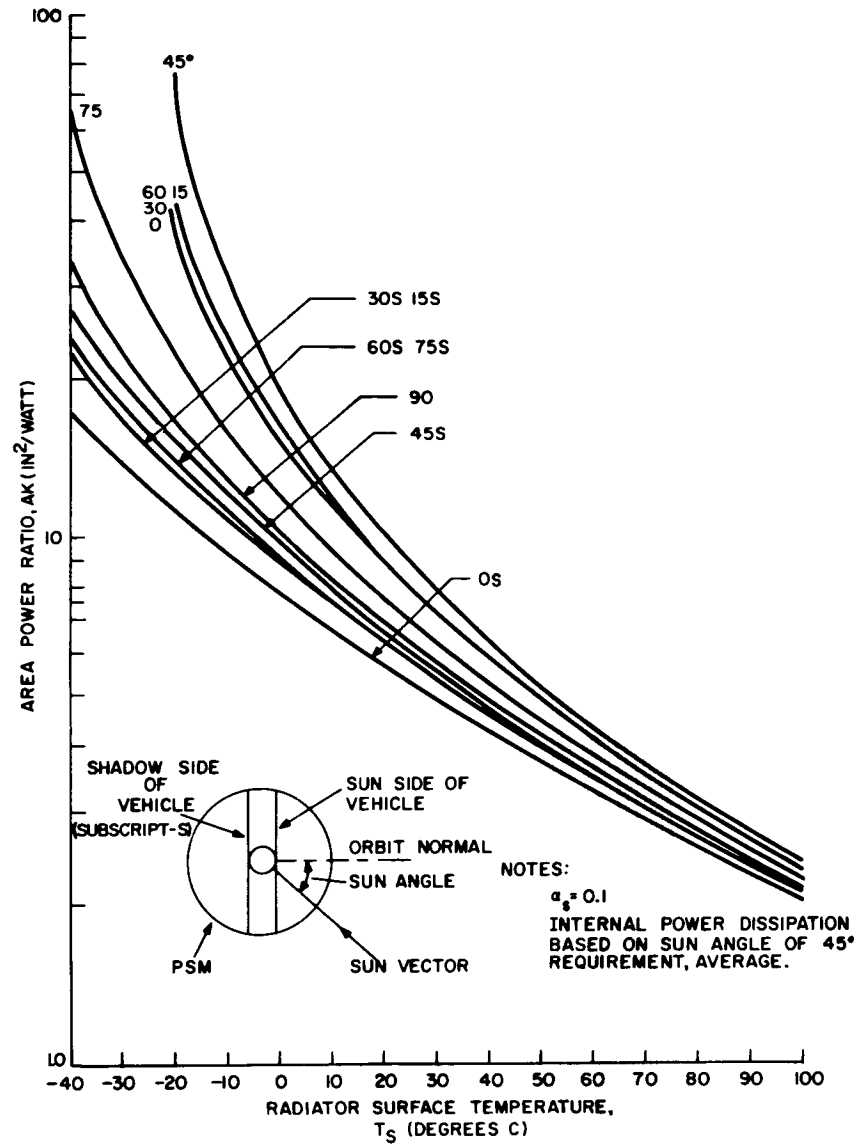

Figure VIII-20. Radiating Area per Unit of Power Dissipation versus Orbit Average Surface Temperature for Various Sun Angles; Sun and Shadow Sides of Orbit Plane at 200-nmi Altitude

TABLE VIII-15. SURFACE FINISH COMPARISON

Surface Finish	Solar Absorption		Solar Power Absorbed (w/in^2)		Area Power Ratio (A_r) $in^2/watt$		No-Sun Condition Equilibrium Temperature °C	
	BOL**	EOL**	BOL	EOL	BOL	EOL	Based on BOL A_r	Based on EOL A_r
Second-Surface Mirror	0.06	0.12	0.045	0.090	5.86	7.95	13	-8
White Paint (PV100)	0.19	0.38	0.142	0.284	13.5	*	-36	—

*A surface temperature of 30°C cannot be maintained at this condition for any finite area-power ratio.
**BOL = Beginning of life; EOL = End of life.

the radiating surface in order to transfer the dissipated power across the joint, and along the radiating surface. The magnitude of the temperature drop (T_c - T_s) is a function of the following:

(1) Contact area between equipment mounting surface and radiation surface.

(2) Contact pressure.

(3) Characteristics of contacting surfaces (roughness, flatness, hardness, etc.)

(4) Size of contact surface relative to total area of radiating surface.

(5) Radiator thickness.

It is considered that the maximum magnitude of this differential can be limited to 20°C for the power conditioning equipment (55°C temperature limit components) and 5°C for the batteries.

c. 200-NMI MISSION ANALYSIS

Because of the relatively short orbit time (92 minutes) for this altitude, the component temperature change due to orbital variation (power dissipation, effective

emittance, incident solar radiation, etc.) will be less than 5°C above or below the orbit average temperature. The maximum allowable value of average radiating surface temperature (T_{sM}) during the orbit will be

$$T_{sM} = T_{cM} - (\Delta T_{cs}) - \Delta T_T$$

where

T_{cM} is the maximum allowable component temperature,

ΔT_{cs} is the differential between component and average radiating surface temperature, and

ΔT_T is the temperature variation due to parameter changes during the orbit.

The minimum allowable value of average radiating surface temperature (T_{sM}) will be

$$T_{sm} = T_{cm} - \Delta T_{cs} + \Delta T_T,$$

where T_{cm} is the minimum allowable component temperatures. Table VIII-16 presents values of these temperatures for the mission phase under consideration.

TABLE VIII-16. TEMPERATURE VALUES FOR 200-NMI MISSION

Component	Maximum Allowable Component Temp. (°C)	Minimum Allowable Component Temp. (°C)	Differential Temp. (°C)	Temp. Variations During One Orbit	Average Radiator Temp. (°C)	
					Max.	Min.
Symbol	T_{cM}	T_{cm}	ΔT_{cs}	ΔT_T	T_{sM}	T_{sm}
Battery	30	15	5	5	20	15
Power Conditioning Equipment	55	0	20	5	30	-15

The temperature range of non-operating (spare) components will be approximately

$$T_{sm} \leq T_c \leq T_{sM}$$

The arrangement of equipment on the various sections of the external radiating surface is shown in Figure VIII-21. The surface area required for these various sections to limit the surface temperature to the maximum allowable value during any orbit was determined from the set of curves presented in Figure VIII-20, which are based on equation (VIII-8) and the orbital average power data. Use of second-surface mirrors having an end of life α_s of 0.1 was assumed for the external surface covering. The power profile for each section varies with the orbit. The power profiles giving minimum and maximum average orbital power dissipation for each section of the radiating surface are shown in Figure VIII-22. These minimum and maximum values occur at sun angles of 90 and 0° respectively.

Two operating modes of the vehicle were considered. The first mode maintains the local vertical fixed with respect to the vehicle axes, while the second mode permits rotation of the vehicle about its roll axis. This mode of operation, as noted elsewhere in this report is acceptable if not too frequent an occurrence. For a polar orbit, rotation about the roll axis may occur twice per year but will occur more frequently for orbital inclinations of less than 90°.

Table VIII-17 gives the radiator surface-area requirements to maintain the upper limits of the temperature range specified for the particular components. The minimum component temperature is given with this radiator area. Included in the table are the results for both Mode I and Mode II. When the roll mode (II) is employed, the surfaces A and D (power conditioning components) are on the sun side of the vehicle and surfaces B and C are on the shadow side.

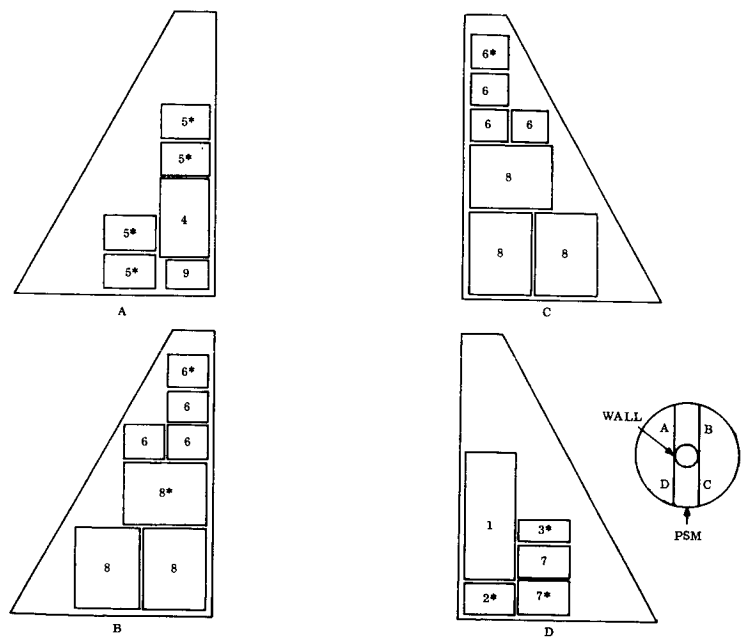

1. PWM REGULATOR ASS'Y
2. PWM REG. CONTROL UNIT
3. PWM REG. MODULE
4. INVERTER ASSEMBLY
5. INVERTER MODULE
6. CHG. ELEC.-TRACKER MOD.
7. CHG. ELEC.-TRACKER CONT. UNIT
8. BATTERY
9. POWER DISTRIBUTION UNIT

*DENOTES SPARES

Figure VIII-21. Proposed Arrangement of Equipment on Radiating Surface

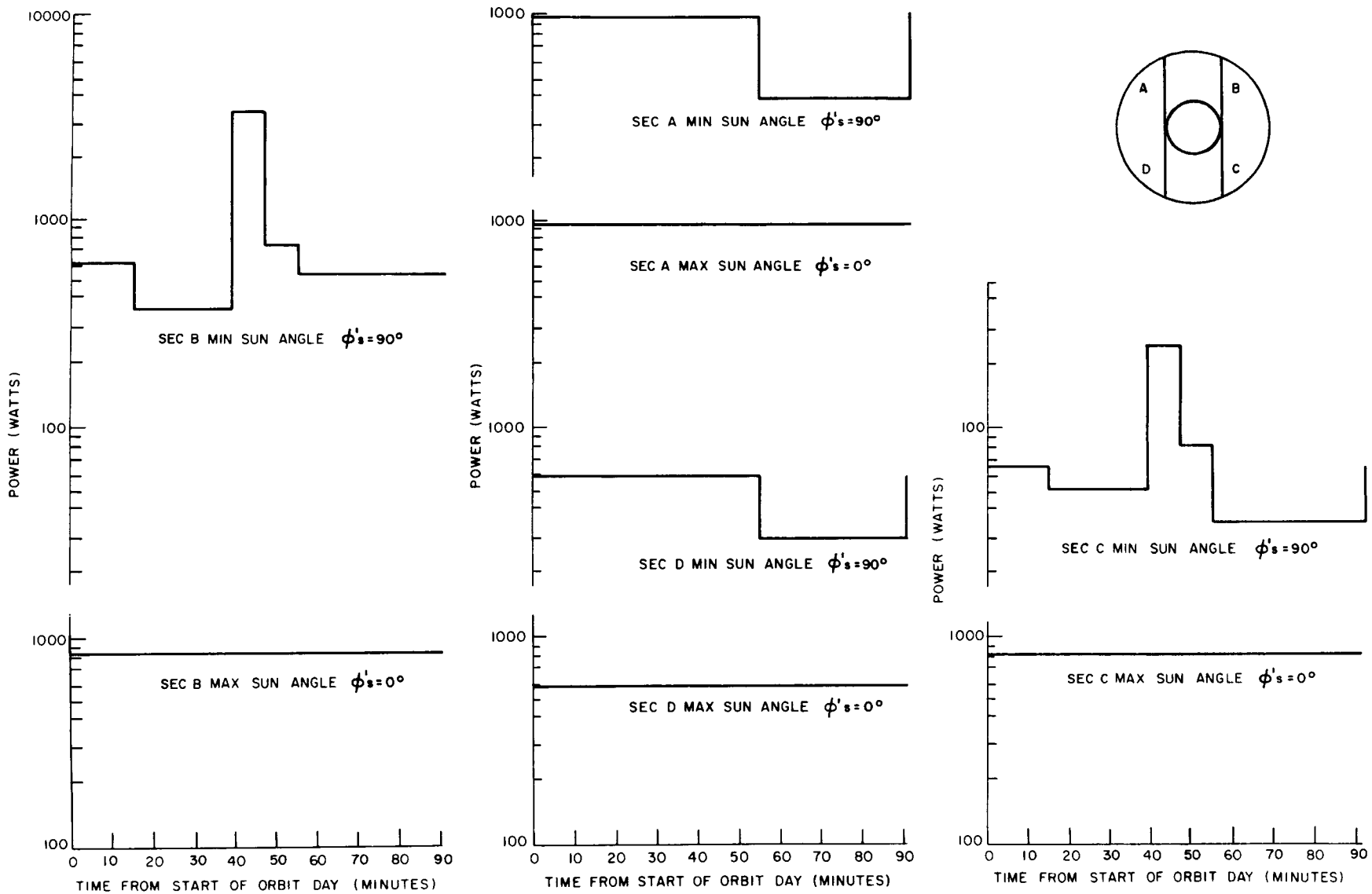

Figure VIII-22. Thermal Dissipation Profiles: Minimum-Maximum Power Profiles, 92-Minute Orbit, 200 NM Altitude

TABLE VIII-17. RADIATION SURFACE REQUIREMENTS

Surface	Component Temp. Limits (°C)	Internal Thermal Dissipation (Watts)	Sun Angle for Maximum Temp. (Degrees)		Radiator Area (Ft^2)		Minimum Component Temperature (Degrees C)	
			Mode I	Mode II	Mode I	Mode II	Mode I	Mode II
A	0 to 55	839	0 to 15	0 to 15	47	47	15	18
B	15 to 30	809	45	15	57	37	-13	9
C	15 to 30	746	45	15	53	37	-10	8
D	0 to 55	524	0 to 15	0 to 15	29	29	17	21

NOTES:

Mode I: No vehicle roll.
Mode II: Vehicle Roll Permitted; Polar Orbit, 2 times per year.
Surfaces B and C are on the shadow side of the vehicle.
Orbit Altitude, 200 nmi

Figure VIII-23 presents curves of orbital component temperature range as a function of sun angle (for operation in both Mode I and Mode II) on surface A (power conditioning equipment) and surface C (battery equipment). These surfaces are on opposite sides of the vehicle.

Note that in both operating modes, the minimum component temperatures on surfaces A and D are above the allowable minimum (0°C) for the electronic equipment but the minimums for surfaces B and C are below that desired (15°C) for the batteries, by 28 and 25°C respectively for Mode I, and 6 and 7°C respectively for Mode II.

The effect of internal coupling has been neglected in all the temperature determinations. In Mode I, the maximum temperatures for the surfaces on one side of the vehicle occur when the temperatures on the opposite side are minimum so that internal coupling could help to reduce the temperature deficiency of the battery sections during the minimum-temperature period. However, the thermal power gain from this internal coupling could not raise the battery temperature to 15°C, even when the temperature difference is maximum at 0° sun angle. At sun angles close to 90°, there is very little difference between the temperatures of these two surfaces, so that internal coupling would have no effect in this operating condition.

It must be concluded that for both operating modes I and II, passive control cannot maintain the battery operating temperature within the desired limits of 15 to 30°C, although in mode II the minimum temperature does not go more than 7° below this limit. A 10°C increase in the allowable battery temperature range would permit the use of passive control in operating Mode II. The difference between minimum and maximum battery temperature is approximately 22°C, which would be less than the 25°C for the revised temperature conditions. If it is necessary to maintain the 15 to 30°C temperature range for the batteries, or even under the revised temperature limits if operating mode II is not allowable, then some type of active control would have to be provided for the radiating surfaces of sections B and C. The effect of an active control system would be to reduce the effective emittance for sun angles where the minimum temperature with passive control is below the allowable minimum. A two-position type of control such as a flap or curtain would be satisfactory if the required range of variation in effective emittance (at sun angles where the temperature is low) is small. However, this is not the case and a modulating control (such as variable-position vanes) is required. The surface-area requirements noted in Table VIII-17 are available with the

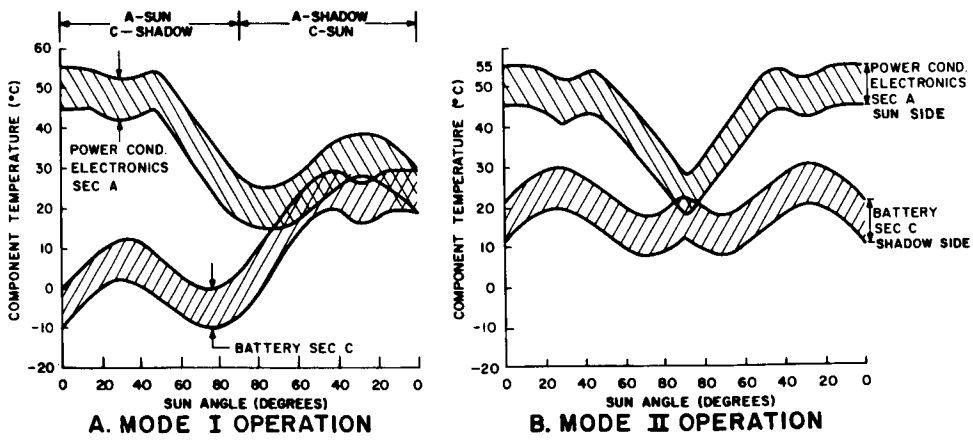

Figure VIII-23. Orbit Component Temperature Range for Sections A and C of Vehicle Surface in Two Operating Modes at 200-nmi Altitude

present layout of the Power System Module. The total surface on one side of the vehicle is approximately 125 square feet as compared to the maximum requirements of 110 square feet for the battery section. The advantage of a second-surface mirror has been clearly demonstrated. Whether the mirrors employ aluminum or silver as the coatings is a subject for future study. The advantage of a silver coating is its lower absorptance value, but a cost increase over aluminum coating would be involved, as the soft silver layer must be protected by a suitable overcoat such as inconel. Noted in Table VIII-15 are the absorptance (α) values for end-of-life conditions for the silver mirror.

d. 19,340-NM MISSION ANALYSIS

The orbit time for this altitude is 24 hours. Component temperatures during this relatively long period may vary considerably from the orbit average, since changes in external environmental factors and power dissipation (due to vehicle position in the orbit) will cause larger transients than was the case for 200-nmi altitude orbits. Thus, the temperature profile during individual orbits must be more carefully investigated for this altitude. The orbit inclination for this mission is 28-1/2°, which gives a sun-angle range of 39 to 90°. The maximum incident solar radiation on the radiating surfaces that must be considered in temperature determination will be approximately 0.80 watt per square inch, as compared with the maximum orbit average of 0.42 watt per square inch for the 200-nmi mission. This will increase the amount of radiating area required per watt of power dissipation to maintain the same average steady-state component temperatures. There is no significant thermal advantage in rolling the vehicle at this altitude, therefore only Mode I need be discussed.

For the synchronous-altitude mission, it is proposed to arrange the equipment on the radiating surfaces as follows (See Appendix H):

Section	Components
A	Inverter assembly, power distribution unit, and four spare inverter modules.
B	Two batteries and two spare battery modules.
C	Same as B.
D	Two PWM regulator control units (1 spare); Six PWM regulator modules (1 spare); Two charger-tracker control units (1 spare); Eight charger-tracker modules (4 spares).

The weight of the equipment complement for each section is as follows:

Section	Weight (lb)
A	533
B	660
C	660
D	399.

Figure VIII-24 shows the power dissipation profiles for these sections for a 90° sun angle (maximum-darktime orbit). The power dissipation for each section during the 100-percent-suntime orbits (sun angle ≤ 81°) will be the following constant values:

Section	Power Dissipation (Watts)
A	955
B	31
C	31
D	756.

It should be noted that only for the batteries is the orbit average power for the 90° sun angle orbit greater than the power for the 100-percent-suntime orbits. This average power is 56 watts. During the 100-percent-suntime orbits, the temperature of the radiating surface will be affected only by changes in the external environment, since the power is constant on all sections. In the 90° orbit, both power and external environmental conditions will vary for all sections.

A typical temperature profile for the battery sections (B and C) during the 90° sun angle orbit is presented in Figure VIII-25, based on a radiating area for each section of 195 square inches. Note that the temperature variation during this orbit is only 8°C. However, because of the relatively large solar input to the radiating surface at the sun angle (39°) where the incident solar radiation of the surface is maximum, the battery mounting-surface temperature would rise to a maximum of 50°C for the 195-square-inch surface area. Therefore, an area of 370 square inches per section would be required to limit the mounting surface temperature to the desired 30°C maximum during this orbit. This surface-area requirement is based on the consideration that internal coupling between the surfaces on opposite sides of the spacecraft will transfer approximately 25 percent of the solar input from the sunlit surface to the surface in shadow. The minimum battery temperature for this same 370-square-inch radiating surface area would be -10°C and would occur for the surface in shadow during the 81° sun-angle orbit, because of the high effective emittance during this orbit due to

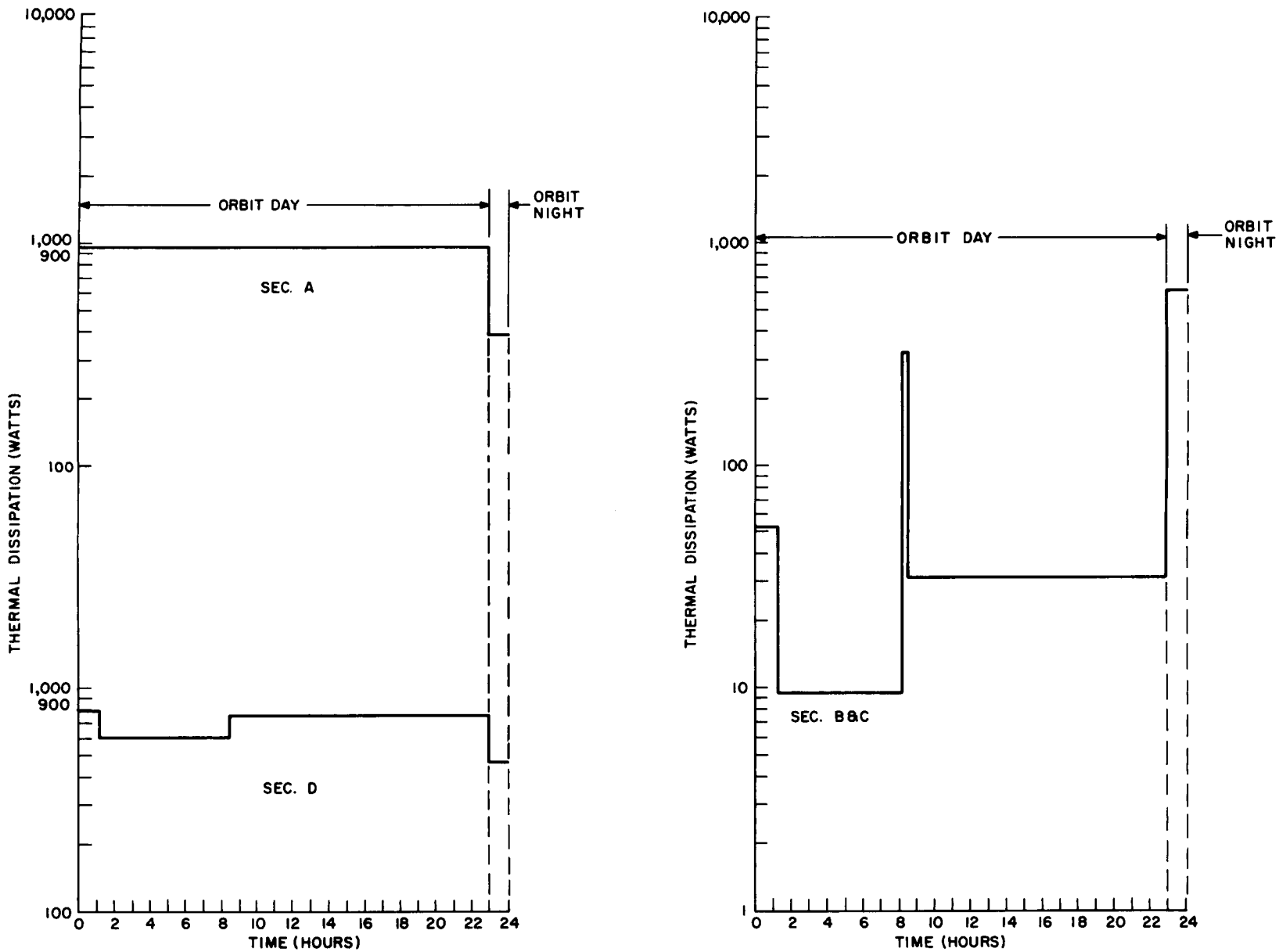

Figure VIII-24. Power Profiles for Sections A, D and B, C.

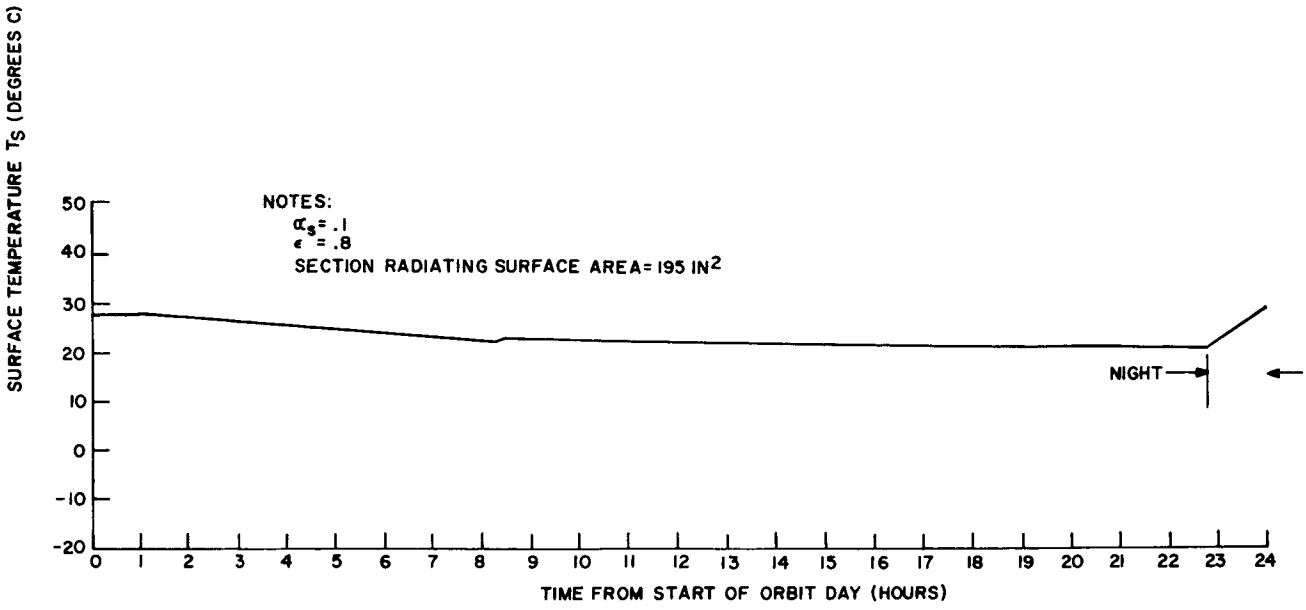

Figure VIII-25. Temperature Of Battery Mounting Surface vs Time From Start Of Orbit Day for 90° Sunangle Orbit at 19400 NM Altitude.

the position of the solar panels. If both battery sections were placed on the same side of the vehicle, some temperature benefit could be gained by a 180° rotation about the roll axis when the sun angle is 90°. This would raise the minimum temperature to approximately -5°C, which is still considerably below the allowable limit of 15°C.

In order to maintain the battery temperature within the desired 15 to 30°C range during the mission, some type of active controller would be required. A circular-shutter type of controller, which has a maximum open area of 50 percent of its gross area, would be 31 inches in diameter in order to provide the required 370 square inches of area when fully open. This size unit would fit readily on the available radiating surface. The total area of active battery mounting surface per section is 1000 square inches, which matches reasonably well with the total controller area of 740 square inches. This type of controller which has been used on various space vehicles and has the advantage over vane-type controllers of having minimum effect on the α_s of the exposed surface. Modulating temperature control could be obtained by use of a fluid-filled bellows-type actuator, which would position the shutter in accordance with temperature requirements.

The electronic equipment sections (A and D) could be maintained within the desired temperature range with passive control, using second-surface mirrors as the external-surface finish.

Table VIII-18 indicates the component temperature limits for the critical orbits and the radiating area required:

TABLE VIII-18. COMPONENT TEMPERATURES

Sun Angle (degrees)	Operating Equipment		Non-Operating Spares	
	Max. Temp. (°C)	Min. Temp. (°C)	Max. Temp. (°C)	Min. Temp. (°C)
39	55	33	35	13
81	29	27	9	7
90	30	20	10	0

Section	Radiating Surface Area (sq. ft.)
A	50
D	35

Component operating temperatures in this table are based on a differential between the component temperature and the average radiating surface temperature of 20°C.

4. Radiator Weight

The substrate of the radiating surfaces must conduct the dissipated power to the surface areas with a reasonable differential between temperatures of the component mounting surfaces and the average radiating-surface temperature. The magnitude of this differential has a very significant effect on the radiating surface area required. For example in the case of the 19,400-nm-altitude mission, the area required per unit of power dissipation to limit maximum component temperature to 55°C is 7.45 square inches per watt for a differential of 20°C. This reduces to 6.0 square inches per watt for a differential of 10°C. However, this could only be accomplished at a significant sacrifice in the weight of the radiator. The thickness of the substrate required for a given differential depends on the material and other parameters previously listed in Paragraph VIII. G.3.b. This thickness can be quite large in the case of components with high dissipation, such as the inverter. It is estimated that the average thickness of an aluminum radiator required to maintain a 20°C differential would be 1.5 inches. The total weight of this radiator would be 1190 pounds.

The weight of the radiator could be reduced considerably by reducing the inverter and PWM regulator assemblies into their component modules and then arranging the individual modules on the substrates so that each module has its own section of surface. In the case of the inverter, this arrangement could reduce the required average thickness of the surface from

1.5 to 0.4 inches, which would mean a weight reduction of approximately 840 pounds, for a total radiator weight of 350 pounds.

In general, the radiator-weight penalty is not considered as totally due to the thermal requirements. Part of this weight is useful to support the components mounted to it, such as the batteries, electronics, and the solar array in the stowed position. The actual chargeable weight has not been determined.

5. Fluid-Loop Heat Transfer System

The application of a fluid heat transfer system to the radiating surface could reduce the weight of the substrate considerably. It is estimated that in the case of the inverter, the use of a fluid system designed to give the same temperature conditions as the 1-1/2-inch-thick conductive radiator ($T_c - T_s = 20°C$) would reduce the required weight by at least 1000 pounds. The weight saving would not be quite so dramatic in the case of the other, lower-dissipation components, but would still be substantial. A second advantage of a fluid transfer system would be the possibility of efficiently distributing a portion of the solar input from sunlit surfaces to surfaces in the shadow, thus reducing the minimum-maximum temperature differential. In the case of the batteries, this could possibly eliminate the necessity of using active controllers in the synchronous orbit, or eliminate the need for vehicle roll (Mode II) to maintain the temperature within the required range. There are certain disadvantages inherent in the use of a fluid system such as:

(1) Possibility of fluid leakage.

(2) Possible reduction in system reliability because of additional operating components required (pump, controls, etc.).

(3) Power requirements for fluid pumping.

Considerable additional study is required in order to thoroughly investigate both the advantages and disadvantages of a fluid loop system.

6. Auxiliary Heater Temperature Control

If sufficient area is supplied in all cases to maintain the maximum battery temperature below the acceptable limit of 30°C, it is noted that with passive control, the battery temperature is below the desired limit of 15°C. It was indicated in previous discussions that active control in the form of rotary shutters or movable vanes could be used to maintain this 15°C limit. An alternate method for obtaining the required temperature control would be the use of auxiliary heaters on the battery radiating surfaces to supply the additional power necessary to keep the surfaces above 15°C during the periods when the external environmental factors are not of sufficient magnitude. The maximum power required by these heaters, which would be supplied by the array, is indicated in Table VIII-19.

The heaters would be actuated by temperature sensors on the battery-mounting surfaces through electronic switching circuits. The application of this type of control system requires

that excess power (over that necessary for the accomplishment of the basic mission) be available from the array at the required periods.

TABLE VIII-19. AUXILIARY HEATER POWER REQUIREMENTS

Altitude (nmi)	Operating Mode	Maximum additional power required to maintain 15°C battery temp. (watts)
200	I	500
200	II	50
19,340	I	30

7. Conclusion

It is apparent that considerably more work is required in the area of thermal analysis and design of thermal-control systems. Conclusions as to which is the preferable control system cannot be made at this time. Definition of mission constraints, such as the influence of the roll mode on the mission, needs clarification; the importance of a single control system for all orbital altitudes and inclinations needs resolution and further study, etc.

The equipment (batteries and power conditioning) have been arranged almost entirely to suit the thermal requirements with very little regard to mechanical or electrical requirements. It is believed that the arrangement as presented is acceptable to the other disciplines mentioned, but further study is necessary. With regard to the equipment arrangement, a case has been illustrated to show where 840 pounds of conductive radiator could be saved by reducing the inverter package to its modules. The penalties exacted to accomplish this are not known at this time.

It has been shown that second-surface mirrors on the radiating surface are more advantageous than white paint because of the higher absorptance values and greater change in thermal properties during a one-year mission. But the problems of placing these mirrors on large surfaces, that will be used for primary mechanical support, has not been sufficiently explored. Further trade-off studies are required with regard to cost, degradation, method of application, and thermal properties prior to the selection of coatings (aluminum or silver).

Finally, a quantitative and trade-off analysis must be conducted to determine the weight, cost, and reliability relationship for passive, active, fluid loop, and auxiliary-heater systems.

In short, more definitive information is required with regard to the satellite mission(s) and a greater degree of thermal analysis is necessary before a control system can be recommended.

H. WEIGHT SUMMARY

Shown in Table VIII-20 is a weight summary for all the items required to fabricate the solar array and maintain normal sun incidence. Also included is the weight of the thermal control system for Mode II at 200 nmi. Note that part of the weight shown for this item (thermal control system) may be utilized for structural support.

Weights of propellants required for attitude control and for orbital maneuvers, as well as momentum storage devices, are not included in Table VIII-20.

Due to the conceptual nature of the study, it was not possible to size all items based upon a stress analysis. Consequently, some of the values listed represent engineering estimates.

TABLE VIII-20. WEIGHT SUMMARY

Item	Weight	
	Lb/sq ft	Lb
Solar Array, 1927 sq ft		
Solar cells and components	0.314	
Aluminum structural frame	0.178	
Aluminum honeycomb, 1/4 in. thick	0.235	
Hinges, locks, and array deployment mechanism	0.053	
Electrical harness	0.008	
Miscellaneous hardware	0.020	
Total	0.808	1558
Deployment Mechanism		
Boom assembly (2 required)		65
Boom actuator assembly (2 required)		8
Array retaining cable		25
Electrical connectors		6
Total		104
Thermal Control System		700
Servo Control System		60
Array orientation drive assembly		
Servo electronics		
Sensors		

LIST OF REFERENCES FOR SECTION VIII

VIII-1. Lockheed-California Company, Modular Multipurpose Space Station Study, Report LR18906, July 18, 1965.

VIII-2. J. P. DenHartog, Mechanical Vibration, McGraw Hill Book Co., New York, 4th Edition, 1956.

VIII-3. "Rocket Engine. Service Propulsion System," NAA-PD Specification MC321-0004 (March 1966).

SECTION IX

ARRAY ORIENTATION ANALYSIS

A. INTRODUCTION AND SUMMARY

This section describes the analyses of the orbital configuration of the satellite. Numerous axes of control and array orientations were considered, with the resultant selection of the "H" configuration (Figure IX-1). The choice of the symmetrical "H" configuration was based on the reduced propellant consumption through elimination of cyclical gravity-gradient torques. This is a most significant consideration if it is assumed that no fuel resupply will be made for the mission duration (one year). Paragraphs IX. C. and IX. D. analyze the effect of "external" perturbations and show the resultant fuel consumption for various missions and configurations. Paragraph IX. E. shows how fuel consumption is affected if some form of momentum storage device (MSD) is utilized to control cyclic perturbations. Two types of MSD are analyzed (reaction wheel and control moment gyro) to generate preliminary tradeoff data. The conclusion arrived at is that at least one axis (pitch) should have momentum storage to conserve fuel.

In Paragraph IX. F. are developed the array-orientation requirements as well as the preliminary analysis of the servo drive. A significant consideration here is the tradeoff and effect of the sun-tracker location.

The final portion of this section contains analyses of preliminary shadowing effects resulting from variation of the sun vector with respect to the orbit. The results indicate that the "H" configuration sustains more shadowing than does the "Z" configuration. Upon further investigation, however, the effect of this shadowing is not as serious as it first appears. If the average orbital array energy is plotted against the mission time, the result is a relatively flat curve. This stems from the fact that worst-case shadowing (50 percent) occurs when the orbit has 100 percent sun time.

Although final decisions regarding details of configuration and orientation cannot be made from this preliminary study, the techniques required to create a "final" design are well developed.

B. CONFIGURATION ANALYSIS

Considerations of stowage, deployment, and design simplicity dictated the use of two solar arrays as the best approach. Since full sun tracking is required, two orientation axes are needed. These axes are called the "μ" axis (which tracks the sun at orbital rate) and the "θ" axis (which tracks the motion of the sun with respect to the orbital plane). The combinations produced by axes location, array position, and axes of rotation were utilized to generate the configurations shown in Figure IX-2.

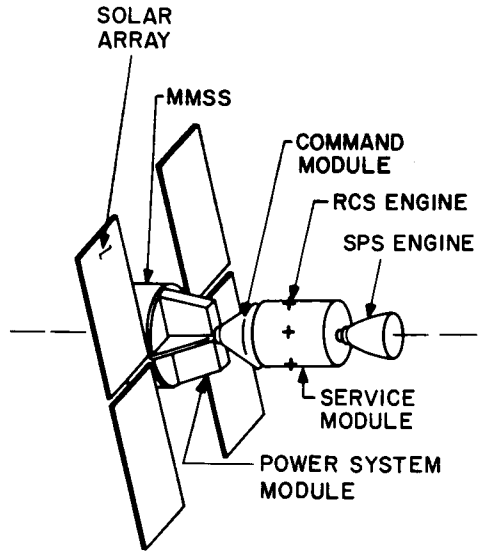

Figure IX-1. Orbital Configuration "H"

A preliminary examination of perturbations on the solar array shows that most effects are independent of shape and position. For example, the magnetic dipole, aerodynamic forces, and solar pressure effects are strictly functions of total array area, provided symmetry is maintained. The gravity-gradient torques, conversely, are a strong function of array shape (aspect ratio) and orientation. Since the gravity-gradient torques are a major perturbation, they are used in conjunction with inertial forces as major selection criteria. Figure IX-3 shows the results of a qualitative analysis of the gravity gradient and inertial effects on the configurations of Figure IX-2. These results, along with considerations of shadow effects, packaging, deployment, and the desirability of simple control motions, were utilized to select the orbital configuration.

The analyses to generate Figure IX-3 are somewhat complicated by variations produced by the position of the sun vector in the orbital plane (ϕ'_s). ϕ'_s is given by:

$$\phi'_s = (90 - \phi_s) = 90 - Cos^{-1} [Cos\ \delta_s\ Sin\ (\alpha_o - \alpha_s)\ Sin\ i + Cos\ i\ Sin\ \delta_s] \qquad \text{(IX-1)}$$

(δ_s and α_s vary with date and may be found in "American Ephemeris and Nautical Almanac".)

$$\alpha_o = \alpha_{o_i} + \alpha_o t \qquad \text{(IX-2)}$$

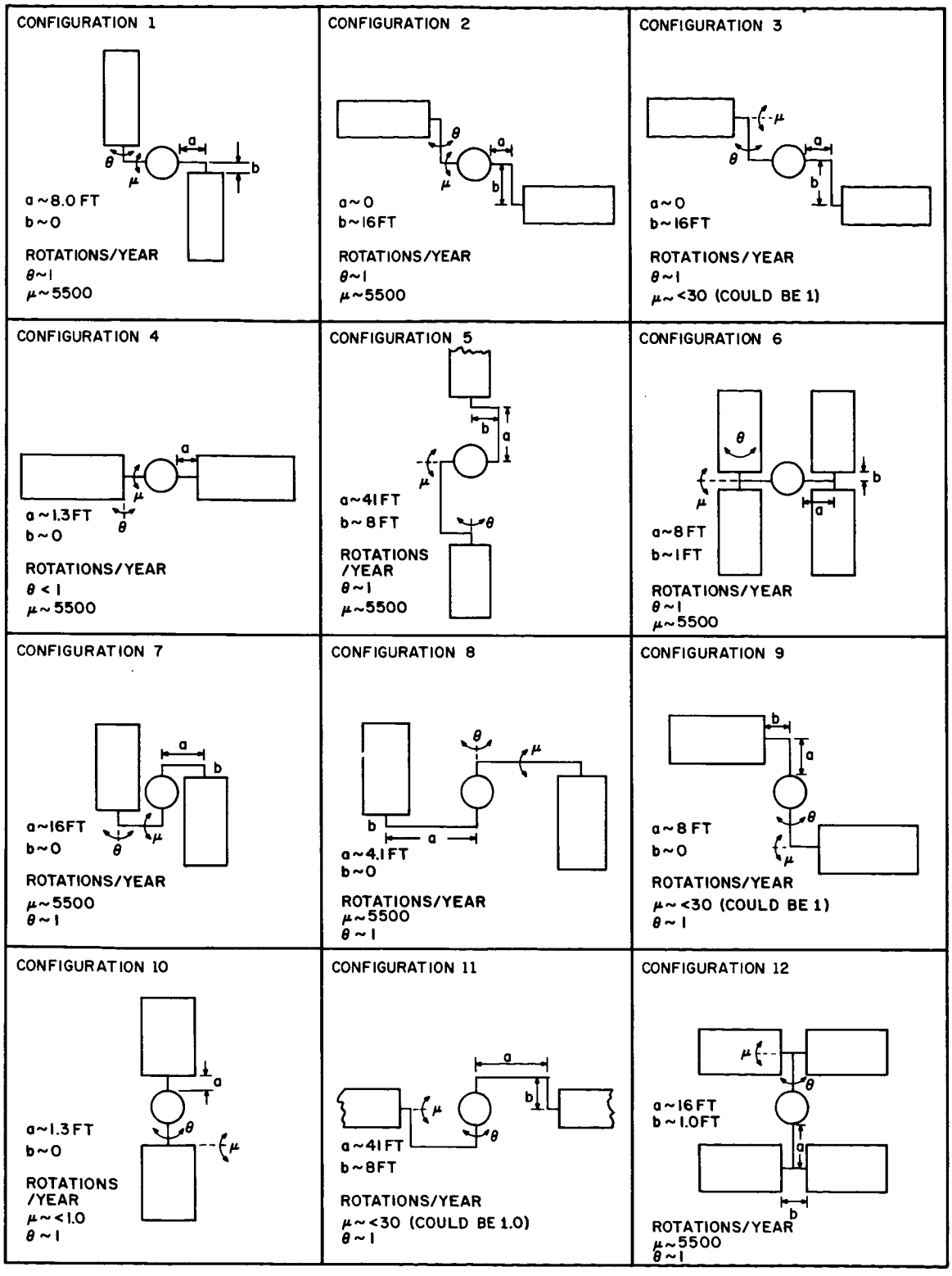

Figure IX-2. Solar Array Configurations

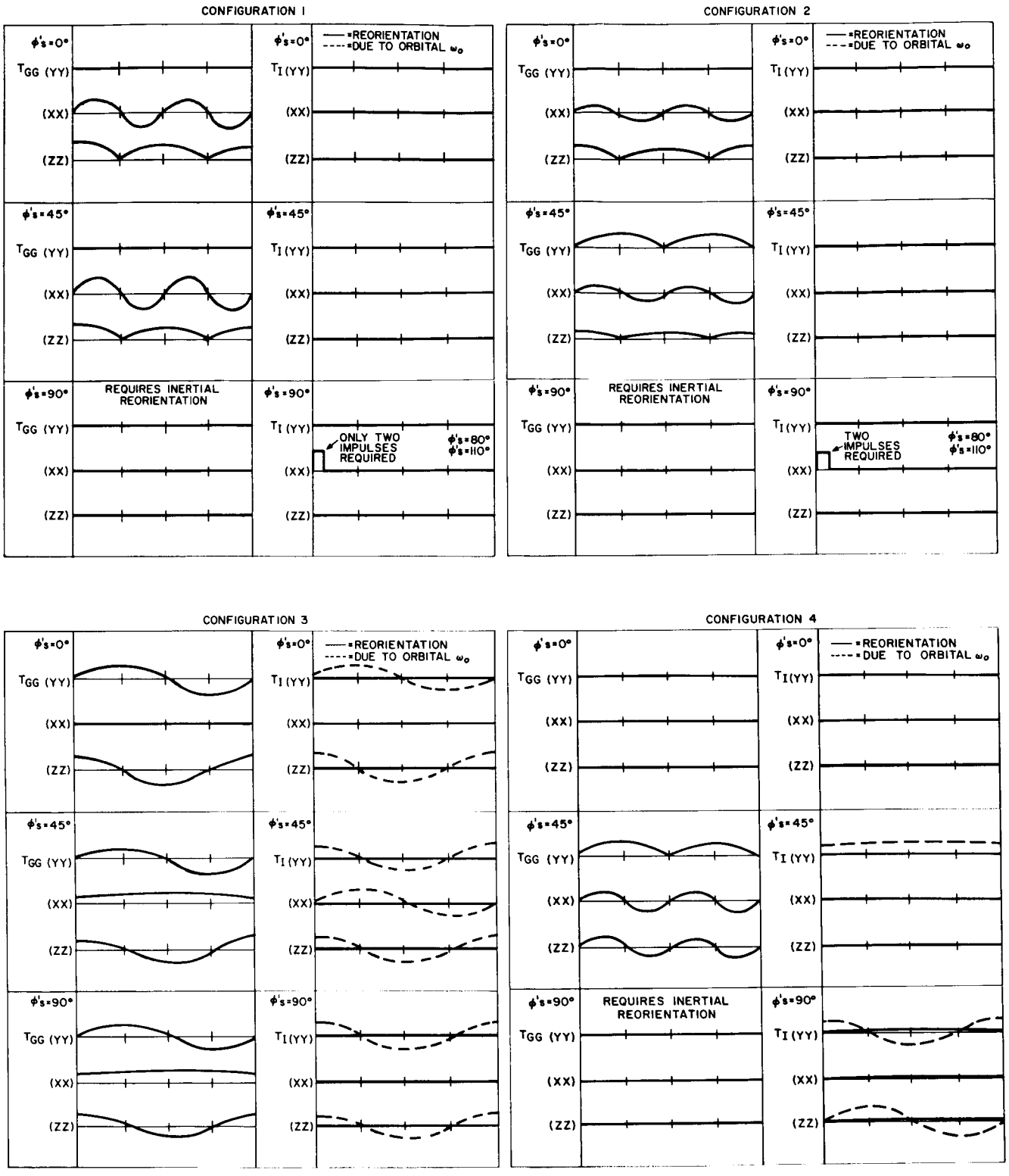

Figure IX-3. Analysis of Gravity Gradient and Inertial Effects on Various Configurations (Sheet 1 of 3)

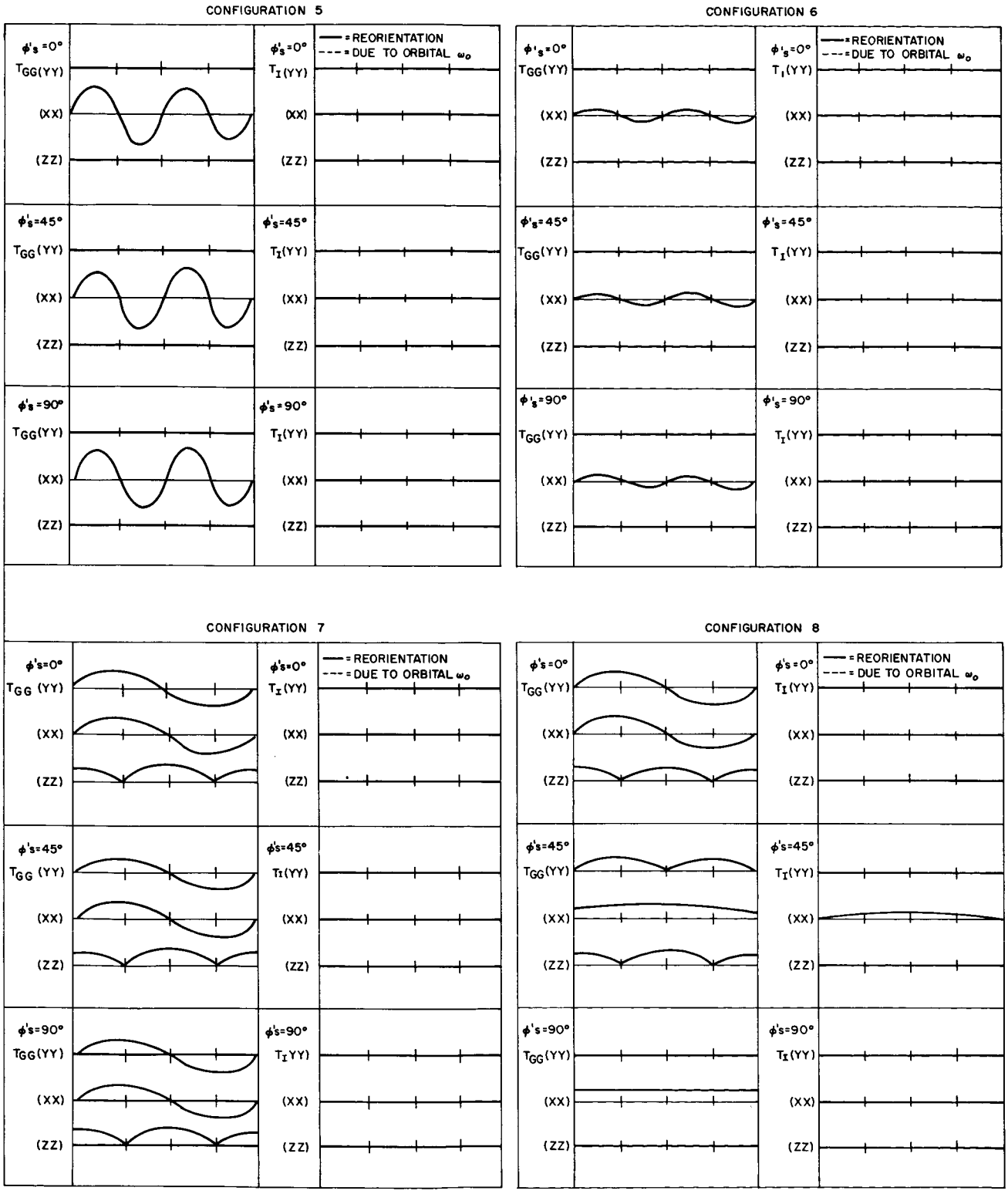

Figure IX-3. Analysis of Gravity Gradient and Inertial Effects on Various Configurations (Sheet 2 of 3)

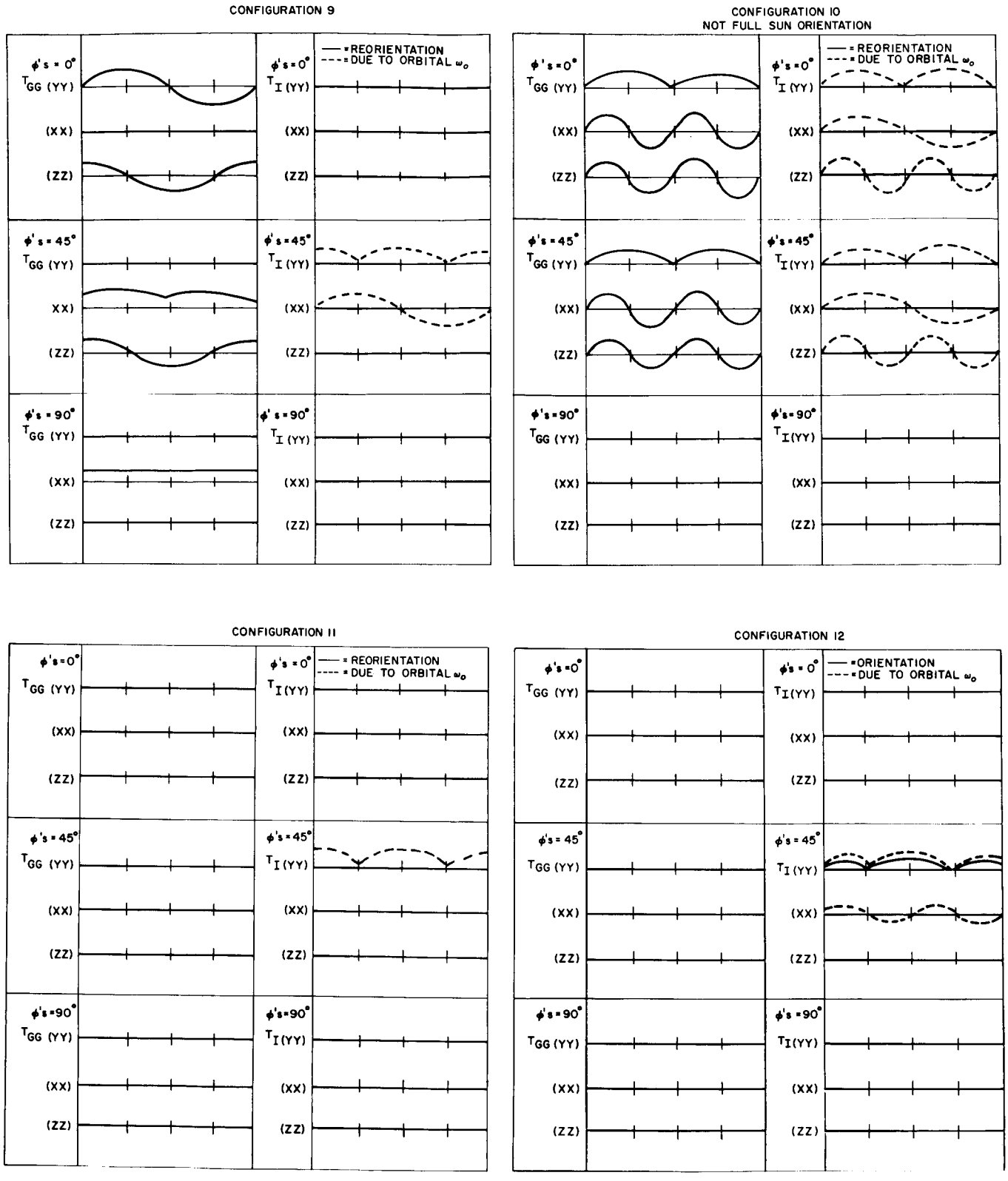

Figure IX-3. Analysis of Gravity Gradient and Inertial Effects on Various Configurations (Sheet 3 of 3)

where α_{o_i} is the right ascension of the ascending node orbit at t equal to 0.and $\dot{\alpha}_o$ is the precession of the orbit plane.

$$\dot{\alpha}_o = (0.23879) \times 10^{14} (a)^{-7/2} \; Cos\; i \;\; (deg/day) \tag{IX-3}$$

For an orbit altitude (h) of 200 nmi, and for an inclination (i) of 28.5°, the precession rate ($\dot{\alpha}_o$) equals -7.212 degrees per day.

The absolute value of the sun angle ($|\phi'_s|$) can vary from 0 to 90°, depending on the orbit and time of launch. The torques for the qualitative analysis are thus shown for $|\phi'_s|$ = 0°, 45°, and 90°.

The array orientation system will maintain the array normal to the sun, while the basic vehicle remains earth-oriented. The vector normal to the array is given in orbit coordinates (Figure IX-4) by:

$$\hat{A} = A_l \hat{\ell} + A_b \hat{b} + A_n \hat{n} \tag{IX-4}$$

where

$$A_l = Cos\; \delta_s \;\; Cos\; (\alpha_o - \alpha_s),$$

$$A_b = Sin\; \delta_s \;\; Sin\; i - Cos\; \delta_s \;\; Sin\; (\alpha_o - \alpha_s) \;\; Cos\; i,$$

$$A_n = Cos\; \delta_s \;\; Sin\; (\alpha_o - \alpha_s) \;\; Sin\; i + Cos\; i \;\; Sin\; \delta_s,$$

and hence

$$\phi_s = Cos^{-1} A_n \tag{IX-5}$$

$$\lambda_s = Tan^{-1} \left(\frac{A_b}{A} \right)$$

Using the array geometry, the required angular orientation of the array with respect to the vehicle (assuming that the vehicle is nominally oriented along the local vertical) is indicated by:

$$\theta = (90 - \phi_s) = \phi'_s \tag{IX-6}$$

$$\mu = \lambda_s - \omega_o t \;\; (t = 0, \; vehicle \; at \; ascending \; node) \tag{IX-7}$$

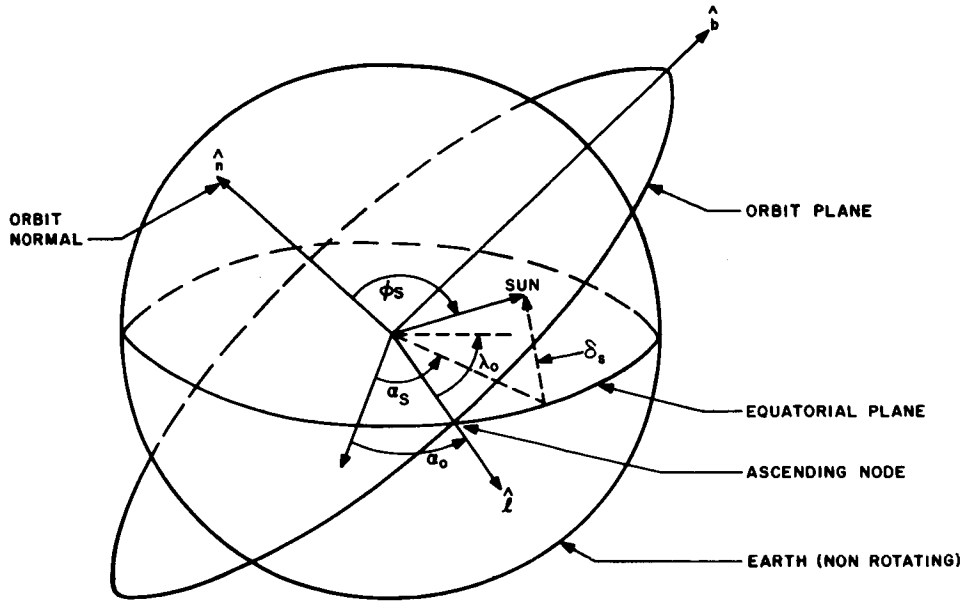

Figure IX-4. Orbit Geometry

Since ϕ_s, and hence θ, is not a function of the satellite position in orbit and since ϕ_s varies slowly, the control of the array about the axis may essentially consist of discrete small motions at infrequent intervals (longer than one day between changes in position). However, μ must be continuously varied at approximately orbital rate with respect to the vehicle (the rate of change of λ_s is, similar to ϕ_s, small relative to ω_o).

The following criteria and ground rules have been established for the IPS concept.

(1) Sun-oriented array;

(2) Earth-oriented vehicle;

(3) Array area, 4900 square feet; and

(4) No interference between control axes and the MMSS or docking ports.

Other criteria included are:

(5) Minimization of array shadowing;

(6) Perturbation effects;

(7) Simple orientation control motions;

(8) Resupply period, 45 days; and

(9) Packaging constraints.

Utilizing these criteria and ground rules for the four basic missions, the "Z" configuration (Figure IX-5) was selected as the initial choice. Although the "Z" configuration met the original requirements, it created a severe problem with gravity gradient torques. Since the largest torque (pitch) was cyclic and thus amenable to momentum storage, it was assumed that propellant resupply could handle the unidirectional torque (roll). With the selection of the "Z" configuration, a full perturbation analysis was initiated. Perturbations considered for this analysis were:

(1) Gravity gradient torques;

(2) Aerodynamic forces;

(3) Residual dipole torques (magnetic); and

(4) Solar radiation pressure.

The four basic missions considered for the analysis were:

(1) 200-nautical-mile, 28.5° inclined orbit with single-compartment MMSS;

(2) 200-nautical-mile, 28.5° inclined orbit with two-compartment MMSS;

(3) 200-nautical-mile, polar orbit with two-compartment MMSS; and

(4) Synchronous altitude, 30° inclined orbit with two-compartment MMSS.

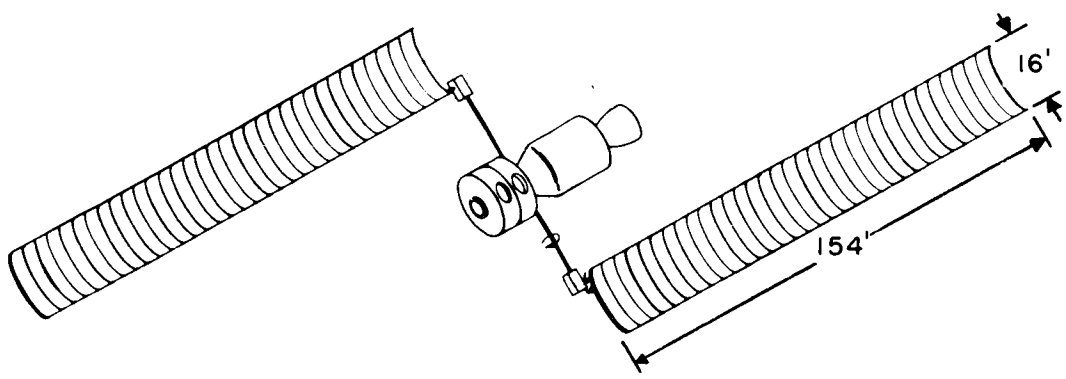

Figure IX-5. Spacecraft in Orbit With a 4900-Square-Foot Solar Array

The only difference between the first two cases is the vehicle configuration which effects perturbations by changing the moment arm between the center of mass and center of force. The difference between missions 2 and 3 is the result of the variations in sun angle (ϕ'_s) that occur during the year. Since the perturbations (except gravity gradient) are affected by the sun angle, a worst-case, 45-day period occurs when the average ϕ'_s for 45 days is near 0. For simplification, the average ϕ'_s for the worst-case 45-day period will be assumed at 12° for all orbits. This estimate is not an over simplification, since it could occur for all orbits. Perturbation effects in the synchronous orbit are negligible with only gravity gradient and solar pressure producing any effect at all. The synchronous mission will therefore not be included in any further analysis.

For the PSM concept, the ground rules were similar with the following major differences:

(1) No resupply for a one-year mission

(2) Array area, 1944 square feet

(3) Two missions:

(a) 200 nmi Polar Orbit (i = 90°)

(b) 200 nmi (i = 28.5°).

Utilizing these ground rules, the orientation axes and configurations were reevaluated. This reevaluation led to the selection of two basic configurations as shown in Figure IX-6 and as follows:

(1) The original "Z" configuration modified for the new area; (6a) and

(2) The "H" configuration. (6b)

The "H" configuration was evaluated for two aspect ratios, i.e., length/width ratios of 13.46:1 and 3.36:1. With these selections, another full perturbation analysis was performed to evaluate the two configurations. (See Paragraphs IX.C and IX.D).

C. PERTURBATIONS AND EFFECTS

As indicated in Paragraph IX.B two complete perturbation analyses were performed. The first analysis was conducted on the "Z" configuration with 4900 square feet of solar array for the four missions. The second analysis included three configurations, an array area of 1944 square feet, and two missions. In addition to the changes in configuration, the analysis was somewhat more refined to give more representative results. The perturbations considered for both analyses were as follows:

- Aerodynamic forces;
- Gravity gradient torques;

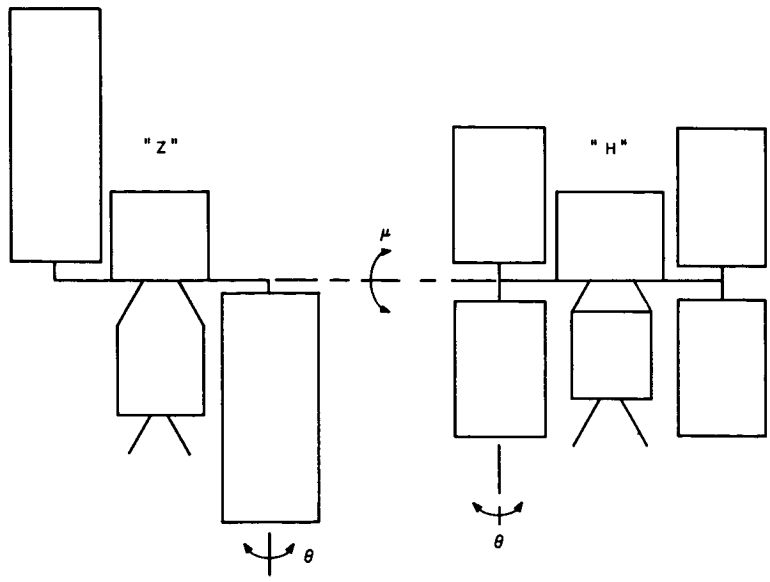

Figure IX-6. Configuration for PSM Concept

- Magnetic dipole moments; and
- Solar pressure effects.

1. Aerodynamic Forces

Aerodynamic forces are caused by the momentum exchange between the atmospheric molecules (and in some instances ions) and the spacecraft. The common terminology for this effect is drag and the resultant force acts to oppose the spacecraft velocity. When the flow is neither normal nor tangent to a flat surface, a lift force is produced due to the re-emission and reflection of molecules. This lift force acts normal to the drag force and in the plane produced by the surface normal and the velocity vector. Since the solar panels are essentially flat, they have a significant lift force in addition to the drag force. The lift force vector is always normal to the velocity vector and thus never adds any linear momentum to the spacecraft. The drag force is always opposing the velocity vector and thus never produces any angular momentum.

The aerodynamic forces are computed as follows:

$$F_C = P_C A C,$$

where F_C is the characteristic force produced on an area A for an aerodynamic coefficient (C) of unity.

$$F_C = \tfrac{1}{2} \rho_\infty U^2 A$$

The drag force $F_D (= F_C C_D)$ and the lift force $(F_L = F_C C_L)$ where C_D and C_L* are the drag and lift coefficients computed as functions of the angle γ between the velocity vector and the normal to the array. These functions are shown in Figures IX-7 and IX-8.

*Computation of C_D and C_L is shown in Appendix K.

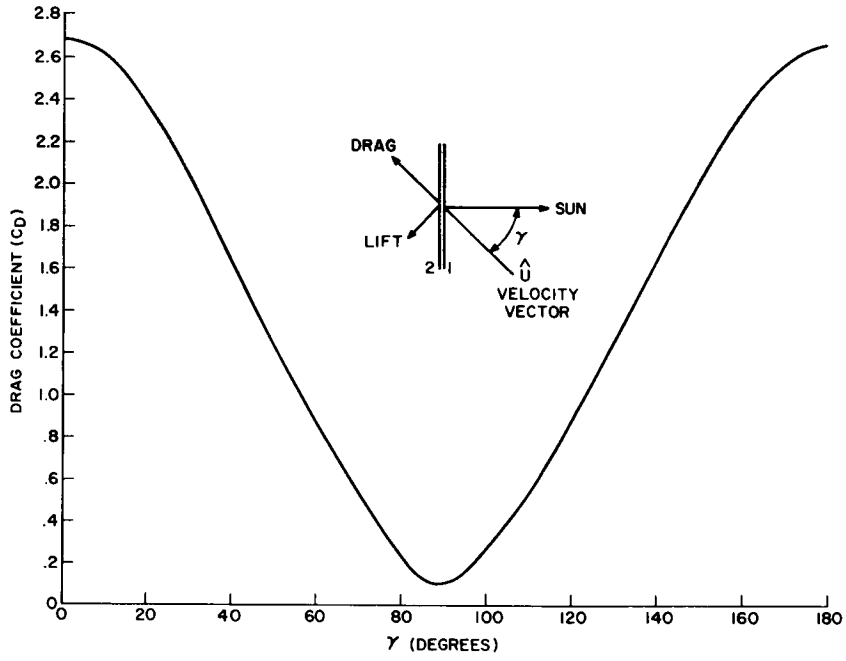

Figure IX-7. Drag Coefficient (C_D) for Solar Panels versus Angle of Attack (γ)

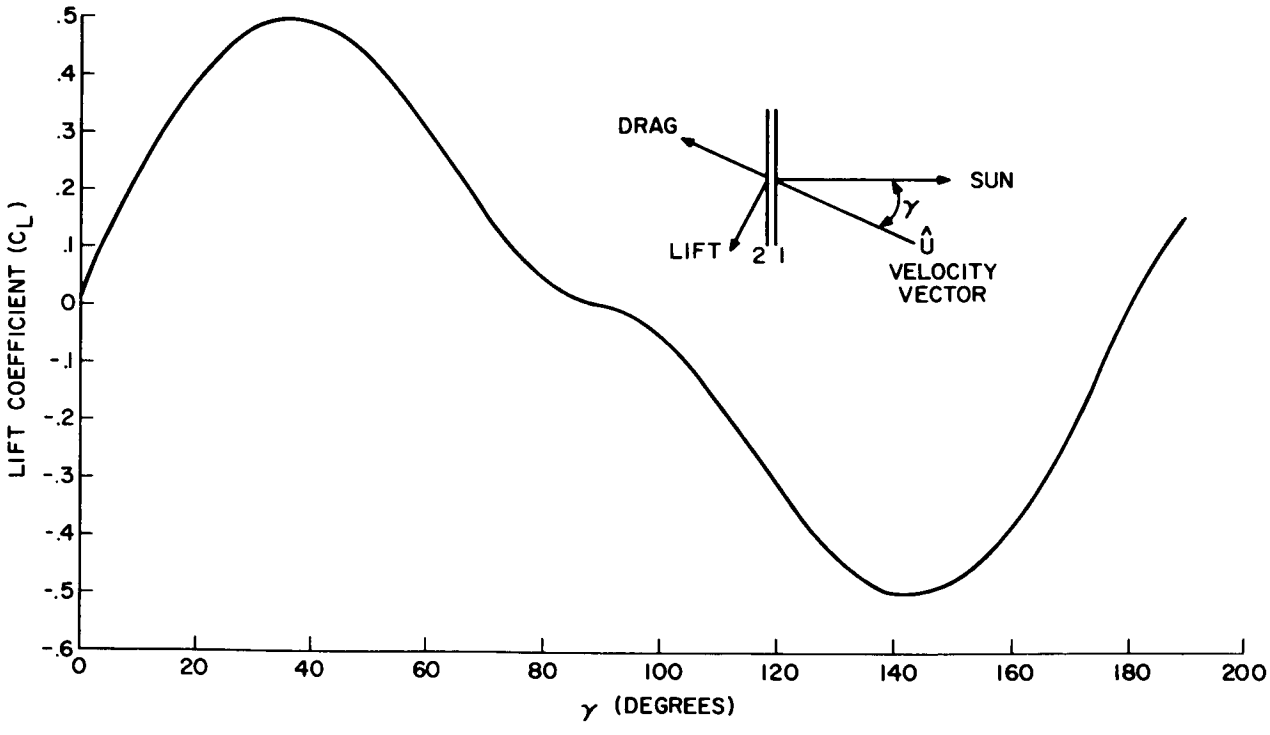

Figure IX-8. Lift Coefficient for Solar Panels versus Angle of Attack (γ)

As the spacecraft makes an orbit about the earth, the velocity vector makes one revolution about the solar array in a plane parallel to the orbit plane. The angle γ will therefore go from some minimum angle (γ_{min}) through ±90° on either side of the solar array. (γ_{min}) is equivalent to ϕ'_s (the angle the sun vector and the orbital plane) and varies slowly from orbit to orbit as a function of the orbit inclination and the orbital precession rate. Since ϕ'_s may be assumed constant for one orbit, the lift and drag coefficients may be conveniently expressed as average values for one earth orbit $(\bar{C}_D, \bar{C}_L)$.

$$\bar{C}_D = \frac{1}{\Delta\gamma}\int C_D \, d\gamma$$

$$\bar{C}_L = \frac{1}{\Delta\gamma}\int C_L \, d\gamma$$

where $\Delta\gamma = (90° - \phi'_s)$.

The values $\bar{C}_D$ and $\bar{C}_L$ are shown in Figures IX-9 and IX-10 and were computed by integration of Figures IX-7 and IX-8.

The body-centered torques produced by the lift force are given by the product of lift force (F_L) and the displacement between center of force will be assumed at the intersection of the vehicle roll axis and the array orientation axis (μ axis). This center of force applies for solar forces as well as aerodynamic forces. For the missions under consideration, the displacement between center of mass and center of force (moment arm) was calculated as in Table IX-1.

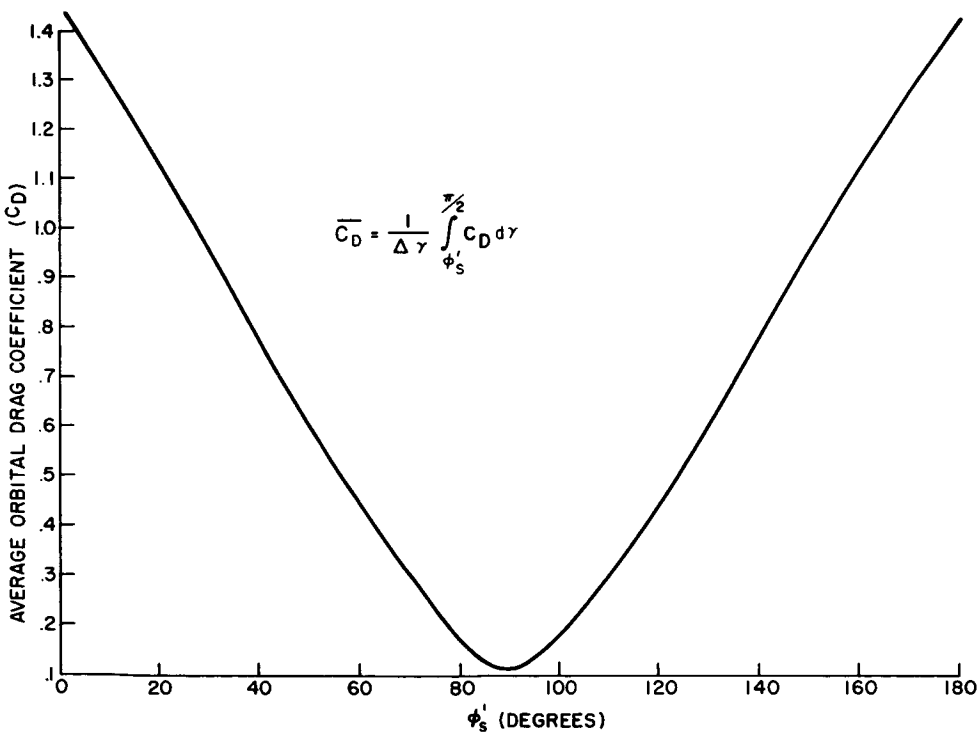

Figure IX-9. Average Orbital Drag Coefficient $\bar{C}_D$ versus ϕ'_s

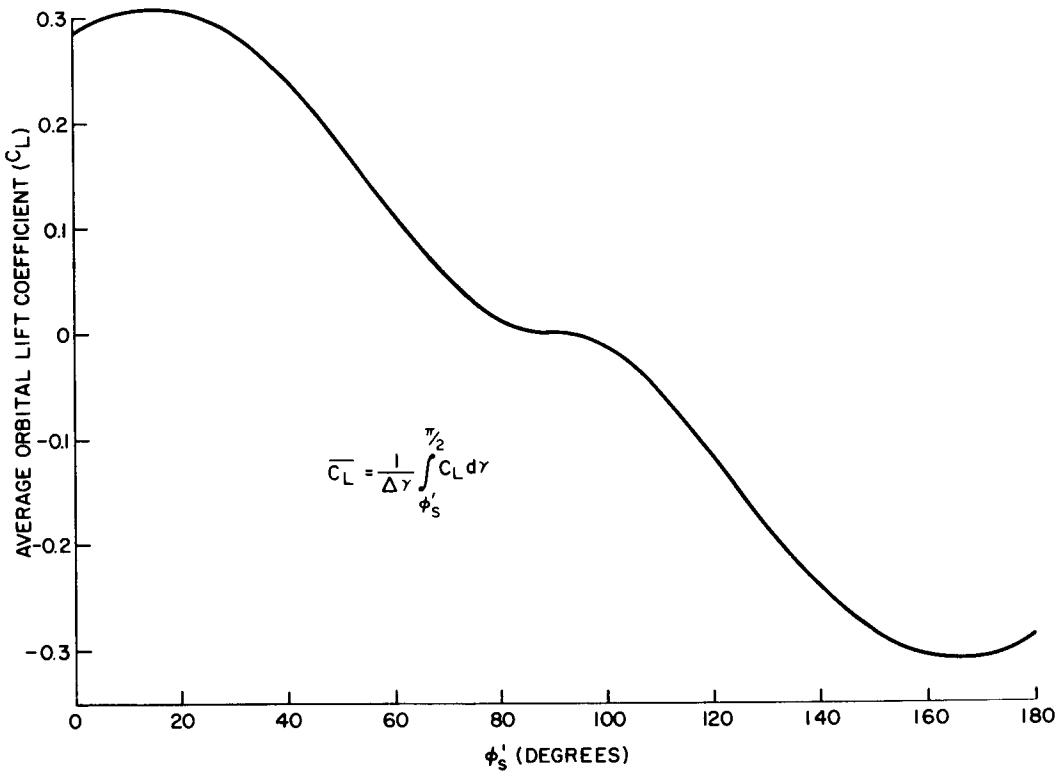

Figure IX-10. Average Orbital Lift Coefficient $\overline{C}_L$ versus ϕ'_s

TABLE IX-1. MOMENT ARMS FOR SEVERAL CONFIGURATIONS

Orbit, nmi	Inclination	No. Compartments	Moment Arm (ft)
200	28.5°	one	11.3
200	28.5°	two	16.5
200	90°	two	15.1

For the PSM effort, the moment arm for both missions is approximately 8.0 feet. The lift torque is cyclic and thus amenable to control with some form of moment storage device (MSD). (See Paragraph IX.E.)

The IPS effort includes a resupply period of 45 days. Therefore, the momentums produced by the aerodynamic forces are calculated for a worst-case, 45-day period as shown in Table IX.2. The PSM effort has no resupply for a one-year mission. The resultant momentums are shown for typical one-year missions in Table IX-3. Both tables show the effects of including a momentum storage device.

The calculations for the worst-case, 45-day period assume the average value of $|\phi'_s|$ as 12°, which is a reasonably good estimate for all three missions. This may be observed from Figures IX-11 and X-12, which show the variations of ϕ'_s for a 200-nmi, 28.5° orbit and a polar orbit over one year.

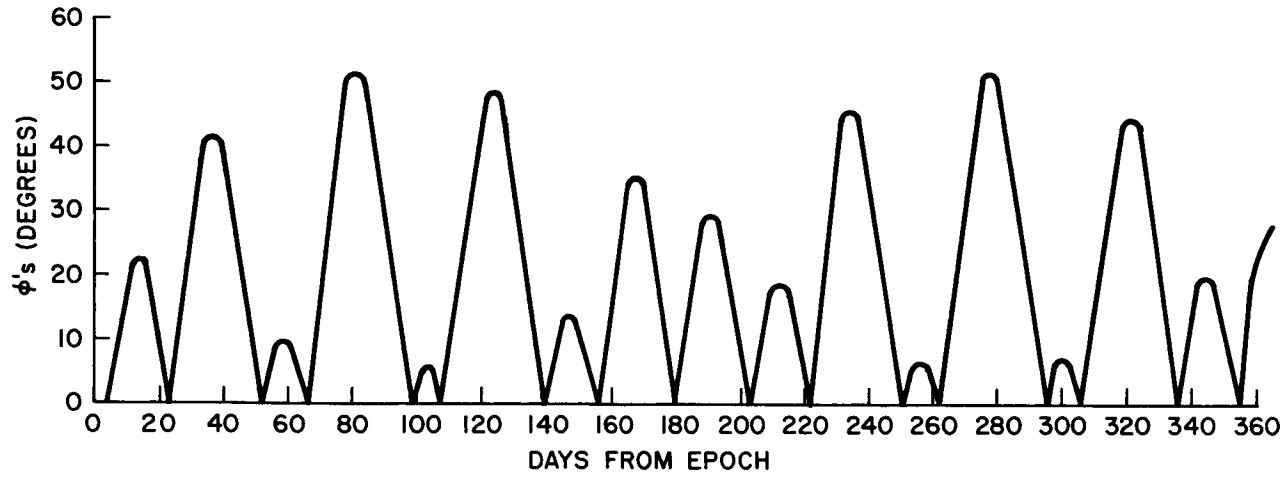

Figure IX-11. Absolute Sun Angle to the Orbit Plane ($|\phi'_s|$) versus Days from Epoch (200-nmi, 28.5° Orbit)

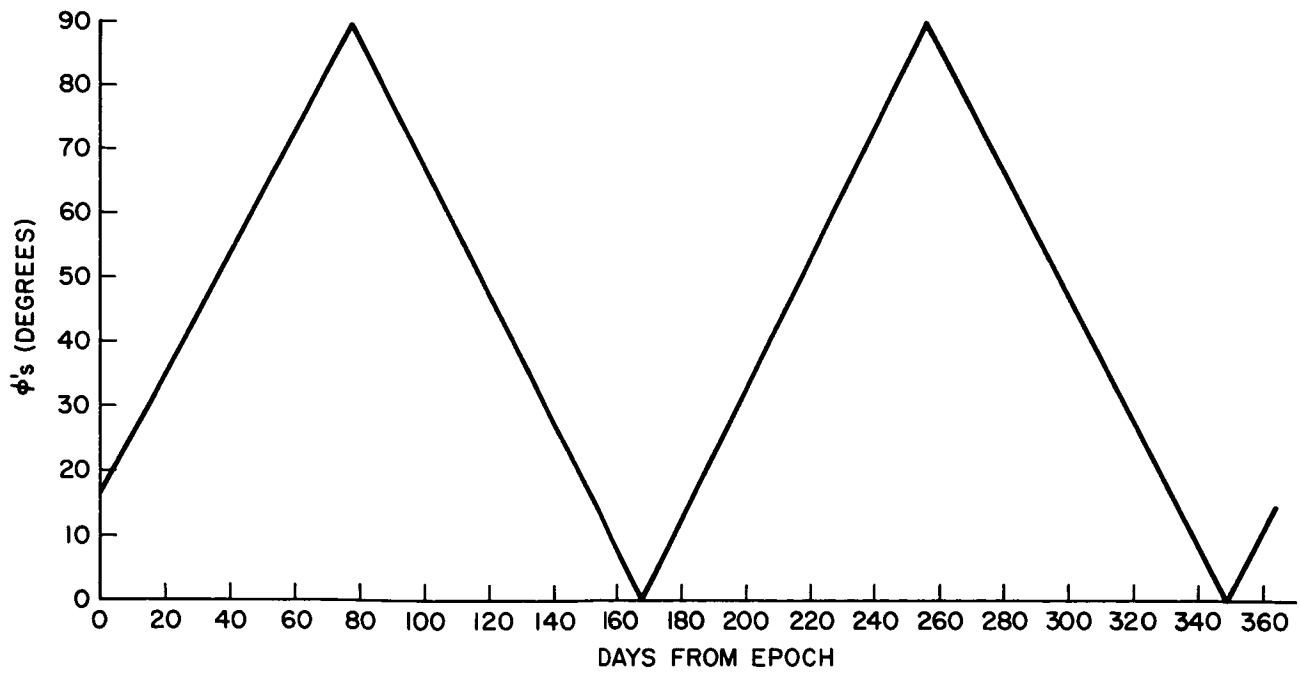

Figure IX-12. Absolute Sun Angle to the Orbit Plane ($|\phi'_s|$) versus Days from Epoch (200-nmi, 90° Orbit)

For the PSM concept, the computations were performed more accurately by plotting the lift and drag forces (Figures IX-13 through IX-16) for the missions and then mechanically integrating the resultant curves.

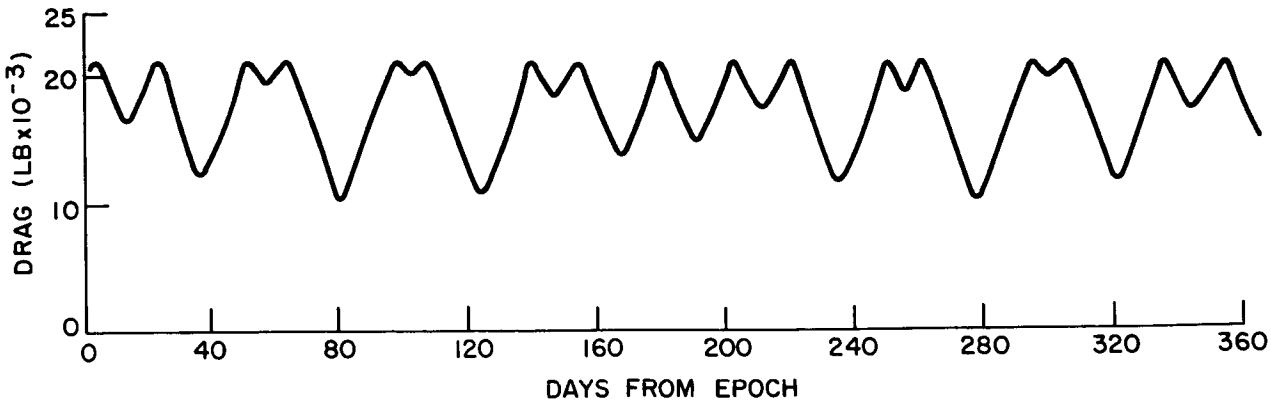

Figure IX-13. Average Orbital Aerodynamic Drag versus Days from Epoch (200 nmi, 28.5° Orbit; Array Area = 1944 Sq. ft.)

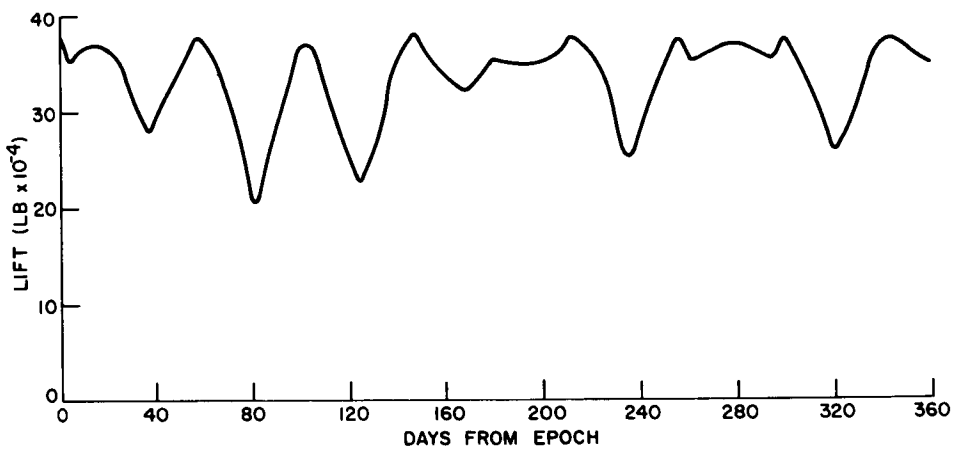

Figure IX-14. Average Orbital Aerodynamic Lift Versus Days from Epoch (200 nmi, 28.5° Orbit; Array Area = 1944 Sq. ft.)

2. Gravity Gradient Torques

The gravity-gradient torque on a satellite in a circular orbit is given by:

$$\hat{T}_{GG} = \frac{3}{2}\,\omega_o^2\,(B-C)\,(\hat{r}\cdot\hat{j})\,(\hat{r}\cdot\hat{k})\,\hat{i}$$

$$+\,(C-A)\,(\hat{r}\cdot\hat{i})\,(\hat{r}\cdot\hat{k})\,\hat{j} + (A-B)\,(\hat{r}\cdot\hat{i})\,(\hat{r}\cdot\hat{j})\,\hat{k},$$

where $\hat{i}$, $\hat{j}$ and $\hat{k}$ are unit vectors along the principal inertia axes and A, B, and C are the corresponding moments of inertia.

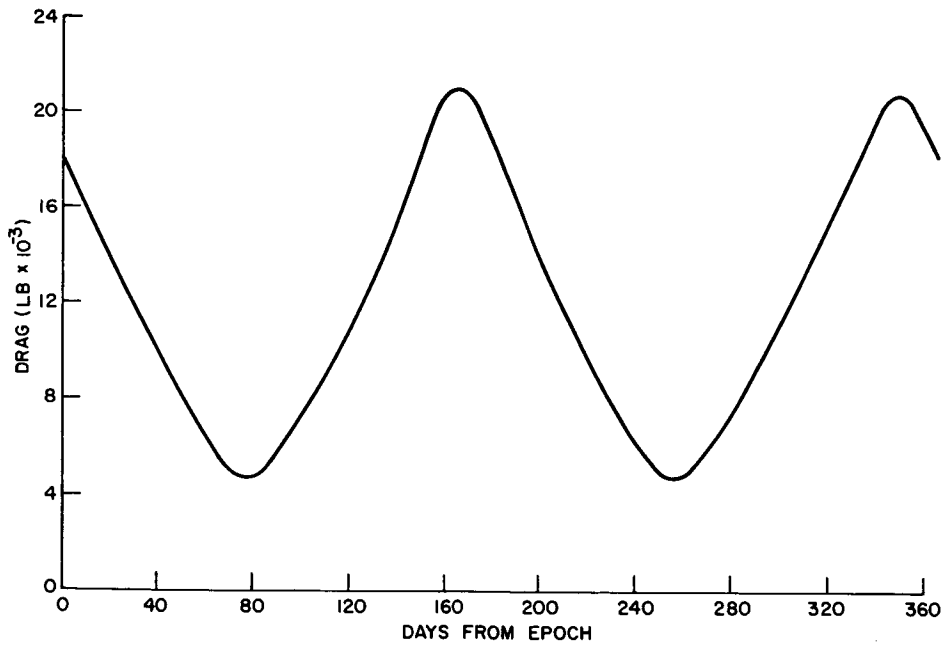

Figure IX-15. Average Orbital Aerodynamic Drag versus Days from Epoch (200-nmi, 90° Orbit; Array Area 1944 Sq. ft.)

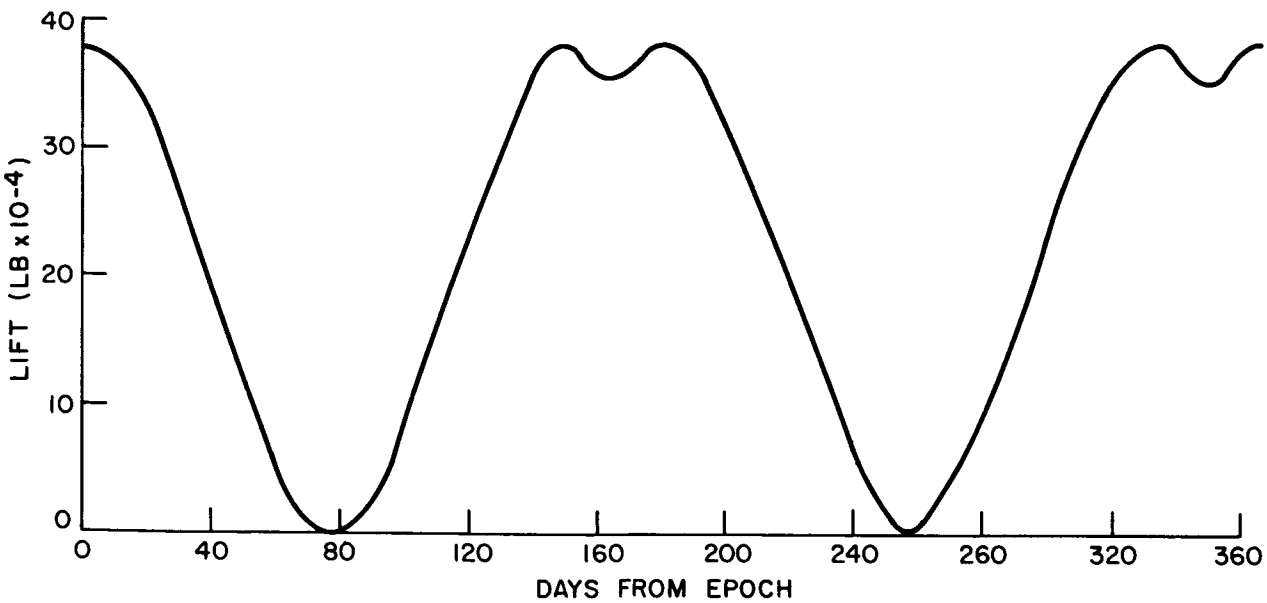

Figure IX-16. Average Orbital Aerodynamic Lift versus Days from Epoch (200-nmi, 90° Orbit; Array Area 1944 Sq. ft.)

Assuming that the roll, pitch, and yaw axes are tightly controlled by the attitude-control system of the vehicle, the transformation from the $\hat{i}\,\hat{j}\,\hat{k}$ system to the $\hat{l}\,\hat{b}\,\hat{n}$ system can be readily made in terms of θ and μ since $\hat{r} = Cos\ \omega_o t\ \hat{\ell} + Sin\ \omega_o t\ \hat{b}$ ($t = 0$ when the spacecraft

is at the ascending node). In the "Z" configuration, the principal moments of inertia are not aligned with the pitch and yaw axes. The result is that a undirectional gravity-gradient torque exists, which must be controlled with the RCS.

In the "H" configuration, the principal axes $\hat{i}$, $\hat{j}$, and $\hat{k}$ will be aligned with the pitch, roll and yaw axes.

Equation (IX-8) reduces to

$$T_{GG} = \frac{3}{2} \omega_o^2 \; Sin\, 2\zeta \, (B-C) \; \hat{i}, \qquad \text{(IX-9)}$$

where ζ is the angle between "long axis" $(\hat{j})$ and local vertical.

With the "Z" configuration, the attitude control system will cause ζ to vary between 0 and 2π at orbital rate. The exception to this occurs for polar orbits when the sun is nearly perpendicular to the orbit plane. In this case the array may be locked to the main body either along the local vertical or perpendicular to the local vertical, thereby greatly reducing the gravity-gradient torque. (This would be of significance primarily for the "Z" configuration, since the undirectional gravity-gradient torque could be eliminated during this portion of the mission. Equation (IX-9) shows that the torque varies cyclically at twice the orbit rate. This suggests that a momentum-storage device (such as momentum wheels or control-moment gyros) might be advantageously used to eliminate the need for mass expulsion.

Figures IX-17 and IX-18 show the gravity-gradient torques for the 4900 square foot "Z" configuration. Figures IX-19 and IX-20 show the gravity gradient torques for the 1944 square foot "Z" configuration and Figure X-21 shows the gravity-gradient torques for the "H" configuration for both aspect ratios.

The total momentums produced by the gravity-gradient torques are computed by integrating the torque for one orbit and multiplying the total number of Orbits. Without momentum storage, the absolute value of torque $|T_{GG}|$ is used under the integral and with momentum storage the sign change is included.

$$H_{GG}/\text{orbit} = \int_o^{2\pi} |T_{GG}| \qquad \text{without MSD;}$$

$$H_{GG}/\text{orbit} = \int_o^{2\pi} T_{GG} \qquad \text{with MSD.}$$

Table IX-2 shows the total momentums produced in 45 days for the 4900 square foot "Z" configuration with and without MSD. Table IX-3 shows the total momentums produced by the 1944 square foot "Z" configurations and the two "H" configurations for one year.

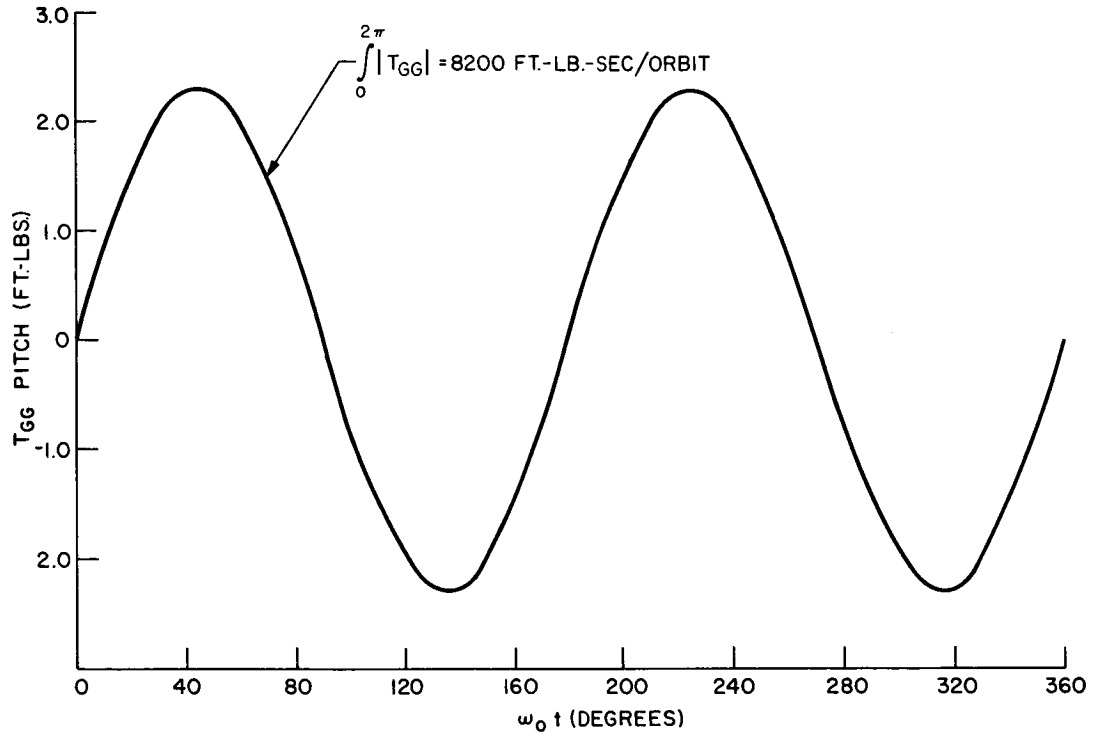

Figure IX-17. Pitch Gravity-Gradient Torque versus $\omega_o t$ ("Z" Configuration, Array Area 4900 Sq. ft.)

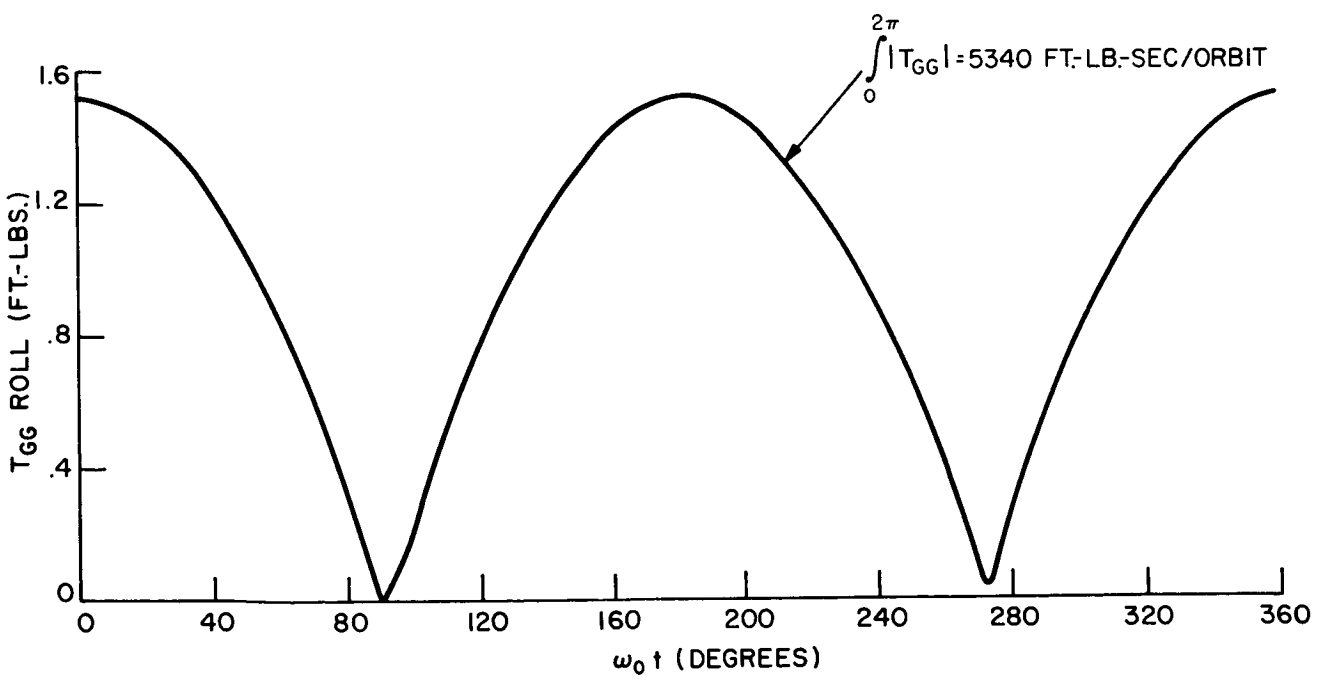

Figure IX-18. Roll Gravity-Gradient Torque versus $\omega_o t$ ("Z" Configuration, Array Area 4900 Sq. ft.)

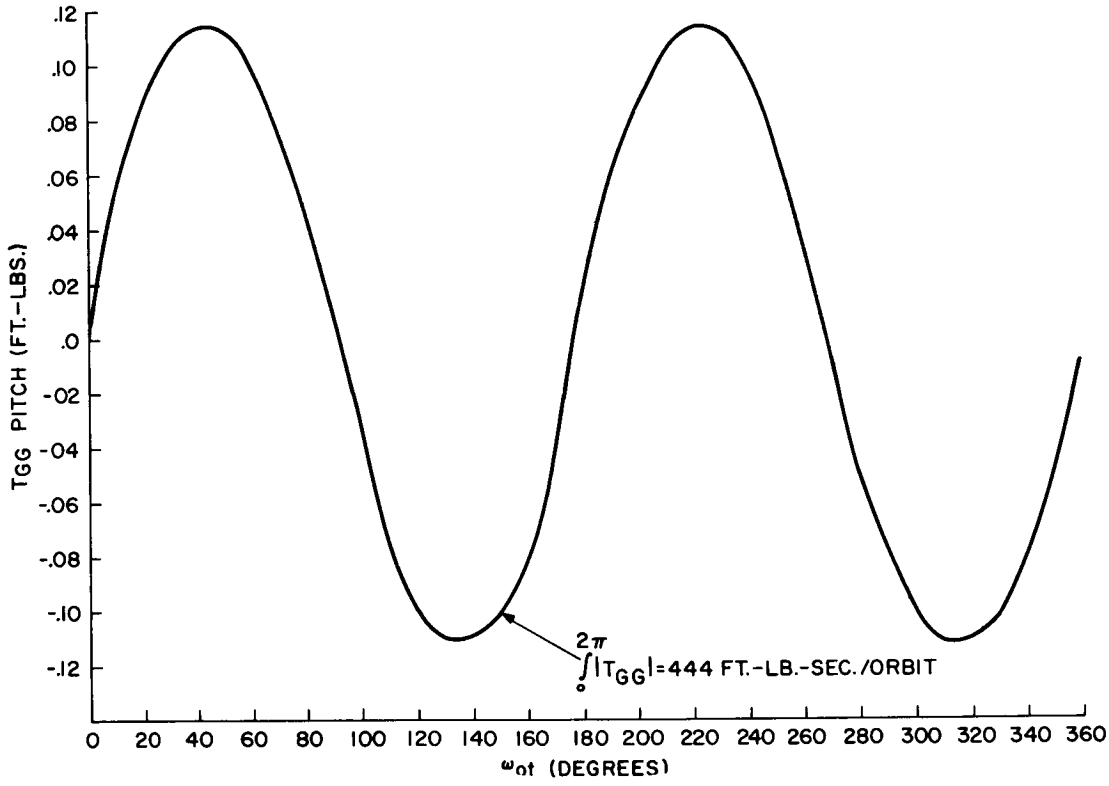

Figure IX-19. Pitch Gravity-Gradient Torque versus $\omega_o t$ ("Z" Configuration, Array Area 1944 Sq. ft.)

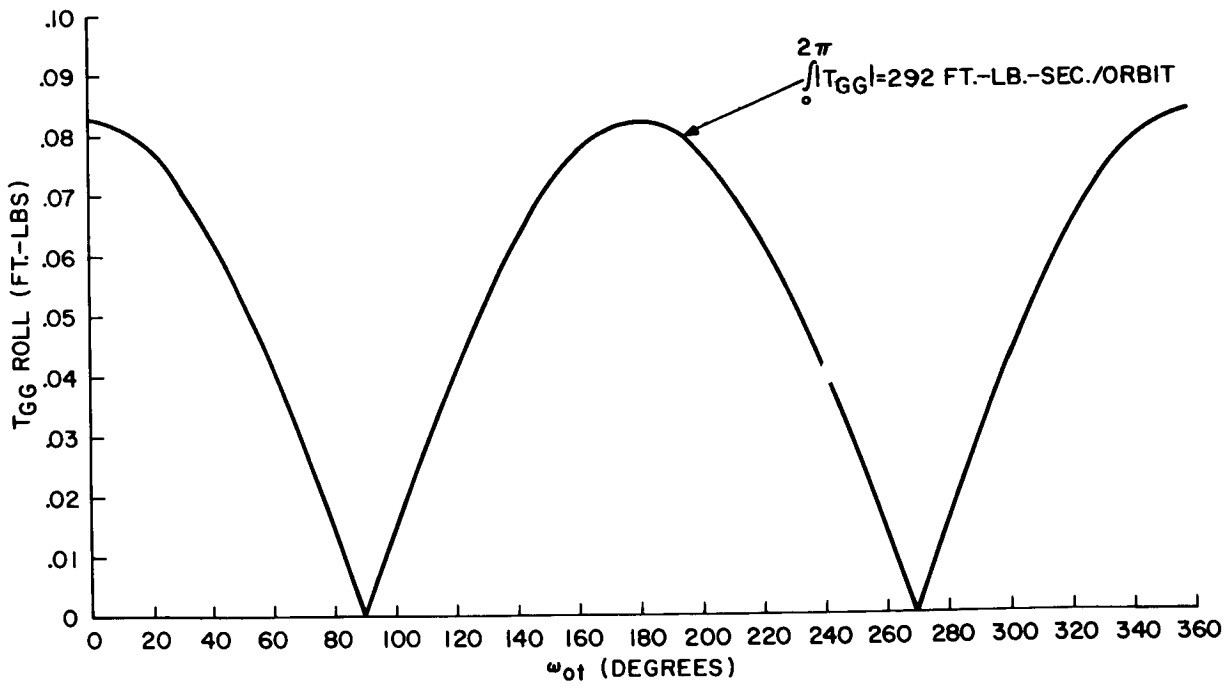

Figure IX-20. Roll Gravity-Gradient Torque versus $\omega_o t$ ("Z" Configuration, Array Area 1944 Sq. ft.)

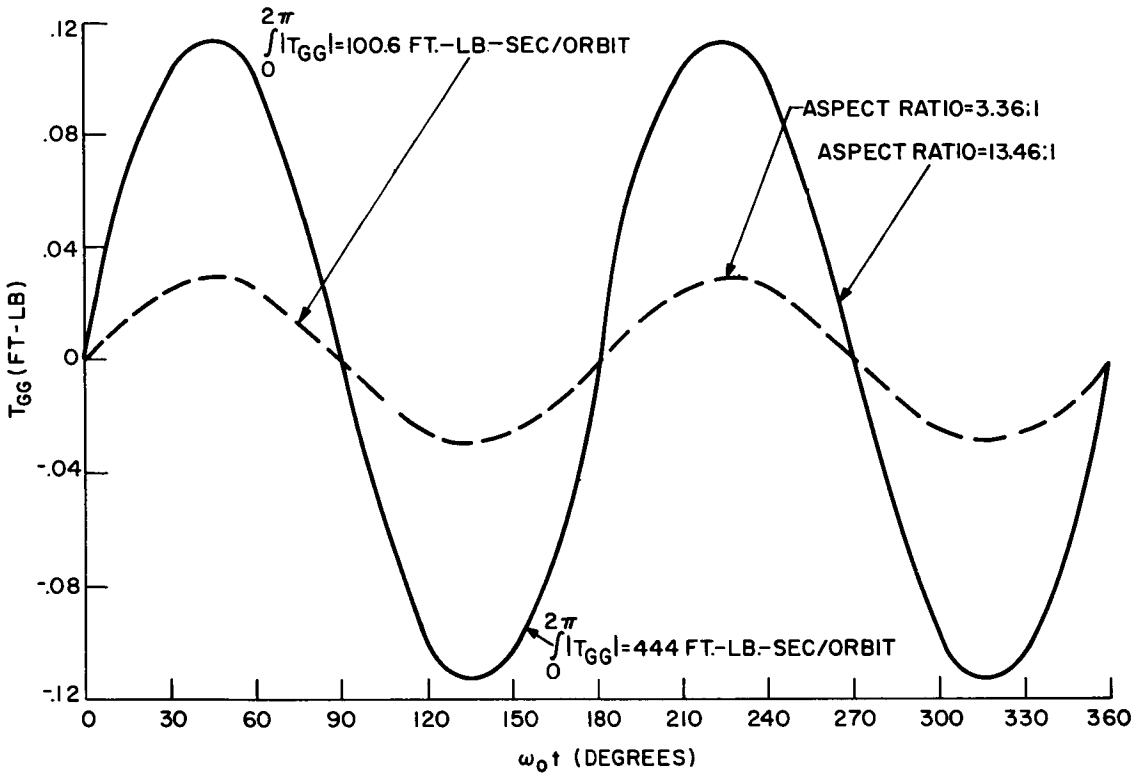

Figure IX-21. Pitch Gravity-Gradient Torque versus $\omega_o t$ ("H" Configuration, Array Area 1944 Sq. ft.)

3. Solar Radiation Pressure

Solar radiation pressure is caused by the momentum exchange between the solar photons and the solar panel. The total "solar" momentum arriving at the panel is $\Sigma\ (\eta/\lambda)$ over the solar spectrum (where η is Planck's constant and λ is the photon wavelength). Part of this momentum is absorbed $[\alpha\ \Sigma(\eta/\lambda)]$, (where α is the effective absorptivity of the solar panel), and the remainder is assumed to be reflected $(1-\alpha)\ \Sigma(\eta/\lambda)$.

The portion of the photons absorbed are converted into electrical energy and thermal energy. A simplifying assumption that does not greatly affect the results is that the thermal energy is dissipated equally on both sides of the panel, therefore producing no net momentum. The net momentum is therefore

$$\Sigma\ (\eta/\lambda)\ \ (2-\alpha).$$

The time rate of change of momentum per unit area equals pressure. Thus $\frac{d}{dt}[\Sigma\ (\eta/\lambda)\ (2-\alpha)]$ is the net solar pressure acting on the panel. $\left[\frac{d}{dt}\ [\Sigma\ (\eta/\lambda)]\right.$ is taken as 9.4×10^{-8} pounds per square foot (Reference IX-3)$\left.\right]$.

Thus for α of 0.78, the solar force is:

$$(F_s) = A\ (9.4 \times 10^{-8})\ (2 - 0.78) = 1.15 \times 10^{-7}\ (A)\ \text{Lb.}$$

where A is the total array area in square feet.

The solar force acts normal to the array at the effective center of pressure and thus describes a cone about the center of force with a half angle of ϕ_s. This vector may be represented by two vectors inertially fixed to the orbital plane; $F_s \sin \phi_s$ which lies in the orbit plane and $F_s \cos \phi_s$ which is normal to the orbit plane.

The effects of the force component in the orbit plane ($F_s \sin \phi_s$) are:

(1) A "solar drag" force that acts along the velocity vector and varies in magnitude as $(-\cos \omega_o t)$.

(2) A pitch torque that varies in magnitude with $(\sin\ \omega_o t)$, where ω_o is the orbital rate, and

t_o occurs when the long axis of the array is normal to the velocity vector on emergence from shadow.

If the orbit were in full suntime, the pitch torque and drag force would add no net momentum per orbit. However, the "solar drag" force would produce an ellipticity change in the orbit. This ellipticity change is small and can be removed by controlling the SPS "burn times" at apogee and perigee during "air drag" compensation.

When the orbit has "dark time", the net linear momentum per orbit produced by the "solar drag" force is

$$\overline{\hat{F}_s t} = F_s \cos \phi_s \int_{t_1}^{t_2} -\cos \omega_o t\ dt, \qquad \text{(IX-10)}$$

where t_1 is the time at entering shadow

and t_2 is the time at emergence from shadow.

The net angular momentum produced by the solar pitch torque is

$$\overline{(\hat{H})\ (pitch)} = \hat{F}_s \sin \phi_s \times MA \int_{t_1}^{t_2} \sin \omega_o t\ dt \qquad \text{(IX-11)}$$

MA is the moment arm, i.e. the distance between the center of mass and the center of solar force. Equation (IX-11) assumes that a momentum storage device is utilized along the pitch axis. Without momentum storage the function is "rectified" before integration, and the integration limits become

$$\int_{t_o}^{t_1} + \int_{t_2}^{T} .$$

Equations (IX-10) and (IX-11) assume that ϕ_s is constant with time which is not true, since ϕ_s is in general a complex function of time. In lieu of a computer program, the following procedure will be used in evaluation.

(1) An average yearly value of dark time per orbit will be estimated along with the corresponding average value of ϕ_s.

(2) The limits of integration t_1 and t_2 will then be computed and the integrations carried out.

(3) The average orbital momentums that result will be multiplied by the number of orbits per year to give the total yearly net momentums.

i.e.: $i = 28\ 1/2°$ Orbit

Average dark time	2140 seconds
Average ϕ_s	70°
t_1	3100 seconds
t_2	5240 seconds
Polar Orbit (i = 90°)	
Average dark time	1492 seconds
Average ϕ_s during dark time	41.5°
t_1	3424 seconds
t_2	4916 seconds
Moment Arm (MA)	7.96 feet
Orbits per year	5680

The component of solar force normal to the orbit plane ($F_s \cos \phi_s$) produces a constant yaw torque in vehicle coordinates. Since the yaw axis rotates with orbital rate, the effect is to produce a cyclic variation in torque in inertial coordinates. The inertial coordinates are chosen to be the vehicle yaw and roll axes at t equal to zero. The resultant inertial yaw torque is expressed by $F_s \cos \phi_s \times MA \times \cos \omega_o t$ and the inertial roll torque is $F_s \cos \phi_s \times MA \times \sin \omega_o t$.

Without momentum storage, the net angular momentum per orbit is

$F_s \cos \phi_s \times MA \times [\tau - (t_2 - t_1)]$, where τ is the orbit period.

Tables IX-2 and IX-3 show the resultant effects of solar pressure for the "Z" and "H" configurations.

4. Magnetic Torques

The vector expression for the torque $\hat{T}$ generated by a dipole moment $\hat{M}$ in a magnetic field $\hat{B}$ is

$$\hat{T} = \hat{M} \times \hat{B}. \tag{IX-12}$$

The solar array, because of its large area and large current carrying requirements, can generate a large dipole moment, which for a loop is equal to the product of the loop area, the current, and the number of turns of wire. This effect can be considerably reduced by careful design of the solar array, i.e. by laying twisted pairs of wires side by side to conduct in opposite directions. However, some residual magnetism will remain and the following paragraphs evaluate the effects of this dipole moment.

Because of the planar layout of the array, it is assumed that the residual dipole will be normal to the solar array panel. This means that the dipole moment will be parallel to the sun vector, i.e.

$$\hat{M} = M_l \hat{\ell} + M_b \hat{b} + M_n \hat{n}$$

and $M_l = M \, Sin \, \phi_s \, Sin \, \lambda'_s$

$$M_b = M \, Sin \, \phi_s \, Cos \, \lambda'_s \tag{IX-13}$$

$$M_n = M \, Cos \, \phi_s ,$$

where ϕ_s is the angle between the sun vector and the orbit normal, and λ_s is the angle between the projection of the sun vector on the orbit plane and $\hat{\ell}$.

This dipole moment exists only when the satellite is in sunlight, i.e., only when the orbit angle (which equals $\omega_o t$ *) satisfies the following inequality:

$$\lambda'_s + (3 - \psi) \pi \geq \omega_o t \geq \lambda'_s + (1 + \psi) \pi \tag{IX-14}$$

where ψ is percent dark time per orbit.

---

*The orbit angle equals $\omega_o t$ only for a circular orbit.

TABLE IX-2. SUMMARY OF MOMENTUM PRODUCED BY PERTURBATIONS FOR A WORST-CASE 45-DAY PERIOD

	200 N. M. i = 28.5° 1 COMPARTMENT		200 N. M. i = 28.5° 2 COMPARTMENT		200 N. M. i = 90° 2 COMPARTMENT	
PERTURBATIONS	WITH MSD**	WITHOUT MSD	WITH MSD	WITHOUT MSD	WITH MSD	WITHOUT MSD
AERODYNAMIC						
DRAG (LB-SEC)	15.3×10^4	15.3×10^4	15.3×10^4	15.3×10^4	15.3×10^4	15.3×10^4
LIFT (FT-LB-SEC)	0	4.27×10^5	0	6.24×10^5	0	5.7×10^5
GRAVITY GRADIENT						
PITCH (FT-LB-SEC)	0	5.75×10^6	0	5.75×10^6	0	5.75×10^6
ROLL (FT-LB-SEC)	3.73×10^6	3.73×10^6	3.73×10^6	3.73×10^6	3.73×10^6	3.73×10^6
SOLAR PRESSURE						
PITCH (FT-LB-SEC)	7210	8100	10520	11830	9640	10860
YAW (FT-LB-SEC)	0	} 3120	0	} 4390	0	} 4170
ROLL (FT-LB-SEC)	1540		2250		2050	
MAGNETIC DIPOLE *						
MAGNETIC FT-LB-SEC	1.72×10^4	2.25×10^4	1.72×10^4	2.25×10^4	9.3×10^3	3.2×10^4

* RESIDUAL DIPOLE 250 AT M^2
NOTE Z CONFIGURATION AREA - 4900 FT^2
**MOMENTUM STORAGE DEVICE

TABLE IX-3. SUMMARY OF MOMENTUM PRODUCED BY PERTURBATIONS FOR 1-YEAR PERIOD

PERTURBATIONS	200 NM	i = 28.5°	200 NM	i = 90°
	WITH M.S.D.*	WITHOUT M.S.D.	WITH M.S.D.	WITHOUT M.S.D.
AERODYNAMIC				
DRAG (LB.-SEC.)	54.7×10^4	54.7×10^4	37.8×10^4	37.8×10^4
LIFT (FT.-LB.-SEC.)	0	8.36×10^5	0	5.73×10^5
GRAVITY GRADIENT				
PITCH (FT.-LB.-SEC.)				
"H" CONFIG. (ASPECT = 13.46:1)	0	25.4×10^5	0	25.4×10^5
"H" CONFIG. (ASPECT = 3.36:1)	0	5.7×10^5	0	5.7×10^5
"Z" CONFIG. (ASPECT = 3.36:1)	0	25.4×10^5	0	25.4×10^5
ROLL (FT.-LB.-SEC.)				
"Z" CONFIG. (ASPECT = 3.36:1)	16.6×10^5	16.6×10^5	16.6×10^5	16.6×10^5
SOLAR PRESSURE				
DRAG (LB.-SEC.)	0	0	0	0
PITCH (FT.-LB.-SEC.)	15700	17980	8850	14950
ROLL (FT.-LB.-SEC.)	5700	} 11800	9960	} 30800
YAW (FT.-LB.-SEC.)	0		0	
MAGNETIC DIPOLE				
RESIDUAL DIPOLE = 100 AT M^2 MAGNETIC (FT.-LB.-SEC.)	3×10^4	7×10^4	2×10^4	10^5

NOTE: ARRAY AREA 1944 FT^2
*MOMENTUM STORAGE DEVICE

An adequate model of the Earth's magnetic field, at satellite altitudes, for attitude-control analyses is that of a dipole aligned with the Earth's geographic polar axis*. The predictability of attitude motions using such a model has been demonstrated many times previously (see References IX-1 and IX-2). The field is represented by:

$$\hat{B} = B_l \hat{\ell} + B_b \hat{b} + B_n \hat{n}$$

where
$$B_l = \frac{3}{2} \frac{V_o}{R^3} \, Sin\ i \ \ Sin\ 2\ \omega_o t \qquad \text{(IX-15)}$$

$$B_b = \frac{3}{2} \frac{V_o}{R^3} \, Sin\ i \ \ Cos\ 2\ \omega_o t = \frac{1}{2} \frac{V_o}{R^3} \, Sin\ i$$

$$B_n = \frac{V_o}{R^3} \, Cos\ i$$

These field equations, then, are seen to have d-c terms and terms varying at twice orbital frequency. The total momentum ($\hat{H}$) added to the system per orbit is derived by integrating equation (IX-12) subject to equation (IX-14):

$$\hat{H} = \left| \frac{1}{\omega_o} \int_{\lambda'_s + (1+\psi)\pi}^{\lambda'_s + (3-\psi)\pi} \hat{M} \times \hat{B} \, d(\omega_o t) \right| \qquad \text{(IX-16)}$$

*A more precise model is a dipole canted at 11.4° to the geographic pole intersecting the earth at longitude W-70.1 in northern hemisphere and W-250.1 in southern hemisphere.

Equations (IX-13) and (IX-15) show that $\hat{M}$ is relatively invariant with time over one orbit when compared with $\hat{B}$.

Hence

$$|H| = \left| \frac{1}{\omega_o} \hat{M} \times \int_{\lambda'_s + (1+\psi)\pi}^{\lambda'_s + (3-\psi)\pi} \hat{B}\, d(\omega_o t) \right| \qquad \text{(IX-17)}$$

From equation (IX-15),

$$\int_{\lambda'_s + (1+\psi)\pi}^{\lambda'_s + (3-\psi)\pi} \hat{B}\, d(\omega_o t)$$

$$= \left\{ 3 \frac{V_o}{R^3} \operatorname{Sin} i \operatorname{Sin} \lambda'_s \operatorname{Cos} \lambda'_s \operatorname{Sin} 2\psi\pi \right\} \hat{\ell}$$

$$- \left\{ \left(3 \frac{V_o}{R^3} \operatorname{Sin} i \operatorname{Cos}^2 \lambda'_s \operatorname{Sin} 2\psi\pi \right) + \left([1-\psi]\pi - 3/2 \operatorname{Sin} 2\psi\pi \right) \operatorname{Sin} i \frac{V_o}{R^3} \right\} \hat{b}$$

$$+ \left\{ \frac{V_o}{R^3} \operatorname{Cos} i \, [1-\psi]\pi \right\} 2\hat{n}$$

Equation (IX-16) becomes

$$\hat{H} = \frac{MV}{\omega_o R^3} \left| \begin{vmatrix} \hat{\ell} & \hat{b} & \hat{n} \\ \operatorname{Sin} \phi_s \operatorname{Sin} \lambda'_s & \operatorname{Sin} \phi_s \operatorname{Cos} \lambda'_s & \operatorname{Cos} \phi_s \\ 3 \operatorname{Sin} i \operatorname{Sin} \lambda'_s \operatorname{Cos} \lambda'_s \operatorname{Sin} 2\pi\psi & -3 \operatorname{Sin} i \operatorname{Cos}^2 \lambda'_s \operatorname{Sin} 2\pi\psi - [(1-\psi)\pi - 3/2 \operatorname{Sin} 2\pi\psi] \operatorname{Sin} i & 2 \operatorname{Cos} i (1-\psi)\pi \end{vmatrix} \right|$$

(1) (2)

---

(1) Determinant
(2) Vector Magnitude

For the "simpler" case of polar orbits

$$
\begin{aligned}
|H| = \frac{MV_o}{\omega_o R^3} \Big\{ & 3 \cos^2 \lambda'_s \sin 2\pi\psi \cos \phi_s + (1-\psi)\pi \\
& - 3/2 \sin 2\pi\psi) \cos \phi_s]^2 \qquad \text{(IX-19)} \\
& + [\, 3 \sin \lambda'_s \cos \lambda'_s \sin 2\pi\psi \cos \phi_s]^2 \\
& + [\, -6 \cos^2 \lambda'_s \sin \lambda'_s \sin 2\pi\psi \sin \phi_s - \left(\overline{1-\psi}\,\pi - 3/2 \sin 2\pi\psi\right) \sin \phi_s \sin \lambda'_s]^2 \Big\}^{1/2}
\end{aligned}
$$

The variation in λ'_s and ϕ_s as a function of time [these are very slowly varying compared with orbit rate, (ω_o)] is very non-linear. Hence, without considerable simplification, a solution to equation (IX-19) (even for this "simple" case) for the minimum momentum requirements would require a computer program. Furthermore, the detailed requirements would be a function of the initial-orbit geometry with respect to the sun. In order to evaluate the order of the minimum momentum requirement, a typical yearly average value for ϕ_s, λ'_s and ψ have been derived for the polar and inclined missions. These are listed in the following:

Inclination, i = 90°	
Altitude, h = 200 nmi	
ϕ_s aver.	41.5°
ψ' aver.	64.5%,
λ'_s	0
Inclination, i = 28.5°	
Altitude, h = 200 nmi	
ϕ_s aver.	70°
ψ' aver.	61.5%,
λ'_s	0.

The yearly momentum requirement as a function of residual dipole moment M is shown in Figure IX-22. For purposes of comparison, the condition of maximum $|H|$ for ψ equal to 0 (neglecting the definitive relationship between ψ and ϕ_s), is also plotted. These results represent an orbit averaged torque and hence neglect the cyclic changes (i.e., change of sign) in torque during an orbit. This suggests the use of momentum storage devices (MSD) to compensate for periodic disturbances. Without MSD, an upper bound on the momentum requirements may be established by maximizing $|H|$ subject to ψ at 0 [again neglecting that ψ is equal to $f(\phi_s)$].

The integrand in equation (IX-17) must be taken as the absolute value of the function $\hat{B}$. Then the momentum requirement per orbit becomes:

$$|H|_{max} = \frac{2\pi MV_o}{\omega_o R^3} \left[1 + 1.855 \sin^2 i \right]^{1/2} \qquad \text{(IX-20)}$$

For the IPS "Z" configuration, a value of residual dipole is assumed at 250 ampere turns square meter. The appropriate values of yearly momentums are read from Figure IX-22 and divided by 8 to obtain the approximate momentums for 45 days. These values are tabulated in Table IX-2. The residual dipole for the PSM effort is assumed at 100 ampere turns square meter. The appropriate values are read directly from Figure IX-22 and tabulated in Table IX-3.

D. FUEL CONSUMPTION ANALYSIS

There are two independent propulsion systems on the service module. One of these systems (RCS) will be utilized for attitude control, while the other (SPS) will be used to effect orbit changes or adjustments.

The RCS thrusters are mounted on the service module in four clusters of four thrusters each, oriented in a cross pattern as shown in Figure IX-23.

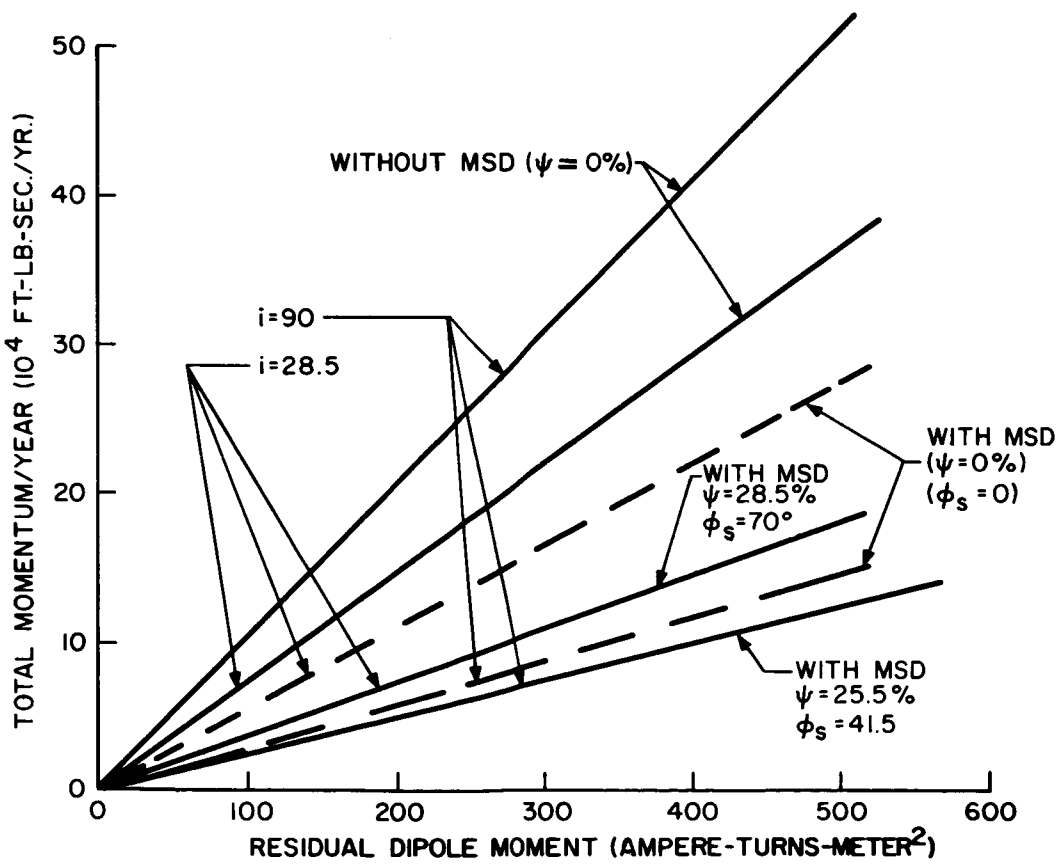

Figure IX-22. Magnetic Disturbances; Total Momentum per Year versus Residual Dipole Moment (h = 200 nmi)

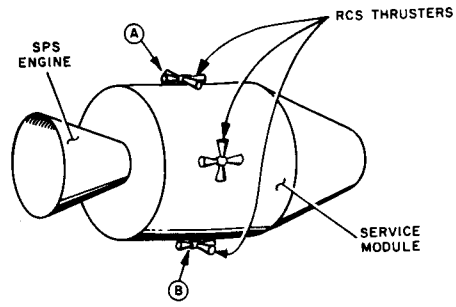

Figure IX-23. Location of Propulsion Systems

It is evident that if a properly selected pair of thrusters is operated, a pure couple is generated in either pitch, roll or yaw; i.e., if (A) and (B) are fired, a pure "clockwise" pitch torque is developed. The torque developed is the product of total thrust and moment arm for the thrusters.

The moment arm assumed for the RCS thrusters is 6.5 feet and the steady-state thrust level is taken at 100 pounds for each unit. The delivered specific impulse for the RCS thrusters is dependent on pulse width and duty cycle. A representative number of 280 seconds is assumed for the RCS specific impulse.

The amount of propellant required to counteract perturbations is found by equating the perturbation angular momentum (H_{pert}) to the angular momentum developed by the RCS.

$$\text{(Propellant weight)} \times \text{(Specific impulse)} \times \text{(moment arm)} = H_{pert}$$

or

$$\text{Propellant Weight} = \frac{H_{pert}}{280 \times 6.5} \text{ lbs.}$$

The propellant weights are listed in Tables IX-4 and IX-5, corresponding to the perturbations in Tables IX-2 and IX-3.

The one exception to the use of the RCS for perturbation correction occurs for aerodynamic drag. Aerodynamic drag produces a linear momentum along the velocity vector that will cause the orbit to decay in a logarithmic spiral until reentry occurs. To correct the orbit, the SPS engine will be fired periodically. The frequency of correction is established by the bounds imposed on the orbit parameters and the restart capability of the SPS engine. It should be noted that each orbit correction could require two engine starts to maintain orbit eccentricity (one at apogee and one at perigee). If minor variations in orbit eccentricity are allowed, then each correction must be made at each succeeding orbit apogee, thus requiring only one start per correction. The amount of fuel required by the SPS engine is found by equating the aerodynamic drag momentum to the delivered SPS momentum.

$$MV_{drag} = \text{(propellant weight)} \times \text{(specific impulse)},$$

or

$$\text{propellant weight} = \frac{MV_{drag}}{\text{specific impulse}}$$

TABLE IX-4. SUMMARY OF PROPELLANT REQUIREMENTS TO CANCEL PERTURBATIONS FOR A WORST-CASE 45-DAY PERIOD IPS CONCEPT

PROPELLANT REQUIREMENTS	200 NMI, i = 28.5° SINGLE COMPARTMENT		200 NMI, i = 28.5° DOUBLE COMPARTMENT		200 NMI, i = 90° DOUBLE COMPARTMENT	
	WITH MSD	WITHOUT MSD	WITH MSD	WITHOUT MSD	WITH MSD	WITHOUT MSD
AERODYNAMIC						
*DRAG	510	510	510	510	510	510
LIFT	0	235	0	342	0	313
GRAVITY GRADIENT						
PITCH	0	3160	0	3160	0	3160
ROLL	2050	2050	2050	2050	2050	2050
SOLAR PRESSURE						
PITCH	4	4.5	5.8	6.5	5.3	6.5
YAW	0	} 1.7	0	} 2.4	0	} 2.3
ROLL	0.9		1.2		1.1	
MAGNETIC DIPOLE	9	12.4	9	12.4	5.1	17.6

NOTES: (1) *SPS ENGINE, I_{SP} = 300 SEC.
(2) RCS ENGINES, I_{SP} = 280 SEC.
(3) RCS MOMENT ARM = 6.5 FT.
(4) RESIDUAL DIPOLE = 250 AMP-TURN-METER^2
(5) Z CONFIGURATION - ARRAY AREA = 4900 FT^2

TABLE IX-5. SUMMARY OF YEARLY PROPELLANT REQUIREMENTS TO CANCEL PERTURBATIONS PSM CONCEPT

PROPELLANT REQUIREMENTS	200 NMI	i = 28.5°	200 NMI	i = 90°
	WITH MSD	WITHOUT MSD	WITH MSD	WITHOUT MSD
AERODYNAMIC				
DRAG*	1823	1823	1260	1260
LIFT	0	460	0	314
GRAVITY GRADIENT				
PITCH AXIS				
"H" CONFIG. ASPECT = 13.46:1	0	1400	0	1400
"H" CONFIG. ASPECT = 3.36:1	0	313	0	313
"Z" CONFIG. ASPECT = 3.36:1	0	1400	0	1400
ROLL AXIS				
"Z" CONFIG. ASPECT = 3.36:1	910	910	910	910
SOLAR PRESSURE				
PITCH	8.6	9.9	4.9	8.2
ROLL	3.1	} 6.5	5.5	} 16.9
YAW	0		0	
MAGNETIC DIPOLE	16.5	38.4	11.0	55

NOTES: 1 - RESIDUAL DIPOLE = 100 ATM^2
2 - SPS ENGINE, I_{SP} = 300 SEC.
3 - RCS ENGINE, I_{SP} = 280 SEC.
4 - RCS MOMENT ARM = 6.5 FT.
5 - ARRAY AREA = 1944 FT^2

The aerodynamic drag momentum shown in Tables IX-2 and IX-3 are based on a "time" averaged atmospheric density of 2×10^{-14} slugs per cubic foot. This density corresponds to a mean altitude of 200 nautical miles, utilizing the 1962 ICAO standard atmospheric model. The propellant requirements shown in Tables IX-4 and IX-5 are based on an effective specific impulse of 300 seconds for the SPS engine. Note that, in case of emergency, the RCS system can be utilized for altitude control since four thrusters will thrust in the same direction as the SPS engine.

Tables IX-4 and IX-5 show that a considerable amount of propellant can be saved by utilizing momentum storage. For example, consider the yearly propellant (RCS) differences for a 200-nmi, 28.5° orbit as summarized in Table IX-6.

TABLE IX-6. FUEL WEIGHTS WITH AND WITHOUT MSD (POUNDS)

Configuration	Aspect Ratio	With MSD	Without MSD	"Δ" Fuel
"H"	13.46:1	28	1914	1886
"H"	3.36:1	28	827	800
"Z"	3.36:1	938	2824	1886

This table shows a saving of more than 1800 pounds of propellant for both the large aspect ratio "H" and the "Z" configuration and 800 pounds for the small-aspect "H". In Paragraph IX.E, these weights will be compared with the potential weight for the MSD required.

E. MOMENTUM STORAGE DEVICE (MSD)

In Paragraphs IX.C and IX.D, reference was made to the use of a momentum storage device (MSD) to control cyclic perturbations. The primary purpose of this section will be to show the effect of MSD on system weight, i.e., net propellant-weight savings versus weight of the MSD. An accurate design analysis and weight breakdown is not possible at this time; however, it is possible to state that a very significant system weight savings results from the use of MSD.

Two types of devices were considered for momentum storage: the reaction wheel and the control moment gyro (CMG). The reaction wheel consists of a "wheel" of sufficiently large inertia, drive by motor. External torques produced by perturbations that occur about the wheel axis are counteracted by a motor torque that speeds up or slows down the wheel appropriately. The effect of this action is to "store" the external momentums in the wheel. The advantage is seen when the external torques are cyclic with respect to time, (i.e.: $\int_{t_1}^{t_2} \text{torque}\ dt = 0.$) Thus the wheel would speed up, slow down, or reverse direction of rotation, while the spacecraft would remain oriented. The CMG accomplishes this same effect with a constant-speed drive. In this case, the reactive torques are developed by

precessing the momentum vector of the wheel. Thus, the reaction wheel develops torques by changing the magnitude of the momentum vector while the CMG changes the direction of the momentum vector.

If two CMG's are put together so that they precess in opposite directions, the effect is quite similar to that of a reaction wheel, that is, the resultant momentum vector changes in magnitude but not in direction, while the drive motors maintain constant speed. The latter configuration of CMG is desirable, since cross-coupling effects are minimized (i.e., the momentum vector remains oriented with respect to the vehicle.)

1. MSD Weight Calculation for "Z" Configuration (4900 Square Foot Area)

The large gravity-gradient torque and associated momentum for the three missions entail large propellant expenditure as described previously. The momentum is cyclic at twice orbital frequency and therefore may be compensated by a momentum storage device (MSD). In addition to the gravity-gradient torque, a nearly sinusoidal torque due to aerodynamic lift exists additively at the same frequency. For the case considered here, it amounts to approximately 5 percent of the gravity-gradient torque. The aerodynamic torque has not been considered in the following evaluation.

As previously mentioned two devices were studied: the reaction wheel and control moment gyro (CMG).

a. REACTION WHEEL

The derivation for a minimum-weight reaction wheel is given in appendix L, together with the assumptions made. The resulting equations are as follows:

$$W_T = \frac{H}{k} \left\{ \frac{\omega_o k_3}{c} \left[(d^2 + n^2)^{1/2} + d \right] + \frac{1.4g}{n} \right\} \tag{IX-21}$$

$$m^3 - \left(\frac{1.4\, c\, g}{\omega_o k_3 \times 10^4} \right)^2 m = \left[\frac{2.8H\, k_4 k\, c\, g}{k_3 \times 10^6} \right]^2 \tag{IX-22}$$

where m is $n^2 \times 10^{-4}$,

and d is $2\omega_o k_4 k H$

Constants are as follows:

c = 1.2 watts per pound,

g = 32.2 feet per second per second,

H = 1035 foot-pound-seconds,

ω_o = 1.164 x 10^{-3} radians per second (90-minute orbit),

k_3 = 1.37 watts per foot-pound per second,

k = 2 feet (reaction wheel radius of gyration), and

k_4 = 8.33 per foot-pound-second (Inland Motor *T-5134).

Substitution into Equations IX-21 and IX-22 results in:

$\dot{\theta}_{m\,(max)}$ = 889 rpm,

$W_{T(min)}$ = 284 lbs,

where

$\dot{\theta}_m$ is the motor speed, and W_T is the total weight.

Of this weight, 44 percent is due to the wheel assembly with the remainder charged to the power supply. Peak power is 196 watts and average armature dissipation is 35 watts.

b. CONTROL MOMENT GYRO

No parametric weight-minimization study was conducted, since a potential vendor was found who is currently developing CMG's of nearly the required capacity. Sperry Gyroscope (Phoenix, Arizona) has built and tested a single-degree-of-freedom CMG with the following characteristics:

• Momentum	500 foot-pound-seconds
• Wheel diameter	22 inches
• Spin-motor power	14 watts
• Weight	85 pounds
• Transverse inertia	0.2 foot-pound per second per second
• Precession-axis friction torque	0.1 foot-pound

For the required 517 foot-pound-seconds, the weight would be 90.0 pounds. Therefore the total system weight for two units would be:

$$2\left[90 + \frac{14}{1.2}\right] = 203 \text{ pounds,}$$

*Inland Motor Corp., Radford, Va. (Subsidiary of Kollmorgen)

consisting of 180 pounds of hardware and 23 pounds of power supply at 1.2 watts per pound. Conventional bearings are used as opposed to air bearings which have dynamic-stability problems under high torques. The wheel is enclosed and operates at 10^{-5} Torr to reduce windage losses. A 3-phase, 4-pole, 400-cps induction-motor drive is used (synchronous speed is 12,000 rpm).

Of the two momentum-exchange devices studied and sized, the CMG configuration weight is approximately two thirds that of the reaction-wheel system where the reaction wheel diameter is 4 feet and the CMG rotor diameter is 2 feet. If the reaction wheel diameter is reduced to 2 feet, the weight increases to 545 pounds, whereas if the diameter is increased to 8 feet the weight is reduced to 166 pounds. Theoretically, the rotating weight of both systems decrease with the increasing radius. The CMG system is bulkier, requiring two devices and space for precession movement. As the radius goes up, the gimbal weight also increases. This may counteract the fundamental advantage of being able to utilize the stress limit of the rotating material. On the other hand, the inertia wheel requires a large diameter to be competitive, but has the advantage of being essentially two-dimensional.

In conclusion, the CMG has a definite weight advantage. However, other vehicle-dependent factors, such as dimension and location restrictions, must be considered in any final decision.

c. ADDITIONAL CONSIDERATIONS

Additional factors to be discussed for a detailed design include: (1) Cross-coupling effects due to the reaction wheel, and vehicle roll and/or yaw rates; (2) Momentum unloading due to any cyclical torques that might exist; (3) Structural design features and their influence on weight; (4) Reliability features of each type of system.

For the PSM concept, three orbital configurations, each with an area of 1944 square feet, were investigated:

Configuration	Aspect Ratio
"Z"	3.36:1
"H"	13.46:1
"H"	3.36:1

(1) "Z" Configuration

An analysis of the reaction-wheel system weight was performed and a minimum-weight equation was derived, based on a tradeoff between the physical weight of the unit and the weight penalty for the power required to energize it. The previous analysis was concerned with gravity-gradient torque only, since this was the overwhelming disturbance. However, the equations developed for this case may be easily generalized in terms of momentum to include the aerodynamic effect, since the aerodynamic torque is additive at the same frequency.

An Inland torque motor which satisfies the requirements is the T-2171 with a stall torque of 0.625 foot-pound. The maximum torque due to gravity gradient and aerodynamics is 0.156 foot-pound, with a corresponding peak momentum of 69.0 foot-pound-second.

The following constants are substituted into Equations (IX-21) and (IX-22):

c = 1.2 watts per pound,

g = 32.2 feet per second per second,

ω_o = 1.164×10^{-3} radians per second,

k_3 = 1.37 watts per foot-pound per second,

k = 1 foot,

k_4 = 87 radians per second per foot-pound, and

H = 69.0 foot-pound-seconds.

The maximum motor speed for minimum weight is 1757 rpm and the minimum weight is 35 pounds with 52 percent due to power penalty and 48 percent due to hardware.

A theoretical (weight) study of control-moment gyros was not undertaken because a potential vendor was found who is well versed in this field and has built CMG's of various momentum capacities. It is proposed that two back-to-back, single-degree-of-freedom CMG's be used to eliminate major cross-coupling effects and to utilize fully the gyro momentum by precessing to 90 degrees. In such an arrangement, since the vehicle is earth-oriented, the CMG's are precessed in the orbital plane at orbital frequency. The resultant torques could be eliminated by using a two-gimbal system to avoid precession in the orbital plane, but weight and complexity would increase. Therefore, the single-degree-of-freedom CMG arrangement was analyzed to determine the torques on the vehicle and those "seen" by the precession-axis torquing device due to orbital precession, vehicle rates, and accelerations. This analysis is shown in Appendix L.

Two back-to-back CMG's could be used, each having the dimensions of a 16-inch-diameter sphere and each weighing 37 pounds, including a power penalty factor of 1.2 watts per pound. Therefore, the reaction wheel system (35 pounds) weighs less than the CMG system (74 pounds) for approximately the same wheel diameter.

Although the reaction-wheel system is lighter in this instance, the CMG has a fundamental theoretical advantage in momentum storage due to its ability to work up to the material stress limit.

Since

$$H = J\omega$$

where J is reaction-wheel inertia, expressed by

$$J = \frac{W}{g} k^2,$$

the specific momentum is

$$\frac{H}{W} = \frac{k^2 \omega}{g}$$

when $k\omega < n_s$,

and

$$\frac{H}{W} = \frac{kn_s}{g}$$

when $k\omega = n_s$ (stress limited).

Therefore, the specific momentum increases with the square of the radius of gyration until the stress-limited speed n_s is reached; thereafter it increases linearly with the radius of gyration. With the reaction wheel, the stress limit is not reached since the "power weight" effectively limits n_s to a much lower value than typical rotor spin velocities. This discussion refers to the rotating weight only. Other practical factors, such as the constant-spin motor power and the weight of stationary parts, must be considered.

The foregoing study was initially applied to a 1035 foot-pound-second momentum storage associated with a larger array. For these conditions, the CMG system weight was less than half the reaction-wheel weight for approximately equal diameter rotors.

The dynamics of the back-to-back CMG system have been investigated, assuming the gyro precession axis to lie on or parallel to the principal axis of the vehicle. For the reaction wheel, gyroscopic coupling to the yaw and roll axis was not investigated. Thus for both devices restrictions on placement and the dynamic effect of location must be investigated before a final choice is made. The lower speed reaction wheel has a bearing-reliability advantage over the high-speed CMG. Momentum dumping and method of control have not been investigated for either the reaction wheel or CMG.

(2) "H" Configurations

The large aspect-ratio "H" panel arrangement has the same pitch gravity gradient and aerodynamic torques as the "Z" configuration, so that the reaction wheel and CMG sizing described for that case are directly applicable. The greatest advantage over the "Z" geometry is the elimination of the unidirectional roll gravity-gradient momentum.

The small aspect ratio "H" configuration has the same area as the above configuration but an aspect ratio of one-fourth the value. Therefore, the aerodynamic moment will be the same but the gravity torque will be approximately one fourth.

The peak disturbance torque is 0.0620 foot-pound. Inland Motor T2157, which weighs 9 ounces and has a stall torque of 0.182 foot-pound, will provide adequate torque reserve.

The same constants are used as in paragraph IX.E.1.c.(1), with the following exceptions:

H is 26.6 foot-pound-seconds, and

k_4 is 909 radians per second per foot-pound.

Substitution of the constants into equations (IX-21) and (IX-22) results in a minimum weight of 16.5 pounds, 61 per cent of which represents power penalty. Maximum motor speed is 1820 rpm. A back-to-back CMG system with the same momentum storage capacity (26.6 foot-pound-seconds) would weigh (including power supply penalty) about 30 pounds.

2. Roll and Yaw Axis Momentum Compensation

Cyclic momentum disturbances in both of these two axes due to aerodynamic, magnetic, and solar-pressure moments are small compared to the pitch momentum. The compensating MSD's would weigh correspondingly less, and on an absolute basis, the weight difference between a reaction wheel and CMG would likewise be small.

Tables IX-7 and IX-8 show the three-axis, propellant-weight penalty caused by cyclic momentum disturbances; all of these may be eliminated by the use of MSD's. Only the weight of pitch-axis MSD's has been calculated, since this axis contributes at least three-quarters of the total momentum. The MSD weights include power system penalty.

TABLE IX-7. NET "Δ" PROPELLANT CONSUMPTION COMPARED WITH WEIGHT OF MOMENTUM STORAGE DEVICE FOR A WORST-CASE 45-DAY PERIOD IPS CONCEPT

Item	Mission		
	200-nm 28.5° 1-compt.	200-nm 28.5° 2-compt.	200-nm 90° (polar) 2-compt.
"Δ" Propellant (3 axes) (pounds)	3400	3507	3488
Reaction Wheel (pitch only) (pounds)	28	28	28
CMG (pitch only) (pounds)	203	203	203

Array Area = 4900^2 ft.

TABLE IX-8. YEARLY NET "Δ" PROPELLANT CONSUMPTION COMPARED WITH WEIGHT OF MOMENTUM STORAGE DEVICE (POUNDS) PSM CONCEPT

Mission, Item	"Δ" Propellant (3 axes)	Reaction Wheel (pitch only)	CMG (pitch only)
200-nm, 28.5°			
"Z" Config., Aspect 3.36:1	1886	35	7
"H" Config., Aspect 13.46:1	1886	35	7
"H" Config., Aspect 3.36:1	800	16.5	30
200-nm, Polar			
"Z" Config., Aspect 3.36:1	1772	35	74
"H" Config., Aspect 13.46:1	1772	35	74
"H" Config., Aspect 3.36:1	685	16.5	30
Note: Array area is 1944 square feet			

F. ARRAY CONFIGURATION ANALYSIS

The first part of this paragraph discusses some of the requirements of the orientation system. Tradeoff data is developed regarding the sun-tracking techniques and the associated system ramifications. The second portion is a first look at the servo drive requirement for the array. While most of this paragraph is of a preliminary nature, the techniques for design and tradeoff analyses are presented.

1. Vehicle-Array Dynamic Interactions

a. GENERAL

This paragraph describes the manner in which the vehicle and the array interact dynamically and the analytical approach necessary to determine the effect of this interaction.

The interactions result from dynamic perturbations such as the orientation of the array to the sun vector, motion of astronauts in the vehicle, docking, altitude corrections, center-of-gravity shifts due to equipment replacement and interchange, and any other disturbances that are of short duration.

The solar array is inertially stabilized on a per-orbit basis. Dynamic perturbations are those "internal" forces that disturb the inertial stabilization of the array and are to be differentiated from the "external" perturbations such as aerodynamic drag, gravity-gradient torque, solar pressure, etc.

(1) Action of Disturbing Torques

The spacecraft is a massive, rigid body (compared to the array) and is stabilized in three axes to maintain proper attitude. Two of the vehicle stabilization axes are oriented about the local vertical (pitch and roll), the third, or yaw axis, is oriented with reference to the orbital plane. The array requires two degrees of freedom with respect to the vehicle to track the sun vector. The dynamic problems stem from the large inertias and flexibility associated with the array.

(2) Array Torquing Reactions

Torquing the array about its own rotational axis μ to maintain normal orientation to the sun vector will introduce a reaction torque in the vehicle. The reaction torque will operate in a direction requiring additional array torquing in the same direction as the original array correction torque, leading to an unstable condition that will rapidly cause the entire vehicle dynamic system to tumble. Correction of this condition is provided by the vehicle attitude-control system.

The dynamic performance of the vehicle stabilization system is highly dependent on the array orientation with respect to the vehicle. The array will have different compliance and inertia about its various axes. Since the array is inertially stabilized and the vehicle is terrestrially oriented, the array physical parameters that the vehicle "sees" about each of its three axes will vary as a function of position in orbit. Detailed analysis and design of the stabilization system will require cognizance of these periodic variations.

b. SUN TRACKING

The discussion thus far has indicated that the array will be oriented normal to the sun vector. One of the first problems to be considered is the determination of the location of the sun tracker. Three choices are available: the vehicle, the array boom, and the array surface.

The tracker requires two degrees of freedom for operation. If mounted on the vehicle, it will require two degrees of freedom with respect to the vehicle, to be capable of tracking the sun vector. If mounted on the orientation drive housing (ODH) one degree of freedom is

the minimum required, since the array drive provides the other necessary degree of freedom. However, two degrees of freedom with respect to the ODH may prove advantageous because its potential response is more rapid than the array-drive servo.

When mounted on the array root or tip, the tracker could have its motion provided by the array drives. As before, however, more rapid response can be provided by one or two degrees of freedom with respect to the array. Table IX-9 discusses some of the advantages and shortcomings of each of these alternatives. The following will elaborate on the two extremes: a two-degree-of-freedom sun sensor mounted with respect to the vehicle, and a zero-degree-of-freedom sensor mounted on the array tip.

(1) Vehicle-Mounted Array, Two Degree of Freedom

In this configuration, the array position is slaved to the sun-tracker position. Since the sun-tracker is mounted on the vehicle, computation will be necessary to translate the sun-vector angle with respect to the three vehicle axes to angles of rotation about the two axes of array rotation. In this mode of operation, highly flexible arrays are permissible because motions will not affect sun-vector tracking. The array servo-drive system can have a low response, sufficient only to take gross errors out of the array orientation. Reaction torques required for vehicle stabilization will likewise have low response requirements, thus facilitating MSD design (Paragraph IX. E).

(2) Outboard Array, Zero Degrees of Freedom

In this configuration, out-of-plane distortions of the array are kept to a minimum. The array servo-drive system must be capable of rapid response, requiring high torques. Reaction torque compensation by the vehicle stabilization system will have high-torque requirements imposed for short-time intervals. Stabilization of the entire dynamic system will be difficult because of the sun tracker location. The remainder of the mounting systems tabulated in Table IX-9 lie somewhere between the two systems discussed. The selection of the proper system will depend on specific mission needs.

c. SYSTEM BLOCK DIAGRAM

Figure IX-24 is a block diagram of the vehicle drive and stabilization system that will serve to represent the manner in which vehicle stabilization, array drive, and sun tracking affect each other. The system illustrated is a two-degree-of-freedom sun tracker mounted on the spacecraft.

Area A of the diagram contains the representation of the vehicle stabilization system. The vehicle servos maintain attitude with respect to the orientation reference. The vehicle plus the array are torqued about the three vehicle axes. (Only one axis is shown for simplicity.)

Motion about the three vehicle axes are separated into components of motion about the two required tracker axes. The sun-tracker servo (Area B) maintains the sun sensor in alignment with the sun vector, driving the sensor with respect to the vehicle. The output of the

TABLE IX-9. ADVANTAGES AND DISADVANTAGES OF VARIOUS SUN-SENSOR MOUNTINGS

Mounted with respect to:	Degrees of freedom with respect to mounting position	Advantages	Disadvantages
Vehicle	2	Rapid response - minimum compliance in mounting. Sun vector located regardless of array position. Sun tracking independent of array deployment or retraction Out-of-plane distortion of array does not affect tracking.	Constant tracking; more than two trackers required because of shadowing. Logic circuitry required to ascertain when tracker is shadowed, and which tracker shall be used. Computation required so that sun-vector relationship to spacecraft axis is translated to array-rotation axis.
Orientation Drive Housing (ODH)	1	Less complex - only 1 degree of freedom Less problem with tracker shadowing Reduced tracking Angle of sun vector with respect to ODH is directly translatable to array rotation.	Reduced response because of dependency on ODH driver servo. Subject to boom compliance. Must be deployed with boom.
Orientation Drive Housing (ODH)	2	Additional degree of freedom improves response rate Tracking separated from boom torsional compliance ODH motion can be used for rough tracking, tracker motion for fine positioning	Deployed with boom. Boom lateral compliance.
Array Root	0	No servo drive required; axes coordinate transfer computation not required; array will have less out-of-plane motions and distortions	Slow response. Difficult to stabilize servo. Deployment and retraction problem. Affected by array distortion, compliance, and vibration.
Array Root	1 & 2	Improved speed of response	Stabilization of tracking loop is difficult because of array compliance. Deployment and retraction problem.
Array, outboard	0	Minimum out-of-plane distortions of solar array.	Extremely difficult servo stabilization problem. Deployment and retraction.
Array, outboard	1 & 2	Improved response of sun tracking	Servo stabilization problem. Deployment and retraction.

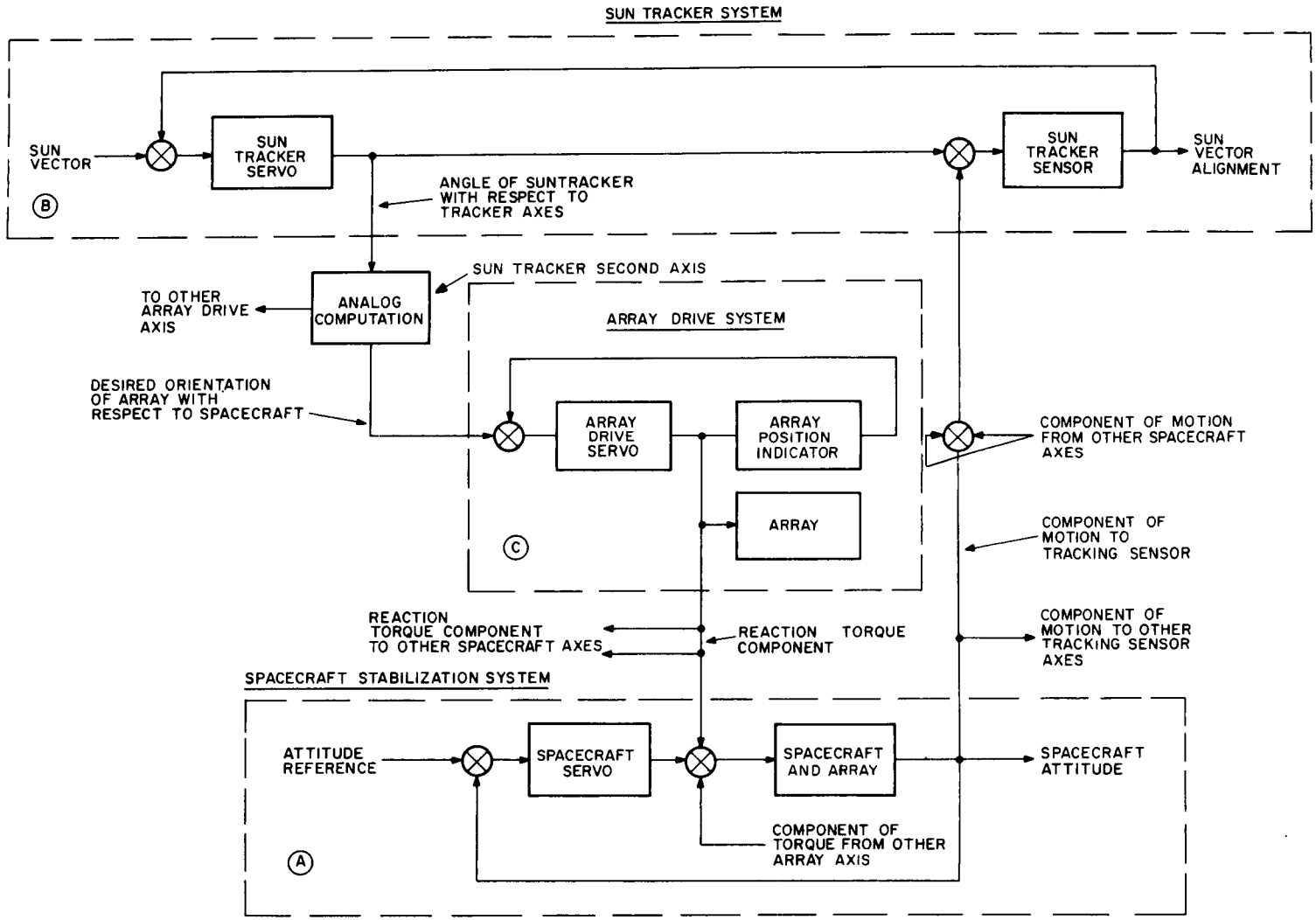

Figure IX-24. Vehicle Drive and Stabilization System

two-axis drive of the sun-tracker servo will be the angular relationship between the sun vector and the instantaneous position of the vehicle axes. The two degrees of freedom of the array are driven with respect to the vehicle so that the array surface is normal to the sun vector. A simple analog computer is provided to relate the angular displacements between sun vector, tracker axes, vehicle axes, and array axes. Area C contains the representation of the array-drive servo. Note that the array proper lies outside the feedback loop, since the array is merely slaved to the sun tracker position, the tracker being removed from the array. Array drive reaction torques disturb the vehicle stabilization servos (area A).

d. ANALYTICAL APPROACH

Prior to the design of the power system, the problems described in the previous paragraph must be thoroughly analyzed. Array vibration and stress, fuel consumption, spacecraft and system stabilization are all parameters which can only be selected after detailed analysis and solution of the problem.

A hybrid computer lends itself to the solution of this type of problem. It would be programmed to fit the basic loops illustrated in Figure IX-24, with an expansion to a complete three-axis interacting loop diagram. In addition, the "static" perturbations, solar wind, drag, gravity-gradient torques, magnetic torques, etc. would be included. Tables for digital storage would be developed for array inertia and compliance as a function of array orientation with respect to vehicle axes, static perturbation as a function of array-vehicle orientation, daily and seasonal sun-vector orientation with respect to vehicle, etc. With a complete program, the vehicle could be "flown" in the computer enabling design tradeoffs to be performed.

2. Orientation Servo System

The function of the orientation system is to position and maintain the array surfaces normal to the sun vector. The system provides control functions in initial acquisition, normal tracking during sunlight and occultation periods, and reacquisition following redeployment of the array.

The basic system concept described in the following is equally applicable to a "Z" configuration requiring 4900 square feet, a "Z" configuration utilizing approximately 2000 square feet, or the "H" configuration of long or short aspect ratio.

For the purposes of this discussion, the sun-tracker sensors are assumed to be located on the array root with zero degrees of freedom allowed. As described previously, other locations may prove to be more advantageous.

a. SYSTEM DESCRIPTION

Two-axis control is required to keep the panels normal to the sun vector. The panels are inertially fixed on a per-orbit basis. The main control is a constant-rate drive about the "μ" axis, which is parallel to the vehicle pitch axis (see Figure IX-25).

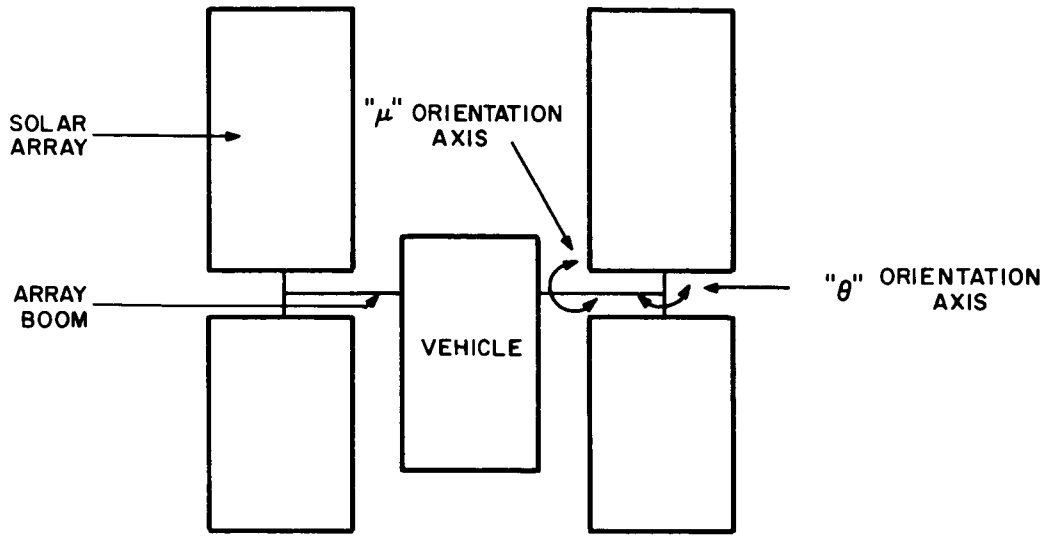

Figure IX-25. Control Axis Configuration

The rate about the second orthogonal axis θ is very small, i.e., a degree per day for the sun's motion in polar orbit and 6 to 8 degrees per day in the 28.5°, 200-nmi orbit. Therefore, the control in this axis could be accomplished manually, with the frequency determined by the satellite orbit. In conformance with the modular design philosophy, the motor-gear train of Figure IX-26 in the θ axis is identical with that in the μ axis; for automatic control, an amplifier must be added. On the other hand, some savings in weight can be realized if the two drive units are not the same. For example, a small geared motor could be used and controlled manually. Another scheme would use a simple relay servo to operate the motor; the final choice would depend on a weight and reliability trade-off. A deadband of typically ±2 to ±5 degrees would ensure negligible array power loss (less than 0.5 percent) while preventing operation of the system in response to small perturbations.

b. MODES OF OPERATION

The modes of operation are best described with reference to Figure IX-26. These are as follows and are described in the following, similarly numbered subparagraphs:

- Initial acquisition; from stowed to operational position.
- Normal

  (a) Sun Tracking; sunlight portion of the orbit.

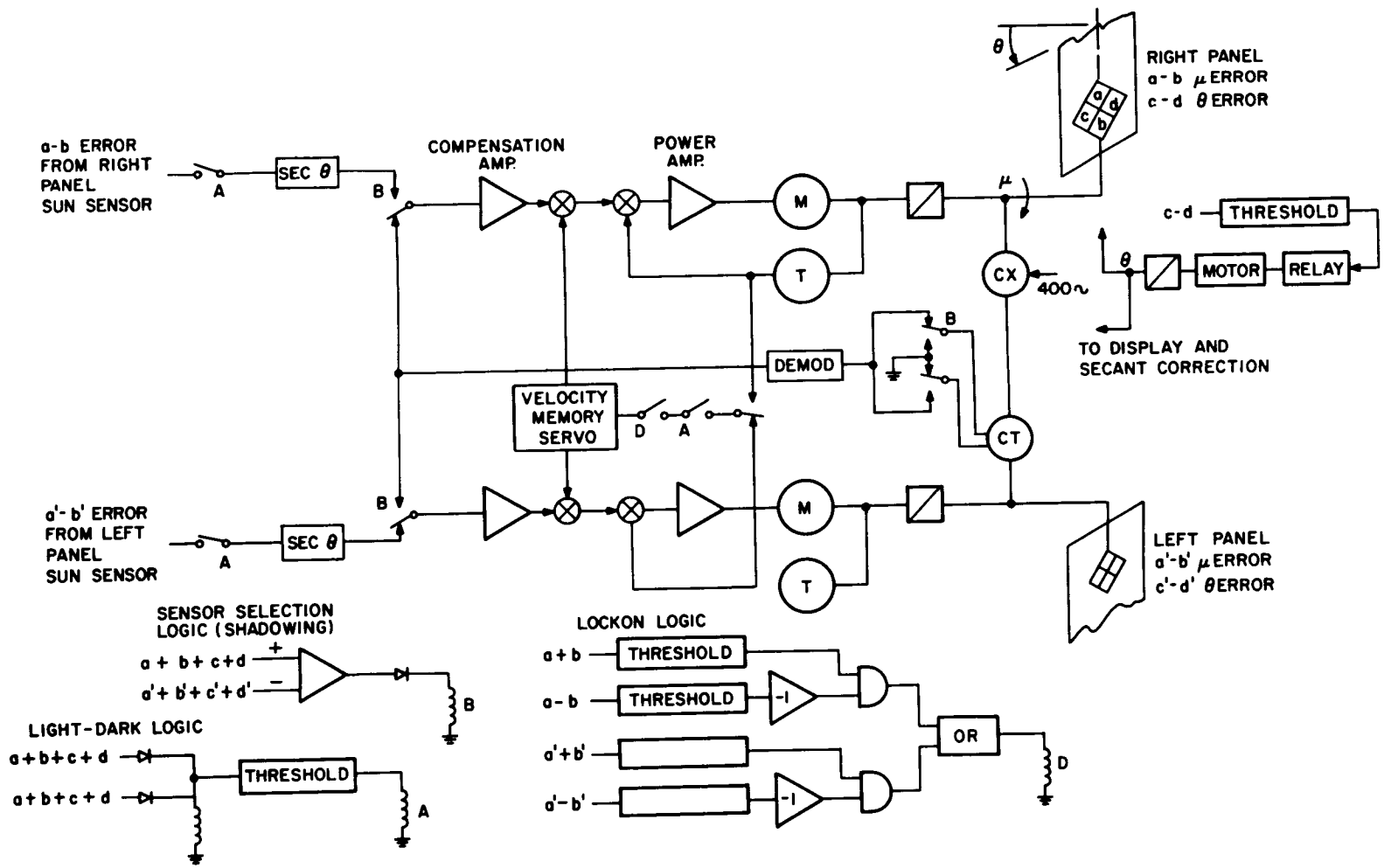

Figure IX-26. Panel Orientation Control System

(b) Occultation; dark portion of the orbit.

Reacquisition; dark-to-sun portion of the orbit.

- Docking and SPS Engine Firing; position array to required orientation for these maneuvers and reacquisition of sun.

- Polar orbit stow.

(1) Initial Acquisition

This can be accomplished automatically or manually. Automatic initial acquisition can be accomplished with a programmed suborbital array rotational velocity so that the sun may "catch up" with the array and a smooth lockon results in the μ axis. A faster lockon may be obtained in the θ axis by mounting solar sensors on the back side of the array panel, which will provide an unstable null that in turn drives the array to the stable null provided by the front-array sun sensors ("c" and "d" of Figure IX-26.)

Manual acquisition can be obtained by switching out the sun-sensor error signals in either or both axes and substituting a slew signal.

(2) Normal Operation

(a) Sun Tracking

The tracking mode is defined when the sun signal from either panel sun sensor exceeds a certain threshold and when the difference signal is less than another threshold is shown by the lock-on logic. This permits the tachometer signal to enter the velocity memory servo. In this mode, the displacement loop is closed and the sun-sensor error is used to drive the panels. The panel dynamics and spacecraft stability and control system must be considered to ensure over-all stability. The low resonant frequency of the panel will dictate a low-bandwidth system. For a 200-nmi orbit, a servo velocity constant of 1/15 is required if the tracking error is to be held to ±2°. Even this requirement for loop gain may be relaxed, since the tracking occurs at practically a constant velocity. An "aided tracking" configuration is used, wherein the average velocity on the active portion of the previous orbit is used to bias the servo.

(b) Occultation and Reacquisition

The sensors are inoperative in the earth's shadow. In order to eliminate reactive torques caused by de-acceleration of the panels, and to have them in the correct position for reacquiring the sun, their velocity is maintained by means of a velocity memory servo. This memory servo averages the velocity during the active portion of the orbit and uses this constant velocity to drive the panels on the dark side. The tachometer loop gain will be limited by the low resonant frequency of the panel. However, the output of the velocity memory servo may be increased to compensate for the finite gain of the tachometer loop and thus minimize the displacement error at the end of the occultation period.

Reacquisition is a transient mode, occurring only at the end of each dark period as the vehicle reenters the sun. Any error accumulated during the dark transit will be reduced as the displacement loop (which is logically controlled by the sun-sensor signals on the illuminated panel) is again closed.

(3) Docking and SPS Engine Firing

Figure IX-26 does not show a control logic function for either docking or SPS engine firing. However, it is reasonable to include this facility to simplify control during these maneuvers.

(4) Polar-Orbit Stow

In a polar orbit (and for the "Z" configuration, when the sun vector approaches the orbit normal), a reduction in propellant requirements necessary to overcome the cyclic-roll gravity-gradient momentum can be achieved. This can be accomplished by eliminating the angular velocity (about the μ axis) of the array relative to the vehicle and orienting the array to minimize the gravity-gradient torque. Another requirement that makes it desirable to stop the panels under these conditions is the secant correction to maintain tracking-loop gain constant as the angle θ increases. This correction is noise-limited as θ increases and obviously fails for θ of 90°.

For these two reasons, a polar orbit stow is desirable as θ approaches approximately 80°. The optimum value of the "stowage" angle would be determined at a future time, taking into account the propellant required to counteract roll momentum, array power loss due to misalignment, and servo tracking loop performance.

G. SHADOW ANALYSIS

During various portions of an orbit and as a function of sun angle, the vehicle may shadow portions of the array and (depending upon array configuration) one array section may shadow portions of another. Evaluation of the shadow patterns is necessary (1) to prepare solar-cell-module layouts that minimize power loss, (2) to determine the additional solar-array area required to compensate for loss of the effective array area, and (3) to define the boom length. The results of this evaluation will be utilized in selecting the array orbital configuration.

The following two basic panel arrangements are considered:

- "H" configuration, shown in Figure IX-6, and
- "Z" configuration, shown in Figure IX-6.

In addition, two boom lengths (10.2 and 18.2 feet) were evaluated for each of the arrangements.

1. Procedure

Three basic techniques are available for determining the degree of shadowing:

- A computer program utilizing the geometry of the vehicle;
- Descriptive geometry, which depends entirely upon geometric layouts; and
- Photographs of a scale model.

Photographs of a scale model were used in this conceptual study to determine the shadow patterns, with the camera acting as the sun. This method was chosen because it was the least costly and presents a physical view of the pattern. The accuracy in using photographs to determine the shadows is estimated as follows:

- Photographic error due to camera-to-object-distance relationship, ±6 percent;
- Scale of model and interpretation of photographs, ±4 percent.

The photographs were interpreted by using a planimeter and by counting the squares of the grid system scribed on the model (see Figure IX-27). The accuracy of counting the squares was compared with the use of the planimeter and found to be within 2 percent. Summation of the errors yields a net accuracy of 2 to 10 percent. Therefore, by utilizing the estimated net accuracy, if a 10-percent shadow is reported in the data, the actual value of shadow percentage lies between 9.0 and 9.8. This accuracy is considered adequate for a conceptual study.

Photographs were taken of the model with sun angles (the angle between the sun vector and the orbit plane) of 30, 45, 60, and 75 degrees. Results for zero and 90° are readily calculated, therefore photographs were not taken at these angles. Photographs were taken for every 15° of the orbit at each sun angle.

2. Results

Figure IX-28 is a plot of the shadow as a percentage of the total array versus the orbit angle as a function of the sun angle for the "Z" configuration, with both long and short booms. Figure IX-29 presents similar information for the "H" configuration. The data presented in these two illustrations were then cross-plotted to represent orbital average shadow as a function of sun angle in Figures IX-30 and IX-31. Included in these illustrations is the data in tabular form. In addition, a plot was made of the percentage of array illumination versus the percentage of suntime for each orbit. This graphical plot is proportional to the energy developed by the array, based upon the assumption that the power generated by the array is directly proportional to the percentage of the array illuminated. This assumption is somewhat optimistic, but may be used for purposes of comparison. Figures IX-32 and IX-33 show the average array illumination versus sun angle for both the "Z" and "H" configurations.

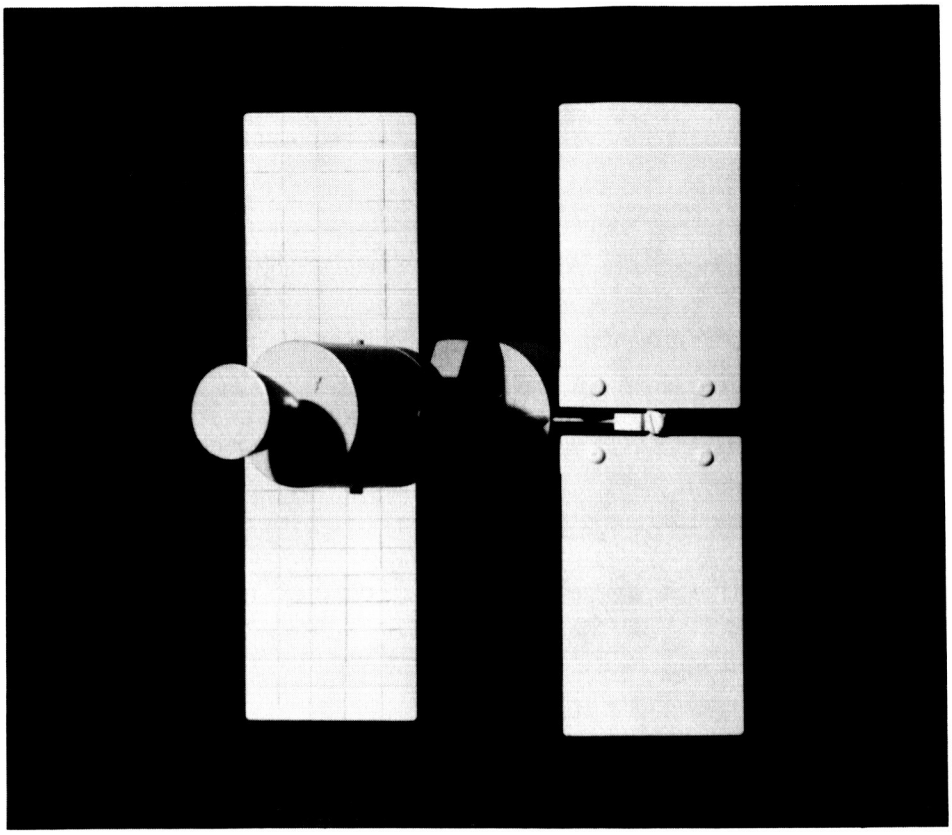

Figure IX-27. Model Used for Shadow Analysis

3. Discussion

The requirement for power from the array is maximum when the sun is in the orbital plane (0°). At this position, the maximum orbital nighttime occurs, i.e., maximum battery discharge with minimum orbital daytime available for battery recharge. In addition, the shortest time is available to generate the required amount of oxygen from the EC/LSS for the longest nighttime period. These three effects enable reduction of the power requirements from the array as the sun angle increases (longer daytime). One of the selection criteria was a set of control axes that permits shadowing to increase as the sun angle increases. Examination of Figures IX-30 and IX-31 reveals that the "Z" configuration exhibits this characteristic and that the "H" configuration also exhibits this characteristic to a much greater degree.

Utilization of the results of the computer program discussed in Paragraph X.E enables determination that in a 100-percent-daylight orbit, the power requirements would be approximately 57 percent of the requirement in a minimum-suntime orbit at 200 nmi. From another aspect, a 43-percent shadow is permissible. (For this calculation, a constant energy requirement was assumed for the EC/LSS.) Data of Figure IX-30 indicates that there is no problem for the "Z" configuration and Figure IX-31 shows that for a five-day period at worst, the "H" configuration array will be deficient in power by a maximum of 7 percent. This degree of deficiency occurs only at a sun angle of 90°. The same conclusions may be drawn from an examination of the array illumination curve (proportional

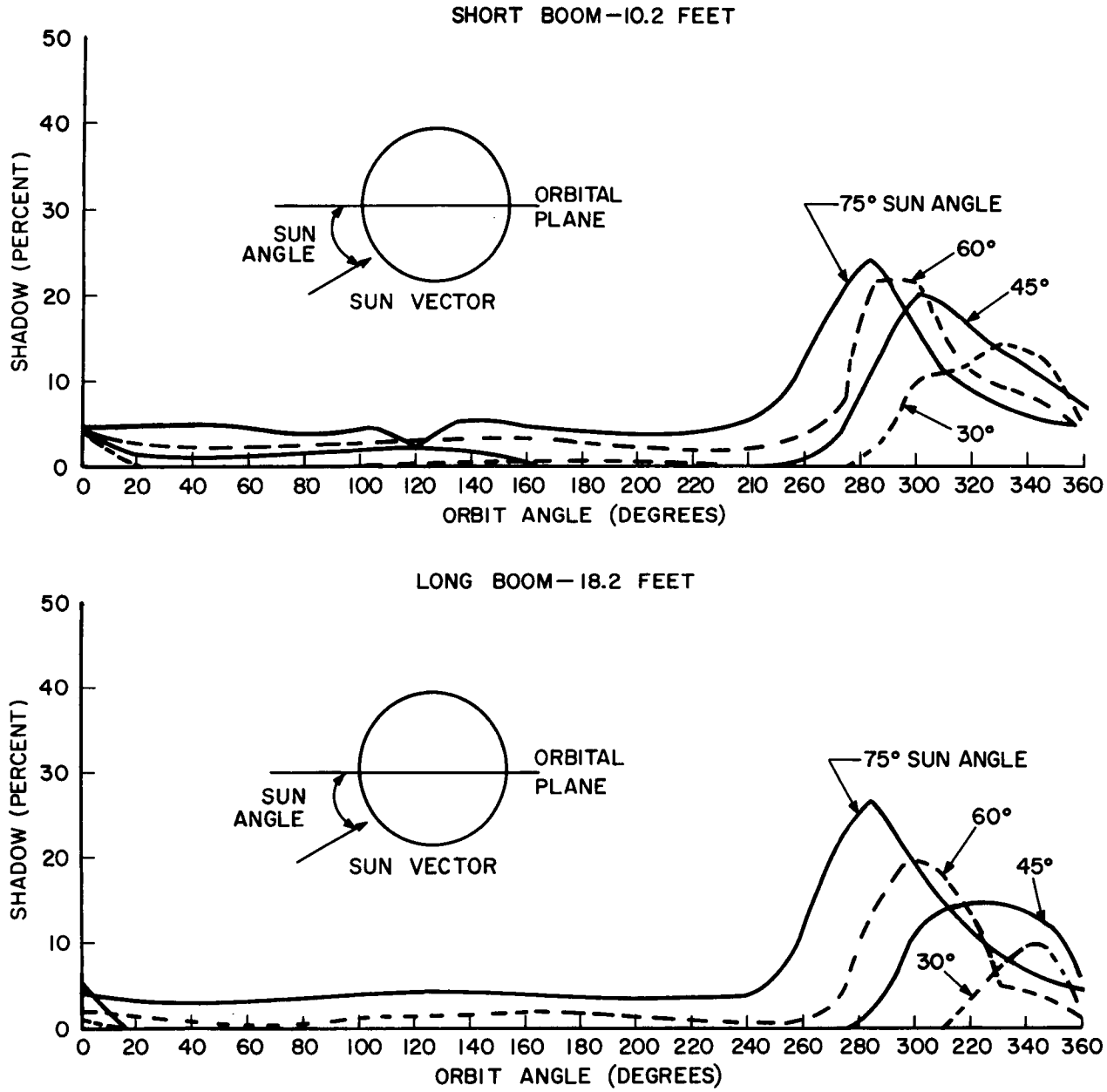

Figure IX-28. Percentage of Shadow versus Orbit Angle for Various Sun Angles ("Z" Configuration)

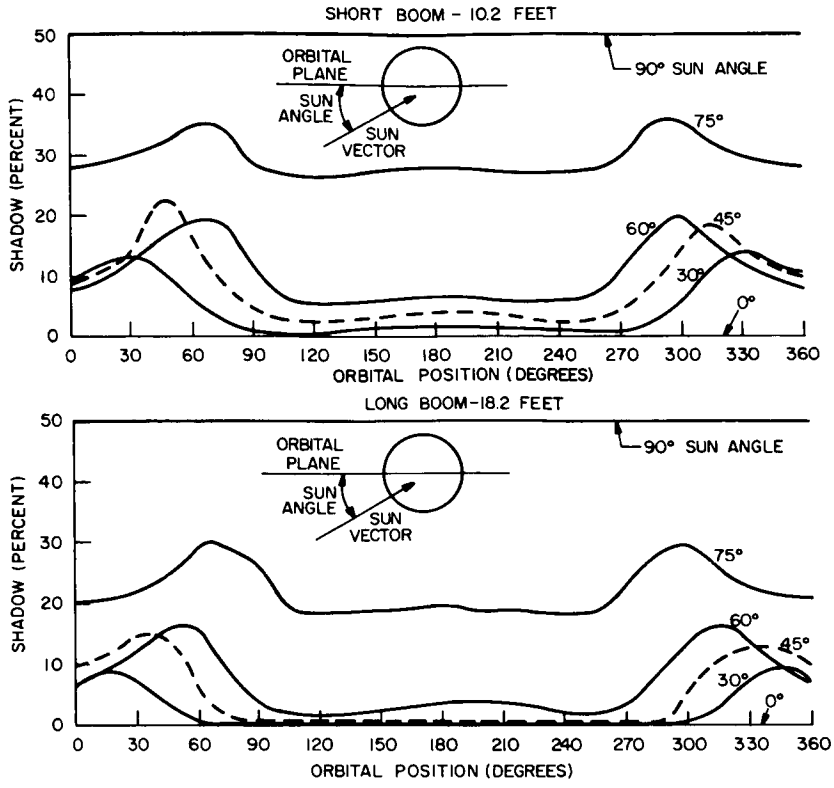

Figure IX-29. Percentage of Shadow versus Orbit Angle for Various Sun Angles ("H" Configuration)

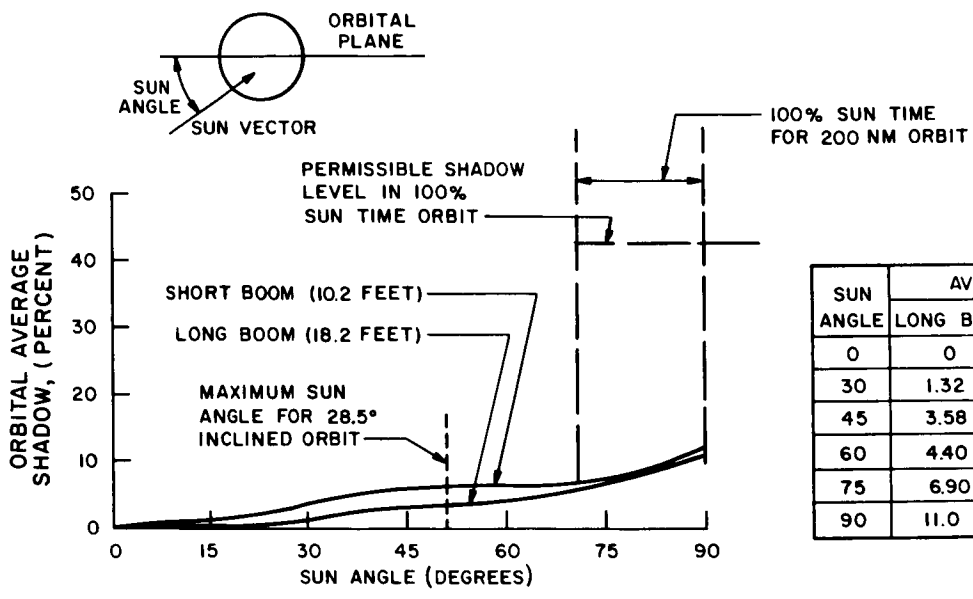

SUN ANGLE	AVG. % SHADOW	
	LONG BOOM	SHORT BOOM
0	0	0
30	1.32	3.95
45	3.58	6.20
60	4.40	6.50
75	6.90	7.28
90	11.0	12.0

Figure IX-30. Average Percentage of Shadow versus Sun Angle ("Z" Configuration)

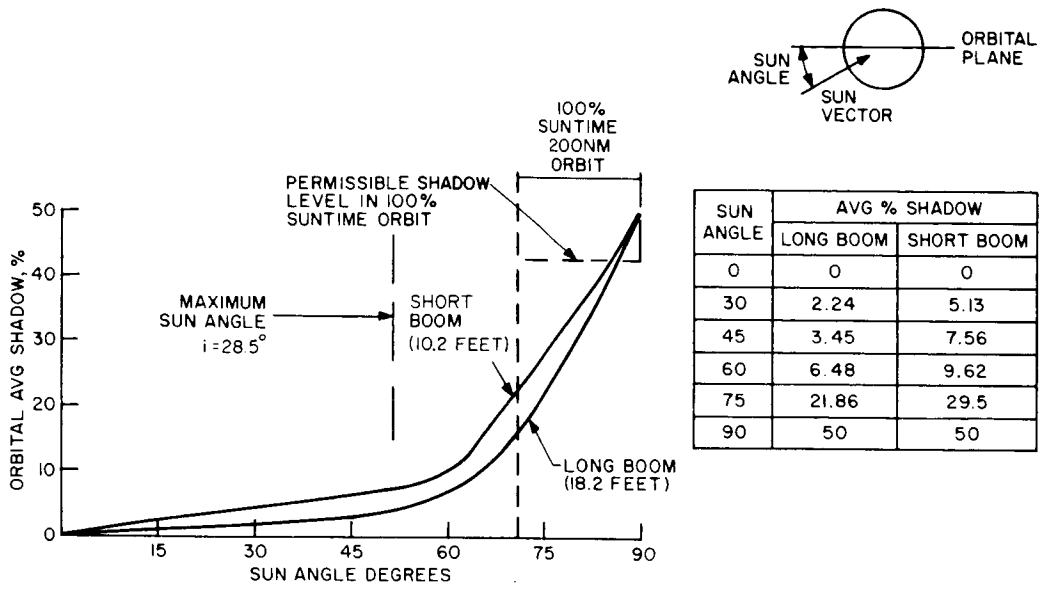

SUN ANGLE	AVG % SHADOW	
	LONG BOOM	SHORT BOOM
0	0	0
30	2.24	5.13
45	3.45	7.56
60	6.48	9.62
75	21.86	29.5
90	50	50

Figure IX-31. Average Percentage of Shadow versus Sun Angle ("H" Configuration)

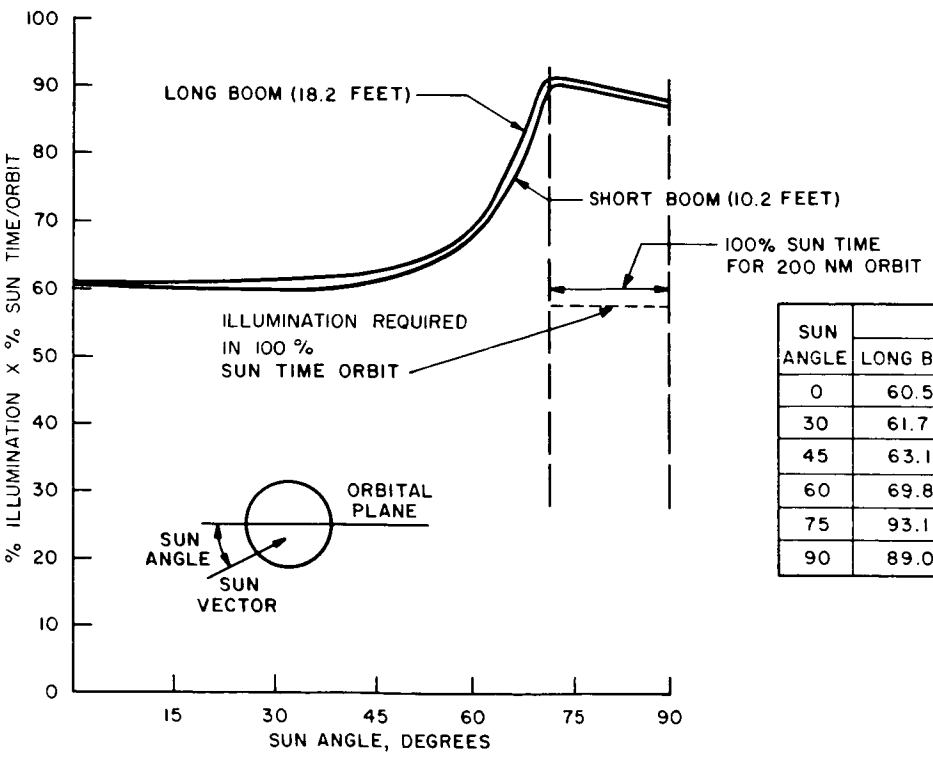

SUN ANGLE	LONG BOOM	SHORT BOOM
0	60.5	60.5
30	61.7	60.0
45	63.1	61.4
60	69.8	68.3
75	93.1	92.7
90	89.0	88.0

Figure IX-32. Average Array Illumination versus Sun Angle ("Z" Configuration)

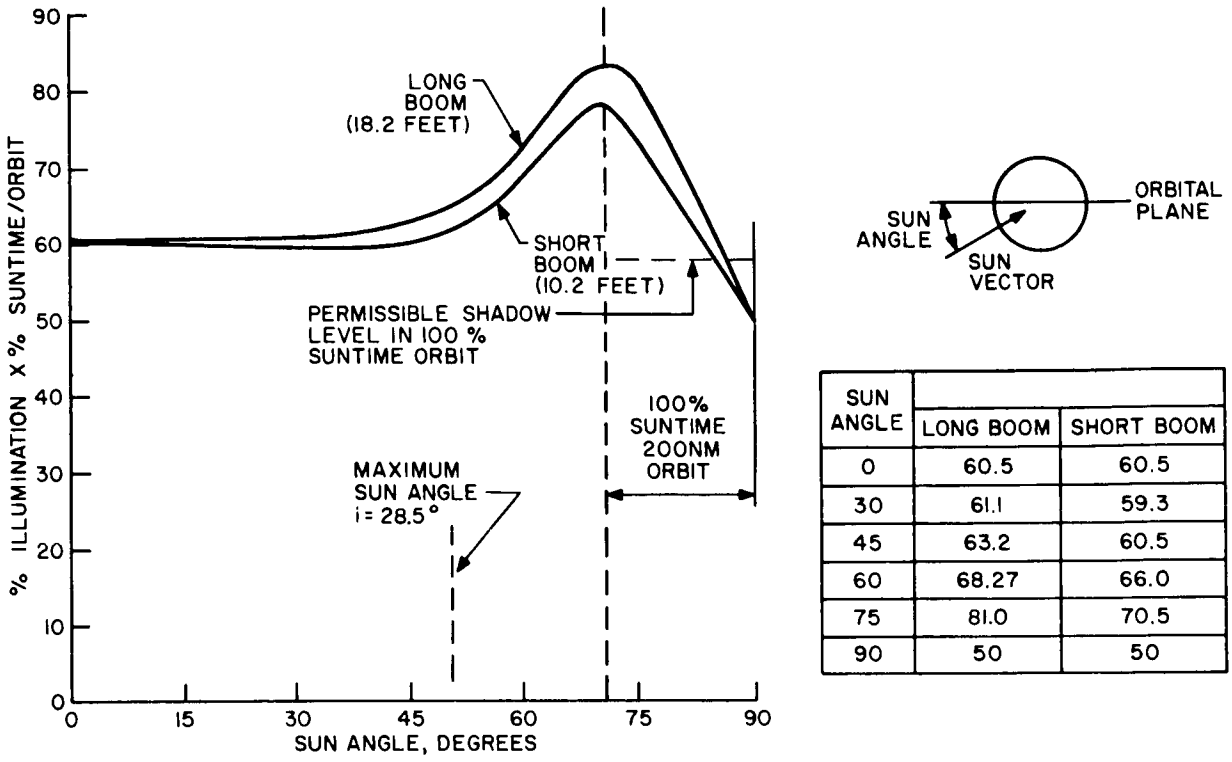

SUN ANGLE	LONG BOOM	SHORT BOOM
0	60.5	60.5
30	61.1	59.3
45	63.2	60.5
60	68.27	66.0
75	81.0	70.5
90	50	50

Figure IX-33. Average Array Illumination versus Sun Angle ("H" Configuration)

to energy developed). The deficiency in power will occur in a polar orbit at a 200-nmi altitude, if launched at such a time that the sun moves through all possible angles with respect to the satellite orbital plane. The array power deficiency does not occur for a 28.5° inclined orbit. If the power deficiency can not be tolerated, two solutions are available; more solar-array area may be added, or the vehicle may be rotated about its roll axis. In the 200-nmi orbit, 6° or less of vehicle roll will be required four times a year at most.

It can be concluded from this discussion that only in special cases (e.g., combination of large inclination angles and time of launch) will small array-power deficiencies occur. These will be of low magnitude for short durations and even in these special cases, vehicle roll can entirely eliminate the power deficiency. Therefore, in connection with shadowing, either the "Z" or "H" configuration is acceptable.

4. Array Boom Length

The sun angle at which array-on-array shadowing starts can be varied by varying the length of the array boom. The expression that defines this angle is as follows:

$$\cos \phi = \frac{W}{2l + D},$$

where

W is the width of the array (17 feet),

l is the boom length in feet,

D is the diameter of the vehicle (17 feet), and

ϕ is the sun angle with respect to the orbital plane.

Figure IX-34 illustrates graphically the relationships of the constants as in the preceding, starting with a minimum boom length of 8.5 feet. With the array control axes as selected, the array-on-array shadowing starts at sun angles where the orbit daytime approaches 100 percent of the orbital period. As the percentage of daytime increases, the energy requirement decreases. Thus, from this point of view, very little is gained by increasing the boom length beyond its present 9.3 feet.

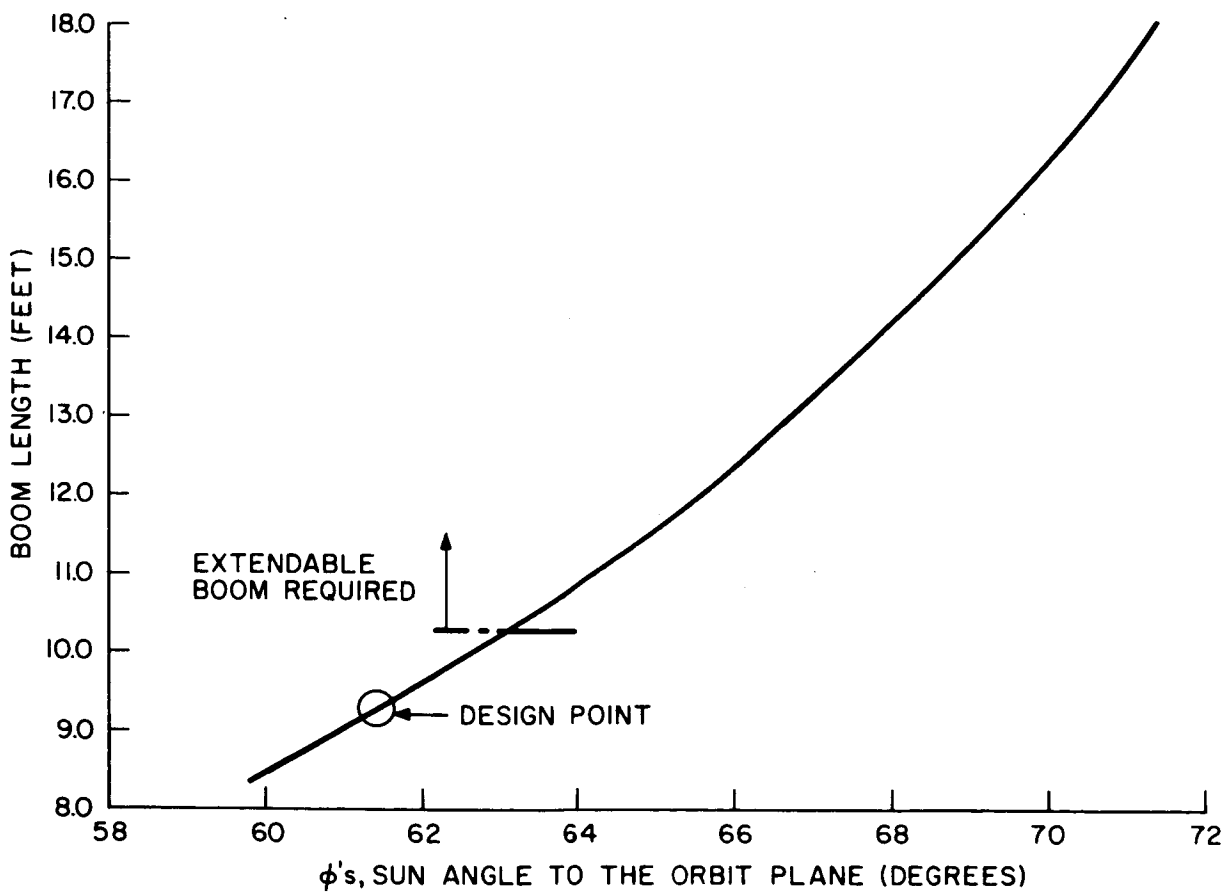

Figure IX-34. Boom Length versus Sun Angle for Start of Array-on-Array Shadowing

LIST OF REFERENCES FOR SECTION IX

IX-1. E. Hecht and W. P. Manger, "Magnetic Attitude Control of TIROS Satellites", American Astronautical Society, Paper #62-44 (March 1962).

IX-2 W. Lindorfer and L. Muhlfelder, "Attitude and Spin Control and TIROS Wheel", AIAA/JACC Guidance and Control Conference, Seattle, Washington, Proceedings, (August 1966).

IX-3. "TRW Systems Space Data Handbook" (Page 49 - Solar Radiation Torques), TRW Space Technology Laboratories Publication.

SECTION X

ELECTRICAL SYSTEMS ANALYSIS

A. INTRODUCTION

This portion of the report summarizes the electrical systems analysis of the power subsystem for the laboratory module.

During the initial phase of the study program, power systems tradeoffs were performed with the object of selecting the optimum configuration for the system block diagram. Various aspects of different power systems were analyzed and compared, including efficiency and solar-cell-array requirements, heat dissipation, reliability, bus-voltage extremes, complexity, and design flexibility. Component data used in this phase was assumed and is accurate only to the extent that it would reflect major trends and permit the selection of a general systems approach.

The power systems tradeoff study resulted in the selection of a parallel tracker system as shown in Figure X-1. The simplified block diagram representation serves to identify the major components and functions and the major interconnections involved. The most outstanding electrical design features of this system are its ability to draw maximum array power (when required) and its relative freedom from excessive heat dissipation. Through electromechanical design, the goal of extensive modularization has been achieved in that all but the heaviest and most reliable internally mounted components, such as busbars and filter banks, are conceived as packaged in the form of eight different, independently replaceable modules, with the initial quantity of each module dependent on the load requirements and frequency of resupply.

As in nearly all other solar-array space-power systems designed to maintain uninterrupted flow of load power in an earth orbit, the selected system involves batteries, load regulators, and a solar array sufficiently large to maintain energy balance under worst-case conditions at the end of design life.

Following selection of the systems approach and identification of the major "black-box" characteristics, detailed component studies were undertaken. Among the major objectives of this phase were crew safety and reliability, definition of a realistic state of the art, accurate estimates of the number and size of the required major components, and identification of the areas requiring futher study. Results of the component studies are given in Paragraph C of this Section.

Presence of the crew has been included as a factor during the conduct of the study. Paragraph D summarizes the projected involvement of the crew in maintaining systems safety, including considerations of systems instrumentation, replacement of faulty components, and redundancy based on detailed reliability studies and a stated probability goal for mission success.

Extensive use has been made of the computer as an aid in the performance of detailed systems analyses. A special computer program has been written to perform complex calculations of the required number and size of solar cells, batteries, and electronic modules, for a range of load conditions and other mission requirements. A detailed description of each function performed by the program, presented in the form of a step-by-step procedure of the analysis of the selected power system configuration, is given in Paragraph E. This portion includes a discussion of a program subroutine developed to yield end-of-life solar-cell characteristics based on raw radiation-flux and component data.

A summary of the results of the computer studies is included in Paragraph F.

Four specific conceptual systems designs have been developed, for two orbit altitudes (200-nmi and synchronous) under two different nominal load profile conditions. (Regarding 200-nmi altitude designs, small differences exist in the required array size depending on the orbit inclination assumed.) In summary, these designs have resulted in recommending nickel-cadmium batteries at low altitudes, silver-cadmium batteries for service in the synchronous orbit, and a resupply interval of one year in all cases. Paragraph G contains a description of the tradeoffs involved, as well as specific recommendations regarding the required components based on detailed component information stored in the computer.

Although a considerable part of this study has been devoted to the analysis of the existing component data in an effort to convey accurate systems information, definition of the exact component characteristics was not included among its major objectives. Because unusually large components will be required to handle the power levels involved (necessitating a good deal of extrapolation of the existing data for smaller components with all the attendant inaccuracies), a search for data more intensive than the usual thorough industry status survey was considered to be beyond the point of diminishing returns. Instead, major emphasis was placed on the electrical-systems studies in the areas of the systems definition, development of useful aids to computation not dependent on specific numerical data, and identification of the pertinent electrical and electromechanical design techniques to be pursued in depth during the course of a detailed design phase based on specific mission objectives.

B. POWER SYSTEM TRADEOFFS

1. General Approach

In view of the large number of variables involved, a parametric study (rather than a detailed study for an accurate determination of any specific quantities) has been performed, aimed at the identification of the major trends. Many simplifying approximations and assumptions were made, but not to the extent of interference with the basic purpose of the study.

In somewhat more specific terms, the approach to the power-system tradeoff study consisted first of the formulation of a set of assumptions and ground rules concerning the load profile. Mission altitude and load requirements have been retained as major variables primarily because significant changes in the orbit altitude or load requirements usually necessitate the greatest changes in the major parameters of a solar-cell power system.

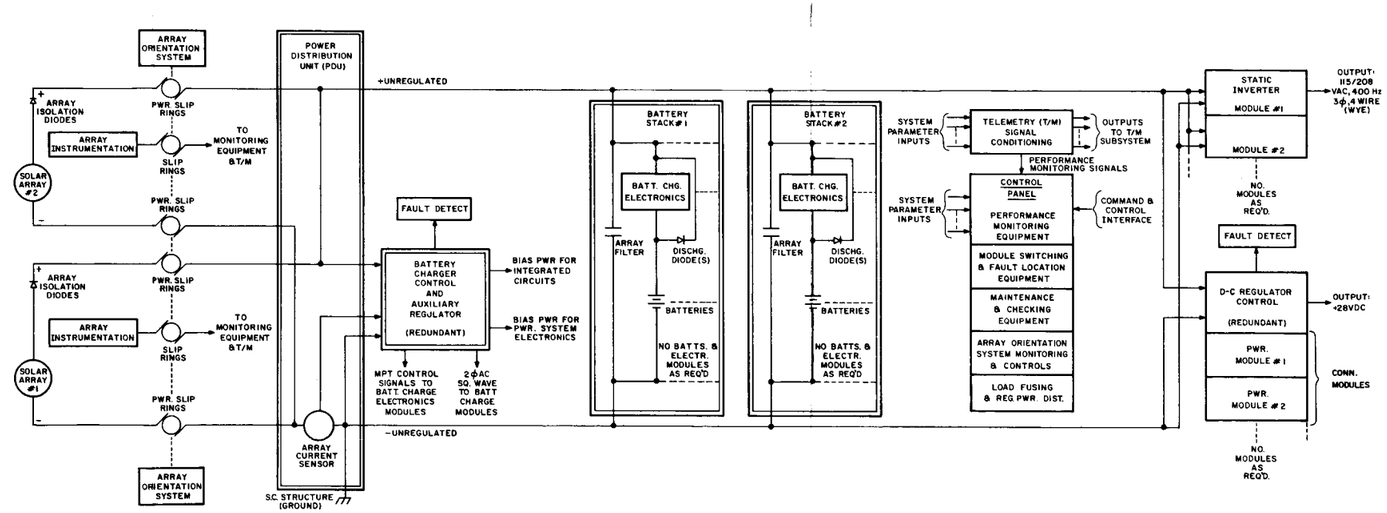

Figure X-1. Laboratory Module Power Supply, Functional Diagram

Additionally, the set of ground rules assumed has been applied to a generalized power-system block diagram in a manner permitting the mathematical model to be changed at will to reflect the performance efficiency of many specific power-system configurations. Several mathematical models were analyzed in detail with the aid of a computer program written especially for that purpose. These fell into two broad categories: the tracking power systems (capable of being tuned continuously to the maximum-power point of a solar array), and the nontracking systems of the more usual variety.

To reflect fairly all the major interrelationships, it has been necessary to perform a certain amount of preliminary work in the areas of orbital analysis and solar-array mechanical and thermal design. A parametric study of the storage system requirements has been performed in order to properly apportion the amount of array power required at all altitudes for battery charging.

Finally, a set of recommendations has been made.

2. Assumptions, Requirements, and Definitions

Certain of the items listed in the following are not directly applicable to the parametric study approach. However, they are mentioned in order to place the end results of the study in the proper perspective.

a. DESIGN PHILOSOPHY

(1) Modular Approach

The power system will consist of multiples of a set of basic building blocks, properly interconnected, with their number dependent on the requirements of the specific mission.

(2) Presence of Crew

Routine maintenance, periodic adjustments, and limited repair will be carried out in flight.

(3) Load Programming

In-flight load programming may be performed.

(4) State of the Art

Present-day state of the art is to be considered, insofar as possible.

(5) Voltage Regulators

Pulse-width-modulated (PWM) down-converter regulators are preferable.

(6) Reliability

The power system will be designed to maintain a probability of mission success of 0.995 or greater.

b. LOAD REQUIREMENTS

(1) Load Voltage

Two load bus voltages are required as follows: (1) d-c: +28 volts ± 1 percent and (2) a-c: 120/208 volts, 3 phase, 400 cps.

Exact proportion of the total load to be delivered at either voltage and respective time-sequencing are not known, but a 65-percent d-c, 35-percent a-c load requirement is probable.

(2) Load-Power Classification.

Examination of a set of typical load-power requirements in a manned mission suggests the following load categories:

(a) Essential Loads. Loads within this category are considered essential to the crew safety and include minimum power necessary to maintain the mission. Examples: ECS/Life Support, Displays.

(b) Non-Essential Loads. Unlike the essential loads, some of these can be turned off, temporarily or permanently, without premature termination of the mission. Example: one or more experiments.

(c) Fixed Loads. When operating normally, these require power continuously. Examples: Navigation and Guidance, Illumination.

(d) Periodic Loads. This category consists of loads which occur on a scheduled basis, although the schedule may be flexible. Examples: Auxiliary Propulsion, Maintenance.

(e) Programmable Loads. The only loads considered to be within this category are the programmable-experiments power.

(3) Load-Power Requirements

Load power requirements for four typical missions are given in Table X-1.

TABLE X-1. LOAD REQUIREMENTS FOR TYPICAL MISSIONS

Characteristic	Voltage (a-c or d-c)	Mission (No.-compartments/altitude/inclination)			
		1/200 NM/28.5°	2/200 NM/28.5°	2/200 NM/90°	2/synch/30°
Fixed Essential Loads					
ECS/Life Support	both	1.25	1.25	1.25	1.25
ECS/Life Support (O_2 regeneration)(1)	both	3.06 kWh(2)	3.06 kWh(2)	3.06 kWh(2)	47.5 kWh(2)
Communications	both	0.21	0.21	0.21	0.26
Data Mgmt	d-c	0.30	0.30	0.30	0.30
Displays	both	0.20	0.20	0.20	0.20
Nav. and Guidance	both	0.20	0.20	0.45	0.25
Stab. and Control(3)	both	0.12	0.12	0.13	0.13
Periodic Essential Loads					
Communications	both				
one hour/day		0.04	0.04	0.04	0.04
10 min., 6 out of 15 orbits		0.05	0.05		
6 min., 3 out of 15 orbits				0.05	
Emergency, 15 min. typical		0.70	0.70	0.70	
Auxiliary Propulsion(3)					
0.1 - 0.6 sec., intermittent	both	0.10	0.10	0.10	
Programmable Essential Loads					
None					
Fixed Non-Essential Loads					
Illumination	d-c	0.24	0.48	0.48	0.48
TV	both	0.12	0.12	0.12	0.12
Experiments	both	0.10	0.10	0.10	0.10
Periodic Non-Essential Loads					
Personnel Systems when required	d-c	0.60	0.60	0.60	0.60
Maintenance	both				
3 hours/day		0.20			
6 hours/day			0.20	0.20	0.20
Programmable Non-Essential Loads					
Experiments(4)	both				
5 kW system		2.26	2.02	1.76	1.91
10 kW system		7.26	7.02	6.76	6.91

NOTES:

(1) during sun-illuminated part of flight
(2) per orbit; other loads in kW
(3) essential/non-essential status unclear; assumed essential for the present
(4) this and the sum of all fixed loads assumed to equal 5 and 10 kW in the respective system.

(4) Load Profile Definition

The load profile is defined as the power-time relationship of the load requirements (power system output) and is assumed to consist of:

(a) the total of all fixed loads and the experiment loads, (i.e., 5 or 10 kW depending on the nominal power level) continuously during both daytime and dark time.

(b) in addition, but only during daytime, the ECS/Life Support (O_2 regeneration) load consisting of:

- 3.22 kW at 200 NM
- 2.09 kW in the synchronous orbit.

During daytime, then, the power delivered to the load is either 7.09, 8.22, 12.09, or 13.22 kW, and during dark time either 5 or 10 kW, depending on the assumed nominal systems power level and altitude. (See Paragraphs X.B.3.d(2)(a) and X.B.3.d.(2)(b) for further specific assumptions.)

(5) Periodic Loads

The preceding assumes a 100-percent duty cycle for the programmable experiment loads. The assumption is made that whenever periodic loads do occur, the experiment loads are reduced by a like amount, thereby maintaining a "flat" profile.

c. NUMERICAL ASSUMPTIONS

The numerical assumptions were as follows:

(1) Orbit-average efficiency factor of all PWM devices (i.e., where applicable, e_c, e_m, e_d, and e_{cb}), is 0.9; as shown in Figure X-2.

(2) Orbit-average efficiency factor of an inverter (e_i) is 0.8.

(3) Average per-cell battery voltages are as follows:

Battery	Charge	Discharge
Ni-Cd	1.5	1.20
Ag-Cd	1.5	1.05

Other specific numerical assumptions are described in the text that follows.

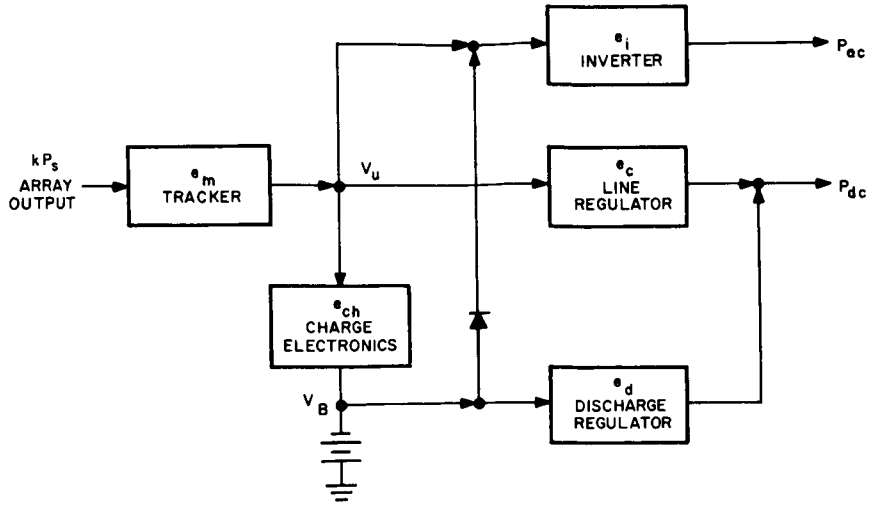

Figure X-2. Generalized Power Subsystem, Block Diagram

3. Block Diagram Tradeoffs

a. GENERALIZED SYSTEM BLOCK DIAGRAM

In view of the fact that several different power-system configurations must be investigated in order to arrive at a logical selection of an optimum approach, it is convenient to devise a generalized power system and write a universal expression for relating the amount of source energy required per unit of load power. The block diagram must be constructed so that, by assigning different numerical values to various component members of the universal equation, an accurate algebraic description of a variety of power-system configurations will result.

The expression referred to is a generalized energy-balance equation. It will be written for the block diagram configuration shown in Figure X-2, where it is assumed that both d-c and a-c regulated load voltages are required. Typical solar-array maximum-power variation (as a function of time in orbit) is shown in Figure X-3, including the thermally induced initial upswing due to the cold array emerging from the earth's shadow. Provisions will be made to include the additional power, resulting when the cold array emerges from the earth's shadow, in the generalized energy-balance equation, since certain systems able to track the array maximum power point will be analyzed later in this report.

It is necessary to define in detail, certain terms to be used:

(1) P_s is the maximum (or near-maximum) array power output when the solar cells reach thermal equilibrium, i.e., the flat portion of the array power-versus-time variation in Figure X-3 is P_s. A power system not capable of actively tracking the maximum power point will receive, on the average, P_s watts from the array when illuminated. In tracking systems, on the other hand, the array output averaged over

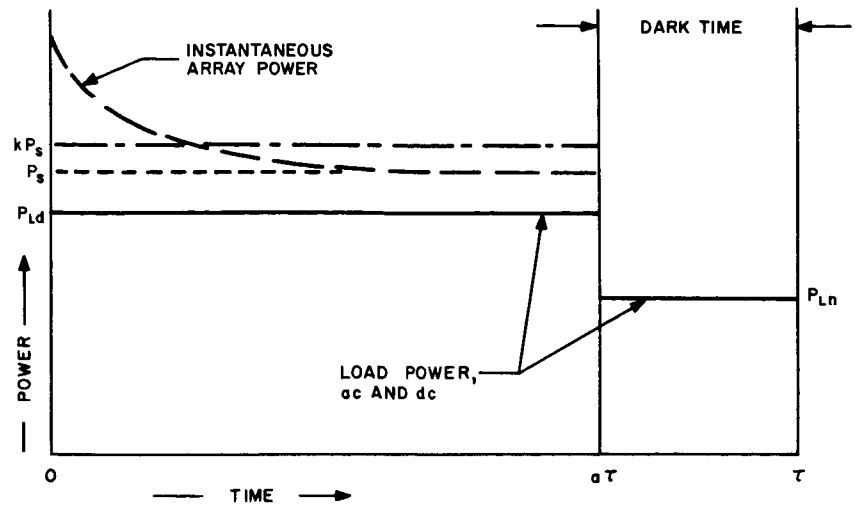

Figure X-3. Generalized Load and Source Power Variation with Time in Orbit

the daytime part of the orbit will be greater (by a factor k). The array power output is defined as $kP_s e_m$ average.

(2) The block described in Figure X-2 by the transfer function e_c defines the path taken by the array energy to the d-c load.

(3) Similarly, e_d defines the path of d-c load energy taken from the battery.

In a simplified case, it can be said that, during daytime, the d-c load is delivered through e_c; during dark time, through e_d.

(4) The a-c load is delivered through block e_i, both daytime and nighttime.

(5) e_{cb} is the transfer function of the block controlling battery charge.

The generalized energy-balance equation for the configuration of Figure X-2 has the following form:

$$kP_s e_m a\tau = \left(\frac{f_d}{e_c} + \frac{f_{id}}{e_i}\right) a\tau P_{Ld} + \left(\frac{f_n}{e_d} + \frac{f_{in}}{e_i}\right) \frac{V_{Bc}}{V_{Bd} e_b e_{cb}} (1-a)\tau P_{Ln}, \qquad \text{(X-1)}$$

where the "f" factors define the amount of load delivered at the a-c and d-c levels at various times.*

*All symbols used in this section are defined in the glossary that appears in back of the cover page for this Section.

By substituting $R = P_{Ld}/P_{Ln}$,

$$f_{id} = 1 - f_d,$$

and

$$f_{in} = 1 - f_n,$$

solving for P_s and simplifying, the Equation becomes

$$P_s = \frac{P_{Ln}}{k e_m e_i} \left\{ \left[1 - f_d \left(1 - \frac{e_i}{e_c} \right) \right] R + \left[1 - f_n \left(1 - \frac{e_i}{e_d} \right) \right] \frac{1-a}{a} \cdot \frac{V_{Bc}}{V_{Bd} e_b e_{cb}} \right\} \tag{X-2}$$

The per-orbit battery discharge, Q ampere-hours, is obtained by multiplying the second part of the right-hand member of equation (X-1) by $e_b e_{cb}/V_{Bc}$. When simplified, the expression for Q assumes the form

$$Q = \left[1 - f_n \left(1 - \frac{e_i}{e_d} \right) \right] \frac{1-a}{e_i V_{Bd}} \tau P_{Ln}. \tag{X-3}$$

Watt-hours discharge therefore equals QV_{Bd}

Applicability of the generalities developed in this Section to specific power-systems approaches will be demonstrated later in this Section.

b. SPECIFIC CONFIGURATIONS

(1) General

Four specific configurations will be analyzed, by operating on the various parts of equation (X-2) as shown in the Table X-2.

Since all four systems must contain factors e_i and e_d (all load power must be regulated at all times), the expression for the per-orbit battery discharge (ampere-hours or watt-hours) remains the same in all cases. Paragraphs X.B.3.b(2) through X.B.3.b(5) will therefore be concerned exclusively with the effect each configuration has on equation (X-2); Paragraph X.B.3.c will summarize the results of a parametric study of the storage battery.

(2) Non-Tracking Series System (PWM Regulator System)

Many power systems of this nature have been built and flown. They include systems using dissipative series regulators, boost regulators, and pulse-width-modulated

TABLE X-2. SYMBOL AND PARAMETER ASSIGNMENTS FOR VARIOUS SYSTEMS

Type of System	k	Symbol Assigned to Steady-State Array Output P_s	e_m	e_{ch}	e_c	e_i	e_d
Non-Tracking Series System	1.0	P_{sso}	1.0	V_{BC}/V_u	e_c	e_i	e_d
Tracking Series System	k	P_{sst}	e_m	1.0	e_c	e_i	e_d
Non-Tracking Parallel System	1.0	P_{spo}	1.0	V_{BC}/V_u	1.0	e_i	e_d
Tracking Parallel System	k	P_{spt}	1.0	e_{ch}	e_c	e_i	e_d

(PWM) switching regulator down-converters developed by RCA for Nimbus. All have one characteristic in common: a d-c voltage regulator is placed in series with the load. Because of its demonstrated superior performance, the PWM regulator system will be singled out for study in this section, although Equation (X-5) applies equally well to any other non-tracking series type system.

Substituting applicable conditions set forth in Table X-2 into Equation (X-2) and for a dissipative type charge regulator,

$$e_{ch} = \frac{V_{Bc}}{V_u} = \frac{V_{Bc}}{\Delta V_{ch_{ave}} + V_{Bc}} \approx 1 \qquad \text{(X-4)}$$

assuming that the average drop across the charge electronics $\Delta V_{cb_{ave}} << V_{Bc}$.

Then,

$$P_{sso} = \frac{P_{Ln}}{e_i}\left\{\left[1 - f_d\left(1 - \frac{e_i}{e_c}\right)\right]R + \left[1 - f_n\left(1 - \frac{e_i}{e_d}\right)\right]\frac{1-a}{a} \cdot \frac{V_{Bc}}{V_{Bd}\, e_b}\right\}. \qquad \text{(X-5)}$$

A simplified block diagram of this power system configuration is shown in Figure X-4. In Equation (X-5), factor e_c is the average daytime efficiency factor of the PWM regulator; during dark time, the factor is e_d; e_i and all other symbols have the same meaning as in the general equation (X-2).

In the PWM regulator system, the storage battery configuration is designed so that the lowest expected battery discharge voltage is slightly greater than the d-c regulated bus voltage

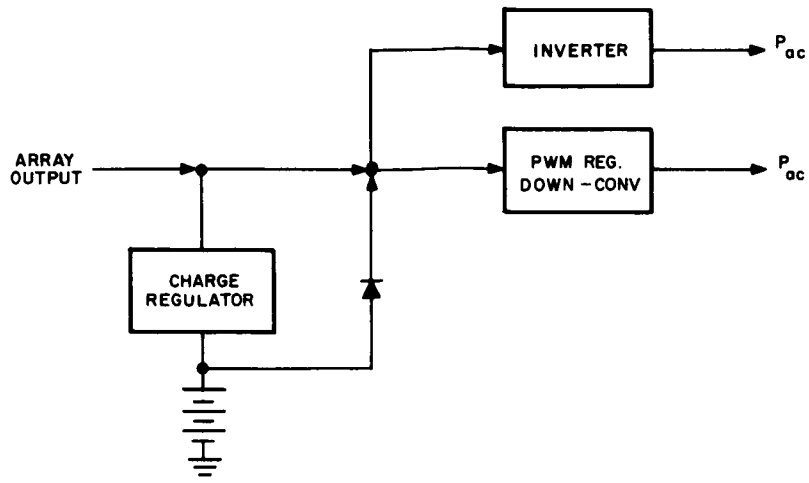

Figure X-4. PWM Regulator System

delivered by the down-converter regulator. The charge regulator is usually of the dissipative series type with the array output voltage always greater than the maximum expected battery charge voltage. The average voltage drop across the charge regulator contributes to its inefficiency, but it can be made quite small by the use of special techniques developed by RCA. The approximation allowed in equation (X-4) is thus held valid, particularly for a large number of series storage cells (25 to 30 or more).

If an orbit-average efficiency factor is assigned to the PWM regulator

$$e_c = e_d = 0.9,$$

and if

$$e_i = 0.8,$$

Equation (X-5) is simplified and becomes

$$P_{sso} = 1.25\, P_{Ln} \left[\left(1 - 0.11\, f_d\right) R + \left(1 - 0.11\, f_n\right) \frac{1 - a}{a} \cdot \frac{V_{Bc}}{V_{Bd}\, e_b} \right]. \qquad \text{(X-6)}$$

(3) Tracking Series System (Series Tracker)

The series tracker configuration shown in Figure X-5 is similar to the PWM regulator system in that the method used to deliver the load power is identical to both. The major differences are in the areas of array-power utilization and charge control.

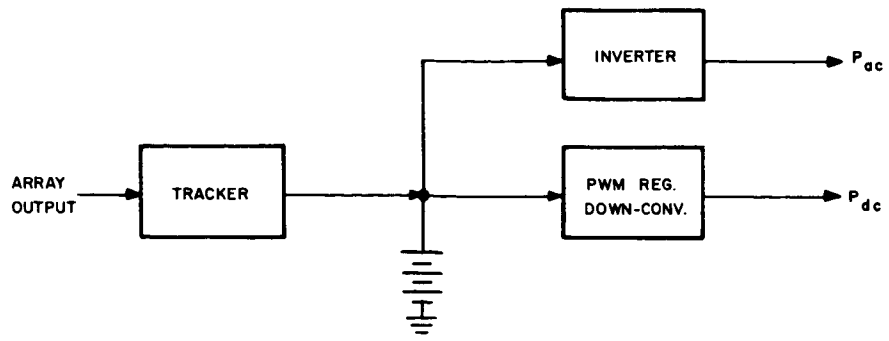

Figure X-5. Series Tracker System

The tracker is capable of following the array maximum-power point and is thus able to take advantage of the initial power upswing illustrated in Figure X-3. Maximum array power (less tracker loss) is available, when required, at the tracker output terminals. The device itself is a duty-cycle-controlled PWM regulator whose output can be cut back in case of excessive battery charge (or excessive array output). A charge electronics box, in the sense of that shown in Figure X-2, is therefore not required. Thus, no special dissipative circuits are needed in this system, provided the tracker input circuits can handle the array-voltage excursion, which is accentuated by low load requirements.

Substitution from Table X-2 into Equation (X-2) results in

$$P_{sst} = \frac{P_{Ln}}{k e_m e_i} \left\{ \left[1 - f_d \left(1 - \frac{e_i}{e_c} \right) \right] R + \left[1 - f_n \left(1 - \frac{e_i}{e_d} \right) \right] \frac{1-a}{a} \cdot \frac{V_{Bc}}{V_{Bd} e_b} \right\}. \tag{X-7}$$

Assuming an orbit-average PWM regulator efficiency factor, i.e., $e_m = e_c = e_d = 0.9$, and $e_i = 0.8$, equation (X-7) becomes

$$P_{sst} = 1.39 \frac{P_{Ln}}{k} \left[\left(1 - 0.11 f_d \right) R + \left(1 - 0.11 f_n \right) \frac{1-a}{a} \cdot \frac{V_{Bc}}{V_{Bd} e_b} \right] \tag{X-8}$$

for the Series Tracker system.

(4) Non-Tracking Parallel System (Direct Energy Transfer System)

The Direct Energy Transfer System (so called because the array energy passes to the d-c loads directly with no series elements between) differs from a series system in that the d-c regulation function is accomplished by a parallel element, i.e., the shunt regulator, as shown in Figure X-6.

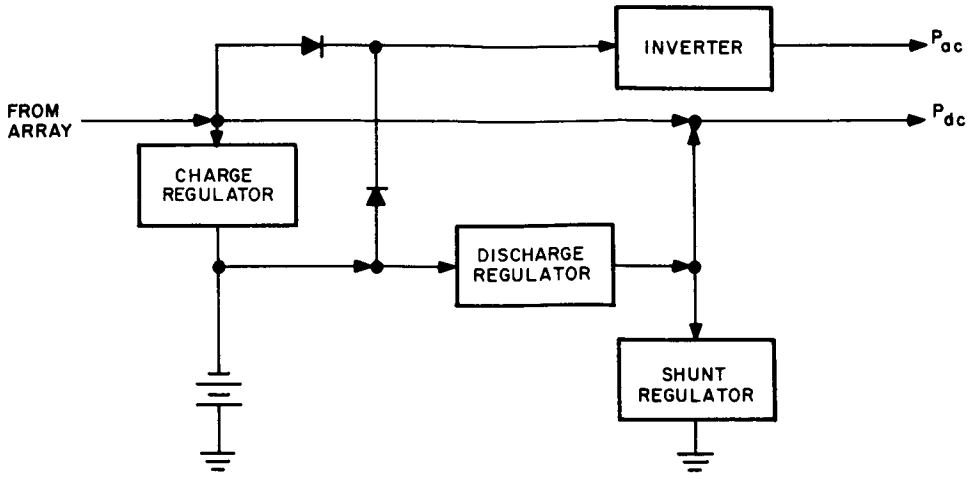

Figure X-6. Direct Energy Transfer System

When the solar array is active, the shunt regulator is ON and maintaining the d-c regulated bus at a fixed level. If the array output exceeds load requirements, the increased shunt-current flow is sensed and the charge regulator is turned on to allow the excess power to be used as battery charge. Any excess over and above the combined battery charge and load requirement is dissipated in the shunt.

During dark time, the shunt current will tend to drop below a predetermined small value. This condition is sensed to turn the charge regulator OFF. The discharge regulator is turned ON proportionally, to satisfy the load requirement and to maintain a small shunt-current flow, thereby assuring a regulated bus voltage at all times.

Many detailed designs of this system have been prepared. One with a modification, has been implemented in the Lunar Orbiter power subsystem. Its principal advantage is the negligible loss incurred during the power transfer from the array to the loads. One of its disadvantages is that, since the principle of operation of this system is based on a fixed array-output voltage, the system cannot be made to track the maximum-power point of the array.

A full or partial shunt regulator (dissipative or non-dissipative) is required in nearly all non-tracking systems as auxiliary equipment to dissipate excess array power. In the system under consideration, it performs a dual role, in addition to dissipating any excess power, it is an essential system element necessary to keep the output bus regulated. Fixed loss in the shunt is relatively small and therefore, does not appear in the energy-balance equation.

Making use of the approximation developed in Equation (X-4), and substituting other pertinent values and parameters into equation (X-2), the energy balance equation for this system becomes

$$P_{spo} = \frac{P_{Ln}}{e_i} \left\{ \left[1 - f_d \left(1 - e_i \right) \right] R + \left[1 - f_n \left(1 - \frac{e_i}{e_d} \right) \right] \frac{1 - a}{a} \cdot \frac{V_{Bc}}{V_{Bd}\, e_b} \right\}. \qquad \text{(X-9)}$$

Using an average discharge-regulator efficiency factor e_d of 0.9, and again assuming e_i as 0.8,

$$P_{spo} = 1.25\, P_{Ln} \left[\left(1 - 0.2\, f_d\right) R + \left(1 - 0.11\, f_n\right) \frac{1-a}{a} \cdot \frac{V_{Bc}}{V_{Bd}\, e_b} \right] \qquad \text{(X-10)}$$

To make the discussion of the direct-energy-transfer system complete, it remains to be said that several variations of the system exist to fit specific mission requirements. Equation (X-9) is written specifically for the condition of a dissipative type charge regulator, and generally for any type of a boost-discharge regulator. Equation (X-2), however, lends itself equally well to a system with a PWM type charge regulator (as will be shown later) and to any other type of discharge regulator, including a PWM-type down-converter or a dissipative series type.

(5) Tracking Parallel System (Parallel Tracker)

The block diagram of this system looks exactly like the PWM Regulator system diagram, Figure X-4, except that a PWM type of charge regulator is used. It is called a parallel Tracker because the tracker unit is in effect, placed across the solar array rather than in series with it as in Figure X-5.

The charge regulator is duty-cycle controlled and is used in such a manner that the maximum-power point of the array is actively tracked when that power can be utilized for the loads and for charging batteries. A parallel tracker system is currently under development*. It is inherently more efficient than the series tracker, since only the battery charging portion of the array energy is subject to the tracker loss.

Depending on the specific load requirements, a parallel tracker may or may not have a separate discharge regulator. None is required if (as is being assumed in this study) daytime battery-discharge energy is comparatively small.

Referring to Equation (X-2) and Table X-2:

$$P_{spt} = \frac{P_{Ln}}{k e_i} \left\{ \left[1 - f_d \left(1 - \frac{e_i}{e_c}\right) \right] R + \left[1 - f_n \left(1 - \frac{e_i}{e_d}\right) \right] \frac{1-a}{a} \cdot \frac{V_{Bc}}{V_{Bd}\, e_b\, e_{cb}} \right\}. \qquad \text{(X-11)}$$

* NASA Contract NAS5-3248

Again assuming e_i as 0.8, and the average PWM regulator efficiencies e_c and e_d, as well as e_{ch}, equal to 0.9,

$$P_{spt} = 1.25 \frac{P_{Ln}}{k} \left[\left(1 - 0.11 f_d \right) R + \frac{1 - 0.11 f_n}{0.9} \cdot \left(\frac{1 - a}{a} \right) \cdot \frac{V_{Bc}}{V_{Bd} e_b} \right]. \qquad \text{(X-12)}$$

(6) Conclusions

Equations (X-6), (X-8), (X-10) and (X-12) relate the end-of-life array power (i.e., minimum) required per unit of load power P_{Ln}. It is expressed parametrically as a function of (1) the array temperature-time profile where applicable, (2) relative amounts of power delivered during daytime and darktime, and (3) the amount of that power delivered at a-c and d-c voltages.

Factor (1-a)/a expresses the effect of orbit altitude in each case (assuming circular earth orbits). V_{Bc}/V_{Bd} depends on the choice of battery, as does the factor e_b. More important, e_b depends on orbit altitude to the extent that varying relative charge rates determine the battery ampere-hour charge-discharge efficiency to be utilized.

c. INVESTIGATION OF THE STORAGE SYSTEM OPERATING PARAMETERS

(1) Purpose

To perform a tradeoff study of the array size required versus altitude, the altitude-dependent operating parameters of the battery must be determined. These parameters are:

- relative charge rate, related to the average charge-discharge efficiency factor e_b expressed as a ratio of ampere-hours;
- cycle life; and
- depth-of-discharge variation of a fixed-size battery.

Once determined, these parameters enable a tentative selection of the battery size. It is then possible to relate the e_b variation, necessary to maintain the battery in energy balance, to the altitude-dependent factor (1-a)/a in Equations (X-6), (X-8), (X-10), and (X-12).

Basic assumptions made are: (1) a maximum life of one year; (2) either a nickel-cadmium (Ni-Cd) or a silver-cadmium (Ag-Cd) battery is used; (3) the altitude range is from 200 to 19,380 nm (synchronous); and (4) the number of cycles per year is the maximum possible at a given altitude.

(2) Specific Assumptions

Specific numerical assumptions to be made are not intended to accurately reflect the properties and limitations of various secondary batteries. They are, however, considered to be typical of the trends exhibited, in keeping with the general study approach stated in Paragraph X.B.2. More accurate battery data is discussed in Paragraph X.C.

(a) Nickel-Cadmium Battery

1. Not to be charged in excess of a 3-hour average rate.

2. Preferably, not to be charged at less than a 15-hour average rate.

3. The efficiency factor e_b varies linearly between the two above rates, so that:

   - at the 3-hour rate, $e_b = 0.82$, and
   - at the 15-hour rate, $e_b = 0.70$

   Then $e_b = 0.01\ (85 - H)$ (X-13)
   where H hours relative charge rate.

4. Efficiency factors assumed are for the worst-case (i.e., highest storage-cell temperature conditions) and are assumed to be independent of depth-of-discharge over the approximate range of 10 to 50 percent.

5. With a 20-hour charge rate, $e_b = 0.4$ (i.e., a charge/discharge ratio of 2.5).

6. Never to be charged at less than a 20-hour rate.

(b) Silver-Cadmium Battery

1. The efficiency-factor-to-charge-rate relationship is

$$e_b = 9.34\ (H + 76.4)10^{-3},\ for\ 3 < H < 20\ hours. \qquad \text{(X-14)}$$

2. Equation (X-14) is presumed to be valid under temperature and discharge depth conditions set forth in Paragraph X.B.3.c.2.a.

3. $e_b = 0.9,\ for\ \ 20 \leq H \leq 30\ hours.$

4. Not to be charged at rates outside the 3-to-30 hour range.

(3) Analysis

Factor e_b can be defined as the ratio of the per-orbit ampere-hour discharge, Q to the per-orbit ampere-hour charge $a\tau I_{cb}$, or

$$e_b = \frac{Q}{a\tau I_{cb_{ave}}} \tag{X-15}$$

The average relative charge rate H equals the ratio of the battery capacity, C, (ampere-hours) to the average charge current

$$H = \frac{C}{I_{cb_{ave}}} \tag{X-16}$$

C and Q are related by the depth of discharge factor d, and $c = \frac{Q}{d}$ a-hrs (X-17)

Substituting equations (X-15) and (X-17) into equation (X-16) yield

$$H = \frac{a\tau}{d} e_b \tag{X-18}$$

Substituting for e_b from equations (X-13) and (X-14) and solving for a τ,

$$a\tau = \frac{100}{\frac{85}{H} - 1} d \tag{X-19}$$

for Ni - Cd, and $3 < H < 15$ hours; and

$$a\tau = \frac{107}{\frac{76.4}{H} + 1} d \tag{X-20}$$

for Ag - Cd, and $3 < H < 20$ hours.

Quantity $a\tau$ is related to the altitude as shown in Figure X-7. Equations (X-19) and (X-20) are plotted in Figure X-8 as lines of fixed relative charge rates, H, and depth-of-discharge, d, vs. altitude.

Since the values H = 20 hours for Ni-Cd, and H = 30 hours for Ag-Cd fall outside the linear relationships of equations (X-13) and (X-14), the corresponding fixed-charge-rate lines are plotted separately by appropriate substitution of H and e_b into equation (X-18).

The cycle-life versus-altitude plot in Figure X-8 reflects the worst-case condition, i.e., the maximum possible number of dark times per year as found by dividing the number of hours per year by the orbital period.

Finally, the lines of fixed battery size show the variation of the depth of discharge with altitude for battery of fixed size. The variation is a direct function of the peak dark time duration $(1-a)\tau$ given in Figure X-7. Thus, size C ampere-hours is arbitrarily assigned to a storage cell size which would undergo a 15-percent depth of discharge at an altitude of 200 nmi; the ratio of dark-time duration at, 10,000 nmi for example to that at 200 nmi, from Figure X-7, is roughly 0.9 to 0.6 hour or 1.5. It follows that the size C battery would discharge to a depth of 1.5 times 15 percent or 22.5 percent at 10,000 nmi as shown in Figure X-8.

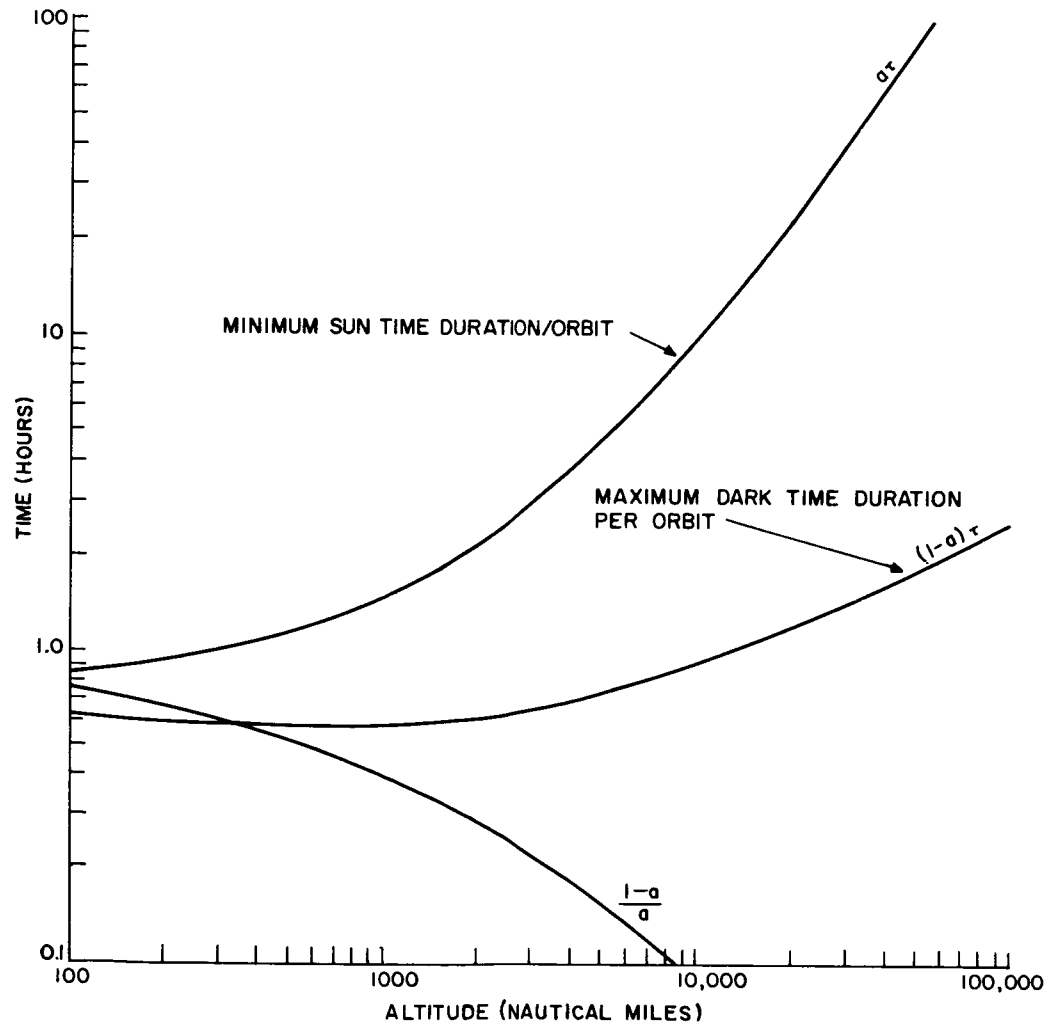

Figure X-7. Earth Orbit Characteristics, Circular Orbits

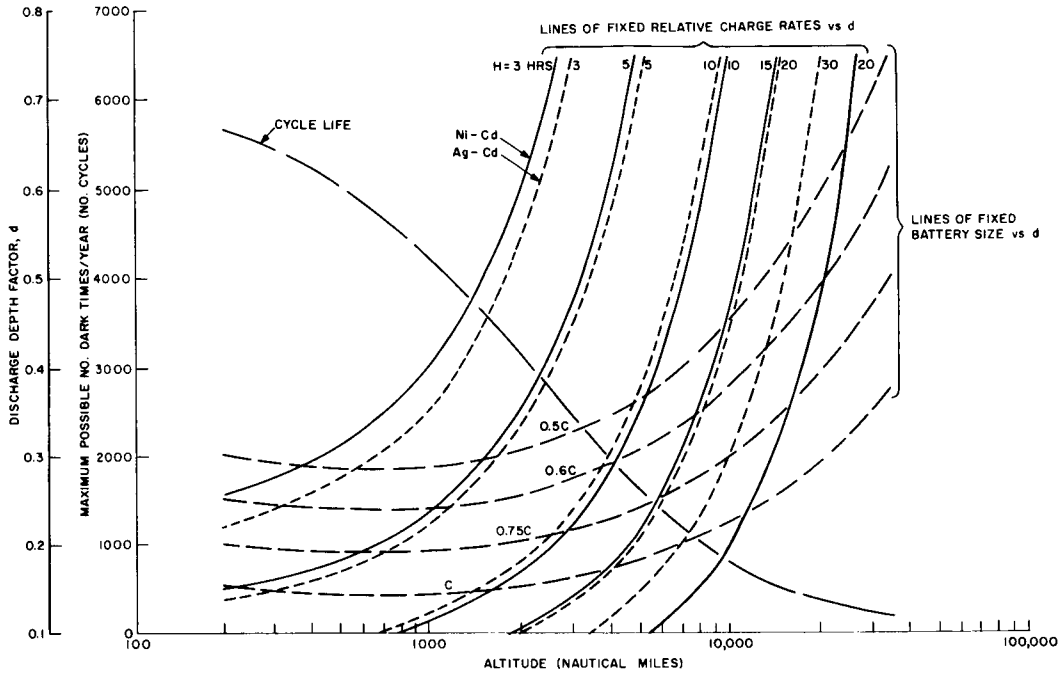

Figure X-8. Battery Operating Characteristics as a Function of Altitude, Earth Circular Orbits

Quantities C, 0.75C, et cetera, shown in Figure X-8, do not, of course, relate to any specific ampere-hour capacity. They are intended only to show relative magnitudes and their variation.

As a separate item, variation of the normalized battery-discharge watt-hours (QV_{Bd}/P_{Ln}) with altitude is shown in Figure X-9. It is calculated from equation (X-3) and applies specifically to the four systems configurations discussed in section X.B.3.b.

(4) Discussion of the Battery Parameters

The curves in Figure X-8 do not relate to any specific load magnitude and are limited to use only when all discharge occurs during dark time.

The lines of fixed relative charge rates are not drawn for a fixed battery size; i.e., for a given constant value of H, the curve implies a different battery capacity for each altitude. The opposite would have been the case if the ratio of dark time to daytime duration, (1-a)/a, were constant at all altitudes. In the actual case, daytime duration (charge time) increases faster than dark time. Thus, to maintain a given H constant without undue overcharge, depth of discharge must be increased with altitude at a rate greater than the rate of dark-time increase. Therefore, a given fixed-H line implies an ever-decreasing battery capacity as the altitude is increased.

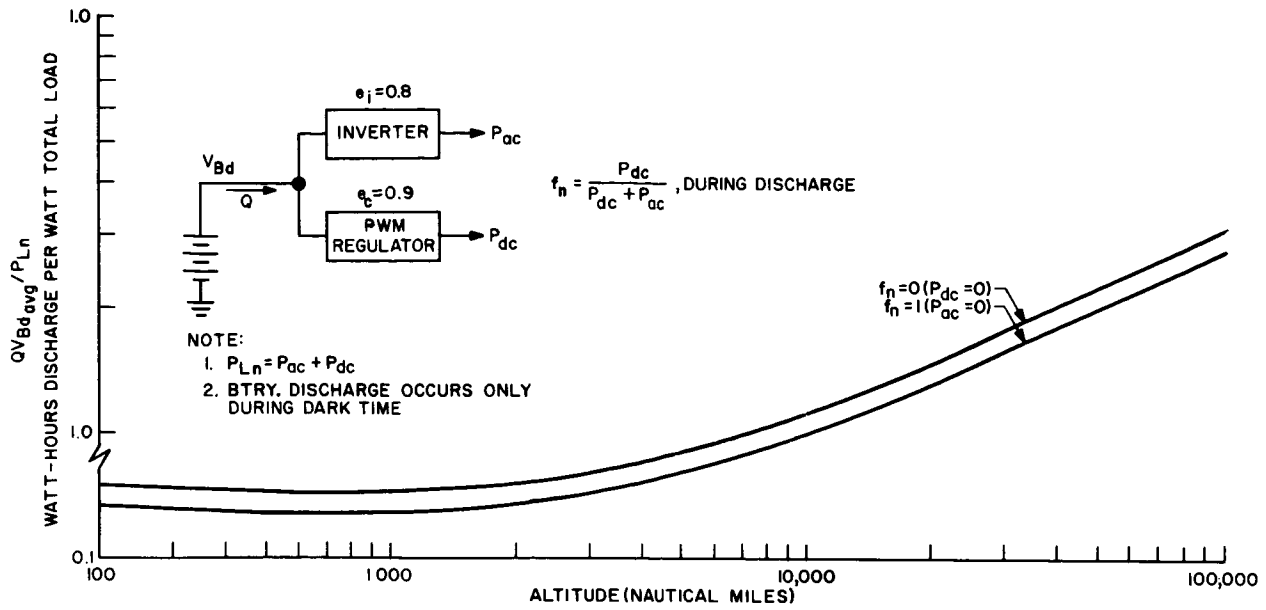

Figure X-9. Battery Watt-Hours Discharge per Watt, $P_{Ln_{ave}}$.

As pointed out previously, the lines of fixed battery size are represented by the relative magnitudes labeled C through 0.5C and show a two-to-one variation in the relative battery size and the resultant variation of the depth of discharge with altitude. In addition to that when these fixed-size lines are superimposed on the fixed-H plots (as shown in Figure X-8) the effect of altitude on the relative charge rate, and other parameters of a fixed-size battery, is illustrated.

For example, assume a Ni-Cd battery discharging to a 15-percent depth at 200 NM (curve is labeled "C" in Figure X-8). Also, assuming for the moment that a one-year life is required, the cycle life will be 5700 cycles (worst-case). Figure X-8 shows that to maintain energy balance, the battery would have to be charged at a 5-hour rate [$(e_b = 0.8$, equation (X-13)] at that altitude. Charge would decrease to a 10-hour rate $(e_b = 0.75,\ d = 0.15)$, and cycle life to 3600 or 3700, at an altitude of about 1,500 NM; to a 15-hour rate ($e_b = 0.7,\ d = 0.17$) and a cycle life of 2000 at most, at 3,700 to 3,800 NM; and, to the 20-hour rate (charge-discharge ratio 2.5, $d = 0.4$) at 11,000 to 12,000 nmi with a cycle life requirement of just under 700. If it were mandatory to operate the same size battery at the synchronous altitude, depth of discharge would be roughly 29 percent, from Equation (X-18), it is found that to maintain H at 20 hours, the charge-discharge ratio would climb to 4 (i.e., $e_b = 0.25$).

This example demonstrates the manner in which Figure X-8 displays the variation of some of the key altitude-dependent parameters of a storage battery. These parameters are significant in selecting either a particular battery type of a given size to cover the entire altitude range of interest, or different battery types and sizes for various altitudes, and pave the way for a detailed weight tradeoff study.

As a general observation, it can be said, based on the trends demonstrated in Figure X-8, that although the Ag-Cd battery is lighter than a Ni-Cd battery of the same electrical size, its use under conditions of varying altitude, due to its other operating characteristics, is somewhat less flexible. At low altitudes, the cycle life is long and requires a larger design margin (lower discharge depth) or more frequent replacement. High charge acceptance, including protective electronics of appropriate complexity, is also required in order to show a significant weight advantage over Ni-Cd at altitudes below 1,000 to 2,000 NM. Also, at the lowest altitudes, the efficiency of a Ag-Cd battery will tend to be lower with a resulting requirement for a larger array.

(5) Tentative Selection of the Battery

It is assumed that the reasoning developed in the preceding sections serves to accurately identify trends in line with the overall objectives of this parametric study. The selection of the battery, as a result of the parametric study approach of Paragraph X. B, cannot, therefore, be regarded as final, since it is not based on either complete information pertinent to the mission or an exhaustive amount of knowledge of the environment to which the battery would be subjected.

Nevertheless, let it be assumed for the present that it is generally preferred to select a reliable, lightweight, single-size battery to operate at all altitudes (within the range of interest) with a given load profile. In principle, either type battery (Ni-Cd or Ag-Cd) could be selected; however, this choice is considered to be beyond the scope of this discussion.

To proceed with the study, let the type of battery selected be Ni-Cd. The lightest-weight nickel-cadmium battery that appears to be feasible is labeled "0.6C" in Figure X-8; its charge rate is within the 3- to 20-hour rate, the per-year cycle life is 5700 cycles or less, with a discharge depth of 25 percent under peak cycle life conditions. Exact variation is shown in Figure X-8, with H and e_b plotted separately in Figure X-10.

From Figure X-9, the electrical size of the tentatively selected battery is of the order of 2.8 watt-hours per watt at load, arrived at by dividing the ordinate of Figure X-9 by the corresponding d factor of a 0.6C-size battery (Figure X-8).

(6) Conclusion

In addition to outlining an approach to the selection of a battery over a range of altitudes, a typical battery has been selected. Plot of e_b given in Figure X-10 permits inclusion of the effects of the trend exhibited by the charge requirements of a Ni-Cd battery on the source of energy employed.

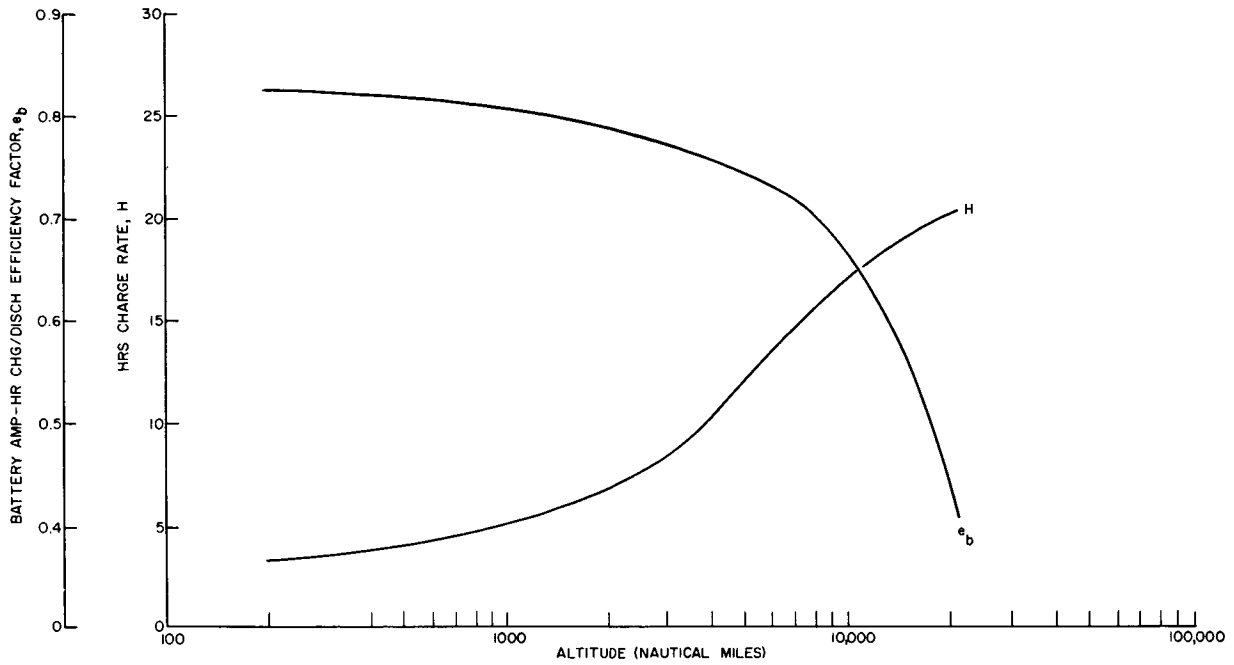

Figure X-10. Typical Variation of Charge Parameters with Altitude, Ni-Cd Battery

d. SYSTEMS-EFFICIENCY TRADEOFFS

(1) Introduction

This portion is concerned with the numerical evaluation of equations developed earlier in this Section for four specific power-system configurations. These equations can be considered as expressions of efficiency to the extent that they relate the size of the array required (P_s) to the load requirement described by P_{Ln}, R, f_d, and f_n.

Definition of the charge requirements assumed in Figure X-10 permits calculation of the solar array required as a function of altitude with a nickel-cadmium battery used in each system.

Generally speaking, the type of power system requiring the least array is considered most desirable, assuming the equality of other factors such as ease of hardware implementation and general mission compatibility.

(2) Solutions of Equations

Solutions for P_{sso}, P_{sst}, P_{spo}, and P_{spt} have been performed by a computer for the following specific conditions:

(a) For a 5-kW system

$$R = \frac{5 + 3.22}{5} = 1.65,$$

where 5 kW is P_{Ln} and where 3.22 kW is the added daytime ECS/Life Support (O_2 regeneration) load in the stated 200 NM-altitude mission. This added load is 2.09 kW at synchronous altitude. An altitude-dependent inverse relationship is apparent, but, since this relationship was unknown at in-between altitudes, the worst case of 3.22 kW was used for all altitudes. (Note: the P_s array output calculations are on the high side by up to about 1.4 to 1.5 kW at the high end of the altitude range.)

(b) Similarly, for a 10-kW mission, P_{Ln} equals 10;

$$R = \frac{10 + 3.22}{10} = 1.322.$$

(c) For the Ni-Cd battery, a V_{Bc}/V_{Bd} ratio of 1.5/1.2 yields 1.25. Some error is introduced by assuming this to be a constant factor for all rates of charge. However, it is seen from Figure X-8 that, generally, the higher the charge rate, the lower the discharge depth. This tends to maintain the voltage ratio reasonably constant. The e_b versus altitude relationship is as shown in Figure X-10.

(d) For the Ag-Cd battery, a V_{Bc}/V_{Bd} ratio of 1.50/1.05 yields 1.43, (if this type of battery is included in the tradeoff study at a later date).

(e) For various fractions f_d and f_n, each ranging from 0 to 1.0.

All calculations were performed assuming unity k factor. It is recalled that this factor relates the average array power output in a tracking system to that of a non-tracking system, and depends on the array temperature extremes, duration of the thermal transient relative to total daylight duration per orbit, and the type of solar cell used. Evaluation of the approximate k value will be made later in this Section; at this point, however, it will be understood that the numerical comparisons presented do not include the beneficial effects of the array-power up-swing illustrated in Figure X-3.

(3) Discussion of the Array Power-versus-Altitude Plots

The curves referred to are given in Figures X-11, X-12, X-13, and X-14.

All show the same trend in decreasing array-power requirement as altitude increases, since the fractional time in the sun increases faster than the corresponding time in the dark

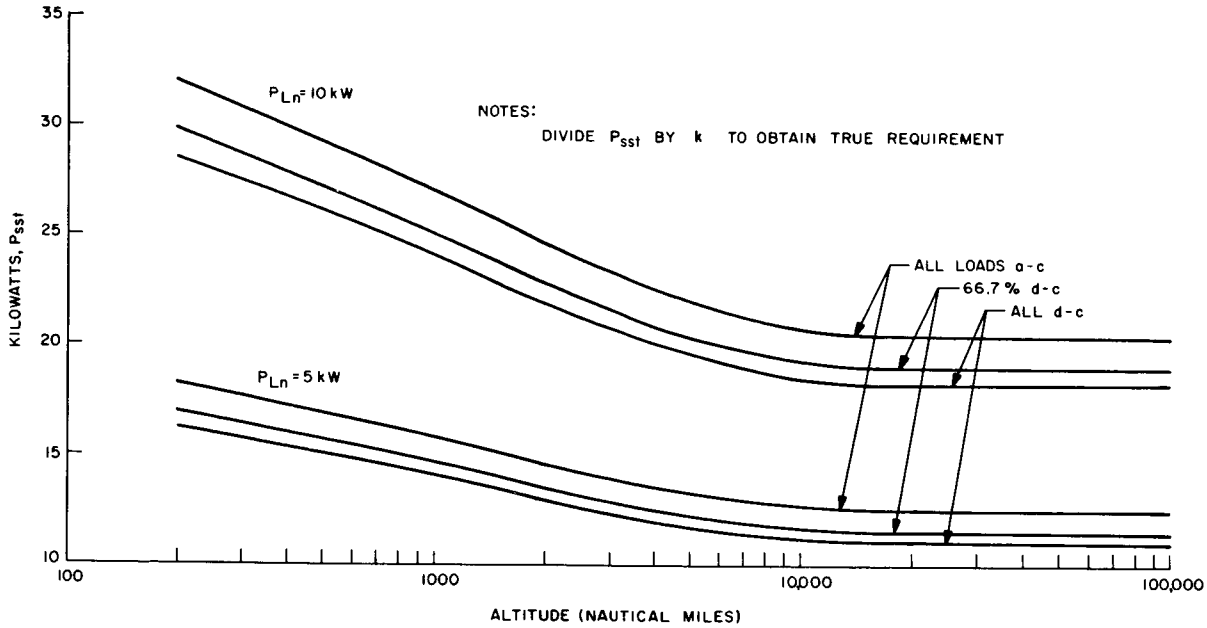

Figure X-11. Non-Tracking Series System with Ni-Cd Battery

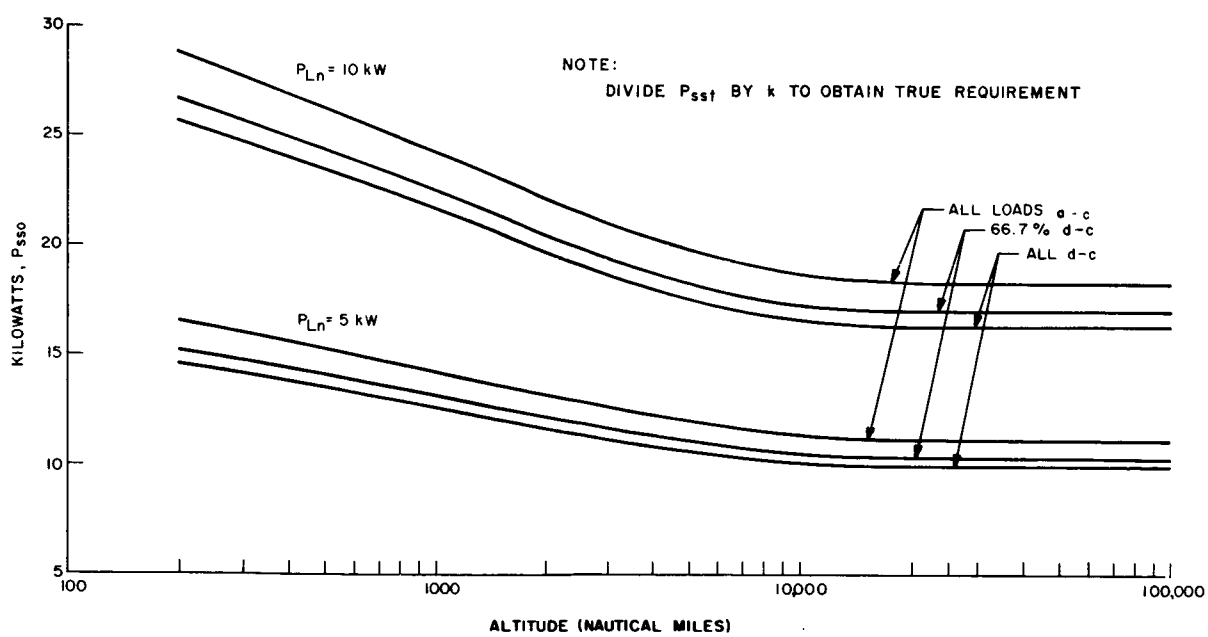

Figure X-12. Tracking Series System with Ni-Cd Battery

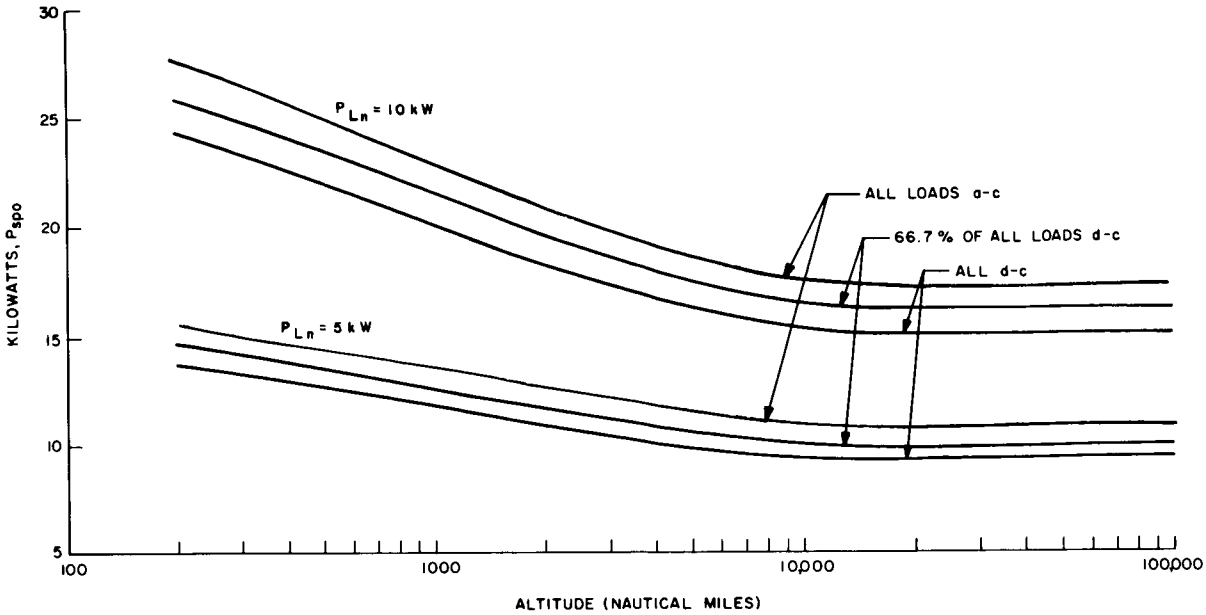

Figure X-13. Non-Tracking Parallel System with Ni-Cd Battery

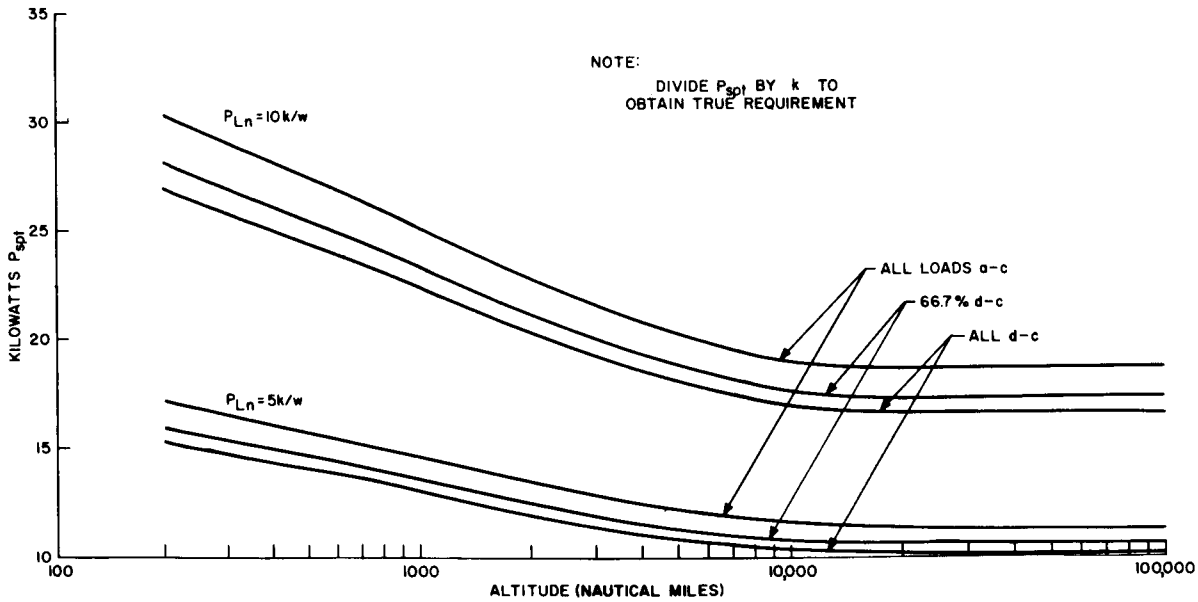

Figure X-14. Tracking Parallel System with Ni-Cd Battery

and since the available charge time is greater at higher altitudes. The rate of decrease of array power with altitude is smaller at higher altitudes. This is due to the nature of the (1-a)/a variation (Figure X-7 and since, in a Ni-Cd battery system (unlike the Ag-Cd battery system), the charge efficiency decreases as the charge time is increased.

At the higher altitudes, a point is eventually reached where the combination of the charge efficiency, e_b, and the available time to charge produces the lowest desirable charge rate (this was assumed to be H of 20 hours for the nickel-cadmium battery and corresponds to an altitude of about 21,000 NM as shown in Figure X-8 for the particular fixed-size battery selected). Therefore, at higher altitudes, this rate of charge must be maintained, at least when there are periodic discharges. This accounts for the flatness of the curves beyond that altitude in Figure X-11, X-12, X-13, and X-14.

Plots for each system are prepared for the condition of f_d equal to f_n in each case, in order to show extreme conditions of a-c/d-c load division. The assumed probable a-c/d-c apportionment mentioned earlier is also plotted. It is seen that as the percentage of the load power delivered at ac increases, more array power is required, since the efficiency of a regulated inverter is lower than that of a PWM d-c voltage regulator.

(4) Discussion of the Power Ratios

(a) General

The power ratios plotted in Figures X-15, X-16, and X-17 apply to the specific condition of:

$$f_d = f_n = 0.667,$$

and reflect the most typical voltage-load requirements in line with the assumption made earlier in this Section. As previously stated, any other combination of the "f" ratios can, of course, be assumed and corresponding power ratios calculated. All would reflect the same basic trends as those shown.

(b) Systems Comparison

Since there are four systems to be compared, six distinctly different power ratios are possible. For a complete discussion, these will be placed in three separate categories and discussed accordingly.

1. Power Ratios of Series-to-Parallel Systems

Two sets of curves are plotted, one for tracking and one for the non-tracking systems. The obvious conclusion drawn from Figure X-15 is that the series systems are less efficient than the parallel systems, requiring anywhere from 4 to 6 percent more array power in the non-tracking configuration and 6 to 10 percent in the tracking configuration. Basically, the daytime operation of a series system is less efficient than that of a parallel system. This, in substance, wholly accounts for the trends later explained in greater detail.

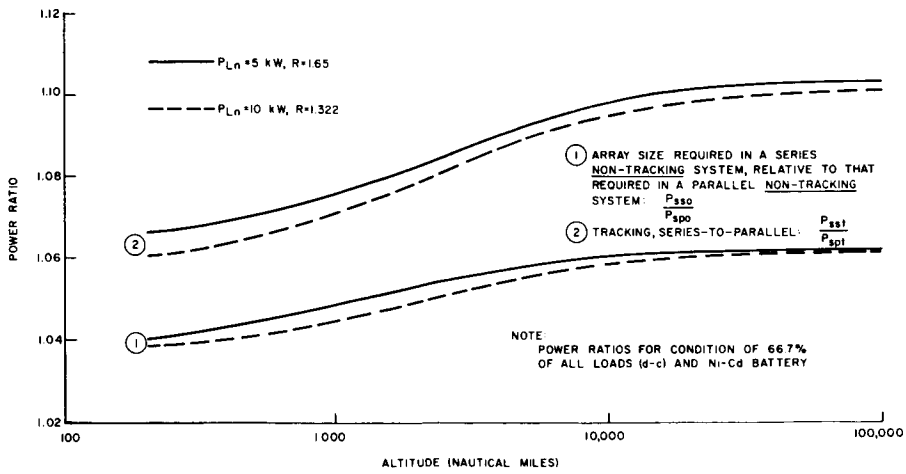

Figure X-15. Power Ratios for Series and Parallel Systems

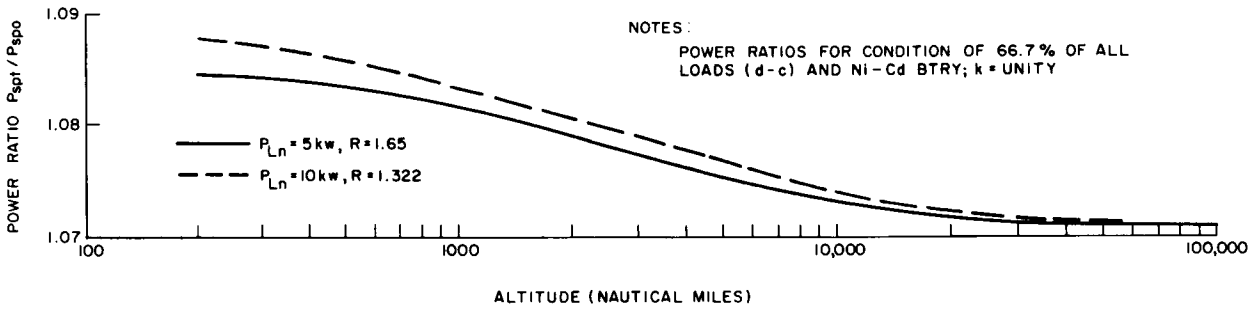

Figure X-16. Power Ratios for Tracking and Non-Tracking Parallel Systems

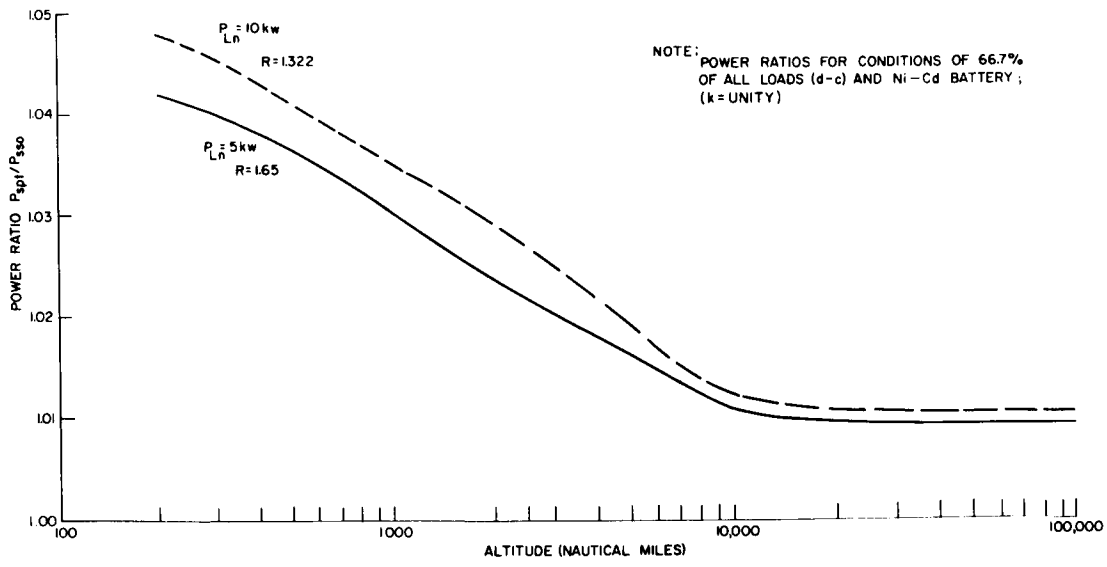

Figure X-17. Power Ratios for Parallel Tracking to Series Non-Tracking System

With increasing altitude, the fractional time in the sun is increasing, and a series system becomes less efficient by comparison with its parallel system counterpart. This is explained by considering the following.

Both non-tracking systems, Figures X-4 and X-6, are essentially identical during dark time. In either case, the d-c bus is supplied by a PWM regulator, and the a-c bus by the inverter. During daytime, the operation is different in that the parallel system does not require a d-c regulator and is thus more efficient. It follows that the longer the relative daytime duration (i.e., the higher the altitude), the more efficient the parallel system. Stated a different way, the P_{sso}/P_{spo} ratio increases with altitude as shown in Figure X-15 (curves labeled "1"). The same basic trend with altitude is exhibited by the curves labeled "2" for the tracking systems, but for a different reason. In a series tracker, Figure X-5, all of the array power is subject to the tracker loss, whereas only a part of that power is handled by the tracker unit in a parallel tracker system. Consequently, the longer the relative daytime duration (the higher the altitude), the greater the proportional amount of the total array energy lost in the tracking mechanism of a series system, and the higher the ratio P_{sst}/P_{spt}. Both sets of curves ("1" and "2") show that the larger the relative daytime load (the larger the ratio R), the more efficient the parallel system. To illustrate the point for the non-tracking system, assume for the moment that R is infinite; in other words, there is no dark-time load. Then all the d-c load is delivered by the parallel system, Figure X-6, directly from the array, causing the energy transfer efficiency to be very high. The series system delivers all the dc to the load through a series PWM regulator with relatively lower resultant efficiency. Figure X-15 reflects this point since for the larger R assumed for the 5-kW system, the series system performs slightly less efficiently than for the somewhat lower R in the 10-kW system. The difference between the dotted and solid curve is, of course, overshadowed to some extent by the continuous precence of the inverter load. Similarly in the tracking systems, the larger R dictates a lower series systems efficiency; relatively speaking, more daytime power is required, increasing proportionally the amount of array power lost in the series tracker.

It is seen that, at very high altitudes, all the curves in Figure X-15 tend to flatten and approach a certain value asymptotically. At very high altitudes,

$$\frac{1 - a}{a} \longrightarrow 0.$$

Substituting this and f_d equal to 0.667 (condition for which all curves in Figure X-15 are drawn) into equations X-6 and X-10, and taking a ratio,

$$\frac{P_{sso}}{P_{spo}} \approx 1.065$$

as $(1 - a) \rightarrow 0.$

This is the value both curves for the non-tracking systems would approach at infinite altitude, with 33 percent of all power delivered at ac. In a similar manner, it can be shown that

$$\frac{P_{sst}}{P_{spt}} \approx 1.11$$

as $(1 - a) \rightarrow 0$, which is exactly equal to the inverse of the assumed average series tracker efficiency factor, e_m.

2. Power Ratios of Tracking and Non-tracking Systems

Examination of equations (X-5) and (X-7) should show that, for k equal to 1, the ratio P_{sst}/P_{sso} equals the inverse of the average series tracker efficiency factor e_m (assumed as 0.9) regardless of altitude (other factors remaining the same). Factor k must therefore exceed 1.11 in order to warrant the use of a series tracker when comparing it with a non-tracking series (PWM Regulator) system.

The ratio P_{spt}/P_{spo}, plotted in Figure X-16, is altitude-dependent. The curve is presented for k equal to 1. In so doing, the ordinate becomes the "break-even" value of which must be exceeded at each altitude in order to produce a net decrease in the array size, through the use of a parallel tracker. The value of the ratio in question (i.e., the required minimum value of k) is seen to decrease as altitude is increased. This is true, since as the relative amount of energy delivered to the load by the battery is decreased (which occurs with increasing altitude), less of the total array energy is subject to the loss incurred in the parallel tracker unit. The same reasoning can be applied to different R values; a lower R means a greater percentage of the total energy delivered to the load by the battery. The dotted curve, therefore, appears slightly above the solid curve in Figure X-16. The limiting value of the P_{spt}/P_{spo} ratio is 1.07 when k equals unity and 66.7 percent of all loads are d-c.

3. Power Ratios of Unrelated Tracking and Non-Tracking Systems

This curve shows the ratios of the tracking parallel system to a non-tracking series system.

Since the ratio for a tracking series system to a non-tracking parallel system is arrived at by multiplying $[P_{sst}/P_{sso} = 1.11]$

by $[P_{sso}/P_{spo}]$ (plotted in Figure X-15), it is not plotted in Figure X-17. The ratio P_{spt}/P_{sso} is plotted, since it exhibits an altitude-dependent variation of its own. Agains, as in Figure X-16, k equals 1 and the ratio values plotted are equal to the break-even values of k required. The basic trends followed by the curves in Figure X-17 are the same as those in Figure X-16 for largely the same reasons. The limiting values of the ratio plotted is unity.

(5) Conclusions

It can be concluded that a parallel type system, either tracking or non-tracking, is more efficient in that is requires anywhere from 4 to 10 percent less array power compared to its series - type counterpart. From the point of view of systems efficiency, the choice between a tracking and a non-tracking system depends entirely on the thermal and optical properties of the solar cells and on the mechanical design of the array, all of which determines the k factor at a given altitude. Depending on the altitude and on which two systems are compared, this factor must be anywhere between unity and about 1.19 (for the assumed a-c/d-c load split), in order to realize a reduction in array size through the use of a tracking system. The material to follow will examine certain specific design aspects at two typical orbit altitudes.

e. EFFECTS OF THERMAL DESIGN ON SYSTEMS CHOICE

(1) General

The thermal aspect to be examined is that of solar-cell temperature as it affects two significant items.

One of these is the duration of the transient temperature variation observed upon emerging from the earth's shadow which determines the value of the orbit-average array maximum power delivered by the solar array into a tracking system. The other is the minimum-to-maximum solar-cell temperature swing, which is related to the choice of the solar-array unregulated bus voltage in certain power systems. Both will be examined in this section on a parametric study basis at two typical altitudes.

(2) Temperature-Time Profiles and Evaluation of Factors "k"

Variation of the solar-cell temperature with time in orbit has been estimated for the 200-nmi and the synchronous-altitude orbit conditions, assuming minimum sun time in each case. A plot of the temperature variation for the 200-nmi orbit is shown at the right in Figure X-18. The assumptions made were as follows:

- Emissivity: front, 0.82

  back, 0.89

- Absorptivity: front, 0.78

  back, 0.20

- Specific heat of the array assembly with an aluminum substrate, $\frac{380 \text{ watt-sec}}{\text{lb-}^\circ\text{C}}$.

- earthshine, neglected at synchronous altitude

- albedo, neglected throughout.

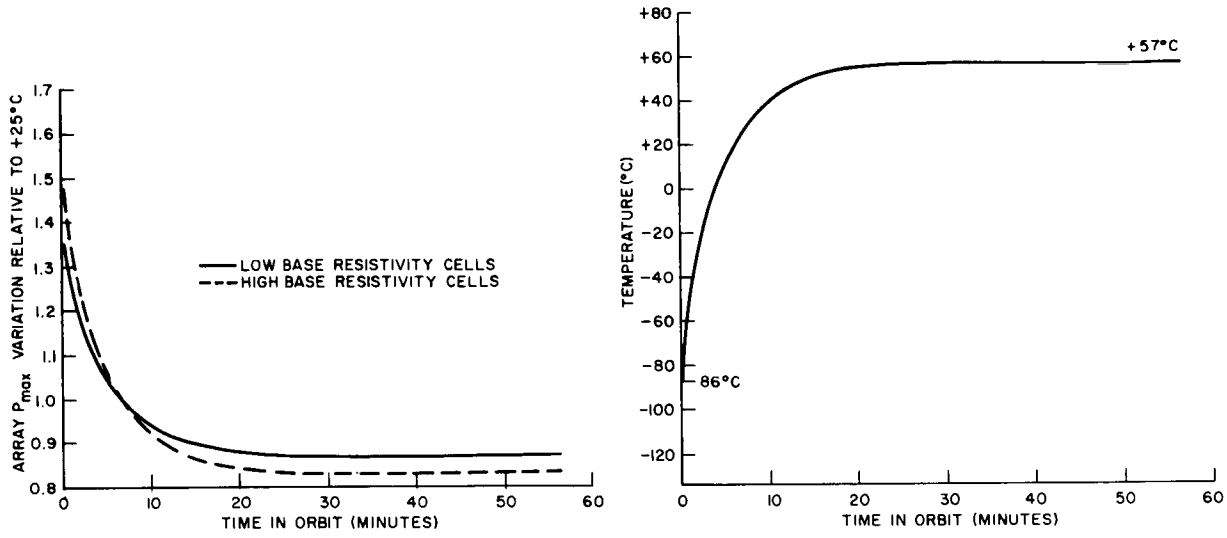

Figure X-18. Relative Solar-Array Output

Temperature variation, particularly the initial transient, is of importance because of its effect on the instantaneous variation on the P_{max}* of a solar cell. Two different types of N-P silicon solar cells will be investigated with the following assumptions:

(a) Low base resistivity cell (typically 1 ohm-cm):

- Maximum-power-point voltage V_{max} of 0.46 volt at +25°C.
- Voltage-temperature coefficient at V_{max} is $-0.0022 \frac{\text{volt}}{°C}$
- $\alpha_1 = \frac{0.0022}{0.46} = -0.0048$ per °C rise

(b) High base-resistivity cell (typically 10 ohm-cm):

- Maximum power point voltage V_{max} of 0.44 volt at 25°C
- Voltage-temperature coefficient at V_{max} is $-0.00265 \frac{\text{volt}}{°C}$
- $\alpha_{10} = 0.006$ per °C rise.

*Maximum power

The preceding voltage-temperature coefficients apply more nearly to radiation-degraded cells, while the V_{max}'s are undergraded values. The computed α's will be slightly on the low side by an amount determined primarily by the charged-particle radiation damage.

The current-temperature coefficient β is assumed to be the same for both type cells, viz:

$$\beta = +0.001 \text{ per °C rise.}$$

It is also assumed that coefficients α and β are constant over the temperature range considered.

Using subscripts "25" to denote the value at +25°C, and "T" at any temperature T,

$$I_T = I_{25} \ (1 + \beta \Delta T), \tag{X-21}$$

$$V_T = V_{25} \ (1 + \alpha \ \Delta T), \tag{X-22}$$

where

$$\Delta T = T - 25°C. \tag{X-23}$$

It can then be shown that

$$\frac{P_T}{P_{25}} = 1 + (\alpha + \beta) \Delta T + \alpha \beta (\Delta T)^2 \tag{X-24}$$

Substituting numerical values α and β into equation (X-24), the power ratios are

for the low base-resistivity cell,

$$r = 1 - 3.8 \times 10^{-3} \Delta T - 4.8 \times 10^{-6} \Delta T^2 \tag{X-25}$$

and, for high base-resistivity,

$$r = 1 - 5 \times 10^{-3} \Delta T - 6 \times 10^{-6} \Delta T^2 \tag{X-26}$$

Equations (X-25) and (X-26) are plotted in Figure X-18. A planimeter was used to determine the values of k for the 200-nmi orbit. These are:

for a low base-resistivity cell array,

$$k = 1.05;$$

and for a high base-resistivity cell array,

$$k = 1.07.$$

Several comments may now be made. First although the computed values of k are relatively low, a significant amount of radiation degradation may lower considerably the assumed V_{max}

values, thereby raising the η's and k's (particularly for the low base-resistivity cell). And, second, the low base-resistivity cell, at a steady-state temperature of +57°C (predicted), produces nearly 5 percent more power, making it a desirable choice in all orbits where the radiation damage is low.

In the synchronous orbit, the predicted solar-cell temperature of an array of 0.8 pound per square foot varied from -138°C minimum to a steady-state value of +57°C* with 90 percent of the temperature rise upon coming out of the dark taking place in less than 20 minutes. Comparing this time interval to the minimum time in the sun (approximately 22.8 hours), it is clear that the resultant values of k would be very low indeed.

(3) Bus-Voltage Considerations

For all systems with the exception of the non-tracking parallel (direct energy transfer) system, a set of guidelines can be established for the unregulated bus voltage level selection:

(a) The minimum voltage must be compatible with the d-c regulated bus voltage of +28 volts as delivered by a PWM down-converter regulator, i.e., it must be no less than about 30 volts.

(b) The maximum voltage must not exceed the rating of the available semiconductor components. This might be within the 100- to 120-volt range.**

(c) Generally, a higher voltage level is more desirable, in order to reduce I^2R losses, to decrease the diode power losses, and to raise the regulator efficiency.

The nominal bus voltage swing will be determined by:

- The solar-array temperature swing as a function of altitude.
- Base resistivity of a silicon solar cell.
- Time-variant voltage degradation at P_{max} (due mostly to radiation), which is also an altitude-dependent factor.

In the direct energy transfer system, the bus voltage is fixed by definition and is usually equal to the desired d-c regulated voltage. The remaining discussion is, therefore, largely inapplicable to this type of a system.

---

* Equality of the steady-state temperatures at the two orbit altitudes is an approximation allowed for the purposes of the parametric study described in Paragraph X.B.

** Subsequent component studies showed the range to be 150 to 200 volts.

The highest possible bus voltage is determined by the beginning-of-life, coldest-array temperature condition of an unloaded array:

$$V_{u_{max}} = \left(1 + \Delta T_{max} \alpha\right) V_{oc} \tag{X-27}$$

This equation is a modification of equation (X-22). V_{oc} is the beginning-of-life open-circuit voltage of the array at +25°C, provided that ΔT is as defined in equation (X-23).

The lowest bus voltage is assumed to equal the maximum-power-point voltage at end-of-life at equilibrium temperature (+57°C); therefore $\Delta T = +32°$.

Then

$$V_{u_{min}} = d_v \, V_{mp} \, (1 + 32\alpha), \tag{X-28}$$

where V_{mp} is the array maximum-power-point voltage at the beginning of life at +25°C, and d_v is the voltage degradation factor relating $V_{mp}(1+32\alpha)$, i.e., the voltage value at +57°C, to that at end of life. At present, it is necessary to determine the total voltage swing throughout mission life. Expressed as a ratio, this is defined by

$$\frac{V_{u_{max}}}{V_{u_{min}}} = \frac{1 + \left(T_{min} - 25\right)\alpha}{1 + 32\alpha} \cdot \frac{V_{oc}}{d_v \, V_{mp}} \, . \tag{X-29}$$

The value of α and V_{mp} have previously been assumed. The following assumptions are added or restated:

V_{oc} : Low base resistivity, 0.58 volt per cell

High base resistivity, 0.56 volt per cell.

T_{min} : 200 NM orbit, -86°C

Synchronous, -138°C.

By making proper substitutions into equation (X-29), it is determined that the values of the ratio defined by that equation, for d_v equal to 1 and for d_v equal to 0.85 as an example, are as follows:

	200-nmi Orbit		Synchronous Orbit	
Base resistivity:	$d_v = 1$	$d_v = 0.85$	$d_v = 1$	$d_v = 0.85$
Low	2.3	2.7	2.66	3.15
High	2.62	3.08	3.12	3.67

It is thus apparent that the voltage swing can easily exceed three-to-one, particularly at higher altitudes. Based on that and other criteria set forth at the beginning of this analysis, the lower end of the voltage range must be minimized and made just large enough to provide adequate charge voltage (particularly in the tracking systems where the voltage swing is large by definition).

In the PWM Regulator system, shown in Figure X-4, if the unregulated bus voltage excursions are limited by one of several types of shunt devices, the bus voltage level can, of course, be set at any value within roughly 50 to 100 volts with the upper limit most probably determined by the reliability of the battery.

f. RELIABILITY ESTIMATE

Appendix F contains a quantitative reliability comparison of the four subsystem configurations considered in Paragraph X. B. 3. b. Comparison was based on equal load and reliability goal requirements.

Results of the comparison indicate that, to achieve an equal probability of success of 0.995 in each system, the parallel non-tracking system must contain the most electronic components, and the series tracking system the least. The series non-tracking and the parallel tracking systems would be approximately equal, from the viewpoint of electronics weight and complexity.

g. PEAK CHARGE RATES IN TRACKER SYSTEMS

(1) Introduction

Since the study is concerned with the tracking, as well as the non-tracking power systems, certain problem areas associated with the tracking-system approach must be discussed. One of the potential problems is the wide voltage swing. Another possible problem area is that of battery peak charge rates.

(2) Statement of the Problem

The typical values of charge rate H versus altitude, computed and reported in Figure X-10, are orbit-average. In a tracker power system, the additional array power generated immediately upon emergence from eclipse is assumed to be absorbed as battery charge. The resultant peak charge rate at that time will be significantly greater than the indicated average. Ability of the battery to absorb the charge at the initially high rate is a potential problem area.

(3) Discussion

The enclosed graph of Figure X-19 illustrates the variation of the peak-to-average charge current ratio with altitude for various daytime-nighttime load distributions. It is seen that, as the altitude and the daytime load increase, and the dark-time load decreases, the peak-to-average charge-current ratio increases.

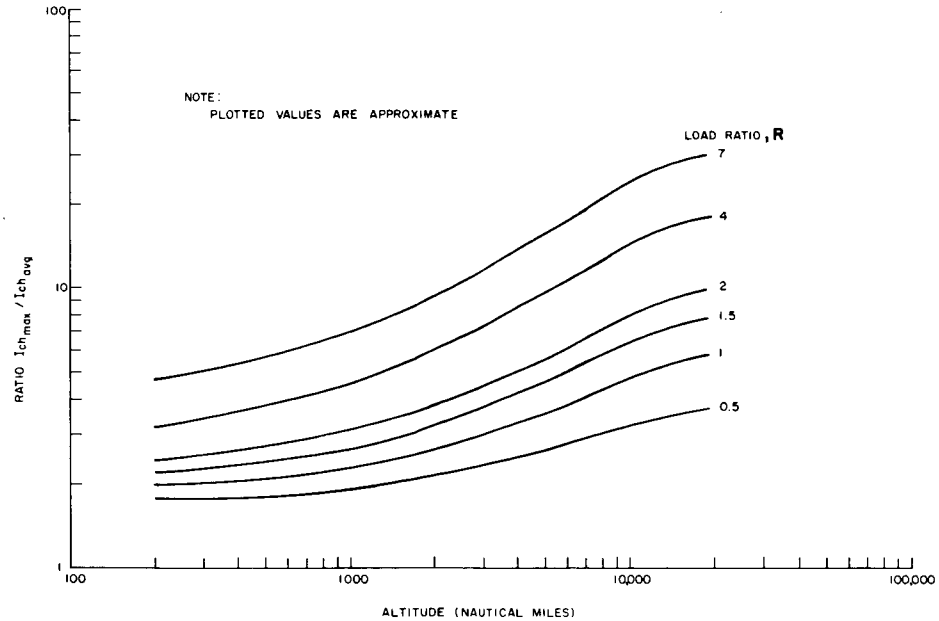

Figure X-19. Peak-to-Average Charge Ratios as a Function of Altitude for Ni-Cd Battery

The method for calculation of the ratios is given in Paragraph (5) of this section, including the extent of the approximations made. Calculations were made for the Ni-Cd battery, using the e_b-versus-altitude relationship assumed in Figure X-10, although the previous analysis permits a recalculation to be made for another set of numbers or for a Ag-Cd battery. It should be noted that the ratios for Ag-Cd will be somewhat lower than those shown in Figure X-19 for Ni-Cd.

Figure X-20 shows both the average and the maximum relationships of H versus altitude for the typical condition of R equal to 1.5; the average H variation is taken from Figure X-10. The maximum H values are obtained by simply dividing the average values by the ratios at corresponding altitudes as in Figure X-19.

Concerning the duration of the battery peak-rate charge, it can be said that it will be very short at end of life and will decrease exponentially to the average value within approximately 10 minutes at the lowest altitudes. At the beginning of life, the peak charge will persist for as long as the array can supply it or until it is limited by some form of a protective mechanism such as an ampere-hour meter or a voltage-temperature limit.

(4) Recommendation

Typical power requirements imply values for the power ratio R of approximately 1.5. Based on this value, it is recommended that the criteria of battery size versus altitude selection developed thus far be further amended to include the effect of the initially high charge rate, so that a sound storage-system design concept results.

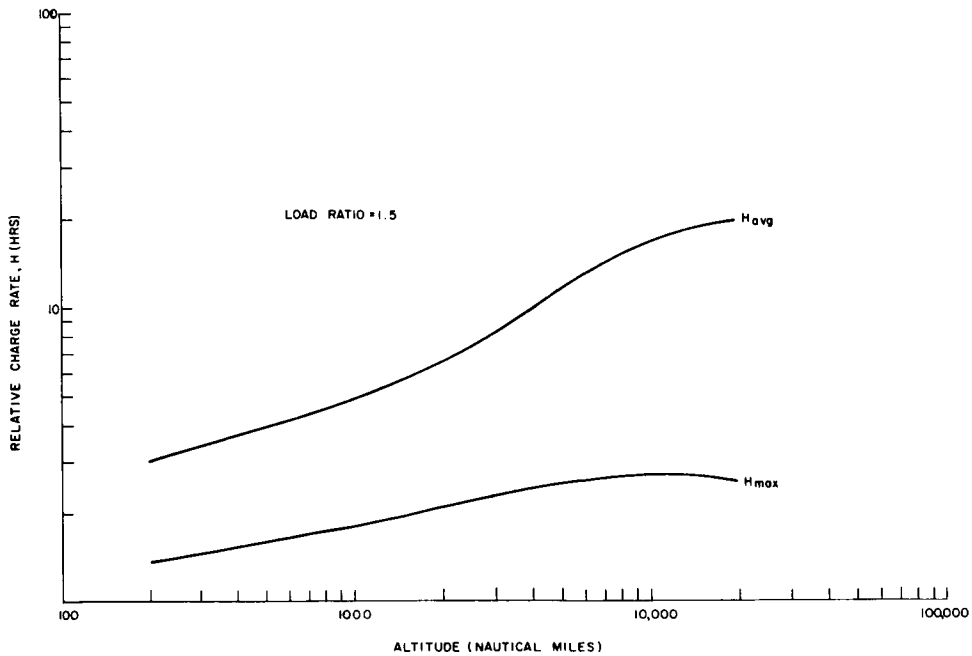

Figure X-20. Average and Maximum Charge-Rate Variation as a Function of Altitude for Ni-Cd Battery

It is noteworthy that, at lowest altitudes, the array power drops to about one-half of its peak value (measured from its steady-state level) within three or four minutes following emergence from eclipse. The recommended solution of the high-charge-rate problem, therefore, is to make provisions in the design of the charge electronics to reject a small part of the array energy contained within the peak by limiting the peak-charge rate.

(Subsequent computer studies showed that the rejection amounts to approximately one percent of the total array energy with the exact amount dependent on the specific input conditions. See Appendix B.)

(5) Calculation of $I_{cb_{max}}/I_{cb_{ave}}$ Ratios

It is desired to calculate the values of the ratio $I_{cb_{max}}/I_{cb_{ave}}$ for various cases of daytime/nighttime load distribution. The parallel tracker system will be used as a model in these calculations.

The approximate value of $I_{cb_{max}}$ (in a parallel tracker system) can be shown to equal

$$I_{cb_{max}} = \frac{1}{V_{Bc}}\left[\left(I_{cb_{ave}} V_{Bc} + P_{Ld}\right)\frac{P_{max_{peak}}}{P_{max_{ave}}} - P_{Ld}\right], \qquad \text{(X-30)}$$

where $P_{max_{peak}}$ is the array output at the lowest temperature measured at the maximum-power-point voltage.

Let the symbols r_H and r_P be defined as follows:

$$r_H = \frac{I_{cb_{max}}}{I_{cb_{ave}}}$$

$$r_P = \frac{P_{max_{peak}}}{P_{max_{ave}}}$$

Substitute the preceding values of r_H and r_P in Equation (X-30) and solve for r_H:

$$r_H = r_P + \frac{P_{Ld}}{I_{cb_{ave}} V_{Bc}} (r_P - 1) . \qquad \text{(X-31)}$$

In a tracking power system,

$$r_P = \frac{P_{max_{peak}}}{k P_{max_{s-s}}}$$

where $P_{max_{s-s}}$ is the steady-state-temperature value of the array maximum power. At lowest altitudes where the k values are likely to be largest, k is still only 1.05 to 1.07 (at least for an undegraded cell under the temperature-time profile conditions predicted, Figure X-18. For other altitudes, the k factor is unknown at present. For the present purposes, let it be assumed that k equals 1.

(Note: this assumption will cause the r_H ratios to be calculated to be slightly on the high (pessimistic) side.) Thus,

$$r_P \approx \frac{P_{max_{peak}}}{P_{max_{+57°C}}} , \qquad \text{(X-32)}$$

since the predicted steady-state solar cell temperature is +57°C. To calculate specific values of r_P, solar-cell base resistivity must be assumed. Low base resistivity will be assumed, because:

- It is a likely choice because of probable low radiation in the specified orbits, and
- It delivers roughly 5 percent more power at the predicted steady-state temperature.

Based on equation (X-25) (which is written for a low-base-resistivity solar cell), it can be shown that the value of r_P as expressed by equation (X-32) is

$$r_P = 1.14\left[1 - 3.8 \times 10^{-3} (T_{min} - 25) - 4.8 \times 10^{-6} (T_{min} - 25)^2\right] . \qquad \text{(X-33)}$$

A further inaccuracy is introduced by equation (X-33) since it is written for a non-degraded cell. This puts the computed ratios r_P and r_H slightly on the low (optimistic) side. Furthermore, equation (X-25) was written assuming the cell voltage and current temperature coefficients linear down to the lowest cell temperatures, an assumption which contributes to the r_H ratios being on the high side.

In equation (X-31), the product ($I_{cb_{ave}} V_{Bc}$) is the average battery charge power and is equal to:

$$I_{cb_{ave}} V_{Bc} = \frac{P_{Ln}}{e_{ave}} \cdot \frac{V_{Bc}}{V_{Bd}} \cdot \frac{1-a}{a} \cdot \frac{1}{e_b} . \qquad \text{(X-34)}$$

In equation (X-34), e_{ave} is assumed to be the average a-c and d-c load regulator efficiency. Let $e_{ave} = 0.85$. Ratio V_{Bc}/V_{Bd} will be taken as 1.25 for Ni-Cd batteries, and 1.43 for Ag-Cd. Substituting these into equation (X-34), and substituting the resultant expressions into equation (X-31),

$$r_H = r_P + \frac{R}{1.47 \frac{1-a}{a e_b}} (r_P - 1), \qquad \text{(X-35)}$$

The expression for Ag-Cd batteries differs only in that the constant 1.47 is replaced by 1.68. In either case, R equals P_{Ld}/P_{Ln}.

Table X-3 contains the various quantities necessary to calculate ratios r_H for a Ni-Cd type battery. The first column is the altitude, followed by the orbital parameter (1-a)/a for the worst-case dark-time condition. The factor e_b is taken from Figure X-10. The next column is the minimum solar cell temperature, T_{min}, for the longest dark-time duration at each altitude. Next is the r_P ratio calculated by using equation (X-33). Finally, the calculated r_H ratios are given, as in equation (X-35) for various values of daytime/dark-time load distribution expressed as ratio R.

4. Results and Conclusions

a. PURPOSE

This paragraph will bring into focus all of the more important considerations brought out in paragraph X. B and submit specific recommendations wherever possible.

b. CHOICE OF COMPONENTS

Specific recommendations in the component area are difficult to make at this time. Nevertheless, certain investigations covered in Paragraph X. B may be helpful in selecting the size and type of the required components. The choice between the low and high base-resistivity N-P silicon solar cell appears to be in favor of the former, provided the radiation-flux level is low. The 2-percent gain in the value of the k factor with a high base-resistivity cell is more than overcome by the 5-percent gain in the steady-state-temperature output-power level for a low base-resistivity cell.

Parametric studies summarized here have proved that a single-size nickel-cadmium battery is feasible, given a fixed set of power requirements and a range of orbit altitudes. Although specific studies were not attempted in the silver-cadmium battery area, preliminary studies showed that the feasibility of a single-size battery of this nature is questionable, since its use is restricted to certain altitudes and lifetimes.

TABLE X-3 CALCULATED VALUES OF r_H ($I_{ch_{max}}/I_{ch_{ave}}$)

Altitude (NM)	$\frac{1-a}{a}$	e_b (Ni-Cd)	T_{min} ^oC *	r_H					
				R = 0.5	R = 1	R = 1.5	R = 2	R = 4	R = 7
200	0.645	0.82	-76	1.77	1.97	2.19	2.42	3.32	4.67
400	0.542	0.815	-78	1.8	2.07	2.34	2.61	3.69	5.31
1,000	0.392	0.8	-83	1.92	2.3	2.68	3.05	4.57	6.83
2,000	0.277	0.782	-89	2.11	2.65	3.19	3.73	5.89	9.14
4,000	0.181	0.751	-98	2.43	3.26	4.09	4.93	8.26	13.26
10,000	0.092	0.66	-114	3.19	4.74	6.29	7.84	14.04	23.34
19,300	0.052	0.45	-130	3.68	5.68	7.68	9.68	17.68	29.68

* for 1 lb/ft^2 array

c. POWER-SYSTEM CONFIGURATION SUMMARY

Tradeoff studies showed that, from the point of view of efficiency, the parallel systems are more desirable than the series systems, (although differences are small), partly because of the presence of the a-c bus. There are, however, other factors that affect the choice of a power-system configuration. Let the non-tracking systems be examined first.

The non-tracking parallel (direct energy transfer) system, Figure X-6, has the advantage of the highest efficiency (i.e., the smallest required array size), It has, however, the following serious disadvantages:

(1) It requires an added "black box" to handle high power dissipation. In addition to the PWM regulator, inverter, and either a charge regulator or a tracker required by all other systems, a shunt regulator is mandatory in this case.

(2) It requires logic circuitry to operate the charge mechanism and the voltage regulator in proper sequence.

(3) Its array-bus voltage would be lowest, i.e., 28 volts. This results in the largest I^2R losses and/or bus-wire size, requires the regulators to have a larger input current handling capacity, and reduces somewhat the efficiency of regulation.

The series non-tracking (PWM Regulator) system, Figure X-4, has been shown to be only slightly less efficient than the parallel non-tracking system. Furthermore, its efficiency is only 4 percent lower at lowest altitudes, increasing slightly at the highest. But at the highest altitudes, the amount of array power required in general, is only about two-thirds of that needed at the lowest. By comparison with its "parallel equivalent", it can be concluded that the slightly lower efficiency of the PWM Regulator system is not particularly objectionable. This system has the following additional advantages:

(1) Extensive test data is in existence and many variations of the PWM system considered have been flown. This system has been subjected to a number of exhaustive analytical and breadboard studies.

(2) It is convertible to a parallel tracker system without a major reconfiguration if a tracker approach should be found more desirable for a specific mission.

(3) Greatest freedom exists in selecting the unregulated (array) bus voltage level. The system need not depend on the presence of extreme voltages at the bus.

For the reasons cited, therefore, the series non-tracker system appears to be more desirable since it more nearly meets the state of the art and flexibility goals.

Of the tracking systems, the series tracker offers no definite advantage over the parallel tracker, either in terms of complexity or efficiency. The choice is, therefore, largely

between the series non-tracking and the parallel tracking systems. To illustrate the efficiency comparison more clearly, the plots of their power ratios have been included in Figure X-17. The ordinate of that plot is the "break-even" value of k required for the parallel tracking system to be equally efficient. It has been shown parametrically that the "k" value is of the order of 1.05 to 1.07 at 200 nmi, and only slightly greater than unity at the synchronous-orbit altitude, which is in keeping with the trend exhibited in Figure X-17. This is to say that, as far as the required array size is concerned, the efficiency of the series non-tracking system is, at its best, very nearly the same as that of the parallel tracker at these two altitudes.

d. SELECTED SYSTEM CONFIGURATION

Finally, the following points must be made clear in choosing between the parallel tracking and the series non-tracking systems approach. Hardware implementation of a series non-tracking system will require a PWM charger to reduce thermal dissipation at the beginning of life and during the array thermal transient. A dissipative charger commonly used in low-power systems would have to be designed to dissipate many kilowatts for the load powers specified and would not, for this reason, be a suitable choice. The advantage of a higher orbit-average charger efficiency assumed in equation (X-4) of Paragraph X.B.3.b (2) would therefore no longer hold. This results in the required array size being very nearly equal to that for a parallel tracker system for k equal to unity. Also, a tracking system, compared to a conventional non-tracking approach, requires a less critical match between the solar array voltage and the remainder of the power system. This adds a measure of design flexibility.

The logical conclusion is that if both systems use a PWM charger, the array size required in the parallel tracker is always lower. If so, and assuming that the major problems to be encountered in the hardware-implementation phase of a high-power system of either type are more or less the same, the parallel tracker of the type presently under development for the Nimbus program appears to be the most logical choice for a variety of manned, earth-orbiting missions.

C. COMPONENT STUDIES

1. Introduction

Component studies have been undertaken in three broad areas, e.g., solar-cell arrays, batteries, and electronics. In all three areas, a detailed analysis of the electrical characteristics has been made, followed by electromechanical designs involving layouts, packaging, bus-bar interconnections, and other peripheral hardware, in order to arrive at accurate and practical estimates of the areas, weights, and volumes involved.

Preliminary designs of all the major components have been prepared, except in certain isolated cases where (1) the hardware involved was clearly well within the state of the art and its detailed treatment would not, therefore, contribute to the existing knowledge; or (2) where a detailed design effort is currently in progress elsewhere in the industry, as is the case with the static inverter.

The contents of this portion of Section X include the description and source of the raw component data used, identify the design and analysis techniques employed in the definition of the major components, and provide a source of the final data stored in the computer program (Paragraph X. E. 2. b(3)) used to evolve specific systems designs.

2. Solar Array

a. PARAMETRIC OPTIMIZATION

(1) Introduction and Background

This paragraph contains the results of a tradeoff study concerned with the determination of the optimum combination of the electrical, mechanical, and thermal parameters of the solar array.

One of the most significant variables involved is the minimum array temperature. This may be, under certain worst-case conditions, lower than -120°C (the lowest temperature to which an array assembly has been qualified at RCA). The worst-case condition is the synchronous-altitude orbit, primarily because at that altitude the spacecraft would encounter the longest dark-time duration, resulting in the lowest end-of-dark-time array temperatures. For this reason, and to achieve a single array-design approach for all altitudes, the work reported is concerned largely with the worst-case orbit.

Since the lowest array temperature is mostly a function of the array back emissivity and weight for a given structural design approach, and since the back emissivity also dictates the in-sunlight steady-state solar-cell temperature (and, therefore, power output), it has been necessary to establish a quantitative relationship among all of these variables in order to define the major parameters of the lightest-weight array which could be design-implemented within, or close to, the existing state of the art.

By way of background, it is true that to raise the minimum array temperature to meet a certain state-of-the-art objective, either the value of the back emissivity must be lowered (thereby raising the in-sunlight temperature and lowering the power generated) or the array weight must be increased. In particular, the array weight (or rather, the array weight density in pounds per square foot) must be evaluated carefully in making temperature predictions. For instance, at least some of the alternate mechanical designs under consideration involve thin honeycomb substrates supported by structural members located several feet apart on the back side of the array. The weight density of the entire array of this nature, if used in temperature calculations, can be misleading in that considerably higher predicted values of the minimum temperature would result, since the weight of the structural supports is not distributed uniformly.

For the purposes of the parameter optimization, therefore, it has been necessary to define two different weight densities: the "effective thermal", or simply thermal weight per square foot (which is that of the assembled solar cells and substrate) and the usual weight density, based on the gross weight of the array. In the discussion to follow, one or the other will be referred to, depending on the particular purpose. Results of this work are described in terms

of the minimum array temperature, the array watts per "total" pound and the back emissivity. Certain conclusions have been drawn, and appropriate recommendations submitted, which are helpful in the selection of the best array configuration including all of its major parameters.

(2) Thermal Design

The solar-panel temperature was determined as a function of orbit altitude. The orbit used in the computation was circular with a 90° sun angle (angle of sun vector to the orbit normal). Effective thermal weight (weight of the solar cells and substrate less the structural frame) used was 0.459 pound per square foot. The cell properties of α at 0.76 and front emissivity ϵ_F at 0.83 and end-of-life solar-cell efficiency of 7.5 percent at 48°C, with α equal to 0.20 and back emissivity ϵ_b equal to 0.90 for the underside of the panel, were used as computation inputs.

Instantaneous values of albedo and earthshine (which vary continuously over an orbit) were computed on an RCA 601 computer for the 200 NM orbit, which is the altitude most subject to albedo/earthshine inputs. These values were subsequently inserted in a computer program that provides transient temperatures of orbiting bodies. A comparative program (which is applicable to a flat-plate configuration oriented to the sun) was run, using average values (Reference X-1) of albedo and earthshine at 200 NM. Comparison of these 200-nmi data is shown in Figure X-21, which indicates that the largest discrepancy observed between the two sets of calculations amounted to 5°C. The temperature-time profiles calculated subsequently were based on average values of earthshine and albedo, since the small amount of discrepancy did not appear to warrant the added complexity of a point-by-point calculation.

To provide the thermal data as a function of altitude, a computer program was run to yield temperature-time curves for nine orbit altitudes, viz., 200, 400, 600, 1000, 2000, 4000, 6000, 10,000 and 19,340 NM. The data obtained has been delivered for storage in the computer program (Paragraph X. E), and is shown graphically in Figure X-22.

(3) Array Analysis

Figure X-23 shows the minimum array-temperature variation in a synchronous orbit as a function of the thermal weight density (defined in Paragraph X.C.2.a.(1)) for various cases of the back emissivity as shown.

Figure X-24 contains a plot of the steady-state solar-cell temperature versus back emissivity, based on the thermal design analysis of the array in synchronous orbit. For the purposes of this study, it is necessary to show a typical plot of the per-cell steady-state power variation with back emissivity. As a typical model, a 2 x 2 cm, low-base-resistivity RCA Mountaintop cell (irradiated at a flux level of 10^{14} 1 MeV electrons per cm^2 equivalent) has been selected. It can be shown that a different 1-MeV flux level selected would not in any way alter the basic conclusions to be reached. As expected, the per-cell power capability is seen to increase as the back emissivity is increased.

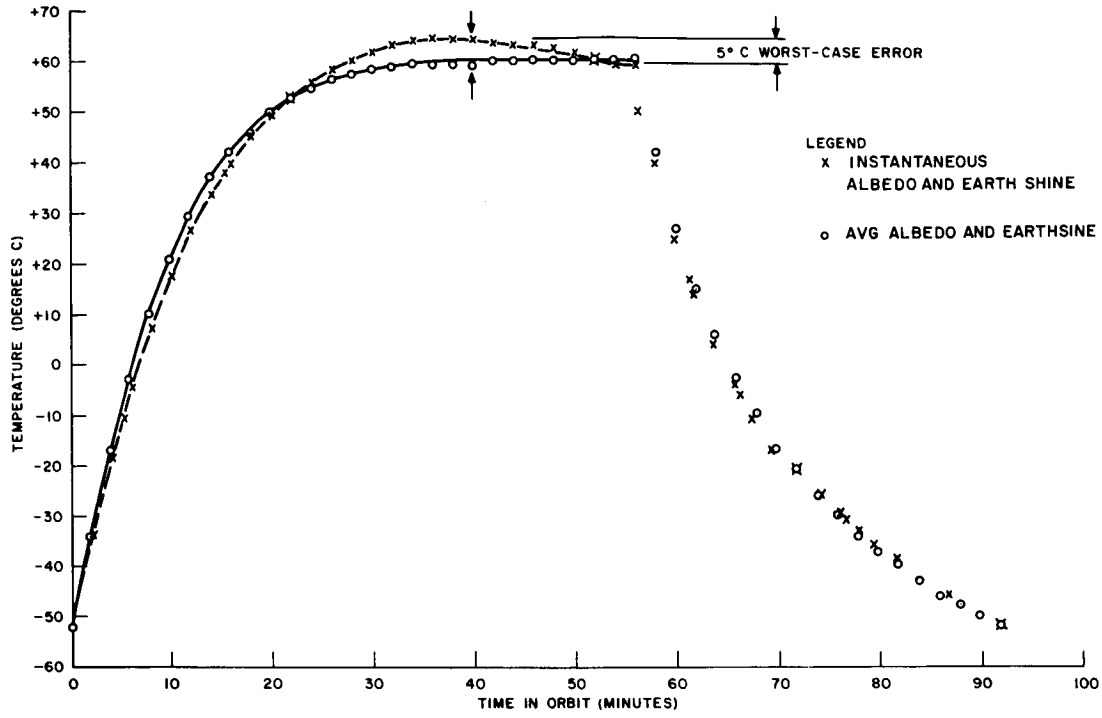

Figure X-21. Temperature Comparison

Figure X-25 is based on the preceding two sets of curves. It consists of plots relating the unique relationship of various parameters necessary to maintain the minimum temperature at a given value. Consider, for example, the -110°C curve. Figure X-23 shows that, if the back emissivity is 0.3, the uniformly distributed panel weight density used in a thermal calculation must be 0.92 pound per square foot to maintain a -110°C minimum. According to Figure X-24 if the back emissivity is 0.3 (which means a steady-state cell temperature of +81°C), the per-cell output capability is about 27.3 milliwatts. This is based on a 2x2-cm cell (roughly 220 per square foot) and yields $220 \times 27.3 \times 10^{-3}$ or 6 watts per square foot. Thus, the -110°C curve in Figure X-25 contains a point described by 0.92 pound per square foot and 6 watts per square foot.

One basis for evaluating a solar array is the watts produced per total array weight, including structural supports. Figure X-26 relates the thermal weight to the actual total array weight. The latter is, of course, greater than the former by the amount of the required supporting structure until the substrate thickness is great enough to provide that no additional structural support is required. It is realized that only certain discrete designs are possible and that, to an extent, it may be naive to draw a smooth curve through the three weight estimates. The study has proceeded based on the smooth curve, however, with the realization that a certain degree of inaccuracy may have been introduced.

A lower limit of feasibility has been assumed as 0.7 pound total array weight per square foot (this includes 0.4-pound-per-square-foot solar cells plus substrate). This may

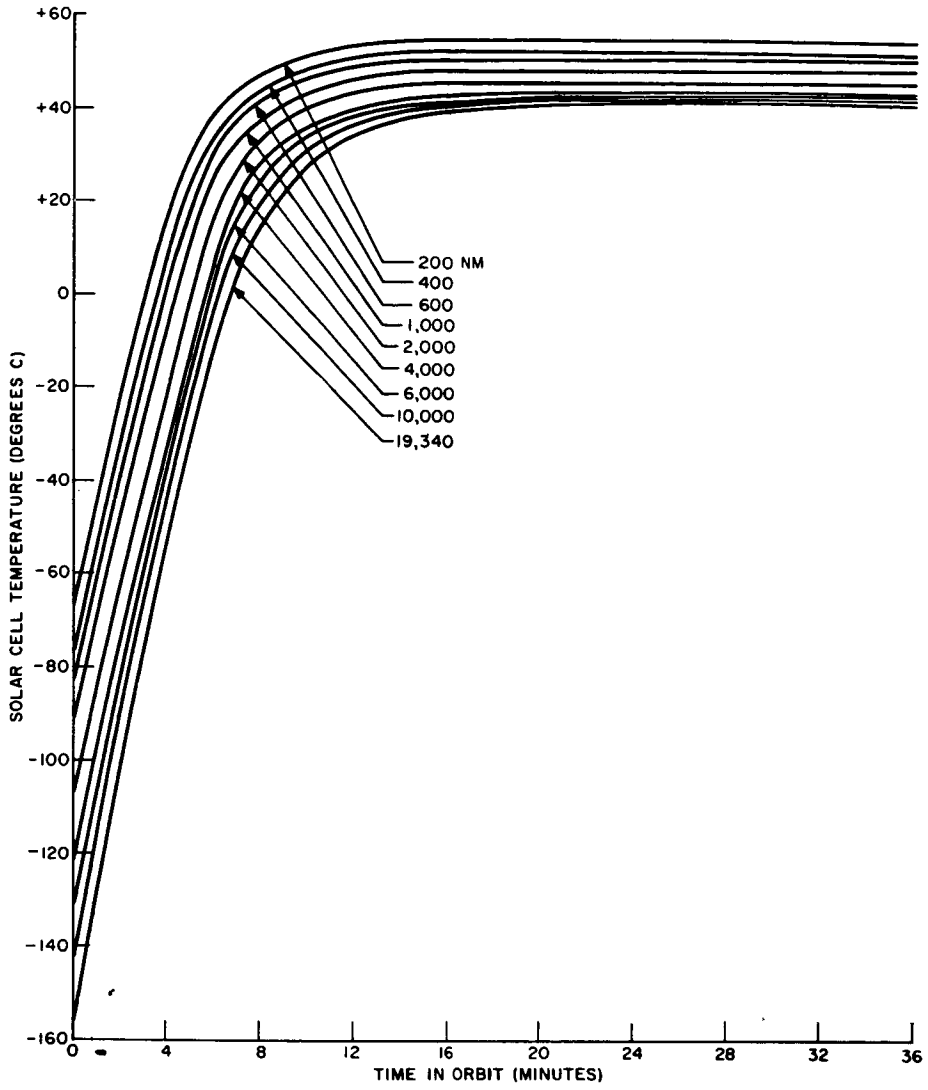

Figure X-22. Temperature-Time Transients vs. Altitude

correspond to a thin-cell design with minimal glass thickness and minimum substrate thickness designed to merely support the cells.

Similar to Figure X-25 in content, Figure X-27 is different in that it describes the conditions to be met in order to maintain a given minimum temperature based on actual or total array weight, rather than the partial weight needed for thermal calculations.

Consider again the -110°C curve. Based on Figure X-23, for a back emissivity of 0.3 the "thermal" weight density is still 0.92 for -110°C. This requires total array weight of 0.94 pound per square foot, according to Figure X-26. It has also been established, as in

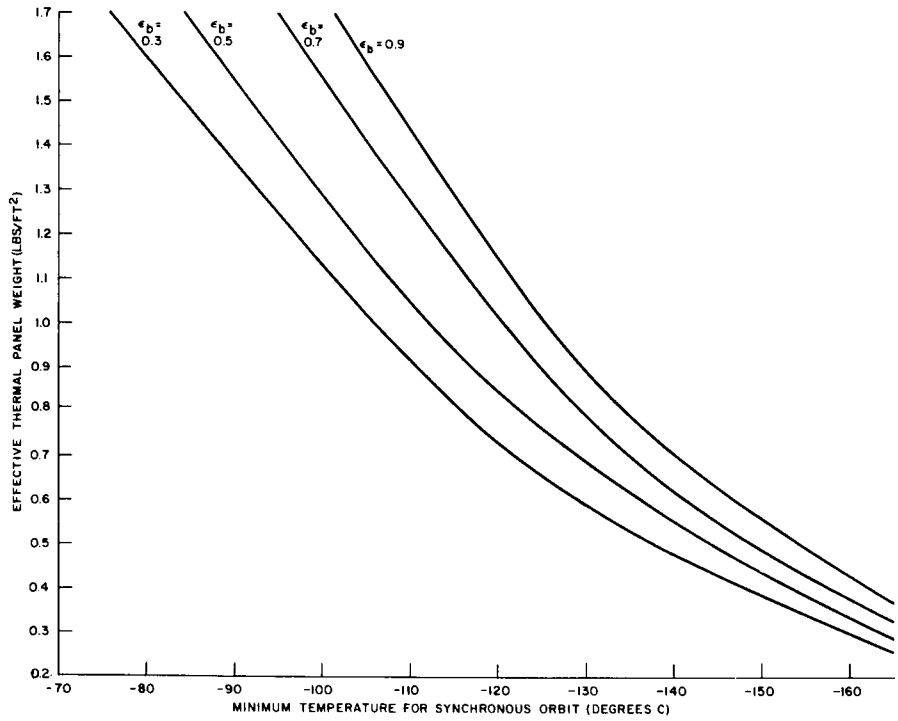

Figure X-23. Effective Thermal Weight vs. Array Temperature for Various Back Emissivities

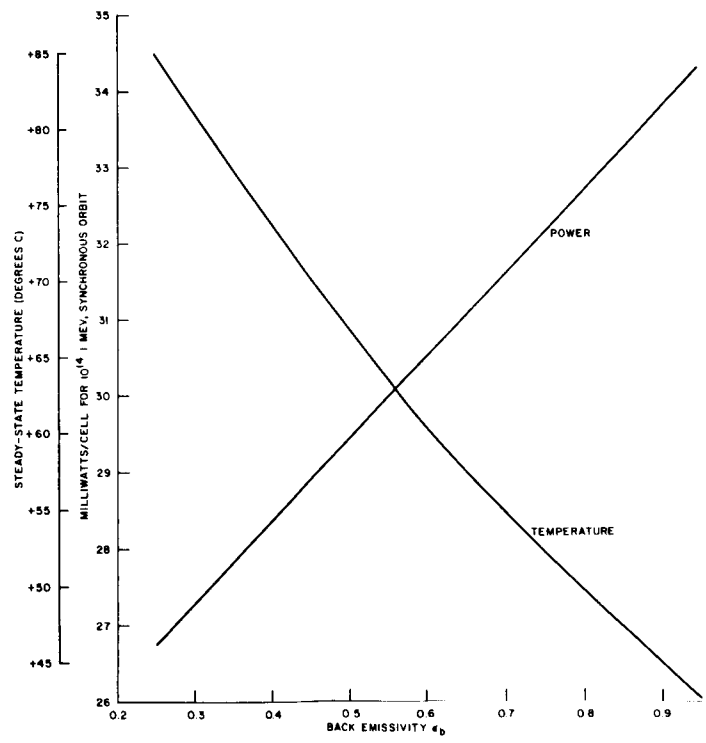

Figure X-24. Solar-Cell Temperature and Per-Cell P_{max} vs. Back Emissivity

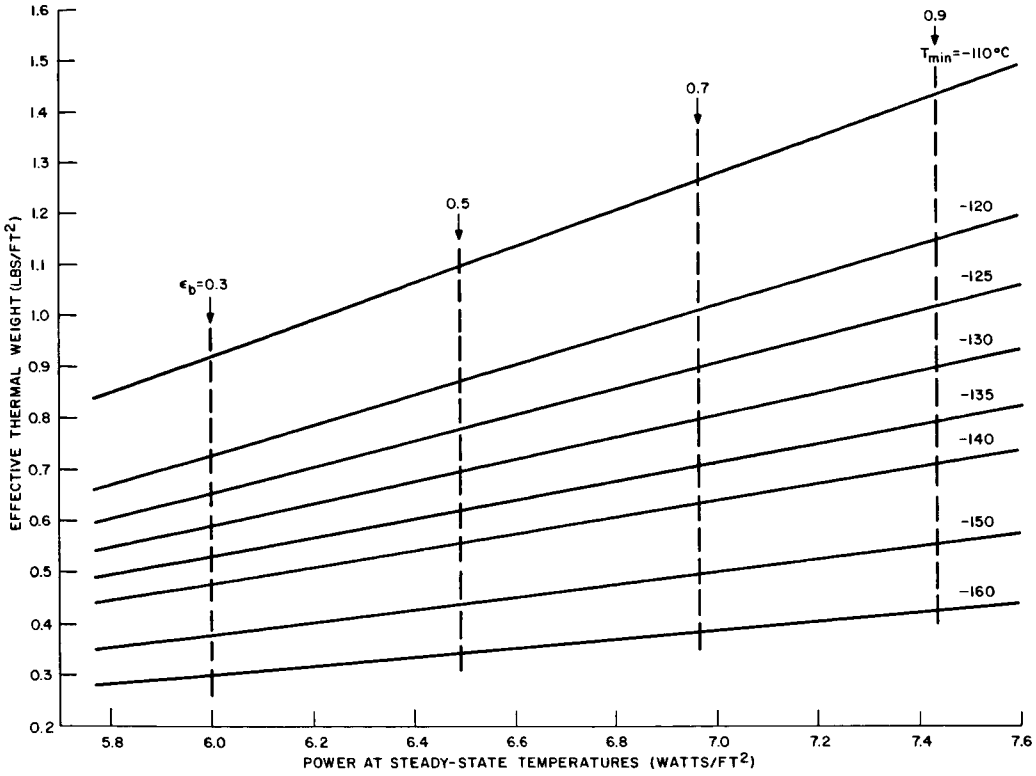

Figure X-25. Effective Thermal Pounds/ft^2 vs. Watts/ft^2 for Various Assumed Low-Temperature Limits

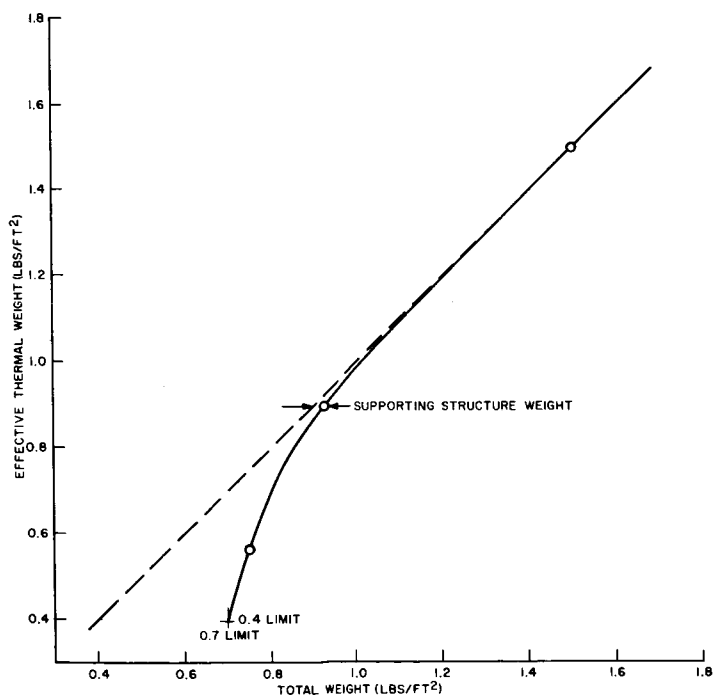

Figure X-26. Relationship of the Effective Thermal Unit Array Weight to Actual Total Unit Weight

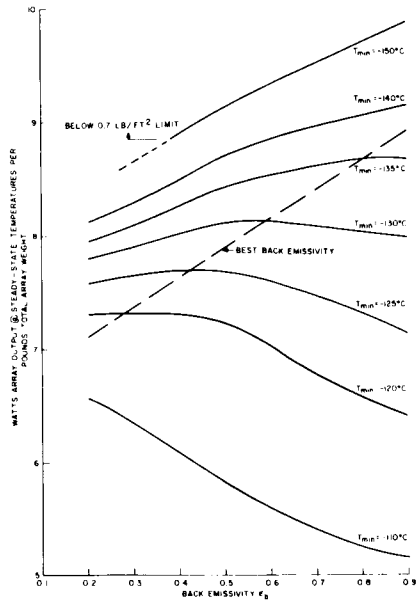

Figure X-27. Array Power Density at Steady-State Temperature vs. ϵ_b for Various Allowable Values of T_{min}

Figure X-25, that a back emissivity of 0.3 means 6 watts per square foot in a synchronous orbit under steady-state temperature conditions. Thus,

$$\frac{6 \text{ watts/ft}^2}{0.94 \text{ lb/ft}^2} = 6.38 \text{ watts per pound of total array weight, for 0.3 back emissivity and } -110^{\circ}\text{C minimum temperature.}$$

Note that for lower back-emissivity values, all the fixed-temperature curves tend to be close together and tend to spread out if the back emissivity, ϵ_b , values are increased. This is due to the combined effect of both the thermal and structural characteristics of the array, resulting in the condition that the lower the back emissivity, the greater the tendency for the array weight to exercise control over the minimum temperature, T_{min}. In other words, if ϵ_b is low, a smaller change in array weight per unit area is required to bring about a given change in T_{min}.

Note also that some of the fixed-temperature curves in Figure X-27 exhibit a fairly well defined peak within the -120°C to -135°C range. As the back emissivity is increased, the per-cell (and per-square-foot) power of the array goes up due to the lowering of the steady-

state temperature (Figure X-24). But, given a fixed T_{min}, the increase in ϵ_b must be accompanied by increased array weight if T_{min} is to remain fixed. Upon further increasing the ϵ_b value, the advantage gained due to increased power is eventually overcome by the increased weight, resulting in a "hump" such as that occurring in the -130°C curve for ϵ_b of roughly 0.55 or 0.6. In the latter case, the use of either lower or higher back emissivities will result in less power per pound; 0.55 or 0.6 is, consequently, an optimum number.

(4) Results and Conclusions

A best straight line has been drawn through the peaks of the curves in Figure X-27. This line, labeled "Best Back Emissivity", defines the approximate location of the optimum values of the back emissivities that result in the largest power output per pound of array weight for a given value of the lowest permissible array temperature.

Based on Figure X-27, Figure X-28 has been plotted to show a more or less practical range of optimum back emissivities as a function of minimum array temperature as well as the resultant power-weight relationship of the array at the in-sunlight steady-state temperature corresponding to the optimum ϵ_b. Although Figure X-28 and all discussion apply specifically to the synchronous orbit as one with the worst-case T_{min}, the resultant weight required per unit of power will be nearly the same at 200 nmi as that listed in Table X-4.

TABLE X-4. OPTIMUM ARRAY DESIGN

Optimum ϵ_b	T_{min} °C, (Fig. X-28)	Lb/Ft^2 Thermal, (Fig. X-23)	Lb/Ft^2 Total (Fig. X-26)	Steady-State Temp., Fig. X-24	Sq. Ft. per 1000 Watts, Fig. X-25	Pounds per 1000 Watts
0.3	-121	0.718	0.81	+81	167	135
0.5	-127.5	0.728	0.82	+67	154	126
0.7	-132.5	0.75	0.83	+55	144	120
0.9	-137	0.76	0.83	+45	134	111

It is evident that the optimum total weight per square foot for the array is approximately 0.82 pound. An appreciable deviation from that number will result in penalties either in terms of extremly low temperature or in weight per unit power produced.

Optimum choice of the remainder of the major array parameters depends primarily on the lowest minimum temperature assumed. For instance, extension of T_{min} by 17° beyond the -120°C temperature qualified for Lunar Orbiter would result in an array weight saving of roughly 18 percent and a very nearly like saving in total area. It is also noteworthy that for a lower T_{min} the total array temperature excursion (T_{min} to T_{max}) is also slightly lower;

this is a reliability consideration. Based on the foregoing, it would appear worthwhile to extend the lower temperature limit to at least -135°C or so, in which case the optimum back emissivity is of the order of 0.8 or 0.85 for an optimum array of roughly 0.82 pound per square foot.

Finally, let the major parameters be determined for the three designs described in Paragraph VII. C. 4. These are defined in the first two columns of Table X-5 and in Figure X-26. Let the performance of each be compared to that at either -137°C as a lower limit or, if that temperature is not achievable given a normal range of back emissivities, at ϵ_b of 0.9. Either of these conditions will enable the three selected designs to yield the most power per unit weight within the T_{min} limitation.

TABLE X-5. DESIGNS UNDER EVALUATION

Lb/Ft^2 Total	Lb/Ft^2 Thermal	ϵ_b (Fig. X-25)	T_{min}, °C (Fig. X-25)	Steady-State Temp. °C; (Fig. X-24)	Sq. Ft. Per 1000 Watts (Fig. X-25)	Pounds per 1000 Watts
0.75	0.568	0.44	-137	+71	157	118
0.92	0.9	0.9	-130	+45	134	124
1.5	1.5	0.9	-108	+45	134	201

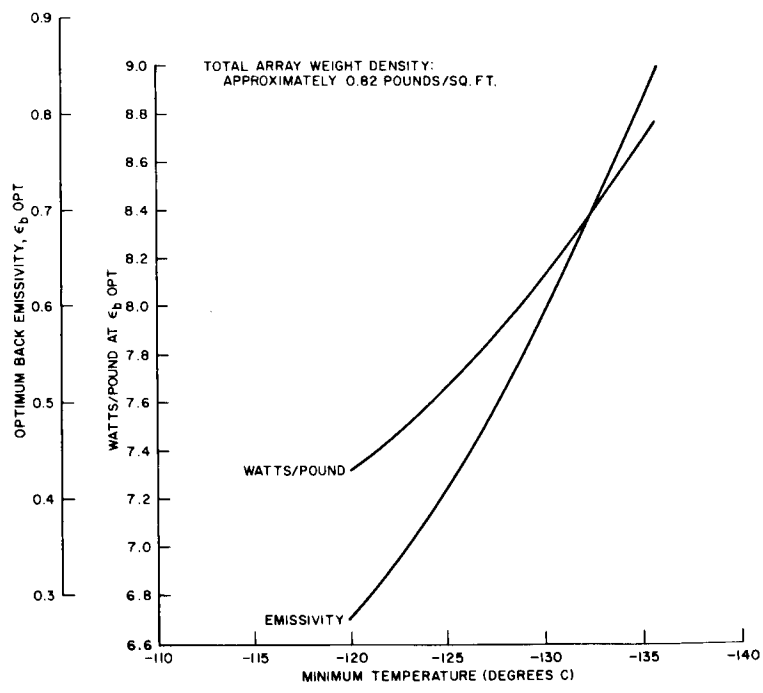

Figure X-28. Optimum Back Emissivity as a Function of Array Temperature

It is seen that the first design, although required to operate at -137°C, requires seven pounds more array weight per 1000 watts than the corresponding optimum design. If the limit were -132.5°C (ϵ_b at 0.3 per Figure X-25), 125 pounds would be required; still five pounds over the corresponding optimum design (ϵ_b equal to 0.7, Table X-4). Further decrease of ϵ_b (beyond 0.3) for this design would probably be impractical.

The second design, although requiring the maximum in the practically achievable high emissivity, is still a few pounds heavier than the best of Table X-4. In table X-4, however it is necessary to reduce T_{min} below -130°C in order to reduce the pounds per unit power produced.

For reasons of weight, the third design approach has not been considered further.

Figure X-29 contains plots based on the tabulated summaries preceding. The lowest plot (heavy line) is for the weight per unit power produced, given the optimum array. The back emissivity varies from 0.3 at about -120°C, to 0.9 at -137°C. Beyond -137°C, the back emissivity is assumed fixed at 0.9 with the ever-decreasing value of total weight per square foot accounting for further temperature decrease down to about -160°C. At that temperature, the "optimum" array is presumed to have reached the lower limit of feasibility in terms of a practically achievable weight density (about 0.7 or 0.71 pound per square foot).

There are two conclusions that can be drawn from this data thus far. First, the lowest temperature to be considered is of the order of -160°C, unless weight densities lower than 0.7 pound per square foot are shown to be feasible. Second, below about -140°C, the "optimum" curve departs from the linear, with the trend showing that the weight saving per degree of T_{min} reduction decreases as T_{min} is reduced.

Weight per unit power curves for the two exact designs (first and second entries of Table X-5) are also plotted in Figure X-29. Since a fixed density is associated with each design approach, only the variation in the back emissivity number accounts for temperature variation under present assumptions. The upper limit of ϵ_b of 0.9 is reached in the 0.92-pound-per-square-foot design at -130°C, and at -150°C in the 0.75-pound-per-square-foot design. In order words, if the lighest array were, for instance, 0.92 pound-per-square-foot, it would be pointless to attempt to qualify for operation below -130°C. At ϵ_b of 0.9, either design is very nearly the same in performance as the hypothetical optimum, from the weight standpoint. The broken-line curves show the required array area per unit of power for the three weight-power curves. In terms of area, the best back emissivity is 0.9.

A detailed discussion on the low-temperature capabilities of the array is included in Paragraph X.C.2.e(5) of this report.

b. SOLAR CELL TRADEOFF ANALYSIS

(1) Introduction

In paragraph X.E.3 of this report, the computer program is described, including the determination of the solar-cell performance during a mission. The input data

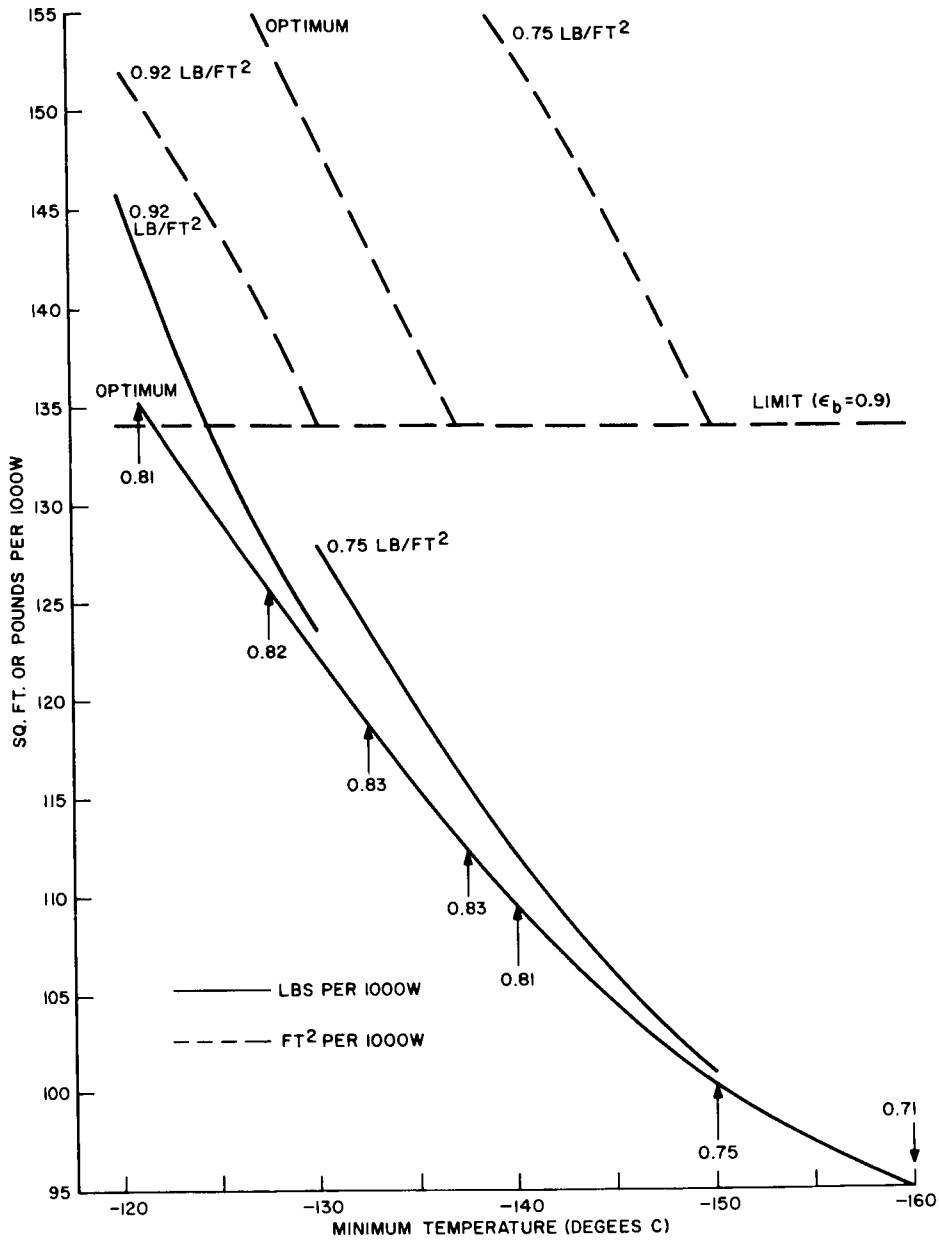

Figure X-29. Weight and Area per 1000 Watts vs. Minimum Temperature

for the computer program are delineated here and the results of computer runs utilizing this data are discussed.

Three orbits are considered, viz., 200 NM, 28.5 degrees; 200 NM, 90 degrees; and, 19,340 NM, 30 degrees. Tradeoffs are presented and a single configuration of cell type and optical-filter substrate thickness are selected, based on the worst-case orbit. The configuration selected for the worst-case orbit is then to be utilized in the other two orbits.

(2) Solar Cell-Selection

(a) General Considerations

A variety of photovoltaic devices is generally available for application on new spacecraft power systems. These devices include conventional silicon solar cells, and thin films. For this conceptual solar-array design and analysis, the silicon solar cell has been selected on the basis of (1) its availability, (2) proven performance on orbiting spacecraft, (3) lower present day cost, and (4) substantiated qualification testing covering a variety of environments including radiation and temperature. While other photovoltaic devices may prove superior to silicon in the future, insufficient data is now available to permit a thorough solar-cell-array analysis with a resultant high degree of confidence in final systems performance.

With the silicon cell established as the basic building block, it is possible to consider the more detailed alternates available. These include (1) cell type (P-on-N or N-on-P), (2) base resistivity, (3) cell area, (4) configuration, and (5) efficiency. Cost is an element of each of the variables identified; each variable is considered in the following.

(b) Cell Type

1. N-on-P Cells. The charged-particle environment in the mission dictates the selection of a cell type that is resistant to radiation damage. The clear superiority of N-on-P cells over P-on-N cells (non-lithium-doped) in this regard has been thoroughly documented (Reference X-2), and the choice of the N-on-P type is justified. In addition, an industry-wide survey indicates that N-on-P cells have been qualified at lower temperature levels than certain other types in thermal cycling test programs. The choice of N-on-P cells is also desirable because they are readily available in large quantities.

2. Lithium-Doped P-on-N cells. (Reference X-3) summarizes the RCA Laboratory development of the radiation-resistant, lithium-doped, floating-zone, P-on-N solar cell. The advantage, as noted in Reference X-3 is that when these cells are bombarded with a flux of charged particles at a rate sufficiently low (but still higher than that expected in space) no degradation is observed in the lithium-containing cells. Presently, three solar-cell vendors (Hoffman, Heliotek, and Texas Instruments) are supplying lithium-doped cells of various types (base resistivity starting material, etc.) to NASA Goddard for evaluation. Preliminary results (Reference X-4) indicate that the 1-MeV flux required to degrade a P-on-N cell without lithium to 50 percent of its initial value does not produce any degradation in the floating-zone, lithium-doped, P-on-N cell. Air-mass-zero efficiencies of the lithium-containing cells obtained by Heliotek in their laboratory average 10.25 percent.

Although these cells are still in the development stage, their utilization in spacecraft power systems is anticipated in the next 12 months. Clearly, any report on a conceptual design would be incomplete without a consideration of lithium-doped cells. In this report various assumptions are made in order to arrive at a comparison of these cells and N-on-P cells. All of these assumptions, in Paragraph X.C.2.b (8) (b), were discussed with Mr. J. Wysocki, now at RCA Astro-Electronics Division, discoverer of the effect of lithium doping on silicon solar cells.

(c) Base Resistivity

Paragraph X.C.2.b (9) (a), a tradeoff analysis, is presented to substantiate selection of the 1-ohm-centimeter cell as a result of comparison with a 10-ohm-cm cell. The analysis is confined to these nominal base-resistivity values because of the overwhelming data and experience available today. Although cells of other nominal base resistivities have been fabricated, insufficient data exists to support their use at this time.

(d) Area, Efficiency, Configuration

In Paragraph X.C.2.e tradeoffs are made on area, efficiency, and configuration based upon maximum power per minimum cost and minimum weight of solar-cell array. The results, restated here, are: 2 x 3 cm in area, 10.5 percent air-mass-zero efficiency, conventional contacts to the cell.

(e) Cell Thickness

The thickness of the cells is 10 mils. Selection of this thickness is discussed in Paragraphs X.C.2.b (5) and X.C.2.b (9).

(3) Charged-Particle Flux

In Appendix E, a study of the space radiation environment for this program is presented. The radiation environment derived from this report for the three orbits under consideration is presented in Tables X-6 through X-9. These fluxes are used in the computer program (Paragraph X.E.3) for determining the damage-equivalent 1-MeV electron flux at the end of one year in the three orbits. This equivalent flux is then used to determine the degradation to the solar cell. A value of 1.0 is used for damage correlation error, D. Postlaunch analysis of various RCA designed spacecraft allows utilization of this conservative value for D, instead of the ultraconservative value of 1.4 recommended in Appendix E.

(4) Optical Filter

The optical filter selected for the solar cells consists of (1) an antireflective coating vacuum-deposited on a 6-mil-thick Corning Glass Works type 7940 fused silica platelet and (2) a blue-reflective coating vacuum-deposited on the underside (solar-cell side) of the platelet. The upper-surface antireflective coating has a peak transmission between

TABLE X-6

SOLAR-FLARE PROTONS, NUMBER/CM^2/YR

ΔE in MeV	100% Attenuation, 200 NM 30° Orbit	50% Attenuation, 200 NM 90° Orbit	No Attenuation, 19.340 NM Orbit 30° Orbit
0 to 1	0	0	0
1 to 2	↑	3.0×10^{10}	6.0×10^{10}
2 to 3		0.75×10^{10}	1.5×10^{10}
3 to 4		4.0×10^{9}	8×10^{9}
4 to 5		2.25×10^{9}	4.5×10^{9}
5 to 6		1.25×10^{9}	2.5×10^{9}
6 to 7		1.0×10^{9}	2.0×10^{9}
7 to 8		5.5×10^{8}	1.1×10^{9}
8 to 9		3.5×10^{8}	7×10^{8}
9 to 10		2.25×10^{8}	4.5×10^{8}
10 to 11		2.0×10^{8}	4×10^{8}
11 to 12		2.0×10^{8}	4×10^{8}
12 to 13		2.0×10^{8}	4×10^{8}
13 to 14		1.5×10^{8}	3×10^{8}
14 to 15		1.25×10^{8}	2.5×10^{8}
15 to 30		9.0×10^{8}	1.8×10^{9}
30 to 100	↓	8.5×10^{8}	1.7×10^{9}
100	0	1.4×10^{8}	2.8×10^{8}

Projection error, A, = 1.0
Detector error, B, = 1.0
Attenuation, C, = 1.0 for 204 NM, 30° orbit,
= 0.5 for 200 NM, 90° orbit, and
= 0 for 19,340 NM, 30° orbit
Damage correlation error, D, = 1.0

TABLE X-7. SOLAR-FLARE ALPHA PARTICLES; NUMBER/CM^2/YEAR

ΔE in MeV	100% Attenuation 200-NM, 28.5° Orbit	50% Attenuation 200-NM, 90° Orbit	No Attenuation 19,340-NM, 30° Orbit
16 to 18	0	2.0×10^7	4.0×10^7
18 to 20	0	1.5×10^7	3.0×10^7
20 to 22	0	1.5×10^7	3.0×10^7
22 to 25	0	1.5×10^7	3.0×10^7
25 to 30	0	2.0×10^7	4.0×10^7
30 to 32	0	1.0×10^7	2.0×10^7
32 to 35	0	1.0×10^7	2.0×10^7
35 to 40	0	1.0×10^7	2.0×10^7
40 to 45	0	1.0×10^7	2.0×10^7
45 to 47	0	5.0×10^7	1.0×10^7
47 to 52	0	6.0×10^6	1.2×10^7
52 to 57	0	6.5×10^6	1.3×10^7
57 to 50	0	2.5×10^6	5×10^6
60 to 80	0	1.6×10^7	3.2×10^7
80 to 100	0	1.0×10^7	2.0×10^7
100 to 200	0	1.12×10^7	$2.25 \quad 10^7$
200 to 400	0	2.25×10^6	4.5×10^6
400	0	5.0×10^5	1.0×10^6

Projection error, A, = 1.0

Detector error, B, = 1.0

Attenuation, C, = 1.0 for 200 NM, 28.5° orbit

= 0.5 for 200 NM, 90° orbit

= 0 for 19,340 NM, 30° orbit

Damage correlation error, D, = 1.0

TABLE X-8. VAN ALLEN BELT PROTONS
NUMBER/CM^2/YEAR

Δ E in MeV	200-NM 28.5° Orbit	200-NM 90° Orbit	19,340-NM 30° Orbit
0.1 to 1	8.03×10^8	1.68×10^8	4.38×10^{15}
1 to 2	3.28×10^8	4.09×10^8	3.4×10^{12}
2 to 3	2.77×10^8	3.36×10^8	1.2×10^{11}
3 to 4	2.56×10^8	2.92×10^8	2.48×10^9
4 to 5	2.19×10^8	1.46×10^8	4.38×10^8
5 to 6	1.46×10^8	2.92×10^8	2.92×10^8
6 to 7	1.46×10^8	2.92×10^8	2.92×10^7
7 to 8	1.46×10^8	1.46×10^8	2.92×10^7
8 to 9	1.46×10^8	1.46×10^8	7.3×10^6
9 to 10	7.3×10^7	1.46×10^8	5.84×10^6
10 to 11	7.3×10^7	1.17×10^8	5.84×10^6
11 to 12	7.3×10^7	7.3×10^7	5.84×10^6
12 to 13	7.3×10^7	5.84×10^7	5.84×10^6
13 to 14	7.3×10^7	2.92×10^7	5.84×10^6
14 to 15	7.3×10^7	8.76×10^6	5.84×10^6
15 to 30	4.2×10^7	5.4×10^7	1.75×10^6
30 to 50	7.3×10^7	5.4×10^7	7.3×10^3
50	2.48×10^8	3.65×10^7	7.3×10^3

Transition Protons:
(Applies only to 19,340 NM, 30° orbit)
Total number/cm^2 with $E > 4$ MeV $= 1 \times 10^7$

Projection error, A, = 2.0

Detection error, B, = 1.0

Attenuation C, (not applicable)

Damage correlation error, D, = 1.0

TABLE X-9. VAN ALLEN BELT ELECTRONS, NUMBER/CM^2/YEAR

E in MeV	200-NM 28.5° Orbit	200-NM 90° Orbit	19,340-NM 30° Orbit	Transition	Total 19,340-NM 30° Orbit
0.04 to 0.25	2.36×10^{12}	1.43×10^{13}	1.07×10^{15}	1.8×10^{14}	1.25×10^{15}
0.25 to 0.5	3.57×10^{11}	3.43×10^{12}	3.29×10^{14}	2.6×10^{13}	3.55×10^{14}
0.5 to 0.75	7.14×10^{10}	1.07×10^{12}	9.29×10^{13}	4×10^{12}	9.69×10^{13}
0.25 to 1.0	1.07×10^{10}	4.64×10^{11}	2.93×10^{13}	2×10^{11}	2.95×10^{13}
1 to 2	2.0×10^{9}	4.71×10^{11}	1.29×10^{13}	6.4×10^{10}	1.3×10^{13}
2 to 3	9.29×10^{7}	4.64×10^{10}	1.14×10^{11}	3.6×10^{9}	1.18×10^{11}
3 to 4	6.0×10^{7}	5.36×10^{9}	1.07×10^{9}	3.6×10^{9}	4.67×10^{9}
4 to 5	4.64×10^{7}	7.86×10^{8}	9.29×10^{6}	3.6×10^{9}	3.61×10^{9}
5 to 6	3.43×10^{7}	1.79×10^{8}	8.57×10^{14}	3.6×10^{9}	3.6×10^{9}
6 to 7	2.71×10^{7}	6.43×10^{7}	7.86×10^{2}	1.22×10^{9}	1.22×10^{9}

Projection error, A, = 2.0

Detection error, B, = 1.0

Attenuation, C, (not applicable)

Damage correlation error, D, = 1.0

600 to 800 millimicrons at normal incidence. The characteristic of the lower-surface blue-reflective coating is defined as follows:

Wavelength (in millimicrons)	Transmission (in Percent)
200 to 370	less than 1
500 to 600	minimum of 85
600 to 1100	minimum of 90
600 to 800	94, minimum average
450 to 1100	94, minimum average
400 ± 15	50

Figure X-30 shows a typical transmission curve of the above-defined Optical Coating Laboratory optical filter before and after bonding.

(a) Optical Filter Substrate

Three types of substrates have been used on spacecraft solar-cell arrays: sapphire, Corning Glass Works type 7940 fused silica, and Corning type 0211 glass (Microsheet). Sapphire was not considered because of its lower emissivity as compared to Corning 7940 and 0211, its initial transmission of 85 percent in the spectral response region of the solar cell, and the higher cost compared to fused silica.

(b) Microsheet and Corning 7940

The initial advantage of Microsheet is its lower cost compared to that of Corning 7940. A blue filter with antireflective coating on a Corning 7940 substrate costs 220 percent more than a similar type filter on Microsheet. The cost difference between a filter on Corning 7940 and a filter on Microsheet in a quantity of 500,000 filters is $680,000.

Reference X-2 presents a comparison of the effect of the radiation on a blue filter and antireflective coating on Microsheet and on Corning 7940 when exposed to 1-MeV electrons and 4.6-MeV protons. Table X-10 is taken from this reference. This data is typical of the charged-particle radiation data that is available on Microsheet and 7940 (References X-5 and X-6). Additional data confirming the results in the table were obtained on various spacecraft programs at RCA and on the Comsat cell evaluation program by Bell Laboratories.

Data of the type contained in Table X-10 for electrons and protons, but of lower energy (the most important area for damage considerations), is not available. The amount of energy that a flux of charged particles in an energy range would deposit in a material can be calculated using accepted or calculated conversion factors. This energy is the dose in rads (hundreds of ergs per gram) and is an indicator of the degree of disturbance that the radiation should cause in the material. Unfortunately, all particles do not give the same amount of damage per rad and, for such effects as loss in transmission, the fluxes of each type of particle must be considered individually.

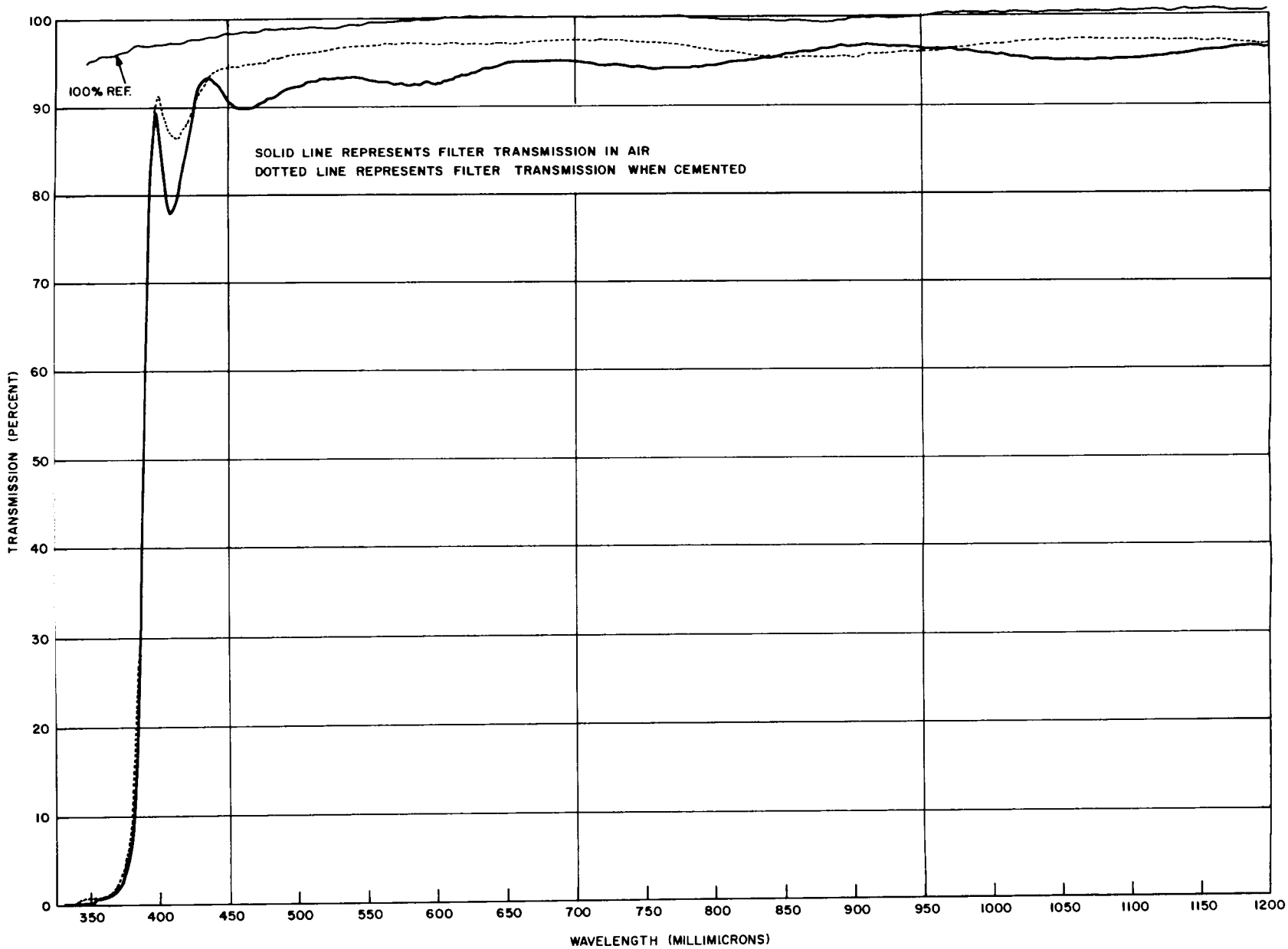

Figure X-30. Blue-Reflecting Solar-Cell Cover on Fused Silica

TABLE X-10. CHARGED-PARTICLE RADIATION DATA FOR MICROSHEET AND CORNING 7940

Material		50% Cut-Off Point	Wavelength (in microns) 0.4	0.45	0.50	0.60	0.70	
1. 6-mil Microsheet with blue filter and antireflective coating	T_o	0.443	--	93.5	96.5	97.0	--	4.6 MeV protons Total dose = 4×10^{11} protons/cm^2
	T_F	0.446	--	88.0	91.5	95.0	--	
	% ΔT	--	--	5.9	5.2	2.1	1.1	
2. 20-mil Corning 7940 with blue filter and antireflective coating	T_o	0.425	←		No Change		→	
	T_F	0.427						
	% ΔT	--						
1. 6-mil Microsheet with blue filter and antireflective coating	T_o	0.444	--	--	96.0	97.5	96.0	1 MeV electrons Total dose = 1×10^{16} electrons/cm^2
	T_F	0.444	--	--	89.0	92.5	92.0	
	% ΔT	--	--	--	7.3	5.1	4.2	
2. 20-mil Corning 7940 with blue filter and antireflective coating	T_o	0.416	--	--	89.0	90.0	91.0	
	T_F	0.425	--	--	88.0	88.0	90.0	
	% ΔT	--	--	--	1.1	2.2	1.1	

T_o is initial transmission

T_F is final transmission

Additional considerations are neutrons, X-rays, and secondary-emission particles. The total flux of neutrons and secondaries is not important compared to the total flux of electrons and protons below 4 MeV. However, the surface dose rate of X-rays of a few kilovolts is 10^6 rads per hour. Corning Glass submitted 6-mil-thick Microsheet and 6-mil Corning 7940 to 50-keV X-rays for a total dose of 10^5 to 10^6 rads in 1962. The results reported to RCA were a 50-percent decrease in transmission in the wavelength region 0.4 to 1.1 microns for the Microsheet and a 0- to 2-percent decrease in transmission in the same wavelength region for the Corning 7940. Additional exposure of Microsheet (125 mils thick) to 50-keV X-rays was made by Corning in 1963. The latter transmission curves are shown in Figure X-31.

Because of the type of data delineated in the preceding, the utilization of Microsheet as an optical-filter substrate material on solar-cell arrays has been limited to missions of short duration (less than 2 months). Nearly all of the solar-cell arrays in space today utilize Corning 7940. Postlaunch analysis of these arrays (Nimbus II, for example) indicate that there is no degradation in transmission of the Corning 7940.

The difference between the cost of Microsheet and Corning 7940 on previous solar-cell arrays (less than 500 watts) was a comparatively small dollar value. This dollar value was a very small percentage of the total cost of the spacecraft and the magnitude of the cost involved was less than the cost of a full-scale investigation of the degradation of Microsheet in a typical radiation environment. On this program, however, even though the difference in cost between the two coverglasses is probably of the same percentage relationship to the total cost of a spacecraft, the magnitude of the cost involved is more than the total cost of some spacecraft. A tradeoff analysis between Corning 7940 and Microsheet is warranted. This tradeoff analysis cannot be performed to any degree of accuracy at the present time due to lack of necessary radiation data on the Microsheet. Therefore, Corning 7940 shall be utilized in the conceptual design of the solar-cell array.

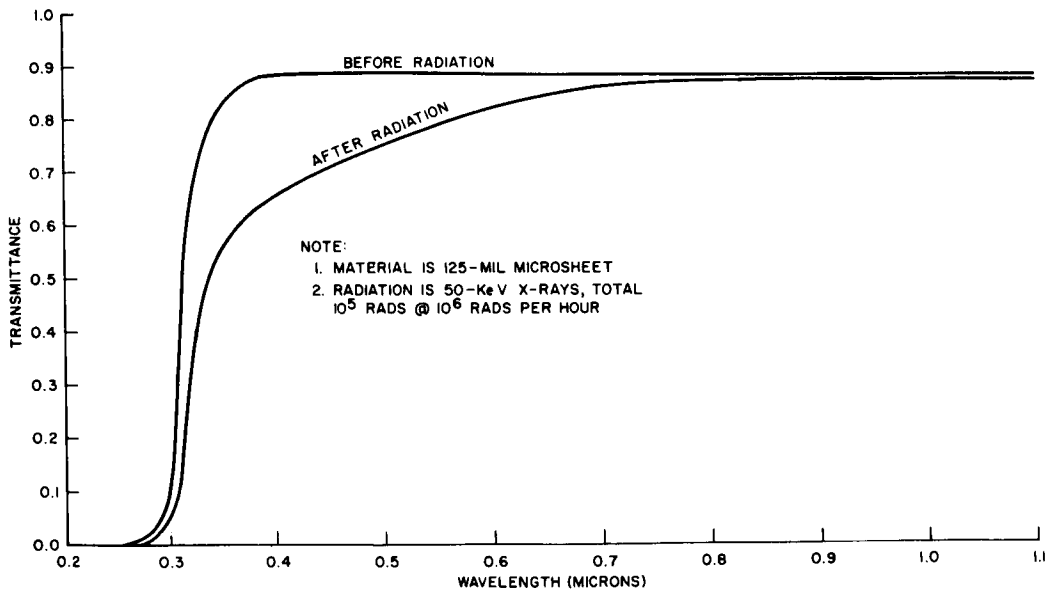

Figure X-31. Transmission Curve for Micro-sheet Before and After Radiation by 50 KeV X-Rays

(c) Thickness

The thickness of the Corning 7940 is determined in Paragraph X. C. 2. b(9)(a) to be 6 mils. Coverglasses less than 6 mils thick may be desirable, but are too costly, both initially and in processing arrays in manufacturing.

(d) Optical-Filter Adhesive

Sylgard 182 shall be considered as the optical-filter bonding adhesive in the conceptual study. Any likelihood of cracked optical-filter coverglasses in thermal cycling (19,340-NM, 28.5^{o} orbit) using Sylgard 182 will be largely dependent on the optical-filter thickness and the extent of the low temperature requirement. In the 19,340 NM, 28.5^{o} orbit the temperature extremes are -156.8^{o}C and +41.86^{o}C. A discussion on low-temperature capability is included in Paragraph X. C. 2. e(5).

(e) Integral Covers

The Corning Glass Works has deposited Corning 7940 directly to N-on-P solar cells for RCA. Thickness of the 7940 ranged from 1 to 10 microns, with the 10-micron-thick coating requiring a much longer period of time for deposition. The decrease in short-circuit current from before to after deposition of the coating was an average of 1.7 percent. Cells with integral coatings were thermally cycled from liquid nitrogen to room air for a total of ten cycles. There was no mechanical damage to the cell or to the integral coating.

The Ion Physics Corp. has a contract from NASA Goddard to develop an integral coating of fused silica with a thickness of 6 mils. The present thickness obtained by Ion Physics is 1 mil. While integral coatings are presently too thin to be used with N-on-P cells because of the minimum amount required of shielding of the solar cell from charged particles, thin integral coatings on lithium-doped P-on-N cells are ideal. A one-micron-thick integral coating on a lithium-doped cell will be thick enough to obtain the same emissivity as that which would be obtained with a 6-mil-thick 7940 cover bonded to the lithium-doped cells, i.e., the equilibrium temperature of the two different cell cover composites will be the same in air mass zero sunlight.

With the addition of an antireflective coating to the top surface of the integral fused-silica cover, the increase in short-circuit current of the cell will be 3 percent. The net effect, therefore, of depositing an integral cover to a lithium-doped P-on-N cell and adding an antireflective coating to the integral cover will be an increase of at least 1 percent in the short-circuit current of the cell. By comparison, when a 6-mil-thick cover with blue filter and antireflective coating is bonded to a cell, using Sylgard 182 adhesive, the decrease in short-circuit current is 4 percent. Following in Table X-11 is a weight comparison between integral covers and organic-adhesive-bonded covers on a per-cell basis, and the effect on the total weight of the solar-cell array.

TABLE X-11. COMPARISON OF WEIGHTS OF INTEGRAL AND BONDED CELL COVERS

	1-micron integral cover	1-mil-thick integral cover	6-mil-thick fused silica cover & 1-mil-thick Sylgard 182 adhesive
Weight per 2x3 cell (in grams)	0.0013	0.0319	0.207
Weight per sq. foot (in pounds)	0.684	0.695	0.750

While the shielding of charged particles provided by a 1-micron-thick integral cover is known, the effect of the remaining low-energy-particle damage to the lithium cell is not know. In particular, the effect of the rate of bombardment of the low-energy particles (less than 1 MeV) in the three orbits considered is unknown. Hence both one-micron and one-mil-thick integral covers should be considered.

(5) Solar-Cell Data

The only N-on-P solar-cell data available to RCA in sufficient quality and quantity is on Radio Corporation of America, Mountaintop, Pennsylvania (RCA MT) solar cells. This data includes I-V (current-voltage) curves, as a function of temperature (before and after irradiation), of 1-MeV electron flux, thermal cycling, base resistivity, intensity, and ultraviolet exposure. This data (taken on Nimbus, TIROS, Relay, ComSat, and Lunar Orbiter programs) has been reduced and incorporated into a computer program for shifting of the cell I-V curve to obtain an I-V curve of a solar cell in an array at end of life and any desirable intermediate points. Many man-months of engineering and technician time was expended to acquire and reduce the data. Additional time was consumed in deriving empirical relationships between the various curves for computerizing the array design. Production of the RCA MT solar cells, however, has been terminated.

RCA has obtained radiation data on various vendors, N-on-P cells from Mr. W. Cherry of NASA-Goddard. All of the cells are bare (without optical filter), 1 x 2 cm in size, and cover a range of efficiencies. All of the cells are nominal 10 ohm-cm, and a nominal 14 mils thick. In addition, data was taken on 8-mil-thick, nominal 1-ohm-cm, Heliotek cells. Table X-12 delineates the number of the samples from each vendor and the 1-MeV electron-flux levels.

TABLE X-12. RADIATION EXPOSURE OF VARIOUS CELLS

Cell Numbers	1-MeV electrons/cm^2
1 and 2	0
3 and 4	0, 10^{13}
5 and 6	0, 10^{13}, 10^{14}
7 and 8	0, 10^{13}, 10^{14}, 10^{15}
9 and 10	0, 10^{13}, 10^{14}, 10^{15}, 10^{16}

I-V curves were measured before and after 1-MeV exposure under a Spectrolab Solar Simulator. The data was reduced and is shown in Figures X-32 through X-37. Absolute efficiency shown in the figures was calculated by the following:

$$100 \frac{P_{max}}{2\ cm^2 \times 139.6\ mw/cm^2} = \textit{air-mass-zero efficiency.}$$

By calculating efficiency as shown, a vendor was penalized for non-optimization of grids and N-strip contact to the active area of the cell. Due to the different range of efficiences from each vendor and the selection of cells from the total of 10 cells to be submitted to the various electron fluxes, it is impossible to compare the cells from various vendors with respect to radiation resistance on an absolute-efficiency basis. Instead, absolute-efficiency curves were normalized using the average values at the various flux levels and the average value of starting efficiency. Comparison between vendors was then made on a relative basis. This was allowed by the experimental fact that cells of the same efficiency and base resistivity will degrade under 1-MeV electron flux at the same rate (within experimental error).

(a) 10-ohm-cm Cells

The data on Hoffman, Heliotek, and Texas Instrument 10-ohm-cm cells is sufficiently close to allow a comparison between them and RCA MT cell data. Figure X-38 shows a comparison of data on 12-mil-thick 10-ohm-cm RCA MT cells with the data on the 14-mil-thick 10-ohm-cm cells of the vendors in Figures X-32 through X-37. The maximum solar-cell damage-equivalent 1-MeV electron flux at the end of one-year life in the worst-case orbit (19,340-nmi, 28.5^{o} orbit) of the three considered is 1.36 x 10^{14} electrons per square cm (see Table X-13).

Based on Figure X-38, and allowing for various errors in the measurements (both electron-flux and efficiency) used to determine this figure, no difference in the radiation resistance is considered to exist for this study at 1.36 x 10^{14} electrons per square cm between RCA MT 12-mil-thick 10-ohm-cm cells and the 14-mil-thick 10-ohm-cm cells of the other vendors.

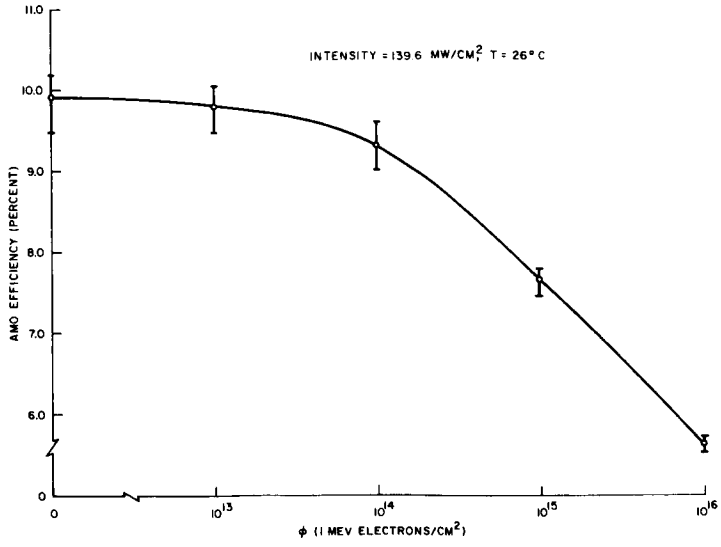

Figure X-32. Irradiation Curve for Heliotek 1-Ohm-Cm, 8-Mil Solar Cell

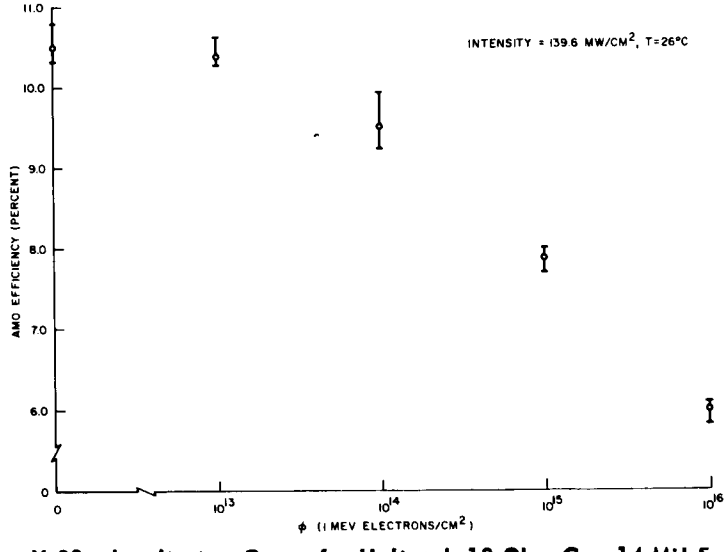

Figure X-33. Irradiation Curve for Heliotek 10-Ohm-Cm, 14-Mil Solar Cell

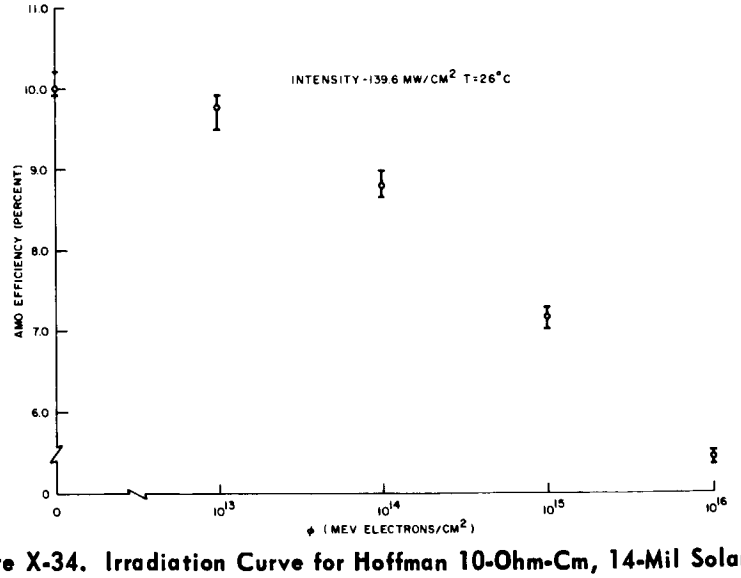

Figure X-34. Irradiation Curve for Hoffman 10-Ohm-Cm, 14-Mil Solar Cell

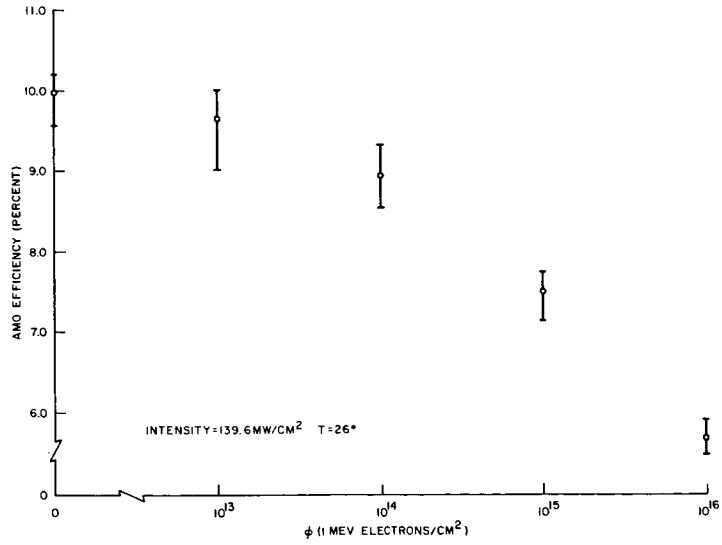

Figure X-35. Irradiation Curve for Texas Instrument 10-Ohm-Cm. 14-Mil Solar Cell

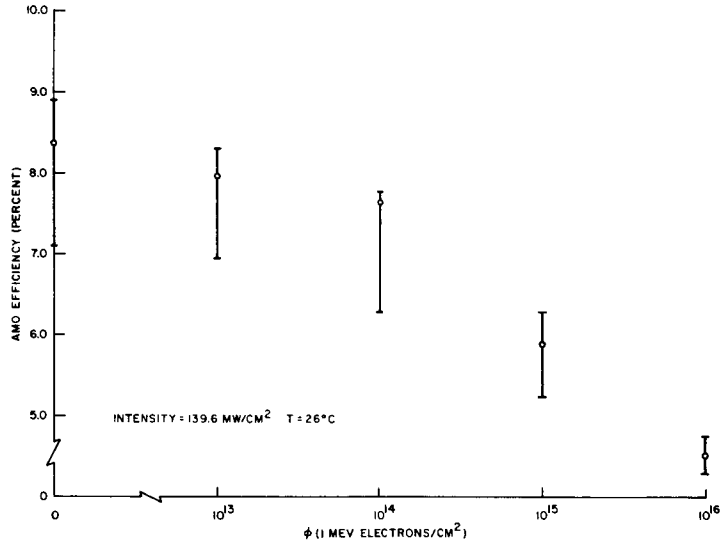

Figure X-36. Irradiation Curve for Westinghouse, 10-Ohm-Cm, 14-Mil Solar Cell

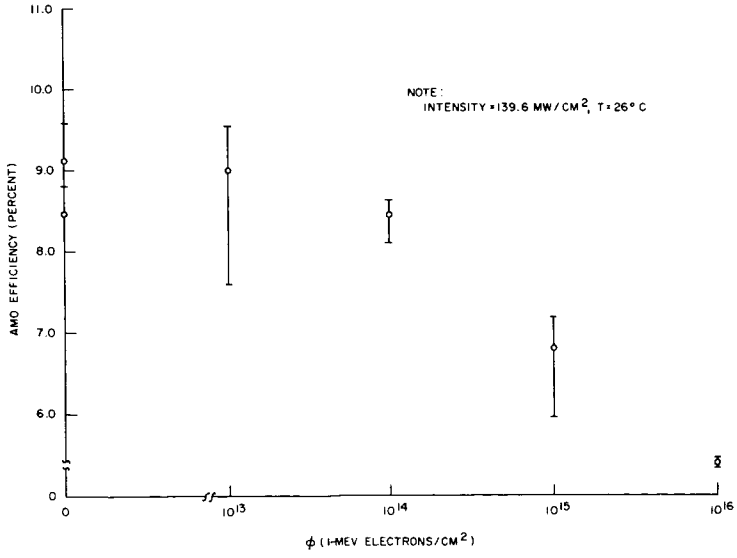

Figure X-37. Irradiation Curve for Ion Physics 10-Ohm-Cm, 14-Mil Solar Cell

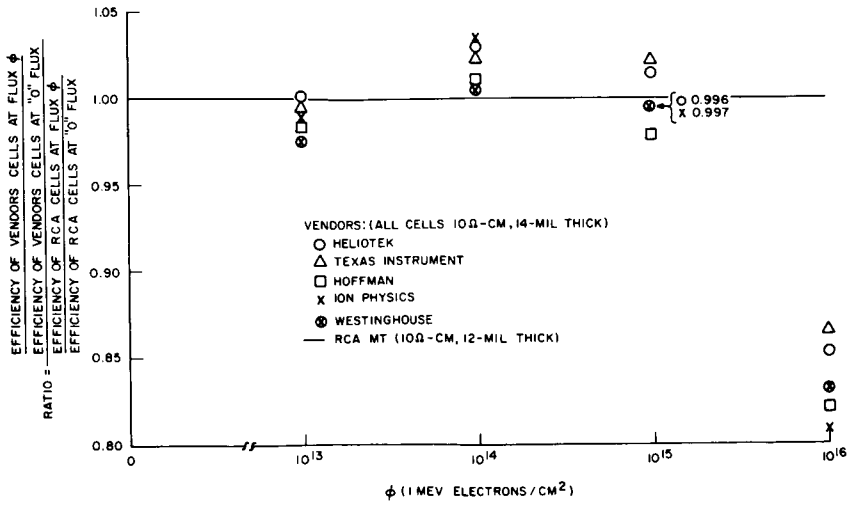

Figure X-38. Radiation Resistance of Vendor Cells vs. RCA Cells

(b) 1-ohm-cm Cells

Figure X-39 shows a comparison of 8-mil-thick 1-ohm-cm cells of Heliotek and 12-mil-thick 1-ohm-cm RCA MT cells. At the equivalent 1-MeV flux level (1.36×10^{14} electrons per square cm) in the worst-case 24-hour synchronous) orbit, the advantage over the RCA cells appears to be approximately 7 percent. However, the initial request for quote for 10.0 and 10.5-percent air-mass-zero efficiency 8- and 10-mil-thick cells showed that the 10.0-percent 8-mil-thick cell costs 30 percent more than a 10.5-percent 10-mil-thick cell. The vendor submitted a no-bid decision on a 10.5-percent air-mass-zero efficiency 8-mil-thick cell.

A similar quote received later showed no difference in cost between a 10.0-percent air-mass-zero efficiency 8-mil-thick cell and a 10.5-percent air-mass-zero efficiency 10-mil-thick cell. A 10.5-percent 8-mil-thick cell is still too uneconomical to be considered. The advantage in power of an 8-mil-thick cell over a 10-mil-thick cell is reduced to 2 percent, i.e., 7-percent advantage following irradiation less 5-percent initial efficiency disadvantage. If any tolerance (say ±3 percent) is placed on the radiation-test results, no power advantage can be reliably demonstrated in using an 8-mil-thick cell. In addition, the 8- and 10-mil thicknesses discussed are nominal; the minimum tolerance on purchased cells is ±2 mils.

Due to the fact that only six 8-mil-thick cells were irradiated to the flux level important in this study, lack of data (such as: tolerance on the radiation tests, tolerance on the thickness of purchased cells, cost difference between 8-mil-thick 10.0-percent and 10-mil-thick 10.5-percent air-mass-zero efficiency cells, and lack of other supporting data — I-V curves as a function of temperature, etc.) and consideration of data that is available on RCA MT cells, a decision was made to use RCA MT data as being typical. Due to the weight advantage of a 10-mil-thick cell over a 12-mil-thick cell and the lack of difference in cost for the 10.5 air-mass-zero efficiency of both cells, a 10-mil-thick cell is used in this conceptual design study.

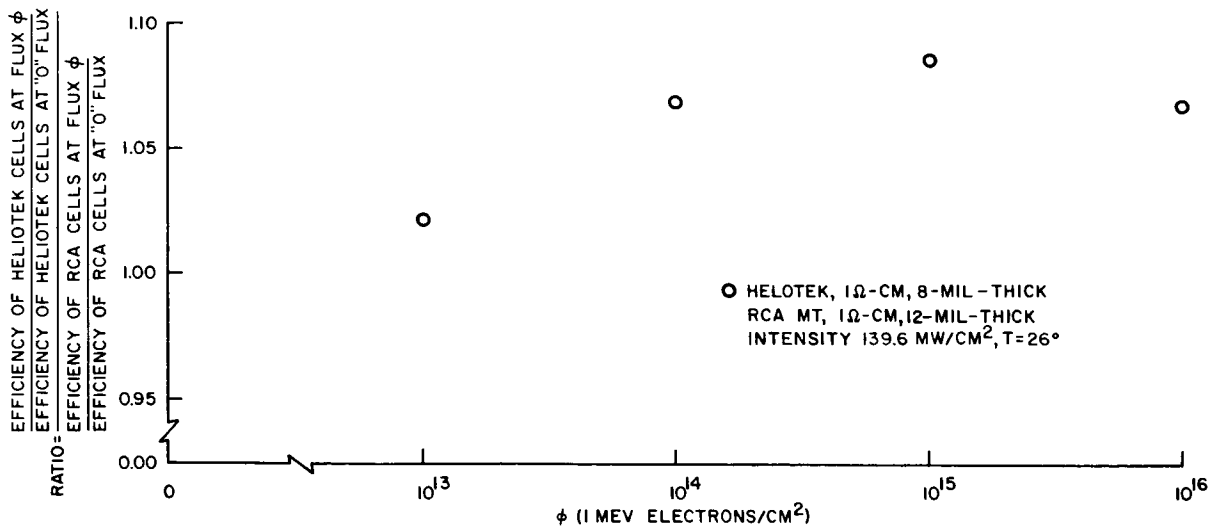

Figure X-39. Radiation Resistance of Heliotek Cells vs. RCA Cells

Based on the assumption that the damage in the worst-case orbit was due to flux only (before completion of the thermal analysis), the solar-cell tradeoff analysis proceeded using RCA MT cell data. However, the true worst-case orbit, from the viewpoint of cell output, is a function of both radiation flux and temperature. This orbit is the 200-NM polar orbit. The equivalent 1-MeV electron flux in this orbit is (Table X-13) 4.17×10^{13}, which is less than 1.36×10^{14} electrons per square cm determined for the synchronous altitude previously used to arrive at the decision to use 10-mil-thick cells instead of 8-mil-thick cells. Lower flux in the worst-case orbit lends greater confidence in the selection of a 10-mil-thick cell.

(6) I-V Curve Construction

One of the inputs to the computer program (Paragraph X. E. 3) is the I-V curves of bare solar cells (1 ohm-cm and 10 ohm-cm). The I-V curves of the 1-ohm-cm and 10-ohm-cm 2 x 3 centimeter, 10-mil-thick, 10.5-percent air-mass-zero efficiency, at a temperature of 27°C were constructed from 1-ohm-cm, and 10-ohm-cm I-V curves of 2 x 2 centimeter, 12-mil-thick, 9.5-percent air-mass-zero efficiency RCA MT solar cells. The RCA MT cell I-V curves are curves of single cells that are 1/N of a module; i.e., the optical filter has been bonded, and the cells soldered into a module (cells connected in parallel).

(a) 1-ohm-cm Cells

The steps in the construction of the I-V curve shown in Figure X-40 are as follows:

1. The current ordinate of the RCA MT 1-ohm-cm curve is multiplied by 1.5. This is the ratio of the active area of a 2x3 cm conventional cell to the active area of a 2x2-cm conventional cell.

TABLE X-13. EQUIVALENT 1-MeV ELECTRONS/CM^2 AT END OF LIFE (1 YEAR)

Orbit		Optical-Filter Substrate Thickness (mils)	Particles Contributing to Equivalent 1-MeV Electron Flux				
Altitude (NM)	Inclination (degrees)		Van Allen Electrons	Van Allen Protons	Solar-Flare Protons	Solar-Flare Alpha Particles	TOTAL FLUX
200	28.5	6	3.31×10^{11}	5.82×10^{12}	0	0	5.85×10^{12}
		9	2.44×10^{11}	4.85×10^{12}	0	0	4.88×10^{12}
		18	1.17×10^{11}	3.22×10^{12}	0	0	3.23×10^{12}
200	90	6	1.66×10^{12}	6.2×10^{12}	3.11×10^{13}	2.72×10^{12}	4.17×10^{13}
		9	1.45×10^{12}	5.14×10^{12}	2.19×10^{13}	2.17×10^{12}	3.06×10^{13}
		18	1.12×10^{12}	2.75×10^{12}	1.29×10^{13}	1.37×10^{12}	1.82×10^{13}
19,340	30	6	6.51×10^{13}	2.78×10^{12}	6.23×10^{13}	5.44×10^{12}	1.36×10^{14}
		9	5.16×10^{13}	$.954 \times 10^{12}$	4.37×10^{13}	4.34×10^{12}	1.01×10^{14}
		18	3.26×10^{13}	$.181 \times 10^{12}$	2.58×10^{13}	2.74×10^{12}	$.614 \times 10^{14}$

2. The resulting I-V curve is then corrected for a positive series-resistance effect.

   By comparison with the other vendors' cells (Hoffman, Heliotek, Texas Instruments) the voltage at maximum power of the vendors' cells was found to be 0.470 volt as compared to 0.460 volt maximum power voltage of the RCA MT 1/Nth-of-a-module cell I-V curve.

   To every current of the I-V curve resulting from Step 1, an incremental voltage (ΔV) was added, where ΔV is defined as:

$$\Delta V = \Delta R \times I = \left(\frac{47}{46} - 1\right)\left(\frac{V_{mpo}}{I_{mpo}} I_{,}\right)$$

   where I is any current at a voltage from 0 to open circuit, and V_{mpo}, I_{mpo} are maximum-power-point voltage and current.

3. The final curve is obtained by adding a ΔI to every voltage point of the curve in Step 2, where ΔI is (177.8 - 164.2) ma. The ΔI is the difference in current at 0.470 volt in the curve of Step 2 and the maximum power current of the final 2 x 3 cm, 10.5-percent, air-mass-zero efficiency cell.

   (b) 10-ohm-cm Cell

The steps in the construction of I-V curve shown in Figure X-41 are as follows:

1. The current ordinate of the RCA MT 10-ohm-curve is multiplied by 1.5.

2. The final curve is obtained by adding a ΔI to every voltage point of the curve in Step 1, where ΔI is (187.8 - 169.4) ma. The ΔI is the difference in current at 0.445 volt (maximum power voltage) in the curve of Step 1 and the maximum-power current of the final 2 x 3 cm, 10.5-percent air-mass-zero efficiency cell. The 0.445 voltage at maximum power (V_{mp}) for the RCA MT cells is identical to the V_{mp} for the other vendor's 10-ohm-cm cells.

(7) Shielding

The cross section of the solar-cell panel shown in Figure X-42 is utilized in calculating the shielding and/or attenuation of the electrons, protons, and alpha particles by various materials in front of and in back of the solar cell. The various materials indicated in the figure are:

(1) Optical-filter substrate, Corning Glass Works type 7940 fused silica.

(2) Sylgard 182, optical-filter adhesive.

(3) Titanium-silver grid lines on top of the solar cell, 1 mil thick.

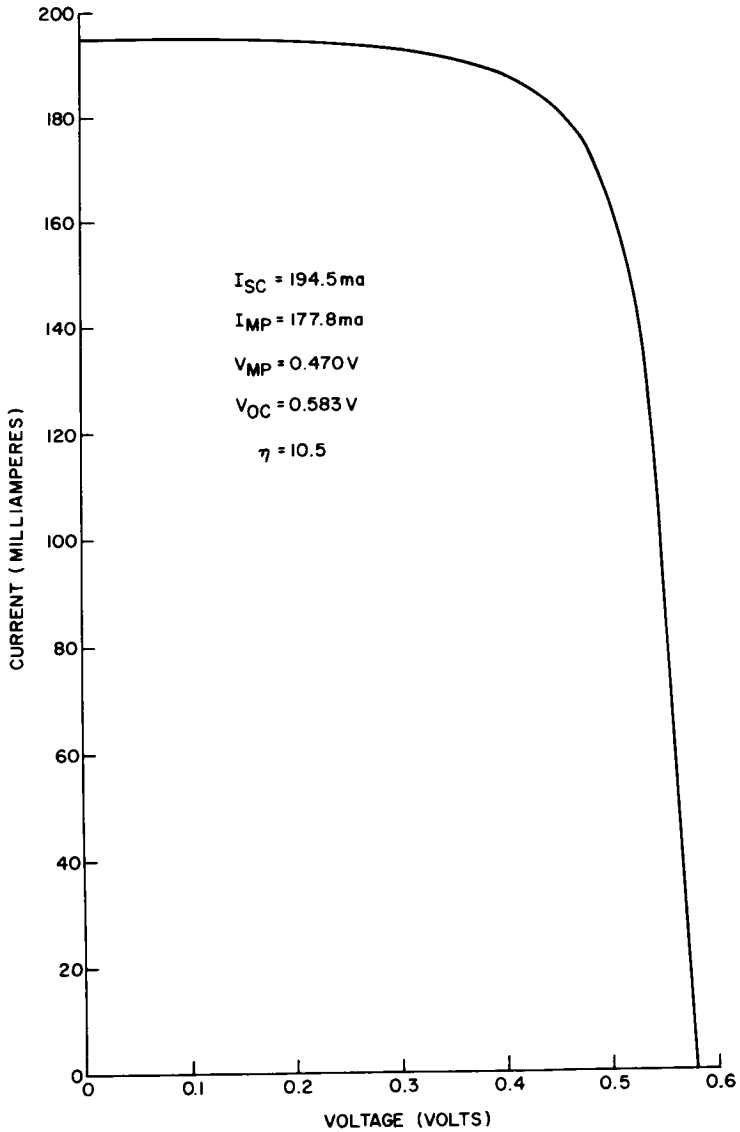

Figure X-40. I-V Curve for RCA MT 1-Ohm-Cm Solar Cell

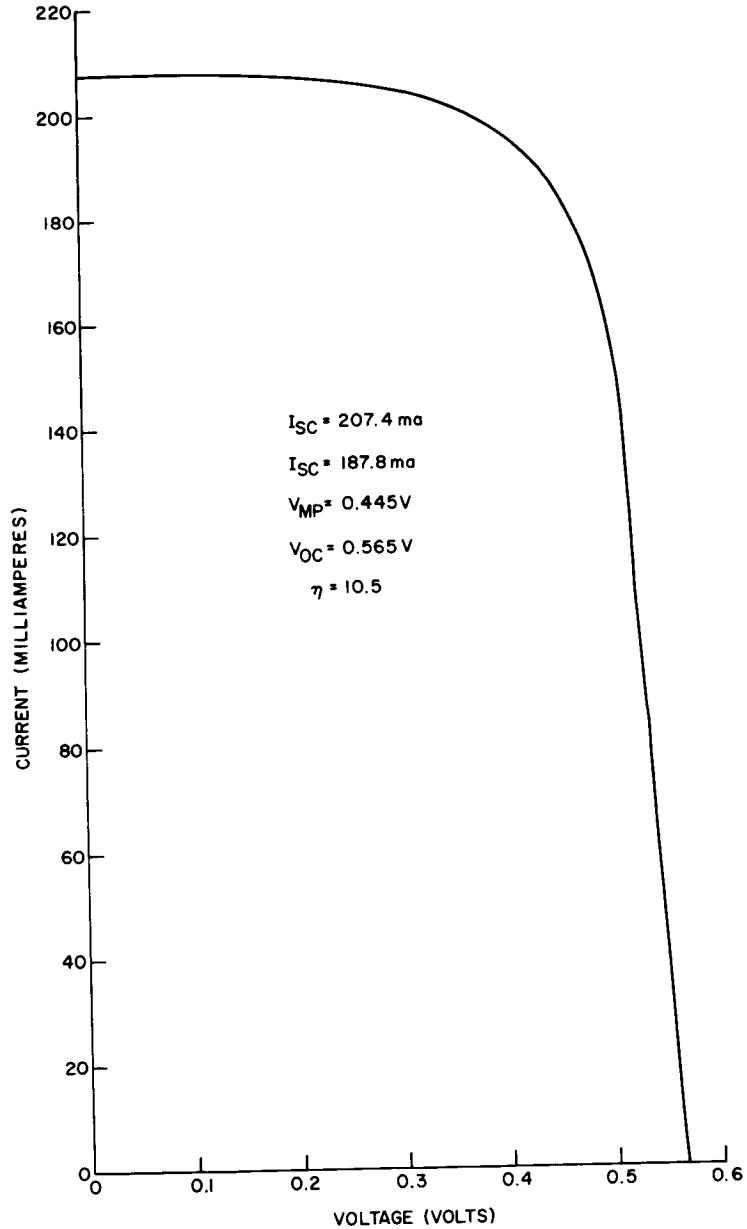

Figure X-41. I-V Curve for RCA MT 10-Ohm-Cm Solar Cell

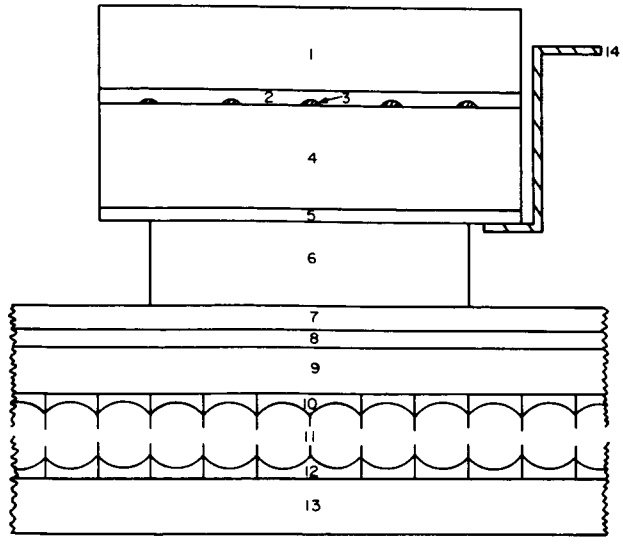

Figure X-42. Cross Section of Solar Array

(4) N-on-P silicon wafer, 10 mils thick.

(5) Titanium-silver P contact to P material of solar cell, 1 mil thick.

(6) RTV 560/580, 6 mils thick.

(7) H-film, 2 mils thick.

(8) H-film adhesive, 1 mil thick.

(9) Aluminum Honeycomb skin, 3.7 mils thick.

(10) Aluminum skin-to-core bonding adhesive FM-1000, 4 mils thick.

(11) Aluminum core, approximately 1/4 inch thick.

(12) Aluminum skin-to-core bonding adhesive FM-1000, 4 mils thick.

(13) Aluminum honeycomb skin, 3.7 mils thick.

(14) Z-tab, connector material to P contact of solar cell.

Items (1) and (2) are used in the frontshielding determination. Items (5) through (13) are used in the backshielding calculation. The results of multiplying the density of a particular material by its thickness and summing the contributions from various materials is presented in the following.

	Mils of Corning 7940 Fused Silica, Item (1)		
	6	9	18
Frontshielding in grams/(centimeter)^2	0.033	0.05	0.100
Backshielding in grams/(centimeter)^2	0.103		

(8) Design Factors

Various factors are herein identified and described that affect solar array electrical performance. Table X-14 presents a summary of these factors. The application of these factors is presented in Paragraph X. E.

(a) N-on-P Cells

1. Cell-Current Design Factors

a. Ultraviolet. RCA and other experimenters (References X-7 and X-8) have determined that solar-cell assemblies (consisting of a solar cell, coverglass-to-cell adhesive, and a filter-coated coverglass) are affected by exposure to ultraviolet irradiation. In general, the results indicate that the optical-filter substrate adhesive contributes to a reduction in solar-cell assembly power due to degradation from ultraviolet exposure. These tests at RCA on the Lunar Orbiter program and on the Comsat Study Program consisted of exposure to ultraviolet radiation of various vendors' cells, various adhesives, various ratios of resin to catalyst for the same adhesive, different catalyst and different resin batches of the same adhesive, different film thicknesses of the same adhesive, and blue filters from the Optical Coating Laboratory on Microsheet and Corning 7940. The degradation to the Corning 7940 substrate with blue filter and antireflective coating, and the Sylgard 182 adhesive is a maximum of two percent.

b. Power Prediction. Several factors contribute to the uncertainty in the prediction of solar-array output power under air-mass-zero conditions. these factors include standard-cell calibration (all measurements of solar cells and panels are referenced to standard cells that are used to calibrate the illumination source or to determine solar intensity in outdoor measurements). Many different techniques are used to calibrate standard solar cells; however, RCA has found that the minimum error is obtained by calibrating the cells using an airplane (Reference X-9) with monthly reference checks of these standards under a stable light source (Reference X-10).

TABLE X-14. SUMMARY OF SOLAR-CELL DESIGN FACTORS

	Maximum, Beginning of Life, N-on-P	End of Life, Worst Case, N-on-P	End of Life, Worst Case, Lithium-Doped, P-on-N
CURRENT			
1. Ultraviolet	1.0	0.98	1.0
2. Power prediction	1.02	0.98	0.98
3. Measurement	1.01	0.99	0.99
4. Solar Constant	1.033	0.967	0.967
5. Angle	0.995	0.99	0.99
6. Shading	1.0	1.0	1.0
7. Micrometeorites and sputtering	1.0	0.97	0.97
8. Radiation damage to optical-filter substrate (N-on-P, P-on-N cells) and Sylgard 182 adhesive (N-on-P cells only)	1.0	1.0	1.0
9. (a) Application of optical filter and adhesive to N-on-P solar cell.	0.97	0.96	
(b) Application of integral cover to solar cell and antireflective coating to integral cover	1.0		1.01
Product of 1 through 9	1.027	0.848	0.90
VOLTAGE			
1. Wiring loss	1.0	0.99	0.99
2. Thermal cycling	1.0	0.98	0.98
3. Measurement	1.01	0.99	0.99

Note: Bare 2 x 3 cm cell, 10-mils-thick, 10.5-percent efficiency, air-mass-zero

By analysis of the method used, correlation of the data for this method, and recognition of the additional errors (such as (1) variations in the values of open-circuit-voltage and short-circuit-current temperature coefficients from the nominal assumed values, and (2) small erros that accumulate in the application of design factors and construction of I-V curves for solar-panel design), the total allowance of ±2 percent is made in the design of solar panels for the errors in power prediction.

c. Measurement. A value of ±1 percent in the uncertainty of solar-panel measurements is based upon an estimate of the errors in the test equipment used for the measurements, due to nonuniformity of the temperature over the panel area, nonuniformity of illumination intensity, and spectral composition of the array of illumination sources. An allowance of ±1 percent in the design of the solar-cell panels for this current-measurement tolerance (or error) will ensure that panels will meet minimum performance specifications when tested under large-area illuminators.

d. Solar Constant. The short-circuit current of a solar cell varies linearly with instensity (for the same relative spectrum) over the range of intensity changes from the reference value of 139.6 mw per square cm at 1 A.U.*, due to the elliptical orbit of the earth about the sun.

e. Angle. The output current (short-circuit) varies cosinusoidally as the angle to the sun vector varies between normal incidence (0°) and 90° incidence. The maximum angular deviation of the panels from normal incidence due to the panel curvature and panel-orientation control system is $\pm 10^{\circ}$. This results in a design factor of $\pm 1.0^{\circ}$ percent. (See Paragraph VII.D.3.) The beginning-of-life value of 0.5 percent assumes no orientation-system tracking error.

f. Shading. The effect of shading of portions of a solar array has been thoroughly analyzed by RCA (see Section IX). However, for the present, the assumption is that there are no items on the spacecraft that will shadow the solar cells on the array. This design factor is therefore 1.0.

g. Micrometeroroid Damage. Measurements have been made of the momentum, kinetic energy, and mechanical impact damage due to dust particles, utilizing various sensors and detectors flown on various spacecraft. Typical data is presented in reference X-11. Reference X-12 and X-13 present results of bombarding cover glassed solar cells with grit silicon carbide and glass spheres. The degradation rates predicted, based upon the results reported in these references, have not been experienced by RCA spacecraft. In reference X-14, it is reported that erosion of thin coatings by micrometeorites often applied to mirrors and lenses is unimportant. It is further reported that, on the first Orbiting Solar Observatory, whatever

*Astronomical Unit

slight errosion does occur (at altitudes near 500 km), far less than 100 Angstroms of material is removed from the surface in one year. The maximum damage to the solar-cell optical filter for this conceptual study is therefore estimated at 3 percent, which corresponds to complete removal of the antireflective coating on top of the optical-filter substrate.

h. Radiation Damage to Optical Filter and Optical Filter Adhesive. Based on the information contained in Reference X 6, the degradation in transmission due to charged-particle radiation is zero for Sylgard 182 and the Corning fused silica platelet with blue reflective and antireflective coating. This design factor is therefore 1.0.

i. Application of Optical Filter and Adhesive to Solar Cell. The decrease in short-circuit current of a solar cell, due to bonding the optical filter to the cell with Sylgard 182 adhesive, is a maximum of 4 percent.

2. Cell-Voltage Design Factors

a. Wiring Loss. The effective increase in series resistance caused by the resistance of wiring the cells into a series string and connecting the series strings in parallel produces a maximum voltage loss of 1 percent of maximum-power voltage.

b. Thermal Cycling. A 2-percent allowance in panel design is included for the degradation in solar-cell output due to thermal cycling. The degradation arises primarily from physical stresses caused by mismatches in thermal coefficients of the contact materials. The 2-percent value is supported by test data accumulated on the Lunar Orbiter program by RCA, and is manifested as electrical degradation averaging 2 percent in voltage at the maximum-power point. The cells on the Lunar Orbiter program experienced 600 thermal cycles between -120 and +120°C. On the Nimbus program, RCA conducted similar tests using a different connector material and design for 1000 cycles over a temperature range of +60°C to -80°C. The maximum degradation was also 2 percent. Since the Nimbus program preceded the Lunar Orbiter program, and because the temperature range was increased on the Lunar Orbiter program without increasing the degradation of the solar cells, it is assumed that comparable connector designs and test results can be achieved on this program.

c. Voltage Measurement Tolerance. A 1-percent allowance in voltage is included in array design because of errors associated with large-area panel measurements.

(b) Lithium-Doped P-on-N Cells with Integral Covers

In order to utilize P-on-N lithium-doped cells in this analysis, several assumptions have to be made.

1. The only effect of adding lithium to the P-on-N cells is to remove the susceptibility of the cell to charged-particle radiation damage; i.e., the short-circuit current temperature coefficients, open-circuit voltage temperature coefficients, and the ultraviolet resistance of the cell, etc., remain unchanged.

2. The radiation resistance of the lithium-doped cell and the characteristics of the cell are unaffected by thermal cycling within the temperature range of the solar array; i.e., within this temperature range, no lithium migration should occur.

3. The number of electrons and protons impinging per hour on the 1-micron-thick integral cover and cell is sufficiently low that hardly any degradation is experienced by the lithium-doped cell (Reference X-3). Should this assumption be proven by test data to be incorrect, a 1-mil-thick integral cover would stop all of the low-protons and reduce the electron flux to a level that would not cause any degradation. The weight/area number would increase slightly. This would be the only effect of using the 1-mil-thick integral cover.

With the above assumptions, the worst-case end-of-life design factors for 1-micron and 1-mil-thick integral covers with anti-reflective coating and lithium-doped P-on-N solar cells are identical with the N-on-P cell with the exception of two cell-current design factors, ultraviolet and application of coverglass.

Since there is no organic adhesive used, the ultraviolet design factor is 1.0. In Paragraph X.C.2.b(4), the application of an integral cover to the cell and an antireflective coating to the integral cover is discussed. The design factor for the integral cover application to the cell is 1.01.

(9) Results

(The design factors, I-V curves, charged-particle flux and shielding values are stored in the computer program described in Paragraph X.E.3. The referenced program has been used to produce results discussed).

(a) N-on-P Cell

The initial step has been to determine the equivalent 1-MeV flux behind the front and back shielding, by the use of the computer program. The results are presented in Table X-13. The worst-case orbit with respect to flux is the 19,340-NMi, 30° orbit.

Utilizing the equivalent 1-MeV flux values, the initial I-V curves (1 and 10 ohm-cm, Figures X-40 and X-41) are then degraded to obtain the end-of-life I-V curves with respect to radiation.

Following that, the program degraded the I-V curves for design factors and then shifted the curves to various equilibrium temperatures. The results are presented in Table X-15

and graphically in Figures X-43 (1 ohm-cm), X-44 (10 ohm-cm), and X-45 (1 and 10 ohm-cm). The differences in power output between 1-ohm-cm and 10-ohm-cm cells (Figure X-45) is due to the differences in temperature coefficients and radiation resistance of the two cell types. The equilibrium temperatures of the solar array in the various orbits are:

200-NM, 28.5°, 90°	+55.04°C,
19,340-NM, 30°	+41.86°C.

1. Cell Base Resistivity. Table X-16 was produced, using Figures X-33 and X-34 and the equilibrium temperatures. Comparison of the maximum power output of 1-ohm-cm and 10-ohm-cm cells reveals that the 1-ohm-cm has greater power output, regardless of the orbit or optical-filter substrate thickness. Therefore, the cell selected for this mission is a 1-ohm-cm cell.

2. Optical-Filter Substrate Thickness. Table X-17 is a rearrangement of Table X-16. Comparison of the power outputs of the three orbits for the same glass thickness shows the worst-case orbit (minimum power output) to be the 200-nmi, 90° orbit. The worst-case orbit is, therefore, a function of both radiation and temperature. Using the values of maximum power from Table X-17 for the 200 NM 90° orbit, the area required for a 1000-watt array composed of 2 x 3 cm cells is calculated

$$\frac{1000\ Watts}{\frac{P_{max}}{Cell} \times \frac{145\ Cells}{sq.\ ft.}} = \text{area required for end-of-life power of 1000 watts}$$

	Optical-Filter Substrate Thickness	Pound/sq. ft.	Area required for 1000 watts at end-of-life (sq. ft.)	Weight of 1000-watt array (pounds)
2x3cm, 1-ohm-cm, 10.5% air-mass-zero efficiency, 10-mil-thick cells:	6 mils	0.75	127	95.3
	9 mils	0.78	125	97.5
	18 mils	0.866	123	106.8

Based upon the objective of minimum total array weight, and in view of the small area advantage gained by increasing glass thickness, the optimum optical-filter substrate thickness is 6 mils.

TABLE X-15. MAXIMUM SOLAR CELL POWER (MILLIWATTS)

Case Number	Orbit & Inclination	Front Shielding (MILS)	Base Resistivity Ω-cm	Temperature °C														
				60	45	30	15	0	-15	-30	-45	-60	-75	-90	-105	-120	-135	-150
SILICON N ON P, END OF LIFE																		
1	200 30	6	1	56.6	61.2	65.8	70.3	74.8	79.4	83.9	88.4	92.9	97.4	101.9	106.3	110.8	115.3	119.8
2	200 30	9	1	56.9	61.5	66.1	70.6	75.2	79.7	84.2	88.8	93.3	97.8	102.3	106.8	111.3	115.8	120.3
3	200 30	18	1	57.5	62.1	66.7	71.4	75.9	80.5	85.1	89.7	94.2	98.8	103.3	107.9	112.4	116.9	121.5
4	200 30	6	10	55.7	61.0	66.3	71.7	76.9	82.2	87.3	92.5	97.6	102.6	107.7	112.7	117.7	122.6	127.6
5	200 30	9	10	56.4	61.7	67.0	72.4	77.8	83.1	88.3	93.5	98.7	103.8	108.9	114.0	119.0	124.0	129.0
6	200 30	18	10	56.5	61.8	67.2	72.6	77.9	83.2	88.5	93.7	98.8	103.9	109.0	114.1	119.1	124.1	129.1
7	200 90	6	1	52.9	57.3	61.7	66.1	70.5	74.8	79.2	83.5	87.8	92.2	96.5	100.8	105.1	109.5	113.8
8	200 90	9	1	53.6	58.1	62.5	66.9	71.3	75.7	80.1	84.4	88.8	93.2	97.5	101.9	106.2	110.6	114.9
9	200 90	18	1	54.7	59.2	63.7	68.1	72.6	77.0	81.4	85.8	90.3	94.7	99.1	103.5	107.9	112.3	116.6
10	200 90	6	10	51.8	56.9	62.0	67.1	72.1	77.1	82.1	87.0	91.9	96.7	101.5	106.3	111.1	116.8	120.6
11	200 90	9	10	52.5	57.6	62.8	67.9	73.0	78.1	83.0	88.0	92.9	97.8	102.6	107.5	112.2	117.0	121.8
12	200 90	18	10	53.7	58.8	64.0	69.2	74.4	79.5	84.5	89.5	94.5	99.4	104.3	109.2	114.1	118.9	123.8
13	19340 30	6	1	49.5	53.7	58.0	62.2	66.4	70.6	74.8	79.0	83.1	87.3	91.5	95.7	99.8	104.0	108.2
14	19340 30	9	1	50.6	54.9	59.1	63.4	67.6	71.9	76.1	80.4	84.6	88.8	93.0	97.3	101.5	105.7	109.9
15	19340 30	18	1	51.9	56.3	60.6	65.0	69.3	73.6	77.9	82.2	86.5	90.8	95.1	99.4	103.6	107.9	112.2
16	19340 30	6	10	48.4	53.3	58.2	63.1	68.0	72.8	77.6	82.3	87.0	91.6	96.2	100.8	105.4	110.0	114.6
17	19340 30	9	10	49.4	54.3	59.3	64.3	69.2	74.1	78.9	83.7	88.4	93.1	97.8	102.5	107.1	111.7	116.4
18	19340 30	18	10	50.8	55.8	60.9	66.0	71.0	75.9	80.8	85.7	90.5	95.3	100.0	104.8	109.5	114.2	118.9
SILICON N ON P BEGINNING OF LIFE																		
19	200 30	6	1	75.0	80.7	86.4	92.1	97.8	103.5	109.2	114.9	120.5	126.2	131.8	137.5	143.1	148.7	154.4
20	200 90 19340 30	9 18	10	71.8	78.3	84.8	91.3	97.8	104.3	110.8	117.3	123.7	130.0	136.3	142.6	148.8	155.0	161.2
END OF LIFE AND BEGINNING OF LIFE, SILICON P-ON-N LITHIUM DOPED																		
21	200 30	6	1	61.4	66.3	71.2	76.1	81.0	85.9	90.8	95.6	100.5	105.3	110.1	115.0	119.8	124.6	129.4
22	200 90 19340 30	9 18	10	59.2	64.8	70.4	76.1	81.8	87.4	93.0	98.6	104.1	109.6	115.0	120.4	125.8	131.1	136.4

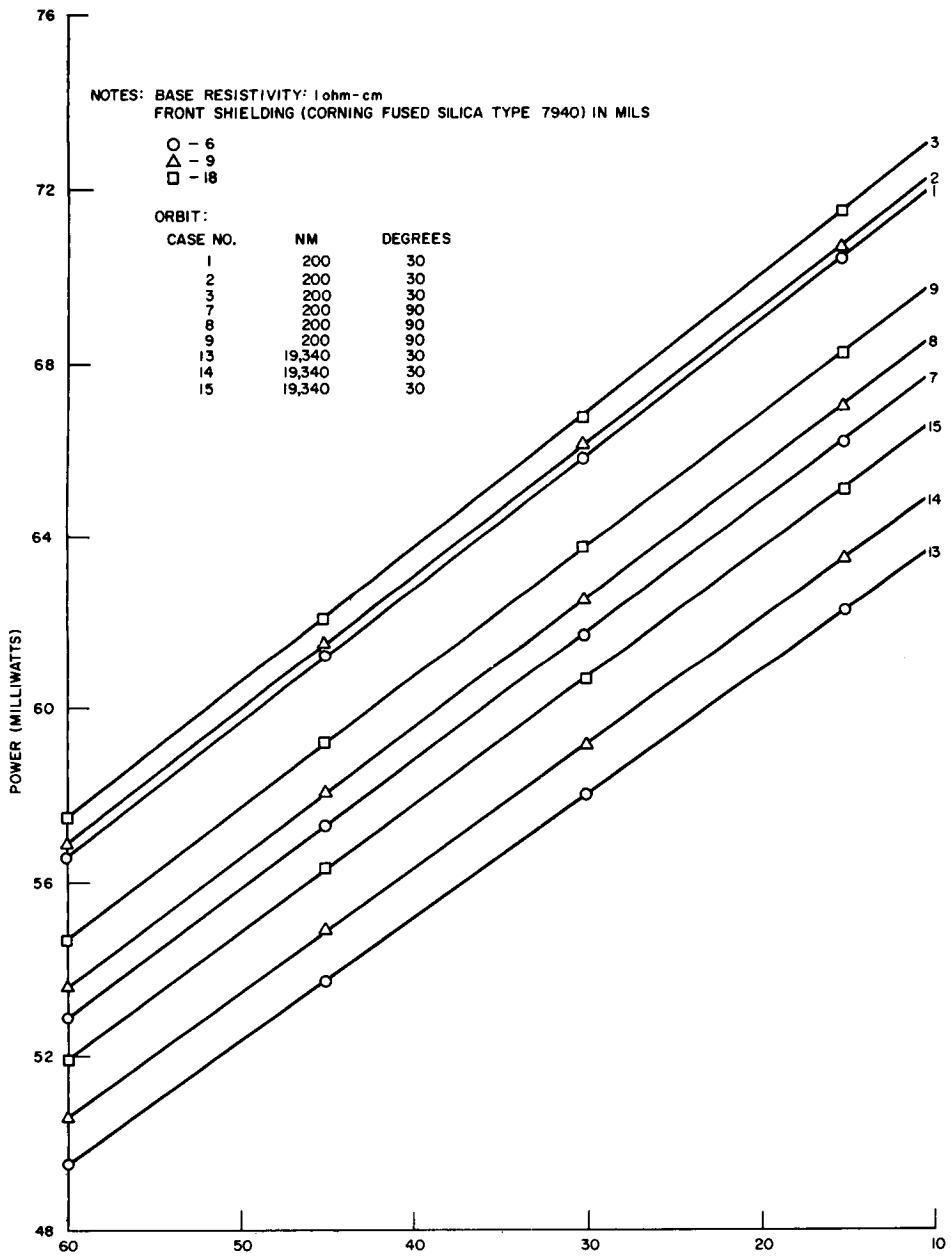

Figure X-43. Maximum Power of 1-Ohm Solar Cells

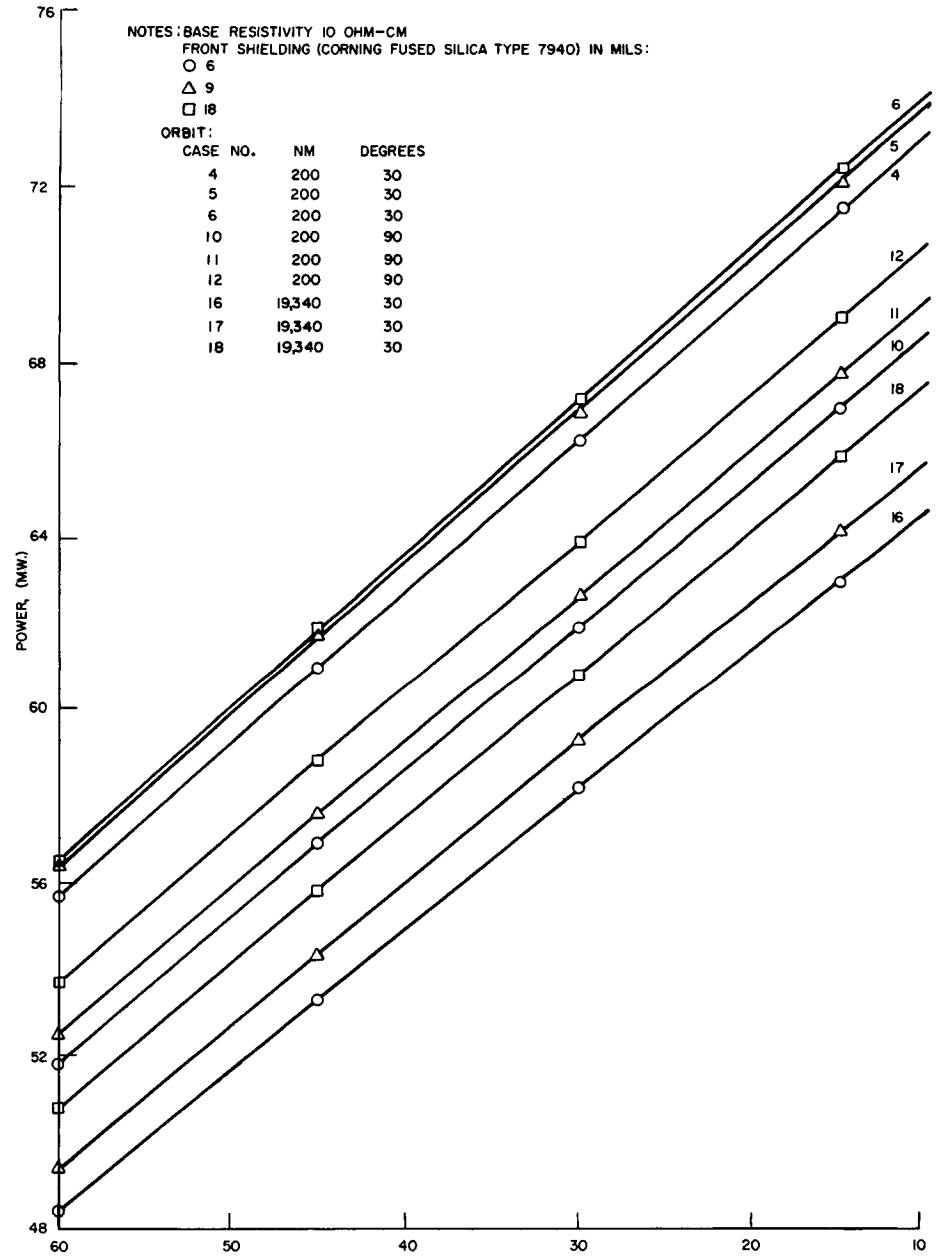

Figure X-44. Maximum Power of 10-Ohm Solar Cells

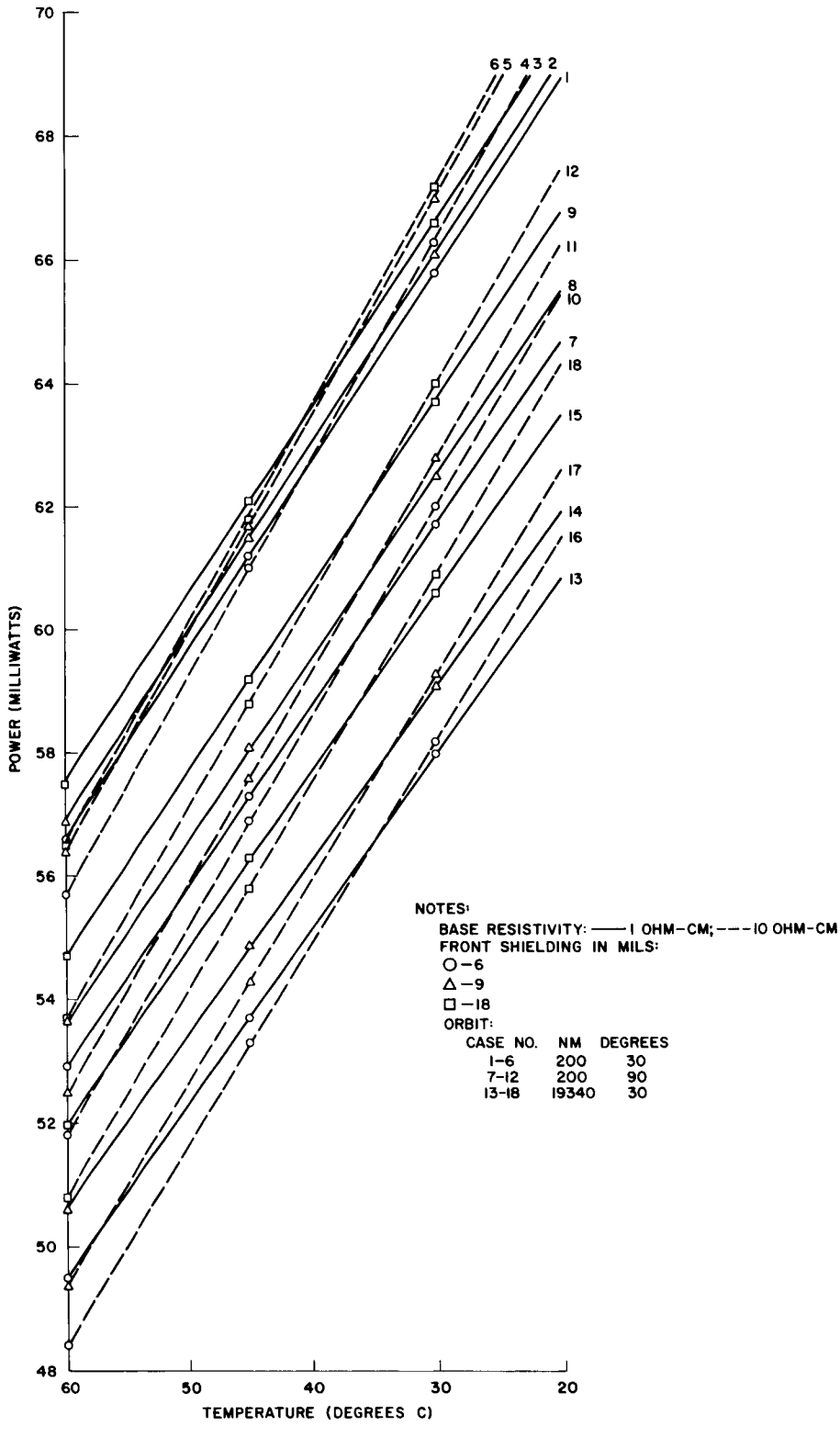

Figure X-45. Maximum Power of 1 and 10-Ohm Solar Cells

TABLE X-16. MAXIMUM POWER FOR CELLS OF 1 AND 10 OHM-CM RESISTIVITY

Orbit		Filter Substrate, Thickness (MILS)	Maximum Power in Milliwatts/2x3cm Cell	
Altitude, (NM)	Inclination (Degrees)		1 ohm-cm	10 ohm-cm
200	30	6	58.1	57.45
		9	58.4	58.15
		18	59.0	58.25
200	90	6	54.35	53.5
		9	55.05	54.18
		18	56.2	55.38
19,340	30	6	54.6	54.3
		9	55.75	55.38
		18	57.2	56.9

TABLE X-17. OUTPUTS OF CELLS WITH VARIOUS FILTER-SUBSTRATE THICKNESS

Filter-Substrate Thickness (MILS)	200-NM 30° Orbit	Maximum Power in Milliwatts/2x3cm 1-ohm-cm cell	
		200-NM 90° Orbit	19,340-NM, 30° Orbit
6	58.1	54.35	54.6
9	58.4	55.05	55.75
18	59.0	56.2	57.2

3. Number of Cells in Series. This is as determined in Paragraph X. C. 2. d.

4. Maximum Current and Voltage. The maximum current to be used in isolation diode selection is defined as 2.033 amperes. This current value is determined from the value of short-circuit current of the maximum, beginning-of-life, I-V curve (0.2033 ampere per series string), 10 series strings in parallel per diode. The peak voltage is determined from the open-circuit voltage of the maximum beginning-of-life I-V curve. The lowest temperature (maximum open-circuit voltage) is -156.8°C in the 19,340-NM, 30° orbit. From Figure X-51, the maximum open-circuit voltage is 0.996 volts per cell. Maximum array voltage may be as high as 140 volts, as discussed in Paragraph X. C. 2. d.

5. Summary of Results. The solar-array design valid for all three orbits is defined as consisting of 10.5-percent air-mass-zero efficiency, 2x3cm, 10-mil-thick, 1-ohm-cm solar cells with 6-mil-thick Corning type 7940 fused-silica optical-filter substrate with blue reflective and antireflective coatings. The number of paralleled series strings per isolation diode is assumed to be ten. Any change in the orbits considered, mission duration, mission launch period, solar array equilibrium temperatures, and/or solar-cell panel thickness (change in backshielding) could (and in most cases will) affect the results derived herein.

(b) Lithium-Doped P-on-N Cells

Based upon the assumptions made in Paragraph X. C. 2. b(8)(b), the maximum power at end of life for lithium-doped P-on-N 1-ohm and 10 ohm-cm cells are presented in Table X-15 and Figure X-46. (NOTE: Worst-case beginning-of-life power will be 5 percent greater than shown, due to absence of micrometeorite and thermal-cycling degradation.) The equilibrium temperature below which 10-ohm-cm cells become more attractive is 15°C (Table X-15). Table X-18 compares the advantages of a lithium-doped P-on-N solar array with the N-on-P 1-ohm-cm cell array selected for the conceptual design.

(c) Universal Earth-Orbiting Solar Array

A comparison of P-on-N lithium-doped and N-on-P cells, where the potential of lithium-doped cells is fully realized, is demonstrated in the design of a solar array that can be utilized in any earth orbit.

The design parameters are simply determined.

1. The minimum-altitude orbit determines the maximum equilibrium temperature (after array weight, emissivities, conductivities, and absorptivities of the array are defined), which in turn is utilized to determine the number of cells in series for a given type of storage battery used in the system.

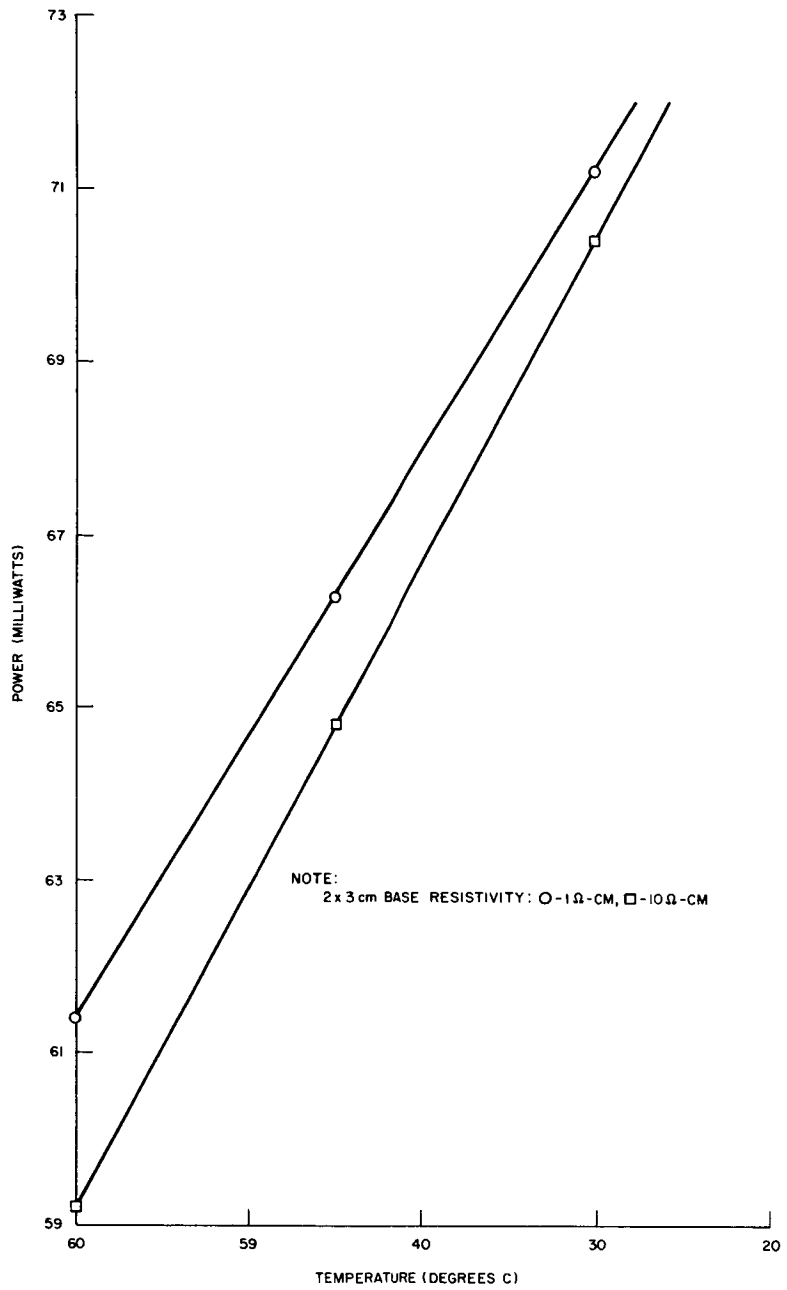

Figure X-46. Maximum Power vs. Temperature for Silicon, P-on-N, Lithium-Doped Solar Cell

2. The orbit with maximum nighttime determines the minimum temperature (after array weight, etc., are defined), which in turn is utilized in selection of materials in making electrical contact to the cells.

3. The orbit in which the maximum flux is intercepted by the array and the duration of the mission determines the thickness of Corning 7940 applied.

TABLE X-18. COMPARISON OF 1-OHM-CM N-ON-P CELL WITH LITHIUM-DOPED P-ON-N CELLS

	200-NM, 90° Orbit	
	Array Area/1000 Watts (sq. ft.)	Weight of 1000-Watt Array (pounds)
N-on-P, 1-ohm-cm cell, 6-mil-thick optical-filter substrate	127.0	95.3
Lithium-Doped P-on-N cell, 1 micron-thick integral coating	106.5 (16%)	74.9 (21.4%)
Lithium-Doped P-on-N cell, 1 mil-thick integral coating	109.5 (14%)	76.1 (20%)

Note: Percentages in parenthesis are area and weight savings of lithium-doped P-on-N cells compared to N-on-P cells.

c. CELL DATA STORED IN THE COMPUTER PROGRAM

Tradeoffs performed in Paragraph X. C. 2. b have led to the selection of a 3 x 3 cm conventional N/P cell with 6-mil cover glass thickness. Selected base resistivity is 1 ohm-cm.

The computer program described in Paragraph X. E contains solar-cell subroutines described in detail in that section. These subroutines have been used to provide data shown in Figure X-47 based on the selected solar cell and its characteristics. This data is stored in the program to enable computer calculations of the array size for any value of the 1-MeV electron flux, if values other than those determined in this study program are assumed (see Table X-13). To make the computer program more versatile, similar data has been determined for a high-base-resistivity, 2 x 3 cm cell with a 6-mil cover (Figure X-48).

d. ARRAY ELECTRICAL DESIGN

The electrical design of an array is performed in four sequential steps. First, the minimum solar-cell voltage requirements are established as determined by the type of battery used and the line drops encountered by the array current in the array-to-battery path. Second, the number of series cells to meet the requirements is calculated. Third, the resultant voltage extremes are found at the array output (unregulated) bus. Fourth, an isolation diode is selected for the solar array, based on the first three steps.

The line drops summarized are based on the bus bar design, (Paragraph X. C. 4. e) and the array mechanical design effort reported in Paragraph X. C. 2. e, past experience, and engineering judgment. The voltage drops for various components have been determined during different phases of this study program but they have not been included as a line-loss compensation factor in sizing array power. The proper number of series cells, however, has been established as described in the following.

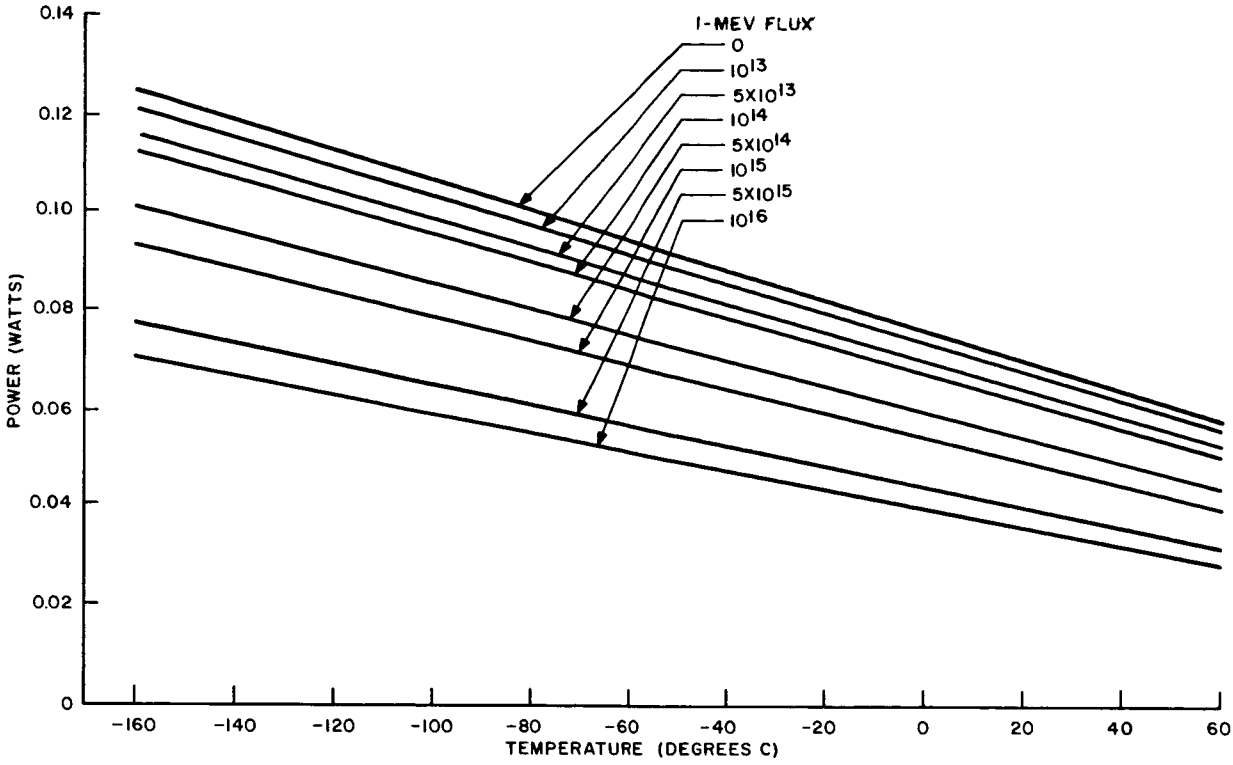

Figure X-47. End of Life, Worst-Case, Solar Cell Maximum Power vs. Temperature and 1-MeV Flux (1 ohm-cm)

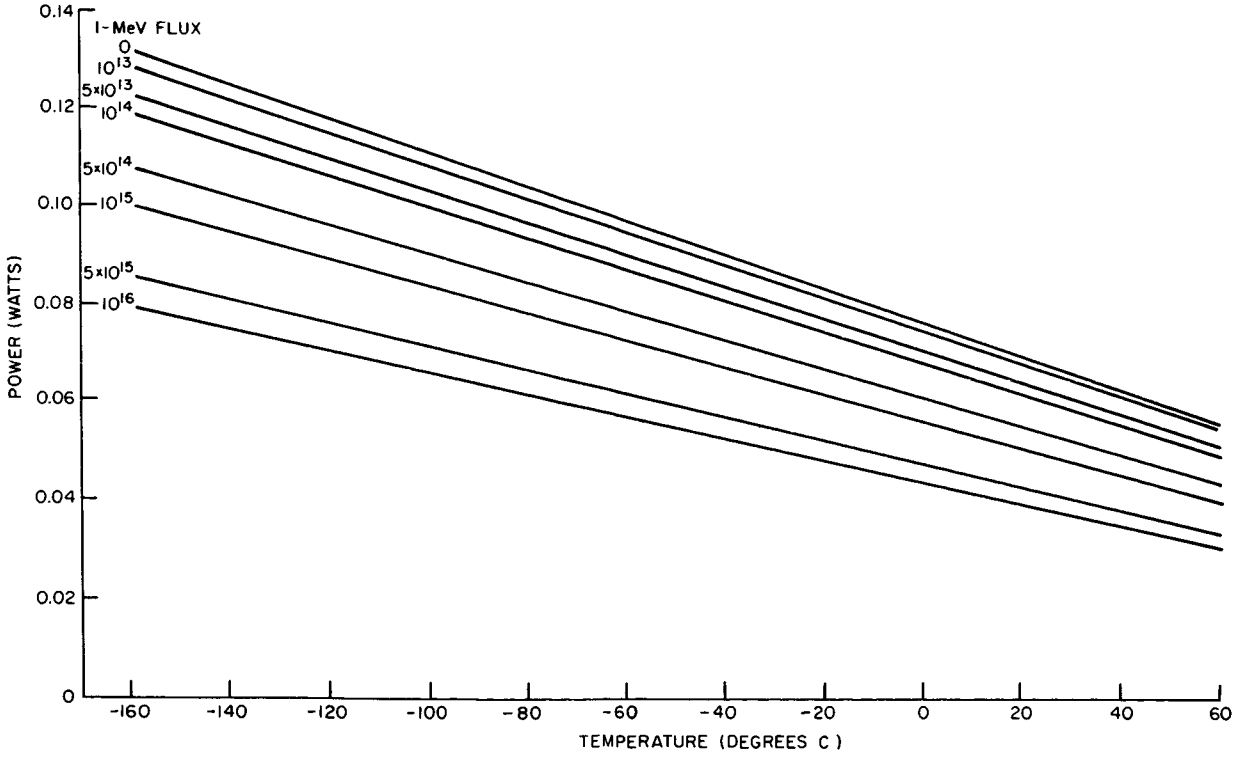

Figure X-48. End-of-Life, Worst-Case Solar-Cell Maximum Power vs. Temperature and 1 MeV Flux (10-ohm-cm)

Figure X-49 is a schematic representation of the various voltage drops that must be overcome by the addition of a sufficient number of series cells. Voltage V_S is measured directly across the solar-cell strings and includes an allowance for cell and module wiring drops. The array-bus drop of 0.5 volt average is a result of the tradeoff study (Paragraph X.C.2.e(4)) involving bus weight versus power loss. Drops across the various sections of cabling running from the slip rings to the charge electronics are based on the bus-bar design parameters discussed in Paragraph X.C.4.e. The slip-ring drop of 50 millivolts is an engineering estimate. The worst-case (largest) value of the minimum required voltage drop across the battery charging electronics is 1.5 volts, as shown. Summation of all the drops around the loop amounts to 5.3 volts.

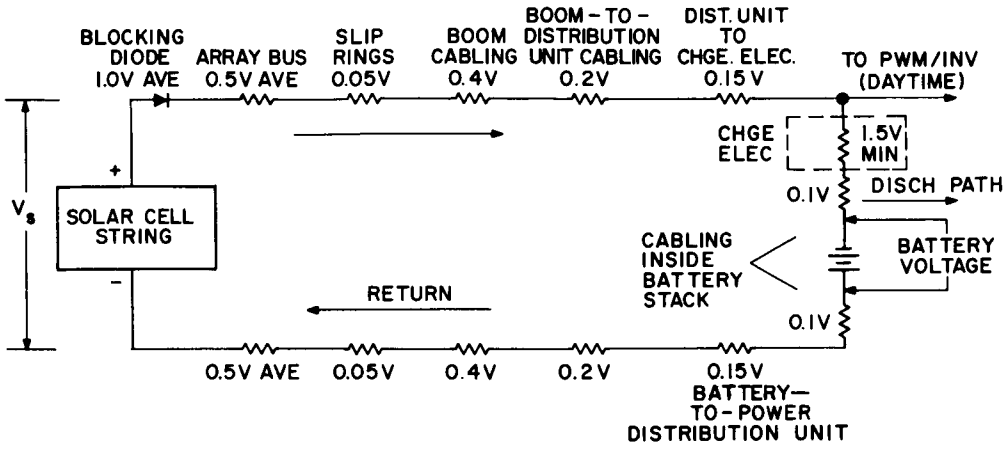

Figure X-49. Power System Voltage Drops, Schematic Diagram

Basing the maximum battery-charge voltage on 1.5 volts per storage cell for a nickel-cadmium (Ni-Cd) battery consisting of 29 series cells, and 1.6 volts per cell for a silver-cadmium (Ag-Cd) battery consisting of 32 series cells, the respective minimum battery-charge voltage requirements are 43.5 and 51.2 volts, respectively. Reflected to the solar cells (voltage level V_S) by the addition of 5.3 volts, the requirements are 48.8 volts minimum, Ni-Cd system and 56.5 volts minimum, Ag-Cd system.

Based on Figures X-50 and X-51, the voltages per solar cell are as follows:

Orbit	At P_{max} Volts at T_{max} (End of Life)	At V_{oc} Volts at T_{min} (Beginning of Life)
19,340-NM, 30°	0.403 V @ +41.86°C	0.9962 V @ -156.8°C
200-NM, 28.5°	0.3935 V @ +55.04°C	0.796 V @ -65.85°C
200-NM, polar	0.3835 V @ +55.04°C	0.796 V @ -65.85°C

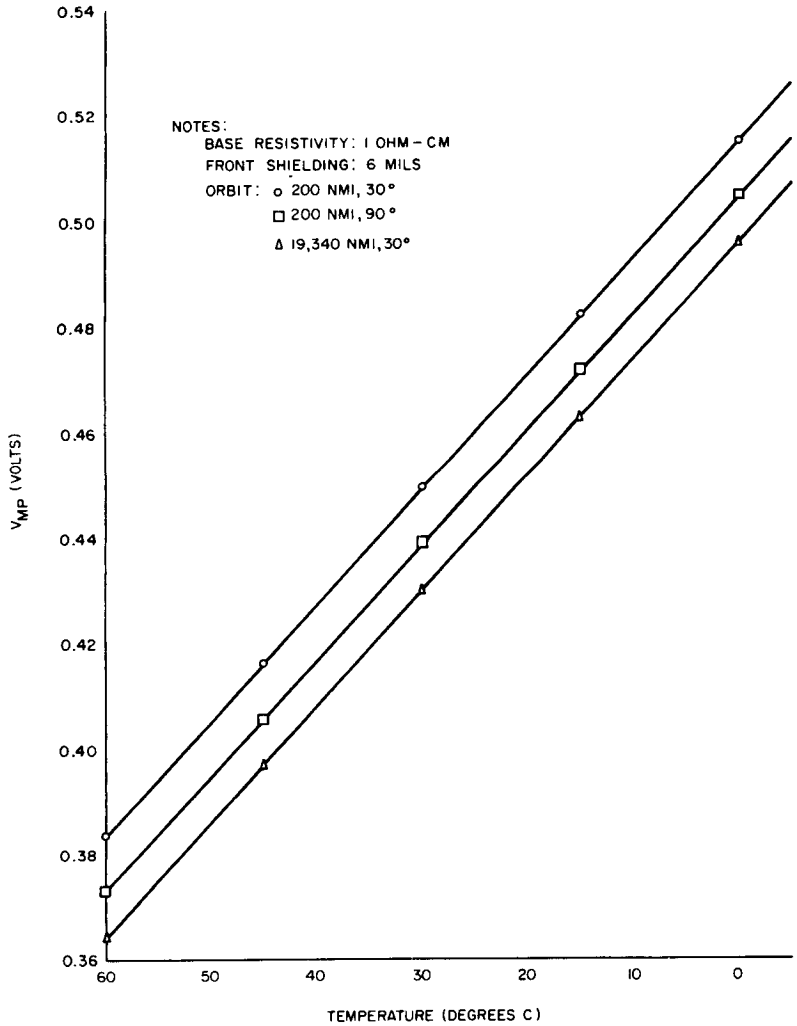

Figure X-50. Maximum Power Solar-Cell Voltages vs. Temperature (Worst Case End of Life)

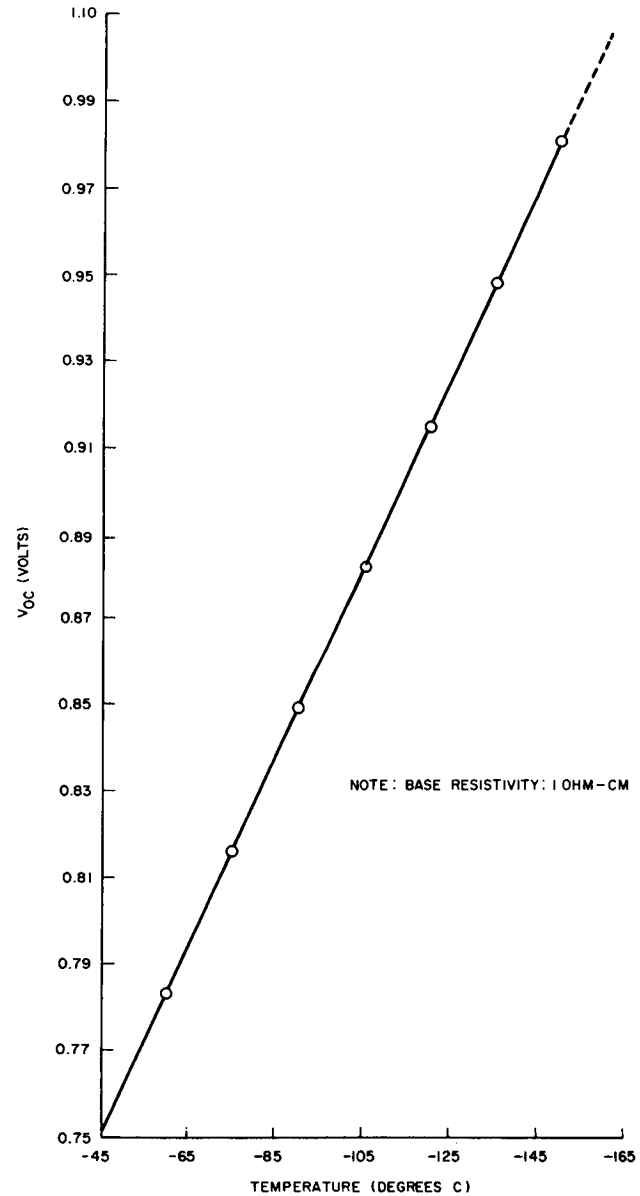

Figure X-51. Open-Circuit Solar-Cell Voltages vs. Temperature (Worst Case End of Life)

Selection of the number of series cells is governed by the condition that a certain minimum voltage must be maintained at the input terminals of the battery-charge electronics, referenced to battery ground.

The maximum-power-point voltage at end of life at steady-state temperature is the lowest per-cell operating voltage needed to determine the minimum required number of series cells N_S. The open-circuit voltage at the beginning of life, at the lowest solar cell temperature multiplied by N_S defines the maximum possible voltage that could appear at the unregulated bus. The maximum bus voltage is a factor in electronic circuitry design. As a sample calculation, assume a 19,340-NM, 30° orbit and an Ag-Cd battery system:

$N_S = 56.5/0.403 = 141$ or more series cells;

$141(0.9962) = 140.3$ volts maximum no-load voltage, unregulated bus.

The following tabulation illustrates the minimum series-cell requirements and the resultant maximum voltages for each individual case of orbit and battery type.

Orbit	Battery	No. Series Cells, N_S	Max. Voltage (Volts)
19,340-NM, 30°	Ni-Cd	122	121.6
	Ag-Cd	141	140.3
200-NM, 28.5°	Ni-Cd	124	98.7
	Ag-Cd	144	114.8
200-NM, 90°	Ni-Cd	128	102
	Ag-Cd	148	117.8

The case of the low-altitude polar orbit and an Ag-Cd battery requires the largest number N_S. Thus, if a single-array electrical design were to be performed to yield adequate end-of-life voltage for all cases, N_S is equal to 148 and the maximum voltages would be 147.4 volts and 117.8 volts in the synchronous and 200-n mi orbits, respectively. If, one the other hand, Ag-Cd type batteries are not flown in the low-altitude missions, as recommended in the discussion of conceptual designs (Paragraph X.G), N_S equals 141 and the corresponding voltages are 140.3 and 112 volts. The latter approach would, therefore, enable a slight voltage reduction. The sample layout shown in Figure X-52 is based on 145 series cells as a typical number.

Worst-case operating parameters for the isolation diodes have been determined to be as follows:

- Reverse voltage: 140 Vdc, nominal;
- Forward current: 2.033 amperes dc (Paragraph X.C.2.b(9)(a)),
- Mounting-surface temperature: +55°C to -140°C assumed.

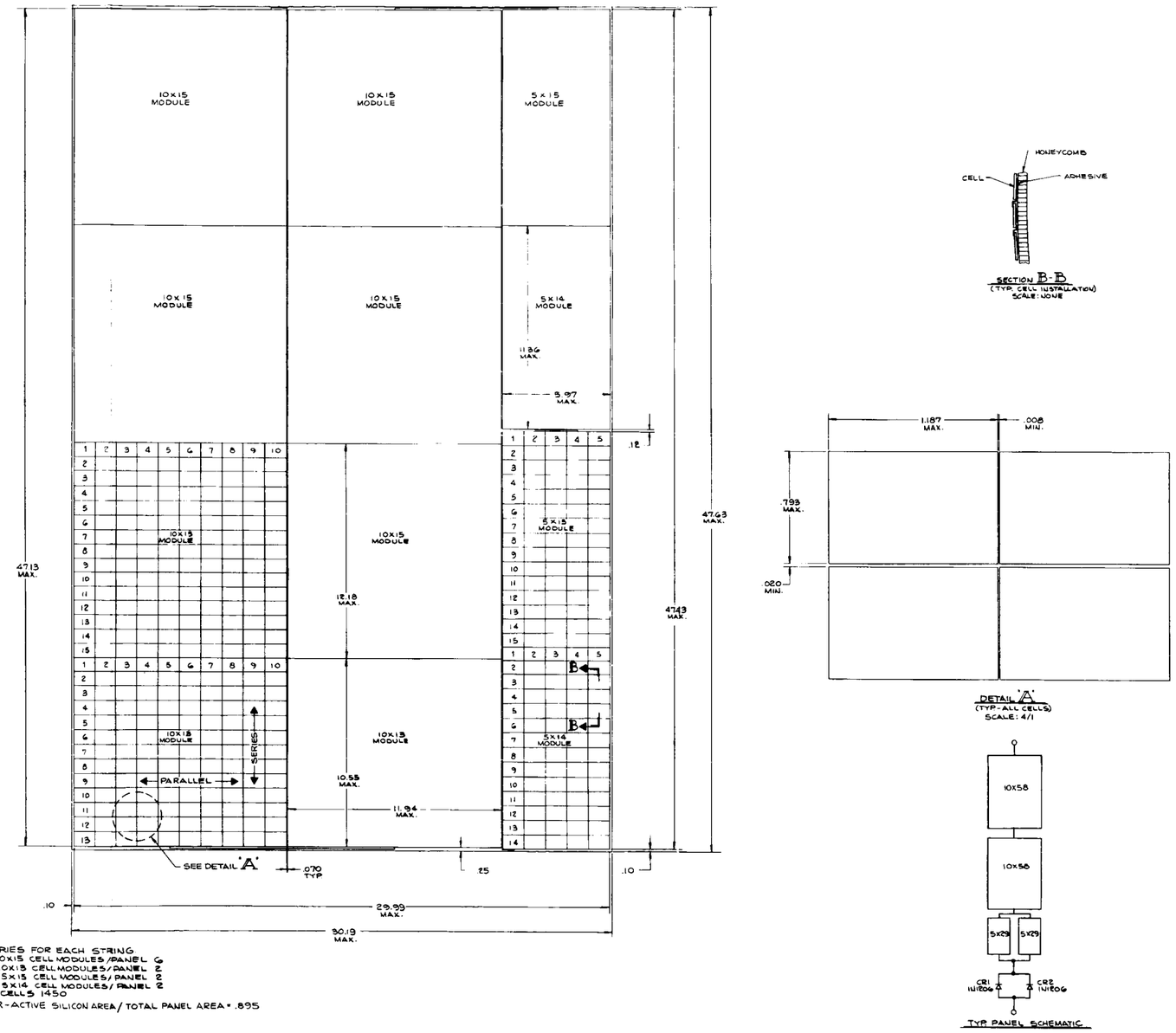

NOTES:

1. 145 CELLS IN SERIES FOR EACH STRING
2. TOTAL NO. OF 10X15 CELL MODULES/PANEL 6
   TOTAL NO. OF 10X13 CELL MODULES/PANEL 2
   TOTAL NO. OF 5X15 CELL MODULES/PANEL 2
   TOTAL NO. OF 5X14 CELL MODULES/PANEL 2
   TOTAL NO. OF CELLS 1450
3. PACKING FACTOR-ACTIVE SILICON AREA/TOTAL PANEL AREA = .895

Figure X-52. Solar-Array Panel Layout

X-93-1

It is felt that these requirements will be most adequately met by a JAN 1N1206 diode (per MIL-S-19500/260). In addition to military qualification, this part was qualified for use in the Lunar Orbiter program, where it also served as a solar-array isolation diode. For the Lunar Orbiter program the 1N1206 was subjected to 300 thermal cycles in vacuum with temperature extremes of -120°C to +120°C; no degradation was observed. The diode carries 0.5 ampere maximum with a reverse voltage of 32 volts (maximum), but is rated in MIL-S-19500/260 for 600 volts $V_{R\ maximum}$ and 12 amperes $I_{forward}$ maximum at T_{case} of 150°C.

For this mission, requalification of the diode will be required in the event that the thermal requirements are more stringent. However, it is felt that no difficulty should be experienced in this area.

The summation of all the drops around the array and battery (path taken by the charge current, Figure X-49) yielded a total drop of 5.3 volts and was used to define the array electrical design in terms of series-string increments. It is also necessary to compensate the array for the power lost due to these drops.

The 1.5-volt drop through the charge electronics is included in the charger/tracker efficiency calculation. This leaves 3.8 volts of drop to be compensated for. If all the drops due to resistors and the diode were to be assumed equal to zero, the array voltage requirements would be, in a Ni-Cd battery system:

$$V_S = 43.5 + 1.5 = 45 \text{ volts minimum required.}$$

The actual requirement, however, is 48.8 volts as determined before in this section, i.e., greater by 3.8 volts. The corresponding array over-design margin required to overcome the drops is, therefore, 48.8/45 or 1.083. Similarly, a system employing Ag-Cd batteries requires an array over-design factor of 56.5/52.7, or 1.071.

The computer program developed for this study does not provide for array over-design due to these losses. It is felt that further optimization of the bus and cable arrangement is in order (aimed at reduction of the amount of over-design required) followed by the inclusion of a realistic numerical over-design coefficient in the computer calculations.

e. ARRAY MECHANICAL DESCRIPTION

(1) Introduction and Summary

The subject matter discussed in this portion is a summary of the study and analysis performed in the solar-cell-array mechanical-design area. The specific areas under investigation were the solar-cell configuration, array weight, solar-cell-module design and array-assembly methods, power transmission, and temperature-cycling capability.

The results of the investigation yielded an array design that employs 10-mil-thick, 2-by-3 cm, conventional-contact cells connected into series-parallel segments with expanded metal connectors, assembled into complete circuits and bonded to the substrate. The power generated by these circuits will be transmitted to the spacecraft by means of tapered aluminum busbars.

Additionally, there appears to be a need to design into a large array such as this, a low-temperature capability somewhat beyond the state of the art in order to arrive at an optimum weight-power ratio. Probable materials for a -150°C array are discussed herein.

(2) Cell Configuration

The selection of the solar-cell mechanical or physical configuration has been accomplished by a parametric comparison of six possible configurations. All configurations considered were single-crystal silicon cells, with the variations consisting of size and contact position. Figures X-53 and X-54 define the dimensions and contacts of the cells considered. The parameters for comparison were defined as follows:

(a) Cell Packing Factor

This is the ratio of the active silicon area to the total area of each cell.

(b) Module Packing Factor

This is the ratio of active silicon within a module to the total module area including appropriate cell-to-cell spacing. A module is defined as a group of cells connected into a series-parallel configuration of approximately 1 square foot in size. The interconnection techniques assumed for conventional-contact cells and wrap-around contact cells are shown in Figures X-55 and X-56 respectively. The additional edge and circuit interconnection areas making up the total panel packing factor should be approximately the same for all cell types with a large rectangular panel of the type being considered for this mission and have, therefore, not been considered in this comparison.

(c) Cell Price Factor

This factor is the ratio of the cell cost per unit area of active silicon to the cell cost per unit area of active silicon of the standard 2-by-2-cm conventional cell.

(d) Cell Assembly Cost Factor

This is the ratio of solar cell array fabrication cost for each cell configuration to the fabrication costs for a standard 2-by-2-cm cell. Fabrication is here defined as those operations necessary to construct a solar array excluding the array support structure or substrate.

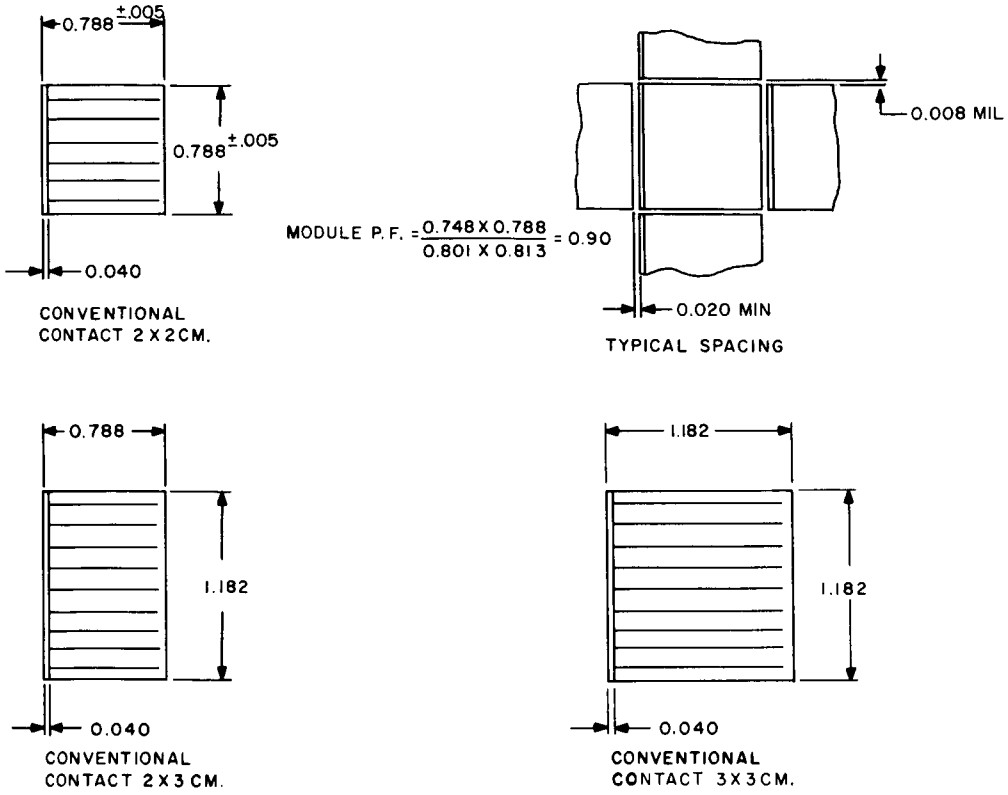

Figure X-53. Dimensions of Conventional Contact Cell

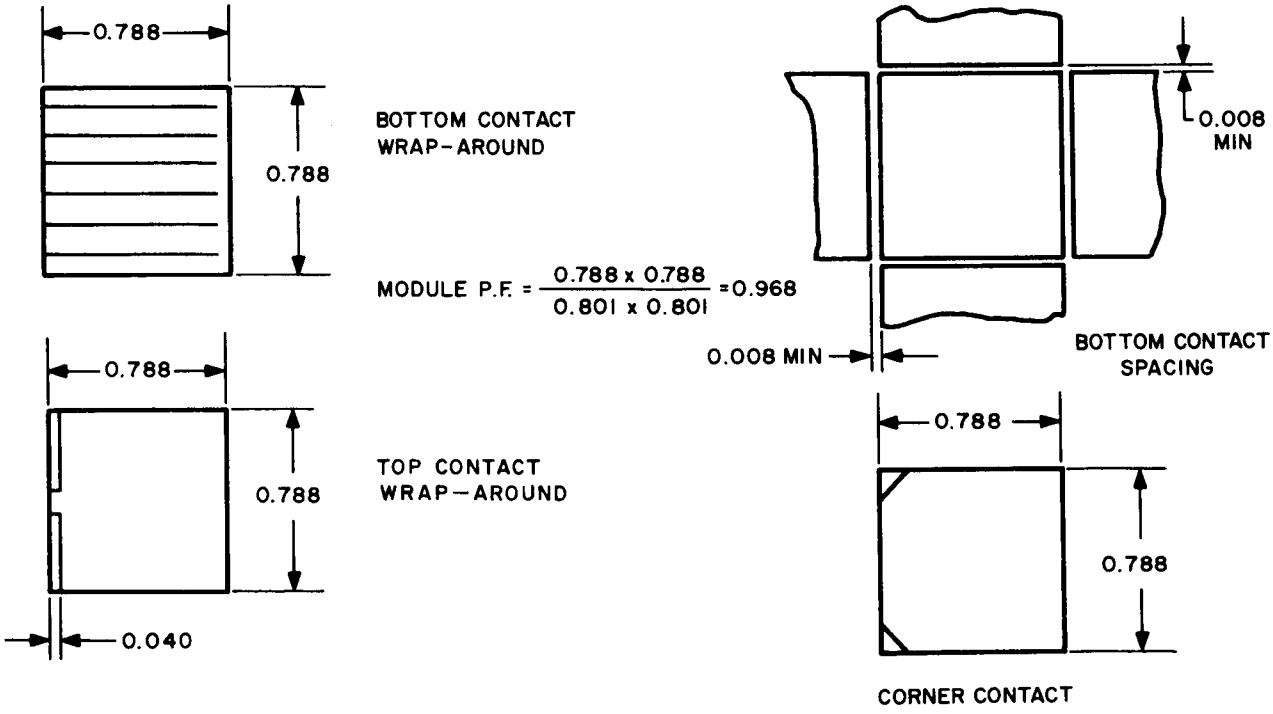

Figure X-54. Dimensions of Other Configuration Cells

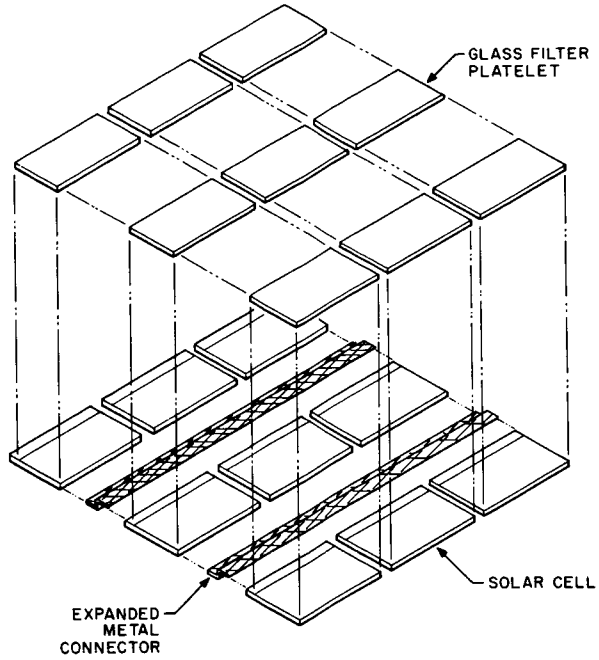

Figure X-55. Interconnection Techniques for Conventional Contact Cells (Exploded View of Typical Portion)

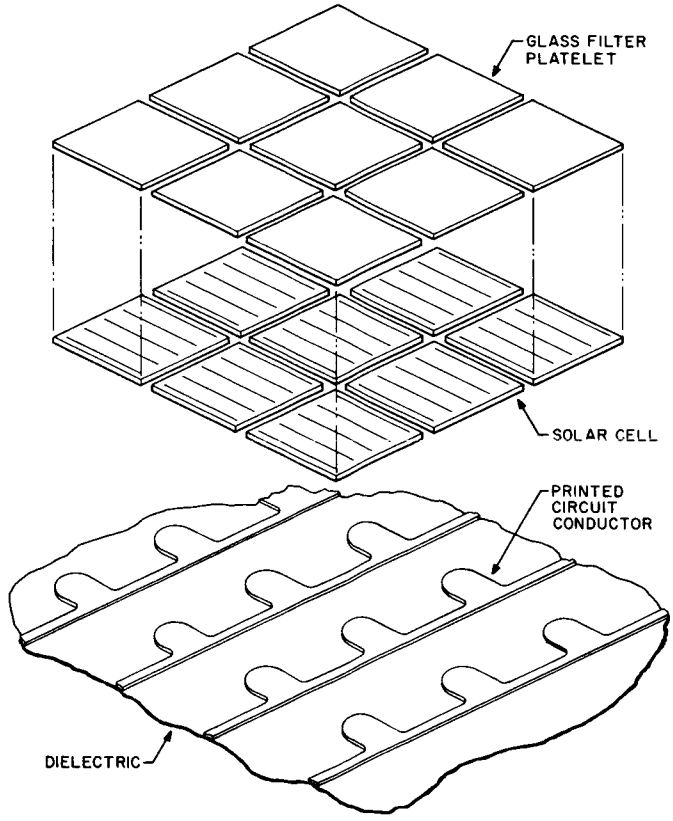

Figure X-56. Interconnection Techniques for Wrap-Around Contact Cells

(e) Weight

This is the overall weight in pounds per square foot of all solar-array components, excluding the supporting structure or substrate.

(f) Reliability

There is insufficient data available on most cell configurations from which to derive failure rates. Therefore, their relative reliability can only be determined by engineering judgment.

For purposes of comparison, all conventional-contact cells have been assumed to be connected into module segments with expanded metal strips, as shown in Figure X-55 and wrap-around bottom contacts to be connected as shown in Figure X-56. The assembly of all cell types will be performed on the modular-segment basis whereby cells are assembled directly into approximately one-square-foot segments, wired together into circuits, and bonded to the substrate.

Table X-19 is a summary of the parameters for each configuration.

(g) Packing Factor

From a packing density viewpoint, the obviously superior cell is the bottom-contact wrap-around, due mainly to the absence of contacts of any kind on the active side of the cell. Also, it is possible to use minimum cell-to-cell spacing since planar-wiring techniques are utilized. With the exception of the bottom wrap-around cell, which is 4 to 6 percent superior, the overall difference in packing factor of the cells considered is within two or three percent.

(h) Cell Price Factor

The cell price ratios are based on a quotation from the Heliotek Corporation, for 1968 estimated prices of the cells under consideration. It is important to remember that the ratios of prices are normalized for equal active silicon area and are therefore a measure of dollars per watt rather than dollars per area.

As can be seen in Table X-19, there is a considerable spread in price between the configurations, with the 2-by-3-cm conventional contact being the most economical and the wrap-around cells being the least economical.

TABLE X-19. SUMMARY OF PARAMETERS FOR VARIOUS CELL CONFIGURATIONS

Cell Configuration	Cell Packing Factor	Module Packing Factor	Cell Price Factor	Cell Assy Price Factor	Figure of Merit
2 cm x 2 cm Conventional Contact	0.95	0.90	1.00	1.00	67.5
2 cm x 3 cm Conventional Contact	0.95	0.91	0.85	0.85	80.5
3 cm x 3 cm Conventional Contact	0.965	0.935	0.94	0.75	78.0
2 cm x 2 cm Wrap-Around Bottom Contact	1.00	0.968	1.05	0.75	74.0
2 cm x 2 cm Wrap-Around Top Contact	0.96	0.91	1.09	1.00	64.0
2 cm x 2 cm Corner Contact	0.98	0.93	0.97	1.00	71.5

Hoffman and Texas Instruments were also contacted for price correlation with the following results:

1. All vendors agreed on the ratio of price for the wrap-around configurations.

2. Due to a lack of yield figures on the larger cells, the vendors were unable to provide realistic price ratios for 2-by-3-cm and 3-by-3-cm configurations.

3. All vendors agreed that the 2-by-3-cm configuration would be more economical on a dollar-per-watt basis than the standard 2-by-2-cm in the quantities required for this type of mission.

(i) Cell Assembly Price Factor

The price of assembling the cells into solar arrays is very definitely a function of cell size and contact configuration as shown in Table X-19. The saving with the larger, conventional-contact cell sizes results directly from the lesser number of cells required per unit area of array, thus reducing the inspection, test, and soldering operations to be performed. The wrap-around, bottom-contact cell, lending itself to the printed-circuit techniques shown in Figure X-55, will provide significant savings in cell assembly. The cells can be assembled directly into pre-insulated circuits which may be readily bonded to the substrate. There is no apparent cell-assembly cost advantage with the edge-contact or top-contact wrap-around cell configurations, as the assembly techniques are very similar to those of the conventional 2-by-3-cm cell.

(j) Array Weight

The weight of the solar array in pounds per square foot is shown in Table X-20 for a nominal 10-mil-thick solar cell and 6-mil-thick fused-silica filter platelet. Since the cell and filter thickness are fixed, the array weight varies approximately with the packing factor. The effects of varying filter-glass and cell thickness are shown in Figures X-57 and X-58 respectively, for a 2-by-3-cm conventional-contact cell. Typical weight breakdowns are shown in Table X-20 for conventional-contact and bottom wrap-around contact configurations.

(k) Figure of Merit

In order to determine the relative merit of each cell configuration, a figure of merit was devised and is defined by the following equation:

$$F = PF_m / (C_{PF} + 1/3\ CA_{PF}) \times 100$$

where

F is the figure of merit, or unit area of active silicon/element of cost,

PF_m is the Module Packing Factor,

C_{PF} is the Cell Price Factor, and

CA_{PF} is the Cell Assembly Price Factor.

The tabulated results for each cell are shown in Table X-19. These results indicate that the 2-by-3-cm conventional-contact cell configuration is considerably more economical than any of the other configurations under consideration in this study. For example, on a 3000-square-foot array, approximately $300,000 would be saved by utilizing a 2-by-3-cm conventional-contact cell rather than the standard size 2-by-2-cm cell.

TABLE X-20. WEIGHTS OF CELL COMPONENTS, POUNDS PER SQUARE FOOT

Component	2 x 2 cm Wrap-Around 8-Mil Cell	2 x 3 cm Conventional 8-Mil Cell	2 x 2 cm Wrap-Around 10-Mil Cell	2 x 3 cm Conventional 10-Mil Cell	2 x 2 cm Wrap-Around 12-Mil Cell	2 x 3 cm Conventional 12-Mil Cell
Solar Cells	0.087	0.081	0.109	0.102	0.130	0.122
Coverglass 6 Mil Fused Silica	0.062	0.058	0.062	0.058	0.062	0.058
Cell to Cell Connectors	0.020	0.012	0.020	0.012	0.020	0.012
Solder	0.007	0.007	0.007	0.007	0.007	0.007
Dielectric	0.017	0.017	0.017	0.017	0.017	0.017
Coverglass Adhesive	0.005	0.005	0.005	0.005	0.005	0.005
Cell Bonding Adhesive	0.015	0.023	0.015	0.023	0.015	0.023
Miscellaneous (Diodes, Terminal Boards, Wire, Tie Downs, Connector)	0.090	0.090	0.090	0.090	0.090	0.090
Totals lbs/ft^2	0.303	0.293	0.325	0.314	0.346	0.334

(l) Reliability

The solar cell contributes to the reliability of the solar array to the extent of its ability to withstand stresses imposed upon it by environmental exposure. This ability is dependent mainly on the integrity of the solder-joint connection between the cell contact and interconnector. Therefore, the silver-titantium-contact strength and solder flow are most significant.

The silver-titanium contact evaporation and sintering and soldering processes, being basically the same for all cell configurations, will produce equally strong or weak connections for any configuration. The only possible variation in reliability between configurations may result from the relative accessibility of solder joints for inspection after bonding.

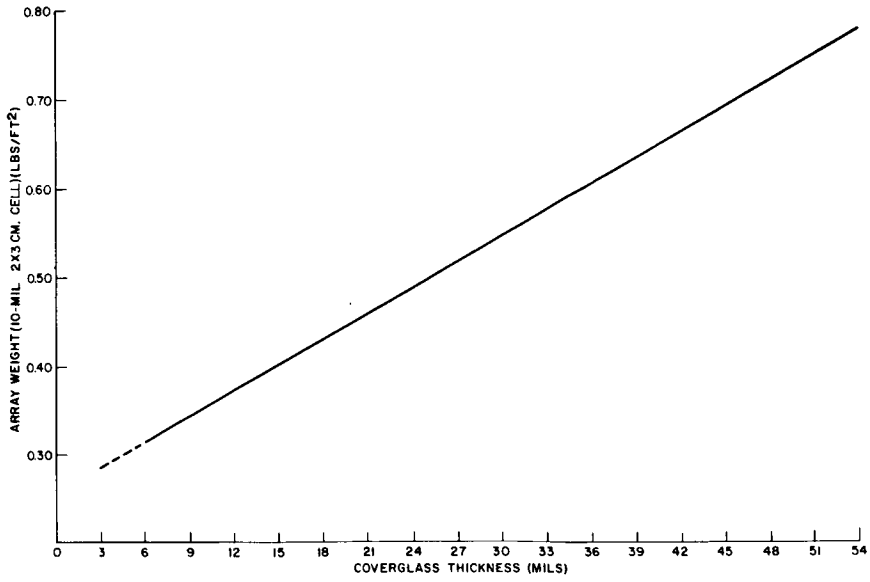

Figure X-57. Array Weight vs. Cover-Glass Thickness

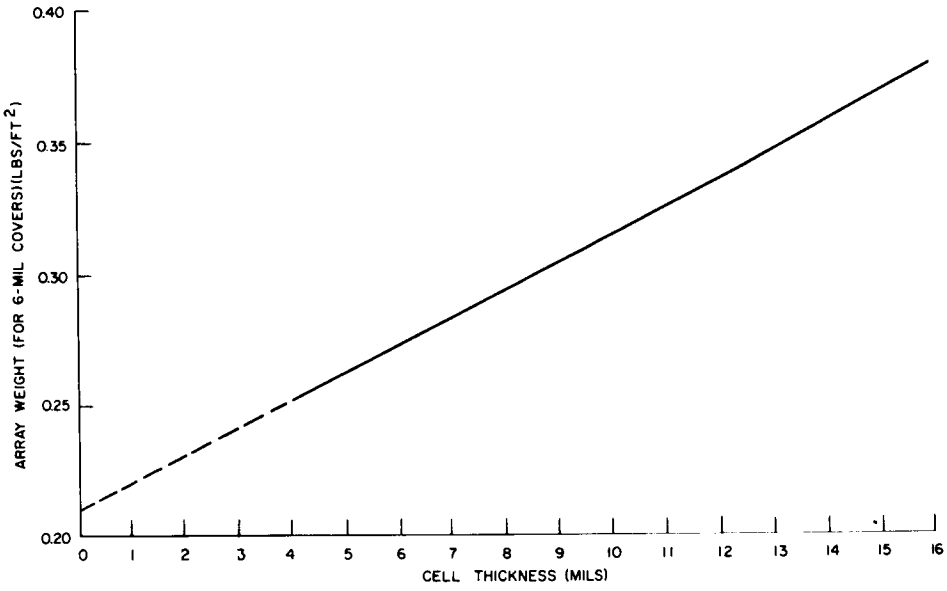

Figure X-58. Array Weight vs. Cell Thickness

The bottom-contact wrap-around configuration presents the largest problem since reliable repair techniques have yet to be developed that allow inspection of a replaced cell joint after the circuit has been bonded to a solid substrate. However, assuming such techniques can be developed for the wrap-around configuration, thorough initial inspection of solder joints should yield equally reliable solar arrays for all configurations under consideration.

(3) Solar-Cell-Array Assembly

(a) Solar-Cell Module

The basic building block of the solar-cell array will be an assembly of series-parallel cells termed a module. The majority of modules will be approximately one square foot in size containing about 150 (2-by-3-cm) solar cells. All series and parallel connections within the module will be made by the soldering of expanded metal strips which are formed into a Z-shape and attached as shown in Figure X-59.

The Z-strip connector material is fabricated from 2-mil-thick sheet metal. The metal is simultaneously slit and stretched, providing a high degree of inherent stress relief in the finished product. Each connector strip is then cut to size and simultaneously formed. Another advantage to the Z-strip series-parallel module configuration is that each cell-to-cell connector need only conduct one-cell equivalent current, which allows the material thickness to be minimum. This provides increased flexibility as compared with other configurations (notably Nimbus and Lunar Orbiter) where 6 to 10 cells were bused together in parallel before series connections were made. There are two possible materials for use as the base connector material, viz, silver and molybdenum. Molybdenum has the important advantage of a close match in thermal coefficient of expansion to the silicon solar cell, and has performed well at low temperatures in the past as described in Paragraph X.C.2.e(4). However, molybdenum must be plated to establish solderability, which is costly. Silver has a considerably higher electrical conductivity and a modulus of elasticity or specific stiffness one-fourth that of molybdenum, therefore requiring less stress relief.

After completion of the soldering operation, individual coverglass platelets (6 mils thick), composed of Corning 7940 fused silica, will be bonded to each cell with coverglass adhesive (Sylgard 182).

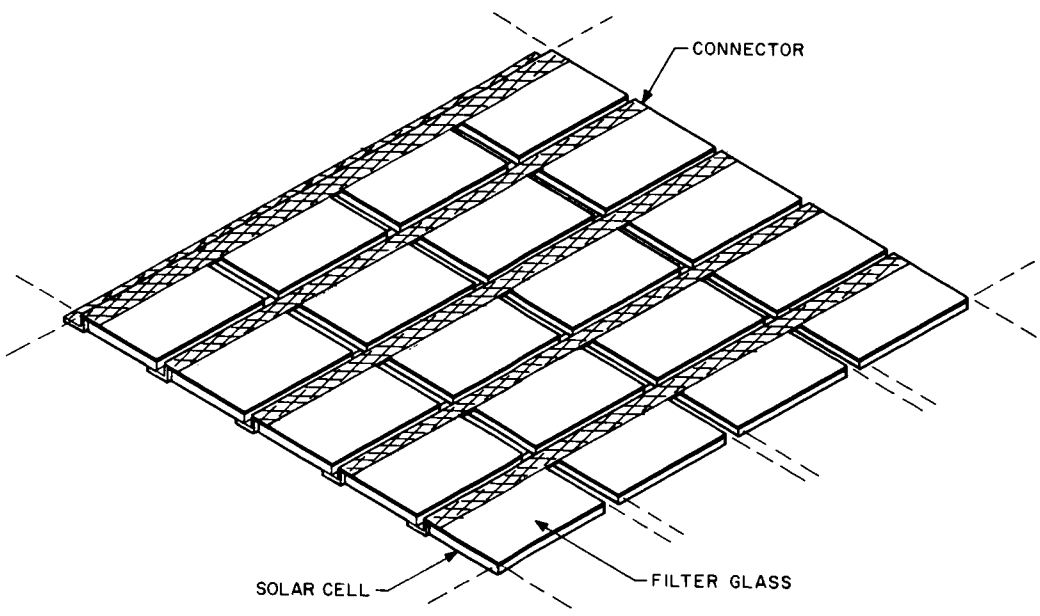

Figure X-59. Typical Portion, Solar-Cell Module

(b) Substrate Insulation

The presently utilized RCA system for insulating the substrate structure prior to the bonding of the solar-cell modules involves the application of a reinforced epoxy polyamid resin (SMP 62/63) system. The SMP 62/63 is reinforced by a two-mil-thick glass cloth, which is bonded with the SMP to the substrate. The use of the cloth ensures a minimum space of two mils between the back surface of the solar cell and the surface of honeycomb. The epoxy system has a minimum dielectric strength of 1000 volts per mil. This system has been qualified successfully on the Lunar Orbiter program but is by no means optimum from a weight and cost standpoint.

A lighter-weight and lower-cost system can be attained by the use of pre-insulated honeycomb skin, since aluminum foils laminated with dielectrics are now becoming commercially available. Such a system would utilize a 2-mil H-film/3-mil aluminum laminate as one face of the honeycomb sandwich, which will have been laminated prior to bonding of the honeycomb sandwich. H-film or 'Kapton' is a polyamide film developed by du Pont which has excellent physical characteristics over a wide temperature range. The dielectric strength of the two-mil film would be 5400 volts per mil. This type of processing will eliminate the need for the time-consuming and expensive surface preparation and bonding required with the reinforced epoxy system, and will reduce the dielectric weight required by 50 percent. Additionally, the H-film offers considerably more temperature stability as discussed in Paragraph X.C.2.e(5).

(c) Solar Cell Bonding

The completed modules will first be wired into strings similar to those shown in Figure X-52 (RCA Drawing SK 1769417) and subsequently bonded to the honeycomb substrate. The bonding operation will be performed by the following methods:

1. A flexible transfer fixture, similar to that shown in Figure X-60, is placed over the module string with the access holes indexed over the center of the cells. For the bowed-panel concept, the transfer fixture, as well as the fixture in which cells are soldered, will be formed in a shape to conform to the panel curvature to avoid inducing stresses during bonding. For a flat panel, a flat fixture would be used.

2. Tape is attached to the cells and fixture as shown and the module string is lifted from its soldering fixture.

3. In parallel operations, the bottom side of the cells and the substrate surface are cleaned and primed.

4. A mask is placed over the bottom side of the cells similar in configuration to the transfer fixture and a controlled amount of adhesive is applied to each cell.

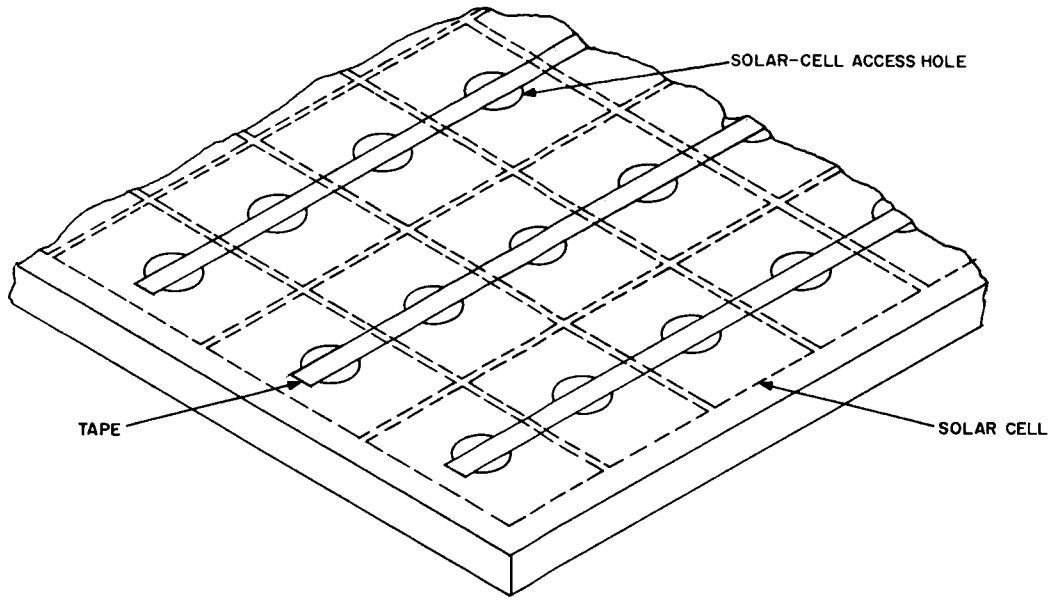

Figure X-60. Solar-Cell Transfer Fixture

5. The module string is indexed to its correct position on the substrate and the transfer fixture is removed.

6. Bonding pressure is then applied through weights with individual rubber cone tips making contact with each cell, to distribute the weight equally.

(4) Solar Array Wiring

The following analysis was performed to determine a minimum wiring weight that will transmit the power generated within each panel back to the array boom, while keeping the voltage drop and voltage mismatch between panels at a low level.

Figure X-61 represents a model of the array current distribution. Each 'P' is composed of four sections approximately 2.8 by 4.0 feet in size, whose composite current output is defined as 'I'. The total array current at the boom is equal to the product of the number of panels and the current. In order to minimize the voltage mismatch between panels along the array, a uniformly varying voltage-drop configuration was chosen. Therefore, the average array voltage drop E_{avg} will be 0.5 E_{total} and will occur at a point one-half that of the total length 'D' of the array.

The cross-sectional area of conductor (A) required at any point along the length is a function of current I (amperes), voltage drop E (volts), and resistance R (ohms) of the conductor. The relationship is given by the following equation, where D_2 is distance along the panel, measured from an arbitrary point as shown in Figure X-61.

$$A \propto \frac{RI}{E} D_2 \qquad \text{(X-36)}$$

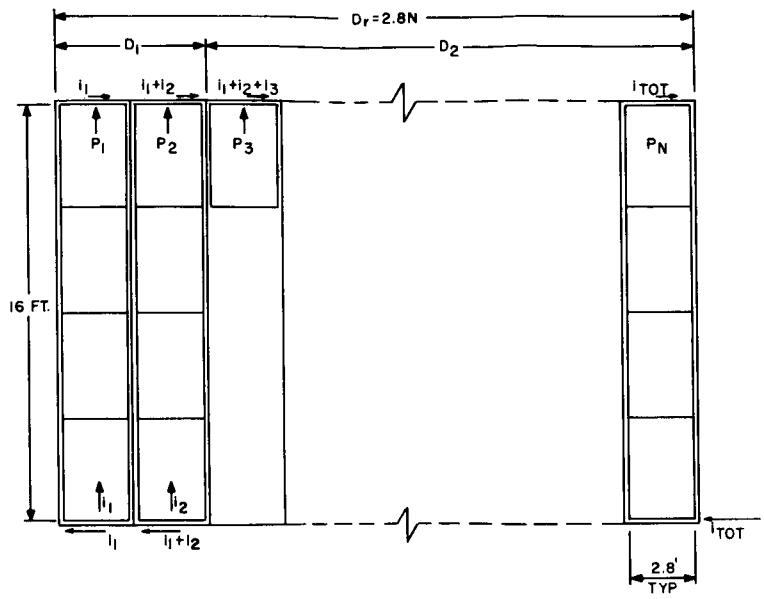

Figure X-61. Array Current Distribution

The current generated at end of life from any panel 'P' has been assumed to be approximately 5.8 amperes for the purpose of this analysis. The current at any point along the array can then be expressed as a function of length as shown by the following.

$$I = \frac{5.8\ amp}{2.8\ ft}\ D = 2.07\ D_1 \qquad \text{(X-37)}$$

Aluminum was chosen as the conductor material rather than the conventional copper in order to minimize weight, since the conductivity-to-weight ratio of type EC aluminum is approximately twice that of commercial copper.

Since the voltage drop, and therefore the cross-sectional area, has been defined as uniformly varying, the total conductor weight, W_{tot}, may be given as:

$$W_{tot} = A_{ave} \times D\ (total) \times Density\ (d) \qquad \text{(X-38)}$$

Substituting equations (X-36) and (X-37) into (X-38),

$$W_{total} = 2.07\ \frac{RD_1\ D_2}{E_{ave}}\ D_T\ d. \qquad \text{(X-39)}$$

Utilizing these relationships, Figures X-62, X-63 and X-64 were generated. Figure X-62 represents the relationship between conductor weight, expressed in terms of pounds per square foot of array area, and the average voltage drop in the conductor. Also shown in this figure is the weight effect of adding series solar cells to compensate for voltage drops.

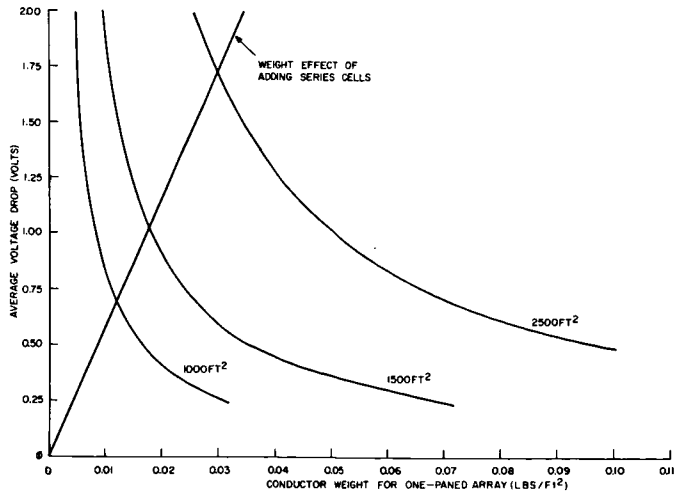

Figure X-62. Aluminum Conductor Weight vs Average Voltage Drop

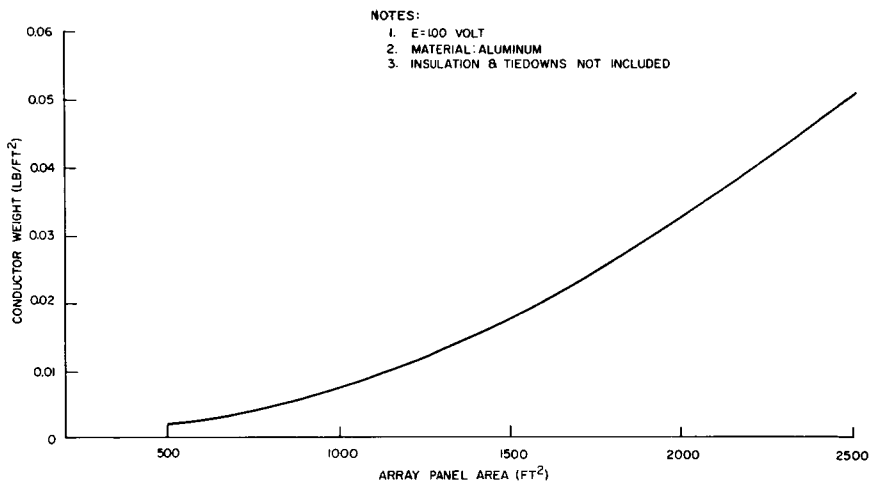

Figure X-63. Conductor Weight vs. Array Panel Area

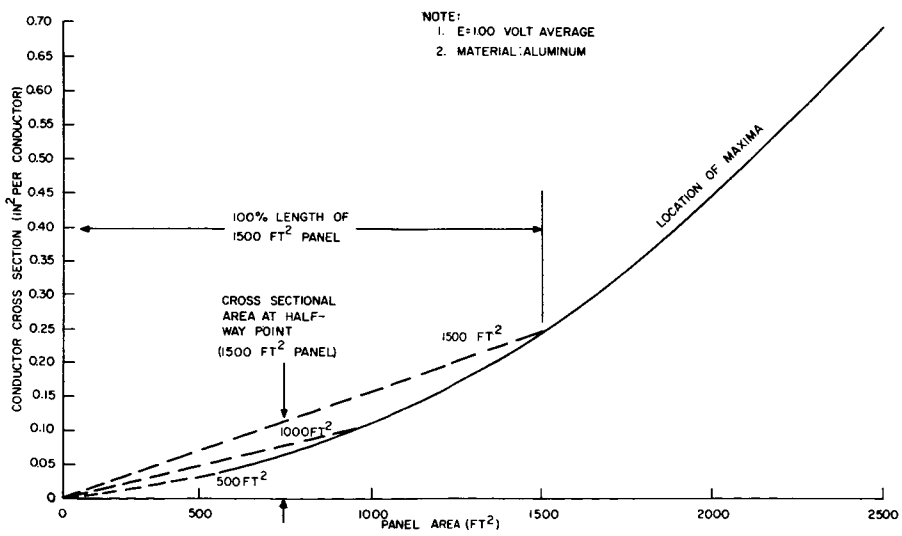

Figure X-64. Maximum Conductor Cross Section vs. Panel Area

In general, for the array sizes (1000 to 1500 square feet per side) under consideration, there is no particular advantage to adding series cells from the weight standpoint. However, for larger areas, there would be a weight advantage to be gained in adding cells and allowing the voltage drop to increase proportionally.

An inspection of these curves indicates that, in the range of 1000 to 1500 square feet per side, the most nearly optimum voltage drop to work toward is 1 volt total (output and return conductors). Increasing the voltage drop above 1 volt will yield small weight advantages.

Figure X-63 is a plot of the array area versus the maximum cross-sectional area per conductor. (The maximum area is located at the boom end of the solar array.)

(5) Temperature Cycling Capability

The temperature extremes between which the solar array will cycle in orbit, being mainly a function of array weight and back surface emissivity, have been determined by a tradeoff analysis of these parameters as they affect array electrical output (reference Paragraph X.C.2.a). The results of this tradeoff indicate that the anticipated temperature extremes for the worst-case orbit (synchronous altitude) will be approximately +40°C and -150°C for an array weighing approximately 0.75 pound per square foot.

The temperature spread in total degrees is less than the previously qualified Lunar Orbiter temperatures of +115°C to -120°C, although the lower limit of -150°C is somewhat beyond the present state of the art. However, considering the results of some recent quick-cycle tests performed at RCA and by reviewing the low-temperature capabilities of the array component materials, it does not appear unreasonable to design and develop a solar array for a 1968 mission that will reliably withstand this temperature extreme.

Figure X-65 shows a typical thermal cycle to which a Lunar Orbiter (LO) module was recently subjected. As can be seen in the figure, this type of cycling is considerably more severe than any anticipated orbital cycle. The LO module tested was drawn at random from a production lot and bonded with RTV 560/580 to a fiberglass substrate. The sample was then thermally cycled 25 times by submersion directly into liquid nitrogen followed by radiant heating. Electrical tests were performed after bonding, and after the 2nd, 5th, 10th, 17th and 25th cycle. The results of electrical tests indicated that no measurable degradation in output occurred through the 17th cycle. Following the 25th cycle, a five-percent degradation was observed at the maximum-power point. A microscopic investigation identified the problem to be a hairline crack in one cell. The appearance and position of the crack indicated that it was most likely caused by insufficient stress relief in the negative connector. The module design proposed in this study, contains considerably more cell-to-cell stress relief than the sample module tested.

The other critical components of the solar array that may be affected by the low temperature and therefore affect array performance are: honeycomb laminate adhesive, insulation, insulation-bonding agent, cell-bonding adhesive, and coverglass adhesive. A review of some of the information available concerning the proposed materials for these applications is shown in Tables X-21 and X-22.

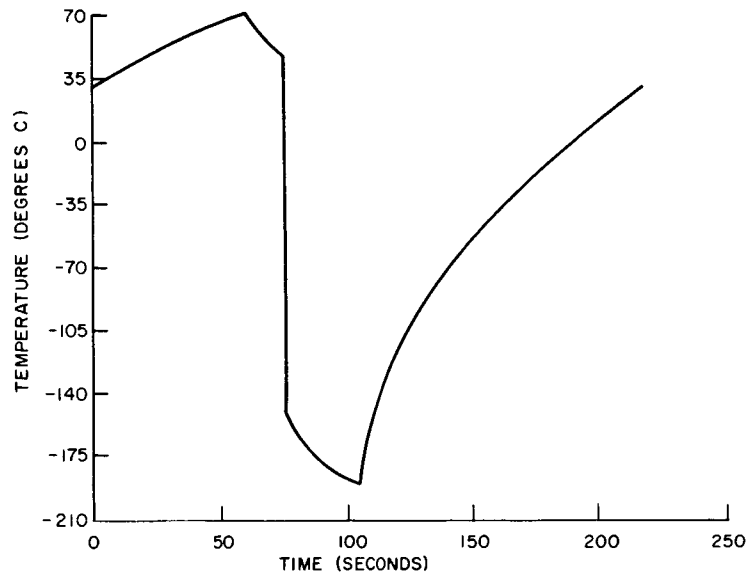

Figure X-65. Temperature-Time Profile, Quick-Cycle Test

Table X-21 identifies the components utilized on Lunar Orbiter panels, which were qualified in flight to -124°C. Table X-22 shows a summary of results of testing performed by the Narmco Research and Development Division of Telecomputing Corporation for NASA, Huntsville, Ala. on adhesives for cryogenic applications. In this evaluation, as can be seen in the table, many of the adhesives retained considerable tensile, shear and peel strength to as low as -252°C. The polyurethane system tested, which maintained the highest coefficient of expansion over the temperature region, consisted of adiprene L-100 urethane elastomer cured with "moca". This material, with the addition of filler material to obtain the desired viscosity, may prove to be a useful cell-to-substrate adhesive.

A material which appears very promising for replacing SMP and scrim cloth as an insulation is 'Kapton' polyamide, film which is commonly known as 'H-film'. This film has been used successfully in applications where the temperatures have been as low as -269°C. The dielectric strength of the material is 7 to 10 thousand volts per mil, depending on the total thickness, over the range of temperatures of 25°C to -195°C. It retains an ultimate tensile strength of 35,000 psi at an elongation of 2 percent at -195°C.

TABLE X-21. LUNAR ORBITER COMPONENTS

Component	Trade Name	Temp, °C
Honeycomb Laminate Adhesive	FM1000	-124
Insulation	Fiberglass	-124
Insulation Bonding Agent	SMP 62/63	-124
Cell Bonding Adhesive	RTV 560/580	-124
Coverglass Adhesive	Sylgard 182	-124

TABLE X-22. EVALUATION OF EXISTING COMMERCIAL ADHESIVES AT VERY LOW TEMPERATURES (Reference X-15)

Type	Adhesive	Coefficient of Linear Thermal Expansion -320°F to 32°F inch/inch/degrees F	Tensile Shear Strength* (psi)		Tee Peel Strength** (lb. per inch)	
			-320°F -196°C	-423°F -252°C	-320°F -196°C	-423°F -252°C
Nylon-epoxy	"Metbond 406"	3.15×10^{-5}	4840	3813	8.3	8.2
Nylon-epoxy	"Metbond 408"	3.33×10^{-5}	4090	2004	4.3	5.3
Nylon-epoxy	AF-40	3.11×10^{-5}	5990	5743	11.7	13.0
Nylon-epoxy	AF-41	2.84×10^{-5}	5010	3402	5.2	4.2
Nylon-epoxy	FM-1000	2.91×10^{-5}	4310	2347	3.1	5.5
Epoxy Polyamide	Resin 3135 and Curing Agt. 7111	3.22×10^{-5}	1514	1552	0	0
Epoxy Polyamide	EC-1933B/A	2.38×10^{-5}	1775	1649	1.7	2.2
Polyurethane	"APCO-1261"	4.12×10^{-5}	1940	-	3.3	-

* Average of eight specimens. Tested per MIL-A-5090D
** Average of six specimens. Tested at head travel of 2 ipm

Note: Adherends: 7075-T6 aluminum
Cure: manufacturer's recommended.
No prime

3. Storage System

a. BATTERY DATA

The curves presented in Figures X-66 through X-69 represent the final battery design data upon which the system calculations are based. This information was used in the battery-weight tradeoff study (Paragraph X.C.3.b) and is included as stored information in the computer program.

The curves of Figure X-66 (Cycle Life versus Depth of Discharge) shown for nickel-cadmium (Ni-Cd) and silver-cadmium (Ag-Cd) batteries are based upon data presented in References (X-21) through X-28). The referenced data, however, are more optimistic than the design values shown in Figure X-66. Some of the typical data points taken from the references (as well as from other sources) are indicated in the figure to demonstrate the degree of conservatism assumed in specifying the battery life and to assist in the battery-reliability appraisals made in Appendix F. For a given temperature, the cycle life characteristics of a battery are primarily a function of the discharge depth. To a secondary degree, they are dependent upon the rate of discharge, amount of overcharge, and the failure criteria of the cycling regime. Cycle-life data are greatly dependent upon factors such as: (1) minimum cell voltage at which failure is defined, (2) the number of individual cell failures that define the failure of a multi-cell pack, and (3) whether electrolyte leakage constitutes a failure condition. The question of reliability and confidence level must also be considered. If published data indicate average or mean time to failure based upon special laboratory conditions for small-scale tests, the data must obviously be derated for design purposes. The data shown in Figure X-66 represent reasonable design values for battery life based upon RCA evaluation of the referenced data.

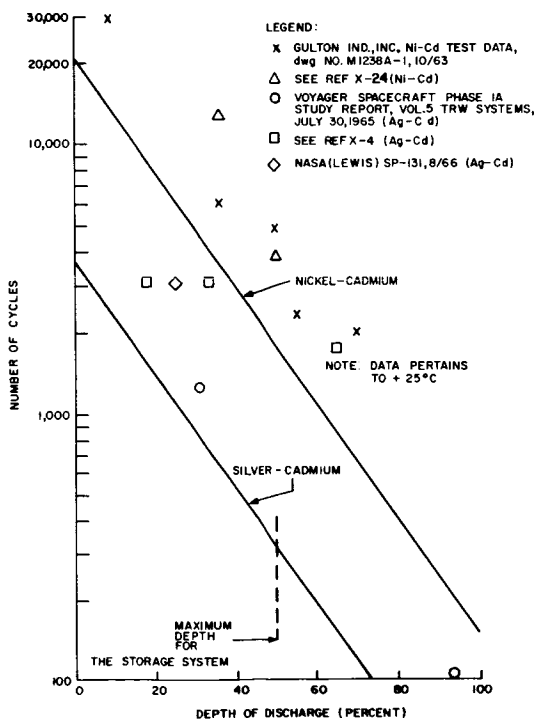

Figure X-66. Cycle Life vs. Depth of Discharge

Note that the depth of discharge is limited to 50 percent. This is due to poor battery performance during cycling at greater depths, the scarcity of applicable data, and the inherent danger of cell reversal during discharge. It is possible to cycle at discharge depths approaching 100 percent, but it would be necessary to monitor cell voltages on an individual basis in order to preclude cell reversal during discharge. (The degree of scattering of individual cell voltages is increased during deep discharges.) The required control system would be complex and the predicted cycle life would be significantly lower than the levels under consideration. Consequently, since the largest portion of test data (from laboratory tests and orbiting satellites) is for depths of discharge less than 50 percent, the discharge will be limited to that value.

The graphs of Figures X-67 and X-68 indicate average charge and discharge voltage curves for Ni-Cd and Ag-Cd batteries after one year of cycling to a given depth of discharge at +25°C. These curves represent average voltages during each operational mode rather than instantaneous values at each state of charge. The curves are, therefore, slightly modified versions of the typical data presented in the referenced reports.

The graph of Figure X-69 is a plot of battery efficiency as a function of charge rate at +25°C for Ni-Cd and Ag-Cd batteries. The literature provides relatively little information on battery ampere-hour efficiency and is often sketchy and indirect. The data shown is the result of engineering evaluation by RCA of the information listed in the referenced literature and the recommendations of the major battery manufacturers.

Figure X-69 also contains the curves indicating the H/e ratio vs. H for each type of battery. (H is the relative charge rate in hours and e is the battery ampere-hour efficiency.) The data is required in this form for the computer input.

Table X-23 lists other data and design factors required for storage in the computer program. The items dealing with battery watt-hours per pound and watt-hours per cubic foot require additional discussion. Note that a special structure has been designed in which to stack batteries (rather than assuming the batteries to be spread over a large area). A portion of this structure serves as support and cooling for the charge electronics. This subject is discussed further in Paragraph X.C.3.d. Although some of the structure is needed for electronics, the total weight and volume are included in Table X-23, as required for system calculations performed by the computer program. The number of series cells per battery listed in Table X-23 is based on the design limitation imposed by any voltage regulators of the down-converter type. Input voltage to these regulators must never fall below approximately 32 volts, reflected to the battery terminals in the power system under discussion. This implies a potential difference of four volts minimum (as measured between the battery terminals and the regulated d-c bus) and is an estimate of the worst-case (largest) summation of the voltage drops due to the regulator switching element, series components of the filters, discharge diode, and all the attendant wiring and cabling. The 32-volt minimum discharge voltage limitation imposed implies 1.1 volts per cell minimum for a Ni-Cd, and 1.0 volt per cell minimum for a Ag-Cd cell, for the number of series cells specified. Specified relative charge rates (i.e., average, minimum, and peak) must be evaluated in conjunction with the charge-control and battery-protection philosophy outlined in Paragraph X.C.3.c. A peak charge rate of 3 hours is specified for the Ni-Cd battery. Lunar Orbiter

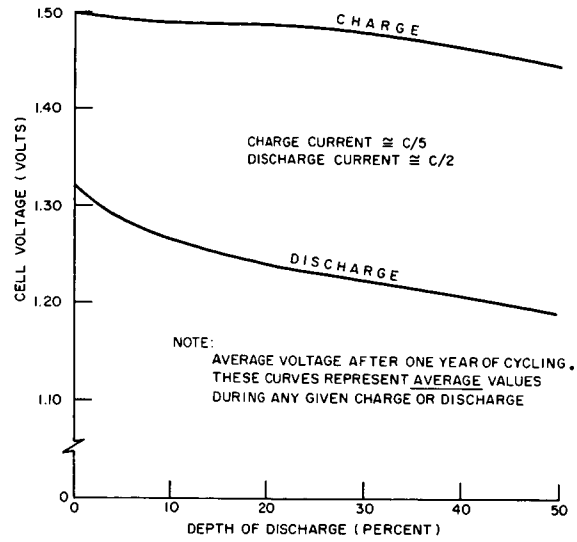

Figure X-67. Cell Voltage vs. Depth of Discharge (Ni-Cd Cell at 25°C)

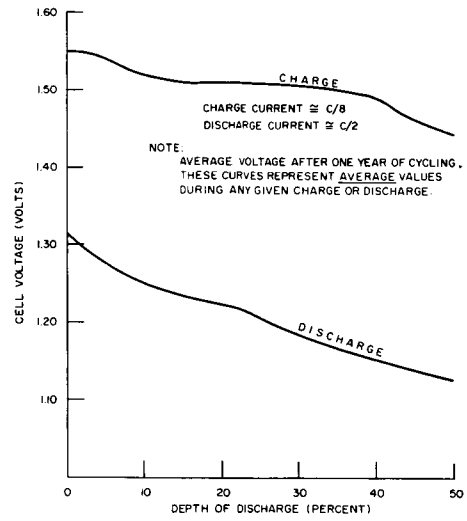

Figure X-68. Cell Voltage vs. Depth of Discharge (Ag-Cd Cell at 25°C)

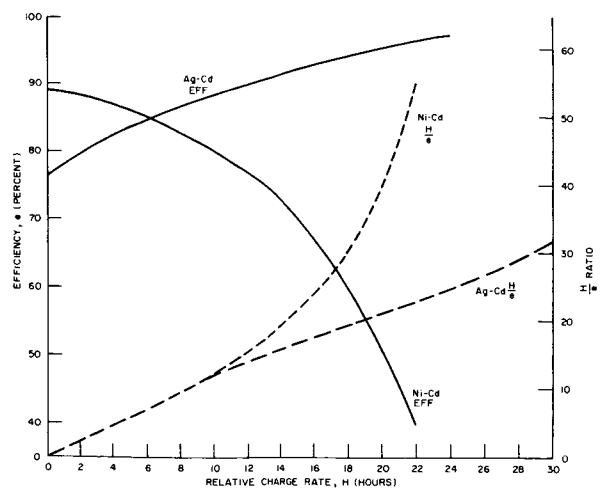

Figure X-69. Battery Efficiency vs. Charge Rate (Ag-Cd and Ni-Cd Cells at 25°C)

TABLE X-23. BATTERY DESIGN FACTORS FOR COMPUTER STORAGE

Item	Nickel-Cadmium	Silver-Cadmium
Maximum depth of discharge	0.50	0.50
H average (maximum)	5	8
H average (minimum)	20	30
H peak	3	5
No. of series cells	29	32
Watt-hrs per pound*	9.2	16.0
Watt-hrs per ft^3 *	950	1,670
Watt-hrs per pound**	7.7	13.2
Watt-hrs per ft^3 †	353	620
Average cell voltage ††	1.20	1.10

* Includes battery modules only. Numbers furnished for information purposes only.

** Includes weight of structural shelf (with cooling coils and busbars) upon which batteries and electronics will be mounted.

†† Based upon external volume of battery and electronics support structure.

†† To full dishcarge; to be used in converting ampere-hours to watt-hours in the computer program.

Ni-Cd batteries have been flown successfully with the peak charge limited to approximately a 4-hour rate but without the ampere-hour meter "stepping" proposed in this storage system. Since the latter feature is particularly effective in protecting against cell overpressure and other adverse effects caused by inadequate control of high charge, a 33-percent increase in the peak rate is believed to be well within the realm of feasibility. Taking into account the somewhat lower capability of the Ag-Cd battery to accept a high charge rate, H (peak) has been specified at 5 hours.

Selection of the minimum charge rate is based primarily on the battery's ability to become recharged efficiently. The H_{ave} (maximum) rates specified are average. These are based on the assumption of a higher charge rate during the initial portion and a lower charge rate in the terminal phases of the charge cycle. The 5- and 8-hour average rates specified for the Ni-Cd and the Ag-Cd batteries, respectively, are within the range of charge rates used in battery test programs conducted thus far and utilized in flight-proven space power systems.

b. BATTERY WEIGHT TRADEOFF STUDY

A technique has been developed to provide an overall view of battery requirements as a function of mission altitude and duration. This results in a comparision (on a weight basis) of Ni-Cd and Ag-Cd batteries for use in different missions. The analysis indicates that neither battery type is superior across the entire range of conditions studied. In general, it can be stated that at the synchronous altitude, the silver-cadmium battery weight is lower than the corresponding nickel-cadmium weight. For altitudes below 2,000 miles, the two systems are almost equal in weight for missions (resupply periods) up to approximately 150 days. However, for longer missions at the low altitudes, the silver-cadmium battery would be heavier than nickel-cadmium. The battery data used in the following calculations is included and discussed in Paragraph X.C.3.a.

The graph of Figure X-70 indicates the maximum number of eclipses to which the satellite will be exposed (during a one-year period) as a function of altitude. This represents the maximum number of charge-discharge cycles the batteries will receive. The graph also contains a plot of minimum sun (charge) time per orbit versus altitude.

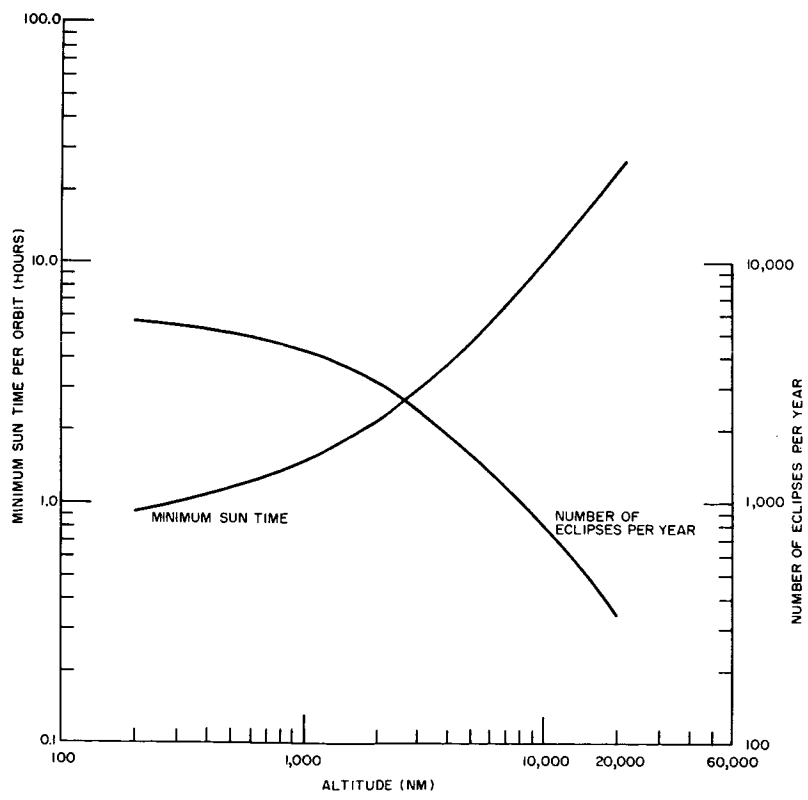

Figure X-70. Orbital Characteristics

The curve of Figure X-71 shows the approximate average watt-hours to be delivered by the battery system (per watt of total load power) versus altitude.

The analytical technique is defined on a step-by-step basis as follows. Steps (1) through (3), in substance, correspond to the procedure developed in Paragraph X.B.3.c, with the end product a plot of the limiting depths of discharge, Figure X-72. The primary difference is in the specific numerical assumptions made (see Table X-23, Paragraph X.C.3.a).

Step (1) For each altitude and mission duration, determine the number of cycles to which the battery system will be subjected. This information is taken from Figure X-70. For mission durations of less than one year, divide proportionally.

Step (2) Refer to Figure X-66 to determine the maximum permissible depth of discharge (based upon cycle life and 50-percent limit).

Step (3) Since the permissible depth of discharge is not necessarily limited by cycle life as calculated in Step (2) (for certain orbits, it will be limited by the maximum allowable recharge rate), the maximum depth of discharge based on recharge rate must be calculated in order to determine which factor will govern. The charge-rate-limited depth of discharge is determined using the following Equation:

$$d = \frac{e_b \, a\tau}{H} . \qquad \text{(X-40)}$$

Quantity H is determined from the data given in Table X-23 of Paragraph X.C.3.a. It is seen that, for Ni-Cd systems, the average charge rate will be limited to C/5 (peak charge current will be C/3). That is, the average current during a charge period shall not exceed C/5. Thus, H_{ave} (max) equals 5 hours.

From Figure X-69, e_b is 0.825 at H equal to 5 for Ni-Cd; for Ag-Cd, H_{ave} (max) is 8 and e_b is 0.835.

Thus for Ni-Cd,

$$d = 0.165\tau a$$

and, for Ag-Cd,

$$d = 0.105\tau a.$$

It is now possible to determine the limiting depth of discharge for each altitude. The value of "a" (related to charge time) is taken from Figure X-70. The limiting d based on recharge rate is not a function of mission duration as is the limiting d based on cycle life. The values of d obtained by each method (cycle-life and charge-limited) are compared. The lower value is used.

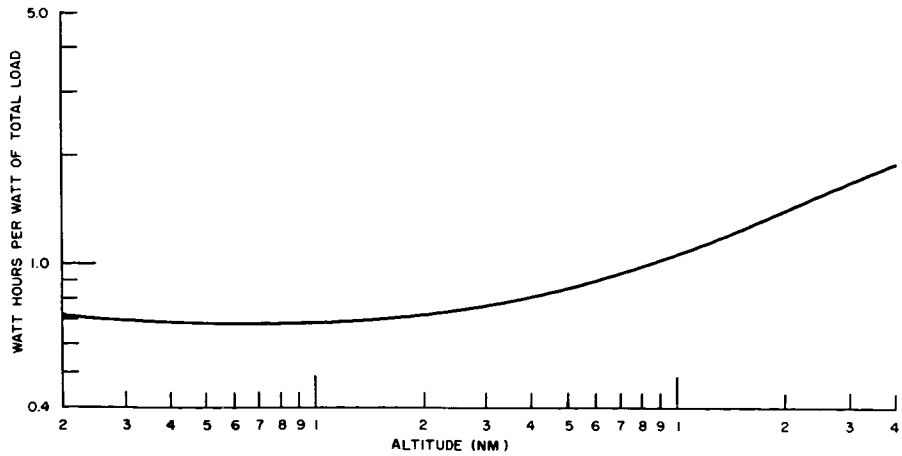

Figure X-71. Battery Discharge Requirements

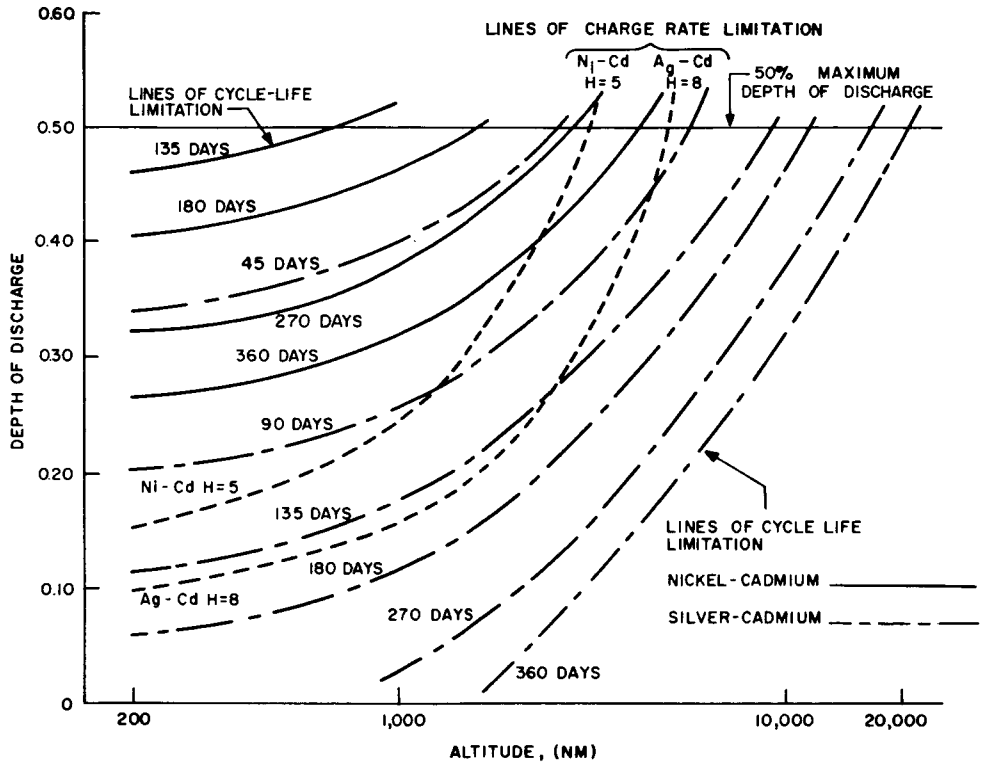

Figure X-72. Depth of Discharge vs. Altitude

In general, it was found that for Ni-Cd batteries, the recharge rate is the limiting factor at altitudes below 2,300 nautical miles (based upon the C/5 maximum average charge rate). At higher altitudes, 50 percent maximum limits d.

The Ag-Cd system is limited by cycle life for most of the conditions studied. Figure X-72 is a plot of the limiting discharge depth for each battery type, mission duration, and altitude. For Ni-Cd, for all mission durations less than

270 days, the depth of discharge is limited by the recharge ability and is therefore independent of mission duration. However, during the 1-year mission, cycle life will limit for altitudes above 2,300 nautical miles.

The Ag-Cd system, however, is very sensitive to mission duration, due to the fact that the depth of discharge is limited by cycle life. Figure X-72 illustrates the manner in which increased mission duration reduces the permissible depth of discharge for any given altitude.

Step (4) After the limiting depth of discharge is determined for each case, the required battery size can be defined by reference to Figure X-71, "Battery Discharge Requirements":

$$WH = \frac{E}{d} \tag{X-41}$$

where WH is Battery size, in watt-hours,

E is Watt-hours of energy required by system (from Figure X-71), and

d is Maximum depth of discharge.

Figure X-73 is a plot of the required battery watt-hours. This graph takes into account the maximum depth of discharge, cycle life, recharge rate, required spacecraft power, orbital parameters, etc. It shows that for most of the missions the Ni-Cd system requires less watt-hours of stored energy per watt of load.

Step (5) Figures X-67, X-68, and X-72 are used to determine the required battery size in terms of ampere-hours. The limiting depth of discharge (from Figure X-72) and the average discharge voltage (from Figures X-67 and X-68) are determined for each mission.

The required battery watt-hours for each mission is divided by the predicted voltage in order to determine battery size in terms of ampere-hours. Figures X-74 and X-75, which represent the required ampere-hours of battery capacity for Ni-Cd and Ag-Cd systems, can now be plotted. Although these curves are similar in shape to the watt-hour curves shown in Figure X-73, they are modified slightly by the voltage variability as a function of discharge depth.

Step (6) Sufficient information has now been developed to permit a calculation of the optimum battery weight for each altitude and mission duration.

Based upon vendors' responses to recent RFQ's*, energy densities of 13 and 22 watt-hours per pound can be expected for Ni-Cd and Ag-Cd Cells, respectively. With allowance for packaging, it is predicted that these factors will be reduced

* Request for quotation.

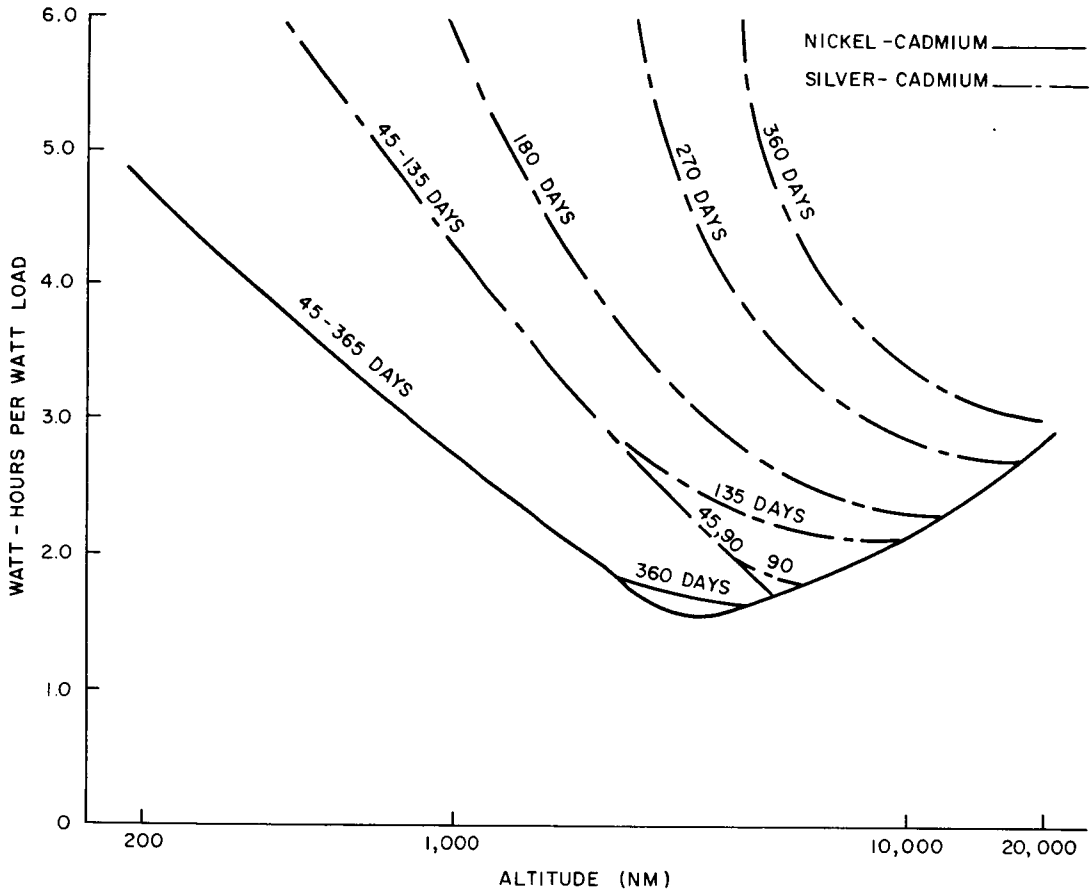

Figure X-73. Required Battery Size, Watt-Hours per Watt Load vs. Altitude

to 10* watt-hours per pound (Ni-Cd) and 17* watt-hours per pound (Ag-Cd). Figure X-76 is a plot of calculated battery weight for each mission. It is seen in Figure X-76 that there are certain combinations of mission duration and altitude for which the Ni-Cd battery system is lighter in weight and other combinations for which the Ag-Cd system would be lighter.

Figure X-77 indicates the "zone" in which each battery system is lighter. The chart shows that the Ag-Cd battery is lighter at the high altitudes and for the short-duration, low-altitude missions. Nickel-cadmium would be lighter for all missions longer than 154 days at altitudes less than 3,000 to 10,000 nautical miles. However, since Figure X-77 does not indicate the magnitude of weight difference for each condition, Figure X-78 was prepared. All ratios that are greater than unity indicate that nickel-cadmium would be lighter. The "unity"

* These values are higher than those listed in the Battery Data Section of this report and are considered to be less accurate. The previously listed data are based upon results of the design effort, which were not available when this weight tradeoff was performed. The ratio of energy densities is essentially unchanged, however, and the effect on the results of the weight tradeoff will be negligible.

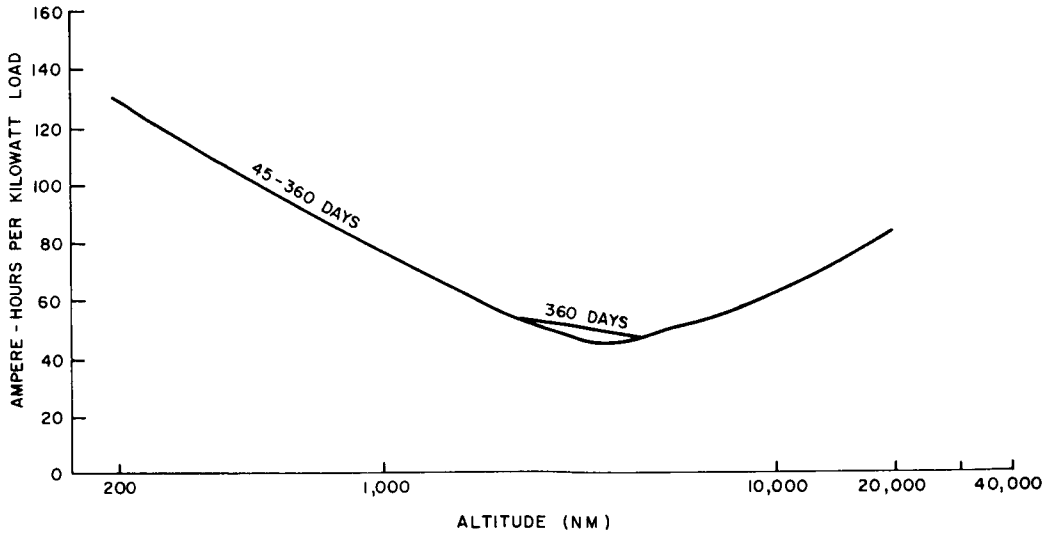

Figure X-74. Required Battery Capacity; Ni-Cd Cells

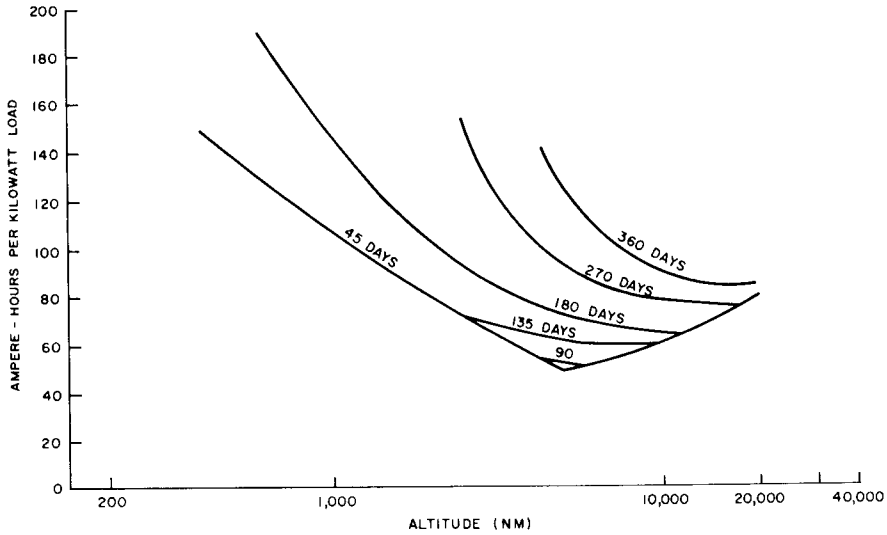

Figure X-75. Required Battery Capacity; Ag-Cd Cells

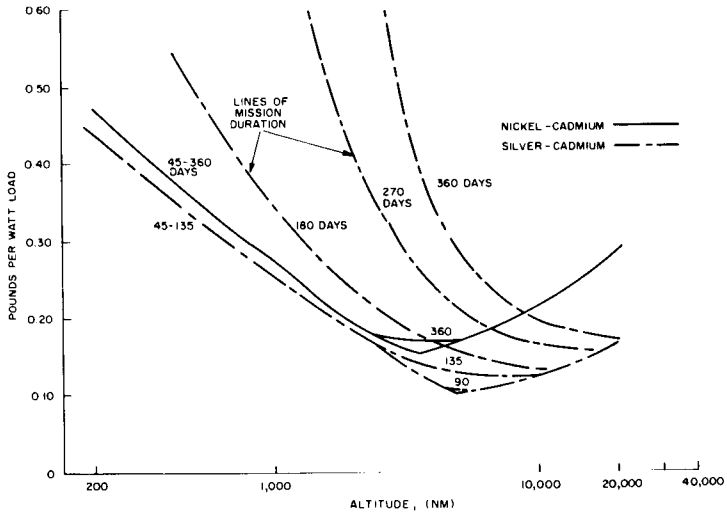

Figure X-76. Required Battery Weight; Ag-Cd and Ni-Cd Cells

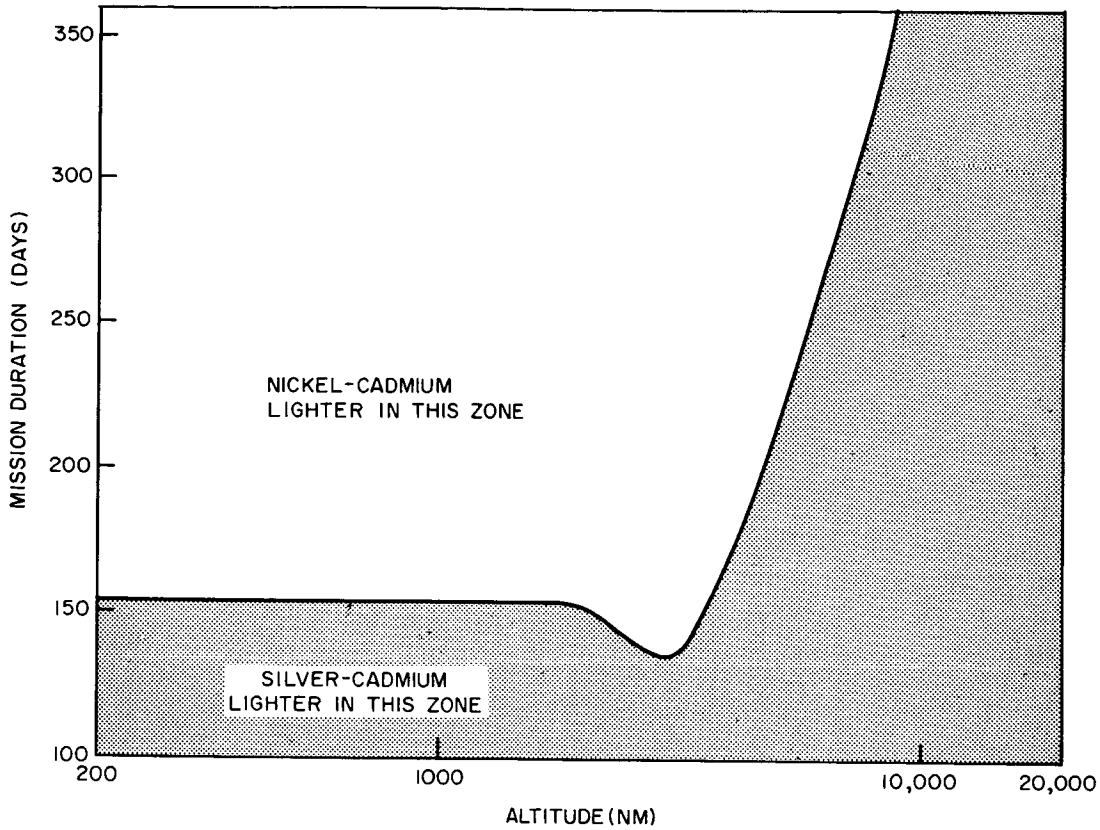

Figure X-77. Battery Weight Comparison

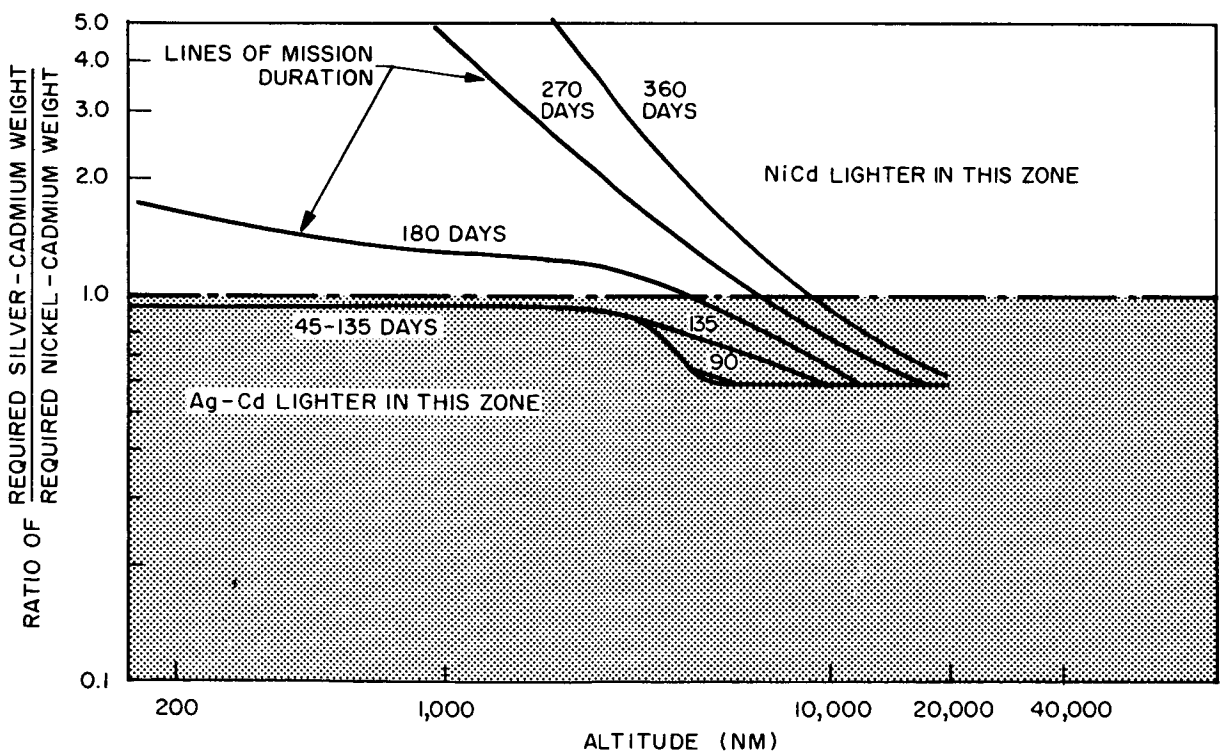

Figure X-78. Battery Weight Ratio

line in Figure X-78 represents the crossover point of equal weight for each system. It is seen that at synchronous altitude, the Ag-Cd battery weight (depending upon mission duration). At altitudes below 19,340 nautical miles, the two systems will be fairly close in weight for missions up to 180 days. However, for longer missions at the low altitudes, the Ag-Cd battery can be as much as 10 times heavier than Ni-Cd.

In conclusion, it can be said that each battery type offers a clear choice, based on weight. Specific mission studies can be restricted to one battery type, but as long as the overall parametric approach is to be maintained, the study must include both Ni-Cd and Ag-Cd battery types.

c. BATTERY CHARGE CONTROL METHODS

(1) Introduction

It is the purpose of this section to present the battery charge control considerations and recommendations. The discussion deals with both Ni-Cd and Ag-Cd systems and will stress control methods with indication of the criteria for selection. The values of limiting functions used are typical rather than "hard" design numbers. This approach is necessitated since many aspects of the projected missions are not fixed and "probable-type" missions will be used as guides. Therefore, assumed data (considered to be reasonably accurate, based upon present understanding of typical projected missions) is employed where necessary.

(2) General Method of Control

This section will describe the general method of charge control with explanations for each limiting factor.

The primary reason for charge control is to assure that the battery will be charged safely and efficiently, with careful attention to battery protection during charge and overcharge. The charge control system must limit overcharge current so that the heat dissipation is not excessive.

The recommended battery charge control system consists of the following major components:

- Ampere-Hour Counter,
- Constant-Current Controller (three levels), and
- Voltage Limiter (temperature dependent).

The system will also contain a high-temperature charge cut-off, and provisions for manual adjustment of control criteria. The principle of operation is as follows:

(a) Charge initially at highest acceptable charge rate, until a predetermined portion of the ampere-hours removed during the previous discharge has been replaced.

(b) Thereafter, reduce charge current to a lower rate, at which most of the charging will take place.

(c) When all of the capacity removed during the previous discharge has been replaced (including additional ampere-hours required due to battery inefficiency), reduce the current to a "trickle" rate for the balance of the charge period.

(d) During each of the three phases described previously, the current can also be limited by the presence of a charge voltage limit that is temperature-controlled.

(e) Reduce voltage limit at the time of the final current reduction at 100-percent state of charge (Ag-Cd only).

The use of a high initial-charge rates permits a relatively higher average recharge rate in a tracker system. By accepting high current for a limited period, the battery can utilize (to a certain extent) the initial surge current available from the (cold) solar-cell array at the beginning of the sunlit portion of the orbit. Figures X-79 to X-86 illustrate typical variations in the available charge current during "daylight" time. The maximum charge level is determined by battery capability (with regard to safe charge acceptance at high rates), current-carrying ability of the charge control units, and total charge energy available as a function of maximum charge rate. The limits were selected such that at the beginning of array life, the high-current limits will probably govern charge rate until the first current-reduction step occurs. At the end of mission life, the high-current limit will govern only for the first few minutes, after which the available charge current will fall below the maximum permissible value.

A value of C/3* was chosen for the high-current limit for Ni-Cd batteries, and C/5* was chosen for Ag-Cd batteries. (C represents nominal battery capacity, when discharged at the 2-hour rate).

Most of the battery charging will occur at the second current level, which will be initiated after the battery is partly recharged; this level will be continued until the point of full charge. The second current level must therefore be high enough to permit efficient recharge, but not so high as to cause premature current limiting (due to high voltage) before the end of charge. The second level for Ni-Cd batteries will be C/5*, and for Ag-Cd batteries, C/8*.

As stated in the preceding, the charge current will remain at the second level until the state of full charge is reached. Full charge is defined as the point at which all of the capacity removed during the previous discharge(s) has been replaced, including the additional capacity required due to battery inefficiency.

It has been experimentally established by RCA in the course of a classified program that some Ni-Cd cells may be fully charged and continuously overcharged at the C/5 rate (at 30°C). Ag-Cd cells may be brought to the point of full charge at the C/8 rate,** but the current must be reduced during the overcharge mode. For the system under consideration, charge

---

* See Paragraph X. C. 3. a

** Manufacturer's maximum recommended rate

current will be reduced for both battery types at the point of full charge. Although the Ni-Cd system may be capable of sustaining continuous overcharge at the C/5 rate, it is desirable to lower the overcharge current in order to reduce the heat dissipation and internal gassing during this phase. During the overcharge period, the input energy is largely dissipated as heat, which must be conducted away from the batteries. Reduced overcharge rates reduce the cooling requirements for the batteries. In addition, there is evidence to indicate that reduced overcharge will result in longer battery cycle life. The current will therefore be reduced to a relatively low rate for extended overcharge periods for both battery types. In addition to the current limiting described, the system will contain a voltage-limiting circuit. This circuit will limit the maximum voltage across the total battery by gradually reducing the charge current. Since battery-charge voltage is sensitive to temperature, the voltage limiting circuit will be temperature-dependent, i.e., the limiting charge voltage will be a function of battery temperature. The system will also be equipped with a high-temperature charge cut-off. If, at any time during the charge phase, the battery temperature rises above a predetermined maximum (typically 35 to 40°C), the charge current will be reduced to a trickle level, until the temperature returns to 30°C. The charge will then be reinstated, with the charge mode determined by the battery voltage, temperature, and state of charge as before. An RCA designed voltage-temperature control has been flight-proven in the Lunar Orbiter power subsystem.

In addition to automatically controlling the charging function, the ampere-hour counter will deliver an indication of the state of battery charge at the end of each charge and discharge period. It will therefore not be necessary for the spacecraft crew to continuously monitor charge and discharge currents. On-board instrumention will provide data for the manual resetting of control levels, if this proves necessary after repeated cycling.

(3) Specific Cases

The following paragraphs describe the manner in which charge control will be implemented for four specific cases. Each of the methods indicated in this section has been introduced and generally described in Paragraph X.C.3.c.(2). The four cases to be considered are:

1. Ni-Cd Battery, Low-Altitude Orbit

2. Ni-Cd Battery, Synchronous-Altitude Orbit

3. Ag-Cd Battery, Low-Altitude Orbit

4. Ag-Cd Battery, Synchronous-Altitude Orbit

(a) Ni-Cd Battery

The nickel-cadmium battery system is characterized by long cycle life, ability to accept relatively high charge current, and ability to sustain continuous overcharge.

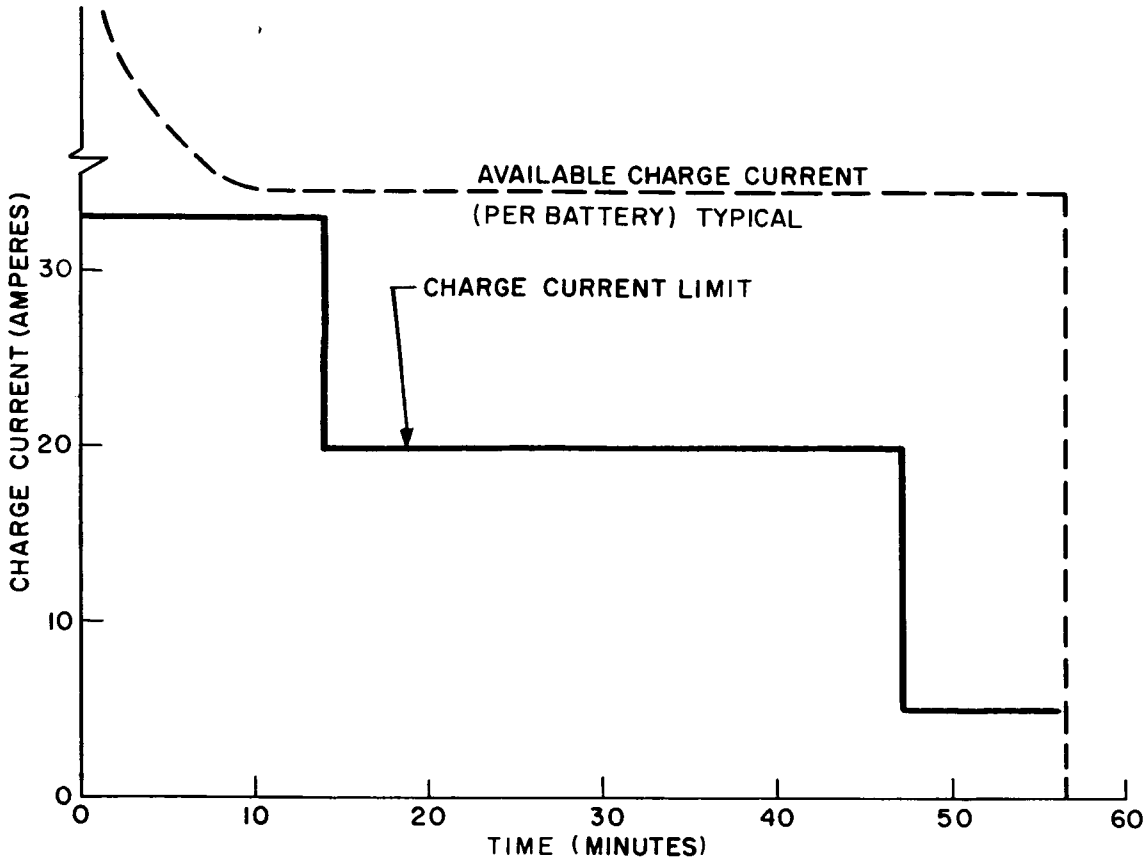

Figure X-79. Beginning of Array Life, Ni-Cd Battery, 200 NM Orbit

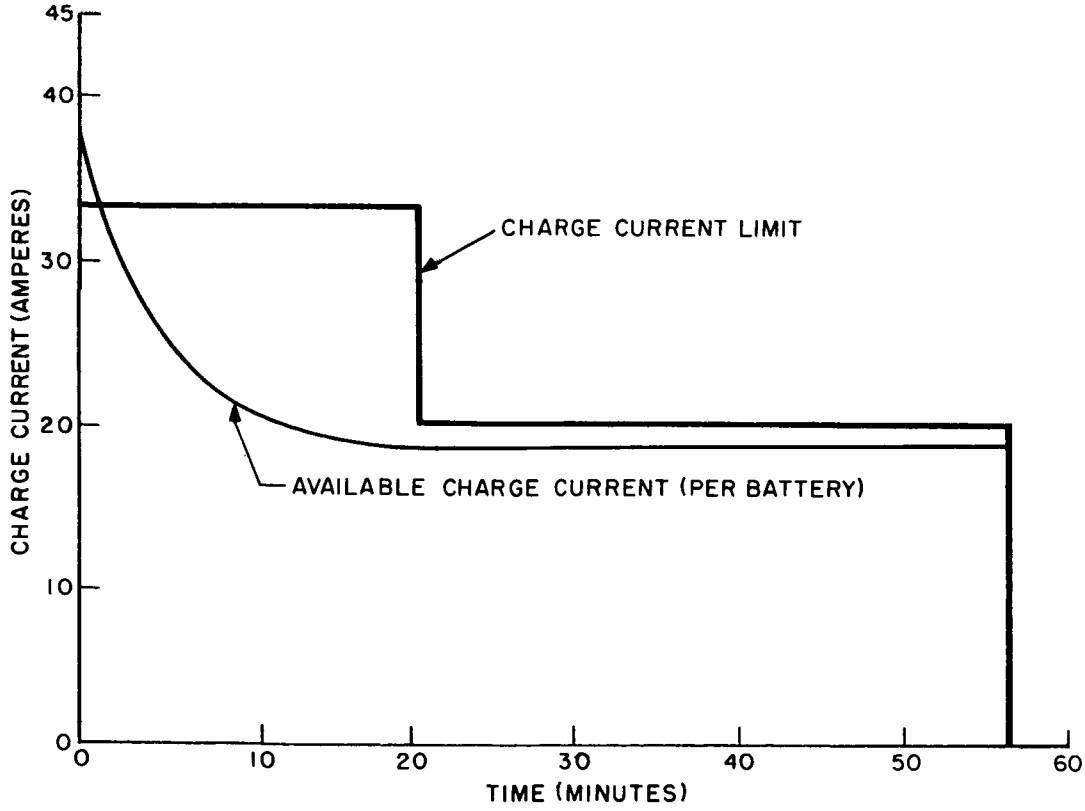

Figure X-80. End of Array Life, Ni-Cd Battery, 200 NM Orbit

The Ni-Cd battery is heavier than the Ag-Cd battery when compared on an ampere-hour basis. However, certain cycle-life and recharge requirements can result in weight tradeoffs favoring Ni-Cd at low altitudes and possibly in the synchronous orbit. (See Paragraph X.C.-3.b.).

1. Ni-Cd Battery, Low-Altitude Orbit (200 nmi). The low-altitude orbit is characterized by low depths of discharge and high recharge rates. The relatively short sunlight period (approximately 57 minutes) and the maximum permissible charge current are the major factors which determine the allowable depth of discharge.

The Ni-Cd battery will initially be charged at a C/3 rate (33.3 amperes for a 100-ampere-hour battery) until 50 percent of the capacity removed during the previous discharge has been replaced. Reference is made to Figures X-79 and X-80, where an assumed typical variation of array power versus time is shown. For the low-altitude orbit, the depth of discharge would be 15.5 percent or 15.5 ampere-hours removed from a 100-ampere-hour battery. During charge, the current limit will remain at 33.3 amperes until approximately 7.75 ampere-hours has been replaced. Therefore, with an undegraded array, the current will be reduced to 20 amperes (C/5) after 14 minutes have elapsed. In Figure X-79, note that the available charge current is well above the charge-current limit.

The current will remain at 20 amperes until the battery has reached a state of full charge (including additional ampere-hours required due to battery inefficiency). For an undegraded array, the full-charge point will occur approximately 9 minutes prior to the end of charge. Therefore, the current will be reduced to C/20 (5 amperes per battery) during the final 9 minutes.

The control parameters will be chosen such that the current "stepping" as a function of state of charge (as determined by the ampere-hour meter) will be the prime controlling mode. The voltage-limit function is intended to serve as additional protection and will not normally limit the charge current. Normally, the charge current will be reduced to a lower step before the battery voltage reaches the temperature-dependent limiting value. However, if there is a significant rise in the battery charge voltage characteristic (due to degradation of a battery cell separator, drying of a cell due to electrolyte leakage, a loose electrical connector between series cells or modules, etc.), the voltage limit will cause a reduction of the current (particularly at the end of charge and during overcharge) until the fault is discovered and corrected. Alternately, if there is a malfunction of the ampere-hour meter, the voltage limit could serve satisfactorily as the prime controller.

For the array end of life, the available charge current remains above the maximum limit only during the initial few minutes of the daylight period. The current then decays, as shown in Figure X-80. The curve depicting available charge current represents one of many possible curve shapes. The ratio of peak-to-average charge current is dependent upon the ratio of daytime loads to nighttime loads.

Figure X-80 shows a typical charge period at array end of life. Note that the first current-reduction step does not occur until 20.5 minutes have elapsed (compared to 14 minutes for the

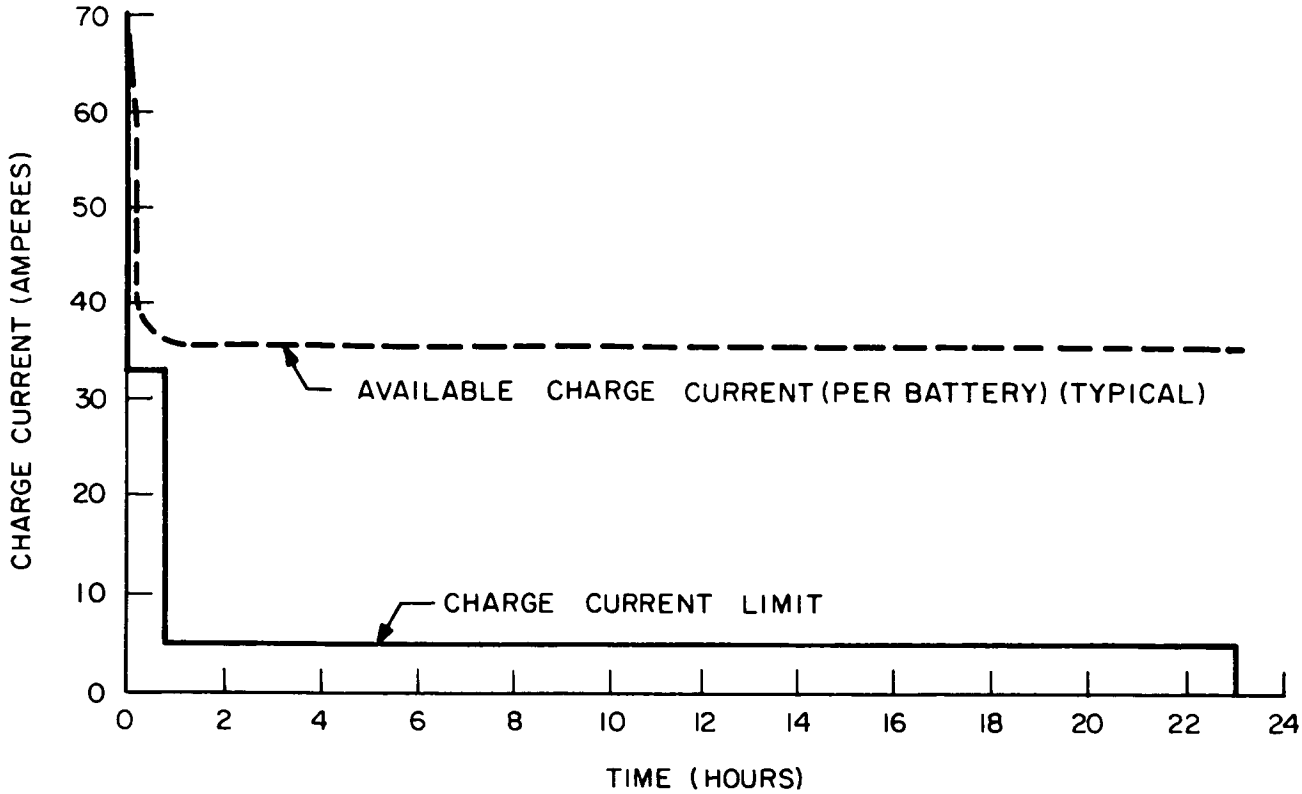

Figure X-81. Beginning of Array Life, Ni-Cd Battery, Synchronous Orbit

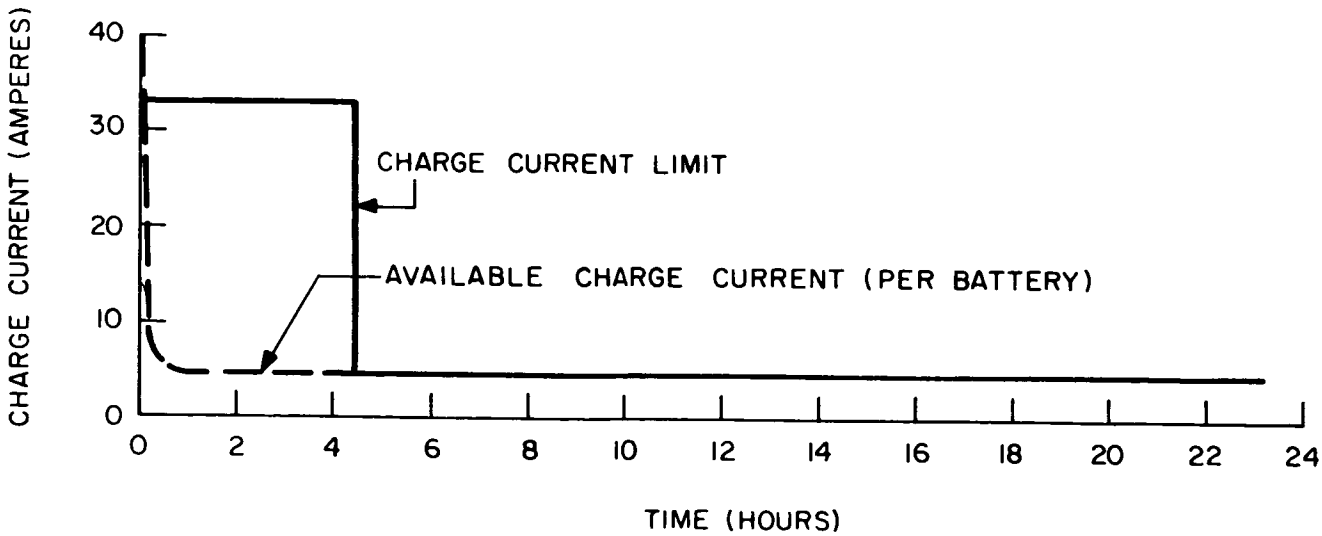

Figure X-82. End of Array Life, Ni-Cd Battery, Synchronous Orbit

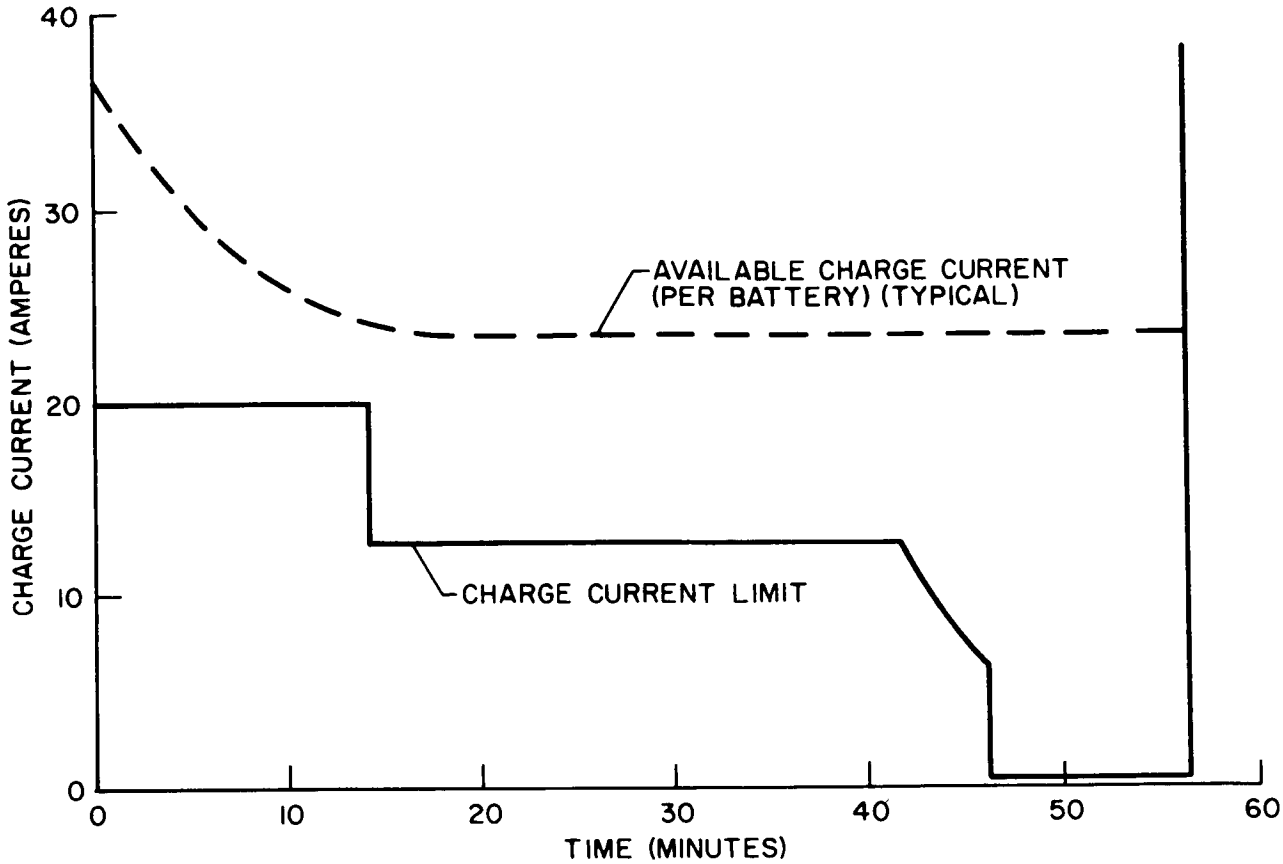

Figure X-83. Beginning of Array Life, Ag-Cd Battery, 200 NM Orbit

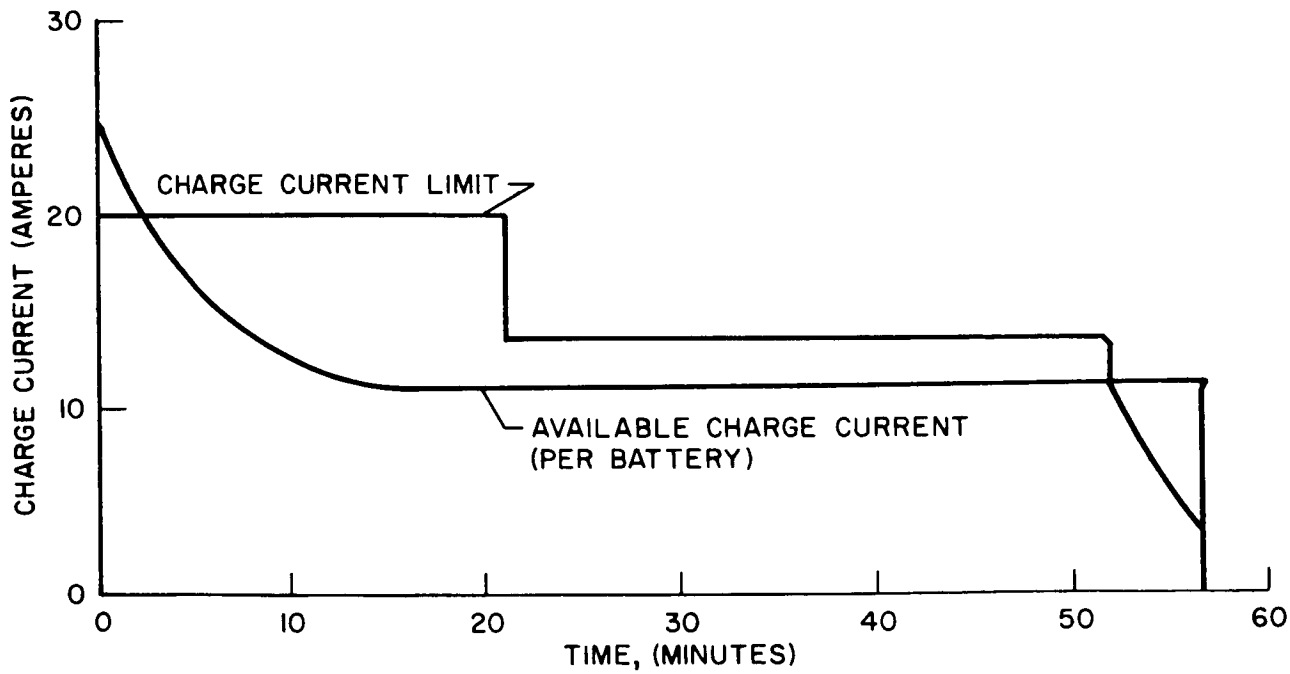

Figure X-84. End of Array Life, Ag-Cd Battery, 200 NM Orbit

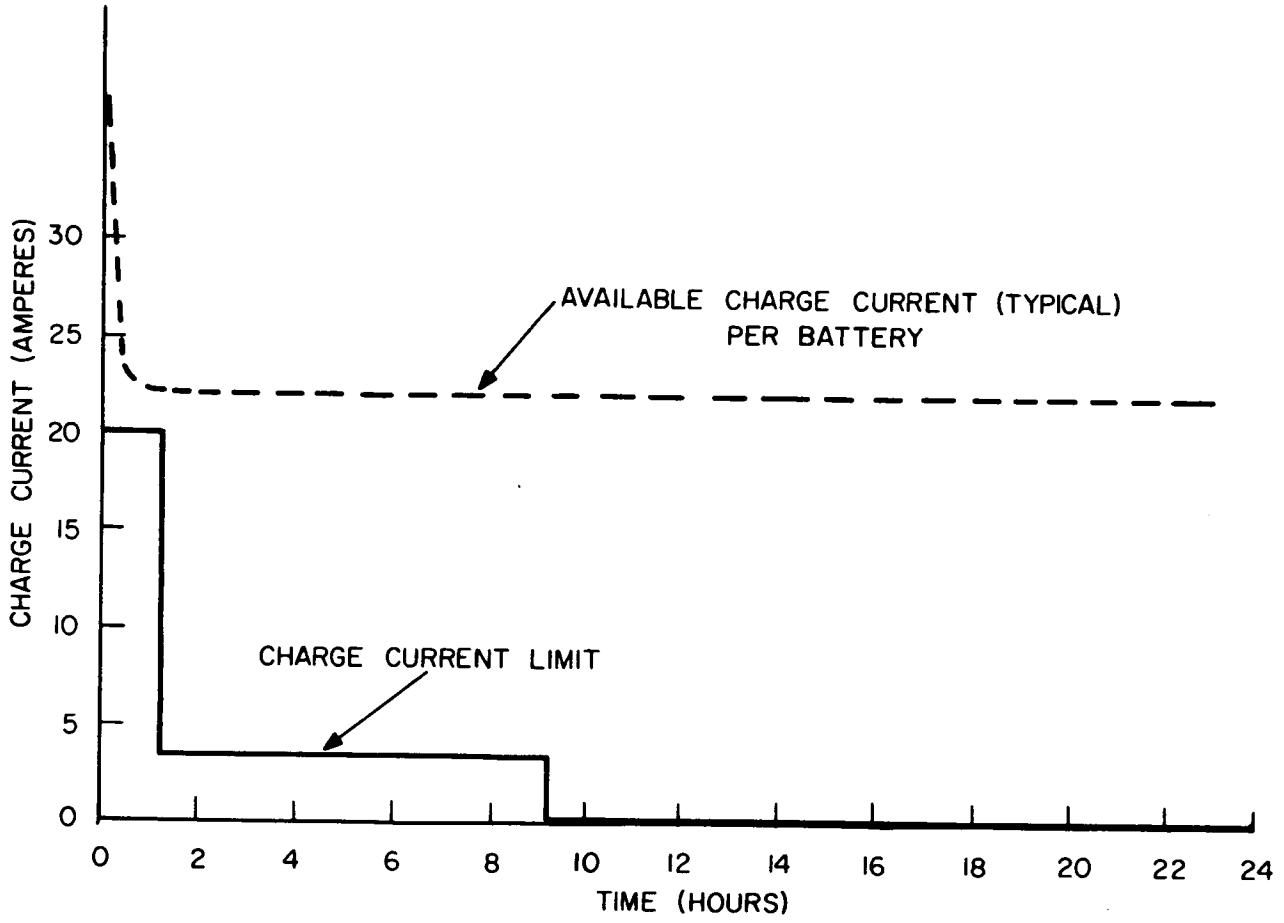

Figure X-85. Beginning of Array Life, Ag-Cd Battery, Synchronous Orbit

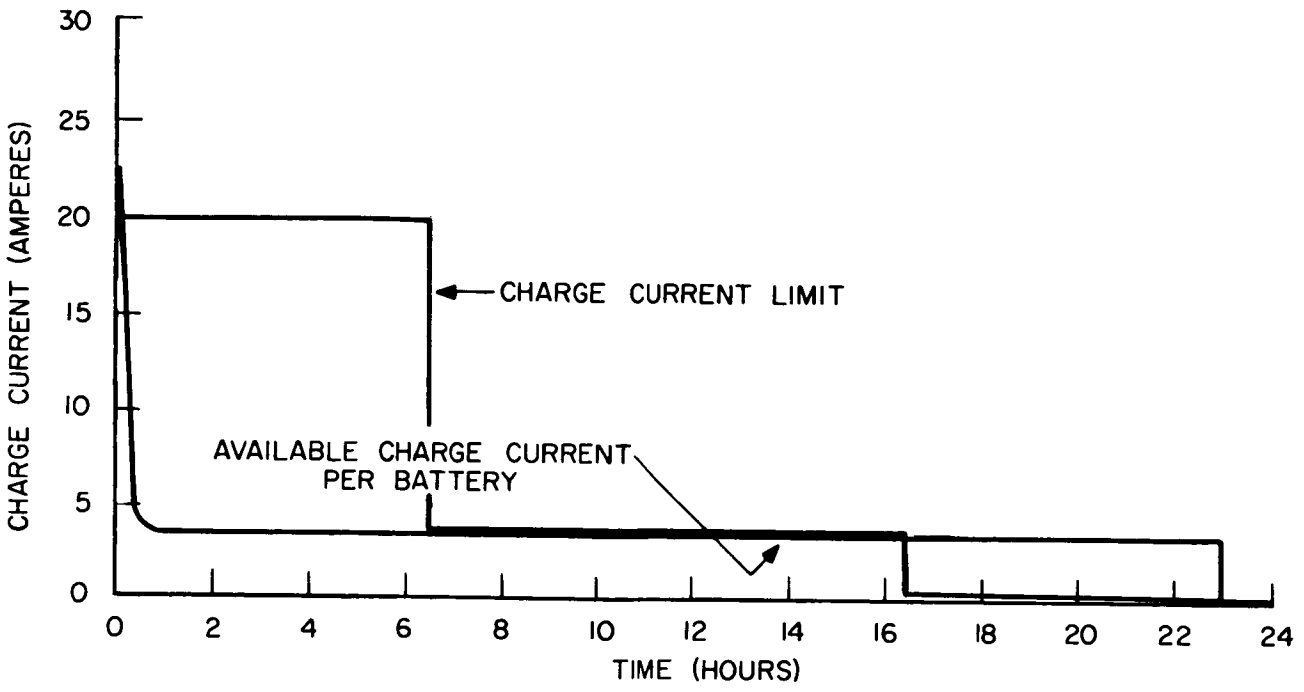

Figure X-86. End of Array Life, Ag-Cd Battery, Synchronous Orbit

array beginning of life) due to the decrease in the array output at end of life. When the current-reduction step occurs, and the limiting value is lowered to 20 amperes, the available charge current will be slightly less. It is seen, therefore, that the battery will accept the full quantity of available current. The array curve shown will permit energy balance with the battery reaching full charge at the end of the daylight period.

2. Ni-Cd Battery, Synchronous Orbit (19,340 nmi). The synchronous-altitude orbit consists of a maximum eclipse period of 70 minutes and a maximum daylight period of 22.8 hours. Due to the long daylight period, there is sufficient time to recharge the battery at low rates and high charge acceptance is not a limiting factor. The battery size is, instead, governed by the maximum permissible depth of discharge, which has been set at 50 percent. The synchronous orbit is therefore characterized (with reference to batteries) by high depth of discharge, low charging rates, and a low cycle life requirement.

Figure X-81 indicates typical charge control of a Ni-Cd battery with an undegraded array. The battery is charged at C/3 until 50 percent of the capacity removed on the previous discharge is replaced. Since 50 ampere-hours were removed (50 percent depth of discharge), the system will replace 25 ampere-hours in 45 minutes. The ampere-hour counter then causes a current step-down to the C/20 rate, which is maintained until the end of the daylight period. The battery will reach the full charge condition after approximately 15 hours and 45 minutes.

As the array degrades, less charge energy will be available at the C/3 rate. Figure X-82 presents a typical curve of the available charge current versus time. Note that the first current reduction step (at 50 percent capacity replacement) does not occur until 4.3 hours have elapsed, compared to 45 minutes for an undegraded array. This is due to the reduced charge current availability. The battery will reach a state of full charge after approximately 19.3 hours have elapsed (based on 50 percent efficiency) at the C/20 rate. C/20 will be the lowest charge rate employed because of the inability to recharge Ni-Cd batteries at lower rates. It is seen in Figure X-82 that all of the charge current available at end of life (except the peak of the initial surge) is accepted by the battery.

Since the battery becomes fully charged before the end of the daylight period, the system may not necessarily require the additional capacity permitted by the high initial current limit. Based upon detailed analysis of predicted end of life array characteristics, it may be possible to eliminate the initial current step. The battery would then be charged at the constant C/20 rate, thus simplifying the control system.

(b) Ag-Cd Battery

The Ag-Cd system is relatively light in weight and is well suited to spacecraft power supply applications. Although the cycle life and recharge capability are limited compared to Ni-Cd, there are mission conditions which favor the use of Ag-Cd batteries, on a weight tradeoff basis.

1. Ag-Cd Battery, Low Altitude Orbit. The charge-control operation for the low-altitude Ag-Cd system is similar to the Ni-Cd control system. The initial (peak charge current, however, will be set at the C/5 rate. After 50 percent of the capacity

removed on the previous discharge has been replaced, the current limit will be reduced to the C/8 level. The current step from the C/5 limit to the C/8 limit will be controlled by the ampere-hour counter, as with the Ni-Cd battery. The next current-limit step will not occur until the battery reaches a state of full charge. However, there will be a current reduction before this point, due to the voltage limit. The voltage limiting function will be temperature-dependent, as in the Ni-Cd control system and will be set at 49.6 volts at +30°C. This corresponds to an average voltage of 1.55 volts per cell for the 32-cell battery. The battery will reach the voltage limit after approximately 95 percent of the energy removed has been replaced. The current will then be gradually reduced while the battery approaches full charge at the constant-potential value. (Figures X-83 and X-84 represent typical charge characteristics for the Ag-Cd system under low-altitude orbital conditions.) When the battery has reached a state of full charge, including required overcharge (as detected by the ampere-hour counter), the current limit will be reduced to a level of approximately C/300. At the same time, there will be a step-down in the voltage limit, to an average of 1.41 volts per cell.

The voltage limit must be reduced when the overcharge phase begins because of possible problems with cell-voltage imbalance. When the total voltage of a series string of cells is limited during charge, the individual cells are not actually controlled and may deviate from the average. Ag-Cd cells are prone to this condition. When limited at 1.55 volts average per cell, the voltages may spread from 1.40 to 1.80 volts per cell. High-voltage cells will undergo internal gassing which is potentially dangerous since the gas recombination characteristics are poor.

The current limit is decreased in order to prevent "thermal run-away", i.e., cell-voltage decrease due to heating causing an increase in current, resulting in more heating, etc. Thus extremely low charge rate (C/300) is required during terminal overcharge.

2. Ag-Cd Battery, Synchronous-Altitude Orbit. For the synchronous-altitude orbit with Ag-Cd batteries, the system design can take advantage of the ability of the battery to efficiently accept charge at low rates. For the purposes of this study Ni-Cd cells will not be charged at currents less than C/20 (that is, all battery charging at rates less than C/20 will not be included in the energy balance calculations due to the inability of the battery to accept charge at low rates). The Ag-Cd system, however, is quite efficient at low charge rates. The C/30 rate was therefore selected as the lower limit for useful charge energy. The control system will then function as follows:

- Charge initially at C/5 limit (up to 50 percent point),
- Charge at C/30 (with voltage limit) (up to full charge),
- Reduce current limit and voltage limit to "trickle" values (C/300 amperes, 1.41 volts per cell).

Figures X-85 and X-86 indicate typical charge performance with an undegraded and a degraded array. Note that the system permits the use of a relatively low-output array at end of life. The projected end of life performance shown in Figure X-86 represents a satisfactory energy-balance situation.

Under synchronous orbital conditions, the Ag-Cd battery will become fully charged before the end of the daylight period. As in the case of the Ni-Cd system, a detailed end of life energy-balance analysis may result in elimination of the initial current step, thus reducing system complexity.

d. BATTERY MECHANICAL CONFIGURATION

(1) Introduction and General Description

The battery system will consist of Ni-Cd or Ag-Cd batteries, depending upon particular orbital and lifetime requirements. This paragraph contains a description of a preliminary mechanical design for both systems.

Since the requirements for the battery system are variable, the total battery size may be varied for different spacecraft loads by adding or removing modular battery units. For the purpose of this study, a worst-case fixed nighttime load of 10 kW maximum was assumed.

Both battery types are assumed to utilize a 100-ampere-hour cell as the nominal basic unit.* Ni-Cd cells are packaged in modules of 5 series-connected cells each. A complete Ni-Cd battery consists of six such modules connected in series. Provisions for carrying up to 16 such batteries on board will be made, including active and spare modules. (This arrangement may apply to the 200-nautical-mile orbit, maximum load, and for mission durations up to one year. These are the conditions requiring the greatest quantity of Ni-Cd batteries.)

Ag-Cd battery consists of four 8-cell modules connected in series. Twenty such batteries are assumed for the 10 kW dark-time load situation. (This is roughly the maximum total quantity of Ag-Cd batteries carried on board, assuming a 200-nautical-mile orbit, for mission durations up to 90 days.)

The batteries are hermetically sealed and mounted in a shelf-like structure that contains electrical interconnections and cooling provisions. The structure also contains the electronic charge controls. The physical arrangement provides for rapid replacement of modules if necessary. The system also contains provisions for monitoring battery performance, pressure-release safety features, and alarm circuits for high pressure and temperature. All of the items described in the foregoing are discussed in detail in the following sections.

(2) Applicable Drawings

The following drawings show the physical and electrical configuration of the batteries. (Further discussion is provided in Paragraph X.C.3.d.(3)).

---

* A 100-ampere-hour capacity is assumed only for the purpose of this section, as a representative cell size. Subsequent computer solutions based on actual mission needs indicate cell sizes which are somewhat different from the number assumed presently. See paragraph X.

(a) Figure X-87 and X-88

The battery support structures for Ni-Cd and Ag-Cd batteries are similar, with the major difference in the number of battery modules contained in each type. The relative position of the structures with respect to the spacecraft chamber is shown in the floor plan in Figure X-87. The modules are supported by shelves that contain cooling coils and gas-exhaust manifolds. Note the gas-exhaust tubing attached to each module.

The electronic charge-control modules are included in the central (vertical) section of the structure, as are the battery busbars. The side walls of the structure consist of corrugated magnesium sections with the front panels hinged for easy access to the inside.

(b) Figure X-89

The battery system wiring details are shown in Figure X-89. In addition to the wiring of a typical module, the method of module interconnection is also shown. Specific electrical connectors are shown for current-carrying and voltage-sensing requirements with wire sizes also listed.

The floor plan of the spacecraft chamber shows the generalized interconnections between the solar panels, the power distribution unit (PDU) and inverter and the battery modules. A five cell nickel-cadmium module is shown in the drawing. The eight cells in a Ag-Cd module are interconnected in a similar manner. The capacitor assembly (array filter) is also shown in this drawing at the top of the battery structure.

(c) Figure X-90

The basic cell outline is shown for both Ni-Cd and Ag-Cd batteries. The details of the pressure-relief valve are shown, as are the details of the cell and module hold-down designs. The ribbed construction of the cast module housing is similar for both battery types as indicated in the drawing. The details of the domed module cover, including the electrical connectors, pressure transducer, and pressure-relief check valve are also presented in the drawing.

(d) Figure X-91

This drawing is a schematic representation of the module and battery wiring. Six modules are connected in series for each battery in this drawing. In addition to the current-carrying wires, the voltage-sensing leads are shown. Note that the voltage leads and current-carrying leads are brought to an electronics module. Required wire sizes are also shown.

(e) Figure X-92

This schematic representation indicates the manner in which the solar-array power is routed to the batteries. As shown, the capacitor assembly is connected

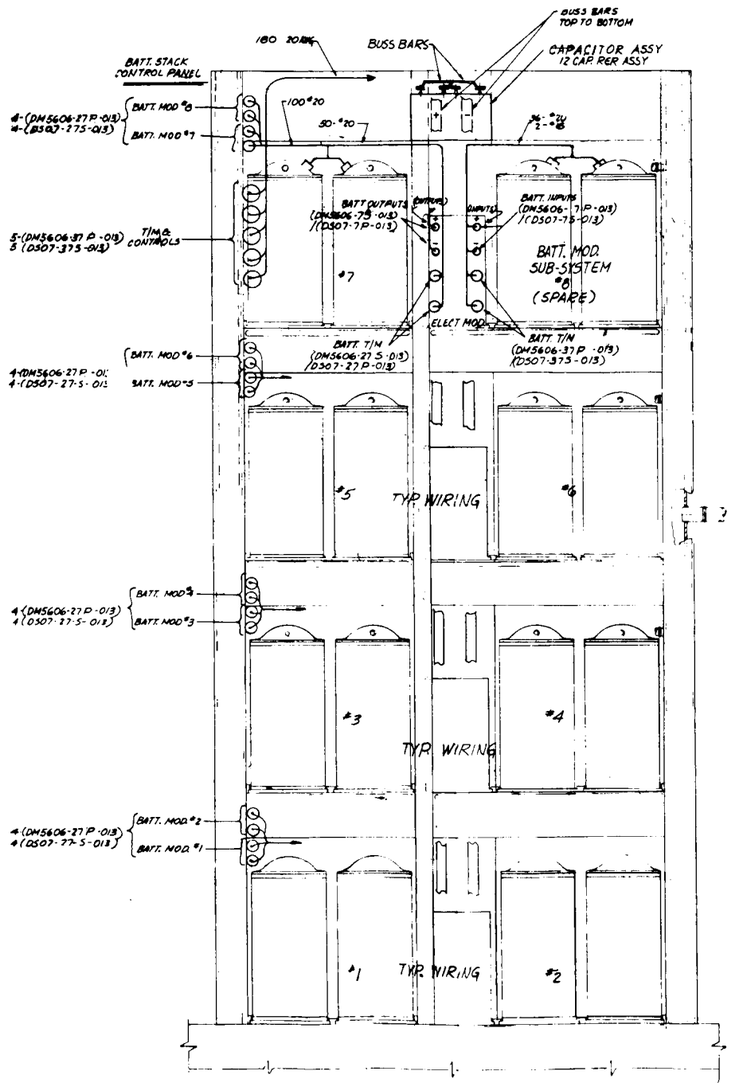

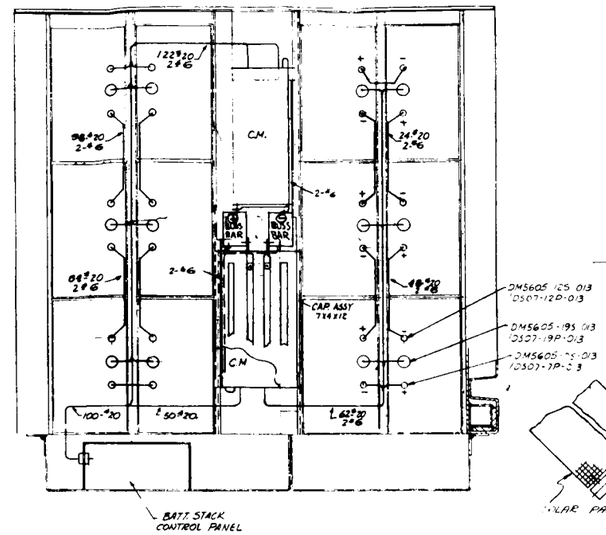

TOP VIEW

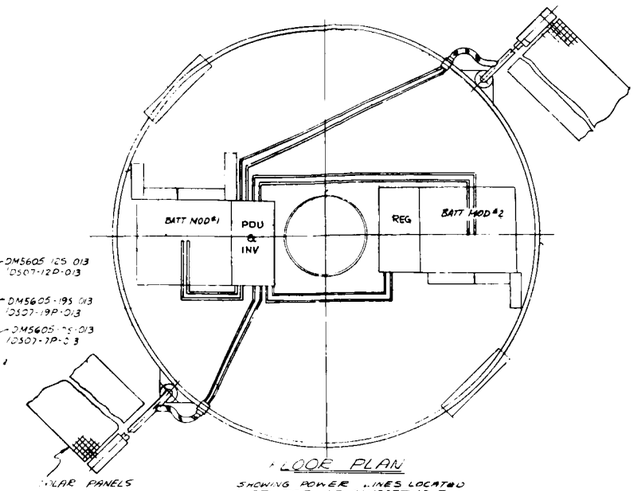

FLOOR PLAN
SHOWING POWER WIRES LOCATED AT TOP OF COMPARTMENT
1/20 SCALE

WIRE REQUIREMENTS		
HARNESS BET. BATT & C.M.	1 UNIT	8 UNITS
WIRE #20	200 FT	2000 FT
WIRE #6	10 FT	80 FT
CONNECTORS: DS07-7P-013	6 REQ	48 REQ
DS07-7S-013	2 REQ	16 REQ
DS07-12P-013	6 REQ	48 REQ
DS07-19S-013	6 REQ	48 REQ
DS07-37S-013	2 REQ	16 REQ
HARNESS BET. C.M. & C. PANEL		
WIRE #20	200 FT	3200 FT
CONNECTORS DS07-27P-013	2 REQ	16 REQ
DS07-27S-013	2 REQ	16 REQ
HARNESS BET. C.M. & BUSS BAR		
WIRE #6	4 FT	32 FT
CONNECTORS DS07-7P-013	2 REQ	16 REQ

ALL CONNECTORS ARE DEUTSCH

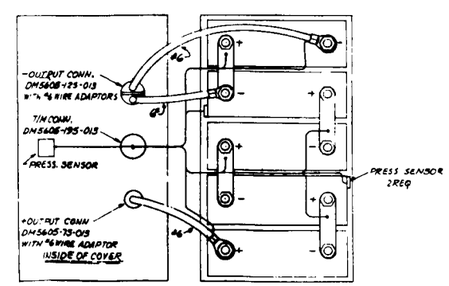

BATTERY MODULE WIRING

Figure X-87. Battery Arrangement, Ni-Cd

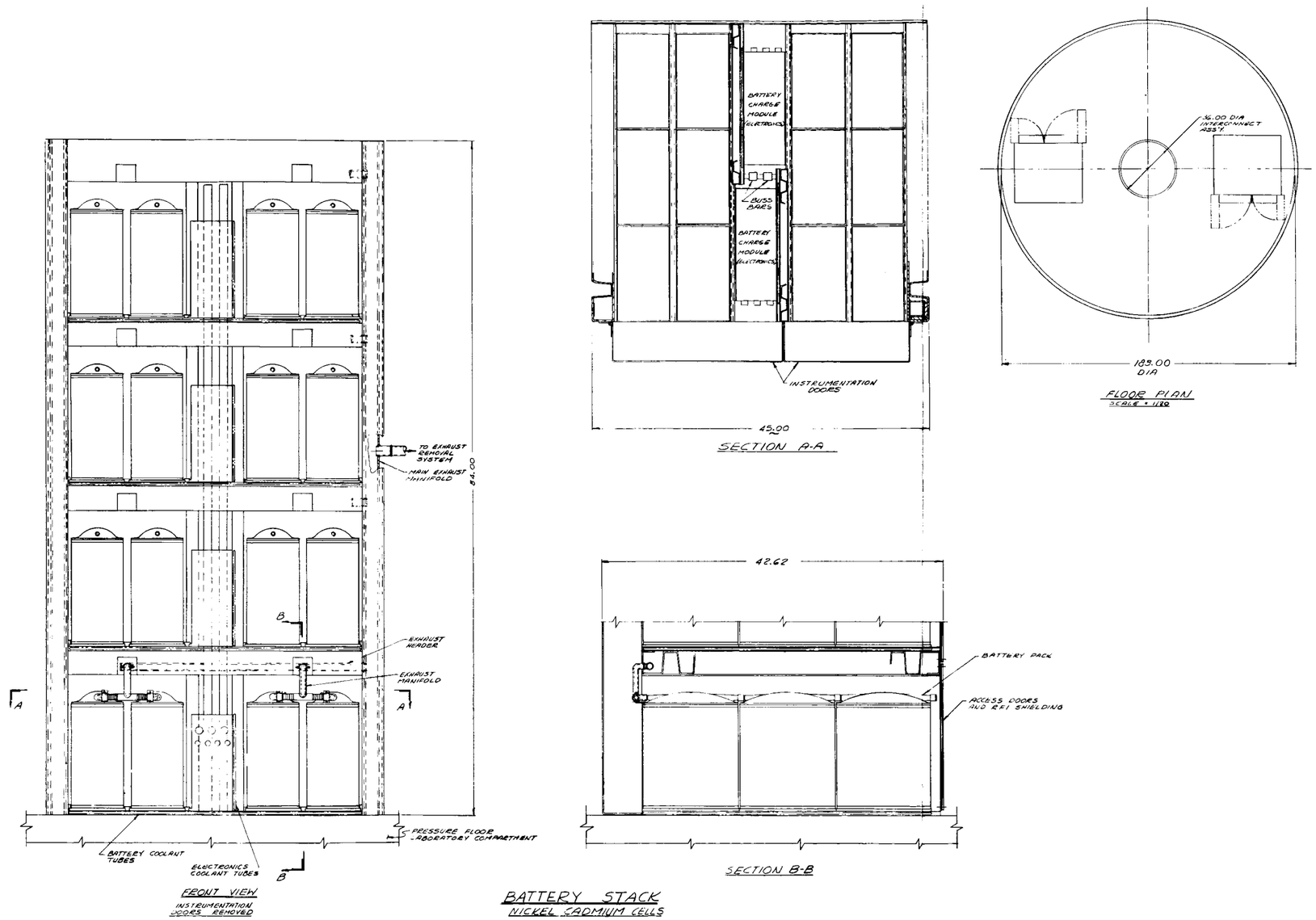

Figure X-88. Battery Arrangement, Ag-Cd

X-135-2

X-135-4

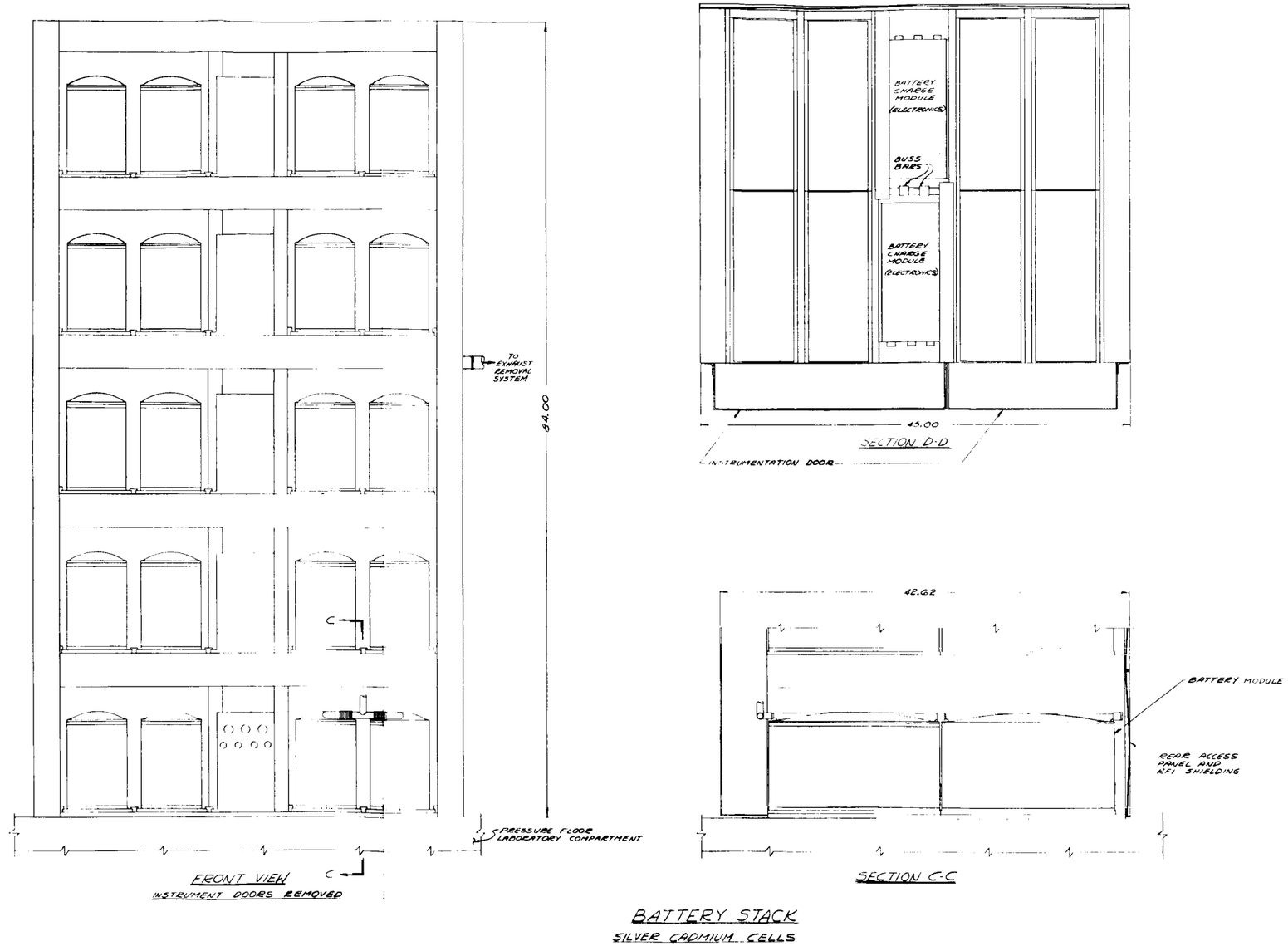

Figure X-89. Battery Stack and Control Module Wiring

[redacted]

X-136-1

X-36-2

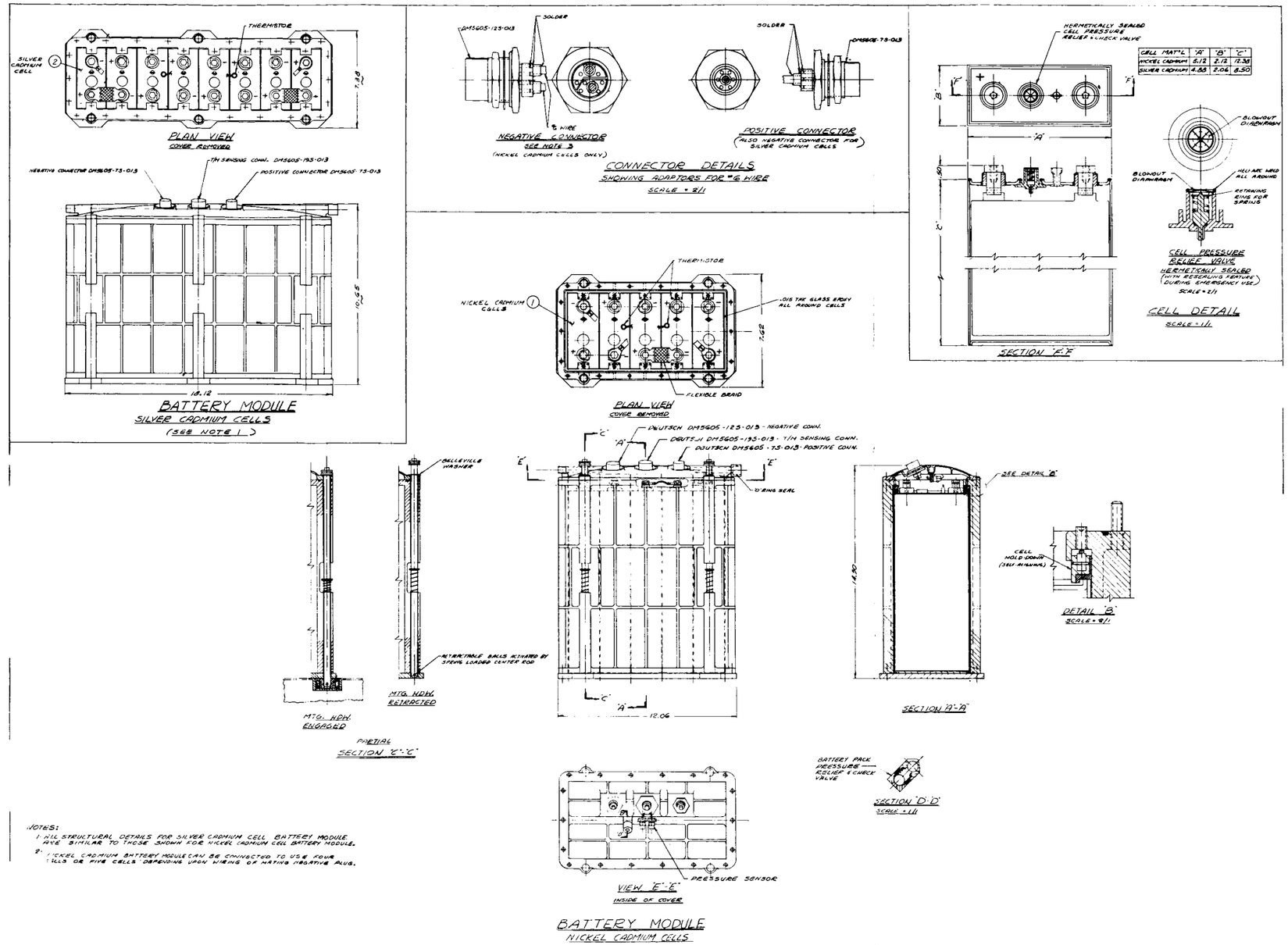

NOTES:

1. ALL STRUCTURAL DETAILS FOR SILVER CADMIUM CELL BATTERY MODULE ARE SIMILAR TO THOSE SHOWN FOR NICKEL CADMIUM CELL BATTERY MODULE.
2. NICKEL CADMIUM BATTERY MODULE CAN BE CONNECTED TO USE FOUR CELLS OR FIVE CELLS DEPENDING UPON WIRING OF MATING NEGATIVE PLUG.

Figure X-90. Battery Module

X-137-18

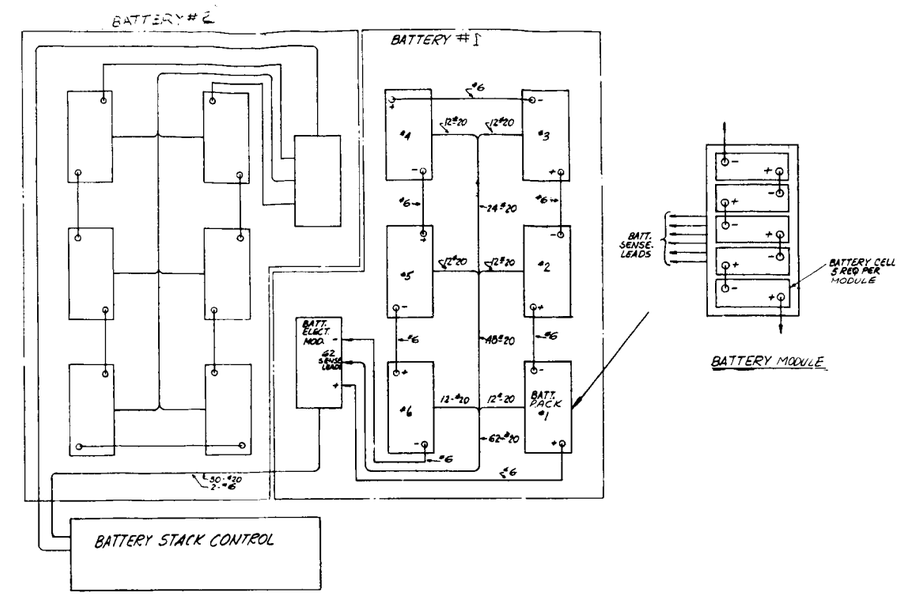

Figure X-91. Battery Module Wiring

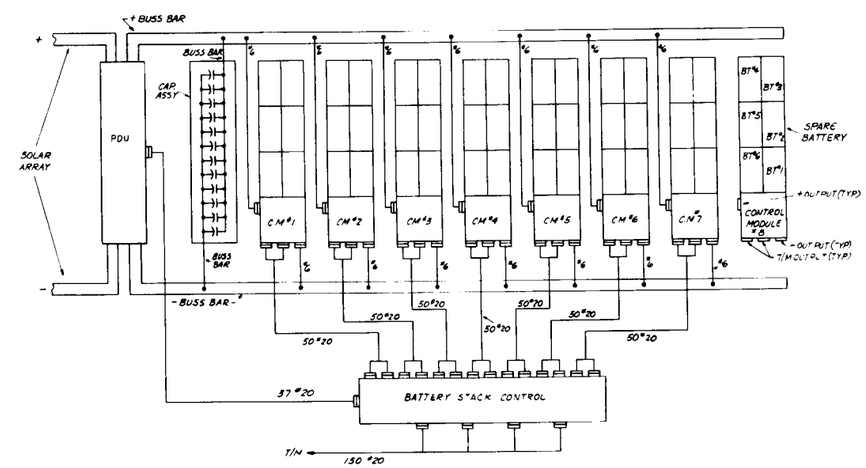

Figure X-92. Battery Stack and Control Unit Wiring

between the battery bus sections. Charge control for each battery is effected by the control module shown adjacent to each battery. Battery telemetry leads are connected to the Battery Stack Control Box.

(3) Module Description

(a) Ni-Cd Modules

The basic Ni-Cd cell has an assumed nominal capacity of 100 ampere-hours, and is hermetically sealed in a stainless steel case. The cell is electrolyte-starved, and designed for long-life applications. It contains a self-sealing pressure relief valve which has a hermetically sealed, welded diaphragm and is fitted with a piercing unit that punctures the diaphragm when the internal cell pressure rises above 80 psig. The pressure will then be relieved, and the valve will reseal itself by means of a spring-loaded conical seal or the equivalent. After the initial venting operation, the cell will again be sealed (although not with the absolute assurance of a welded seal). The sealing mechanism is designed to open and reseal as many times as needed to relieve overpressure.

The positive terminal of the cell will be insulated from the metal case and the negative terminal will be electrically common with the case. Both cell terminals will contain provisions for screw-type connections.

The cells are packaged in a 5-cell module, electrically insulated from one another and from the module housing, but in intimate mechanical (and thermal) contact with the walls of the module housing.

The module packaging material is magnesium, and consists of a machined cast housing, a domed cover, and a flat bottom plate. The main body of the housing is a rectangular section with reinforced, ribbed walls. The primary function of this section is to restrain the cells during periods of internal pressure generation. Magnesium was selected for the module housing because of the relatively high strength-to-weight ratio and the fact that battery electrolyte (potassium hydroxide) will not attack magnesium. Aluminum would be seriously corroded in the event of an electrolyte leak.

The cells are held in place by means of insulated hold-down clips, which automatically compensate for small variations in cell height. The clips hold the cells firmly against the bottom plate. The domed cover and bottom plate are machined pieces, fitted to the rectangular section and sealed with O-rings. The major mode of heat transfer is through the cell bottom to the module bottom plate and then to the mounting structure. Since the bottom of the cell is recessed, it lends itself to the bonding of a magnesium slug, thus providing a wide contact area for good heat transfer. The slug is bonded with a thermally conductive (but electrically insulating) epoxy. The bottom module plate is machined to fit matching grooved tracks which are built in as part of the structure. The housing contains quick-disconnect captive bolts, which are self-aligning with a matching set of receiving adapters for locking the module in place. In operation, the module slides into place (within the grooved tracks) and the captive bolts are depressed and given approximately three-quarters of a turn. The bolts contain a ball-and-cam type spring-loaded locking mechanism. The module is thus

locked in place when the bolts are turned. In this manner, the modules can be quickly mounted or removed for servicing if the need arises. The module cover is a domed, cast section designed to accommodate pressure and structural requirements. It contains the electrical connectors for power takeout and individual cell-voltage sensing, the pressure-sensing transducer, and the outlet port for vented gases. All connectors in the cover are hermetically sealed, with quick-disconnect provisions.

The pressure sensing transducer will initiate an alarm and cause the charge to be terminated or reduced if a cell "blows a seal" and vents gas to the module interior.

The cells will be interconnected by means of copper busbar sections with terminal connections made by means of screws in the terminals.

The spacecraft system requires a minimum of 29 Ni-Cd cells. Since six 5-cell modules contain 30 cells, one of the modules must be wired so as to allow the use of only four cells. In order to preserve versatility and to limit design and production to one type module, each of the modules will be capable of serving either as a 4-or a 5-cell unit. During spacecraft integration, an appropriate connection can be made to each module. In the course of detailed systems design, the use of all 30 series cells can be explored as an alternate.

The total weight is 66 pounds, with the cells weighing 50 pounds. Since the module is rated at 600 watt-hours, the packaged module energy density is 9.2 watt-hours per pound.

(b) Ag-Cd Modules

With reference to construction details, the Ag-Cd module is similar to the Ni-Cd module except that there are 8 cells instead of 5. The assumed cell capacity is again 100 ampere-hours, but the cell-case material is a plastic. Since the cell case is plastic there will be no need for additional electrical insulation between cells and housing. The positive and negative terminal feed-through areas are potted with epoxy resin in order to ensure a reliable seal. These cells are also fitted with resealable pressure-relief valves, although they are far less likely to vent gas under normal operating conditions than are the Ni-Cd cells. Ag-Cd cell is an extremely low-pressure system, since the charge current and overcharge current are particularly well controlled. The system is also very efficient during charge. The combination of high charge efficiency and absence of any appreciable overcharge results in a low heat dissipation factor. Therefore, since there is no significant pressure buildup or dissipation of heat, the plastic cell case can be utilized.

The complete module weighs 55.0 pounds, of which the cells weigh 40 pounds.* Since the module is rated at 880 watt-hours, the packaged module energy density is 16.0 watt-hours per pound.

---

* Based on 100-ampere-hour cell capacity

(4) Structure and Overall Integration

The structure in which the batteries are housed consists of shelf-type compartments. For the missions under consideration, it is necessary to stack the batteries vertically to assure a compact packaging approach and to minimize the required floor space. The walls and shelf areas are constructed of corrugated magnesium, with coolant passages as an integral part of the structure. Coolant is provided for each module position in order to control battery temperature. The coolant is piped to one main line which is connected to the spacecraft cooling system.

Each of the module compartments contains track guides for module alignment and hold-down, as well as receptacles for the quick-connect mounting bolts. The structure extends from the compartment floor to the ceiling, and can be utilized as structural support for the compartment. The gas venting system is also integrated as part of the structure, and functions as follows:

Each of the modules contains a gas-port tube in the cover that interconnects with the tube of the adjacent module. The modules are all interconnected with a lead to a common exhaust system. The opening on each end of the module exhaust tube is designed for quick connection with the neighboring module. The connection is sealed by an O-ring type of flange. One of the end modules in each battery will require a cap seal on one end of the tube. In the module, the interior space above the cells is separated from the exhaust tube by a one-way check valve. Therefore, if gas is vented by a cell, it will be funneled directly to the exhaust system, and will not flow into the adjacent modules. The exhaust manifold system will be constructed of a suitable magnesium alloy. A flexible bellows joint has been provided as part of the exhaust tubing that is attached to each module to allow for slight relative movement between the modules (caused by mechanical tolerance build-up, vibration, and thermal differentials).

A large portion of the structure is intended for support of associated electronics. The structure contains the busbars to which the batteries are connected, the battery charge controllers, the capacitor bank (mounted at the top), the power distribution unit, and the inverter. It is estimated that approximately 20 percent of the structure weight is required for support and cooling of the various electronic assemblies. The front of the structure contains hinged instrument panels for charge-control monitoring, current adjustments, etc. The back of the structure is covered with removable magnesium access panels. The entire structure is completely enclosed, thus providing RFI* shielding.

As shown in the applicable drawings, there are two such structures for the application described herein. For the worst-case mission conditions, which require Ni-Cd batteries, 14 active 100-ampere-hour batteries are assumed for the present purposes, plus two spares. Each of the structures will therefore contain 7 active batteries, and 1 spare battery (each consisting of six 5-cell modules). Other combinations of active units and spares may be required, depending upon the mission and reliability requirements. The

---

*Radio-Frequency Interference

present packaging approach involving Ag-Cd batteries is based on the requirements of 18 active 100-ampere-hour units and two spares. Each of the two structures will contain 9 active batteries and 1 spare battery, each battery consisting of four 8-cell modules.

Assuming the number of batteries as in the preceding, the fully loaded Ni-Cd battery structure will weigh 3,760 lbs, including batteries, RFI shielding panels, instrument panels, cables, exhaust system, busbars, and coolant coils. Since the floor area occupied by the battery housing structure is 11.6 square feet, the bearing pressure on the spacecraft chamber floor will be 324 pounds per square foot (psf). This is a relatively high loading pressure, and must be taken into account during all operations that occur when the spacecraft is not in a weightless environment.

Similarly, with the silver-cadmium batteries, the total structure weight will be 2,670 pounds with a resultant floor load of 230 psf.

(5) Heat Dissipation

The following discussion is presented in order to demonstrate the method of calculating approximate heat dissipation for each operational mode of the battery.

(a) Ni-Cd (100-Ampere-Hour Cell), Low Altitude Mission

Figure X-93 is an idealized version of charge and discharge curves, plotted in terms of cell voltage versus ampere hours. The solid line above area "A" represents a simplified discharge curve (the dotted line "a" indicates the actual shape of the curve). Since the Ni-Cd battery will be discharged to an approximate depth of 16 percent, assuming a 200-nmi circular orbit, the average level of the discharge curve was assumed to be 1.25 volts (per cell). For the given depth of discharge, 16 ampere-hours will be removed assuming a 100-ampere-hour cell. The area "A", Figure X-93, represents the electrical energy removed per cell during discharge: 1.25 volts x 16.0 ampere-hours equals 20.0 watt-hours.

The solid line that is the upper boundary of zones "B" and "C" represents a simplified charge curve (the dotted line "b" indicates the approximate shape of the actual curve). The average charge voltage was assumed to be 1.45 volts. Since the ampere-hour efficiency of the cell is approximately 90 percent for the given conditions, an input of 17.8 ampere-hours is required to maintain energy balance during repetitive cycling. Area "C" then represents the total required overcharge energy. A gross energy-balance calculation shows that the total watt-hours into the system is 1.45 volts x 17.8 ampere-hours, or 25.81 watt-hours. The electrical energy removed from the system is 1.25 volts x 16 ampere-hours, or 20.0 watt-hours. The difference of 5.81 watt-hours is assumed to be dissipated as heat over the entire charge-discharge cycle.

It is, therefore, seen that the average heat dissipation rate during the entire charge-discharge cycle is 5.81/25.81, or 19.4 percent of the total charge energy. In a general case, the orbit-average heat dissipation can be calculated as above, once the average values for charge rate, charge voltage, and charge time are established. It is of further interest to

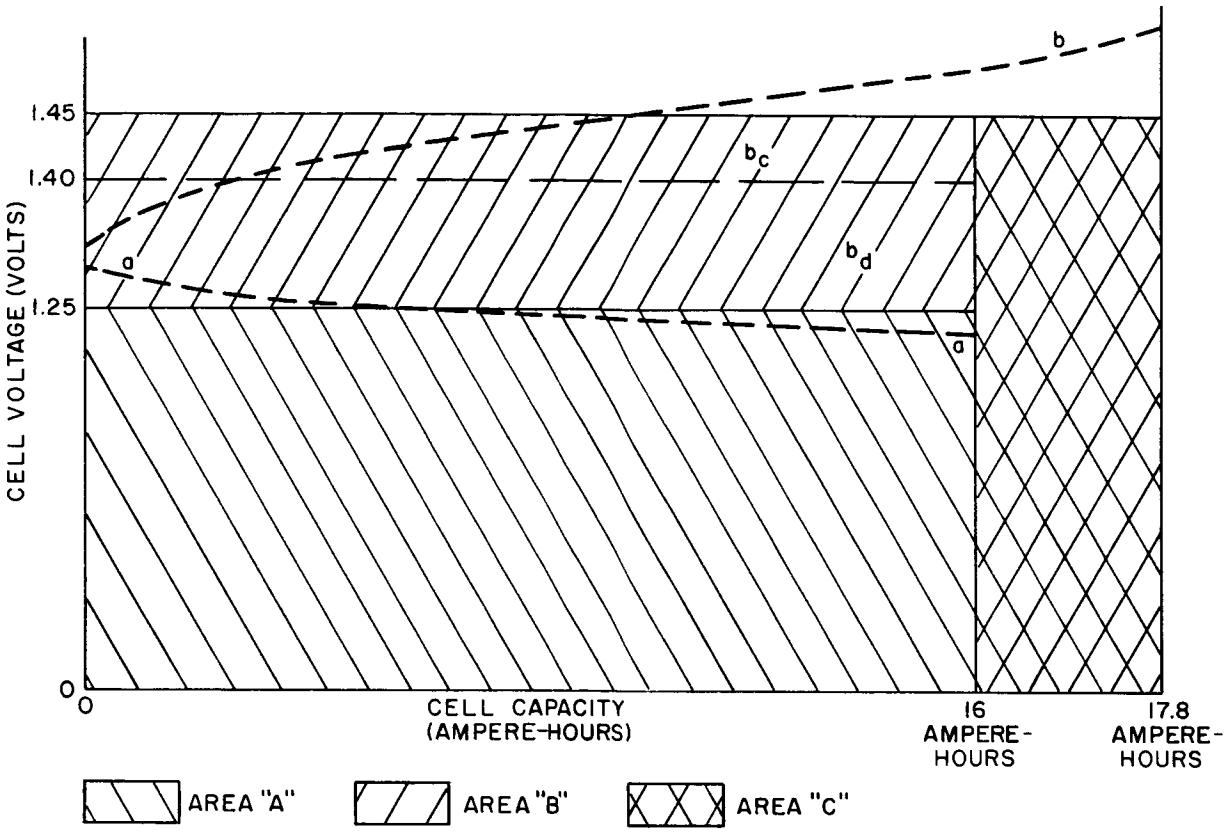

Figure X-93. Storage Cell Voltages

estimate actual heating rates during the three major phases of the charge-discharge cycle. The following calculations will have no effect, however, on the average rate as calculated previously.

During the overcharge portion (area "C") all of the input energy is assumed to be dissipated as heat. This portion of the cycle usually results in heat dissipation rates which are far in excess of those developed during charge (area "B") and discharge. A small portion of the input energy does perform useful work (charging) during this overcharge portion, but the total heat dissipation is essentially unchanged. Compared to the 19.4-percent orbit-average dissipation ratio, the 100-percent factor during overcharge governs the requirements for heat-dissipation capability. Since the overcharge heating rate is far above the average, the charge and discharge rates must be (as a group) below the average. As shown in Figure X-93, the heat dissipation during charge and discharge (combined) is (1.45 - 1.25) x (16 ampere-hours), or 3.2 watt-hours. This is 16 percent of the total energy input during the charge period defined by area "B".

In order to divide the energy loss between charge and discharge modes, it is assumed that the instantaneous rise in cell voltage at the start of charge is due to polarization and IR losses. A similar assumption is made for the immediate drop in voltage at the start of discharge. If a hypothetical open-circuit voltage during cycling is postulated, it can be assumed that the heat losses due to voltages higher than the open circuit voltage occur

during charge. This would be area "b_c" in Figure X-93. Discharge losses are shown in area "b_d". A value of 1.40 volts per cell was taken as the dividing line, due to cell-voltage characteristics observed during cycling, and because it yields results which agree with experimental data. For example, it is known that the heating rate during early charging is negligible and that the charge is often endothermic (battery absorbs heat). Calculations based upon the above listed assumptions indicate that 3.5 percent of the total charge energy goes to heat:

$$100\left(\frac{1.45 - 1.40}{1.45}\right) = 3.5 \text{ percent}$$

It has been observed that significant heating occurs during discharge. The calculations agree, indicating that 12 percent of the total energy is converted to heat.

$$100\left(\frac{1.40 - 1.25}{1.25}\right) = 12 \text{ percent}$$

1. Heat Balance Calculations, Ni-Cd

- Overall:

Watt-hours in = 17.8 (1.45) = 25.81

Watt-hours out = 16 (1.25) = 20.00

difference (heat) = 5.81 watt-hours per cell

- During individual phases of the charge/discharge cycle:

Heat during charge = (1.45-1.40) 16 = 0.80

Heat during overcharge = 1.45 (17.8-16) = 2.61

Heat during discharge = (1.40-1.25) 16 = 2.40

Total energy 5.81 watt-hours per cell

2. Heat Rate During Each Phase

- Discharge; $\frac{2.30 \text{ WH heat}}{20.00 \text{ WH electrical}} = 0.12$, or 12 percent

Heat dissipation during discharge = 0.12 (VI), watts per cell.

VI = battery voltage x battery current (discharge)

- Charge; $\frac{0.80 \text{ WH heat}}{1.45\ (16) \text{ WH electrical}} = 0.0345$, or about 3.5 percent

  Heat dissipation during charge = 0.035 (VI), watts per cell.

- Overcharge; heat = 1.00 (VI), watts per cell.

(b) Ag-Cd (100-Ampere-Hour Cell), Synchronous Orbit

The method of calculation is identical to the method described in Paragraph X.C.3.d(5)(a). The input values have been changed, to reflect the characteristics of the Ag-Cd battery corresponding to 50 percent discharge depth.

Average charge voltage	=	1.44 volts
Average discharge voltage	=	1.125 volts
"Ideal" voltage	=	1.40 volts
Required overcharge	=	0.035

- Heat evolved during overcharge =

  (1.44-1.40) (50.0 ampere-hours) = 2.00 watt-hours per cell

  heat rate $= \frac{2.00 \text{ VI}}{1.44\ (50)} = 0.028$ (VI), watts per cell

- Heat evolved during discharge =

  (1.40-1.125) (50.0 ampere-hours) = 13.75 watt-hours per cell

  heat rate $= \frac{13.75 \text{ VI}}{1.40\ (50)} = 0.197$ (VI), watts per cell.

4. Electronics

a. DESCRIPTION OF THE MAJOR BLOCKS

All electronic circuits, except for certain filter networks discussed later in this section, are contained within a set of replaceable modules. See Figure X-94. There are three major electronic equipment assemblies shown in Table X-24: charger/tracker, d-c regulator, and inverter.

The charger/tracker assembly consists of a number of power modules equal to the number of batteries in the system. Each power module is a replaceable charger unit, complete except for bias power. In addition, the assembly includes two redundant control modules packaged together with the failure detection and switchover module, but independently replaceable. Each control module consists of the circuits shown in Figure X-94 and in Table X-24. Relays are used to switch over from one control module to the other in the event of malfunction. In order to avoid a momentary removal of the bias power during the switching process, make-before-break switching will be used. Malfunctioning of the failure-detect module will not cause a power system failure unless it is followed by a failure in the active control module.

The d-c regulator assembly consists of the power modules (whose number is chosen on the basis of d-c load and reliability requirements), two redundant d-c regulator control modules, and a failure-detect module. As in the charger/tracker assembly, all modules are replaceable. Malfunction of both the failure-detect module and an active control module are necessary to disable the regulated d-c bus.

The Inverter Assembly is assumed to consist of two or more active, self-sufficient power modules electrically connected in parallel.

As indicated in Table X-24, seven different types of electronic modules are required. The choice of this number is based on engineering judgment, taking into consideration the ease of replacement and the desirability of minimizing interference with operating assemblies and functions at a time when a faulty module is being replaced. As a result of a detailed design effort, however, the number of different module types may well be reduced by combining functions into a lower number of replaceable blocks.

The solar array filter and the input/output filters for the d-c regulator are non-replaceable items in this system, because these functions are extremely difficult to service. For safety of personnel, the system would have to be shut down in order to repair or replace these units. In lieu of replaceability, these filters will be designed in such a manner that a large portion of the components might fail without impairing the intended functions and that any such failure would cause no permanent damage to other portions of the system.

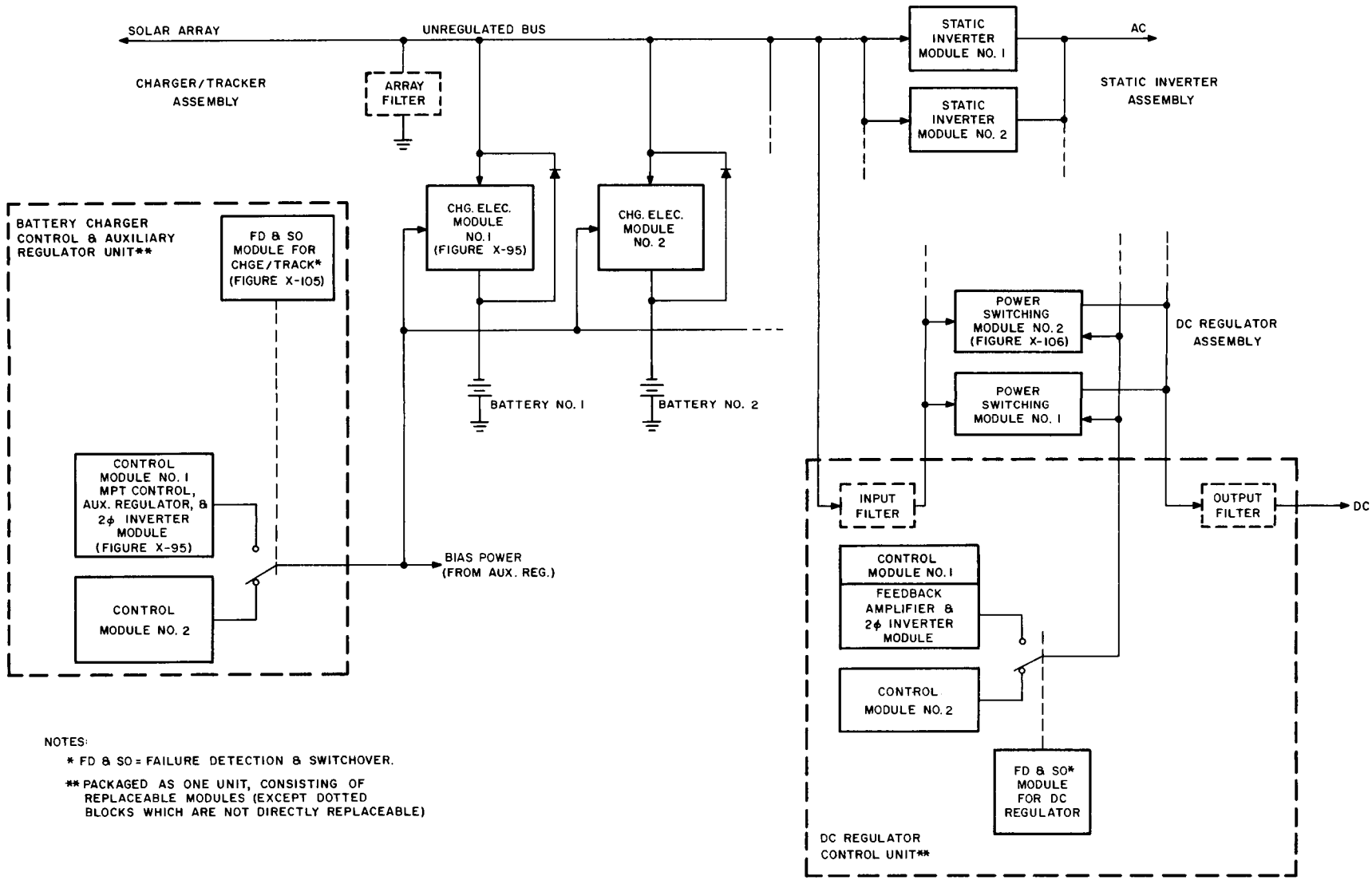

NOTES:

* FD & SO = FAILURE DETECTION & SWITCHOVER.

** PACKAGED AS ONE UNIT, CONSISTING OF REPLACEABLE MODULES (EXCEPT DOTTED BLOCKS WHICH ARE NOT DIRECTLY REPLACEABLE)

Figure X-94. Power Supply, Electronics Modules

TABLE X-24. ELECTRONIC MODULES

Assembly	Module	Description	Reference Paragraph
Charger/Tracker	Power	Power Switching Network	X.C.4.b(1)(b)3.a
		Battery Protective Functions (voltage, temperature, current limit, amp/hr accumulator)	X.C.4.b(1)(c) and X.C.4.b(1)(e)
		Current Equalization Circuits	X.C.4.b(1)(b)3.b
		Switch-Out Circuits	X.C.4.b(1)(d)
	Control	MPT Control	X.C.4.b(1)(b)3.b
		Two-phase Inverter	X.C.4.b(1)(b)3.a
		Auxiliary (Bias) Regulator	
	Failure Detect & Switchover		
D-C Regulator	Power	Power Switch and Driver	X.C.4.b(2)(b)
		Pulse Width Modulator	X.C.4.b(2)(b)
		Current Limit Circuit	X.C.4.b(2)(b)
		Switch-Out Circuit	X.C.4.b(2)(c)
	Control	Feedback Amplifier	X.C.4.b(2)(b)
		Two-phase Inverter	
	Failure Detect & Switchover		X.C.4.b(2)(c)
Inverter	Power		X.C.4.b(3)

b. MAJOR COMPONENTS

(1) Charger and Tracker Electronics and Battery Protection

The function of the battery charge electronics is to effect the maximum safe transfer of energy from the source (solar array) to the energy storage devices (batteries). This is done taking into account the load requirements (which are satisfied first), the requirements of the batteries as determined from the discharge during the previous orbital

dark period, the inherent limitations of the batteries and the instantaneous capability of the source. The various operating modes are as described below. A functional diagram is presented in Figure X-95.

The battery charge electronics has two normal modes of operation, charge and discharge, corresponding to orbital day and night, as well as two protection modes.

(a) Discharge Mode

The discharge mode occurs during the darktime portion of the orbit. Operation of the battery charge electronics in this mode is as follows:

The beginning of the spacecraft night is characterized by the loss of output from the source (solar array). The solar array bus voltage falls until it is slightly lower than the battery voltage; when this occurs, the discharge diodes conduct. The batteries now supply the load power requirements through the discharge diodes. Note that, with the discharge diodes conducting, the battery charge electronics, with the exception of the current monitoring circuits, is ineffective.

The current monitoring function senses the battery current magnitude and direction, performs a time integration and accumulates the battery charge and discharge ampere-hours in separate digital memories. Since the cycle of operation begins at the end of orbital day, the ampere-hour accumulator receives an "end of day" indication that resets all memories to zero. During orbital night, battery discharge is sensed by the battery-current magnitude and direction sensors. The total ampere-hour discharge is computed and stored in the discharge memory of the ampere-hour accumulator. This quantity is used for telemetry, display and performance monitoring, and control functions to be described for the charge mode of operation.

(b) Charge Mode

1. Introduction. Since in the parallel tracker type of space power system the charge and tracking functions are inseparable, a description of the operating point control will be offered prior to a detailed discussion of the charge philosophy and its implementation.

2. Array Operating Point Control. This section briefly describes the principles employed to track the maximum power point of a solar array.

By changing the load resistance presented to the array, the operating point can be changed, as shown in Figure X-96.

By using a pulse width modulated regulator (PWM) and suitable filters, the load can be made to appear to the source as having any value from its inherent impedance to infinity. For the present purposes, let an ideal PWM device be assumed, in which case the power P_o delivered to the load equals the array output power P_s as shown in Figure X-97.

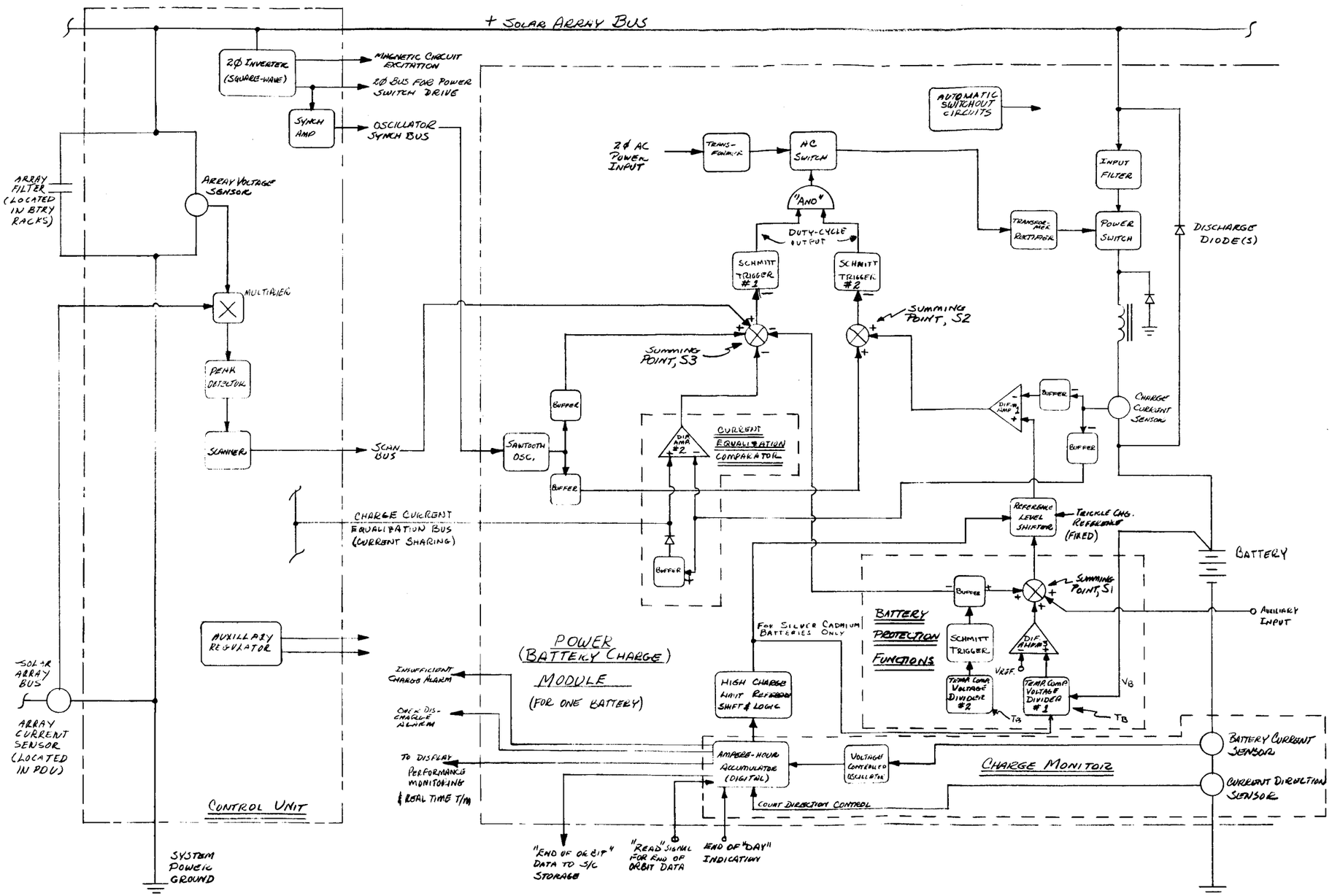

Figure X-95. Battery Charge Electronics, Functional Diagram

X-150-2

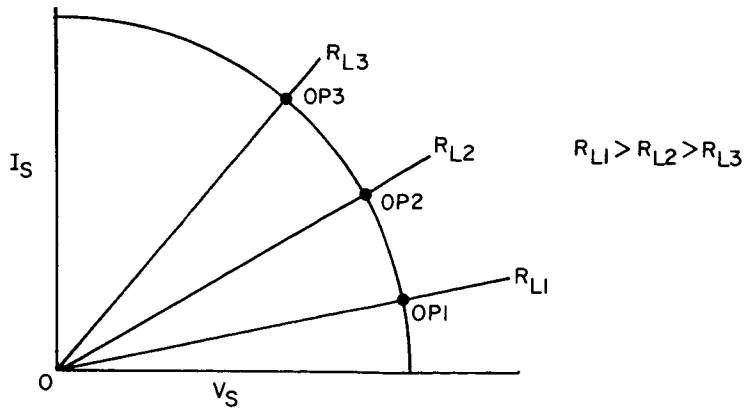

Figure X-96. Variation in Operating Point with Change of Impedance

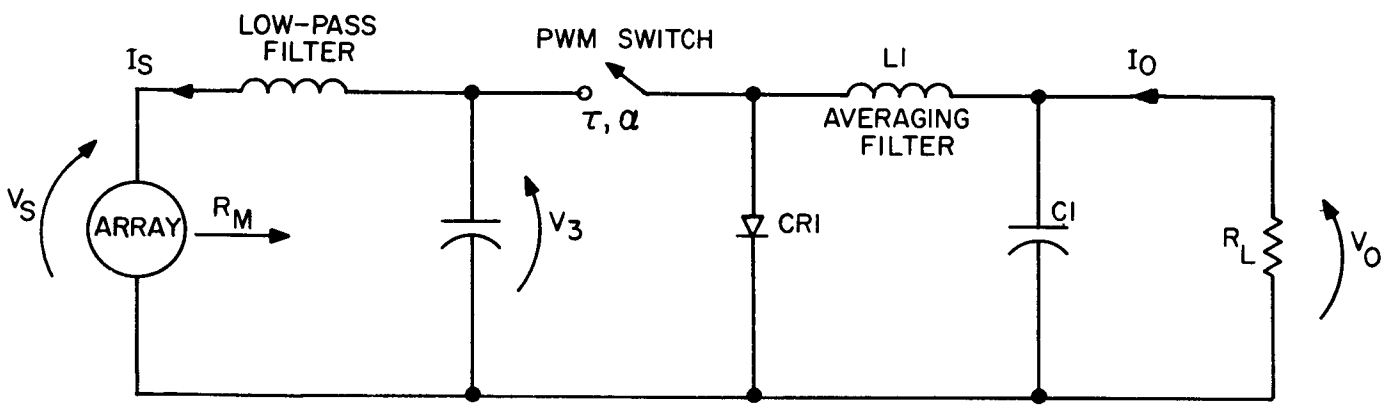

Figure X-97. Ideal PWM Impedance Transformer

$$P_s = \frac{(V_s)^2}{R_m} = P_o = \frac{(V_o)^2}{R_L} \; ; \; R_m = R_L \left(\frac{V_s}{V_o}\right)^2 , \qquad \text{(X-42)}$$

where

P_s is solar array output power required under steady-state solar-cell temperature conditions

V_o is output voltage, and

R_L is load resistance.

V_s is solar array voltage

The voltage across R_L is substantially ripple-free and is given by

$$V_o = \alpha V_s, \tag{X-43}$$

where α is the duty cycle and

$$R_m = R_L \left(\frac{V_s}{\alpha V_s} \right)^2 = \frac{R_L}{\alpha^2} . \tag{X-44}$$

It can be seen that as the duty cycle α is changed from 1.0 to 0.0, the load resistance presented to the array is varied from R_L to infinity. This is shown graphically in Figure X-98. Thus the operating point is controlled by controlling α.

Assuming an ideal (non-dissipative) PWM as before, power delivered to the load, P_o, equals array output power, P_s, and all the array power is delivered to the load resistor.

By selecting R_L to intersect the $I_s - V_s$ characteristic at a voltage lower than the maximum power voltage, a value of α can be found which will result in maximum transfer of array power to R_L, as shown in Figure X-99.

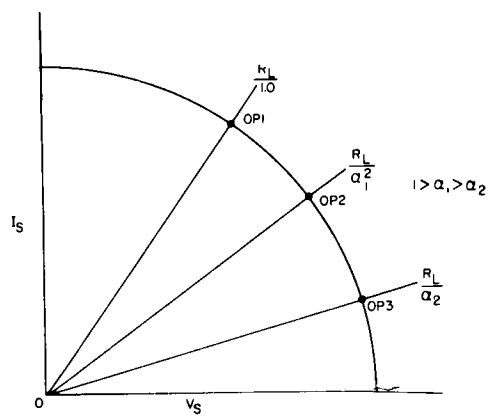

Figure X-98. Variation in Load Resistance with Variation in α

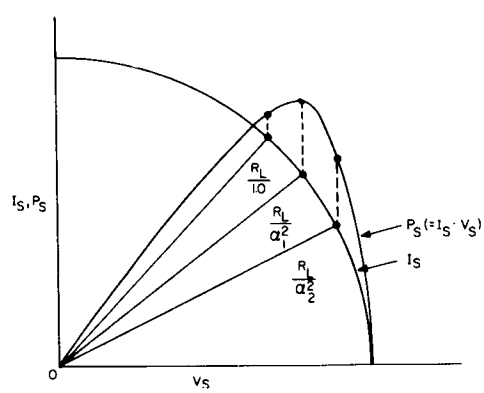

Figure X-99. Determination of Maximum Power Transfer

Substitution of a battery for R_L doesn't change control capability, as shown in Figure X-100.

The average output voltage is now determined by the battery and

$$V_o = V_B = \alpha V_s$$

or

$$V_s = \frac{V_B}{\alpha} \tag{X-45}$$

The short-term I-V characteristic of a battery can be assumed to be almost vertical as shown in Figure X-101.

The battery voltage is reflected to the PWM input terminals modified by the duty-cycle α, and it appears as a low-impedance signal to the array. This causes the array voltage to be fixed by this low impedance with the array current flow determined by its I-V characteristic. This appears graphically as shown in Figure X-102.

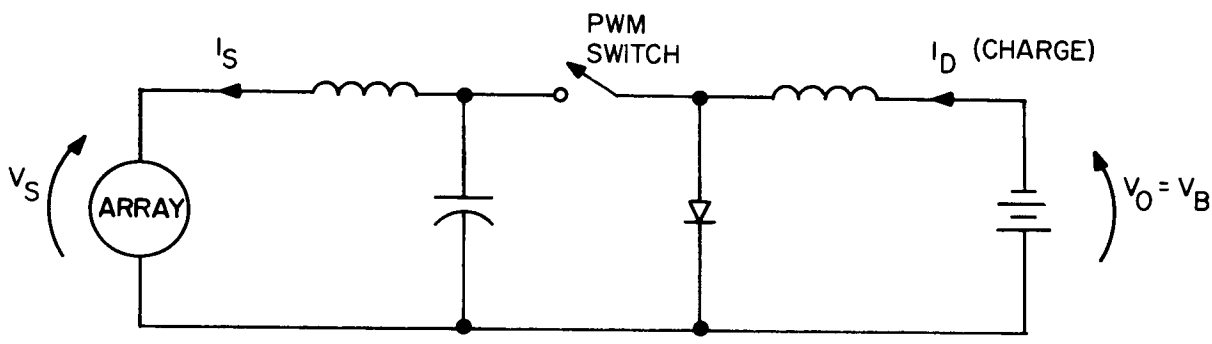

Figure X-100. Substitution of Battery for R_L

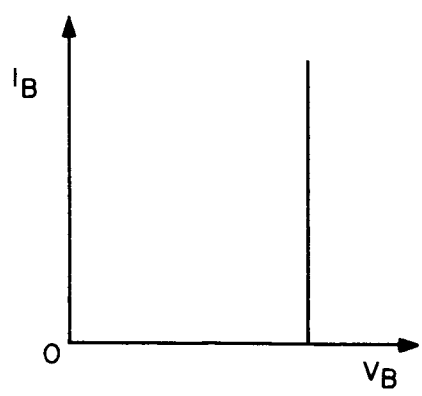

Figure X-101. Short-Term Characteristic of Battery

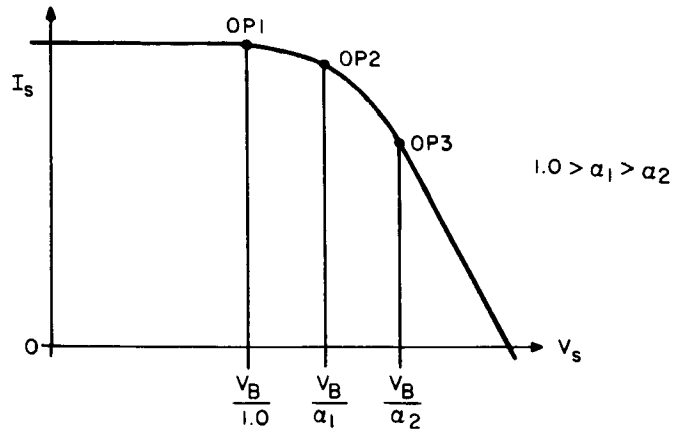

Figure X-102. Array Current Flow with Respect to I-V Characteristic

Therefore, by proper choice of the duty cycle α in a PWM device, the battery voltage (as reflected to the array terminals) can be varied over a range and maintained at the particular voltage operating point (OP) of the array that corresponds to its maximum voltage-current product.

3. Charge Control. Normal charge mode occurs during the daylight portion of the orbit and can be considered for three cases of source capability. In the first case the array is able to supply more power than the batteries and spacecraft loads require; in the second case, the array can supply both the battery and load requirements, but only if active control of the operating point is used as described in the preceding section; and in the third case, the array can no longer satisfy the requirements of both load and batteries.

It is important to note again that the ampere-hour discharge history of the batteries during the preceding night-time period is known to the charge electronics, as discussed in Paragraph X.C.4.b(1)(a).

a. Excess Array Capability. In the case of excess array capability, the source has more power available than the loads and batteries require and the array is operated on its I-V characteristic at a point, other than the maximum power point, determined by the actual total instantaneous system load requirements. See Figure X-96.

The sensor, detector, and scanner functions are not required in this case and are not permitted to control operation of the battery charge modules (that is, the array maximum power point is not tracked in this mode).

A two-phase square-wave inverter is used to provide drive and synchronization for all the battery charge modules.

Details of the operation of a battery charge module in this mode are as follows: Assume the battery voltage and temperature are within acceptable limits and there is no signal to the reference level shifter from the battery protective function. The ampere-hour accumulator has stored in its memory the ampere-hour discharge of the battery accumulated during the

previous spacecraft night. Upon activation of the array, as the spacecraft enters the daylight portion of the orbit, the batteries begin to charge. The battery current magnitude sensor and the current direction sensor then cause the ampere-hour accumulator to begin computing and accumulating the total ampere-hour charge. The ampere-hour accumulator and high charge limit reference shift and logic cause the reference-level shifter output to indicate that a maximum charge rate (of the order of C/3) is allowable. This rate is preset and is designed into the equipment; however, manual adjustment is possible if the need arises.

Since there is excess array power available, the batteries will charge at the maximum allowable rate. The charge current magnitude sensor senses the charge current, and an analog indication of this value is fed to difference amplifier No. 1 (see Figure X-95) where it is compared with a signal from the reference-level shifter. If the current sensed is greater than the maximum allowable current, the output to summing point S_2 increases. Also, at point S_2, the synchronized sawtooth signal that determines operating frequency of the semiconductor power switch is added to the current error signal. This combined signal is threshold-detected by Schmitt trigger No. 2. The Schmitt trigger output controls the a-c switch, which alternately applies and removes the drive to the power switch. An increasing output from the difference amplifier No. 1 results in a decreasing duty cycle "ON" time of Schmitt trigger No. 2 and ultimately a decreasing "ON" time of the power switch; this decrease tends to reduce the charge current.

The charge current magnitude sensor output is also fed to the charge current equalization comparator, where it is compared to the current levels in other battery charge modules. An error signal is generated and is fed to summing point S_3 resulting in adjustment of the duty cycle to compensate for unequal charge currents in the power modules of the charger/tracker assembly. At the summing point, S_3, the scanner signal and the sawtooth signal are added. The signal at this point determines the duty cycle of the power switch. Since the available array power is greater than the total power demand, the deliverable current (if the array were at the maximum power point) is greater than the limiting current as determined by other functions. Note that the "AND" function input to the a-c switch allows the modulator (Schmitt trigger), which is "ON" for a shorter period of time, to control the duty cycle. Therefore, the current limiting function (which requires the shorter duty cycle) controls, and the maximum power tracking function has no effect.

The ampere-hour accumulator continuously computes and stores the battery history. As it does this, the present ampere-hour charge (real-time) is continually compared with the discharge history of the previous night by the high charge limit reference logic. When the ampere-hour charge-to-discharge ratio reaches a preset value such as 0.5, the maximum allowable charge rate reference is reduced. The resulting reference level shifter output is such that a new, lower maximum charge rate is established. This rate is also preset and designed into the system. When this decrease in maximum allowable charge current occurs, the action of all functions is as described above, except that the array is operated at a different quiescent point.

A third automatic adjustment is made to the maximum charge rate after the batteries become fully charged. This rate is for "trickle charge", the lowest charge rate limit employed.

The operation under conditions of excess array capability can be summarized as follows. The charge current is limited to preset values which have been determined for safe battery charging. The source (solar array) is fixed at an operating point which satisfies the demands of both the loads and the batteries. This condition would normally occur during the beginning of a mission before the array has degraded or later in the mission if load power requirements are lowered below the design level. Note that the transition between this operating case and cases to be discussed below is automatic.

b. Sufficient Array Capability. In the case of sufficient array capability, the solar array source has enough power to satisfy the requirements of the loads and the batteries only if active control is exercised over its operating point. If a fixed operating point were used (as in a non-tracking system), the batteries would not be fully recharged during each orbit, and the spacecraft would not be in a state of positive energy balance.

The power tracker control unit is designed to detect the maximum power point of the source and to exercise control over the battery charger power modules so that the source is operated at or near that point.

The array voltage and current sensors provide signals that are proportional to those parameters. These signals are then multiplied together to yield an instantaneous power analog. The analog signal is then fed to the peak detector, which monitors the instantaneous power.

Noting that a battery charge power module is essentially a constant-frequency pulse width modulator, the output (battery) voltage is proportional to the input (array) voltage by a factor equal to the duty cycle. The output voltage is effectively fixed by the battery so that variation of the duty cycle causes the array voltage to vary. If these variations in duty cycle are controlled, then the operating point of the array is being controlled. In this system, control of the duty cycle is derived from detection of the source maximum-power point.

The scanner generates a signal that is capable of varying the duty cycle over its entire range. The scanner is free-running and automatically reverses if it reaches either the 0 or the 100-percent duty-cycle extreme without detecting maximum power.

To understand the acquisition and tracking of the maximum power point, assume that the scanner is indicating zero percent duty cycle and its output is changing towards an indication of 100 percent duty cycle. As the scanner output changes, the duty cycles of the battery charge power modules increases and the source voltage decreases as determined by battery voltage and the instantaneous duty cycle. The charge modules are PWM-regulated down-converters; the basic assumption is that the source has a point of maximum power and that this point corresponds to a voltage greater than the battery voltage. As the source voltage decreases, the source power output increases. The instantaneous power is sensed, and the analog is fed to the peak detector, which compares this power level to the previous level that was sensed. If the most recent information indicates an increase in source power output relative to the previous indication, then the new information replaces the old information in a memory device and the process repeats. If the most recent information indicates a decrease in source output power, then a signal is sent which causes the scanner to reverse direction (towards zero-percent duty cycle) and again the most recent information replaces

the older information in the memory device. Note that it is necessary to pass the maximum-power point in order to detect the peak power and that as the duty cycle decreases, the source output power is again increasing and the entire process repeats. In this manner the source operating point continually makes small excursions to either side of the maximum-power point, and the system tracks that point, making internal adjustments automatically. Operation does not depend on the initial conditions of the scanner.

The battery charge power modules act in response to sensed battery conditions and to duty cycle information received from the power tracker control unit.

Assume that the battery voltage and temperature are within acceptable limits and that the instantaneous charge current is less than the maximum allowable value as determined by the ampere-hour accumulator and the high charge limit reference logic. The duty cycle as determined from the signal level at summing point S_2, Figure X-95, is greater than the duty cycle as determined at the summing point S_3, and the inputs to junction S_3 control the system operation as a result of the "AND" function.

The charge current sensor provides an analog indication of charge current; this indication is transmitted to the charge current equalization comparator, where it is compared with the signals from other battery charge modules. If the signal for the current level in the power module under consideration is greater than signals from the other modules, then the diode will conduct and the signal will be fed to the other modules. In this case the input to both sides of difference amplifier No. 2 are equal, there is no output and, therefore, no change in duty cycle. If the signal level in the module being considered is less than that received from the other modules, then the diode will not conduct, and an error signal is fed to the difference amplifier No. 2. This causes a decrease in signal level at summing point S_3, which results in an increase in duty cycle and a corresponding increase in charge current. This process continues until all modules are carrying equal currents.

The duty cycle of the power switch is determined by the signal output of summing junction S_3, Figure X-95. The inputs to S_3 are (clockwise from output): scanner inhibit signal from battery protection function, charge current equalization error correcting signal, synchronized sawtooth for determining operating frequency, and the scanner signal for determining the approximate duty cycle.

The charge monitor and high charge limit reference shift logic function in this mode in the same manner as described under Excess Array Capability (Paragraph X.C.4.b(1)(b)3.a.) except that the limit value of current is not reached. (If the charge current should ever become greater than the allowable value determined by the charge monitor, then the limiting action will occur as described previously.)

The operation under the conditions of sufficient array capability can be summarized as follows: The load demand is satisfied and the maximum available remaining power is used to charge the batteries. This is true because the battery charge electronics actively track the maximum power point of the source and adjust the operating point to coincide with that point.

In this system, a condition of this nature would ordinarily occur towards the end of a mission (as the array degrades) and during portions of the mission where the load power requirements are unusually high, but do not exceed array capability.

c. Insufficient Array Capability. In the case of insufficient array capability, the source power is not adequate to supply the loads and recharge the batteries in each orbit. The control circuits cause the source to operate as its maximum power point.

Operation of the power tracker control unit is as described for the case where the maximum power point of the source is tracked. The operation of the battery charge power modules is controlled by the battery conditions such as voltage and temperature, and by the power tracker control unit.

The ampere-hour charge monitor also functions as previously described, except that at the end of spacecraft day, an indication of insufficiently charged batteries will be generated. The ampere-hour accumulator has stored in its discharge memory the history of the battery during the previous orbital night and has also accumulated the ampere-hour charge returned to the batteries over the entire day time. The significant difference between this case (insufficient source capability) and the previous case is that, if the source capability is insufficient, the total ampere-hour discharge is greater than the ampere-hour recharge (per orbit) and the system is not in a state of positive energy balance.

(c) Normal Battery Protection Modes

When certain system parameters do not agree with limiting or allowable values as determined by the system and "black box" design specifications, the battery charge electronics operate in the protected modes. These modes serve to reduce stress applied to the batteries, thereby extending their useful life.

The system parameters of interest are:

1. Maximum battery voltage,

2. Maximum battery current,

3. Maximum battery temperature, and

4. Battery state-of-charge.

Note that, in the previous discussions of operating modes, it was assumed that the protective functions were not in effect, except for current limiting. If at any time during the spacecraft operation, the system parameters previously described are not within the established limits, the storage system (or a portion thereof) will automatically operate in the applicable protected mode.

1. Battery Voltage Limit. The maximum end-of-charge voltage of the battery and its variation with temperature are known from extensive testing. Sensing of the battery voltage to ensure that the maximum value is not exceeded is accomplished by the temperature-compensated voltage divider No. 1. Compensation for battery temperature is such that all points on the voltage-temperature curve for the battery appear as the same signal level at the No. 1 divider output, Figure X-95. This output is compared to a fixed reference by difference amplifier No. 3. If the battery voltage is below the maximum value, there is no output from the difference amplifier. If battery voltage is greater than the allowable maximum, then a signal is fed to the reference level shifter; the shifter output then indicates that the maximum charge current should be something less than the preset maximum rate. This level is continuously variable and controllable between maximum and trickle charge rates by difference amplifier No. 3, which acts as a feedback amplifier in a voltage regulator in this mode of operation. System action is similar to that described for the case where the current limit reference is shifted by the ampere-hour indicator. The reduction in current level is proportionally controlled (as opposed to a switching operation), and is sensitive to battery voltage changes of a few millivolts. Each battery charge power module (and battery) is independent of the other power modules. This function automatically resets when the battery voltage decreases below the limit value.

The voltage-temperature control technique is not new; it was successfully used by RCA in the Lunar Orbiter program.

2. Battery Current Limit. The charge current must be limited according to the state of charge of the batteries. The charge current is limited by appropriate high-current reference signals applied to the reference level shifter by the high charge limit reference logic. This process has been described previously. Each battery and battery charge power module independently determines its own correct limiting current.

3. Battery Temperature Cut-off. The battery charging process must be reduced if the battery temperature exceeds a limiting value. A temperature-sensitive component of the temperature-compensated voltage divider No. 2, Figure X-95, is located on or near the battery to sense temperature. If battery temperature exceeds a preset limit, the output of the divider exceeds the threshold level of the Schmitt trigger. Firing of the Schmitt trigger causes a signal to be sent to the reference-level shifter, which immediately establishes the "trickle charge" rate as the maximum allowable current. The trigger output is also fed to summing junction S_3 to inhibit operation in response to the scanner signal. The high-temperature protection function automatically resets when the battery temperature decreases below another preset balue. This differential is desirable to afford stability of operation. Each battery is independently protected.

4. Battery State-of-Charge Alarms. The ampere-hour monitor makes possible many types of protection. The one criterion that signifies proper operation of a spacecraft power system is positive energy balance. The ampere-hour accumulator has the complete discharge and charge history of the battery in its memories during each orbit. At the end of spacecraft day, an "end-of-day" indication is furnished to the accumulator. Upon receiving this indication, the accumulator compares the effective ampere-hour charge with the ampere-hour discharge. If the difference is positive (positive energy balance), no alarm

is sounded. If the indication is negative, an alarm signal is furnished to the display and performance monitoring equipment.

The charge and discharge ampere-hour accumulations can be automatically transferred to other on-board storage for future reference and to provide a charge history, if needed. After this data transfer, the ampere-hour accumulator's memories are cleared for renewed use.

An indication of excessive depth of discharge is also provided. Section X. C. 4. b(1)(e) describes the ampere-hour meter in greater detail.

(d) Protection Against Power Module Failure Modes

It is desired to disconnect the battery charger power module in the event of over-current, over/under-voltage, over-temperature, or over-pressure. Figure X-103 shows a scheme by which this may be accomplished. When any of the parameters exceed their desired values, the output of its sensor drives a flip-flop, which in turn sounds an alarm and passes a signal through an "OR" gate to switch a latching relay. This relay disconnects the battery charger module from the power subsystem. The module must then be repaired or replaced manually.

In addition, excessive temperature in the charge electronic system will automatically cause the charger to be switched to a trickle-charge mode (low-dissipation mode) and sound an alarm.

(e) Ampere-Hour Meter Design

The ampere-hour meter will be of the digital type, with integrated circuits and magnetic current sensing. Figure X-104 is a functional diagram of the ampere-hour meter. Operation is best described by following an orbital period.

The orbit begins at the onset of spacecraft night with the batteries fully charged and the counters set to zero. As the battery begins to discharge, the current sensor produces an output voltage proportional to current. The voltage-controlled oscillator (VCO) integrates this voltage and produces an output pulse for every 0. 1 to 0. 15 ampere-hour measured (depending upon rated battery capacity). The current-direction sensor steers the VCO pulses to the appropriate counter (charge or discharge accumulation).

As the discharge counter accumulates VCO discharge pulses, a resistor network simultaneously converts the counter's digital information to an analog signal. This action continues until spacecraft day when the battery begins to charge. At this time, the current-direction sensor steers the VCO charge pulses to the charge counter. The discharge accumulated during the dark period remains stored in the discharge counter. Any battery discharge occurring during spacecraft day is merely added to this accumulation by the direction sensor action. Should the discharge accumulation exceed some preset limit, an alarm will be sounded by the over-discharge sensor (a count recognition gate).

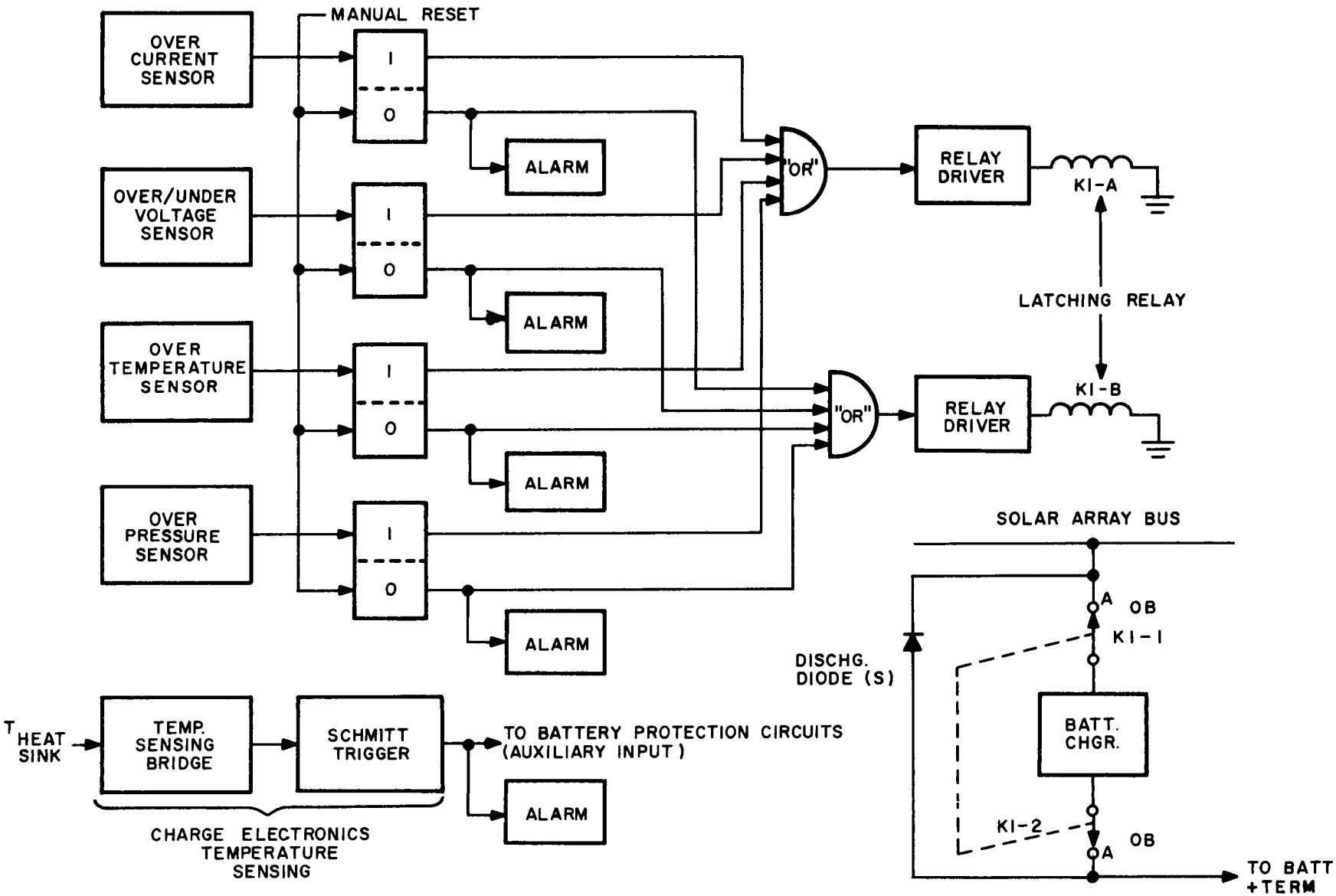

Figure X-103. Battery/Battery Charger Automatic Protection, Functional Diagram

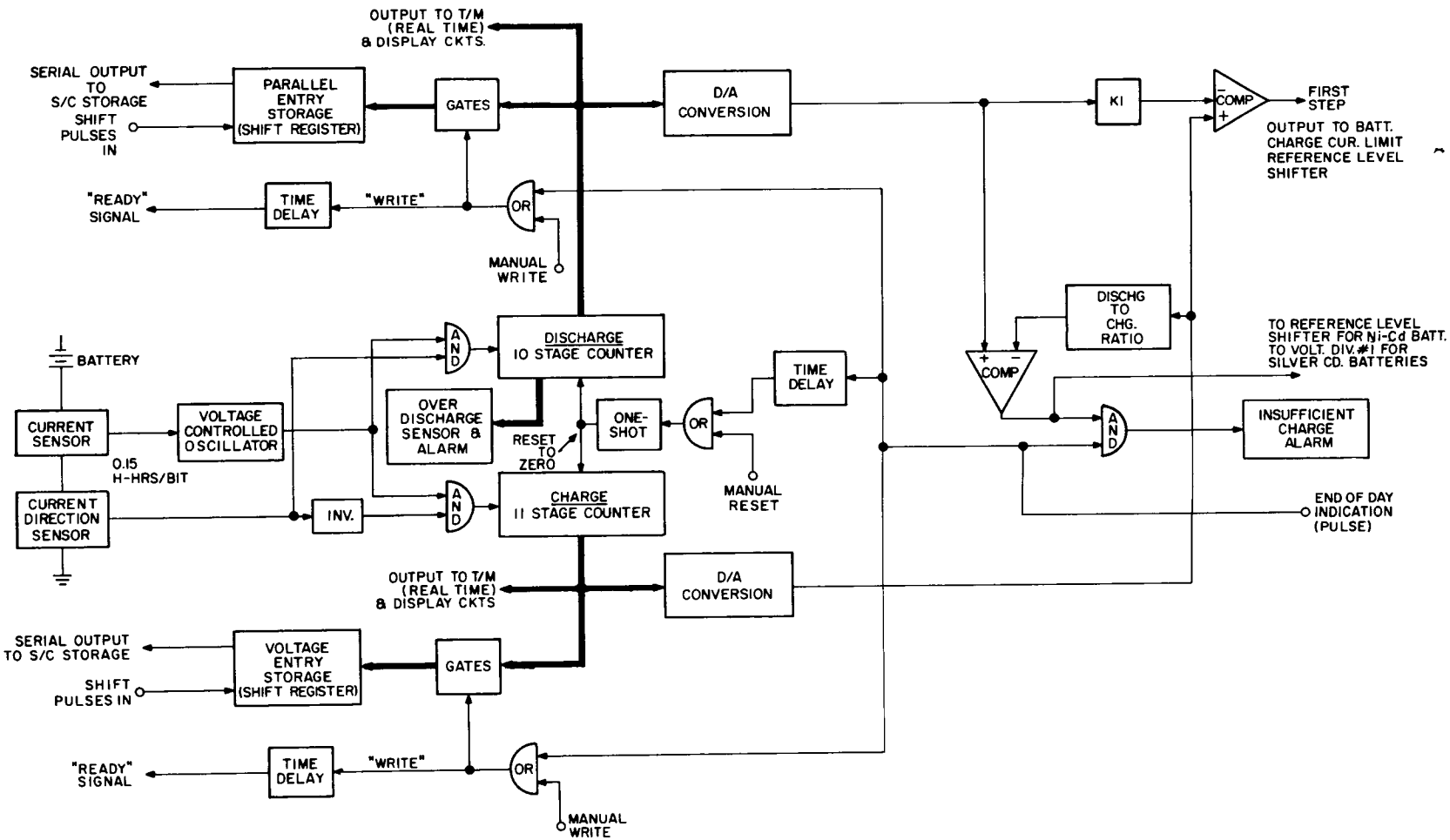

Figure X-104. Battery-Charger Ampere-Hour Meter

As the charge counter accumulates VCO charge pulses, another resistor network performs a simultaneous digital-to-analog conversion. The analog output of the discharge counter is compared with that of the charge counter. The discharge analog, however, is modified by block K_1, which is a simple voltage divider. When the charge indication equals or exceeds K_1 times the discharge indication, an output (labeled "First Step") is delivered to the battery charger and causes the high charge current limit to be reduced to some lower level. When the batteries become fully charged, a signal from the comparator circuit which compares the discharge accumulation with the discharge-to-charge ratio will reduce the charge current to a trickle-charge level.

At the end of the orbit, a pulse is received from the array orientation subsystem indicating the onset of spacecraft night. If the charge returned to the battery during spacecraft day is insufficient, this pulse in conjunction with the signal from the comparator circuit will activate the insufficient-charge alarm. In either case (sufficient or insufficient battery charge), the end-of-day indication pulse will cause the charge and discharge digital accumulations to be entered into shift registers (where they will await entry into a spacecraft central storage) and will cause a time delay to be initiated. After sufficient time has elapsed for entry of the data into the shift registers, a "ready" signal is transmitted to the spacecraft storage enabling it to read the data by delivering shift pulses at its own rate and receive the information in a serial form. Two channels are required: one for charge and the other for discharge data. When the time delay has expired, after a period of time sufficient to allow complete data transfer to the shift registers, the counters will be reset and the operation will begin for the next orbit.

The insufficient-charge alarm will be an indication to the crew to reduce nighttime programming during that orbit or to make appropriate corrections during the ensuing daytime.

Also included are the following:

- Manual counter reset
- Manual write commands to initiate data storage at any time
- Parallel outputs permitting simultaneous digital display and telemetry.

(f) Failure Detection and Switchover for Battery Charger Control Module

Circuitry is provided to cause automatic switchover to a redundant control module in the event of failures in either the MPT control, the two-phase inverter, or the auxiliary regulator. The logic for implementing this protection is shown in Figure X-105. In all cases, detection of a failure results in either a pulse or step voltage waveform being delivered to a flip-flop through an "OR" gate as shown. Change of state in the flip-flop will (through the relay drivers and relay coils) cause all relays to change states, thereby switching from the unit having a failure to an operating unit. A manual switchover is also provided as back-up. The two-phase inverter fault detection circuit is shown in the figure. One of the two redundant inverters is connected through a latching relay to pulse-absence detectors (PAD), one PAD per phase. Should the inverter fail, the PAD would generate an output pulse which would cause switchover as described above.

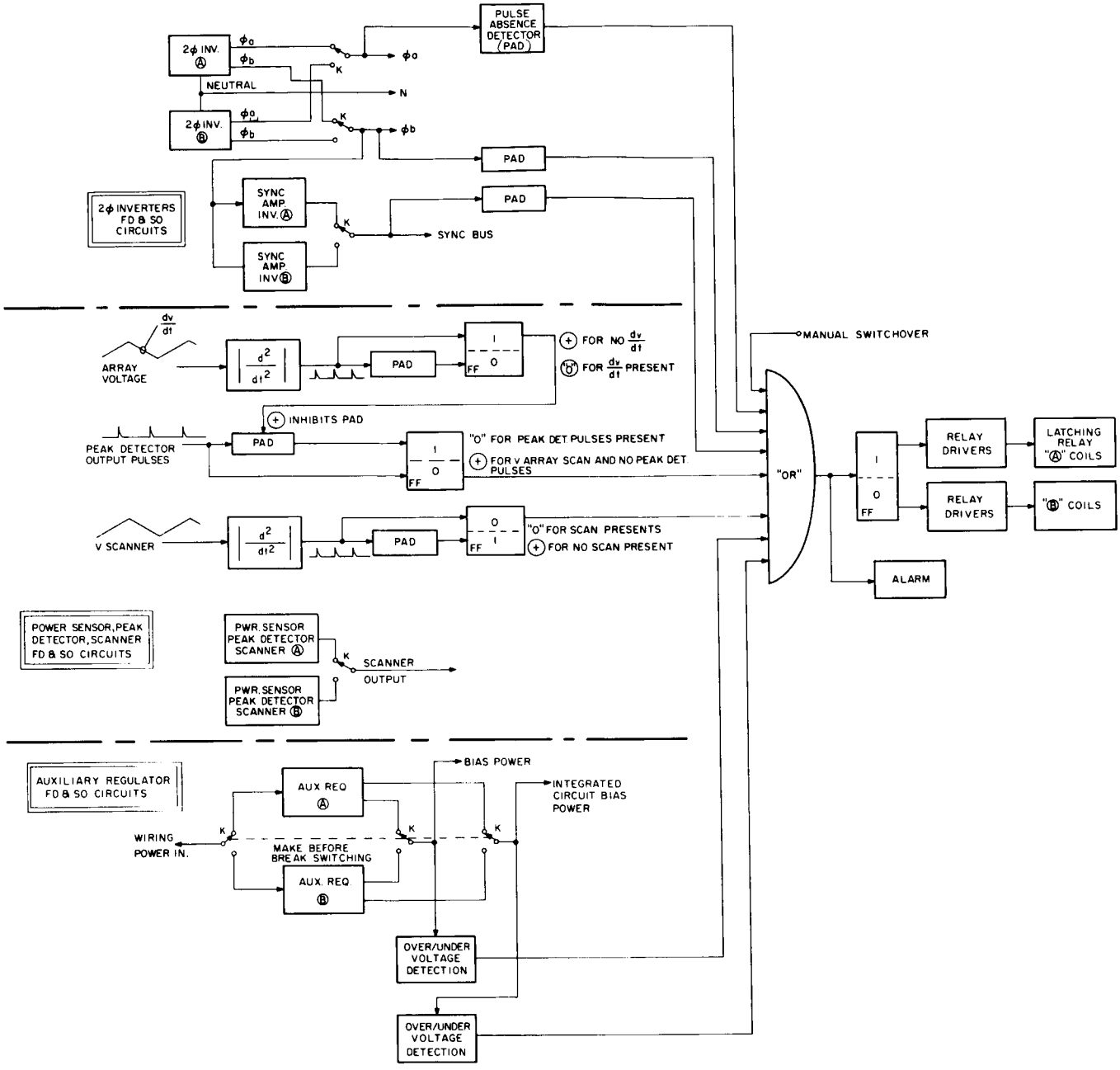

Figure X-105. Failure Detection and Switchover (FD & SO) Logic for Battery Charger Control and Auxiliary Regulator Unit

The configuration of the power sensor-scanner failure-protection circuits is shown in Figure X-105. The triangular waveform of the scanner is differentiated twice to yield a series of pulses. A pulse-absence detector monitors the resulting pulse train and will issue an output signal some predetermined time after it has received its last input pulse. The PAD output causes switchover as described above.

Failure in the power sensor or the peak detector circuits is more complex, as indicated in Figure X-105. The logic of this circuitry is as follows:

Peak detector pulses are present if

- Both the power sensor and the peak detector are operating properly.
- The scanner is operating properly and is causing the battery-charge electronics to search (or scan) for the maximum power point (in which case the array voltage is constantly changing).

Peak detector pulses may be absent under normal conditions if

- All battery modules are operating in a normal battery protection mode.
- The array output is not present, as during spacecraft night.

These considerations lead to the logic shown in Figure X-105. Presence of a changing array voltage and absence of peak detector pulses indicates a failed power sensor or peak detector. In this case, switchover action occurs as described above.

Auxiliary regulator protection is much the same as the previously described methods. Output voltages are monitored for excessively high or low conditions. Either condition can trigger switchover as previously described.

In this case, make-before-break switching is specified, in order to minimize switching transients in the system if switching occurs for some reason other than a failed auxiliary regulator.

(2) D-C Load Regulator Assembly

(a) General Description

Efficient d-c voltage regulation is obtained through pulse-width-modulation (PWM) techniques. Figure X-106 is a functional diagram of the regulator. It consists basically of an input filter, an output capacitor bank, redundant voltage sensing and error amplification and a number of paralleled power-switching modules. Current limiting is included in the power-switching networks. Over/under-voltage protection is also provided in the regulator. As in the case of the charger/tracker assembly, all circuits, except for the input filter and the capacitor bank, are contained within three types of replaceable modules.

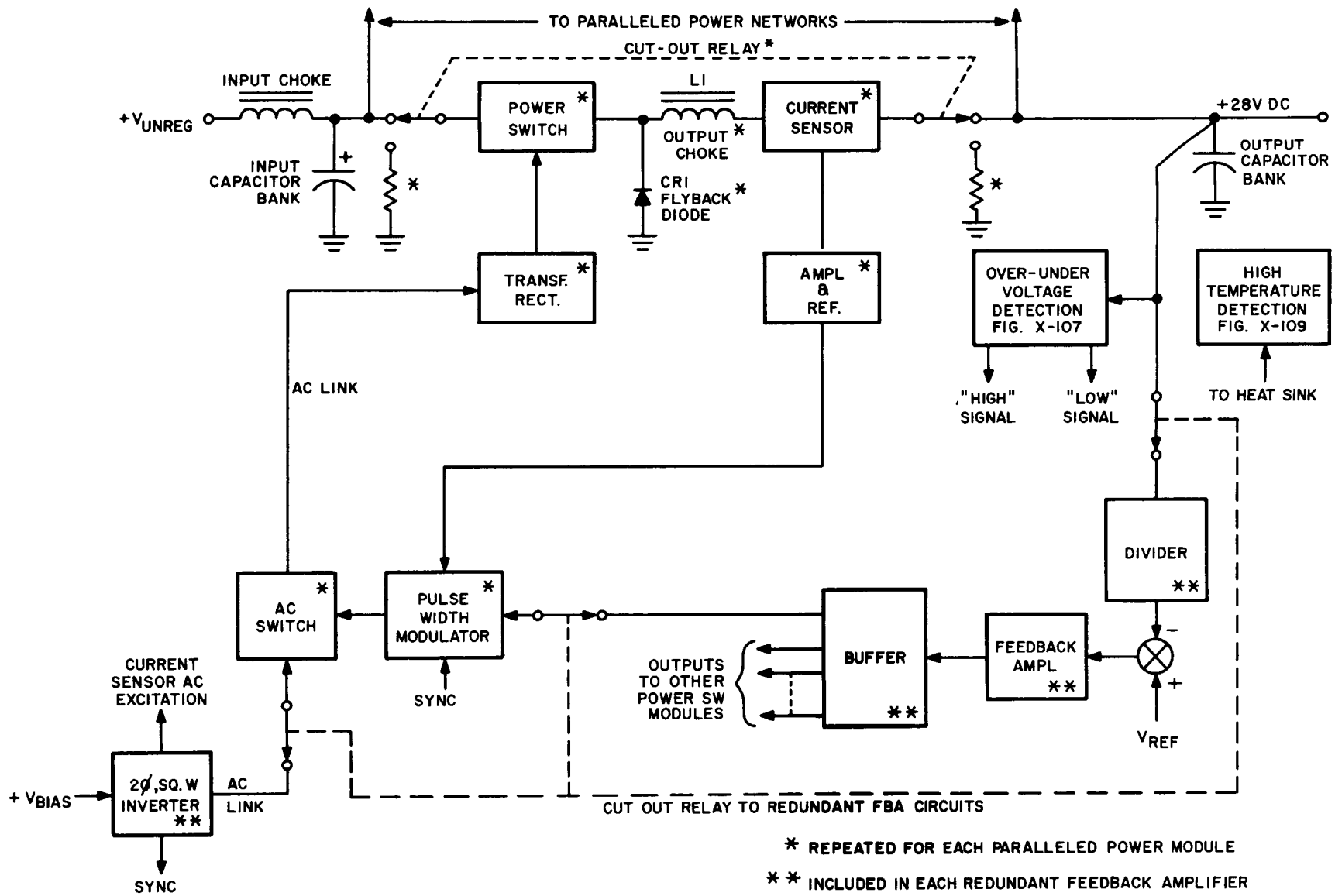

Figure X-106. D-C Regulator, Logic Diagram

(b) Normal Regulator Operation

Output voltage control is achieved by the modulating action of the power module(s). The power switch is turned on and off at a constant repetition rate with a variable, controllable duty cycle, ratio of "on time" to total period. The net effect of this action is to alternately connect and disconnect the input voltage as it appears across the input capacitor bank to the output filter composed of L_1, CR_1, and the output capacitor bank. The time-average of this resulting "pulse train" is equal to the output voltage of the regulator.

The input filter is intended to smooth the high ripple content of the power drawn by the switching network, thereby preventing large voltage and current excursions from appearing on the input bus. The output capacitor serves to smooth the regulator output and to present a low dynamic impedance to the regulator loads at frequencies beyond the regulator response. Voltage sensing and error amplifier networks, as the names imply, sense output voltage and compare it with a reference, and then amplify the error and deliver the amplified error to the power control or power switching networks for purposes of output voltage correction. The power switch is controlled by the signals from the pulse-width modulator (PWM) in conjunction with the outputs of the two-phase square wave inverter.

Each individual power switching module will be capable of delivering up to 50 amperes d-c (maximum) at +28 volts from an input bus. The bus voltage will be in the range of 30 to 150 volts, as determined by semiconductor component availability. Note that there is no provision for actively forcing load sharing among power networks. The need for this sort of function with the attendant circuit complexity is obviated by virtue of the current-limiting function indicated by the current sensor and current-limit detector. As the 28-volt bus load increases, one power module will probably tend to deliver the total load or a major portion of the load due to normal component tolerances. Should the load be large enough to cause the current through any one power module to reach the limit value (some value in excess of 50 amperes), that network will become current-limited and will supply no further current to the load. Further load increase will then be supplied by another power module. This process will continue until the total load is somewhat in excess of the rated total regulator load, whereupon further current demand will result in reduction of the bus voltage due to the current-limiting function. When the load is no longer excessive, the bus voltage will automatically recover, and normal voltage regulation will be resumed.

(c) Failure Mode Protection Circuits

1. Over/Under-Voltage Protection Mode. Table X-25 shows the logic to be employed in over/under-voltage protection for the d-c regulator system. This logic may be implemented as shown in Figure X-107. The +28 volt bus voltage is applied to a difference amplifier by way of a voltage divider and response-shaping network. A comparison with a reference voltage is made and the difference is amplified. Depending upon the direction of the deviation from the desired +28 volts, the amplified difference signal is delivered to either of the two Schmitt Triggers, which will produce a step output change should the bus voltage deviate by a preset amount.

TABLE X-25. POWER SUPPLY, +28 VDC BUS OVER/UNDER VOLTAGE PROTECTION LOGIC

Major Symptom	Additional Symptoms	Cause	Circuit Action	Visual/ Audible Indication
Undervoltage	Low or no current	Open FBA and/ or power switch drive.	Switch FBA and power switch drive circuits to redundant units.	Yes
	Current limit operation	Load fault	Inhibit O/U protective functions and allow fault to clear.	Yes
Overvoltage	Excessive power network current	Shorted power network.	Remove defective power network automatically.	Yes
	(Current equal to or greater than the limit value in one or more power networks)	Shorted FBA	Power networks will current limit with high bus voltage. After built in time delay, FBA will be switched.	Yes
	Low power network current	Shorted FBA	Built in time delay after overvoltage indication, switch FBA if bus is not corrected.	Yes
	(Current less than or equal to the limit value in any power network)	Shorted power network	Wait for FBA switchover, if bus is not then corrected, load regulator with a current in excess of limit value for one power network. Excessive current in shorted power network will trigger cut out.	Yes

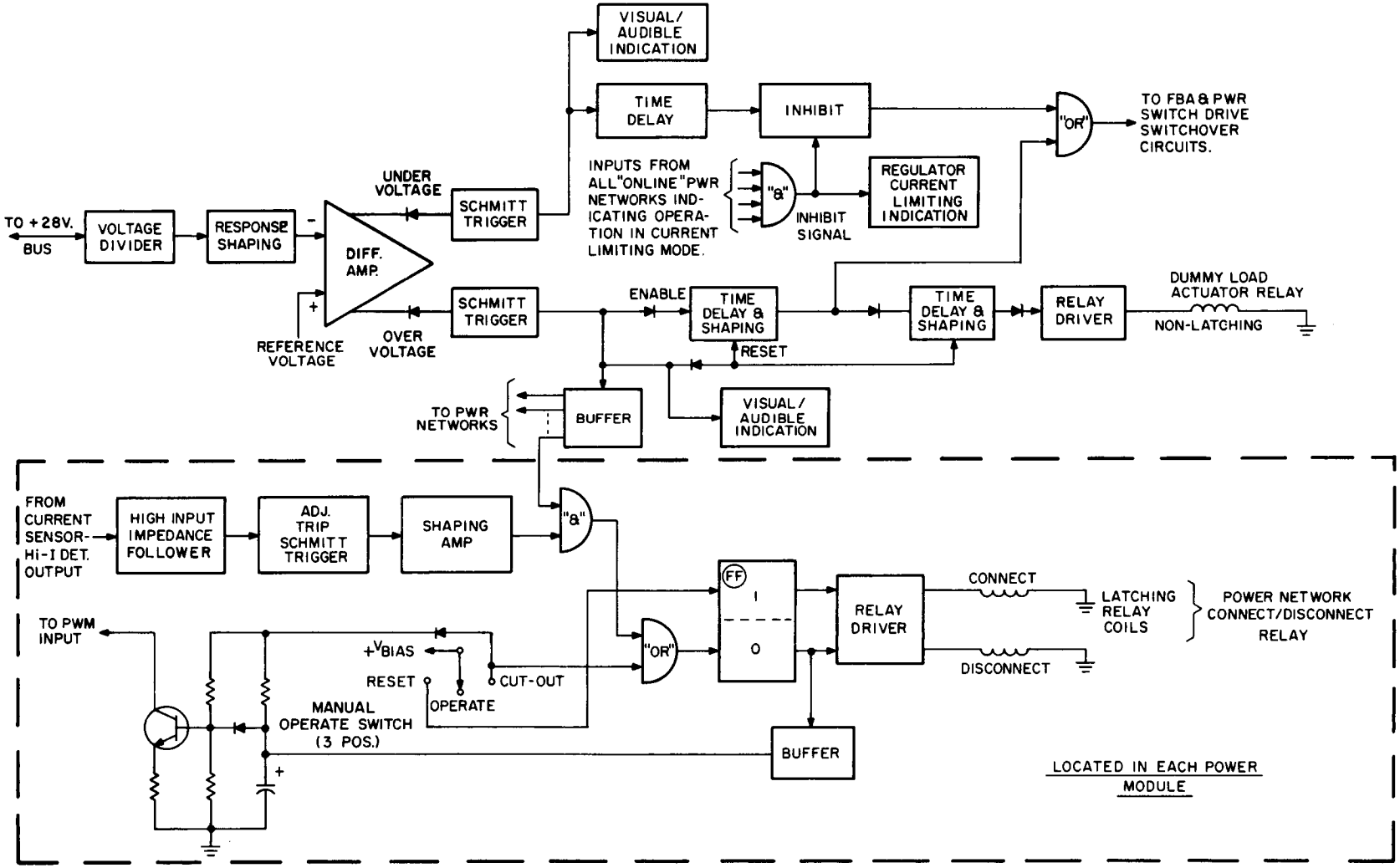

Figure X-107. Functional Diagram of + 28 VDC Over/Under Voltage Protection

If the voltage is too low, the Schmitt trigger output is delayed in order to allow current limit mode indications to reach the protection circuits. Without the current limit indications present, the delayed output would cause the regulator feedback amplifier (FBA) and the power switch drive circuit (control module) to be replaced by redundant units.

If the voltage is too high, the logic and therefore the circuit action is considerably more complex. Figure X-108 is an abbreviated functional diagram for this case. Here, as for the undervoltage case, the chain of events is initiated by the Schmitt trigger output, which is delivered simultaneously to a time delay and an "AND" function. As indicated, in order that an output be derived from the "AND" function, the presence of both the overvoltage condition and an excessive power switch current is required. Under these conditions the affected power module is immediately disconnected by means of a relay from the regulator system.

If a short-circuited power switch is not the cause of the overvoltage condition or if the total current through a short-circuited power switch is not of sufficient magnitude to affect this action, the path containing the time delay functions becomes active. After delay number 1 has elapsed, in a period of time adequate to allow a defective power switch to be disconnected in the presence of a high current, the FBA and power switch drive circuits are exchanged as is done in the case of an undervoltage condition. Simultaneously, another delay (number 2) is initiated. Should the exchange of the FBA and the power switch drive circuits result in normal 28-volt operation, the Schmitt trigger output will disappear, thus resetting both delays and allowing no further protection circuit action. But if the 28-volt bus is not returned to normal operation (thereby indicating insufficient current through a short-circuited power switch), the second delay will run to completion and will apply a dummy load by means of a non-latching relay. This load will cause a current flow of sufficient magnitude through a shorted power switch to cause that switch to be disconnected.

In addition to the automatic mode of operation, the possibility of manual operation is provided in order to facilitate service checks and to provide a positive means for inserting a

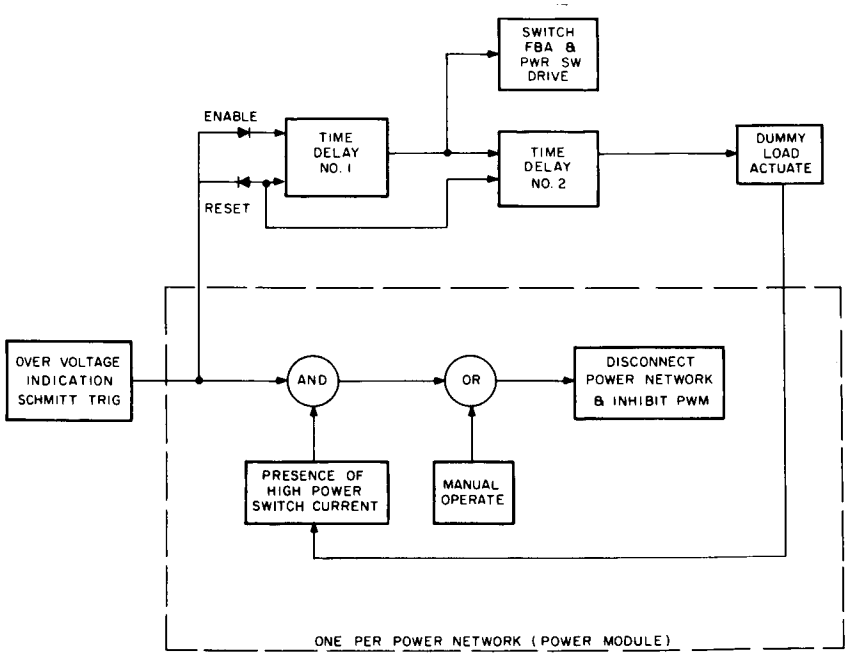

Figure X-108. Over Voltage Protection, Functional Diagram

new power module should the need arise. This network will allow the new power module to be inserted in the system without turning off the entire 28-volt regulator.

There is one remaining major failure type that the foregoing protection method will not detect and act upon. A single open power module may be detected only through periodic maintenance checks of the system. The occurrence of such a failure is not considered immediately detrimental to system performance unless that module is called upon to deliver load current. Because it cannot do so, the remaining power modules will either supply the load or will reach the limit of current. Should the system current-limit with an open power module, a false under-voltage condition will be sensed, the FBA and the power switch drive circuits will be switched, and an alarm will be given. The operator will then take command, inspect the system, and replace the defective circuit.

2. High-Temperature Protection Circuit. If the heat sink temperature exceeds a certain value, all non-essential loads on the d-c regulator should be disconnected. This can be accomplished by the circuit shown in Figure X-109. The temperature-sensing circuit will cause the flip-flop to change states when the temperature exceeds the desired maximum value. This will operate the alarm and pass a signal to the relay driver, which will switch the latching relay and disconnect all non-essential loads.

(3) Inverters

A number of manufacturers of both static and rotary inverters were consulted regarding the relative merits and disadvantages of their products. It is a consensus among suppliers of inverters that for a space application the best weight and efficiency would be found in static inverters. Most common types of rotary inverters contain brushes but these units do not have efficient or long-lived commutation when operated in a vacuum. Brushless rotary inverters are capable of operating in a vacuum, but the efficiency is limited to approximately 60 percent (the same as for brush type rotation).

The only accurate weight information on rotary inverters is for non-space-qualified stock units containing brushes. These data are shown in Figure X-110, but it should be recognized that space qualification requirements will add significantly to these weights.

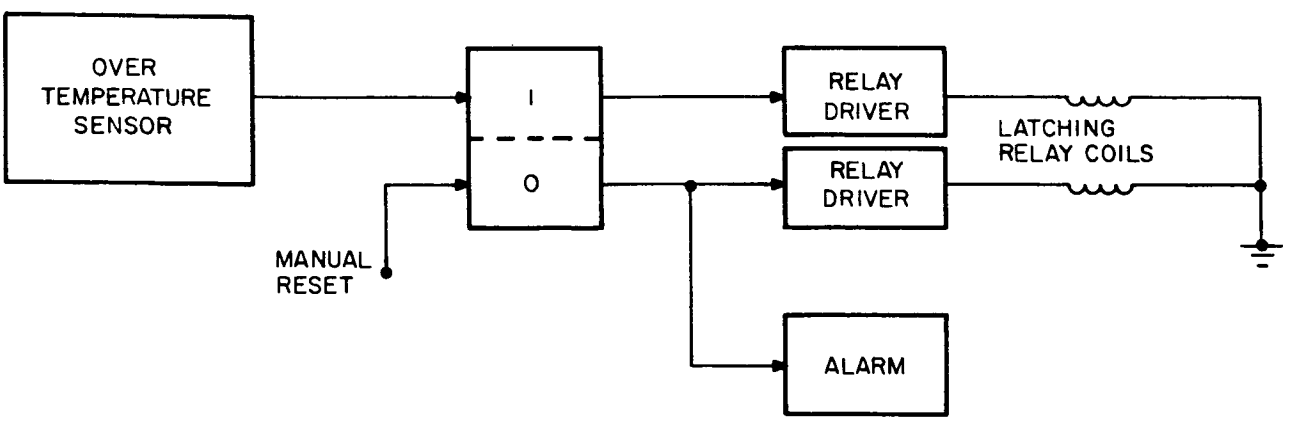

Figure X-109. High-Temperature Protection Circuit for D-C Regulator

The information obtained for static inverters was, in general, estimated since inverters of the required size are not available from stock. Efficiencies as high as 85 percent may be expected. Figure X-110 is a curve showing the relationship of weight to KVA at the maximum efficiency, for static inverters meeting the requirements of MIL-STD-704 in a space application.

Therefore, in view of the data at hand the most that can be said is that the relative weights of each are comparable. If the efficiencies are taken into account, static inverters will result in the lightest system for supplying equal loads.

Lower efficiency aggravates the already difficult cooling task associated with rotary inverters. The rotating member must have a fluid coolant. This, of course, requires a sealed system since operation in space vacuum is a necessity. The static inverter, on the other hand, may be adequately cooled by means of conduction and radiation, which is more acceptable in the spacecraft system.

For location within a spacecraft with a "shirtsleeve" environment, it is highly desirable that the sound level be low; in this respect the static inverter is again preferable to the rotary.

It should be noted that the Apollo spacecraft utilizes static inverters for similar reasons. For the numerous reasons just presented, static inverters are selected for this study.

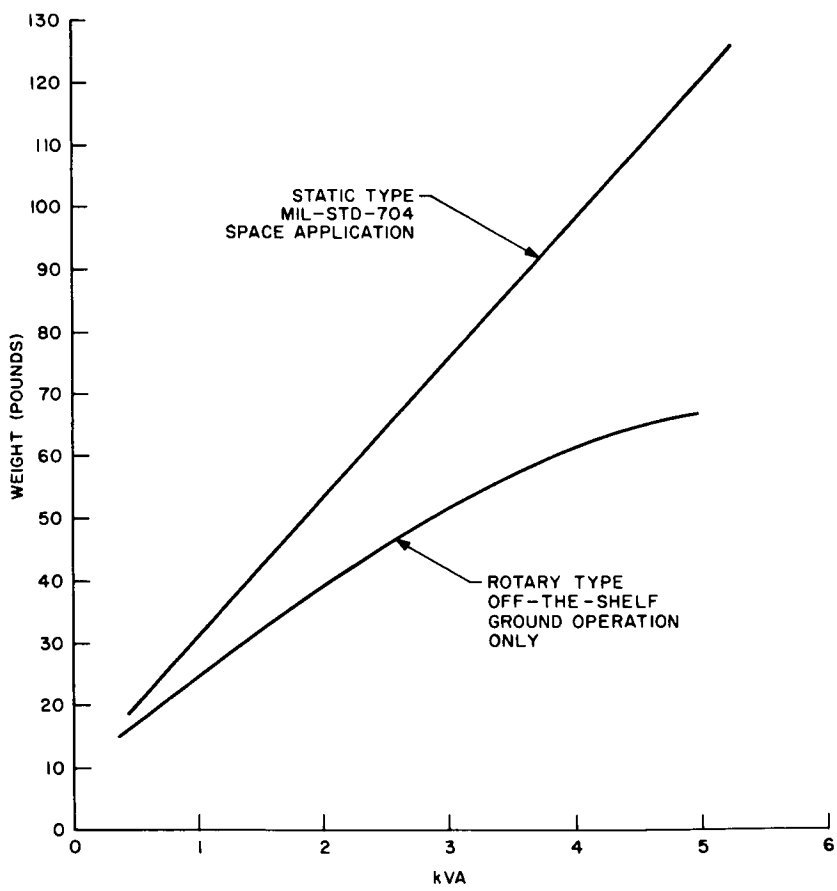

Figure X-110. Inverter Weight vs. Power Rating

c. ELECTROMAGNETIC COMPATIBILITY (EMC) CONSIDERATIONS

Because the nature of EMC is such that parametric analysis is quite difficult, it is felt that the best approach at this time is to present recommendations and a brief plan for assuring electromagnetic compatibility. Compatibility among the various elements of an electronic system is of prime importance. Interference limits must be considered to be fully as important as other operating characteristics. Indeed, the limits relating to EMC are to be recognized as another set of input-output requirements: susceptibility to interference is equivalent to an "input" requirement, and emission of interference is an "output" requirement.

Selection of EMC criteria for this mission should be based upon anticipated system requirements rather than upon some more rigid and perhaps less appropriate basis such as a standard specification. A flexible approach of this nature is more desirable in view of the problems involved in the conditioning of very large power magnitudes by switching techniques. However, MIL-I-6181 has been used as a guide in developing EMC goals.

In the interest of quality of power-system performance and of overall system cost, it would be most advantageous to provide some degree of flexibility in the mission EMC criteria. More specifically, the initial criteria should be subject to review as the design and development program proceeds; revisions would be based upon hardware performance in much the same manner as the hardware performance is subject to the EMC specification. This will allow the EMC criteria to reflect the real needs of the spacecraft as they are determined, as well as the performance of the power subsystem. A complete understanding of all existing design margins (or lack thereof) will also accrue from this process.

Any electronic device must be designed to operate without malfunction under a specified set of environmental conditions. The ambient electromagnetic field is clearly an important component of the operating environment. Insensitivity to electromagnetic interference (EMI) must be designed into each unit from the start, along with insensitivity to temperature and vibration. Similarly, the units must be designed so that they will not produce harmful electromagnetic fields and signals, just as it is necessary to ensure that they will not produce amounts of heat or vibration which would be harmful to the system or to components.

The implementation of EMI control measures is to be considered as a continuous effort throughout the entire development program. It is therefore necessary that all personnel involved in hardware design and selection be made aware of the goals of the EMI program. Certain stages in the hardware development will be taken as major evaluation points in determining the steps necessary to ensure effective EMI control.

- The behavior of the breadboard prototype will be analyzed, especially with respect to waveforms and to locating gross sources of EMI.

- As packaging and component layouts are developed, the drawings will be evaluated for possible EMI control improvements. From the viewpoint of EMI control, packaging (which includes component arrangement and case design) should accomplish two basic objectives. First, the outer envelope serves as the primary means

for reducing the amount of interference radiated by the unit. Second, the proper arrangement of components assists in reducing the level of conducted interference. It is clear from preliminary design analysis that the portions of the circuit which carry heavy currents, such as the power switching networks, will have a much greater tendency to produce EMI than will the low-level circuits such as differential amplifiers. It is advantageous to arrange components so that the low-level circuits are protected from the fields produced by the high-current sections as well as to contain these fields within the equipment. This is to be achieved by creating separate compartments, or "vaults", to house the most obvious EMI offenders. The vaults are to be completely sealed, and all leads penetrating the walls of the vault are to be provided with EMI filters. These procedures have been followed in the mechanical unit designs made for this program, Paragraph X.c.4.d. Selection of satisfactory materials for the equipment case is of great importance in controlling radiated EMI. The choice is necessarily a compromise involving strength, workability, weight, cost and EMI shielding effectiveness.

- A series of preliminary EMI tests will be conducted on the first complete prototype unit. Any necessary changes will be incorporated at this time.

- Formal EMI qualification tests will be conducted on the prototype unit.

- Continual review and up-dating of EMC requirements as previously mentioned will occur throughout the system design and development.

d. ELECTRONIC PACKAGING CONCEPT

(1) D-C Regulator

The regulator packaging concept is shown in Figure X-111. The control package contains non-replaceable input and output filters, two replaceable plug-in control modules having redundant regulator controls, and a replaceable failure detection and switchover module. Connections between the modules and the remainder of the control package are made through one or more connectors; the modules are retained in position by means of floating through-bolts, which will mate with threaded inserts in the mounting (heat sink) surface. Removal of a module will be achieved by merely loosening the through-bolts and pulling the module forward out of the assembly. A handle or other means to facilitate removal may be included.

Power modules are electrically connected to the control package through a connection box as shown. The plug-in directions indicated in the figure will allow any power module in a regulator assembly to be removed without disturbing operation of the regulator. Since the connection boxes contain only wiring, their removal is not anticipated.

The final design of the compartments and the filtering arrangement will take into account EMC considerations.

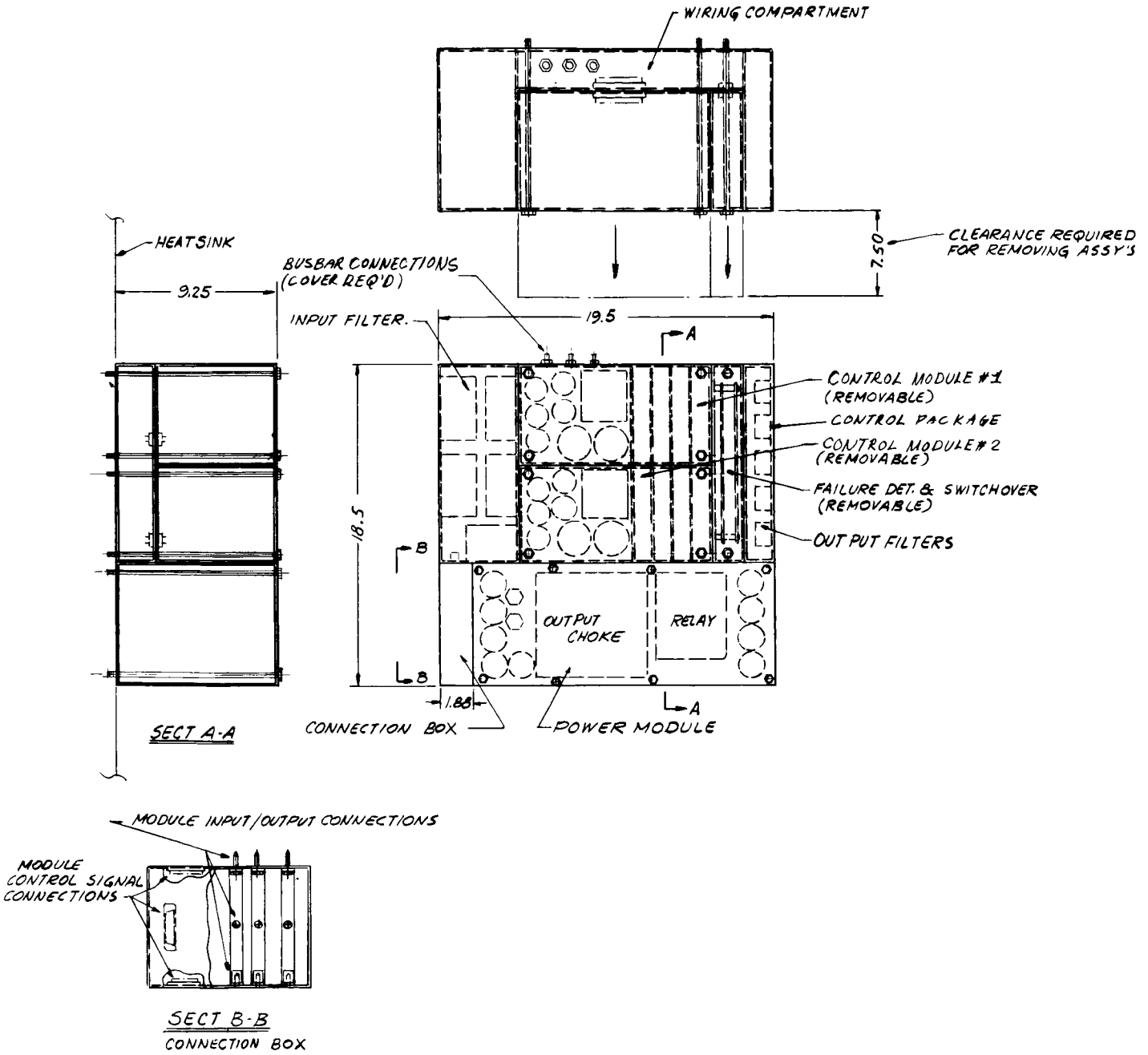

Figure X-111. D-C Regulator Concept

(2) Battery Charge Power Module

The battery electronics power module is divided internally into three separately compartmented sections: input-output, power switching (a source of EMI), and low level and noise-sensitive electronics. Figure X-112 is a sketch of this package.

Major heat producers are mounted as close as possible to heat-sinked surfaces. Heavy items are mounted on the external walls where possible. All connections to the power switching compartment will have feed-through filters, and the compartment will be constructed in such a manner as to conform to EMC requirements.

(3) Battery Charger Control and Auxiliary Regulator Container

Figure X-113 presents a packaging concept for these functions. The assembly consists of two redundant control modules, a failure detection and switch-over module and a housing containing wiring and input/output connectors.

Replacement of modules is effected in the same manner as described for the d-c regulator control package.

(4) Power Distribution Unit

Figure X-114 shows a sketch of the unregulated power distribution unit (PDU). This unit consists of two main busbars (positive and negative unregulated power); terminations for array, batteries, inverters and d-c regulators; and insulators.

Also included in this figure is a sketch showing assembly of the PDU, battery charger control and auxiliary regulator container, and the inverters, mounted on one surface of battery rack No. 2. Not indicated are the current sensors for the MPT control power sensor which are located in the PDU.

e. BUSBAR DESIGN

The purpose of the study reported in this section is to provide estimates of the minimum size and weight of the power distribution buses external to the power supply packages, but internal to the MMSS module. Figure X-115 shows a floor plan of the MMSS module with equipment locations and busbar routing as indicated.

Table X-26 presents busbar measurements scaled from Figure X-115.

(1) Array-to-PDU Conductors

It can be shown that

$$\frac{W_T}{I_S} = \frac{\gamma \rho}{2V_D}\left(L_{A1}^{\ 2} + L_{A2}^{\ 2}\right) \text{ pounds} \qquad \text{(X-46)}$$

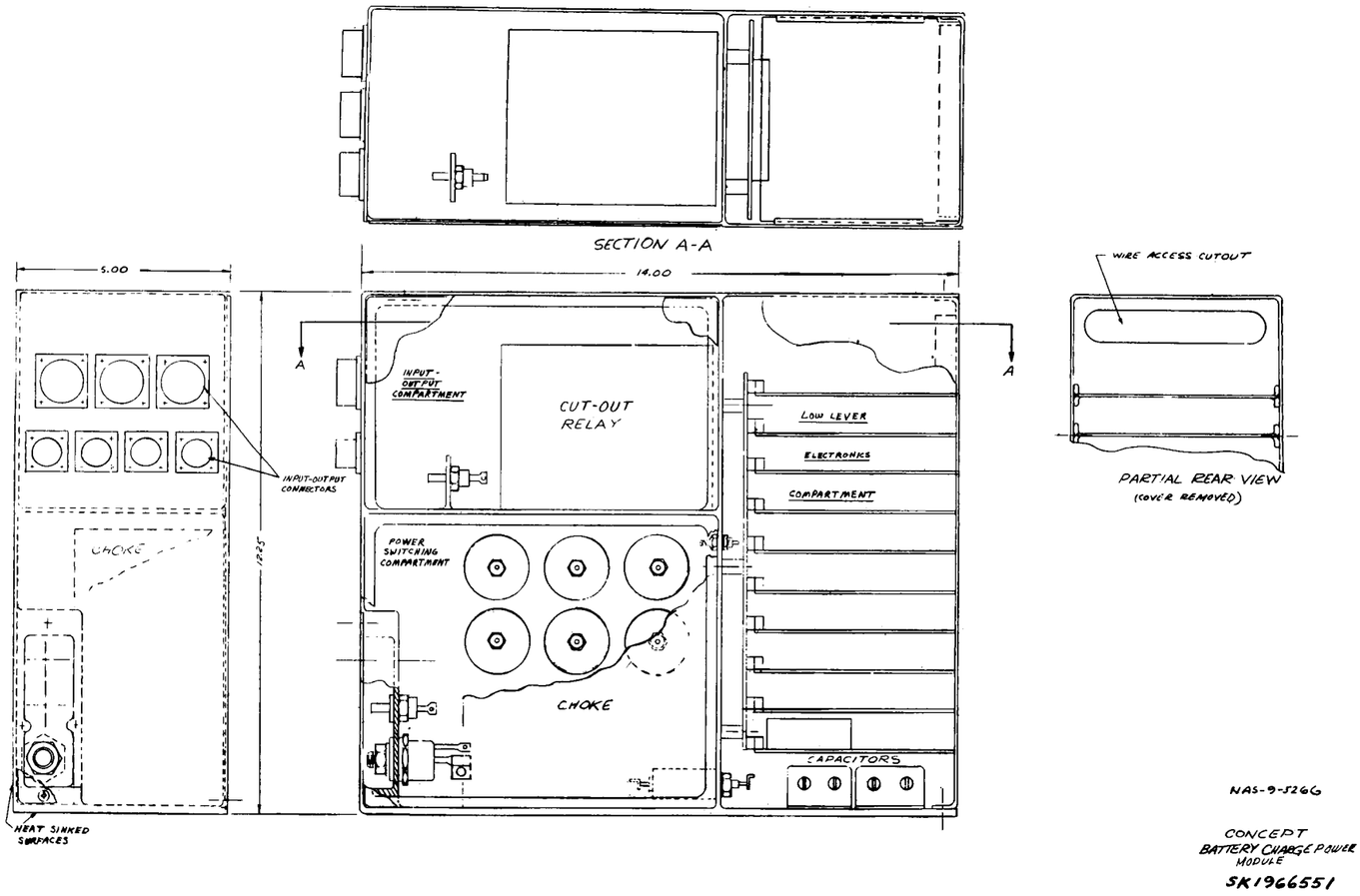

Figure X-112. Battery Charge Power Module (Concept)

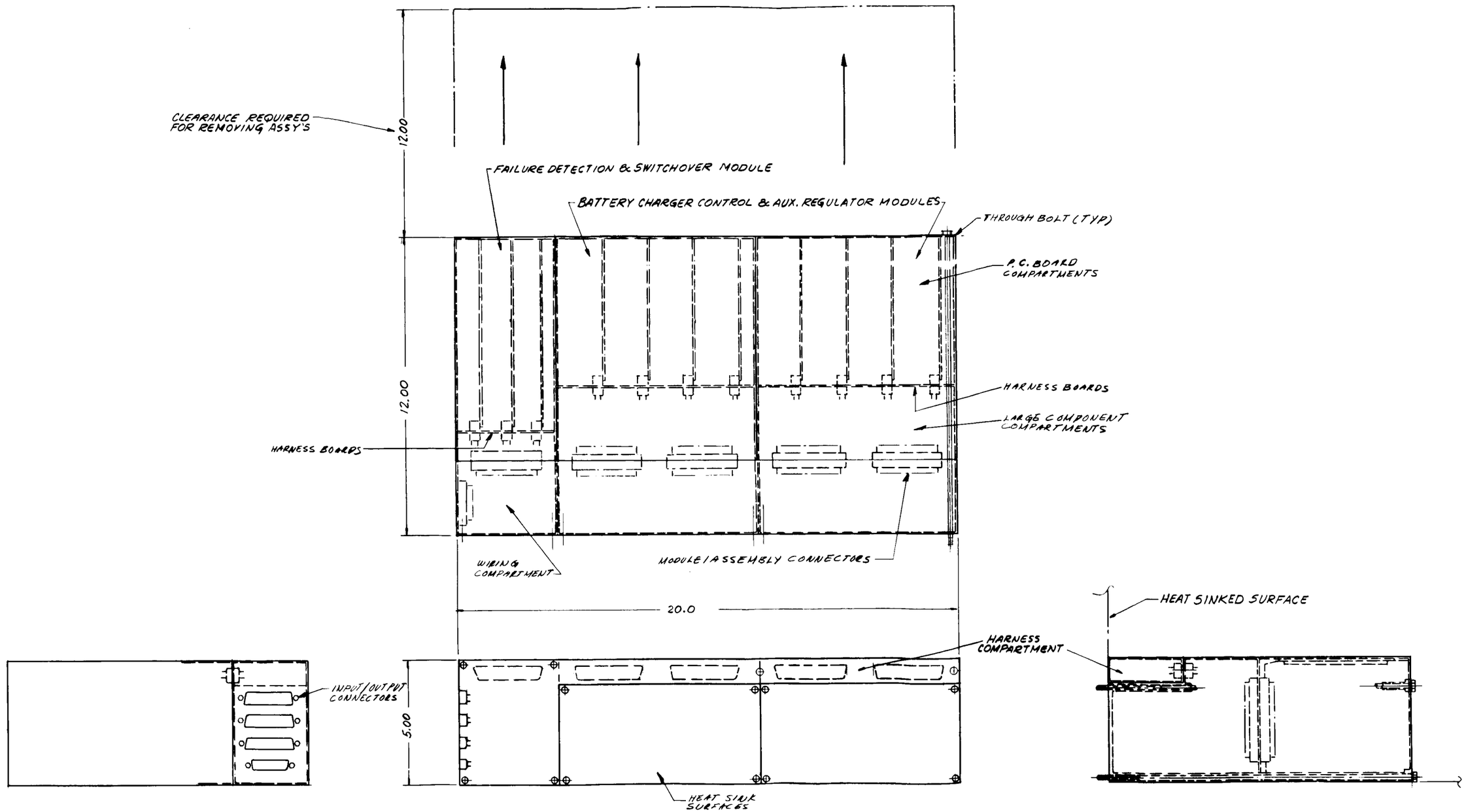

Figure X-113. Battery Charger Control and Auxiliary Regulator Container

X-178-2

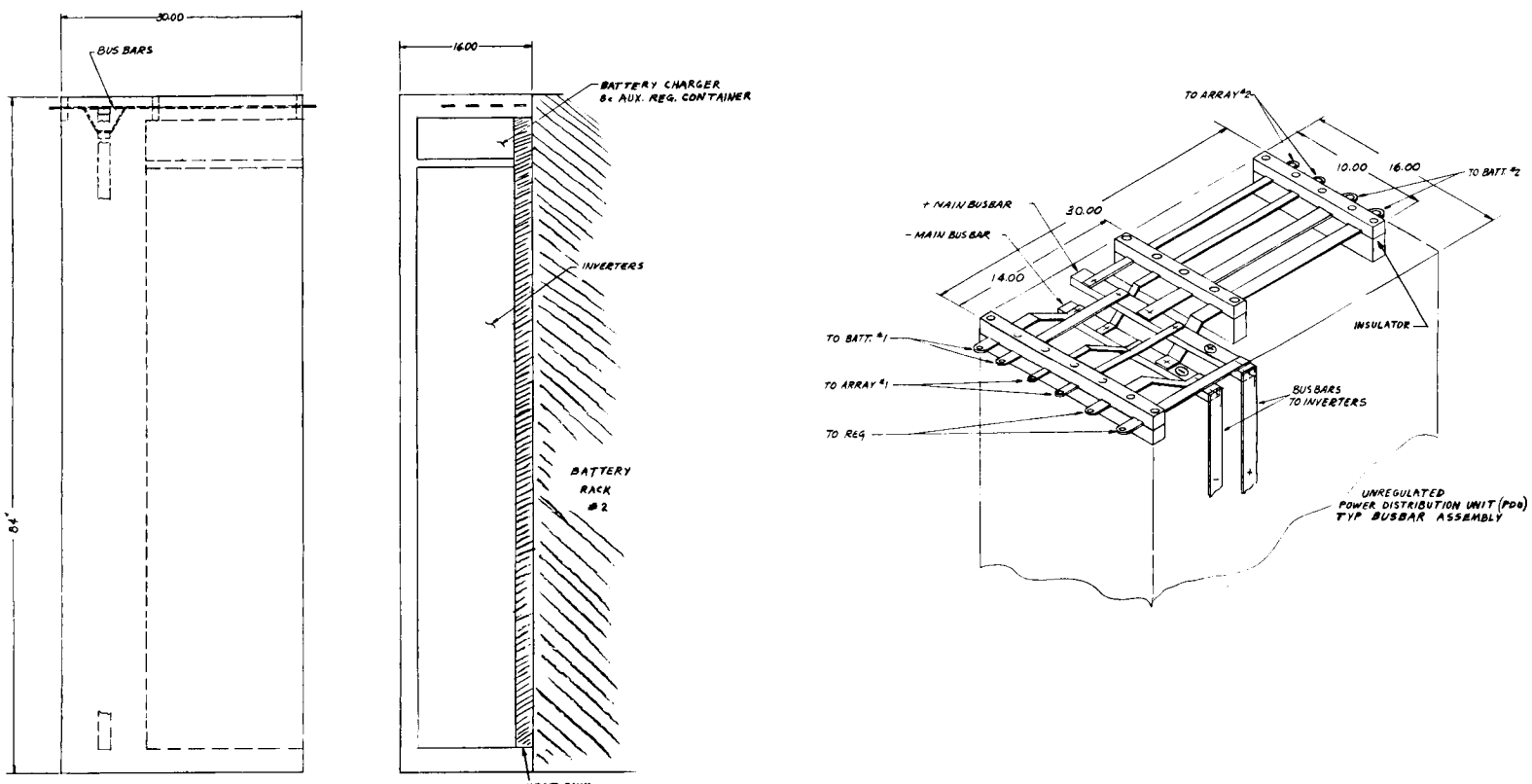

Figure X-114. Unregulated Power Distribution Unit, Busbar Assembly

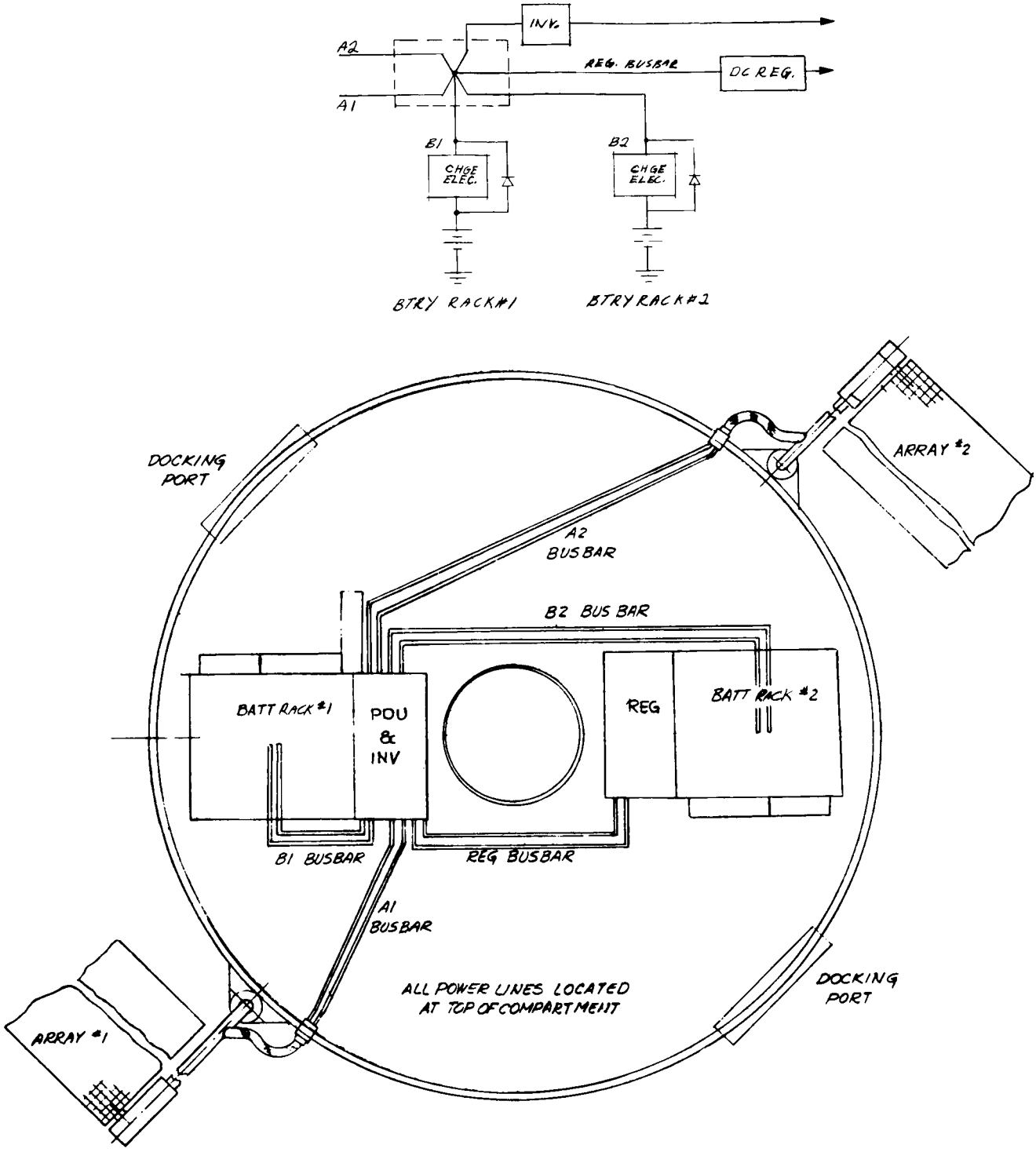

Figure X-115. MMSS Floor Plan Showing Power Equipment and Busbar Routing

TABLE X-26. LENGTH OF BUSBAR RUNS

Run	Designation	One-Way Length (inches)	Total Conductor Length (inches)
Array No. 1 to PDU	A1	64	128
Array No. 2 to PDU	A2	133	266
Battery Stack No. 1 to PDU	B1	81	162
Battery Stack No. 2 to PDU	B2	151	302
PDU to D-C Regulator	Reg.	112	224

where

W_T is Bus weight

γ is volume density in pounds per cubic inch,

ρ is conductivity in ohm-inches,

V_D is permissible bus voltage drop,

L is conductor length, and

I_S is total array current.

Then, if

γ is 0.0974 for aluminum and
0.321 for copper,

ρ is 1.12×10^{-6} for aluminum and
0.679×10^{6} for copper, and

L_{A1} is 128 inches and

L_{A2} is 266 inches,

the curves shown in Figures X-116 and X-117 may be plotted.

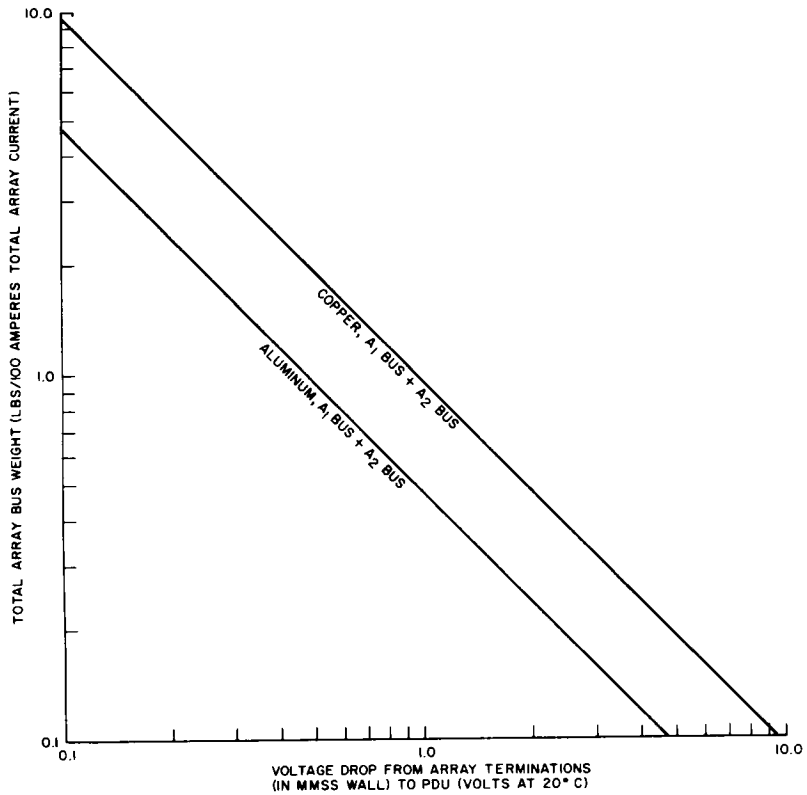

Figure X-116. Array Bus Weight vs. Voltage Drop

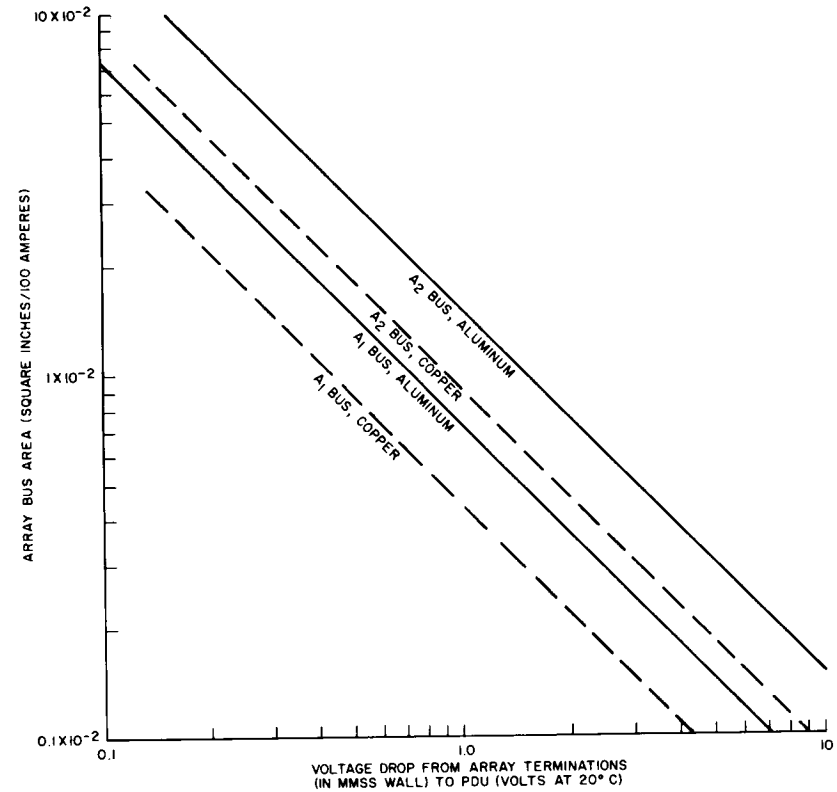

Figure X-117. Array Bus Area vs. Voltage Drop

(2) Battery-PDU-Regulator Conductors

Battery-to-Regulator busbar voltage drop is limited by end-of-discharge voltage of the battery, battery isolation diodes, and minimum allowable voltage input to the regulator.

The assumptions are (Figure X-118):

- $V_{Batt.}$ end-of-discharge minimum is 31.9 volts;
- Typical diode drops for 1N1334 diode (Westinghouse type 327F) at 30 to 50 amperes DC, ΔV_D is 0.8 volt;
- Minimum regulator input voltage $V_{reg.}$, allowing for power switch saturation resistance, diode drops, and resistance within the regulator assembly: $V_{reg.}$ is 30.7 volts;
- Voltage drop in battery stack is 0.1 volt.

Then, V_{Bus} is 0.3 volt, this being the difference between the low battery voltage less battery and diode drops (31.9 - [0.8 + 0.1] = 31.0) and minimum regulator input voltage (30.7).

For any section of busbar,

$$W = \gamma AL \tag{X-47}$$

where A is cross-sectional area, and

$$R = \rho \frac{L}{A}.$$

$$WR = \gamma \rho L^2;$$

since

$$R = \frac{V}{I},$$

$$\frac{W}{I} = \frac{WR}{V},$$

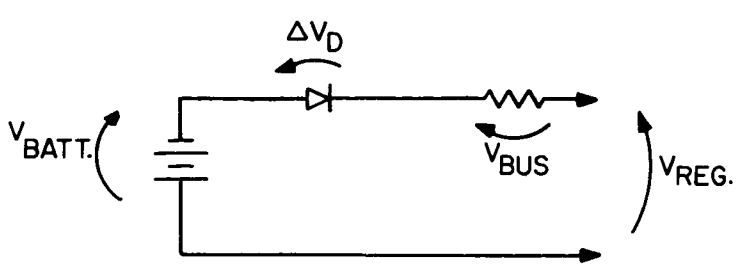

Figure X-118. Parameters for Battery-PDU-Regulator Assumptions

and weight per unit current is

$$\frac{W}{I} = \frac{\gamma \rho L^2}{V} \tag{X-48}$$

For the system comprising bus bars B_1, B_2, and $B_{reg.}$, the circuit diagram in Figure X-119 applies.

The battery voltages V_{B1} and V_{B2} are assumed equal, and equal currents $I_B/2$ are assumed taken from each. Since the voltage drops are equal, each being V_1, then R_{B1} is equal to R_{B2}.

The total weight of this system is the sum of the weights of the three parts (expressed per unit current):

$$\frac{W_T}{I_B} = \gamma \rho \left[\frac{(L_{B1})^2}{2V_1} + \frac{(L_{B2})^2}{2V_1} + \frac{(L_{BReg})^2}{V_2} \right] \tag{X-49}$$

Then, let β be exactly equal to

$$\left[\frac{(L_{B1})^2}{2V_1} + \frac{(L_{B2})^2}{2V_1} + \frac{(L_{BReg})^2}{V_2} \right]$$

From the constraints of the problem,

$$V_1 + V_2 = 0.3 \text{ volt.}$$

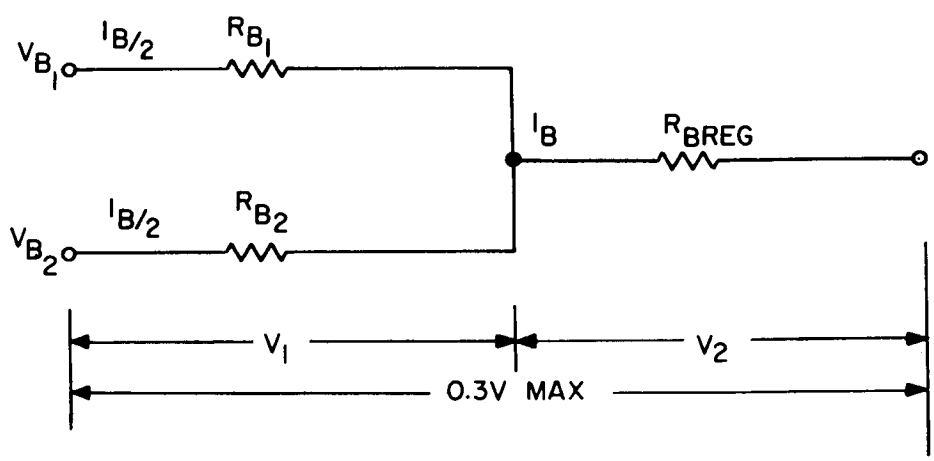

Figure X-119. Bus Bar Resistance Relations

By assuming several values for V_1 and V_2, β may be searched for a minimum value. This, of course, will minimize the weight within the problem constraints.

Figure X-120 is a plot of β versus V_1 with a minimum occurring for V_1 at approximately 0.155 volt. Utilizing this result and the equations immediately preceding the busbar constants are determined; results are given in Table X-27.

TABLE X-27. BATTERY-REGULATOR BUSBAR CONSTANTS

Parameter	Material	
	Copper	Aluminum
Total Weight, $\frac{W_T}{I_B}$ (lb/100 amperes)	15.8	7.96
Regulator Bus Area, $\frac{A_{reg.}}{I_B}$ (in^2/100 amperes)	0.105	0.173
Battery Bus No. 1 Area, $\frac{A_{B1}}{I_B}$ (in^2/100 amperes)	0.0355	0.0585
Battery Bus No. 2 Area, $\frac{A_{B2}}{I_B}$ (in^2/100 amperes)	0.0662	0.109

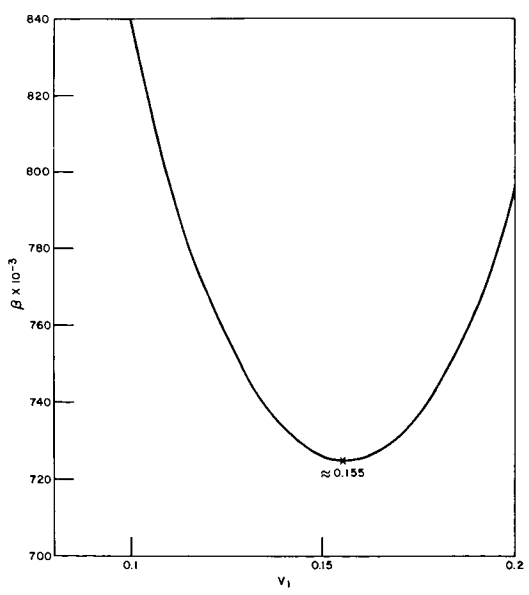

Figure X-120. Plot of β vs. V_1

f. DATA AND ANALYSIS

(1) General

The following information has been derived both from vendors' inverter data, and from a configuration analysis of the d-c regulator and the battery charge electronics. Maximum ratings are based upon component types presently available either as catalog items or through selection based upon certain performance criteria. Selection criteria have been discussed with vendors and have been determined to fall within normal product parameter distribution.

(2) Maximum Capability per Module

- PWM voltage regulator: 1400 watts (at 28 volts d-c)
- Inverter: 1750 watts (at 0.7 PF)
- Charge Electronics: 50 amperes

The information for PWM voltage regulator and charge electronics is based solely upon power transistor capability for switching up to 55 amperes with safe derating. Some of the power transistors capable of this performance are:

- Solitron Devices, Inc. MHT8923 family (selected for BV_{ceo} greater than 150 volts). Devices from this and similar families have been employed at RCA for several years and have been flown successfully in TIROS, Lunar Orbiter, and other programs in power supply equipment. The MHT8905 (lower voltage, selected version of the 8923) has been designed into the Nimbus B power system, where it serves as a main switch in a 500-watt switching regulator.

- Silicon Transistor Corp. STC 2502. This device, although not previously used by RCA in power supply designs, appears to have excellent qualities and adequate performance characteristics.

The inverter capability has been estimated jointly by RCA and Westinghouse Aerospace Electrical Division, who is developing a modular static inverter under Contract NAS 3-9429 (see Reference X-16).

(3) Efficiency

It is possible to describe the curve showing efficiency as a function of percent of full load, where the full load is between 50 percent and 100 percent of the per-module peak output, given in the preceding section.

(a) Regulator Efficiency

PWM d-c regulator efficiency, designated e_c, can be defined as follows (see Figure X-121):

$$e_c = \frac{P_o}{P_{in}} = \frac{P_o}{P_o + P_d} \tag{X-50}$$

where P_o is 28 volts x I_o and P_d is the sum of the loss components, so that

$$P_d = P_{dr} + P_{dsat} + P_{dsw} + P_{dcr} + P_{dsh}. \tag{X-51}$$

P_{dr} is fixed resistance loss $(= I_o{}^2 R_F)$

P_{dsat} is power switch saturation loss which is expressed as

$$\left[I_o{}^2 R_{sat} + V_{base\ drive} \times I_{B\ (max)} \right] \alpha$$

P_{dsw} is switching loss, which is expressed as

$$2\, t_r\, f_{sw}\, V_{in}\, I_o$$

P_{dcr} is flyback diode loss (see Figure X-122)

P_{dsh} is fixed shunt loss within power module.

The following is a list of circuit constants involved in the power-loss terms preceding and their values as used in the analyses:

Regulator output current;	I_o	= 2.5 to 50 amperes
Fixed module resistance,	R_F	= 10 milliohms
Power switch saturation resistance,	$R_{sat.}$	= 20 milliohms
$V_{basedrive}$ x I_B max (based upon 50 ampere I_O max)		= 20 watts
Power switch rise time,	t_r	= 1.0 microsecond
Regulator switching frequency,	f_{sw}	= 9.6 kHz
Low-level electronics loss,	$P_{dsh.}$	= 7.4 watts
Regulator input voltage,	V_{in}	= 53 volts, day = 36 volts, night

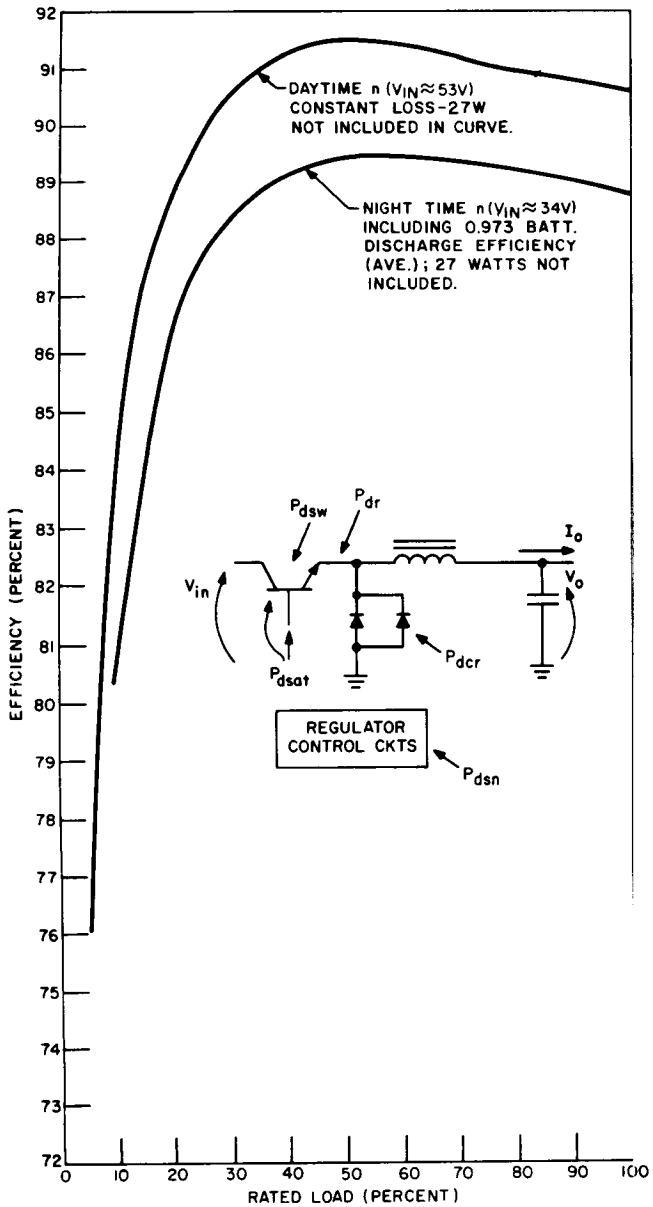

Figure X-121. D-C Regulator Efficiency (Estimated)

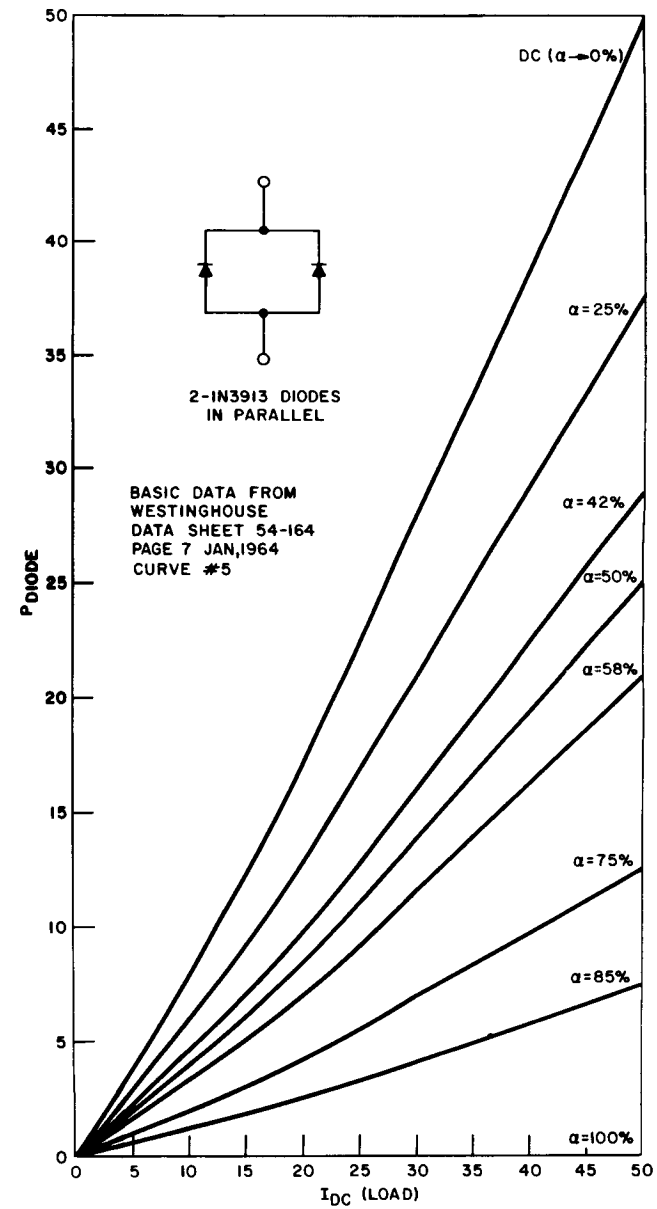

Figure X-122. Typical Power Dissipation in Flyback Diodes vs. Regulator Load Current

Input voltages are average values for anticipated variations of array and battery. Nighttime input voltage includes loss due to battery discharge diodes.

Regulator duty-cycle α is 0.58, day; 0.85, night.

This is based upon resistance and diode drops within the regulator.

Flyback diode loss, P_{dcr} is as in Figure X-122.

An additional efficiency factor (due to battery discharge diodes and bus resistance) of 97.3 percent was taken into account in making the regulator nighttime efficiency calculations.

The resulting curves, Figure X-121, show efficiency as a function of the percent of rated load. Also indicated is the regulator fixed loss (independent of the number of modules) of 27 watts.

(b) Inverter Efficiency

The inverter efficiency as a function of the percent of full load has been derived from various data accumulated during a vendor survey made early in this study. The curves of Figure X-123 reflect a mean efficiency based upon estimated 2.5-kVA inverter performance. An inquiry (made at the Westinghouse Aerospace Division on December 22, 1966) regarding the inverter efficiency revealed that the results of Westinghouse studies were in good agreement with the data in Figure X-123. The latest estimates are:

Percent efficiency	Percent full load
82	100
81	75
78.5	50

(c) Battery Charger Efficiency

Battery charger efficiency was calculated in a manner identical with that for the regulator. There are, however, differences in the operating parameters.

Differences are as follows:

- P_o equals 42.3 V x I_o, where 42.3 V. is assumed to be an average battery charge voltage.
- As a result of the P_o calculation, α is 85 percent (daytime only).
- Fixed shunt loss P_{sh} is 10 watts (estimated).

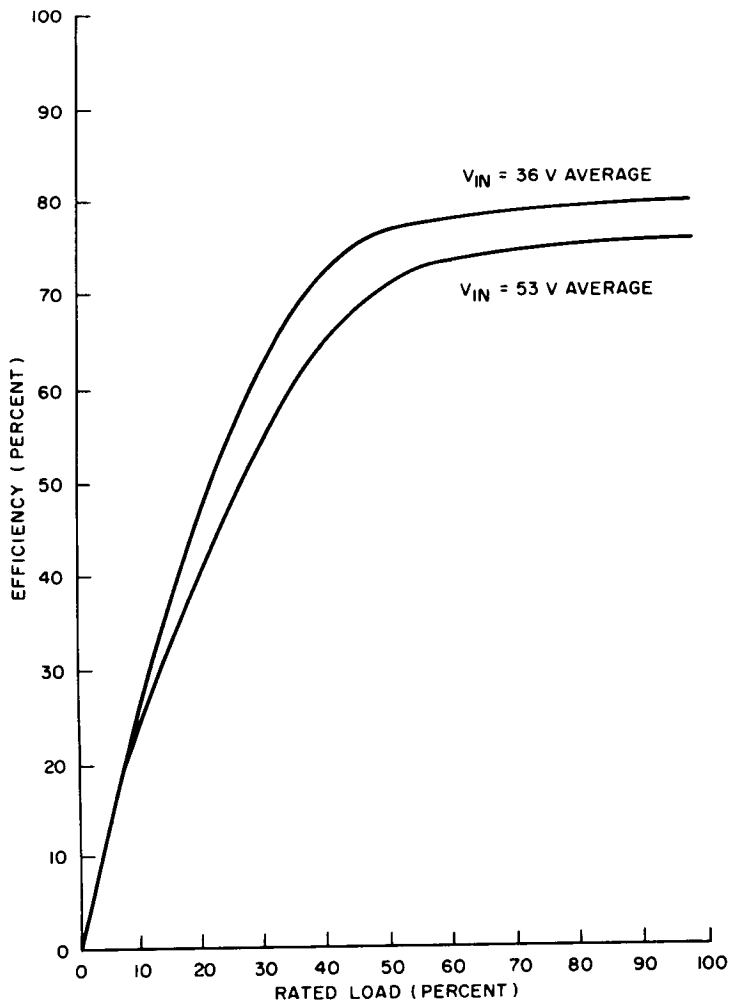

Figure X-123. Inverter Efficiency

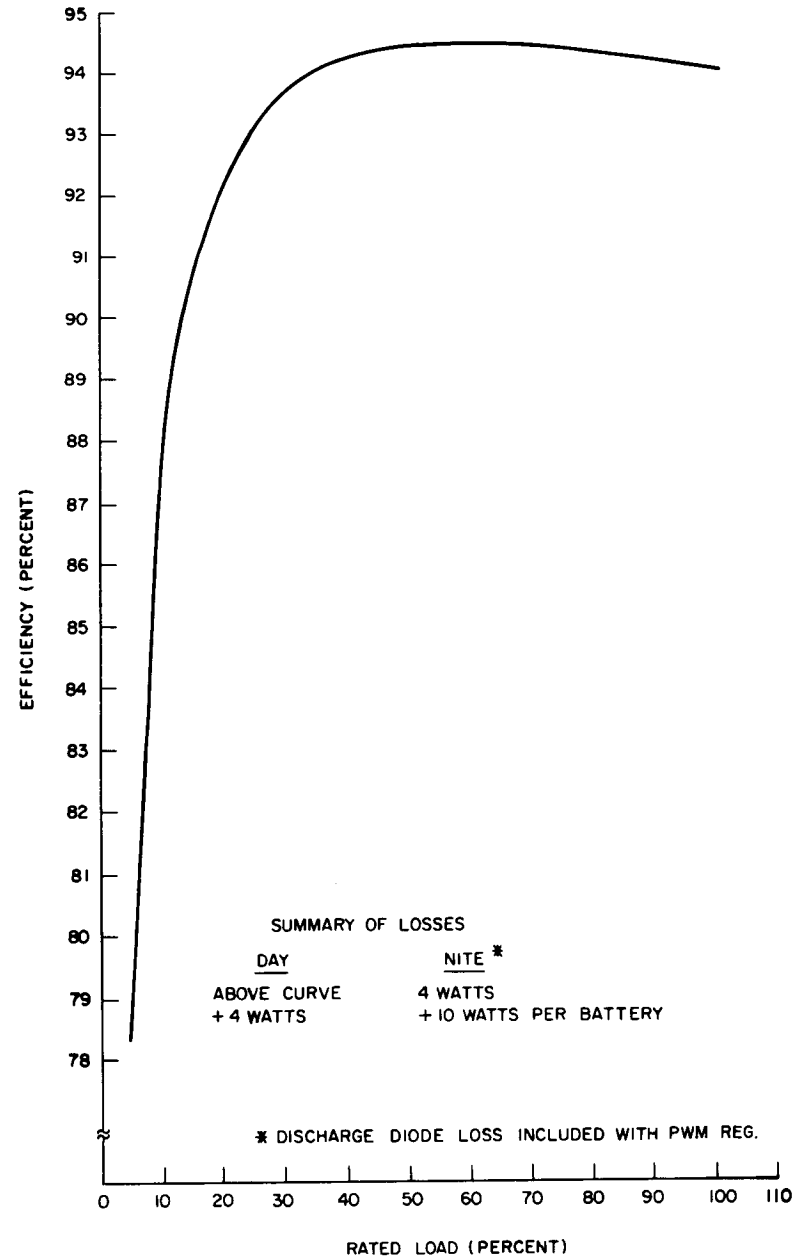

Figure X-124. Battery Charge Electronics Power Transfer Efficiency vs. Percent of Rated Load

Figure X-124 shows the relationship of the charge electronics efficiency to the load. Also indicated is a summary of fixed losses.

(4) Weight

The following parametric data was generated from vendors' inverter information and from the size and weight information (Paragraph X.C.4.f(6)) for the d-c regulator and the battery charger assemblies.

(a) Inverter Weight versus VA Rating (Figure X-125)

The curve represents a mean of vendors' data for inverters over the indicated rating range. Data from the Westinghouse Aerospace Division however, indicated that the weight shown was on the high side; a 70-pound module was stated to have a full load capability of 3.6 kVA.

(b) Regulator and Battery Charge Electronics Module Weights versus Maximum Rating

These curves (Figures X-126 and X-127) were derived by first estimating weight for the maximum-output module using an estimated parts count and including packaging. This was then reduced by an amount equal to the weight reduction in electrical components due to lower output ratings. Because of the range of maximum ratings involved (two to one), it was felt that the total weight would not change appreciably more than the component weight.

(5) Specific Volume

The curves (Figures X-128 and X-129) for the d-c regulator and battery charger assemblies were computed from the estimated weights and volumes for these functions. The total volume and weight in each case includes both fixed and modular values. This information is presented with the power module rating as a parameter.

The inverter specific volume is taken to be 0.0181 cubic feet per pound; this value is a mean of various vendor inputs.

(6) Size and Weight Data

Table X-28 presents estimated size and weight data for the component modules of the d-c regulator and battery charger assemblies. This information is based upon conceptual mechanical designs (see Paragraph X.C.4.d) and estimated parts counts for the respective modules.

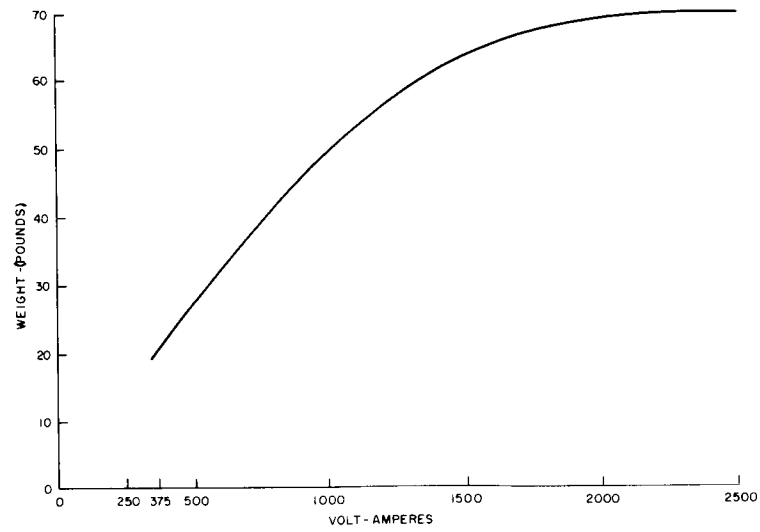

Figure X-125. Weight vs. Volt-Ampere Rating for Static Inverter (120/208 Volts, 3ϕ, 400 Hz)

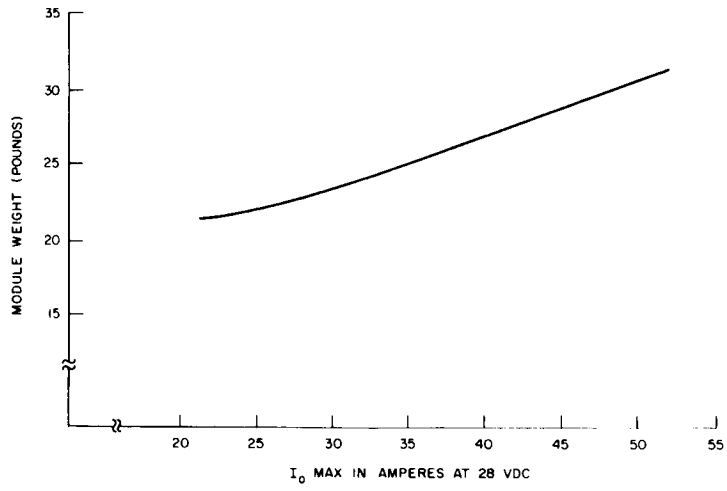

Figure X-126. D-C Regulator Power Module Weight vs. Maximum Output Current Module

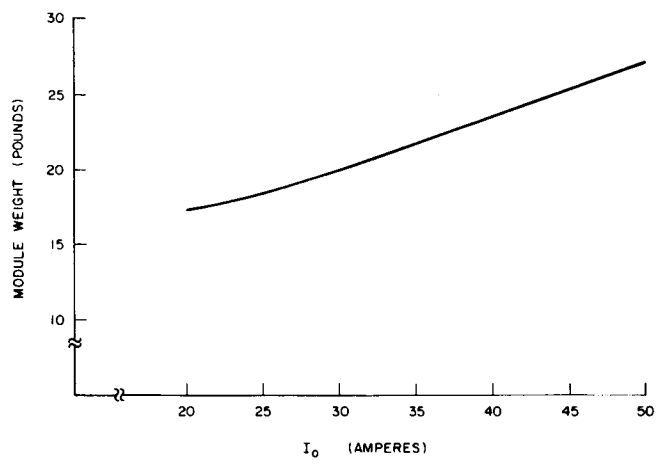

Figure X-127. Battery Charge Electronics Power Module Weight vs. Maximum Charge Current

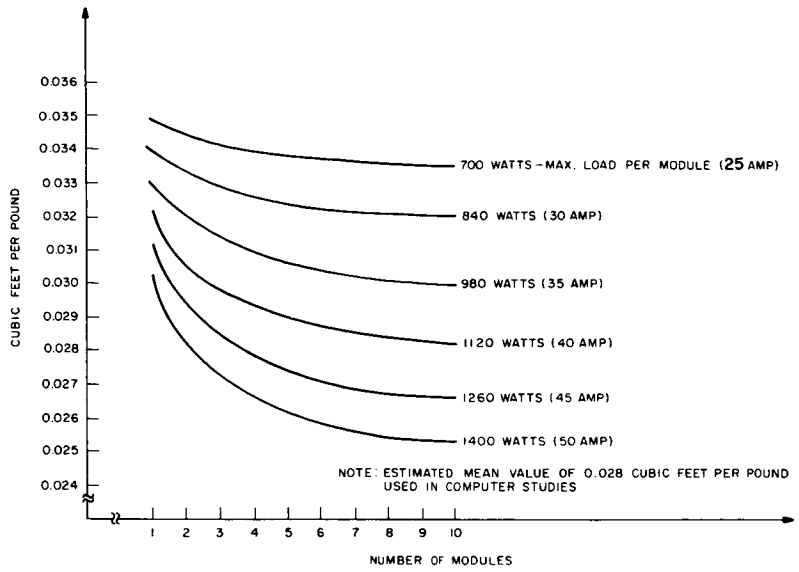

Figure X-128. D-C Regulator Assembly, Specific Volume vs. Number of Power Modules

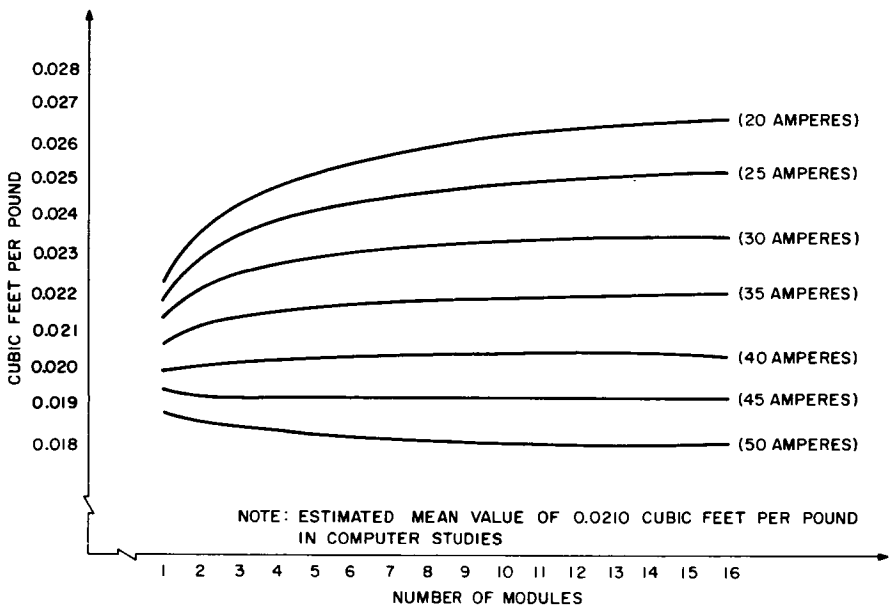

Figure X-129. Battery Charge Electronics Assembly, Specific Volume vs. Number of Power Modules

TABLE X-28. ESTIMATED SIZE AND WEIGHT DATA

Package Designation	Size (Inches)	Volume (Cubic Inches)	Weight, Pounds			
			Container	Electrical Components & Potting	Hardware Wiring Connections, Brackets/ Boards	Total (pounds)
1. Battery Charge Electronics Power Module (Maximum Rating)	14 x 5 x 12.2	854	5.0	18.06	4.06	27.1
2. D-C Regulator Control Unit (Fixed)	11.5 x 19.5 x 9.25	2074	11.6	16.55	5.35	33.5
3. (a) D-C Regulator Power Module	17.62 x 9.25 x 7.0	1141	10.0	15.1	1.5	30.4
(b) Connection Box (Maximum Rating)	--	--	2.3	--	1.5	30.4
4. Battery Charger Control & Auxiliary Regulator Container (Fixed)	12 x 20 x 5	1200	10.9	18.2	5.4	34.5

D. SYSTEM OPERATIONAL PHILOSOPHY

1. Introduction

The operational philosophy of a power subsystem in a manned space vehicle application is intimately tied to safety and reliability. Webster defines safety as:

"Freedom from danger or hazards---

---Quality of being devoid of whatever exposes one to danger or harm---

---Of or pertaining to the safeguarding from accident---"

By virtue of the foreign environment in which the mission is to take place, there is, by definition, no freedom from danger or hazard nor can the quality of being devoid of whatever exposes one to danger or harm exist. However, safeguards can be provided against accident or hazard.

Therefore, system safety can be achieved if successful measures are taken to protect the crew and mission from accident or hazardous circumstances despite component malfunctions within the power system.

This can be achieved in three ways:

(1) Through inspection and preventive maintenance;

(2) Through implementation of automatic protection where crew reaction time is too slow to avoid catastrophic or hazardous circumstances; and

(3) Through application of appropriate techniques to enhance system reliability.

In general, the guidelines employed are as follows:

(1) Maintain Power Supply System (PSS) load interface whenever possible.

(2) Protect PSS from load malfunctions.

(3) Protect PSS from internal malfunctions.

(4) Where possible, rely on the crew to take preventive action in order to avoid malfunctions.

2. The Protective Process

Since the most adequately designed and constructed system may sustain random failures and/or wearout of some components, the need for replacement and periodic resupply becomes

evident. A requirement for replacement is preceded by recognition of marginal operation or location of a defect. This may be achieved through either of two methods:

(1) Perform a maintenance and monitoring function.

(2) Wait for a malfunction to occur.

In either case, having established the condition, replacement or repair may be effected. Figure X-130 shows the aforementioned protective processes in schematic form. Here, as indicated, maintenance checking and performance monitoring is carried out on a routine periodic basis. The advent of performance degradation is followed by location and replacement of a defective component. Resupply will then restore the appropriate number of spare components. Occurrence of a malfunction initiates automatic protective action followed by location, replacement, and resupply as before.

3. Inspection and Preventive Maintenance; Performance Degradation

a. GENERAL

Performance degradation is any condition generally resulting from normal degradation of components and which results in small-magnitude changes in system performance. These changes may be noted over a period of time and will, in general, exhibit a trend. If not corrected in time, this may become a malfunction. Performance degradation will be accounted for by maintenance checks and observation of system parameters. Measurable quantities such as regulated voltages, battery end-of-charge and discharge voltages, depth of discharge and the like will be monitored. These parameters will be available for measurement on board or via telemetry, or both. Maintenance checks will be tests and/or observations made on parameters not generally available for continuous monitoring (such as individual battery cell voltages).

Periodic inspections of the power system both on board and via telemetry may be made on a routine basis. One brief inspection per day or per orbit of parameters such as battery state of charge, bus voltages and system currents is sufficient. More detailed inspections should be made on a weekly basis and include examination of equipment performance parameters such as regulation, efficiency, battery cell voltage balance and operation of all automatic protection circuits. Location of a faulty component or an out-of-specification condition indicates the need for immediate maintenance action.

b. PARAMETERS

(1) On-Board Monitoring

Table X-29 lists the power system parameters suggested as indices of system performance for on-board monitoring of the spacecraft. For convenience, the power system has been broken down into seven categories or groups of equipments.

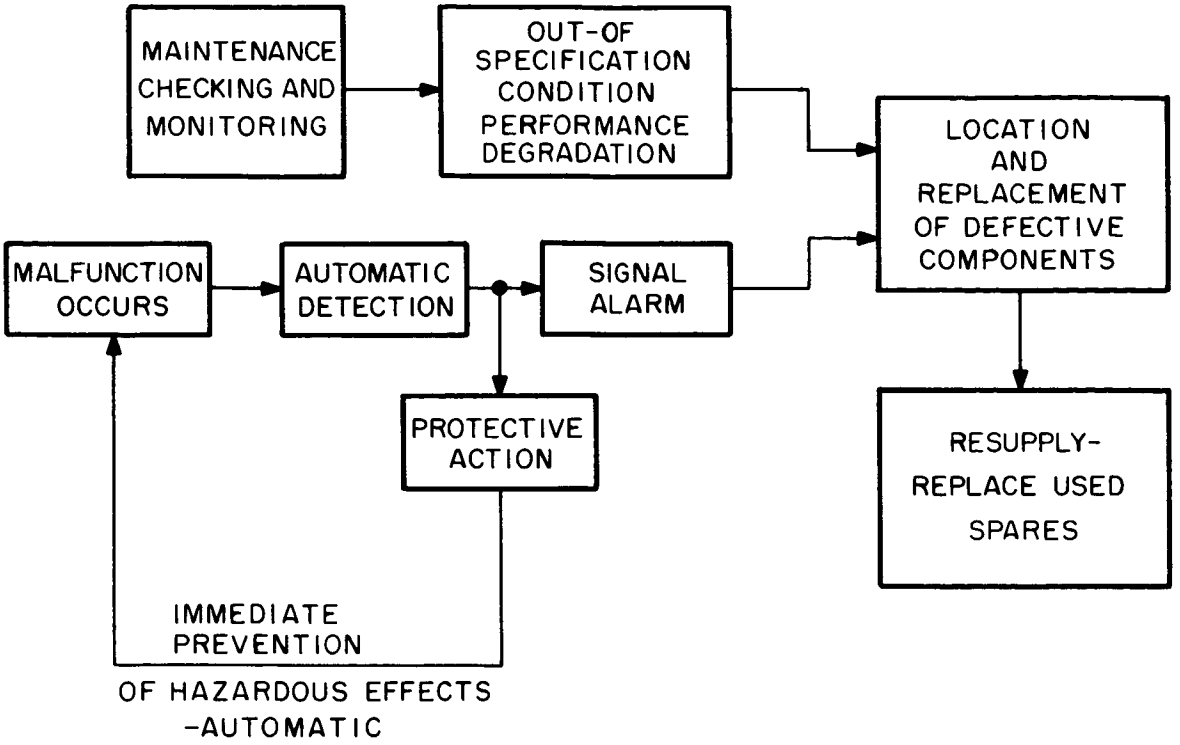

Figure X-130. Schematic Representation of Protective Processes

TABLE X-29. POWER SYSTEM PARAMETERS TO BE MONITORED ON BOARD

Equipment Group	Metered Performance Parameters
1. D-C Regulators	Load voltage Load current Operational status of power modules and FBA (i.e., on or off) Temperature
2. Inverters	Load voltage Load current Frequency Load power factor Module status (on or off) Temperature
3. Batteries	Terminal voltage Current Temperature State-of-charge

TABLE X-29. POWER SYSTEM PARAMETERS TO BE MONITORED ON BOARD (Continued)

Equipment Group	Metered Performance Parameters
4. Battery Chargers	Temperature Operational status of redundant elements (i.e., on or off)
5. Solar Array	Voltage Current Temperature Sun sensors
6. Redundant Auxiliary Regulator	Voltage Current Operational status (on or off) Temperature
7. Ancillary Equipments includes: Telemetry and status monitoring Malfunction detection and protection Maintenance checking	None

* A minimum number of meters will be used. Test points will be available for each parameter allowing individual measurements as desired.

(2) Recommended Telemetry Points

Telemetered points listed in Table X-30 represent complete instrumentation of the power subsystem. Continuous analysis of these points by a ground facility would assure the ultimate in systems safety, reduce crew participation time, and serve to warn the crew of impending failures.

4. Automatic Protection; Malfunctions

A malfunction is defined as any condition resulting from a damaged, destroyed and/or seriously degraded component which causes generally large-magnitude changes in system performance. A malfunction will occur suddenly with no obvious prior trend of degradation. Malfunctions may be classified as external or internal types. External or load malfunctions will usually be manifested as excessive current drains on the power system. Protection against such overloads will be inherent in the regulator and inverter designs. This is due to built-in current limiting features. However, to conserve energy and prevent possible damage to the general spacecraft loads due to an undervoltage condition, a faulted load should be disconnected in as short a time as possible. This action may be achieved simply and

TABLE X-30. POWER SUBSYSTEM TELEMETRY POINTS

Equipment Group	Telemetry Points
DC Regulators	Regulated DC voltage Regulated DC load current (total) D-C Regulator Control Module status (on or off) D-C Regulator Power Module status (on or off) D-C Regulator heat sink temperature D-C Regulator over-under voltage indication D-C Regulator current limiting indications D-C Regulator input voltage (unregulated bus)
Batteries	Battery voltage (total) Battery charge current (per battery) Battery discharge current (per battery) Battery temperature (per battery) Battery charge/discharge accumulations (per battery) Battery over-discharge indication (per battery) Battery insufficient charge indication (per battery) Battery charger over/under voltage indication (per battery) Battery over pressure indication (per battery) Battery over current indication (per battery) Battery over temperature indication (per battery)
Battery Charger	Charge Electronics Control Module status (on or off) Battery Charger Power Module status (on or off) Battery Charger electronics heat sink temperature
Inverters	Static Inverter AC output voltage (per phase) Static Inverter AC load current (per phase) Static Inverter Power Module status (on or off) Static Inverter load power factor (per phase) Static Inverter frequency Static Inverter heat sink temperature Static Inverter over-under voltage indication Static Inverter current limiting indication Static Inverter high temperature indication Static Inverter output voltage (line to line)
Auxiliary Regulator	Auxiliary Regulator voltage (per regulator) Auxiliary Regulator current (per regulator) Auxiliary Regulator heat sink temperature (per regulator) Auxiliary Regulator over-under voltage indication (per regulator) Auxiliary Regulator current limiting indication (per regulator)

TABLE X-30. POWER SUBSYSTEM TELEMETRY POINTS (Continued)

Equipment Group	Telemetry Points
Solar Array	Solar Array voltage Solar Array current Solar Array temperature Solar Array paddle deployment Solar Array panel strain Solar Array orientation indications

inexpensively through appropriate fusing techniques. Selection of fuse types* and ratings must necessarily await a detailed system design. However, there are several types and techniques available for space application. Points to be considered in fuse selection will be steady-state derating, load current peak-to-RMS ratios, starting surges and ambient temperature effects.

Internal malfunctions are not handled in so straightforward a manner. In most instances, internal malfunctions will occur in a short time period and could be catastrophic in nature; for example, a short-circuited d-c regulator power module would result in excessive voltage on the d-c bus, perhaps as high as 100 volts. Crew reaction time must be considered here and automatic safety equipment must be included to cope with such situations. Occurence of a malfunction in the latter case is detected automatically. At this point, two things occur simultaneously, the crew is notified via an alarm (visual or audible indicator) and protective action takes place to immediately prevent any hazardous effects. As an example, the shorted power module mentioned previously would cause an overvoltage condition. An overvoltage indicator would light and the defective module would be automatically switched out of the system. Since the d-c regulator would contain at least one operating, redundant power module, the loss of one module would not reduce desired regulator capability. After the crew has had time to respond, the defective module can be manually removed from the system and replaced.

5. Crew Participation

a. PRESENCE OF THE CREW AS A FACTOR IN SYSTEMS SAFETY

An unmanned spacecraft generally contains spare components which may be switched into operation either via ground command or automatically. The adaptability of these systems, however, is limited by the number of spares and the complexity of the circuitry required to perform any but the simplest of detection and switching functions. The manned spacecraft, however, not only has the convenience of a human operator but also the presence of this operator will allow certain functions to be performed which would otherwise require large quantities of circuitry and ground command capability.

* "fuse" indicates replaceable as well as resettable types.

The power system design philosophy has been directed toward automatic operation only in cases where even a short-duration failure would interfere with the delivery of the rated loads. The human operator will be involved with the replacement of faulty modules in emergency situations and in the performance of brief maintenance tasks. The adopted design philosophy would, therefore, both minimize crew participation as well as provide for automatic correction of critical-component failures.

b. CRITICAL COMPONENT FAILURE

A critical failure component is defined as one which, unless immediately corrected, would cause the load delivery to be disrupted. Feedback amplifier failure in the d-c regulator assembly would fall into this category: i.e., unless a redundant control module is automatically switched in delivery of the regulated DC bus voltage would cease.

After automatic action takes place and an alarm is initiated, it is incumbent upon the crew to locate the malfunction and effect a repair.

c. NONCRITICAL COMPONENT FAILURE

An example of noncritical component failure would be the malfunctioning of an inverter power module. The inverter assembly will include one or more actively redundant modules; temporary loss of one will not cause the a-c load delivery to be interrupted. Faulty components resulting in noncritical failures will be replaced manually, following automatic removal from the active circuit in the event that continued presence of a faulty unit could trigger further failures.

d. LOCATION

When an alarm is heard, it will draw immediate attention to the control panel where any critical or noncritical malfunction will be indicated automatically. Fault location initially consists of a simple, visual search of the panel for one or more lighted indicators.

e. CORRECTIVE ACTION

Once a fault has been located, corrective action will take place. The nature of the action is dependent upon the nature of the fault. A static inverter malfunction is the simplest to correct. Malfunctioning inverter module will be electrically removed by automatic apparatus. Required crew action consists of physical removal of the module from the inverter assembly by loosening several fasteners and sliding the module out of its location. A spare module will then be inserted and electrically connected to the system by activating manual controls which would both reset the automatic fault detection apparatus and establish module operation. Proper operation may then be ascertained by re-examining the control panel and searching appropriate test points with built-in metering equipment. The crew must then establish communications with a ground station in order to describe the malfunction and request a replacement module which would be delivered on the following resupply vehicle.

A d-c regulator malfunction will cause similar action, except that the regulator would have more than one type of replaceable module, as described in section X.C.4. A battery system malfunction would be the most difficult to handle since this is the most complex portion of the power supply. There are three types of replaceable electronic modules plus the battery modules in this system. Although location and replacement methods for a defective module are generally the same here as in the other areas of the power system, some judgment must be employed in ascertaining the effects of reduced energy storage capacity even for a short period of time. Communications with a ground station must be established and an analysis made to determine the possible need for reducted load programming or other measures which might be necessary to allow the storage system to be returned to full capability.

Loss of one of the solar array panels or slip ring assemblies would constitute the most serious malfunction. The crew would immediately reduce spacecraft loads to the barest essentials in an effort to conserve battery energy. This would provide maximum time for a repair-or-abandon decision and its execution.

f. MAINTENANCE

In order to prevent malfunctions and uncover untimely degradations, a program of periodic maintenance is recommended. As already suggested in section X.D.3, it is desirable to have two on-board inspection routines, one every day (or orbit) and one every week. In addition, some planned maintenance tasks may be performed.

g. DAILY INSPECTIONS

The daily inspection will be kept as short as possible in an effort to minimize crew participation. Checks made will show system performance and will be based primarily upon terminal behavior. Pertinent system voltages and currents will be monitored at the control panel with built-in metering equipment. The typical procedure will consist of setting a selector switch to a desired parameter and depressing a "read" button or toggle-type switch. System temperatures will be read in the same manner.

The entire checking procedure should require no more than 15 minutes of crew time per day.

h. WEEKLY INSPECTIONS

The Weekly inspection will provide a more detailed assessment of power system status. Each performance parameter listed in Table X-29 should be observed and compared with specified values. In addition, observations will be made of the following:

(1) Battery cell voltages will be checked for balance with other cells in the same battery.

(2) All test points (to be specified) will be read.

(3) All automatic protection circuits will be exercised to ascertain proper operation.

(4) Dummy loads will be applied to regulator and inverter outputs to load these circuits to rated capability. This will provide an operational check on these important portions of the system.

(5) Planned rotation of spare and operating battery modules can be made at this time.

The weekly inspection should require no more than 1.5 hours of crew time providing there are no out-of-specification conditions observed. Observation of such a condition will prompt immediate action.

6. Equipment Reliability and Redundancy Recommendations

a. DISCUSSION

The total functional reliability model for the power system is presented in Figure X-131. The individual probabilities of success are based on approximate part type population counts with continuous operation of the element over the mission life, 1 year of 8760 hours (see Appendix F). Since the required probability of success for the system throughout the mission is at least 0.995, it is apparent from the data shown that greater reliability is required from certain of the individual black boxes. The redundant elements of the d-c regulator, the MPT control circuits, the two-phase inverter for the battery charge electronics, and the auxiliary regulator have designated probabilities of success which reflect their redundant nature. The solar array, within the constraints of this study, is assumed to have unity probability of success. Worst-case design of the solar array provides for an adequate margin for all possible degradation modes. Therefore, the reliabilities here are sufficiently high at the outset, and any attempt to improve them would have to be made in the course of a detailed design effort.

The probabilities of success of the filter banks based upon parts count are appreciably below the mission reliability goal: 0.98600 and 0.98322, respectively, compared with the goal of 0.995. Since the filters are conservatively designed, a higher probability of success can be justified. For example, the solar-array filter bank consists of 24 capacitors in parallel, but only 18 are necessary for satisfactory filtering. Each capacitor has a failure rate (assigned by RCA Engineering Reliability) of 80 failures in 10^9 hours. This yields a probability of success of 0.9993 for each capacitor. The probability of success of the entire solar-array filter is expressed by the first six terms of the binomial expansion, $(P+Q)^{24}$, where P, the probability of success = 0.9993 and Q, the probability of failure = 0.0007. This means that as many as six of the 24 filter capacitors can fail before system failure occurs. The resulting probability of success is 0.999946. Therefore, it is justifiable to assign the composite aggregation of the input-output filters of the regulator and the solar-array filters a total probability of success of 0.9999.

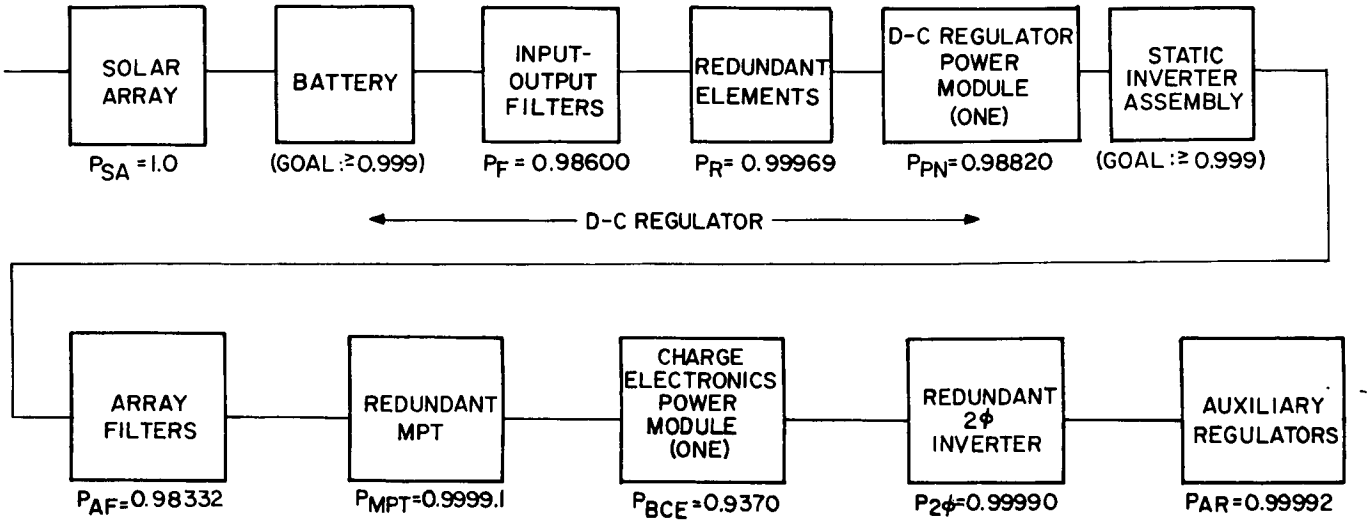

Figure X-131. Reliability Mathematical Model, Power Subsystem

The six elements considered so far have a combined mission probability of success of 0.99932, determined in the following manner:

$$P_s = (P_F) \cdot (P_{AF}) \cdot (P_R) \cdot (P_{MPT}) \cdot (P_{2\phi}) \cdot (P_{AR}) \qquad \text{(X-52)}$$

$$= (0.9999) \cdot (0.99969) \cdot (0.99991) \cdot (0.99990) \cdot (0.99992)$$

$$= 0.99932$$

To obtain a goal of 0.995, the remaining four subsystem elements require a total P_S of 0.9957 as shown below:

$$0.99932\ P_s = 0.995$$

$$P_s = 0.9957 \text{ total (See Figure X-132)}$$

Since

$$(0.9957)^{1/4} \approx 0.999$$

The required probability of success can be achieved if the remainder of the probability of success allocations are as follows:

Battery Charge Electronics Power Modules (all)

$$P_s \approx 0.999$$

D-C Regulator Power Modules (all)

$$P_s \approx 0.999$$

Static Inverter Power Modules (all)

$$P_s \approx 0.999$$

Batteries (Total)

$$P_s \approx 0.999$$

b. REDUNDANCY APPORTIONMENT FOR ELECTRONIC POWER MODULES

For the battery charger power modules, the probability of success is P_{BCE} = 0.937 per module for one year. The binomial expansion $(P + Q)^n$ was used to determine the required number of modules for a total P_s of 0.999. The calculations were made for a variable baseline number of modules of 1 to 10, with various resupply intervals. Therefore:

$$P = e^{-\frac{t}{MTBF}} \qquad \text{(X-53)}$$

Where

MTBF is mean time between failures

t is mission duration or resupply interval

In the expression $(P + Q)^n$ given above

Q is 1 - P

n is number of modules required

Sample Calculation: Determine the number of modules required for a P_s of 0.999 with a baseline of 5 modules and a resupply interval of 90 days (2160 hours). The MTBF of one module was determined to be 1.41×10^5 hours based upon an estimated parts population.

$$P_s = e^{-0.0153}$$

$$= 0.98482$$

$$(P + Q) = (0.98492 + 0.01518)^{5+X}$$

where X is the required number of spares.

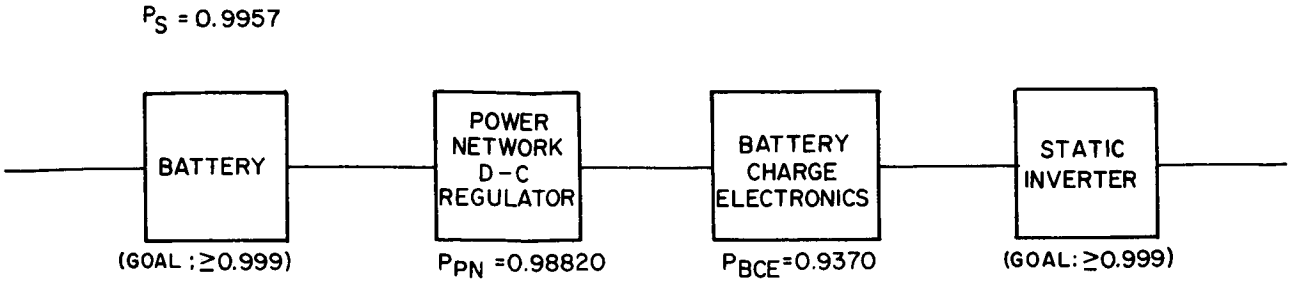

Figure X-132. Portion of Subsystem to be Allocated

Binomial expansion tables were used to determine the probability of survival of at least 5 modules from a set of (5 + X) modules, each having a reliability of 0.98492. The binomial expansion tables show that the probability of survival of at least 5 of 7 modules of reliability 0.98 is 0.999737. The P_s for 5 of 6 modules is 0.994313. Therefore 2 spares are required for a total P_s of 0.999 over a 90-day period.

All results for the battery charge electronics power module calculations are shown in Table X-31. Similar calculations were made to determine the required number of d-c Regulator power module spares for variable baseline and resupply intervals. The results of these calculations are shown in Table X-32. For the static inverter power modules, calculations were performed using various MTBF's, since the specific inverter configuration and associated MTBF are as yet undetermined. The results for the inverter are shown in Tables X-33, X-34, and X-35.

TABLE X-31. BATTERY CHARGE ELECTRONICS, POWER MODULES

Number of Baseline Modules	Number of Spares* for Resupply Interval of			
	45 Days	90 Days	180 Days	1 Year
1	1	1	1	2
2	1	2	2	2
3	1	2	2	3
4	1	2	2	3
5	2	2	2	3
6	2	2	3	4
7	2	2	3	4
8	2	2	3	4
9	2	3	3	5
10	2	3	4	5

$P_s \geq 0.999$ for the interval
* Operating plus non-operating spares

TABLE X-32. DC REGULATOR, POWER MODULES

Number of Baseline Modules	Number of Spares* for Resupply Interval of			
	45 Days	90 Days	180 Days	1Year
1	1	1	1	1
2	1	1	1	1
3	1	1	1	1
4	1	1	1	2
5	1	1	2	2
6	1	2	2	2
7	1	2	2	2
8	1	2	2	2
9	1	2	2	2
10	1	2	2	3

$P_s \geq 0.999$ for the interval
* Operating plus non-operating spares

TABLE X-33. INVERTER MODULES

Number of Baseline Modules	Number of Spares* for Resupply Interval of			
	45 Days	90 Days	180 Days	1 Year
1	2	2	4	6
2	2	3	5	8
3	3	4	6	
4	3	4	6	
5	3	4		
6	3	5		
7	4	6		
8	4	7		
9	4	7		
10	5	7		

$P_s \geq 0.999$ for the interval (module MTBF = 20,000 hours)
* Operating plus non-operating spares

TABLE X-34. INVERTER MODULES

Number of Baseline Modules	Number of Spares* for Resupply Interval of			
	45 Days	90 Days	180 Days	1 Year
1	1	2	2	4
2	2	2	3	5
3	2	3	4	6
4	2	3	4	6
5	2	3	4	7
6	3	3	5	
7	3	4		
8	3	5		
9	3	5		
10	4	5		

$P_s \geq 0.999$ for the interval (module MTBF = 40,000 hours)
* Operating plus non-operating spares

TABLE X-35. INVERTER MODULES

Number of Baseline Modules	Number of Spares* for Resupply Interval of			
	45 Days	90 Days	180 Days	1 Year
1	1	2	2	3
2	2	2	3	4
3	2	2	3	4
4	2	2	3	5
5	2	3	4	5
6	2	3	4	6
7	2	3	4	
8	2	3	5	
9	3	4	6	
10	3	4	6	

$P_s \geq 0.999$ for the interval (module MTBF = 60,000 hours)
* Operating plus non-operating spares

c. BATTERY RELIABILITY ANALYSIS

The reliability apportionment ($P_s = 0.999$) for the total battery portion of the power supply will be handled by techniques similar, but not identical, to those employed for the regulator power networks and the inverters. In establishing battery reliability, a straightforward and basic approach has been adopted. Sections X-B and X-C-3 contain a description of the methods and techniques by which the battery size is selected for any altitude and mission life. This has been based on cycle life, charge acceptance, and maximum discharge depth considerations. A basic assumption, that the combination of criteria developed for sizing the battery will result in an equally reliable component for any mission condition, has been made. For example, a Ni-Cd storage cell, discharged to 16-percent depth in a 200-nmi orbit and which has to undergo 5700 charge-discharge cycles in one year and be recharged at an average charge rate of C/5 (5-hr relative), has a probability of survival number equal to that of a different-size Ag-Cd cell, designed to discharge to 48-percent depth and be recharged at a C/30 rate and survive 365 cycles, as it would in a synchronous orbit application. This probability of survival number would be the same for any other storage cell size selected for another set of mission requirements, as long as the selected cell parameters agree with, or are within, the selection criteria developed in the study.

The above ground rule is an approximation. For instance, the Ni-Cd battery mentioned in the preceding paragraph for the 200 nmi altitude application is in reality adequate for up to 600 days of orbiting, based on cycle life data included in Figure X-66. The Ag-Cd battery mentioned later, based on 48-percent depth and cycle life data, is just adequate for one year's worst-case cycling. The two systems are not equally reliable since the Ni-Cd at the lower altitude is more reliable in that it is not stressed to the limit of its cycle life capability during a one-year mission. Tables X-36 and X-37 give spares and reliability apportionments for the two battery types just discussed. The scope of the present study does not, however, include estimations of the effects of degree of stress on the probability of survival. So long as the storage system is operated within the criteria set forth, equal probability of survival is assumed and no allowance is made for increased reliability due to lower-than-rated cycle life. To that extent, the spares apportionment for the batteries in Tables X-36 and X-37 are worst-case.

The case of the two storage systems used as an example in this section is based on computer runs 1, 2, 5, 6, 9, and 10 (See Appendix B). These runs were used as the basis for the conceptual designs of the power system in section X. G. Considering the existing status of the appropriate storage cell data (particularly in terms of the absence of generally accepted test standards), the approximation developed is believed to be adequate under the circumstances. It is strongly recommended that a follow-up storage cell test program be pursued prior to hardware design, to simulate and test the specific mission environments contemplated.

Numerically, the present approach is based on a fixed probability of survival (P_s) of a storage cell. The storage cells have the following characteristics:

$P_s = 0.9987$/cell (see Appendix F)

TABLE X-36. SPARES AND RELIABILITY APPORTIONMENTS FOR NICKEL-CADMIUM MODULES

Baseline Number of Modules*	Number of Spares	Total P_s
6	2	0.9999
12	2	0.9997
18	2	0.9990
24	3	0.9998
30	3	0.9997
36	3	0.9994
42	3	0.9990
48	4	0.9998
54	4	0.9997
60	4	0.9995

P_s = 0.9935 for each module

* Increments of six are used since there are six modules per battery in the nickel-cadmium system.

TABLE X-37. SPARES AND RELIABILITY APPORTIONMENTS FOR SILVER-CADMIUM MODULES

Baseline Number of Modules*	Number of Spares	Total P_s
4	1	0.9990
8	2	0.9998
12	2	0.9997
16	2	0.9993
20	3	0.9999
24	3	0.9999
28	3	0.9998
32	3	0.9996
36	3	0.9994
40	3	0.9991

P_s = 0.9897 for each module

* Increments of four are used since there are four modules per battery in the silver-cadmium system.

Nickel-Cadminum: 5 cells/module
Silver-Cadmium: 8 cells/module
$P_S = (0.9987)^5 = 0.9935$/Ni-Cd Module
$P_S = (0.9987)^8 = 0.9897$/Ag-Cd Module

The number of spare modules required to maintain a battery reliability of greater than 0.999 for a variable baseline number of modules has been determined using the following relationship:

A probability of survival of at least S, requiring elements from a set of N redundant elements of reliability P is represented by:

$$P(S,N) = \sum_{x=s}^{n} p^x (1-P)^{n-x} \binom{n}{x} \qquad \text{(X-54)}$$

where

$$\binom{n}{x} = \frac{n!}{(n-x)!\,x!}$$

For example, the probability of survival of 6 out of 8 nickel-cadmium modules is represented by:

$$P(6,8) = \sum_{x=6}^{8} (0.9935)^x (0.0065)^{8-x} \left(\frac{8!}{(8-x)!\,x!}\right)$$

Binomial probability tables were used to solve this expression for P (6, 8) =

$$P(6,8) = 0.999946$$

Similar calculations were performed to determine the values tabulated in Tables X-36 and X-37.

The following example illustrates the technique used in forming Tables X-36 and X-37:

Given: Nickel-Cadmium Modules of $P_S = 0.9935$
Baseline of 30 modules

Find: The required number of spare modules to maintain a P_S greater than 0.999.

From the binomial probability tables, the approximate numbers are:

P_S for 30 modules with zero spares is 0.73971

P_S for 30 modules and one spare is 0.96162

P_S for 30 modules and two spares is 0.99601

P_S for 30 modules and three spares is 0.99968

Therefore, three spares are required for a 30-module nickel-cadmium baseline to maintain a total P_s greater than 0.999.

d. SUMMARY OF REDUNDANCY RECOMMENDATIONS

The number of spares required to achieve 0.999 probability of success in certain portions of the subsystem for a mission duration of 1 year is high as can be seen from the data presented in the Tables. This is especially noticeable in the static inverters. For example, if two inverter modules are required, to obtain a P_s of 0.999 with a module MTBF of 20,000 hours and a mission duration of 1 year, 8 spare modules are required. If it is assumed that there is a scheduled resupply within 90 days (2160 hours), only 3 spare inverter modules are required at the start of the mission to obtain a P_s of 0.999 for 90 days. If at the end of 90 days, all inverters are still operative, there would be no need to obtain additional inverters through resupply and the probability of success over the next 90-day interval is unchanged (i.e., still 0.999) since the failure rate of the modules does not change.

The random nature of circuitry failure rates indicates that the likelihood of a failure on the first day of the mission is the same as that for any other time during the mission regardless of the accumulated operating time (providing wearout time is much greater than mission duration). In the event of inverter failures prior to resupply time; spare inverters, equal in number to those which failed, can be requested and the inverter complex restored to a 0.999 reliability. The resupply capability is used here to maintain a continuous reliability of 0.999 throughout the mission. Specific redundancy recommendations cannot be made at this time since the mission requirements are variable. Therefore, Tables X-36 and X-37 are presented and should be referred to when specific missions are selected.

Tables X-31 through X-35 cover the redundancy apportionment recommended for the electronic power modules. The remaining four electronic modules, i.e., failure detect and control (charger/tracker and d-c regulator, see section X.C.1, Table X-29) should have one spare unit of each kind (four in all) per flight; this would constitute a minimum of 50-percent non-operating spares as an added safety feature in the event of any premature failures. Although this will increase reliability, the probabilities of success for these portions of the system are already so high that the resultant improvement in total system reliability may be considered negligible at this time. Tables X-36 and X-37 summarize the spares recommendations for the batteries, in terms of the number of spare modules required. Since the tabulations are based on the assumption of equal cell reliability for all mission conditions (obtained by varying the battery operating parameters to fit each mission), the resupply interval does not appear as a variable. At the end of the specified resupply interval, both the baseline battery assembly and the spare modules would be resupplied.

7. Probability of Crew Survival

The assumption is being made that in case of a catastrophic failure in the spacecraft, the crew would abandon the laboratory and board the command module to attempt a safe descent. In the process of abandoning the spacecraft, a small fraction of the rated power system output will be required. It is assumed that this amount of emergency power would be available as long as at least one of the baseline batteries is operating. To limit the

analysis to a set of worst possible conditions, the probability of at least one battery operating (equated here to the probability of crew survival) will be determined for the conditions of only four baseline Ag-Cd batteries of 100-ampere-hour capacity each (lowest number required in conceptual designs, section X.G.), with all batteries connected through power diodes to a common point where the emergency power would be tapped. Let it also be assumed that replacement of faulty battery modules cannot be made during an emergency situation of the type discussed in this section.

As in section X-D. 6.c

$P_s = 0.9987/\text{cell};$

for 32 cells,

$P_s = (0.9987)^{32} = 0.9593/\text{battery of 32 cells}$

The failure rate of the power diode will be assumed to be 17 failures per 10^9 hours:

$$P_{sd} = e^{-\lambda t} = e^{-(17 \times 10^{-9})(8.76 \times 10^3)}$$
$$= e^{-1.49 \times 10^{-4}}$$
$$= 0.9999$$

where

λ is 17×10^{-9}

t is 8760 hours (1 year)

The probability of success of one battery-diode combination is

$$P_s\,(b\text{-}d) = (0.9999)\,(0.9593) = 0.9592$$

The probability of survival of 1 out of 4 of these combinations is, approximately,

$$P_s\,(b\text{-}d) = 0.9999976$$

Thus, the probability of crew survival in terms of the availability of emergency power is also 0.9999976. If the number of series cells per battery is lower as in a Ni-Cd system, or if the number of baseline batteries is greater, or if some array power can be assumed to be present, the probability of survival would increase beyond the worst-case number calculated.

The amount of stored energy associated with the calculated number is (assuming nominal 100-ampere-hour cells):

$100\,(32)d = 3200d$ watt-hours,

where 32 is approximately the minimum discharge voltage at the diode output, and d is the discharge depth. If d is not allowed to exceed 0.5 as recommended in sections X.C.3, the minimal stored energy is 1.6 kilowatt-hours available in an emergency based on the assumptions stated.

E. COMPUTER PROGRAMS

1. Summary of the Programs Developed

Modern methods employed in design and analysis of space power systems depend on detailed analyses of the mission requirements and the effect of these requirements on several components of unrelated properties. Design sophistication required by present-day standards and the vast amount of information which must be considered in the process calls for heavy reliance on the computer approach. This section describes the computer programs developed by RCA as parametric study and design tools specifically for use in this study program.

The first program written is referred to in Paragraph X.B.3.d(2). It was used to solve equations (X-6), (X-8), (X-10), and (X-12) in Paragraph X.B.3.b, to obtain data for the plots of Figures X-11 through X-17 to assess the efficiency performance of the various power-system configurations. Following selection of the parallel tracker as the proper system choice, another computer program has been written to perform a series of detailed system designs using the parallel tracker as the model configuration. The contents of this section are devoted exclusively to the latter program.

For the present purposes, the computer program to be described will be treated as consisting of two parts, although both are delivered to the customer as one program in Fortran IV format. One is the main part, dealing with system design. The other part is used to perform solar-cell "tradeoffs" and to calculate the end-of-life performance of a fully degraded solar cell. It can be used in conjunction with the main program to perform array designs.

The program has been used at RCA to perform the parametric system studies (Paragraph X.F) and the conceptual designs (Paragraph X.G). The program, in Fortran II format, was run on the RCA 601 computer with approximate running time of ten seconds per solution. Fourteen standard IBM cards were required to completely define a set of mission requirements and machine instructions to initiate a solution. The program was subsequently converted to Fortran IV format.

All component data is stored in the computer, but may be changed or updated as desired by the user. A complete solution is delivered as a printout of the mission requirement inputs, system constraints selected by the program based on these inputs, intermediate results of interest, and final results of the computation performed.

Paragraph X.E.4 contains a description of the available program options and of the fourteen IBM cards used to initiate computer solutions.

2. Main Program

a. INTRODUCTION AND GENERAL DESCRIPTION

Description of the Main Program emphasizes the functional aspects of the engineering approach rather than the mechanics of computer implementation described in Appendix C. A description of the required input information is given in terms of the mission requirements

and stored component data. The program itself is described as the performance of a number of individual major functions, which results in a solution composed of a set of numerical program outputs related to the optimum characteristics of the system major components.

Detailed information is provided regarding the major parameters of the entire system, as well as the operating parameters of the individual components, and the degree to which the components would be stressed in actual flight.

Another important feature of the program is that it can help define the range of missions that the power system can support, when provided with a set of known (or assumed) hardware characteristics. This, as well as the other functional uses, can be performed under simulated conditions of variable total load, orbit, altitude, individual load at a given voltage, or charged particle-radiation environment, within certain limitations.

The program will not automatically select the best component type to be used. It is limited to the determination of the optimum parameters for the particular type of component for which data has been stored. For example, if it is desired to minimize the physical size of the energy source (solar array) by way of selecting the best solar cell, and if several options exist in this area, data for each option must be stored in the computer one at a time and several resultant solutions must be compared on an individual basis.

Many individual functions performed rely on weighted average values of component efficiencies, voltages, and other quantities. Although much depends on the accuracy of the input data, small inaccuracies will nevertheless accrue in the process of computation based on average values. A wide range of mission requirements can be tolerated. However, the program is written primarily for missions where there is a fixed total daytime load, and where dark-time loads are required, although the two loads can be vastly different.

Finally, the program applies specifically to the space power system configuration of a parallel tracker. It can apply to certain other systems provided some modification is made of the existing program.

b. INPUT INFORMATION

(1) General

All input information consists of the mission requirements and stored component data.

This mission requirements encompass a variety of independently variable inputs such as load, life, and altitude that would be continuously programmed to obtain a set of computer solutions following the format as outlined in Paragraph X.E.4. On the other hand, the stored component information represents a relatively permanent record, subject to periodic updating as better data is made available.

(2) Mission Requirements

(a) Load. Fixed daytime and dark-time total load power requirements are independently programmed as respective quantities P_{Ld} and P_{Ln} watts. Under the assumption of both a-c and d-c loads present, inclusion of the fraction of total power to be delivered at dc during daytime (f_d) and during dark time (f_n) is also required.

(b) Mission altitude (nautical miles). This is limited to circular earth orbits, although a more flexible approach can be adopted.

(c) Cycle Life. This consists of a number expressing the ratio of the total number of orbits involving dark time to be encountered during life to the maximum possible number of such orbits per year at the assigned altitude. During the computer study phase, this input has been identified with the resupply interval.

(d) Charged-Particle flux. The equivalent 1-MeV electron flux corresponding to (1) the selected solar-cell type, backshielding, and coverglass thickness, as determined by the Solar Cell Program, Paragraph X.E.3, and (2) to the in-orbit life-time. Three options exist, as discussed in Paragraph X.E.4.

(3) Stored Component Information

Where applicable, graphical form of the stored data is as referenced in other sections of this report.

(a) Battery. The program is designed to maintain both nickel-cadmium and silver-cadmium battery data storage. Either can be called upon as a basis for a system solution with individual solutions subsequently compared. The data are described below.

1. Cycle life versus depth of discharge. Figure X-66.

2. Maximum safe depth of discharge d_{max} that must never be exceeded. Used in conjunction with 1 preceding, as an upper limit, d_{max} is 0.5.

3. Maximum average charge rate H_{ave}(max); 5 hours for Ni-Cd, 8 hours for Ag-Cd.

4. Minimum average charge rate H_{ave}(min); 20 hours for Ni-Cd, 30 hours for Ag-Cd.

5. Peak instantaneous charge rate H_{peak}, to limit the charge-current surge. 3 hours for Ni-Cd, 5 hours for Ag-Cd.

6. Relationship between the average charge rate and the effective ampere-hour charge-discharge efficiency factor, e_b. Figure X-69.

7. Number of series cells per battery. 29 for Ni-Cd, 32 for Ag-Cd.

8. Per-cell charge and discharge voltage. Several factors, such as rates of charge (or discharge) and cell temperature, influence the battery terminal voltage. Depth of discharge was chosen as the one factor which has a particularly important effect on voltages. This factor is determined by the program for each new solution sought and is readily taken advantage of as a direct means of relating battery performance to the particular mission. Both voltages (Figures X-67 and X-68) are expressed as time-weighted average values.

9. Per-cell average discharge voltage (to full discharge). Used in converting total stored ampere-hours to watt-hours. 1.2 for Ni-Cd and 1.1 for Ag-Cd.

10. Watt-hours per pound. 7.7 for Ni-Cd, 13.2 for Ag-Cd; includes bus bars, supporting structure and shelves.

11. Watt-hours per cubic foot. 353 for Ni-Cd, 620 for Ag-Cd; includes volume of peripheral equipment as in 10. preceding.

(b) Electronics. Individual parameters are stored for the three major black-box assemblies: PWM* regulator, inverter, and charge electronics. Each assembly is assumed to consist of one or more modules, with the number dependent on the load-power magnitude. Stored quantities are largely on a per-module basis.

1. Maximum full load per power module. Per-module peak output capability, amperes or watts as the case may be, based either on equipment availability, on projected load requirements range, or on a practical upper limit for each module type. The program will determine the exact full-load rating required for each module, within the maximum limitations stored. The assumption is made that power modules built to lower-than-maximum full-load rating stored are equally available or feasible. Stored numbers are: 50 amperes per charger/tracker module, 1400 watts per PWM regulator module, and 1750 watts per inverter module.

2. Charge electronics power module efficiency versus fraction of full load, Figure X-124, where the full load is as determined by the program. It is assumed that the shape of the curve is basically the same over a wide range of absolute full-load values. It is further assumed that the numerical values of the ordinate will remain unchanged over a two-to-one range of absolute values of the full load (a range of practical usage in the program).

3. PWM regulator power module efficiency versus fraction of full load. In this and in the inverter power module case to follow, the same assumptions apply as those made for charge electronics. In addition, a distinction is being made between the lower input voltage during dark time and the higher input voltage during daytime as it affects the device efficiency. Two curves are therefore stored, as shown in Figure X-121.

*Pulse Width Modulated

4. Inverter module efficiency versus fraction of full load, Figure X-123.

5. Module weight versus maximum required per-module output, Figures X-125, X-126, and X-127.

6. Fixed weight. In general, three numbers stored; one for each of the three assemblies. The fixed weight is due to modules other than the power modules, and is assumed to be independent of the number or size of the particular power modules involved. The numbers are: PWM regulator, 33.5 lb, charger/tracker assembly, 34.5 lb, zero pounds for inverter. See Paragraph X.C.4.f(6), Table X-28.

7. Electronics volume, cubic feet per pound. Three numbers are stored: PWM regulator, 0.0280; inverter, 0.0181; charger/tracker, 0.0210. (See Paragraph X.C.4.f(5).)

8. Weight ratio. A fixed factor of 1.1 to account for the weight of peripheral equipment such as telemetry, cabling and harnessing, and special equipment, if present.

9. Volume ratio. A fixed factor of 1.1 as in 8. to account for added volume of peripheral equipment.

(c) Energy Source. Specific information stored in the program applies to a solar-cell array with all information, except pounds per square foot, stored on a per-cell basis.

1. Maximum power per solar cell versus cell temperature for the selected solar-cell type, (Figures X-47 and X-48) produced by means of the Solar Cell Program, Paragraph X.E.3. A family of curves for a range of total equivalent 1-Mev flux values to be encountered. Power per cell is the effective maximum-power-point output at end of life, including all degradation factors. It is based on a detailed analysis of the solar-cell test data, coverglass type and thickness, backshielding, and many other factors considered in the process of reduction of the initial cell output to that related to a practical solar array and described in Paragraph X.E.3. Data are stored for cells of both low and high base-resistivity. Either can be called as an option. See Paragraph X.E.4.

2. Effective area per cell, including the packing loss: 0.0069 square foot per cell.

3. Specific weight of the array assembly, pounds per square foot. Weight includes solar cells, substrate, structure, and any added weight attributable to the solar array. Stored data is given in Figure X-57, as a function of coverglass thickness to which the weight of the backshielding is added.

(d) Temperature. Array temperature profiles are shown in Figure X-22, a family of curves over a range of altitudes showing solar-cell temperature variation as a function of time during the sun-illuminated portion of the orbit.

(e) Orbital Parameters. Minimum fractional time in the sun and the orbital period versus a circular orbit altitude are stored. Also, the maximum possible number of dark times per year calculated as the ratio of the number of hours per year to the duration of the orbital period at the corresponding altitude. See Figures X-7 and X-8.

c. DETAILED DESCRIPTION OF THE APPROACH

(1) Introduction

For discussion purposes, details of the program operation will be described in terms of eight interdependent functions. Emphasis will be placed on both the analytical aspect of the power system design and on the block diagram logic developed as a first step towards implementation of the analysis in computer language.

The manner in which all the input information (referred to in Paragraph X.E.2.b) is used will be discussed in conjunction with each applicable function. It will be shown that a number of intermediate-step parameters is generated, some or all of which can be delivered in addition to the program outputs listed in Paragraph X.E.2.d.

(2) Battery Parameters Function, Figure X-133.

The object of this function is to determine the operating parameters of the storage battery, these are:

(a) depth of discharge factor d, a parameter related to the use of the battery in the discharge mode. It is based on the maximum discharge depth, maximum charge rate, and cycle life limitations.

(b) relative charge rate H (hours), a significant operating parameter when the battery is under charge, determined by the charge time, discharge depth, and charge efficiency.

The input requirements consist of the following battery data: minimum and maximum values of the orbit-average charge rate H_{ave} (min) and H_{ave} (max); relationship of the charge rate to the ampere-hour efficiency expressed as the H/e_b versus H variation; cycle life; the maximum allowable discharge depth d_{max}; mission altitude; life; and the orbital parameters as a function of altitude.

Initially, calculation is made of the orbital period τ and the minimum fractional time in the sun, a, needed to establish the charge time duration, the number of charge-discharge cycles the battery will undergo during life at the assigned altitude, and the numerical values of the ratio of charge rate, H, to effective battery efficiency, e_b, under conditions of the two limiting charge rates, H_{ave} (min) and H_{ave} (max).

The design-parameter or critical depth-of-discharge factor, d, is next calculated. Two separate values are determined; first, d_1, based on cycle life. Since the (d) versus cycle-life

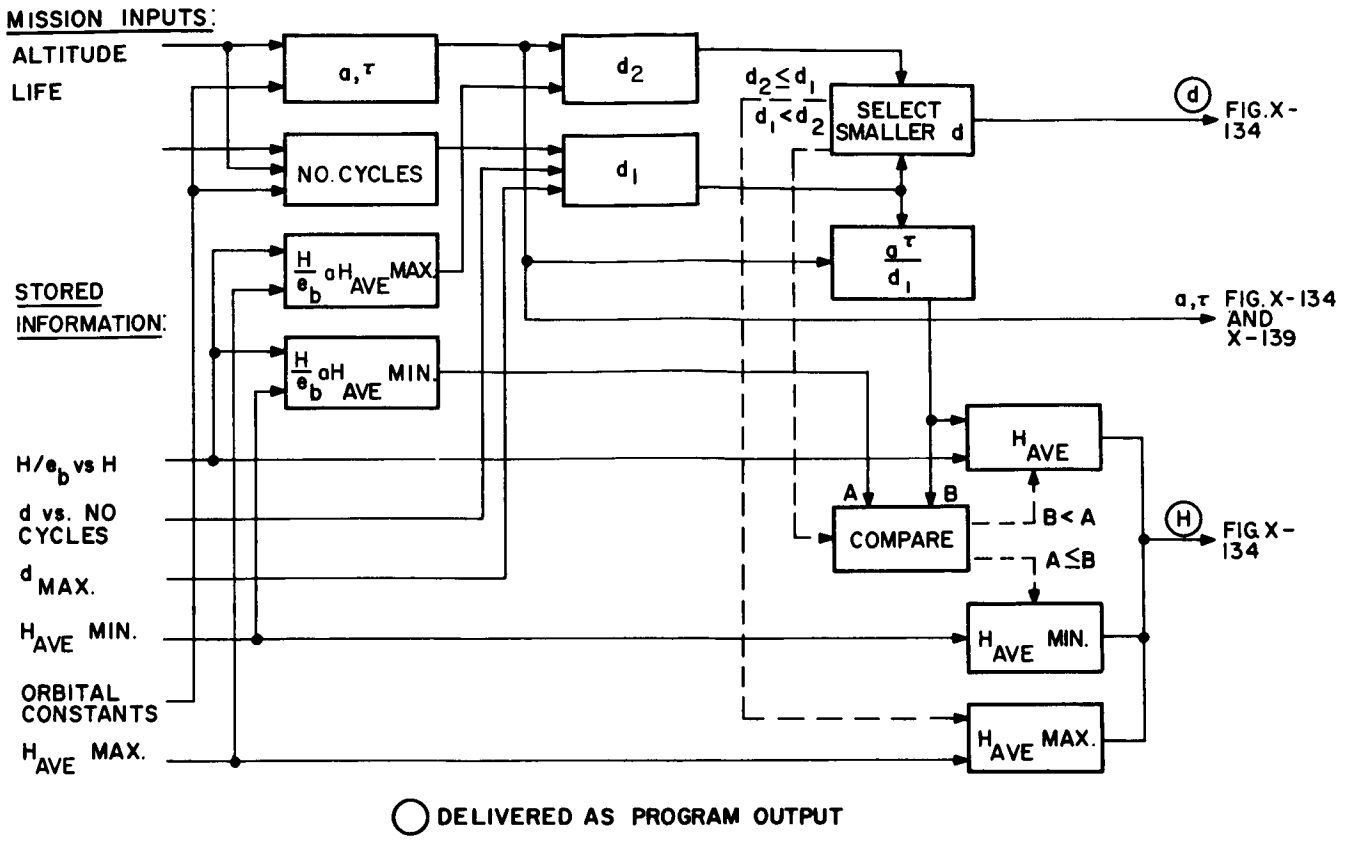

Figure X-133. Battery Parameters Function

data is limited by d_{max}, the resultant d_1 contains the maximum discharge depth criterion, regardless of how low a cycle life may be required. The second value, d_2, is based on the maximum value of the average charge rate H_{ave} (max), calculated by using the expression

$$d_2 = \frac{e_b \, a\tau}{H_{ave} \, (max)} \, . \qquad \text{(X-55)}$$

For clarity, note that H_{ave} (max) corresponds to a low numerical value of H and a high value of average charge current.

The Battery Parameters Function uses this equation (X-55) to solve for d_2; equation (X-55) is, in turn, obtained by solving equation X-20 of Paragraph X.B.3.c(3) for d. Product a τ is determined elsewhere in the function as discussed. The value of H/e_b used is that corresponding to H_{ave} (max) in this case.

The part of the Battery Parameters Function that determines the discharge depth factor is terminated upon comparing the two factors d_1 and d_2, and selecting the smaller of the two as the critical value of the discharge depth to be used in the design of the storage system. Depending on which of the two d values is the smaller, one of two possible actions is initiated to determine the design value of H in the remaining portion of this function.

If the maximum-charge-limited value of d (i.e., d_2) is equal to or less than the cycle-life-limited fraction d_1, an appropriate path is enabled as shown by broken line on the diagram, and the system value of the average relative charge rate is simply $H = H_{ave}$ (max). If, on the other hand, the discharge depth is determined by cycle life (d_1 greater than d_2, and d equal to d_1), the critical value of H can be determined by either the efficiency of the battery or by the minimum charge rate limitation H_{ave} (min), depending on specific circumstances as described below.

Condition $d_1 < d_2$ enables an event shown by the block labeled "compare" in the figure. For discussion purposes, quantity A is the value of H/e_b if H is equal to H_{ave} (min); B is the value of that fraction (H/e_b equal to a τ/d) if d equals d_1 where d_1 has been determined beforehand. Since the "H/e_b versus H" function is monotonic, the higher the numerical value of H/e_b the higher the corresponding numerical value of H, and the lower relative charge rate. It follows that the highest permissible value of H/e_b is that corresponding to H equal to H_{ave} (min). If B equal to $a\tau/d_1$ turns out numerically higher than A (A equal to or less than B as in Figure X-133), too low a charge rate (too high a value of H) is indicated. The Function then forces the output value of H to assume the value of the lowest permissible rate, i.e., H_{ave} (min). But, if B is less than A, the indicated numerical value of H hours is within the H_{ave} (max)-to-H_{ave} (min) range, the value of H is H_{ave} and its specific numerical value is determined by referring to stored information H/e_b versus H.

The output value of H is thus determined via one of three possible paths. It is H_{ave} (max) (as is most often the case at low altitudes), it is H_{ave} (min) (as is the usual case at high altitudes), or it is an in-between value, H_{ave}, if the mission under analysis is one involving an in-between-altitude orbit.

(3) Battery Design Function, Figure X-134

The key operating parameters d and H were determined solely by reference to the device characteristics. The Battery Design Function uses these and other stored or calculated quantities to determine the electrical and physical size of the battery.

Most significant is the calculation of the per-orbit discharge, Q in ampere-hours. This quantity is a function of the dark-time load requirement, discharge time, electronics efficiency, and the particular battery configuration. Numerically, it has been shown to equal

$$Q = \left[1-f_n \left(1-\frac{e_{in}}{e_{ch}}\right)\right] \frac{1-a}{e_{in} V_{Bd}} \tau P_{Ln} \qquad \text{(X-56)}$$

where

f_n is fraction of d-c power to be delivered during dark time,

e_{in} is inverter efficiency, dark time,

e_{ch} is efficiency factor of charger tracker,

a is minimum fractional sun time,

V_{Bd} is average battery discharge voltage,

τ is orbital period, and

P_{Ln} is fixed dark time total load requirement.

in equation (X-3) of Paragraph X.B.3.a. Subscripts "n" in the preceding equation (X-56) indicate the dark-time (low) input voltage values of the efficiency factors for the regulating electronics.

The solution of equation (X-56) is performed by this Function using programmed load information, orbital parameters, average electronics efficiencies (determined elsewhere by the program as shown in Figure X-134), and a calculated value of the average battery discharge voltage, V_{Bd}. The latter is calculated simply by multiplying the number of series storage cells by the average discharge voltage per cell that corresponds to the critical depth of discharge factor d delivered by the Battery Parameters Function. Likewise, the average battery charge voltage V_{Bc} is determined by table reference of an appropriate per-cell average charge voltage followed by multiplication by the number of series cells. V_{Bc} is delivered to other functions performed by the program.

After Q has been determined, the battery capacity C is found using the relationship C equals Q/d.

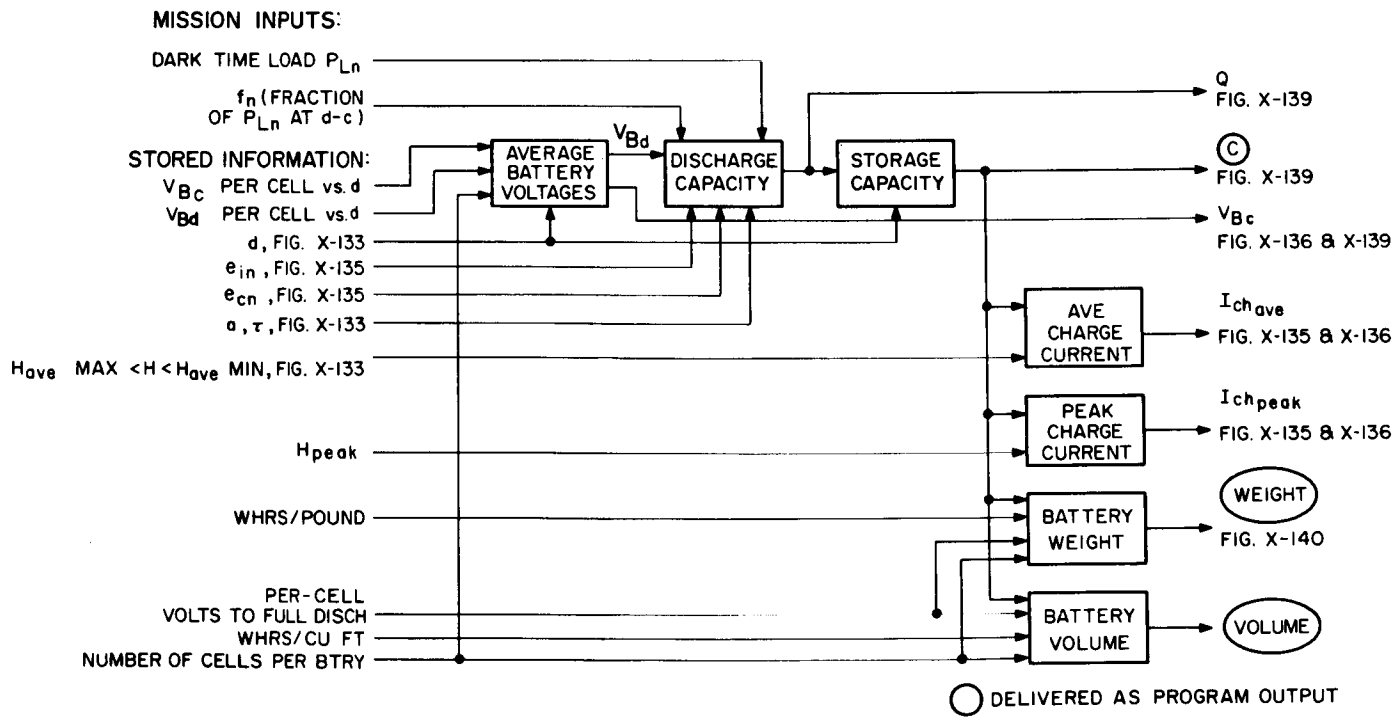

Figure X-134. Battery Design Function

Other parts of the program require calculated values of the average charge current I_{ch}(ave) as well as the largest possible safe charge current I_{ch} (peak). Both current values are calculated by dividing C by the appropriate H quantity as shown in Figure X-134.

The remaining function of the Battery Design is to establish the physical characteristics of the storage system, i.e., volume and weight. Additional stored inputs required are the watt-hours per cubic foot and per pound, and the average per-cell voltage at full discharge. The function converts C ampere-hours to watt-hours by multiplying C by the above per-cell voltage and by the number of cells, and then by dividing the product by the appropriate characteristic parameter.

(4) Electronics Function, Figure X-135.

Various design parameters are calculated for the inverter, the PWM d-c load regulator, and the charge electronics. These are: efficiencies, number of power modules, per-module power design requirements, weight, volume, and other quantities. Identical logic is used to perform calculations for both the inverter and the d-c regulator. A slightly less complex approach is possible in the charge electronics, since it is active only during daytime. See Figure X-135.

In the inverter case, mission inputs regarding load are used to determine the inverter power module parameters. Thus, during dark time, the amount of a-c load power is $(1-f_n)\ P_{Ln}$; during daytime, it is $(1-f_d)\ P_{Ld}$. The two quantities are calculated and compared, and the larger of the two selected to size the inverter.

Sizing of the inverter assembly proceeds in the following manner. The largest load to be delivered is divided successively by 1, 2, 3...n, until the ratio becomes equal to, or less than the stored amount of the maximum permissible per-module output power. The lowest whole number n to meet this criterion becomes the number of inverter power modules required. The largest total load to be delivered, divided by n, is the required per-module power rating. It cannot exceed the maximum permissible full load stored and is the value of the maximum load to which the inverter power modules would be designed to meet the requirements of these specific mission inputs.

The two average efficiencies of the power module thus designed, viz. daytime (e_{id}) and dark time (e_{in}), are now determined. Let it be supposed that the larger of the two loads as determined in the preceding paragraph had occurred during daytime. The daytime efficiency factor e_{id} would, therefore, correspond to the e_{id} factor stored for the 100-percent load condition, since the electrical size of the power modules has been selected to just meet the peak load demand.

The dark-time efficiency factor corresponds to an assumed lower load condition in this case. To determine e_{in}, the total dark-time load is divided by the number of power modules, and the resultant ratio divided by the daytime per-module load calculated. The result is the fraction of the full load delivered during dark time. The e_{in}ave versus percent load table is entered to determine the value of the efficiency factor sought.

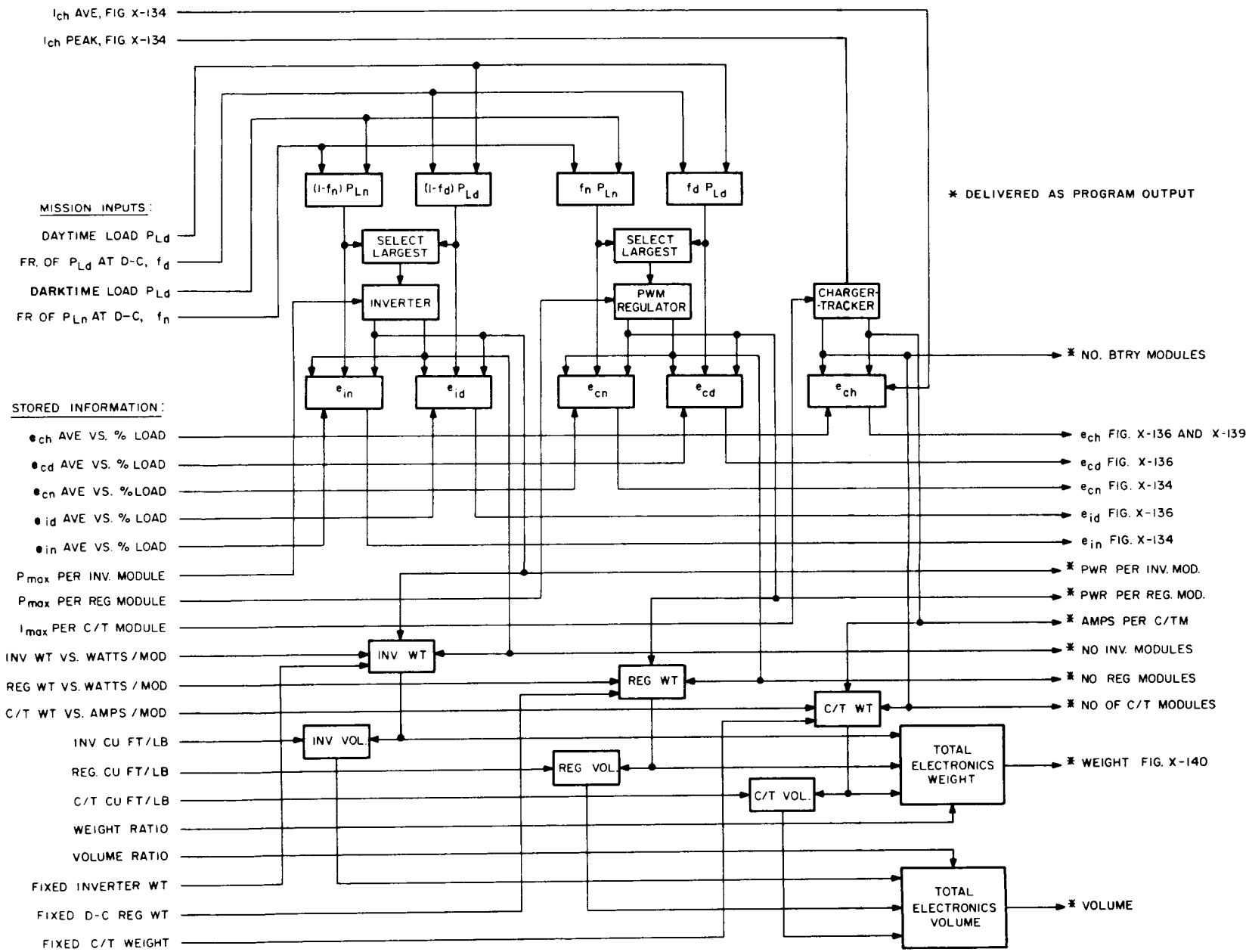

Figure X-135. Electronics Function

The remainder of the inverter calculation is the determination of the weight and volume. Module weight information is stored as pounds per maximum output. Based on that and the number of power modules, total module weight is determined. To the total power module weight, the fixed inverter weight is added (fixed weight is assumed to be zero in the inverter case). The result is the total weight of the inverter assembly. The volume is found by multiplying the calculated weight number by the cubic-feet-per-pound factor stored for the inverter.

From Figure X-135, it is evident that the method of calculating the PWM regulator assembly parameters is, in every way, the same as that described for the inverter.

For the charge and tracking electronics, the maximum permissible total battery charge current I_{ch} (peak) is used to find the number of power modules and the design value of the per-module peak current. I_{ch} (peak) is successively divided by whole numbers 1 through n, until the ratio is equal to or less than the peak capability of the device as stored under "Stored Information". The number of charge electronics power modules (and, therefore, the number of battery modules), as well as the peak current design value per power module are thus determined. To calculate the average efficiency factor e_{ch}, the total average charge current required (I_{ch}ave) is divided by the calculated number of power modules, and divided again by the per-module peak-current design value. The resultant ratio is the fraction of full load from which e_{ch} is determined. Weight and volume are determined in the same manner as explained for the inverter.

The last operation performed by the Electronics Function is the determination of the total weight and volume of all the regulatory and protective electronics. The three individual weights and volumes are added, and each sum multiplied by a corresponding fixed factor (assumed equal to 1.1 at present) to account for peripheral electronic equipment.

(5) Source Requirements Function, Figure X-136

This function establishes the source power requirements to which the solar array must be designed. These requirements consist of two parts. First is the amount of power needed to supply the daytime load requirements (see Paragraph X.B.3.a).

$$\text{source power to load} = \frac{P_{Ld}}{e_{id}} \left[1-f_d \left(1-\frac{e_{id}}{e_{cd}}\right)\right]. \qquad \text{(X-57)}$$

Second is the amount of battery-charge power,

$$\text{source power to battery} = \frac{V_{Bc}}{e_{ch}} I_{ch(ave)} . \qquad \text{(X-58)}$$

Both magnitudes, as defined by the equations, are reflected to the unregulated bus (array output bus) with their sum and individual values delivered to the Array Design Function, as shown in Figure X-137.

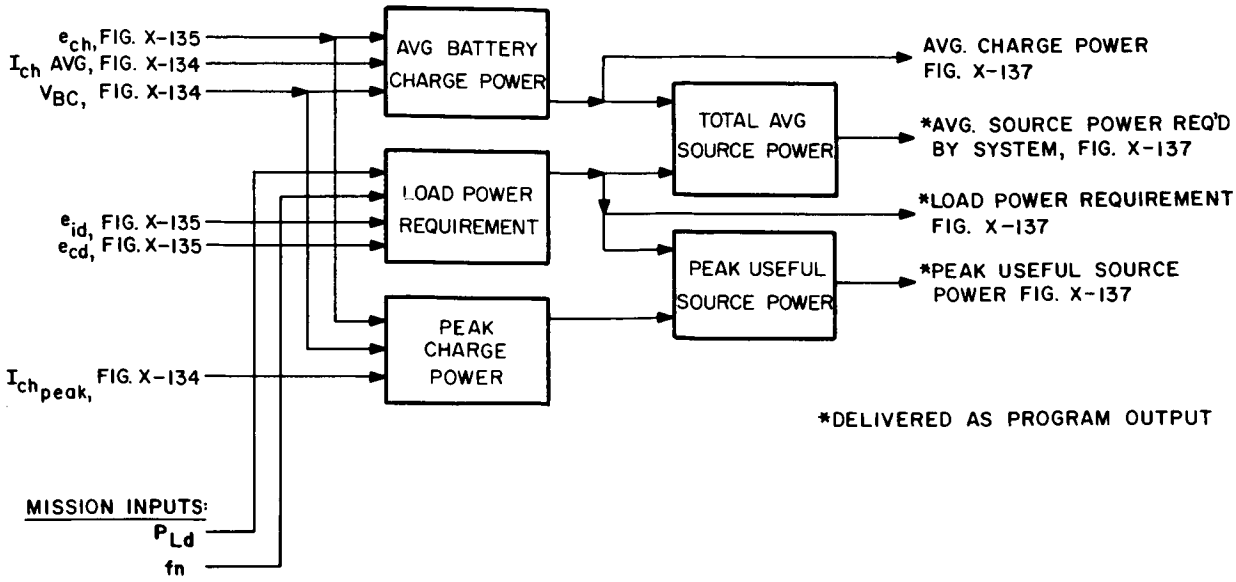

Figure X-136. Source Requirements Function

In addition to that, the peak useful source output power is calculated. Its magnitude is based on the value of I_{ch} (peak) rather than I_{ch} (ave). It is the maximum source power which can be absorbed by the power system at any time as dictated by the load and the maximum allowable value of the relative charge rate H_{peak}.

(6) Array Design Function, Figure X-137

For a given mission input regarding the charged particle radiation level, an appropriate per-cell maximum power versus temperature characteristic is selected from stored data shown in Figure X-47 or X-48. Also, the appropriate temperature-time variation corresponding to the mission altitude is selected from the stored temperature data, Figure X-22, Paragraph X.C.2.a(2). The two selected characteristics enable the program to determine the average per-cell power delivered during the sun-illuminated part of the orbit.

The "first-cut" number of cells is found by dividing the source power requirement determined by the Source Requirements Function, Figure X-136, by the orbit-average maximum power per cell. The remainder of the Array Design Function performs a modification of the first-cut number of cells in order to make the array design compatible with the limitations imposed by the battery on a tracker power system.

In a tracker system, all of the added solar-cell power available during the thermal transient is presumed to be absorbed by the battery. However, if this statement is taken literally and if the large current surge available during the initial 2 to 3 minutes is delivered to the batteries unchecked, excessive relative charge rates of the order of one hour or less may result. (See Paragraph X.B.3.g.) For this reason, the program has been designed to take the H_{peak} limitation into account. The first step in that direction was taken in the Battery Design

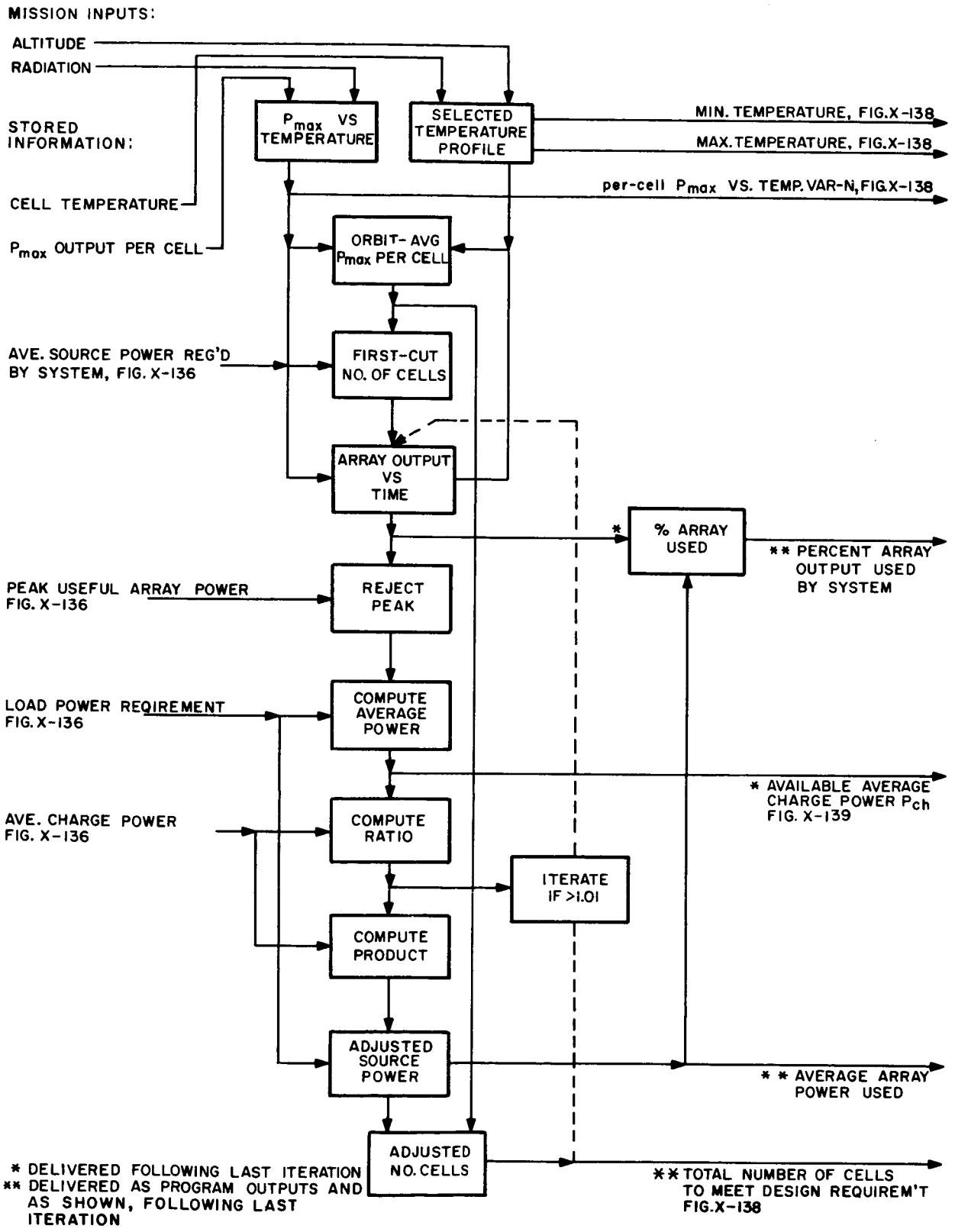

Figure X-137. Array Design Function

Function where the total peak charge rate which must not be exceeded (I_{ch} (peak)) was calculated.

In effect, this limitation amounts to the rejection of a small part (1 to 2 percent maximum) of the total available array energy. Despite this rejection, a tracker system can still tap a large block of source energy not utilized in a non-tracking system.

The "first-cut" number of solar cells calculated thus far by the Array Design Function does not as yet reflect the small amount of added cells needed to compensate for the rejected excess energy. The compensation process is accomplished in the following manner.

Array output power variation versus time is computed by the program, using the first-cut number of cells. Then, the positive difference between this variation and the peak useful array power (computed by the Array Requirements Function) is subtracted, thus providing the variation in array output versus time, with a clipped peak. When the load power requirement is subtracted from the latter variation, the remainder is the instantaneous variation of the array output versus time, delivered as battery charge. Average battery charge is then computed, and a ratio of the required battery charge (from Array Requirements Function) to the available average charge is computed. The ratio is always greater than unity.

If the ratio is greater than 1.01 (i.e., if the available charge energy deficiency exceeds one percent following clipping), an "iterate" path is enabled (this is discussed later in this section). In any event, the required battery-charge power is multiplied by the ratio, and the resultant product added back to the array power intended to supply the daytime loads. The sum equals the adjusted average array power requirement delivered as "Average Array Power Used". Dividing the latter by the orbit-average per-cell power calculated previously yields the adjusted number of cells required per array.

If the "iterate" path is open, the adjusted number of cells is returned to the block labeled "Array Output versus Time", in Figure X-137, and used in place of the first-cut number of cells. The entire sequence is repeated until the resultant ratio is 1.01 or lower, causing the "iterate" path to close.

Each successive iteration has the effect of adding a few more cells to the array, until the battery charge-power availability matches the requirement within one percent or better. In actual computer runs, only one or two iterations are needed. To define the amount of array overdesign needed to compensate for the rejected array energy, the amount of average source power available from the array prior to clipping is compared to the final adjusted array average power used. The result is delivered as a program output in terms of "percent array output used by system".

(7) Array Output Function, Figure X-138

Additional array parameters are computed by this Function shown in Figure X-138. The per-cell minimum and maximum power (at the maximum power point) is computed, using the selected cell characteristics (Figure X-137) and the temperature extremes.

Area and weight are calculated in a manner which is self-explanatory.

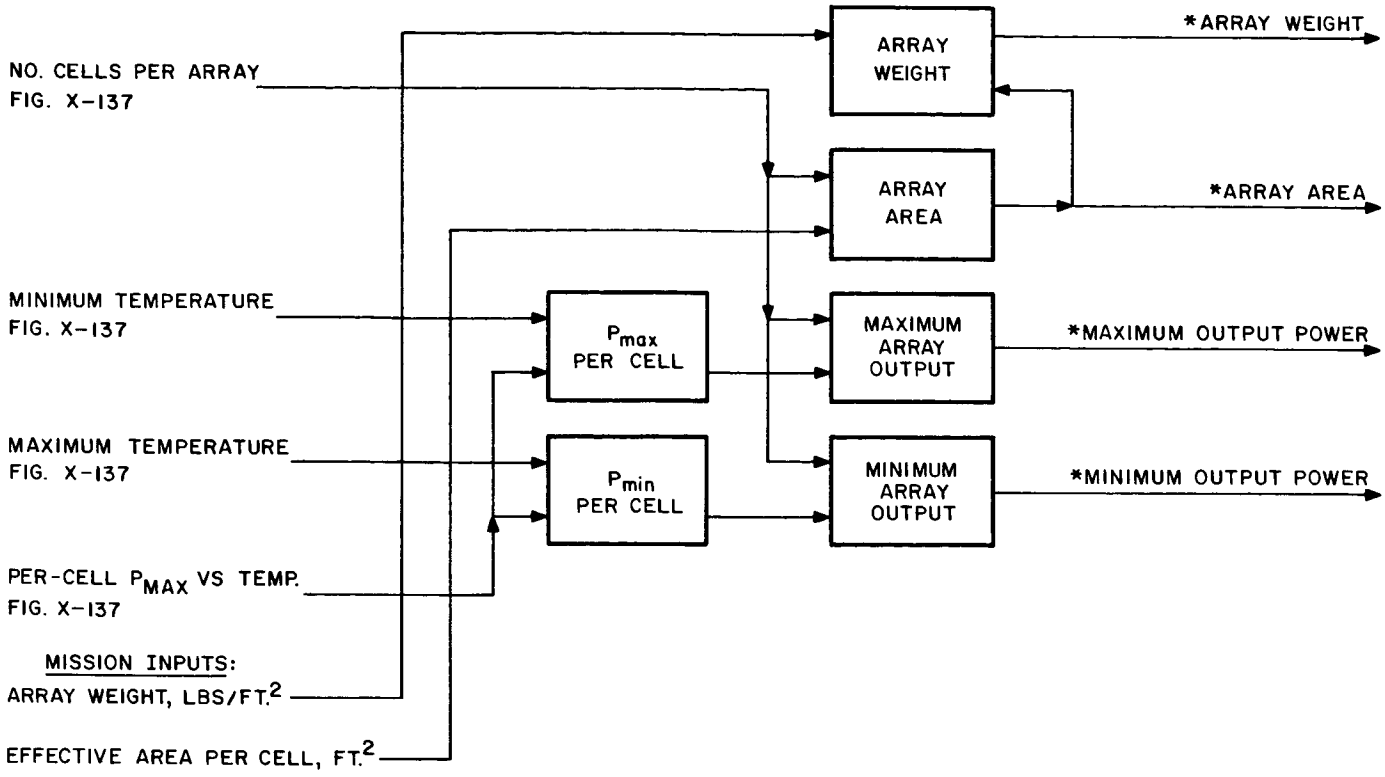

Figure X-138. Array Output Function

(8) Self-Check and Monitoring Function, Figure X-139

The required value of the average charge rate H was determined by the Battery Parameters Function, Figure X-133. This Function calculates the actual rate, based on the charge-energy availability for the design performed. The value of the function is based on all the preceding design functions performed (Figures X-134 through X-137). The required and calculated values of H, as determined by the program, are usually within 0.2 percent or less thus yielding confidence regarding the validity of the other systems parameters determined in each solution.

The method of calculation of H in Figure X-139 is based on solving for the ratio of the C to $I_{ch_{ave}}$, where $I_{ch_{ave}}$ is defined as $P_{ch} e_{ch}/V_{Bc}$, and P_{ch} is found in Figure X-137.

Another calculation performed by this Function is that of the effective ratio of ampere-hours charge to ampere-hours discharge (where the latter equals Q). The inverse of that ratio is the effective battery efficiency, e_b in ampere-hours.

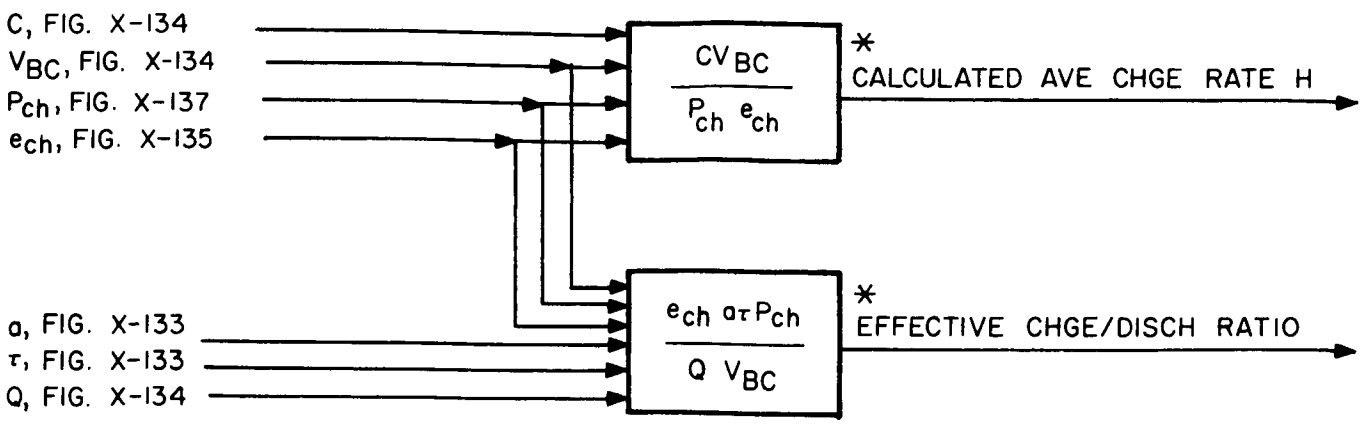

Figure X-139. Self-Check and Monitoring Function

(9) Total weight Function, Figure X-140

This Function performs the summation of the battery, electronics, and array weights, and delivers the total system weight as a program output.

d. MAIN PROGRAM OUTPUTS

The program outputs include the quantities that are the result of the computer calculations performed. They are printed out along with the mission input parameters, selected by the user, and certain intermediate quantities, determined by the program in the course of performing a solution.

A list of parameters selected for delivery as program outputs is shown in the following, together with numerical quantities as determined by the program based on the conceptual design run of a baseline system (computer run No. 1, Appendix B) for a 200-nmi, 28.5° inclination orbit requiring 8.22 kW daytime load and 5 kW dark-time load for a one-year mission. Two-thirds of all loads draw power from the d-c regulated bus. An oriented solar array and a nickel-cadmium battery are used in the power system. Note that the following parameters apply to a baseline system as determined by the computer, i.e., excluding spares and redundancy enhancement.

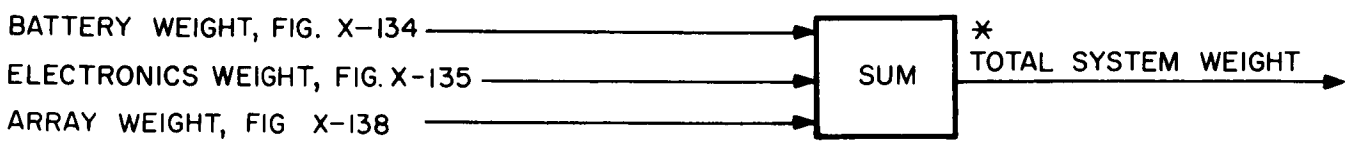

Figure X-140. Total Weight Function

(1) Battery

Capacity, ampere-hours total (all batteries):	610.97
Maximum number of cycles:	5740
Maximum depth of discharge:	16 percent
Required average charge rate:	5.00 hours
Calculated average charge rate:	5.01 hours
Effective charge/discharge ratio:	1.164
Battery weight:	2761.3 pounds
Battery volume:	60.23 cubic feet
Number of battery packs (non-redundant):	5

(2) Solar Array

Average array power used:	15.275 kW
Average array power required by system:	15.287 kW
Percent useful array power:	98.79%
Maximum array power:	23.583 kW
Peak useful array power:	19.008 kW
Minimum array power:	14.488 kW
Array area:	1719.67 square feet
Array weight:	1279.44 pounds
Number of cells (2x3 cm) required:	249,228

(3) Electronics

Number of modules and per-module peak load design value,

PWM regulator:	4,	1370.7 watts d-c each
Inverter:	2,	1368.6 watts a-c each
Charge electronics:	5,	40.73 amperes each
Electronics weight:		488.59 pounds total
Electronics volume:		11.01 cubic feet total

(4) Power System Weight: 4529.32 pounds total, baseline

e. MODIFICATION OF THE MAIN COMPUTER PROGRAM TO PROVIDE SOLUTIONS BASED ON DISCRETE MODULE SIZES

The changes in the Main Program necessary to permit computer solutions based on a truly modular hardware approach in the electronics and battery area are described functionally. At present, the program solves for the optimum electronics module sizes, for the optimum total battery capacity, and for the number of battery modules. This approach is most suitable to parametric studies where firm component size information is not ordinarily available.

Should it be desired to convert the program to a purely modular approach and obtain solutions based on known module sizes, it is recommended that the modifications outlined in this subsection be implemented as an added program option while still maintaining the present "parametric" approach intact. This subsection can be used as an initial guide to appraise the extent of the modifications.

As will be seen from the following discussion, only one added stored component input is required, i.e., the "battery ampere-hours per module". (See Paragraph X.E.2.c.)

(1) Solution for d by the Battery Parameters Function is performed as before, but not delivered anywhere except to determine Storage Capacity C and the average battery voltages, Battery Design Function.

(2) C thus found is delivered only to a new block, labeled A in Figure X-141.

C is divided by the "a-hrs per module" input. The ratio is rounded off to the next-higher integral number and delivered as "number of battery modules".

The number of modules is multiplied by the per-module ampere-hour capacity input; the product is the actual baseline capacity C_a, delivered by the Battery Design Function in place of the previous C. The actual depth of discharge d_a is the ratio of Q and C_a, where Q is determined exactly as before.

(3) Solution for H. Factor d_a is fed to the Battery Parameters Function and action is initiated as if d_1 were smaller than d_2 as stated previously. In the modified program, the other possible alternative action (d_2 equal to or less than d_1) is never initiated since increased capacity C_a (greater than C) discharged to shallower depth d_a (less than d equal to d_2) will not result in rates exceeding H_{ave} (max) (provided proper computation of d_2 and d has been made in the first place).

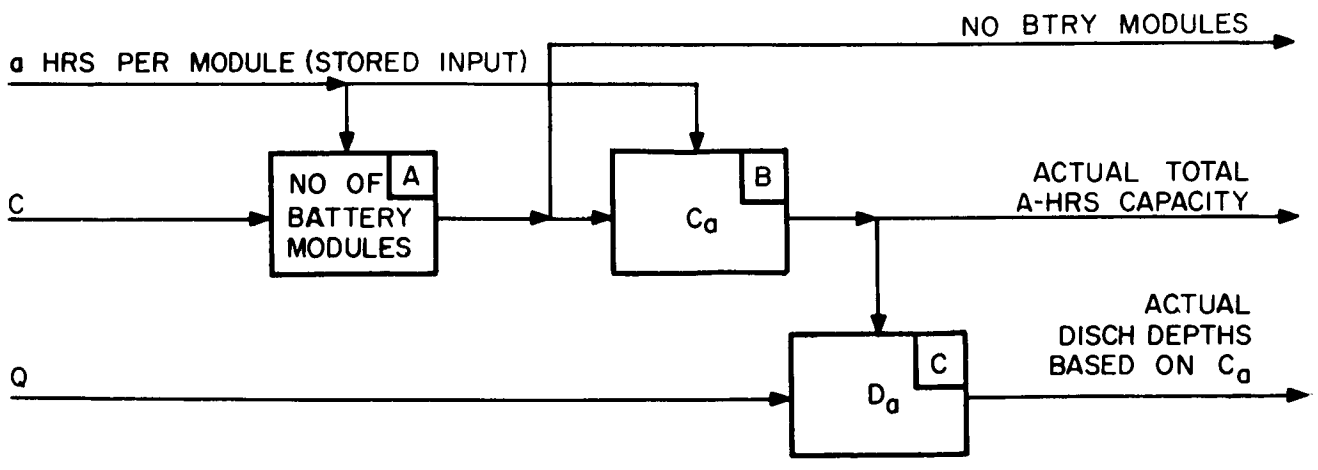

Figure X-141. Adjustment of C and d for Modular Hardware Approach

Thus, the average charge rate as now computed will be either H_{ave} or H_{ave} (min) and delivered to the Battery Design Function as before for I_{ch} (ave) calculation and as a program output called "Required Average Charge Rate".

(4) Other effects of redefined C and discharge depth. I_{ch} (peak) is found as before except that the capacity is now C_a. For all practical purposes, battery weight and volume calculation should be left unchanged, i.e., C_a is converted to watt-hours and divided by watt-hours per pound and watt-hours per cubic foot.

(5) Charge Electronics. Exactly the same approach is used as before, except that three of the stored inputs must bear the relationship

$$\text{peak amperes per module} = \frac{\text{battery module capacity, ampere-hours}}{H_{peak}}$$

(6) PWM Regulator and Inverter. Presently, the program selects the peak design value of the per-module load within a maximum limitation stored. The new method would make the peak design value equal to the stored maximum.

The "larger of the two loads" would be divided by the maximum per-module load and the ratio rounded off to the next-highest integral number. That number would be the number of baseline modules. Each load, daytime and dark-time, would then be divided by that number, and divided again by the stored "maximum load per module". The result is equal to the fraction of full load in each case. The two fractions are entered into the "efficiency vs. load" tables to find the efficiency factors (four in all). The efficiency factors would be handled in the same way as described in Paragraph X.E.2.C.

3. Solar Cell Program

a. INTRODUCTION

The purpose of this subsection is to describe the techniques used to determine solar-cell performance as influenced by the environmental parameters encountered during a given mission.

Three computer subroutines have been developed that implement these techniques to provide the required solar-cell information to the Main Program (Paragraph X.E.2). The three subroutines are as follows:

(1) PHI. This subroutine converts the charged-particle raw flux encountered by a solar cell during its flight lifetime to an equivalent 1-MeV electron flux as a function of the coverglass and backshielding thicknesses selected.

(2) DEGRADE. This subroutine simulates degradation of the solar-cell output characteristics (I-V curve) to account for the reduction of output power caused by the charged-particle flux to which the cell is exposed.

(3) STASH. This subroutine operates on the solar cell I-V curve to account for all other degradation factors besides charged-particle irradiation, i.e., current, voltage, and series-resistance degradation factors as well as temperature effects.

Figure X-142 presents a flow chart of the calculations involved in the three solar-cell subroutines. Blocks 1 through 10 on the flow chart constitute subroutine PHI, blocks 11 through 25 constitute subroutine DEGRADE, and blocks 26 through 31 constitute subroutine STASH; blocks 32, 33, 34 are located in the main program to determine total solar array weight.

The equations and tabulated data presented in the following discussion were empirically derived from laboratory measurements on 1 and 10 ohm-cm solar cells from the RCA Mountaintop, Pa. plant. Similar data for other manufacturers' solar cells may be obtained from a laboratory measurements program.

The Solar Cell Program may be used separately or in conjunction with the Main Program. It can be used to determine the effective, degraded, solar-cell output by using either an assumed value of the 1-Mev flux ϕ_T, in which case the PHI subroutine is bypassed, or by calculating ϕ_T from the raw flux data N_e, N_p, N_{fp}, and Nfa. In either case, resultant cell data is either printed out or fed automatically to the Main Program. An example of the use of the Solar Cell Program as a separate analytical tool is in the determination of the solar-cell parameters needed to perform the tradeoffs discussed in Paragraph X.C.2.b and in calculation of the solar-cell data stored in the Main Program (Paragraph X.E.2.b(3)(c) 1).

b. CALCULATION OF THE 1-Mev ELECTRON FLUX

(1) General. Solar-cell-parameter (short-circuit current, maximum power and open-circuit voltage) degradation due to charged-particle irradiation is usually defined as a function of the damage-equivalent, normally incident (DENI) 1-MeV electron flux because of the preponderance of data existing for bombardment of solar cells with this low energy, monoenergetic particle. Converting orbital fluxes to a DENI 1-MeV electron flux thus obviates the necessity for exact simulation of the orbital irradiation environment to determine the resulting solar-cell degradation.

(2) Orbital Fluxes. The charged particles that produce damage in solar cells are the electrons, protons, and alpha particles encountered in the launch-to-orbit transition during the orbit lifetime and during a solar flare occurrence. The estimated orbital fluxes are introduced to the computer in the following formats:

(a) Table X-38. Electrons within an energy range ΔE, encountered during the transition and orbital lifetime, are summed to give the total electron flux N_e within each energy range of interest.

(b) Table X-39. Protons within an energy range ΔE, encountered during the transition and orbital lifetime, are summed to give the total trapped proton flux N_p within each energy range of interest.

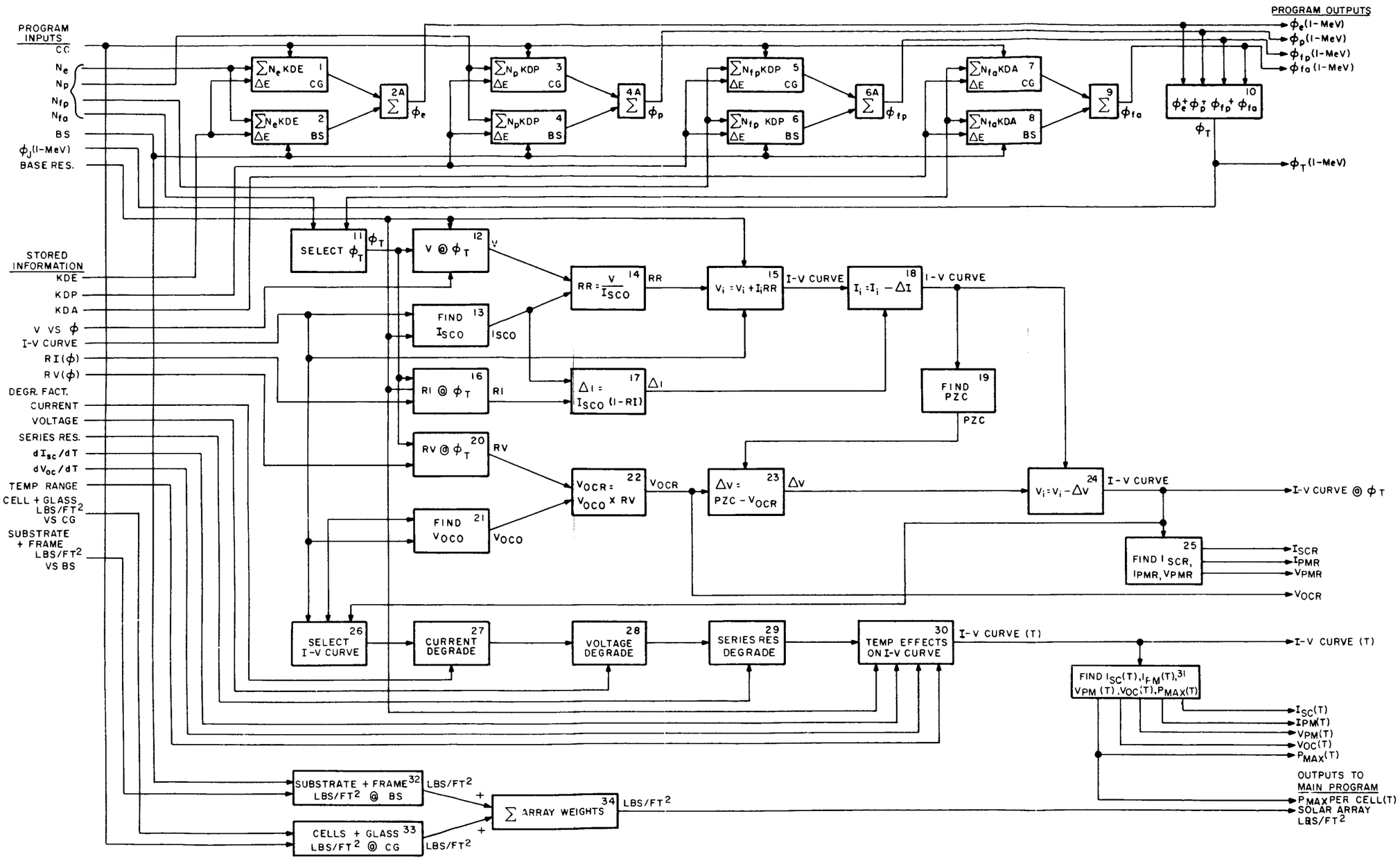

Figure X-142. Computerized Study Flow Chart Solar-Cell Subroutine

X-235-1

TABLE X-38. ELECTRON FLUX FORMAT

Energy Range No.	ΔE (MeV)	Transition Electrons (No./cm^2)	Orbital Electrons (No./cm^2/yr)	Total Electrons (No./cm^2/yr)
1	0 to 0.25			↑
2	0.25 to 0.5			
3	0.5 to 0.75			
4	0.75 to 1.0			
5	1.0 to 2.0			N_e
6	2.0 to 3.0			
7	3.0 to 4.0			
8	4.0 to 5.0			
9	5.0 to 6.0			
10	6.0 to 7.0			
11	7.0 to 8.0			↓

TABLE X-39. PROTON FLUX FORMAT

Energy Range No.	ΔE (MeV)	Transition Protons (No./cm^2)	Orbital Protons (No./cm^2/yr)	Total Protons (No./cm^2/yr)
1	0 to 1			↑
2	1 to 2			
3	2 to 3			
4	3 to 4			
5	4 to 5			
6	5 to 6			
7	6 to 7			
8	7 to 8			
9	8 to 9			N_p
10	9 to 10			
11	10 to 11			
12	11 to 12			
13	12 to 13			
14	13 to 14			
15	14 to 15			
16	15 to 30			
17	30 to 100			
18	> 100			↓

(c) Table X-40. Solar-flare protons within an energy range ΔE, encountered during a solar-flare occurrence, are considered as a flux per year N_{fp} over the energy range of interest.

(d) Table X-41. Solar-flare alpha particles within an energy range ΔE, encountered during a solar-flare occurrence, are considered as flux per year N_{fa} over the energy range of interest.

TABLE X-40. SOLAR FLARE PROTON FLUX FORMAT

Energy Range No.	ΔE (MeV)	Total Protons (No./cm^2/yr)
1	0 to 1	
2	1 to 2	
3	2 to 3	
4	3 to 4	
5	4 to 5	
6	5 to 6	
7	6 to 7	
8	7 to 8	
9	8 to 9	N_{fp}
10	9 to 10	
11	10 to 11	
12	11 to 12	
13	12 to 13	
14	13 to 14	
15	14 to 15	
16	15 to 30	
17	30 to 100	
18	> 100	

TABLE X-41. SOLAR FLARE ALPHA PARTICLE FLUX FORMAT

Energy Range No.	ΔE (MeV)	Total Alphas (No./cm^2/yr)
1	16 to 18	
2	18 to 20	
3	20 to 22	
4	22 to 25	
5	25 to 30	
6	30 to 32	
7	32 to 35	
8	35 to 40	
9	40 to 45	N_{fa}
10	45 to 47	
11	47 to 52	
12	52 to 57	
13	57 to 60	
14	60 to 80	
15	80 to 100	
16	100 to 200	
17	200 to 400	
18	> 400	

(3) Damage Factors. The flux of each type of charged particle in each energy range described in Paragraph X.E.3.b(2) must be multiplied by a factor to obtain the equivalent 1-MeV flux. These damage factors are presented in Figures X-143 through X-145,* which show the number of DENI 1-MeV electrons for each electron, proton, and alpha particle in the energy ranges of interest as a function of solar-cell-shielding thickness. The

* The basic data for Figures X-143 and X-144 were obtained from Reference (X-17). Figure X-145 is based on a discussion with the authors of Reference (X-18).

shielding shown in Figures X-143 through X-145 is defined as grams per square cm; the equivalent thickness of coverglass (fused silica) and backshielding (aluminum) is listed in Table X-42.

Average damage factor values have been obtained from Figures X-143 through X-145 for each energy-range number for the three particle types for the five shielding thicknesses. The average damage factors are shown in Table X-43 for electrons, in Table X-44 for protons, and in Table X-45 for alpha particles. Note in Table X-43, X-44, and X-45 that the

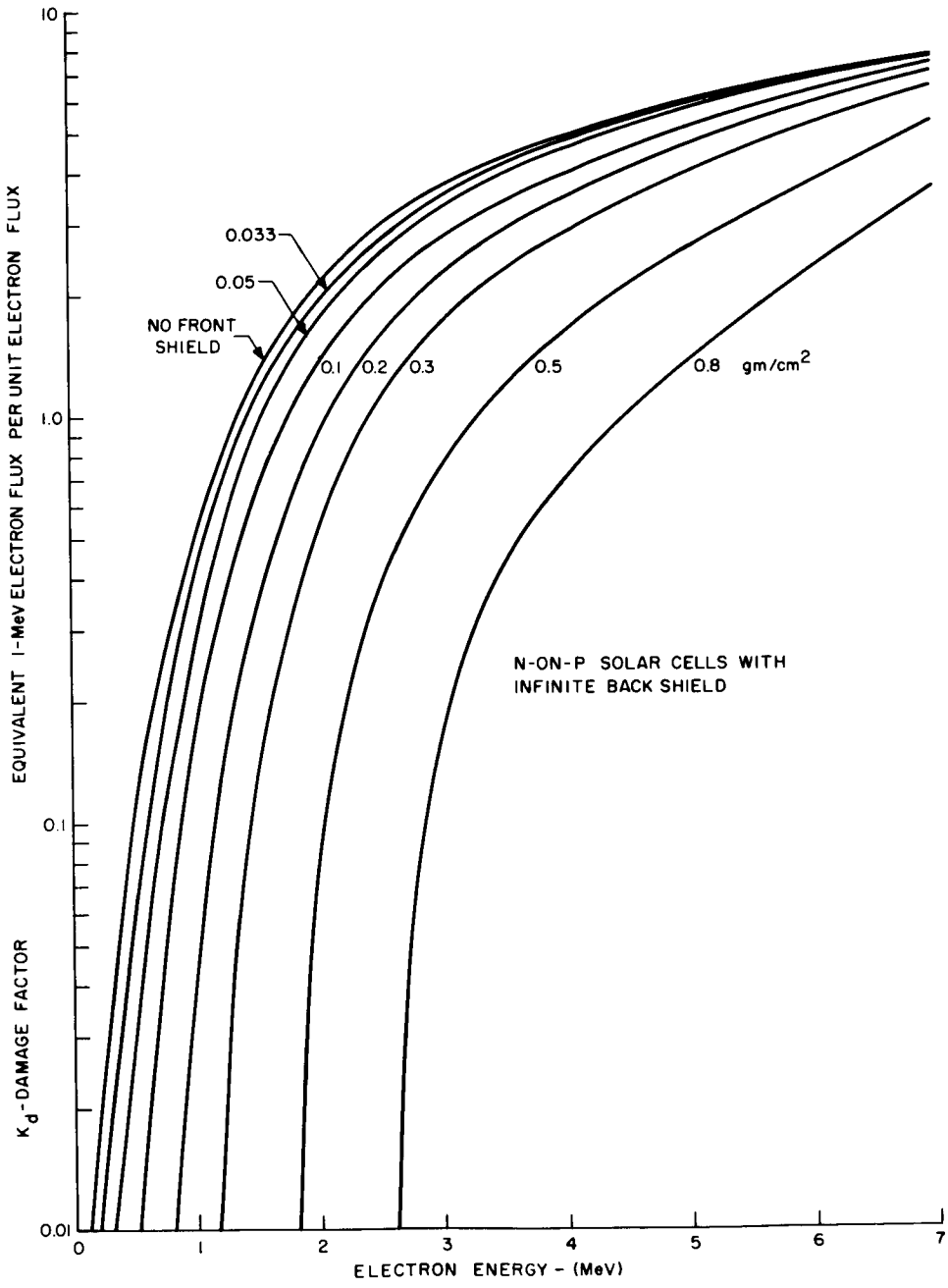

Figure X-143. Damage Equivalent for Normally Incident 1-MeV Electron Flux vs. Monoenergetic Isotropic Electron Flux

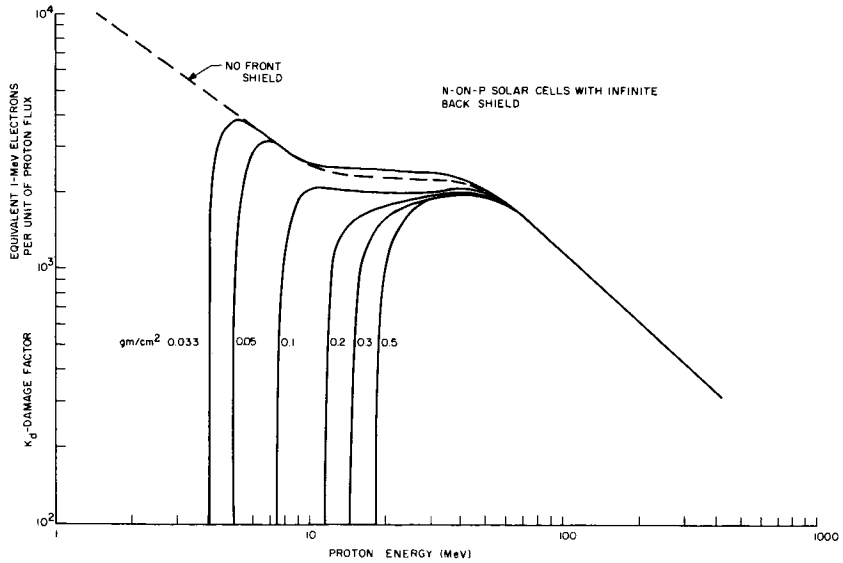

Figure X-144. Damage Equivalent for Normally Incident 1-MeV Electron Flux vs. Monoenergetic Isotropic Proton Flux

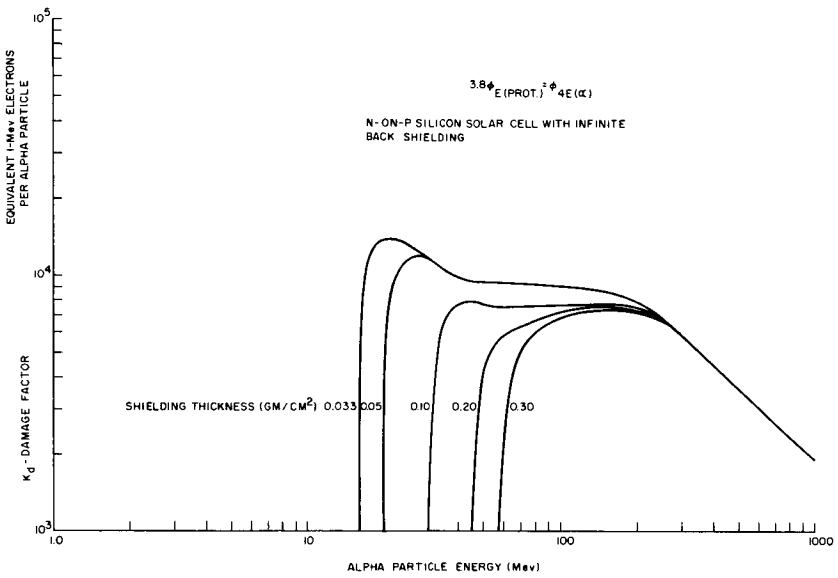

Figure X-145. Damage Equivalent for Normally Incident 1-MeV Electrons per Omnidirectional Alpha Particle

TABLE X-42. EQUIVALENT THICKNESS OF SHIELDING

Grams per Square Cm	0.033	0.05	0.1	0.2	0.3
equivalent mils of coverglass:	6	9	18	36	54
equivalent mils of aluminum:	5	7.5	15	30	45
definition of shielding number for computer "look-up":	1.0	1.5	3.0	6.0	9.0

TABLE X-43. DAMAGE FACTORS FOR ELECTRONS

Energy Range No.	Shielding Number				
	1.0	1.5	3.0	6.0	9.0
1	0	0	0	0	0
2	0.03	0.02	0	0	0
3	0.13	0.08	0.03	0	0
4	0.30	0.20	0.10	0.02	0
5	1.15	1.02	0.75	0.47	0.25
6	2.70	2.50	2.05	1.55	1.10
7	4.15	3.92	3.38	2.85	2.15
8	5.30	5.15	4.60	4.10	3.30
9	6.15	6.10	5.70	5.30	4.60
10	7.30	7.30	6.80	6.50	5.85
11	7.80	7.80	7.70	7.50	7.0

TABLE X-44. DAMAGE FACTORS FOR PROTONS

Energy Range No.	Shielding Number				
	1.0	1.5	3.0	6.0	9.0
1	0	0	0	0	0
2	0	0	0	0	0
3	0	0	0	0	0
4	0	0	0	0	0
5	3000	0	0	0	0
6	3700	2000	0	0	0
7	3500	3100	0	0	0
8	3100	3100	200	0	0
9	2800	2800	1400	0	0
10	2700	2700	2000	0	0
11	2600	2600	2100	0	0
12	2500	2500	2100	100	0
13	2500	2500	2100	1000	0
14	2500	2500	2000	1400	0
15	2500	2500	2000	1500	100
16	2500	2500	2000	1800	1500
17	2300	2300	2000	2000	2000
18	1000	1000	1000	1000	1000

TABLE X-45. DAMAGE FACTORS FOR ALPHA PARTICLES

Energy Range No.	Shielding Number				
	1.0	1.5	3.0	6.0	9.0
1	10000	0	0	0	0
2	13000	0	0	0	0
3	14000	7000	0	0	0
4	13700	11000	0	0	0
5	12500	12000	0	0	0
6	11500	11500	2500	0	0
7	11000	11000	5200	0	0
8	10400	10400	7200	0	0
9	9800	9800	7900	0	0
10	9500	9500	8000	1700	0
11	9500	9500	7800	3650	0
12	9500	9500	7700	5300	0
13	9500	9500	7600	5700	1600
14	9400	9400	7600	6300	4000
15	9200	9200	7600	7000	6400
16	8600	8600	7700	7400	7100
17	7000	7000	7000	7000	7000
18	4000	4000	4000	4000	4000

shielding thicknesses have been assigned dimensionless numbers, so that the same damage-factor tables may be used for both coverglass and aluminum shielding. For example, a proton in energy range number 12 (12 to 13 MeV) has an associated damage factor of 2100 behind either 18 mils of coverglass or 15 mils of aluminum backshielding, both of which have a shielding number of three.

Any one of the five coverglass thicknesses (6, 9, 18, 36, or 54 mils) and aluminum back-shielding thicknesses (5, 7.5, 15, 30, or 45 mils) may be selected for a computer run by the inputs "CG =_____ mils" and "BS =_____ mils" (see Paragraph X.E.4).

(4) Machine Computation of 1-MeV Electron Flux. Equivalent 1-MeV electron flux is computed by subroutine PHI. The required data for the computation are:

Program Inputs:
- CG (mils)
- BS (mils)
- N_e (table)
- N_p (table)
- N_{fp} (table)
- N_{fa} (table)

Stored Information:
- KDE (table)
- KDP (table)
- KDA (table

The block numbers refer to the flow chart, Figure X-142.

ϕ_e (1-MeV equivalent of transition and orbital electrons; blocks 1, 2, 2A):

$$\phi_e = \sum_{1}^{11} N_e KDE \Big|_{CG} + \sum_{1}^{11} N_e KDE \Big|_{BS} \tag{X-59}$$

ϕ_p (1-MeV equivalent of transition and orbital protons; blocks 3, 4, 4A):

$$\phi_p = \sum_{1}^{18} N_p KDP \Big|_{CG} + \sum_{1}^{18} N_p KDP \Big|_{BS} \tag{X-60}$$

ϕ_{fp} (1-Mev equivalent of solar flare protons; blocks 5, 6, 6A):

$$\phi_{fp} = \sum_{1}^{18} N_{fp} KDP \Big|_{CG} + \sum_{1}^{18} N_{fp} KDP \Big|_{BS} \tag{X-61}$$

ϕ_{fa} (1-MeV equivalent of solar flare alpha particles; blocks 7, 8, 9,):

$$\phi_{fa} = \sum_{1}^{18} N_{fa} KDA \Big|_{CG} + \sum_{1}^{18} N_{fa} KDA \Big|_{BS} \tag{X-62}$$

ϕ_T (1-MeV equivalent of total encountered fluxes; block 10):

$$\phi_T = \phi_e + \phi_p + \phi_{fp} + \phi_{fa} \tag{X-63}$$

After computation, the values of ϕ_e, ϕ_p, ϕ_{fp}, ϕ_{fa}, and ϕ_T are printed out and the value of total 1-MeV flux, ϕ_T is sent to subroutine DEGRADE.

c. IRRADIATION DEGRADATION OF SOLAR-CELL I-V CURVE

A solar cell exposed to charged-particle irradiation experiences a reduction of short-circuit current, open-circuit voltage, and, of course, a decrease in its maximum output power. This degradation is a function of the total integrated particle flux to which the cell has been exposed and of the base resistivity of the cell. The short-circuit current and maximum-power current of a 10 ohm-cm cell degrade less than those of a 1 ohm-cm cell at a given 1-MeV flux level, and the maximum-power voltage of a 1 ohm-cm cell degrades less than that of a 10 ohm-cm cell at a given 1-MeV flux level. For 1-MeV fluxes up to about 10^{15} electrons per square cm, the relative power degradation of a 1 ohm-cm and a 10 ohm-cm cell is about the same, but for higher flux levels the output power of a 10 ohm-cm cell degrades more slowly than that of a 1 ohm-cm cell. Figure X-146 shows the relative degradation of short-circuit current and maximum-power current of 1 and 10 ohm-cm RCA

solar cells as a function of 1-MeV flux. Figure X-147 shows the relative degradation of maximum-power voltage of the low and high base-resistivity cells as a function of 1-MeV flux. Figure X-148 shows the relative degradation of open-circuit voltage of the RCA cells as a function of 1-MeV flux (the relative degradation of this parameter is independent of base resistivity).

In addition to reducing the I-V curve short-circuit current and open-circuit voltage, irradiation changes the I-V curve shape, such that a "squarer" curve is obtained after irradiation. By comparing the pre- and post-irradiation I-V curves recorded in the laboratory, it was determined that the change in the shape of the I-V curve could be graphically illustrated by adding a negative series-resistance effect to the unirradiated curve to obtain the proper post-irradiation curve shape. The value of this resistance increases with the 1-MeV flux level and is also dependent on the base resistivity of the solar cell. Figure X-149 presents a plot of "Volts at I_{sc}" versus 1-MeV flux for the 1 and 10 ohm-cm RCA cells. The value of series resistance to be used for I-V curve shape correction is obtained by entering the appropriate base-resistivity curve in Figure X-149 at the desired flux level and reading the value of the ordinate "Volts at I_{sc}". The voltage value is then divided by the value of initial undegraded short-circuit current of the cell (I_{sco}) to yield the proper value of series resistance (called RR for radiation resistance, in the flow chart).

The sequence for irradiation degradation of an I-V curve is:

- Undegraded curve shape is corrected to proper irradiated curve shape.
- New curve shape is translated to give correct irradiated short-circuit value (I_{scr}).
- Curve shape is translated to give correct irradiated open-circuit voltage value (V_{ocr}).

Irradiation degradation is the first step in the process of I-V curve degradation. This first degradation is performed on a room-temperature (+25 to +30°C) I-V curve.

The solar cell I-V curve is degraded for irradiation in subroutine DEGRADE. The required data for this operation are:

Program Inputs:
- Base Resistivity (1 or 10 ohm-cm)
- Total 1-MeV flux, ϕ_T (optional)

Stored Information:
- V versus ϕ_T (Table from Figure X-149)
- ϕ_T computed by subroutine PHI (optional)
- I-V curve (Table of X-40 and X-41 points, 1 or 10 ohm-cm)
- RI (ϕ) equations
- RV (ϕ) equations

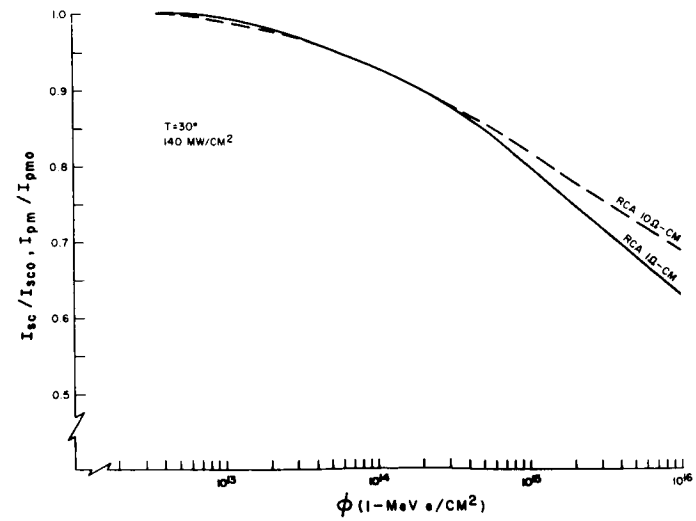

Figure X-146. Air-Mass-Zero Short Circuit and Maximum-Power Current Degradation

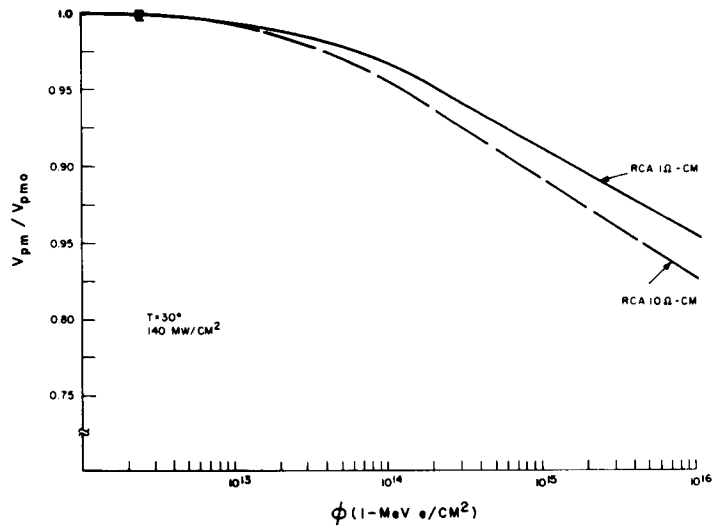

Figure X-147. Air-Mass-Zero Maximum-Power Voltage Degradation

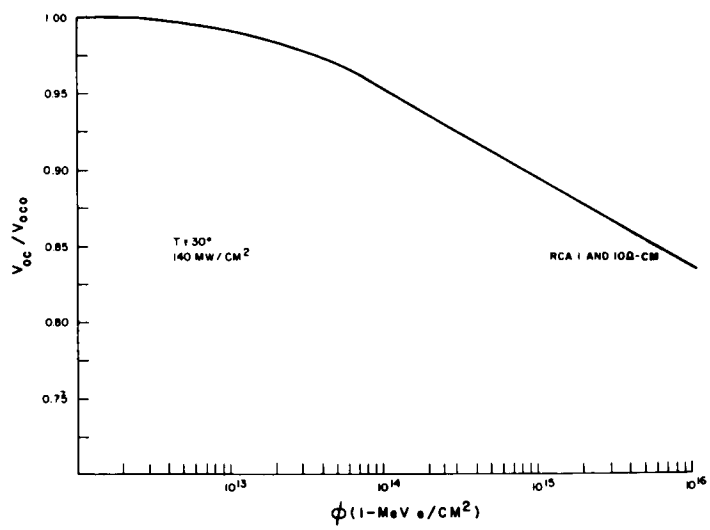

Figure X-148. Air-Mass-Zero Open Circuit Voltage Degradation

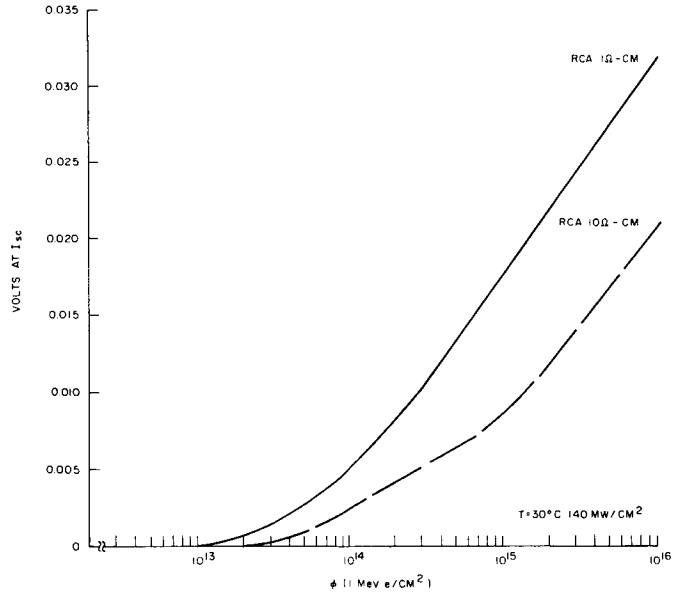

Figure X-149. I-V Curve Shape Change

ϕ_T is selected by the user to be either an input number of 1-MeV electrons or else the 1-MeV value of ϕ_T calculated previously in subroutine PHI from orbital fluxes. This selection is shown in block 11 of the flow chart.

For I-V curve shape correction (blocks 12, 13, 14, 15), the I-V curve is selected according to the base resistivity (1 or 10 ohm-cm) specified in the input. Its short-circuit current (I_{sco}) is determined and V is found at ϕ_T from Figure X-149. Then RR is computed as $RR = V/I_{sco}$. The I-V curve shape is corrected by the iterative procedure:

$$V_i = V_i + I_i \, RR \tag{X-64}$$

where V_i and I_i are the current and voltage pairs representing the tabulated I-V curve

The short-circuit current relative degradation plotted in Figure X-146 can be described by a set of equations (RI):

<u>10 ohm-cm</u>

$$RI = 1 - 2.78 \times 10^{-7.34} \, (\phi_T - 5 \times 10^{12})^{0.41},$$

for $5 \times 10^{12} < \phi_T < 10^{15}$, (X-65)

and $RI = 2.806 - 0.1325 \log_{10} \phi_T$ for $\phi_T \geq 10^{15}$. (X-66)

<u>1 ohm-cm</u>

$$RI = 1 - 7.13 \times 10^{-8.31} \, (\phi_T - 4 \times 10^{12})^{0.451},$$

for $4 \times 10^{12} < \phi_T < 10^{15}$, (X-67)

and $RI = 3.3 - 0.167 \log_{10} \phi_T$ for $\phi_T \geq 10^{15}$. (X-68)

For short-circuit current correction (blocks 16, 17, 18), the value of RI is computed from one of the preceding equations (X-65), (X-66), (X-67), or (X-68), depending on the base resistivity and value of total 1-MeV flux ϕ_T. A value ΔI is computed as:

$$\Delta I = I_{sco} \ (1-RI). \tag{X-69}$$

The value ΔI is subtracted from each I-V curve current point I_i:

$$I_i = I_i - \Delta I. \tag{X-70}$$

The open-circuit-voltage relative degradation plotted in Figure X-148 can be expressed by a set of equations (RV):

<u>1 and 10 ohm-cm</u>

$$RV = 1 - 0.0222 \ \left(\log_{10} \frac{\phi_T}{3x10^{12}}\right)^{1.67} \tag{X-71}$$

$$3 \times 10^{12} < \phi_T < 10^{14}$$

and

$$RV = 1.779 - 0.0588 \log_{10} \phi_T \quad \phi_T \geq 10^{14} \tag{X-72}$$

For open-circuit voltage correction (blocks 19 through 24), the value of undegraded open-circuit voltage (V_{oco}) is determined from the undegraded I-V curve of the selected base-resistivity. The value of RV is computed from equation (X-71) or (X-72), depending on the value of total 1-MeV flux ϕ_T. The irradiation-degraded open-circuit voltage (V_{ocr}) is computed as:

$$V_{ocr} = V_{oco} \times RV. \tag{X-73}$$

The open-circuit voltage of the current-corrected I-V curve (called PZC for point of zero current) is found, and a voltage increment ΔV is calculated:

$$\Delta V = PZC - V_{ocr}. \tag{X-74}$$

The value ΔV is subtracted from each I-V curve voltage point V_i:

$$V_i = V_i - \Delta V \tag{X-75}$$

The resultant I-V curve has been properly degraded for irradiation. It is printed out and also sent to subroutine STASH. Block 25 determines the values of short-circuit current, maximum-power current, and maximum-power voltage (I_{scr}, I_{pmr}, and V_{pmr}) of the irradiation degraded I-V curve, which, along with the already-determined V_{ocr} (block 22), are printed out.

d. DEGRADATION OF SOLAR-CELL I-V CURVE FOR FACTORS OTHER THAN IRRADIATION

Any factor, other than charged-particle irradiation, that results in degradation of a solar cell I-V curve, can be treated as one of the following effects:

(1) Equivalent illumination intensity change (includes corrections for reduced current due to off-normal illumination, standard-cell tolerance, solar-constant variation, ultraviolet damage to coverglass and adhesive, etc.).

(2) Translation effect on I-V curve (voltage measurement error).

(3) Temperature Change.

(4) Equivalent external series-resistance change (includes wiring loss, etc.).

The current degradation factor, (1) preceding, reduces the output current of the solar cell and produces a corresponding voltage degradation of the I-V curve.

The voltage degradation factor (2) produces a uniform incremental decrease in voltage of all points of the I-V curve, but does not affect the value of short-circuit current.

The temperature change of the solar cell (3) produces a decrease in open-circuit voltage and an increase in short-circuit current for a positive temperature change and opposite effect for a negative temperature change. In addition, the I-V curve shape changes with temperature; i.e., as the solar cell temperature is raised, the knee of the I-V curve becomes depressed, progressively increasing at higher temperatures. Conversely, as the solar-cell temperature is lowered, the knee of the output characteristic becomes sharper and yields a more efficient I-V curve shape that improves with decreasing temperatures. Exact behavior of the I-V curve at the lower temperatures experienced by the solar array (below -100°C for some orbits) is not presently known. Laboratory measurements under the appropriate simulated environmental conditions are recommended before final design of hardware for a low-temperature solar array.

A series resistance degradation factor (4) produces a loss of voltage along the I-V curve that is proportional to the output current at each point along the I-V curve.

A detailed description of the techniques for correcting an I-V curve for the degradation factors described is presented in Reference 19. The procedures described in Reference 19 have been incorporated for use in this computer program.

Correction of the I-V curve for all degradation and environmental factors other than charged-particle irradiation is done by means of subroutine STASH. This subroutine has been used successfully with other RCA developed Space Power computer programs and will not be covered in detail in this report. The required data for the I-V curve degradation are as follows:

Program Input: Base Resistivity (1 or 10 ohm-cm)

Stored Information:
- I-V curve (table of I and V points, 1 or 10 ohm-cm)
- Degradation factors (current, voltage, series resistance)
- Temperature coefficients (for 1 and 10 ohm-cm)
- Temperature range of interest.

For I-V curve selection (block 26), the I-V curve, either 1 or 10 ohm-cm, may be taken from subroutine DEGRADE (irradiation degraded) or from the stored input table (unirradiated).

For current, voltage, and series resistance degradation (blocks 27, 28, 29), the selected I-V curve is corrected for the effects of current, voltage and series resistance degradation factors as described in Reference 19.

For temperature effects on I-V curve (block 30), the I-V curve shape is changed and translated as a function of temperature over the entire temperature range of interest. The I-V points of the curve are stored at each specified temperature in the range and also printed out.

Block 31 determines the short-circuit current (I_{sc}), maximum-power current (I_{pm}), maximum-power voltage (V_{pm}), open-circuit voltage (V_{oc}), and maximum power (P_{max}) of the fully-degraded solar-cell I-V curve and prints out these parameters at every temperature specified in the range of interest. The calculated table of P_{max} per cell as a function of temperature is also sent to the main program for use in the system calculations.

e. SOLAR-ARRAY WEIGHT

Solar-array weight per unit area is a function of the coverglass and backshielding thicknesses selected. The effective backshielding thickness cannot be specified exclusively on the basis of the irradiation protection it affords the solar cells, since the structural and thermal performance of the solar array is also influenced by the substrate properties. Selection of a substrate to meet the solar-array thermal and mechanical requirements would, therefore, define the backshielding irradiation protection provided. The required data are as follows:

Program Inputs:	Coverglass Thickness (mils) Backshielding Thickness (mils of aluminum)
Stored Information:	Weight of Cells + Glass Weight (table of lbs/ft^2 versus coverglass thickness in mils) Substrate + Frame Weight (table of lbs/ft^2 versus backshield thickness in mils)

In Block 32, the substrate-plus-frame weight at the specified backshielding thickness (BS, in mils of aluminum) is looked up.

In Block 33, the solar-cell-plus-coverglass weight, at the specified coverglass thickness (CG, in mils of coverglass), is looked up.

In Block 34 the outputs of blocks 32 and 33 are summed and the value of total solar array weight, in pounds per square foot, is stored. When the main program has determined the required size of the array in square feet, the total array weight is computed and printed out.

f. SUMMARY

This subsection has described the computer subroutines used to (1) calculate the 1-MeV flux from the orbital flux rates, (2) degrade the solar-cell I-V curve for charged particle irradiation, temperature and other environmental and degradation factors, and (3) compute the array weight per unit area. The variables affecting the solar cells that the computer user may specify are defined in Paragraph X.E.4. These are:

- solar-cell base resistivity,
- coverglass thickness,
- backshielding thickness,
- 1-MeV electron flux, and
- temperature range of interest (function of altitude).

The solar-cell subroutines may be run separately without the Main Program for the purpose of performing solar-cell and radiation-effects studies.

4. Program Options

The computer program is versatile, allowing the exercise of several options. The desired option is selected by proper coding of the fourteen IBM cards (N-codes) necessary to initiate a solution. This subsection covers the description of the options and the mechanics of the solution initiation.

Standard IBM cards are used. All fourteen N-code cards must be present, and must have appropriate numbers punched, regardless of the option exercised. The following are the values for the various N-codes.

N-Code Card No.	Numerical Value Punched
1	Daytime load in watts
2	Nighttime load in watts
3	Fraction of daytime load at dc
4	Fraction of nighttime load at dc
5	Resupply (fraction of a year)

N-Code Card No.	Numerical Value Punched
6	Flux (1 MeV electrons). Three options exist, with numerical value punched on card No. 6 indicated to identify each option. See cards No. 12 and 13. (a) Value: -1.0. Calculate the equivalent 1-MeV electron flux from raw flux data stored. Value punched on card No. 12 is 1.0, to initiate STASH subroutine in the solar-cell program. Card No. 13 is punched 0.0. (b) Value: 1-MeV electron-flux value chosen for the solution, between limits of 0.0 and 10^{16}. For instance, 5.0×10^{14} is punched on the card as 500000000000000.0. PHI subroutine in the solar-cell program will not be initiated. Card Nos. 12 and 13 as in (a). This option is used if a 1-MeV flux value, other than that resulting from the raw flux data stored, is assumed. (c) Value: as in "b". This option is used if it is desired to use P_{max} -vs.-temperature-vs.-flux solar-cell data stored in the Main Program (see Paragraph X.E.2.b(3)(c)1), rather than data calculated by the Solar-Cell Program. Card No. 12 is 0.0, to inhibit STASH; card No. 13 is 28.0 (special code corresponding to the serial number of the solar-cell data table stored in the Main Program).
7	Altitude, nautical miles
8	Coverglass thickness, mils. If options 6b or c are exercised, the numerical value of the 1-MeV flux punched is assumed to be the correct value for the glass thickness punched on card No. 8.
9	Backshielding thickness, mils of aluminum. Same comment applies as for the glass thickness under options 6 b or c.
10	Solar-cell base resistivity, 1.0 or 10.0 ohm-cm cell data stored in either the Solar-Cell or the Main Program, depending on option selected on card No. 6.
11	Battery type. Punched value: 0.0, Ni-Cd; 1.0, Ag-Cd.
12	Value punched: 1.0, to initiate a new STASH solution; 0.0, to use the output of a preceding STASH solution, an option exercised to save computer running time in cases where no changes in solar-cell parameters are called for in a set of several consecutive runs.

N-Code Card No.	Numerical Value Punched
13	Source of solar-cell data. Punched value: 0.0, use output of STASH (solar-cell program); 28.0, use cell data stored in the Main Program.
14	Program selection. Four options exist: (a) Value: 1.0. Exercise the Solar-Cell Program only. Output is a single solution of the STASH subroutine. (b) Value: 2.0. Another Solar-Cell Program run, different data. Option used when more than one consecutive STASH subroutine solution is required. (c) Value: 3.0. Exercise the entire program, including Main. Single solution, then stop. (d) Value: 4.0. More than one solution in sequence, involving the entire program including Main.

F. PARAMETRIC SYSTEMS STUDY

1. Introduction

The parametric data presented in this study is based on the computer runs tabulated in Appendix B. The purpose is to provide, by means of graphs, an appreciation of the orders of magnitude involved. Specific, detailed magnitudes, as well as additional information, can be determined from Appendix B by selecting the horizontal row tabulation nearest to the specific mission requirements under consideration.

Only baseline system requirements are considered here. No redundant solar-array panels or battery or electronics modules are included in the component sizes or weight and volume magnitudes plotted. For a discussion of how redundancy and other reliability provisions affect system sizes and weight, reference is made to Paragraph X. G dealing with reliability augmented, conceptual design systems.

2. Preprogrammed Input Information

The specific numerical assumptions were intended to cover the effect of each significant variable over a reasonable range. The assumed input information was as follows:

a. Orbit: 200 NM, 28.5° inclination;
200 NM, 90° inclination;
19,340 NM, (24 hr.), 30° inclination.

b. Battery type: silver-cadmium (Ag-Cd) and nickel-cadmium (Ni-Cd).

c. Resupply (fraction of a year), 0.125, 0.25, 0.5, 1.0.

d. Nighttime load: 2, 4, 5, 6, 8 and 10 kW.

e. Ratio of daytime load to nighttime load ($R = \frac{\text{Day Load}}{\text{Night Load}}$); 1.3, 1.5, 1.7.

f. Fraction of day and night load at dc (f_{dc}): 0, 0.667, 1.0.

g. Solar Array: Solar-cell efficiency, 10.5 percent at air mass zero, +27°C;
Solar-cell area, 0.0069 square foot per cell;
Cover glass, 6 mils;
Total array weight, 0.744 pound per square foot.

h. 1-MeV Fluxes: 5.85×10^{12} for 200-NM, 28.5° orbit;
4.17×10^{13} for 200-NM, 90° orbit;
1.356×10^{14} for 24-hr., 30° orbit.

i. Battery and electronics data as in Paragraph X. E. 2. b(3)(a) and X. E. 2. b(3)(b).

As a demonstration of the computer capability to analyze and design power systems for any altitude condition within the 200 to 19,340-nmi range, computer runs Nos. 13 through 44 have been made and tabulated in Appendix B. The variable-altitude data has not, however, been plotted.

3. Effect of Load Variation on Array Area

The solar-array area required to support a given value of nighttime load for one year is shown in Figure X-150 for the three orbits considered. These curves apply to the typical set of conditions where f_{dc} is 0.667 and R is 1.5. The 200-NM, 90° orbit requires more array area than the 200-NM, 28.5° orbit because of the greater damage to the array in the polar orbit by charged-particle radiation. The 24-hour orbit suffers the greatest radiation damage but the batteries are charged at a much lower rate than in the low-altitude orbits (since the ratio of satellite daytime-to-nighttime duration is much greater at the high altitude). This results in less array power required and consequently, the least array area required for a given load.

Figure X-151 presents the array area required to support a given nighttime load for one year in the 200-NM, 28.5° and the 24-hour, 30° orbits as a function of the a-c/d-c ratio of the load. More array power and area is required for the loads with a higher a-c component because of the lower efficiency of the inverters compared with the PWM d-c voltage regulators.

The solar-array area required to support a given nighttime load for one year as a function of three daytime-nighttime load ratios (R = 1.3, 1.5, 1.7) for the two inclined orbits is shown in Figure X-152. The greater array power and area required for the higher values of R is due to the fact that the array must supply a bigger daytime load in addition to recharging the batteries.

4. Effect of Array Area on Array Weight, Number of Solar Cells, and Array Power

The effect of the area of the solar array on total array weight is presented in Figure X-153, and is described by the following relationship:

Total array weight = 0.744 lb. per sq. ft of array area x total array area in sq. ft.

Figure X-153 also shows the number of 2- by 3-cm solar cells versus array area as defined by the relationship:

No. of solar cells = total array area (in sq. ft.)/0.0069 sq. ft. per cell

The values of maximum, average, and minimum solar array power during the daytime portion of the orbit versus array area are shown in Figure X-154 for the three orbits. In the two 200-nmi orbits, the profiles for solar-array temperature versus time are assumed to be identical and the difference between the array power curves for these two orbits is due to the greater radiation degradation in the polar orbit. The synchronous orbit sustains the greatest radiation damage, but since the minimum and steady-state temperatures are lower

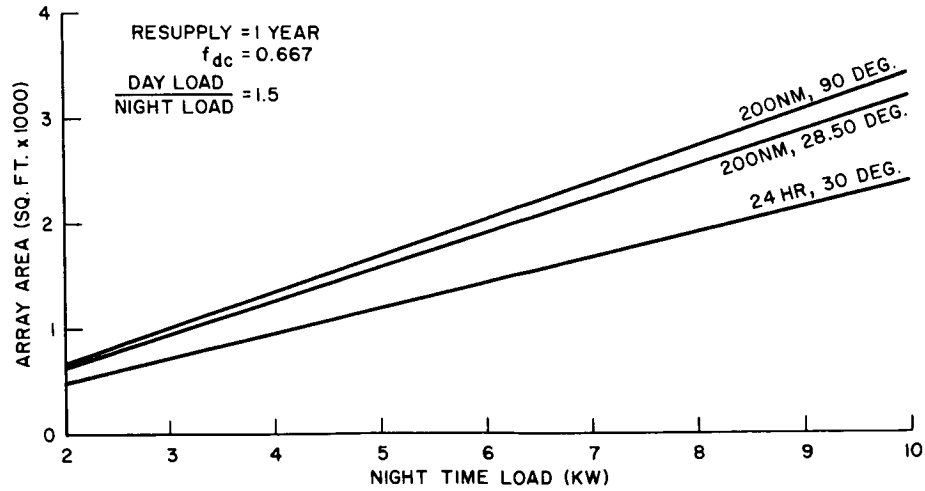

Figure X-150. Solar Array Area for Three Orbits vs. Night Load

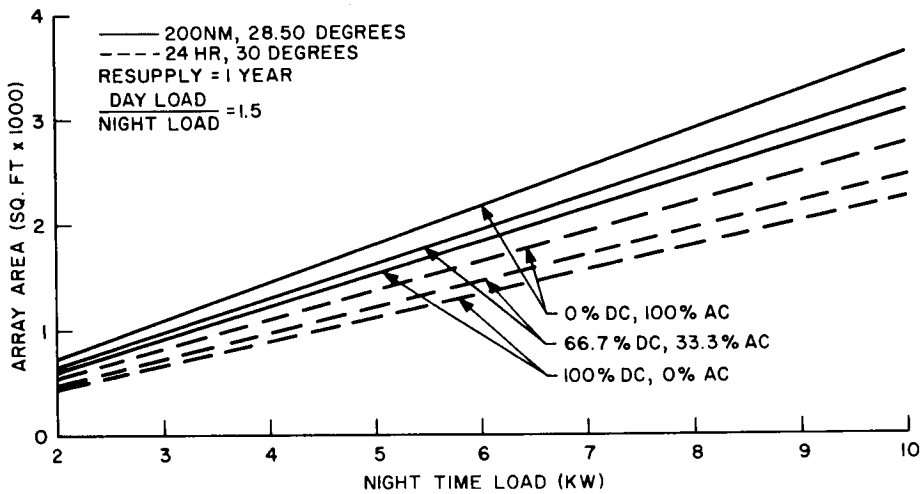

Figure X-151. Solar Array Area for Three a-c/d-c Ratios vs. Night Load

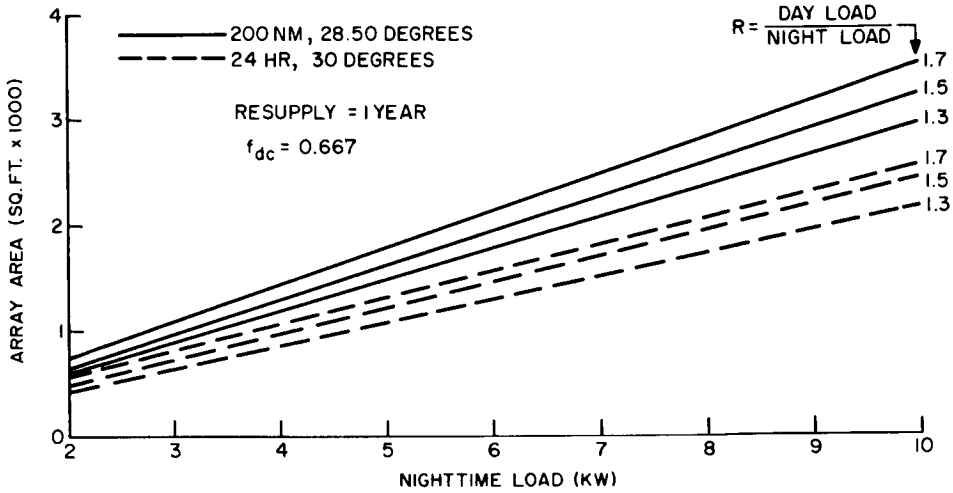

Figure X-152. Solar Array Area for Three Values of R vs. Night Load

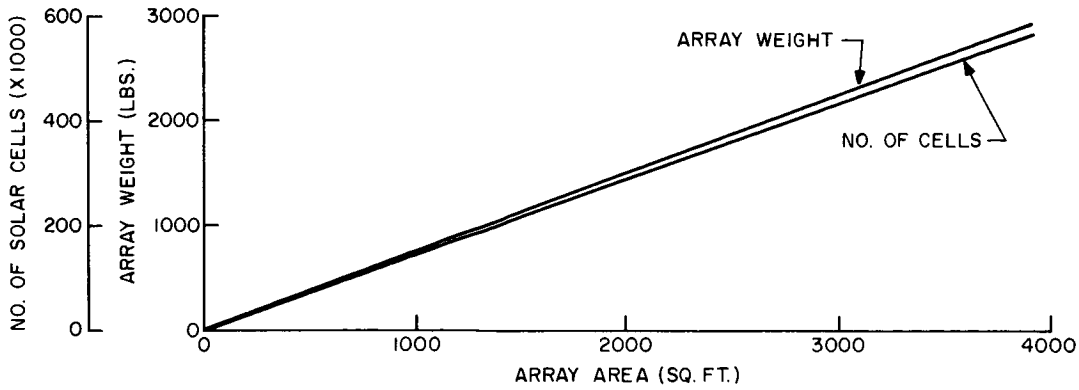

Figure X-153. Total Array Weight and No. of Solar Cells vs. Array Area

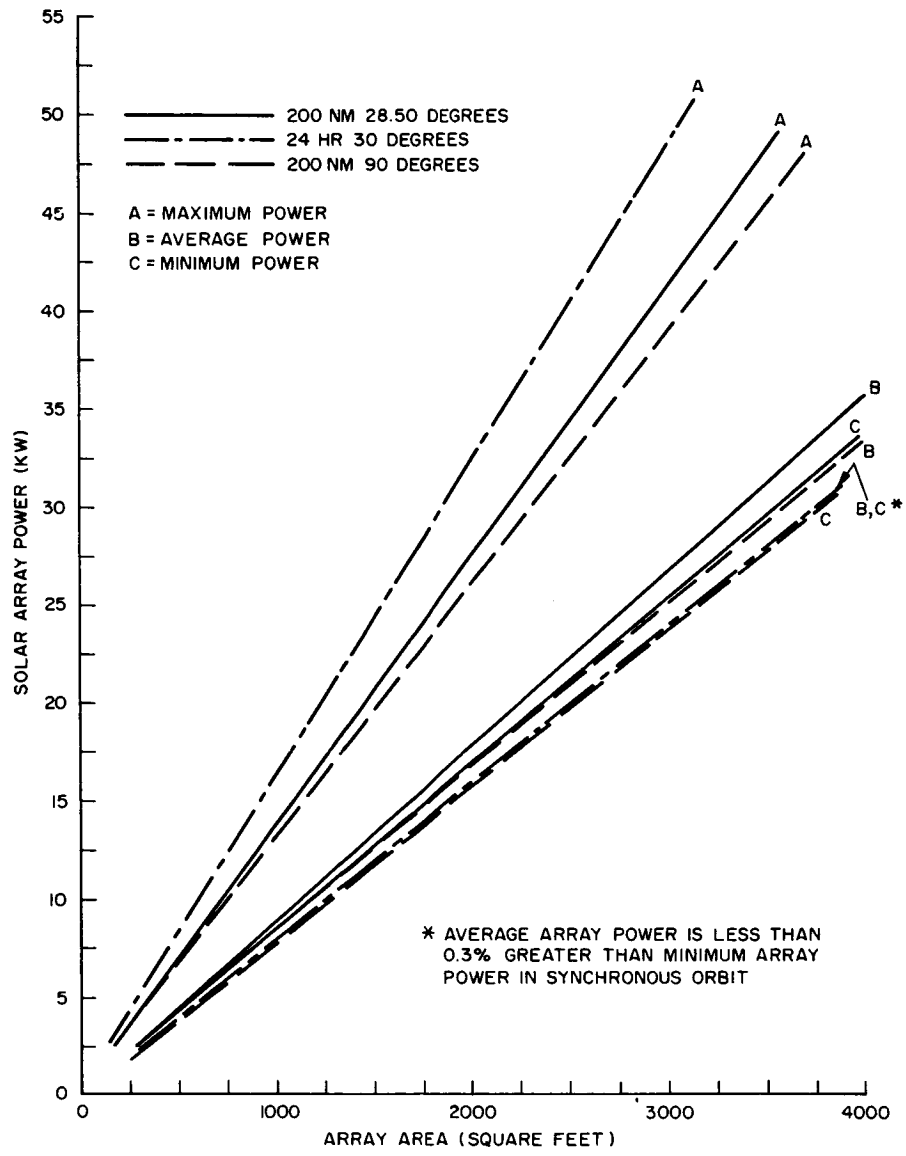

Figure X-154. Solar Array Power in Three Orbits vs. Array Area

than in the 200-NM orbits, the result is higher values of maximum and minimum array output power. Since the array temperature transient in the 24-hour orbit takes place during a very short portion of the daylight period, the average array P_{max}* power in this orbit is only about 0.3 percent greater than the minimum array power. The minimum array power is that obtained at the steady-state (highest) array temperature which is present during 1345 minutes of the 1368 minute daylight portion of the synchronous orbit.

5. Effect of Load Variation on Required Battery Capacity

The baseline-system battery capacity required to support a given nighttime load for one year as a function of the fractional portion of the load at dc (f_{dc}) is shown in Figure X-155 for the two inclined orbits. A Ni-Cd battery is shown for the 200-NM orbit and an Ag-Cd battery for the 24-hour orbit, because this combination results in the minimum storage-system weight as determined in Paragraph X. C. 3. Basically, a greater capacity is required for the lower altitude because the batteries are maximum-charge-rate-limited due to the relatively small percentage of sun-time in the orbit with a resulting depth of discharge of only 16 percent. In the 24-hour orbit, only 365 charge-discharge cycles (at most) can be encountered in one year and the batteries may be discharged to almost 50 percent of their capacity and recharged at the minimum charge rate.

In both orbits, higher capacity is required for greater percentages of a-c loads because of the lower efficiency of the inverters compared with the PWM regulators.

Figure X-156 presents the required battery capacity as a function of battery resupply interval for a given nighttime load for the two inclined orbits. In the 200-NM orbit, Ag-Cd batteries result in minimum system weight for a resupply interval of 0.25 year. Resupply at intervals greater than 0.25 year and up to 1.0 year yield a lighter-weight system if Ni-Cd batteries are used. In the low-altitude orbits, the Ag-Cd batteries are cycle-life limited and the Ni-Cd batteries are charge-rate limited. The synchronous altitude requires that Ag-Cd batteries be used for all resupply intervals, including one year, in order to achieve minimum system weight. For a resupply interval of 0.5 year at this altitude, the batteries are maximum-depth-of-discharge limited, while at a resupply interval of one year, they are cycle-life limited, thus requiring a slightly greater capacity (about 4 percent) for the one-year mission.

6. Effect of Battery Capacity on Battery Weight and Volume

Weight and volume as a function of battery capacity are presented in Figure X-157 for Ni-Cd and Ag-Cd batteries. The weights and volumes include the structural shelf upon which the batteries will be mounted, as well as the cooling coils and electrical busbars. It is seen that the Ag-Cd batteries have almost twice the effective energy density as the Ni-Cd batteries.

---

*Maximum power

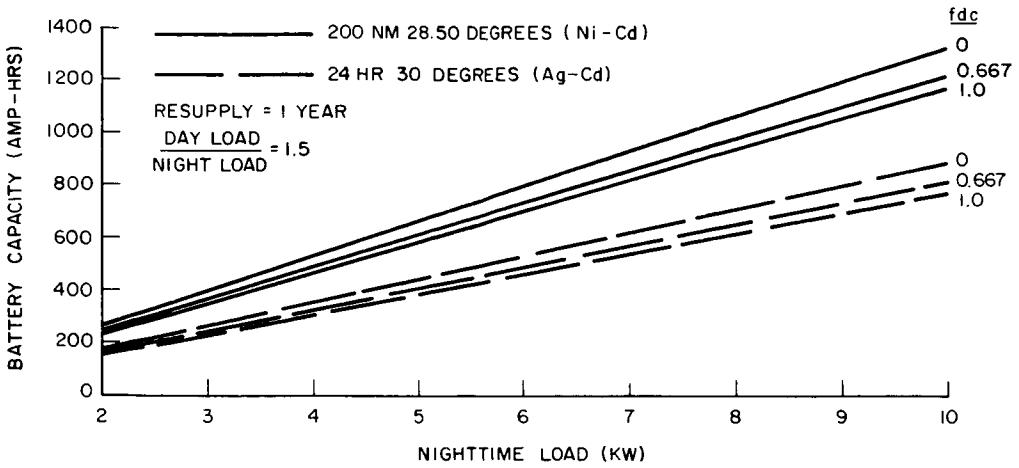

Figure X-155. Required Battery Capacity for Three A-C/D-C Ratios vs. Night Load

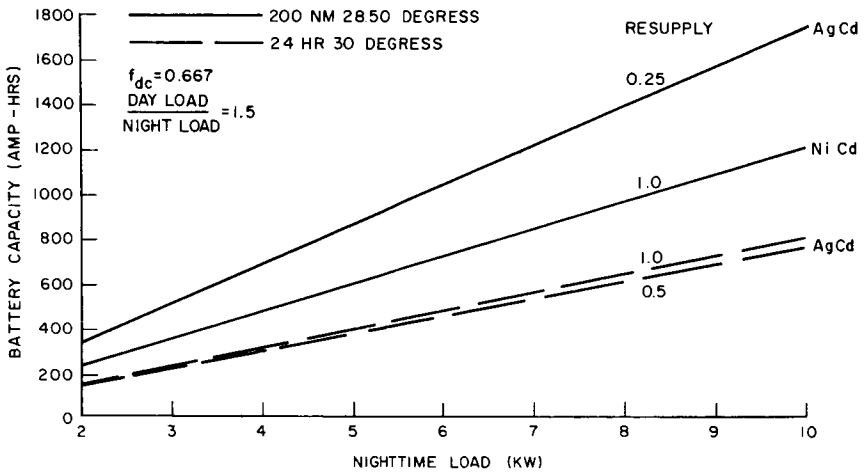

Figure X-156. Required Battery Capacity for Three Resupply Intervals vs. Night Load

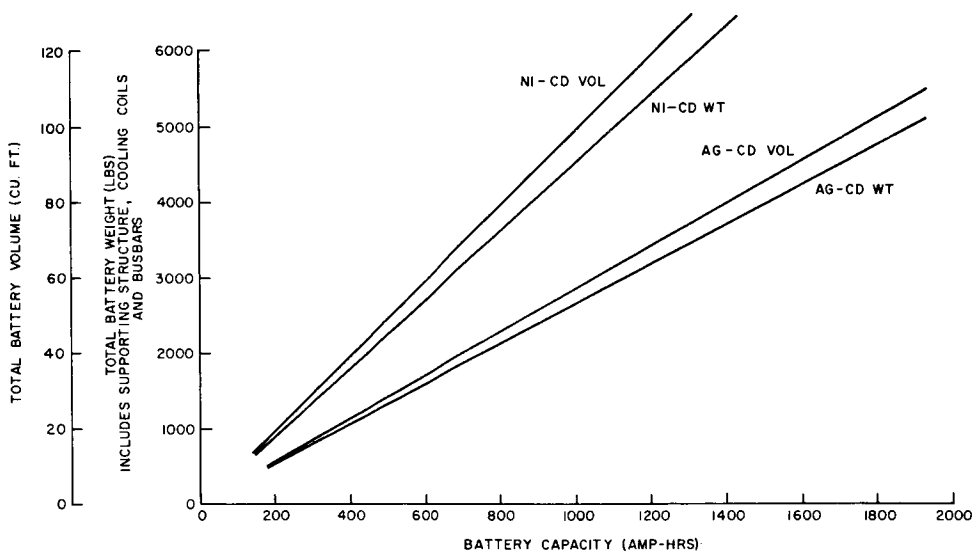

Figure X-157. Battery Weight and Volume vs. Battery Capacity

7. Effect of Load Variation on Total Electronics Weight and Volume

Figures X-158 and X-159 present the weight and volume, respectively for the total electronics (PWM d-c voltage regulators, inverters, and battery charge electronics) for a given nighttime load, as a function of the fraction of load at d-c. Linear interpolation between the 0 and 100 percent d-c load curves may be assumed, allowing for a small degree of inaccuracy. The plotted data points in each figure show the typical deviation from a straight-line characteristic of weight and volume versus nighttime load, caused by the fact that these relationships are not based on fixed factors of watts per pound and watts per cubic foot but are instead dependent upon the absolute per-module peak-load design requirement.

Electronics weight and volume versus nighttime load for f_{dc}* equals 0.667 with the ratio of day load to night load a variable (R, equal to 1.3, 1.5, and 1.7) are presented in Figures X-160 and X-161, respectively. The comments for Figures X-158 and X-159 apply to Figures X-160 and X-161 as well.

All values of electronics weight and volume include a 10 percent factor to account for such items as busbars, connectors, intermodule cabling, telemetry circuits, and power distribution unit.

8. Effect of Major System Parameters on Total System Weight

Total power system weight (consisting of the solar array, battery, and electronics weights discussed earlier in this section) as a function of resupply interval, nighttime load, fraction of load at d-c and ratio of day load to night load ($1.3 \leq R \leq 1.7$) for the three orbits considered in this parametric study is presented in Figures X-162, X-163, and X-164.

System weight in the 200-NM orbits for resupply intervals between 0.25 and 1.0 year is shown in Figure X-162. Use of Ni-Cd batteries results in the lightest-weight system for these conditions. The polar orbit system weight is about 1.5 percent greater than that for the inclined orbit. This is due entirely to the larger solar array required to supply the power at the end of one year in orbit since there is more radiation degradation of solar cells in the 90° orbit.

Determination of total power system weight from Figure X-162 is described through the following example:

What is the baseline weight of the power system to support a nighttime load of 7 kW for one year in the 200-NM 90° orbit with 25 percent of the load at d-c (75 percent at a-c) and a daytime load to nighttime load ratio of 1.5?

Step 1. In Figure X-162, enter the abscissa at the value of nighttime load, 7 kW (point Ⓐ), and move away from the abscissa parallel to the adjacent "f_{dc}" lines until the desired value of f_{dc} (0.25) is reached (point Ⓑ).

*Fraction of power at d-c

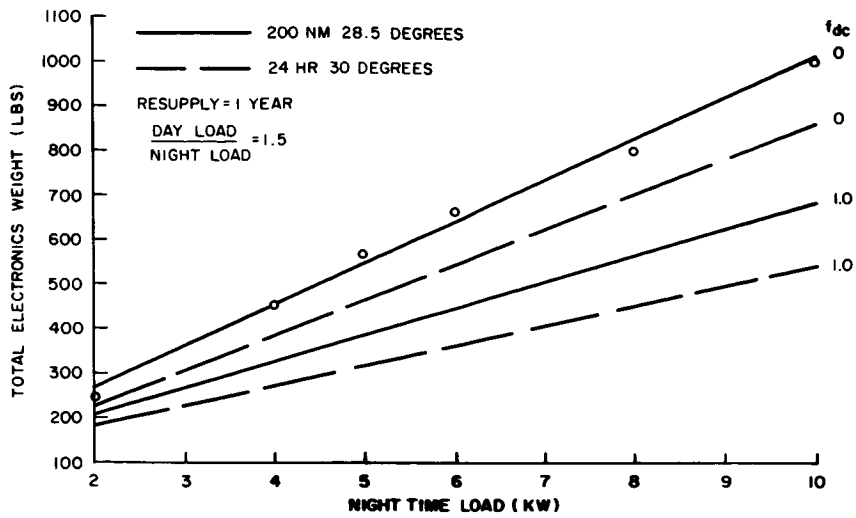

Figure X-158. Electronics Weight for 0 and 100-Percent D-C Loads vs. Night Load

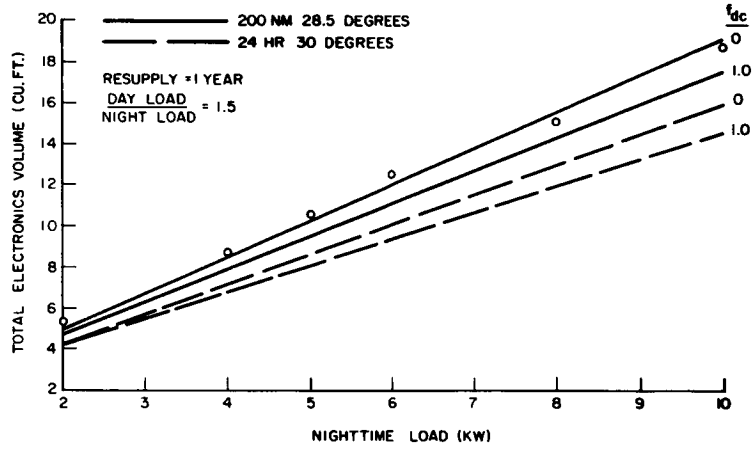

Figure X-159. Electronics Volume for 0 and 100-Percent D-C Loads vs. Night Load

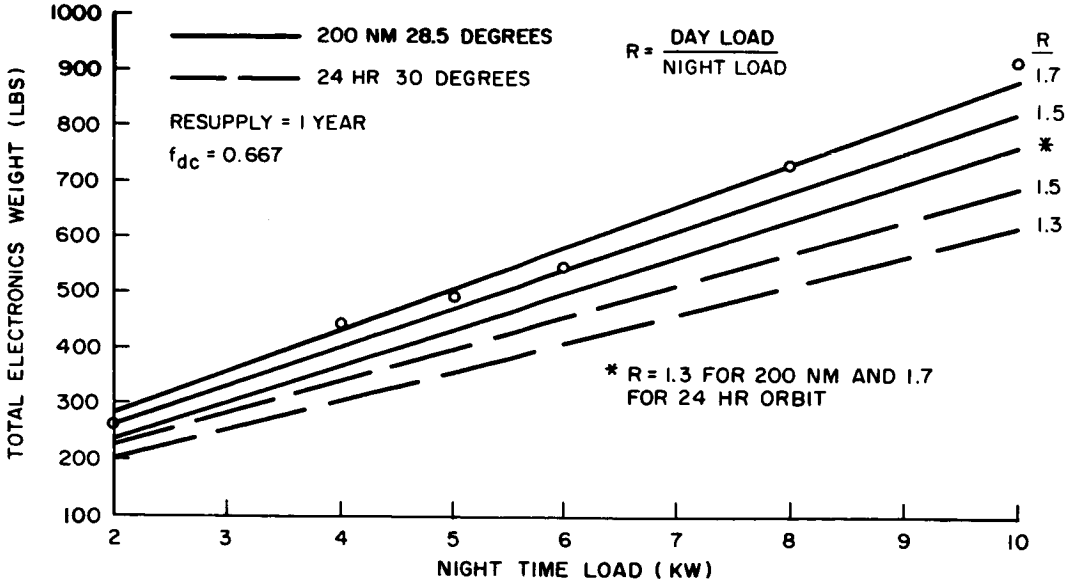

Figure X-160. Electronics Weight for Three Day/Night Load Ratios vs. Night Load

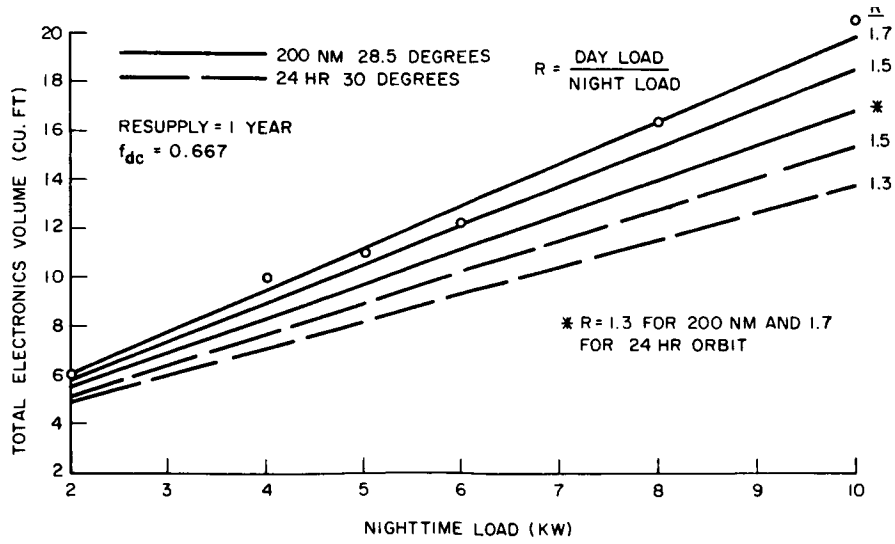

Figure X-161. Electronics Volume for Three Day/Night Load Ratios vs. Night Load

Step 2. Move vertically from Ⓑ until the proper curve (200 NM 90°) is intercepted (point Ⓒ).

Step 3. Move horizontally to the left from Ⓒ , past the ordinate, until the column "R" = 1.3" is intercepted (point Ⓓ).

Step 4. Move from Ⓓ in a direction away from the ordinate, parallel to the adjacent "R lines" until the desired value of R (1.5) is reached (point Ⓔ).

Step 5. Move horizontally to the right from Ⓔ until the ordinate is intercepted (point Ⓕ). Read the value of total power system weight from the last point of interception at the ordinate, i.e., 6750 lbs.

System weight in the two 200-n mi orbits for resupply intervals of up to 0.25 year is shown in Figure X-163. This Figure applies to systems with Ag-Cd batteries because this type of battery results in a lighter-weight system for short resupply intervals.

NOTE: Figure X-162 may be used for systems with Ni-Cd batteries and resupply intervals of less than 0.25 year if it is understood that such a selection will not provide the minimum baseline system weight.

Figure X-163 must not be used for a resupply interval greater than 0.25 year, or large optimistic weight errors may result.

Figure X-164 presents total power system weight in the synchronous orbit. Ag-Cd batteries are used for all values of resupply intervals up to one year in this orbit. The curve labeled "0.5 yr." in Figure X-164 actually applies to resupply intervals up to about 0.9 year, since the battery capacity required up to 0.9 year is determined by the maximum depth-of-discharge

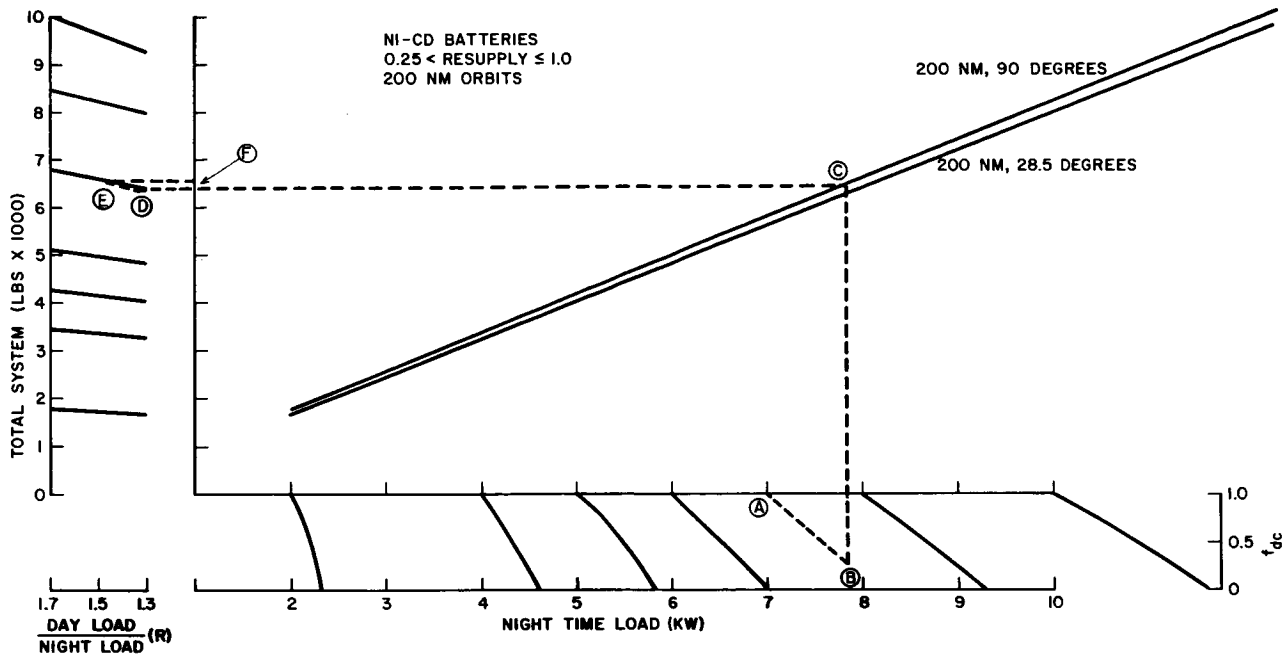

Figure X-162. Effect of System Operating Parameters on Total System Weight, Ni-Cd Batteries, 200 NM Orbit

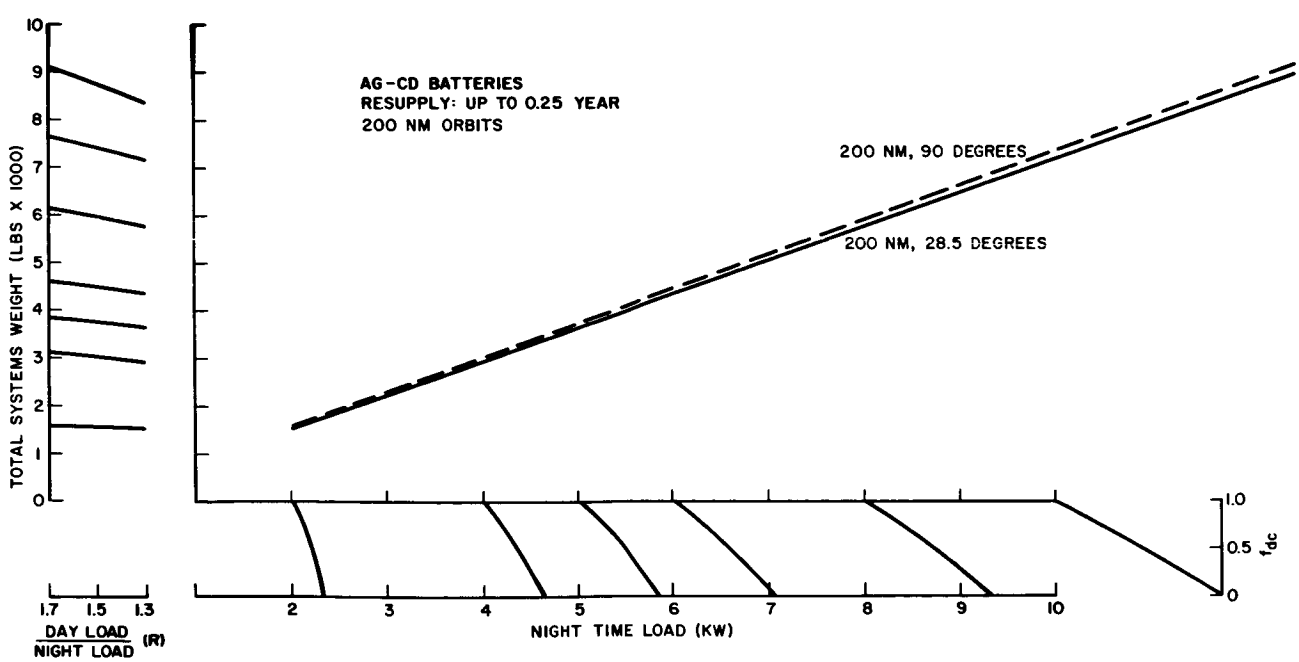

Figure X-163. Effect of System Operating Parameters on Total System Weight, Ag-Cd Batteries 200 NM Orbit

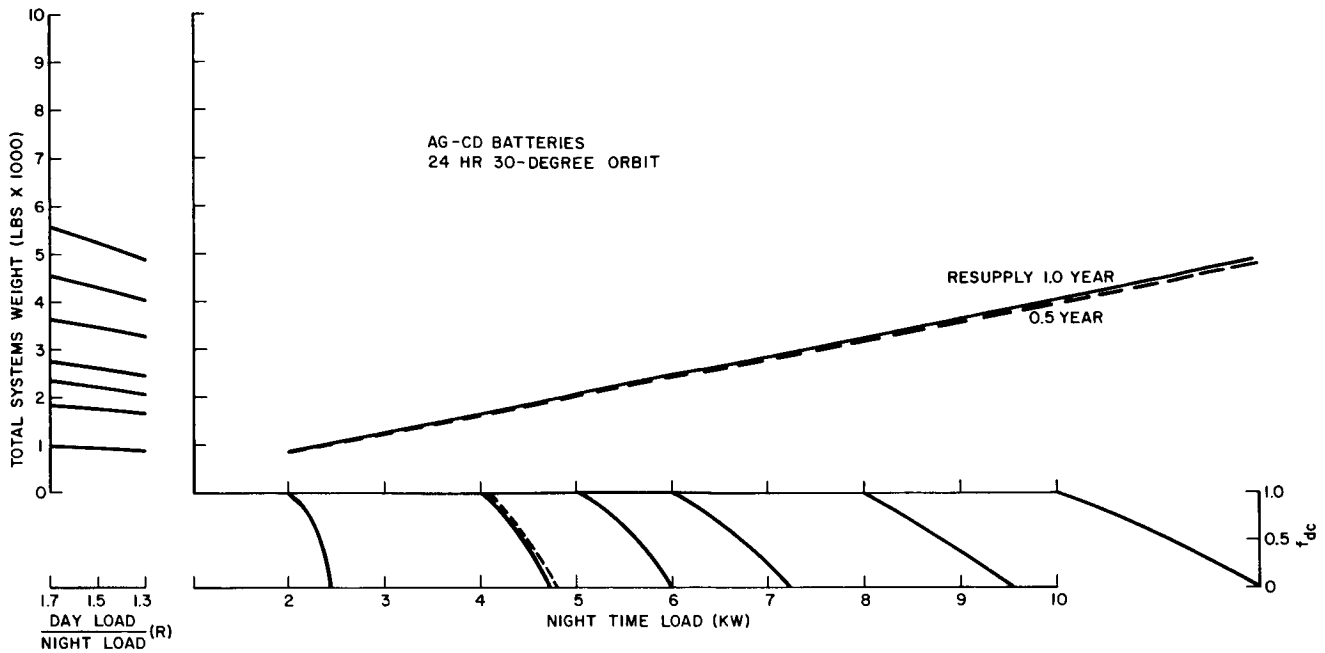

Figure X-164. Effect of System Operating Parameters on Total System Weight, Ag-Cd Batteries, Synchronous Orbit

limit. For resupply in excess of 0.9-year, the batteries are cycle-life-limited, and require a greater battery capacity so that the permissible depth of discharge is not exceeded. The additional battery capacity is the only factor slightly increasing the system weight for the 1.0-year resupply interval.

9. Conclusions

Section X.F summarizes the highlights of a parametric study of a baseline power system for three typical orbits. Only minimum electrical requirements are considered, with no redundancy included. The following major power system trends were exhibited:

(1) Effect of nighttime load on solar-array area, battery capacity, and electronics weight and volume.

(2) Effect of solar-array area on solar-array weight and number of solar cells required.

(3) Effect of battery capacity on battery weight and volume.

The variable parameters considered in the study were resupply interval, type of battery (Ag-Cd or Ni-Cd), nighttime load, fraction of load at d-c and ratio of day load to nighttime load. Composite plots showing the effect of all of the above variables on total power

system weight are presented for the three orbits. All of the power system trends and magnitudes of component size, weight, and volume show a linearly increasing value with nighttime load. For a given nighttime load, varying the fraction of load at d-c between 0 and 1.0, or varying the ratio of day load to nighttime load from 1.3 to 1.7, produced a change in the total system weight of less than 16 percent and 8 percent, respectively.

The total power system weight in the synchrous orbit for a given set of load conditions is only about 50 percent of that in the 200-nmi orbits, primarily because the higher energy density Ag-Cd batteries can be used and charged at a much lower rate with resultant reduction of both battery weight and solar-array weight.

G. CONCEPTUAL POWER SYSTEM DESIGNS

1. Introduction

This section is concerned with the conceptual power systems designs. The computer program, which has been used to provide solutions upon which the specific designs were based, has been heavily referenced.

One of the basic ground rules assumed was that resupply applied primarily to the electronics modules and the batteries. The solar array has been assumed to have been designed for the entire mission duration of one year and, consequently, has been treated as a non-resuppliable item.

Contents of this section, as well as the basic approach to the conceptual designs, have been subdivided into three steps as follows.

First, the computer solutions that define the baseline power systems (no spares, no redundancy) have been augmented to include spare and redundant equipment, using recommendations made in Paragraph X.D. The result is a tabulation of the total effective systems parameters, such as weight at liftoff, for a selected set of twelve design cases.

Second, the resupply interval has been appraised critically insofar as it affects both the total liftoff weight and the subsequent weight to be resupplied. It became very clear that a tradeoff was required between a system that is light at liftoff with a heavy resupply requirement and a system that is slightly heavier when launched initially, but requiring either very little or no resupply. To accomplish this second step, it has been necessary to define a resupply philosophy, i.e., exactly what is to be resupplied, in what quantity, and how often. Based on the experience gained in this study, the philosophy assumed appears to be reasonable.

Third, a specific recommendation has been made concerning the exact makeup of the power systems for 5 and 10-kW power levels in all three orbits. This is covered in Paragraph X.G.4, which summarizes the conceptual designs.

The power profiles and orbits used as models are described in detail in Paragraph X.B.2. The power system configuration is a parallel tracker; the system is of modular construction to provide a flexible mission approach and to facilitate replacement. The electronic modules have been identified and described in Paragraph X.C.4.a. In addition, the batteries consist of a number of replaceable battery modules connected in series.

2. Discussion of the Conceptual Design Cases

Reference is made to Table X-46 which contains data for the various cases discussed in Paragraph X.G.1.

TABLE X-46. SUMMARY OF CONCEPTUAL DESIGN CASES

Design Case No.	Computer Run No.	P_{Ln} KW	Orbit NM/°	Battery	Resupply	Electronic Power Modules and Battery Modules								Calc. AMP Hrs per Cell	Added Redundant/Spare Hardware						Total Weight at Liftoff
						Baseline No. Modules				Total* No. Modules					Weight, Lb.		Volume, cu ft		Total		
						PWM	Inv	C/T	B	PWM	Inv	C/T**	B+		Elec	Btry	Elec	Btry	Weight Lb.	Volume, cu. ft.	
1	1	5	200/28.5	Ni-Cd	1	4	2	5	30	6	7	8	33	122	516	276	10.3	6.1	792	16.4	5321
2	3	5	200/28.5	Ag-Cd	0.25	4	2	4	16	5	4	6	18	220	251	292	5.2	6.4	543	11.6	4638
3	5	5	200/90	Ni-Cd	1	4	2	5	30	6	7	8	33	122	516	276	10.3	6.1	792	16.4	5409
4	7	5	200/90	Ag-Cd	0.25	4	2	4	16	5	4	6	18	220	251	292	5.2	6.4	543	11.6	4727
5	9	5	Synch	Ag-Cd	1	4	2	2	8	6	7	4	10	204	491	272	9.8	5.8	763	15.6	3235
6	11	5	Synch	Ag-Cd	0.5	4	2	2	8	5	5	4	10	195	321	260	6.4	5.5	581	11.9	3003
7	2	10	200/28.5	Ni-Cd	1	7	3	9	54	9	9	14	58	135	636	407	12.7	8.9	1043	21.6	9546
8	4	10	200/28.5	Ag-Cd	0.25	7	3	7	28	9	6	9	31	250	351	499	7.3	10.6	850	17.9	8488
9	6	10	200/90	Ni-Cd	1	7	3	9	54	9	9	14	58	135	636	407	12.7	8.9	1043	21.6	9699
10	8	10	200/90	Ag-Cd	0.25	7	3	7	28	9	6	9	31	250	351	499	7.3	10.6	850	17.9	8642
11	10	10	Synch	Ag-Cd	1	7	3	4	16	9	9	7	18	203	586	270	11.6	5.8	856	17.4	5240
12	12	10	Synch	Ag-Cd	0.5	7	3	4	16	9	7	6	18	194	421	260	8.6	5.5	681	14.1	4966

* Baseline plus spare and redundant modules.
** Charger / Tracker
+ Battery

a. HORIZONTAL ROWS

The first six rows are relevant to the designs where the continuous load is five kilowatts (PLn is 5kW). These are then the 5-kW systems. The next six are the 10-kW systems. Within each group of six, three different orbits are specifically investigated for two different resupply intervals. The reason for including two resupply intervals in each orbit will be later explained in detail.

b. VERTICAL COLUMNS

The first column refers to the design case number used for reference purposes in this section. This is followed by the number of the computer run used to produce the baseline design (Appendix B) and the specific mission input conditions assumed to produce the computer solution, i.e., continuous load (P_{Ln}), orbit, and battery type.

Next is the "Resupply" column. For each combination of orbit and P_{Ln} (six in all), the case of a resupply interval of one year (1.0) has been investigated. With one year as the total mission lifetime, a unity resupply means that no resupply may occur during that year. The design case cited is, therefore, worst-case from the viewpoint of total weight at liftoff, due to the additional redundant hardware.

In some cases, computer solutions were obtained for resupply increments of 1, 0.5, 0.25, and 0.125 years for both types of battery even though the battery weight tradeoff studies clearly define the resupply interval ranges where each of the two battery types considered is likely to yield the lowest total system weight. The solutions verified the previous studies by showing that, in general, there exists a resupply interval for each orbit below which the total baseline systems weight can be lowered by changing to a different type of battery. (See Figure X-77.)

As an example, see the tabulated cases No. 1 and 2 for the 200-NM, 28.5° inclination orbit with a 5-kW continuous load. These two cases are a summary of several runs for different resupply intervals, which yielded either one of two possible fixed baseline system weights. One was for a nickel-cadmium (Ni-Cd) system for any resupply interval of one year or less, while the other, with a lower weight, was for a silver-cadmium (Ag-Cd) system with a resupply internal of 0.25 year or less. Any runs for the Ag-Cd, and a resupply interval of 0.5 or more, yielded solutions of total weight greater than that for the Ni-Cd cells of like interval. Resupply of 0.25 is, therefore, the only other interval tabulated (in addition to the one-year maximum) in cases 1 and 2, 3 and 4, and 7 through 10, where the 200-NM altitude orbits were involved.

Specific reasons why one type of battery is lighter than another for a given orbit and resupply are stated in the battery weight tradeoff studies, Paragraph X.C.3.b. For the present, it is useful to recall that the resupply interval affects the storage system size only if the combination of the battery operating parameters is such that the cycle life is the critical sizing factor. In a majority of other cases, either the maximum charge rate or the peak discharge depth are the factors which govern the battery size. Thus, the cycle life implied by the programmed "resupply" has nothing to do with the selection of the physical characteristics of the baseline storage system.

The latter argument is not wholly applicable to the electronics since the number of baseline components is never a function of the mission length but is, instead, a function of the electrical-load power profile and, in part, of the type of battery used. Weight of electronics is, therefore, less subject to variations in the baseline systems concept. For this reason, and due to the fact that the electronics weight is lower than that of the batteries in general, the battery weight is primarily responsible for major variations of the total systems weight.

Following the tabulation of the required number of baseline components in Table X-46, the total number of components is listed. The difference between the two is the number of spare modules recommended in Paragraph X.D.

The total number of modules includes the following.

(1) Electronics Power Modules

Baseline requirement, plus redundant and spare units based on Paragraph X.D.6. One of the added units is connected in the active circuit; the remaining additional units are spares. Thus, for Case No. 1 there are 4 baseline PWM Regulator Modules and a total of 6. This means that the active circuit consists of 5 units and that there is one spare. Exception: there are no actively redundant C/T modules (all added C/T power modules are inactive spares).

NOTE: 40,000 hours mean time between failures is assumed for Inverter modules in apportioning redundancy.

(2) Battery Modules

The tabulated numbers refer to the number of replaceable battery modules (six per Ni-Cd battery and four per Ag-Cd battery). Spare module apportionment is based on Tables X-36 and X-37 of Par. X.D. For example, in design case No. 1, Table X-46, five baseline Ni-Cd batteries are required; at six modules per battery this means 30 baseline modules. From Table X-36 of Paragraph X.D, three additional spare modules are needed , for a total of 33 battery modules. The three spares are rotated periodically to assure equal wear.

The next vertical column is the calculated ampere-hour capacity per cell. The total number of ampere-hours computed has been divided by the number of active batteries, to arrive at the ampere-hour capacity per storage cell. From the table, it is seen that all the Ni-Cd modules would consist of cells within the capacity range of 122 to 135 ampere-hours. The Ag-Cd cells are within 194 to 250 ampere-hours. (If it is subsequently established that manufacture of such large Ag-Cd cells would entail unnecessary risks, half-size cells of roughly 97 to 125 ampere-hours may be used and the number of batteries and charge electronics doubled with little effect on the computed total weight.)

The added weights and volumes of the redundant and spare equipments are tabulated next, as follows:

(3) Added electronics weight consists of redundant and spare modules. Specifically, these are:

(a) Power Modules

By reference to Appendix B and component weight data, Paragraph X.C.4, the power modules are as listed in Table X-47.

TABLE X-47. POWER MODULE BREAKDOWN

System	PWM Regulator		Inverter		C/T	
	Watts	Pounds	Watts	Pounds	Amps (approx.)	Pounds
5kW	1370	30	1368	70	43.88	25
10kW	1259	29	1467	70	49.92	27

(b) Other Electronics Modules

In each design case, one of each of the following four types of electronics modules is assumed, carried as a spare for all resupply intervals (up to one year):

PWM Regulator Assembly:
- One control module (in addition to the two redundant modules);
- One failure detect module;
- Weight of both: 15 pounds.

C/T Assembly:
- One control module (additional module as above);
- One failure detect module;
- Weight of both: 16 pounds.

An additional 31 pounds of spare electronics is thus assumed to be required.

(4) Added battery module weight is determined as a proportion of the weight of the baseline modules as determined by computer (additonal battery volume is determined in a similar manner).

The next column refers to added volume. In the case of electronics, this had been determined by calculating the weight added to each of the three assemblies (PWM d-c regulator, inverter, and charger/tracker), and dividing by the following factors (Paragraph X.C.4.f.(5)):

- PWM Regulator assembly: 0.0280 cubic foot per lb.
- Inverter Assembly: 0.0181 cubic foot per lb;
- C/T assembly: 0.0210 cubic foot per lb.

Total added weight and volume is computed by the summation of the respective quantities for the electronics and battery. In computing the added weight and volume, no allowance is made for racks and shelves to be used to store spare modules, since the the individual weights were based on packaged, assembled, and mounted operating equipment.

The total systems weight column is the sum of the baseline system weight as determined by the computer and the total added weight of redundant and spare electronics and battery modules.

c. SUMMARY

Table X-46 defines the specific hardware requirements for individual missions in each of twelve cases. The following sections will recognize the similarities which exist between different missions in terms of the required power system equipment. The number of design cases will be reduced and specific module sizes, to the considered during the detailed design phase, will be recommended.

3. Resupply as a Weight Factor

a. RESUPPLY PHILOSOPHY

Under the presently assumed ground rules, batteries and electronics may be subject to resupply.

It is necessary at this point to recognize that batteries and electronics are to be replaced as a result of (or in anticipation of) two essentially different failure modes. The batteries are primarily subject to wearout failures. They are selected and sized on the basis of one of several limiting design criteria, but each design has an inherent ability to support a certain cycle life. Exceeding that cycle life can be assumed to result in frequent failures thus rendering the original equipment useless.

Electronic component failures are predominantly random phenomena in properly designed circuits. Failure of one replaceable group of components can occur at any time and will not normally trigger an avalanche of failures in other groups of components.

It can, therefore, be concluded that the operating batteries as well as the "roving" spare battery modules must be replaced by fresh units at specified time intervals. Electronic hardware is replaced as failures occur with a sufficient number of redundant and spare components maintained on board to meet the reliability requirements.

More specifically, the following ground rules, concerning the resupply philosophy, are established:

(1) Resupply the entire storage system including spares within a time limit corresponding to the resupply interval or the rated cycle life.

(2) The number of resupplied electronics power modules is equal to the number of failures during the previous resupply cycle.

(3) Other electronics. Four other electronics modules (31 lb) are assumed carried at liftoff and not subsequently resupplied.

b. EFFECT OF RESUPPLY-CYCLE DURATION ON LIFTOFF AND RESUPPLY WEIGHTS

The initial discussion will concern the 5-kW systems.

(1) 200 NM Orbits (28.5 and 90° Inclination)

In each of the two orbits in question, the Ni-Cd system is the heavier one at liftoff. No resupply during the one-year mission is specified for the Ni-Cd system. The Ni-Cd batteries are rated in excess of one year's cycling (16 percent discharge depth is assumed safe for up to 600 days at 200 NM; see computer runs Nos. 1, 2, 5, and 6 of Appendix B and Figure X-66). If it were necessary to absolutely minimize the liftoff weight, no Ni-Cd batteries could be removed regardless of the frequency of resupply settled for, since the battery size is determined by the maximum change rate. If in-between resupply were provided anyway, some electronics weight could be removed, with the possibility that all of the removed weight might have to be resupplied. In design cases 1 and 3, the liftoff weight saving would amount to 265 pounds of electronics power modules only if the one-year resupply is reduced to 45 days. In other words, the small weight reduction achieved cannot be justified unless frequent resupplies are scheduled to maintain the electronics stock in the event of random failures.

The Ag-Cd systems in question (design cases 2 and 4) are lighter at liftoff by about 682 pounds, but more frequent resupply is mandatory with the total weight to be resupplied considerably in excess of the 265 pounds required in the Ni-Cd system.

The Ag-Cd battery in each of the two cases has been designed for 10 percent depth of discharge, as dictated by the maximum charge-rate limitation in the low-altitude orbit. That depth is safe to 2300 cycles according to the available cycle life data. This corresponds to 0.4 year (145 days) in the 200nmi orbit under worst-case cycling, an interval between the discrete resupply intervals of 0.25 and 0.5 year assumed in the computer study. The amount of battery module weight to be replaced, however, is 2170 pounds, computed in the following manner:

Baseline Ag-Cd battery weight, 4 batteries (16 modules) packaged, based on Appendix B computer run No. 3 or 7:	2340 pounds;
Two spare modules (Paragraph X.D. Table X-37) including structure, 2 (2340)/16 = 292 lbs, entered in Table X-46, Paragraph X.G:	+ 292 pounds
Total storage system, 18 modules:	2632 pounds.

Weight of the replaceable Ag-Cd modules amounts to 82.5 percent of the total weight chargeable to the storage system (computed from the ratio of 13.2 and 16 watt-hours per pound). Therefore, the net weight of 18 modules to be replaced is 0.825 (2632) or 2170 pounds. Note that the remaining 17.5 percent of the total weight accounts for storage racks and structure included in the liftoff weight number, but not resupplied thereafter.

If the battery life is taken as 145 days, this weight would have to be resupplied at least twice, but more probably three times during the one-year mission. In addition to that, there is the possibility of replacing up to 195 pounds of electronics (the weight difference between the spares weight for a no-resupply one-year mission and that for a scheduled resupply of 0.25).

It is thus apparent that even though an initial weight saving of about 682 pounds can be realized with the Ag-Cd system at liftoff, the total hardware to be resupplied may well amount to an additional 6705 pounds (3 x 2170 plus 195) which in itself is heavier than the entire Ni-Cd system of 5300 to 5400 pounds with no resupply.

(2) Synchronous Orbit

The Ag-Cd battery of the design case No. 6 system is sized to discharge to 50 percent in compliance with the maximum depth-of-discharge limitation imposed in this study. According to cycle life data, Figure X-66, at that depth 330 cycles is assumed as safe (0.9 year under worst-case conditions). As such, this design is very nearly like the design case No. 5, where an Ag-Cd battery is used in a no-resupply one-year mission at the expense of a slight reduction in the discharge depth (i.e., 48 percent). The total systems weight difference between the two is due primarily to the additional weight of electronics modules (approximately 170 pounds) carried in the latter system to support it beyond the 0.5-year resupply. For all practical purposes, then, case No. 6 need no longer be considered as a separate design.

(3) Summary

The 10-kW design cases can be analyzed in a very similar manner with essentially the same conclusions reached. Table X-48 is a summary table for both the 5kW and 10kW conceptual designs.

TABLE X-48. RESUPPLY INTERVAL AS A WEIGHT FACTOR

Parameter	Values			
1. System/Altitude	5 kW/200 NM	5 kW/synch	10 kW/200NM	10 kW/synch
2. Liftoff Weight (pounds), no resupply	5321	3235	9546 (3)	5240
a requires battery type	Ni - Cd	Ag - Cd	Ni - Cd	Ag - Cd
b assuming 45-day resupply of electronics, liftoff weight (to be resupplied) can be reduced by (pounds)	265	265	390	363
3. Minimum Weight (pounds) at liftoff	4638 (1) (2)		8488 (2) (3)	
a can be achieved by using battery	Ag - Cd		Ag - Cd	
b which reduces mandatory resupply to	90-145 days		90-145 days	
c and requires a total resupply weight for a one-year mission of:	6705 lb		11, 814 lb	
consisting of: electronics	195 lb		264 lb	
batteries	6510 lb		11, 550 lb	
4. Based on Design Cases (Table X-46)	1 through 4	5	7 through 10	11

(1) 88 pounds more array weight for 90° inclination.
(2) reduced slightly if resupply is 45 days (by 25 to 100 pounds).
(3) 153 pounds more array weight for 90° inclination.

4. Final Recommendations

A nickel-cadmium battery system is recommended for all missions projected for the 200-NM orbits. If, due to critical weight requirements, it becomes necessary to reduce the liftoff weight of the power system to a bare minimum, a weight saving of about 15 percent can be realized through the use of silver-cadmium batteries. The penalty paid for this weight reduction would be a resupply weight of roughly 140 percent of the original total Ag-Cd system weight at liftoff. Characteristics of both the 5- and 10-kW power systems recommended for 200-NM orbits are listed in Table X-49.

For the synchronous-orbit mission, the silver-cadmium battery system approach is best from the point of view of weight (it can be shown that nickel-cadmium systems would require about 70 percent more battery weight in this orbit). Recommended system characteristics for the synchronous orbit are also listed in Table X-49.

In all recommended systems, the no-resupply approach is preferred as far as the battery modules are concerned.

Recommended electronic module sizes are based on the largest required for the twelve design cases as determined by computer. This introduces a very small error in some of the individual total systems weights tabulated. On a per-module basis, it would amount at most to 1.5 pounds per PWM regulator power module, less than one pound in the inverter, and about three pounds per charge electronics power module.

Although the specified ampere-hour capacity per storage cell is nominal, it is within 5 percent of the exact capacity determined by the computer in each individual design case.

TABLE X-49. FINAL RECOMMENDATION; CONCEPTUAL DESIGNS

Mission	Total Weight at Liftoff (Pounds)	Solar Array (1)			Storage System (3)					Electronics (3)					Computer (Appendix B) Run No.
		Avg. Power kW	Area (ft^2)	Weight (Pounds)	Type of Battery	No. Btry Mods	Cell Size Amp-hr	Weight (Pounds)	Volume (cu. ft.)	No. Power Modules			Weight (Pounds	Volume (cu. ft.)	
										PWM	Inv	C/T			
200NM, 5kW	5321(1)	15.28	1720	1279	Ni-Cd	33	130	3037	66.3	6	7	8	1005	21.3	1
10kW	9546(1)	26.72	2999	2231	Ni-Cd	58	130	5904	128.8	9	9	14	1411	30.1	2
Synch, 5kW	3235	10.39	1309	974	Ag-Cd	10	200(2)	1359	29	6	7	4	902	19.2	9
10kW	5240	16.98	2138	1591	Ag-Cd	18	200(2)	2434	51.9	9	9	7	1215	26	10

(1) 1.6 percent more total weight, 6.5 percent more array weight in polar orbit.

(2) or 100 amp-hr, if the number of C/T modules and batteries is doubled.

(3) weights, volumes, and number of modules include redundant equipment.

All missions: no resupply
1370-watt D-C Regulator power modules
1467-watt Inverter modules (power factor = 0.7)
50-amp C/T power modules

LIST OF REFERENCES FOR SECTION X

X-1. Dr. C. G. Gordon, "Spacecraft Thermal Design", Internal RCA Publication.

X-2. W. C. Cooley and R. J. Janda, "Handbook of Space Radiation Effects on Solar Cell Power System", NASA SP 3003 (1963).

X-3. J. J. Wysocki, B. Goldstein, N. Almehleh, and P. Rappaport, "Analysis of Radiation Damage in Silicon Solar Cells and Annealing or Compensation of Damage by Impurities", prepared under NASA Contract No. NAS 5-1931 (May 1966).

X-4. J. J. Wysocki, A. G. Holmes-Siedle, and B. Goldstein, "Parameters Which Affect Stability of Advanced Experimental Solar Cells to Charged Particle Radiation", Semiannual Report No. 1, prepared under NASA Contract No. NAS 5-10239 (November 1966).

X-5. W. Luft, "Effects of Electron Radiation on N-on-P Silicon Solar Cells", TRW Space Technology Laboratories Publication.

X-6. D. L. Reynard, "Irradiation of Solar Cell Cover Slides and Adhesives with 1 MeV Electrons".

X-7. R. E. Mauri, "Evaluation of Optical Properties and Environmental Stability of Solar Cell Adhesives", Lockheed Missiles and Space Co. (April 1964).

X-8. J. Simpson, "Environmental Testing of Solar Cell Cover Glasses and Adhesives for ComSat Program", Memorandum for Record (November 1964).

X-9. H. W. Brandhorst, Jr., and E. O. Boyer, "Calibration of Solar Cells Using High-Altitude Aircraft", NASA TN D-2508 (February 1965).

X-10. H. K. Gummel, and F. M. Smits, "Evaluation of Solar Cells by Means of Spectral Analysis", Bell System Technical Journal, Vol. 43, No. 3, pp 1103-1121 (May 1964).

X-11. R. J. Naumann, "Pegasus Satellite Measurements of Meteoroid Penetration", NASA TM X-1192 (December 1965).

X-12. B. Ross, "Design Criteria for Satellite Power Supplies Using Radiation Resistant Solar Cells", ASME Airation and Space Hydraulic and Gas Turbine Conference, Los Angeles, Calif. (March 1963).

X-13. J. A. Fager, "Effects of Hypervelocity Impact on Protected Solar Cells", General Dynamics Convair Corporation Report No. GDC-CHD-65-011.

X-14. C. Wolff, "The Effect of Earth's Radiation Belts on an Optical System", Journal of Applied Optics, Vol. 5, p 1838 (1966).

X-15. M. B. Smith and S. S. Susman, "Adhesives for Cryogenic Application", Narmco Research and Development Division, Telecomputing Corporation.

X-16. Westinghouse Aerospace Electrical Division, Modular Static Inverter, Contract No. NAS 3-9429.

X-17. W. L. Brown, J. D. Gable, and W. Rosenweig, "Results of the Telstar Radiation Experiments", Bell System Technical Journal, Figures 32 and 33 (July 1963).

X-18. F. J. Liederback and A. G. Holmes-Siedle, "A Study of the Space Radiation Environment for Manned Orbital Power Supplies", RCA, Princeton, New Jersey (September 1966).

X-19. H. D. Harmon and R. Rasmussen, "Temperature, Illumination Intensity and Degradation Factor Effects on Solar-Cell Output Characteristics", Supplement to IEEE Transactions on Aerospace and Electronic Systems (July 1966).

X-20. P. Rappaport and A. Frink, "Sealed Nickel-Cadmium, Silver Cadmium, and Silver-Zinc Batteries", USASRDL, American Rocket Society Paper 2511-62, September, 1962.

X-21. W. Ingling and W. Clark, "Evaluation of Secondary Batteries", Cook Electric Co., 17th Annual Power Sources Conference, 1963.

X-22. R. Shair, "Sealed Secondary Cells for Space Power Systems", Gulton Industries, AIAA Paper No. 64-455, July 1964.

X-23. R. Shair, "Primary and Secondary Electro-chemical Cells for Space Vehicle Power Supplies", NASA Scientific and Technical Information Facility No. N64-17997, Gulton Industries, 1963.

X-24. Quality Evaluation Laboratory, NAD Crane, Indiana, "Evaluation Program for Nickel-Cadmium Sealed Cells", First Quarterly Report of Life Cycling Test, QE/C 64-274, 15 June 1964.

X-25. P. Bauer, "Characteristics of Three Electrode, Sealed Nickel-Cadmium Cells", TRW STL, 1964.

X-26. Twiner and Willis, "High Temperature Effects on Sealed Nickel-Cadmium Batteries", Bell Telephone Laboratories, 20th Annual Power Sources Conference, 1966.

X-27. A. Frink, "Sealed Cadmium-Silver Oxide Batteries", USAERDL, 17th Annual Power Sources Conference.